
NUCLEI
Experiment

Isomeric Ratios in Reactions Induced by Gamma Rays and Fast Neutrons in the Isotopes of Re, Ir, and Au

Yu. P. Gangrsky^{*}, N. N. Kolesnikov¹⁾, V. G. Lukashik²⁾, and L. M. Melnikova

Joint Institute for Nuclear Research, Dubna, Moscow oblast, 141980 Russia

Received April 22, 2003

Abstract—Isomeric ratios were measured in the (γ, n) and $(n, 2n)$ reactions leading to the formation of ^{184}Re , ^{190}Ir , and ^{196}Au odd–odd nuclides. The measurements were performed by the activation method implemented for Re, Ir, and Au samples of natural isotopic composition that were irradiated with 14.7-MeV neutrons and bremsstrahlung photons of endpoint energy 22 MeV. Isomeric- and ground-state nuclei formed in these reactions were identified by their x- or γ -ray spectra and by their half-lives. The isomeric ratios were calculated on the basis of the statistical model, and the results were compared with experimental data, whereby it was possible to determine parameters that characterize the dependence of the level density on the excitation energy and angular momentum. The effect of the nuclear structure on these parameters is discussed. © 2004 MAIK “Nauka/Interperiodica”.

INTRODUCTION

Investigation into the structure of nuclei involves determining the dependence of the level density on the excitation energy and angular momentum. These dependences are an important source of information about collective and single-particle properties of excited nuclei. Their comparison with the results of calculations performed within various models provides a basis for choosing parameters of these models and for describing the properties of excited nuclei.

Various methods are used to study such dependences experimentally. Measurement of the ratios of the cross sections or yields for reactions leading to nuclear levels of substantially different angular momenta (usually, one of these levels is the ground-state level, while the other is an excited one) is one of the most efficient methods. Various systems of excited states participate in the population of each level, and the probabilities of their population allow one to derive information about some properties of these systems. The sensitivity of measurements of cross-section ratios is considerably higher if the excited state is isomeric; that is, it is characterized by a rather long lifetime (for example, in excess of 1 s). In this case, it is possible to separate in time the excitation of nuclei and measurement of the spectrum of radioactive radiation emitted in their deexcitation and to perform the measurement at a much

lower level of background radiation. This extends the possibilities of investigations significantly; therefore, measurement of cross sections for reactions leading to isomer formation or of the ratios of cross sections for reactions producing isomeric and ground states (isomeric ratios) has become one of the main lines of investigations of level densities in excited nuclei. A vast body of data on isomeric ratios in photonuclear reactions and the possibility of deriving new information about the structure of nuclei from these data are surveyed in [1, 2]; similar information about $(n, 2n)$ reactions is given in [3].

The objective of this study is to measure isomeric ratios for the production of ^{184}Re , ^{190}Ir , and ^{196}Au odd–odd nuclides (which occur in the transition region between spherical and deformed nuclei) in (γ, n) reactions at an excitation energy around a giant dipole resonance and in $(n, 2n)$ reactions at a neutron energy of 14.7 MeV. In this region of nuclei, the structure of low-lying excited states undergoes changes. An analysis of isomeric ratios on the basis of the statistical model could make it possible to explore the changes in the properties of higher lying levels (up to the neutron binding energy), which determine isomeric ratios. We imply here the level density and its dependence on the excitation energy and angular momentum.

The choice of the above nuclides was motivated by a high level density in them even at relatively low excitation energies, this making it possible to describe these nuclides on the basis of the statistical model. In addition, the ^{190}Ir and ^{196}Au nuclei have two isomeric states each, with the result that information about

¹⁾Moscow State University, Vorob'evy gory, Moscow, 119899 Russia.

²⁾Institute for Space Research, Russian Academy of Sciences, ul. Profsoyuznaya 84/32, GSP-7, Moscow, 117810 Russia.

* e-mail: gangr@jinr.ru

Table 1. Spectroscopic features of the ground and isomeric states of the nuclides under investigation

Nucleus	Z	N	β_2	E_i , keV	J^π	Nucleonic configuration	References
^{184}Re	75	109	0.21	0	3^-	$\pi 5/2 [402] + \nu 1/2 [510]$	[5]
				105	8^+	$\pi 5/2 [402] + \nu 11/2 [615]$	
^{190}Ir	77	113	0.17	0	4^+	$\pi 3/2 [402] + \nu 11/2 [615]$	[6]
				26	7^+	$\pi 3/2 [402] + \nu 11/2 [615]$	
				175	11^-	$\pi 11/2 [552] + \nu 11/2 [615]$	
^{196}Au	79	117	0.12	0	2^-	$\pi 3s1/2 + \nu 2f5/2$	[7]
				85	5^+	$\pi 2p3/2 + \nu 1i13/2$	
				595	12^-	$\pi 1h11/2 + \nu 1i13/2$	

the isomeric ratio appears to be richer in this case. It should also be noted that (γ, n) and $(n, 2n)$ reactions leading to the same final nuclei with close excitation energies supplement each other well (in the former, an angular momentum of $1\hbar$ is introduced in the nucleus at all photon energies, while, in the latter, the mean angular momentum is about $5\hbar$ at a neutron energy of 14.7 MeV).

Although isomeric ratios are known for a number of reactions resulting in the formation of the nuclei in question (they are quoted below along with our data for the sake of comparison), they do not provide a complete pattern of isomeric ratios in the nuclear region under investigation. Moreover, they are often insufficiently accurate or were obtained under different conditions of measurements of the yields of the nuclei in the isomeric and ground states. In this study, we measured the isomeric ratios under identical conditions in all cases and determined the yields in the different reactions from the same γ lines, whereby we were able to improve the accuracy and reliability of our results.

PROPERTIES OF THE NUCLIDES UNDER STUDY

As was mentioned above, the nuclides in question belong to the transition region between spherical and deformed nuclei; therefore, the properties of low-lying excited states change sharply in them. In the Nilsson scheme, the single-particle states of ^{184}Re and ^{190}Ir for a deformed potential are identified in terms of the $11/2[505]$ and $3/2[402]$ proton and the $11/2[615]$, $9/2[505]$, and $7/2[503]$ neutron orbits. It is precisely these orbits that form the spectrum of low-lying excited states. The presence of high-angular-momentum levels among them leads to the appearance of high-spin isomers. According to the Mayer scheme, the single-particle states in ^{196}Au have the

following configurations for a spherical potential: the $h_{11/2}$, $d_{3/2}$, and $s_{1/2}$ proton and the $i_{13/2}$, $f_{5/2}$, and $p_{3/2}$ neutron orbits.

Table 1 gives the spectroscopic features of the ground and isomeric states of the nuclei under investigation: their energies E_i , spins–parities J^π , nucleonic configurations, and quadrupole-deformation parameters β_2 for the ground state. The features of the radioactive decay of these nuclei in the ground and isomeric states (half-lives $T_{1/2}$, energies E_γ of γ lines, their fractions I_γ per decay, and full-internal-conversion coefficients α)—they are necessary for identifying them and for determining their yields—are listed in Table 2. In a number of isomeric states, these nuclei are deexcited in low-energy, high-multipolarity radiative transitions characterized by large internal-conversion coefficients. In those cases, the intensity of γ radiation was very low, and we measured the areas of x-ray L lines in order to determine the respective yields. The energies E_x of the most intense of them ($\alpha_{1,2}$ lines, whose fraction per decay is 84% [4]) are also displayed in Table 2. The data in Tables 1 and 2 are systematized in [5–7].

EXPERIMENTAL PROCEDURE

The isomeric ratios in the relevant (γ, n) reactions were measured by using a beam of bremsstrahlung photons with an endpoint energy of 22 MeV from a microtron electron accelerator. In the case of the $(n, 2n)$ reactions, we employed 14.7-MeV neutrons obtained at a neutron generator in the interaction of deuterons accelerated to 120 keV and a tritium target.

The targets used were identical for either type of reactions. The targets were made from metallic foils of natural isotopic composition that were 20, 30, and 50 μm thick for Au, Ir, and Re, respectively. They had the shape of a disk 15 mm in diameter. The irradiation was performed in “close” geometry; that is,

Table 2. Features of the radioactive decay of the nuclides under study

Nucleus	J^π	$T_{1/2}$	Decay mode	E_γ , keV	I_γ , %	α	E_x , keV	References
^{184}Re	3^-	38 d	ε	903	39	0.021	8.610	[5]
	8^+	169 d	ε	792	38	0.012		
				105	75	6.5		
^{190}Ir	4^+	11.8 d	ε	187	70	0.42	9.117	[6]
	7^+	1.12 h	i.t.	26.3	10^{-6}	10^6		
	11^-	3.25 h	ε	616	97	0.014		
^{196}Au				562	97	0.023	9.686	[7]
	2^-	6.18 d	β^-, ε	357	88	0.041		
	5^+	8.2 s	i.t.	64.6	4×10^{-3}	240		
	12^-	9.7 h	i.t.	148	43	0.32		
				188	32	0.23		

Note: ε and i.t. denote electron capture and isomeric transitions, respectively.

the targets were arranged in the immediate vicinity of the braking target (tungsten disk 3 mm thick) or the tritium target (tritium implanted in titanium). This enabled us to harness a considerable fraction of the bremsstrahlung or the neutron flux. Their intensity at the irradiated target amounted to 10^{12} s^{-1} (in the energy range 7–22 MeV) and 10^{10} s^{-1} , respectively. Such intensities made it possible to obtain reasonably high yields of the nuclides being studied even for low isomeric ratios.

After been irradiated, the targets were transported into a room protected from γ rays and neutrons, and their γ spectra were measured there. In these measurements, we employed a HpGe detector of volume 200 cm^3 , a Ge(Li) detector of volume 60 cm^3 (their resolutions for ^{60}Co γ lines at $E_\gamma = 1331 \text{ keV}$ were 2.0 and 2.2 keV, respectively), and a silicon detector 2 mm thick (its resolution for the ^{55}Fe x-ray line at $E_x = 5.4 \text{ keV}$ was 0.340 keV). The choice of detector for the measurement depended on the γ -line energies in the spectrum. In the case of the short-lived isomer ^{196m}Au ($T_{1/2} = 8.2 \text{ s}$), the irradiated target was transported to the detector by a pneumatic rabbit (the transportation time was 2 s).

The measured γ spectra were processed by means of a code that made it possible to separate γ lines of close energies in a complicated spectrum. For each detector, the dependence of the photon-detection efficiency ε on the photon energy was determined with the aid of a set of calibration sources. From an analysis of the γ spectra, we deduced the areas S of the γ lines associated with the products originating from the decay of the nuclei being studied. These areas are

related to the yields of nuclei in the ground or isomeric states by the equation

$$Y = \frac{S(1 + \alpha)f(t)\tau}{\varepsilon I_\gamma t}, \quad (1)$$

where t is the time of the measurement; τ is the lifetime of the nucleus; and $f(t)$ is the factor that takes into account the accumulation of nuclei within the irradiation time, their decay prior to the beginning of the measurements, and the population of the ground state owing to the isomer decay.

EXPERIMENTAL RESULTS

Because the yields of nuclei in the isomeric and ground states were measured by using the same targets under identical conditions of irradiation, the isomeric ratios in the relevant (n , $2n$) reactions can be considered as the ratio of the respective yields:

$$\text{IR} = \frac{\sigma_{\text{is}}}{\sigma_{\text{gr}}} = \frac{Y_{\text{is}}}{Y_{\text{gr}}}. \quad (2)$$

In (γ , n) reactions, this ratio is only approximate because the bremsstrahlung spectrum is continuous and because, for reactions leading to the formation of the isomeric and ground states, the excitation functions have different forms. In this case, the measured isomeric ratios can be represented as

$$\text{IR} = \frac{Y_{\text{is}}}{Y_{\text{gr}}} = \frac{\int_{B_n+E_{\text{is}}}^{E_{\text{max}}} \sigma(E)N(E)dE}{\int_{B_n}^{E_{\text{max}}} \sigma(E)N(E)dE}, \quad (3)$$

Table 3. Experimental and calculated values of the isomeric ratios in question

Nucleus	Levels	Isomeric ratios			
		(γ, n)		$(n, 2n)$	
		experiment	calculation	experiment	calculation
^{184}Re	$8^+(\text{is.}), 3^-(\text{gr.})$	0.019(3)	0.019	0.20(4)	0.19
		0.018(5) [9]		0.15(8) [12]	
^{190}Ir	$7^+(\text{is.}), 4^+(\text{gr.})$	0.15(3)	0.18	0.26(5)	0.17
	$11^-(\text{is.}), 4^+(\text{gr.})$	$8(2) \times 10^{-4}$	7.4×10^{-4}	0.07(2)	0.04
^{196}Au	$5^+(\text{is.}), 2^+(\text{gr.})$	0.10(3)	0.26	0.11(3) [13]	0.50
		$6.0(4) \times 10^{-4}$	5×10^{-4}	0.08(2)	0.09
		$6.1(4) \times 10^{-4}$ [14]		0.10(1) [15]	

where $\sigma(E)$ and $N(E)$ are, respectively, the reaction cross section and the number of photons in the bremsstrahlung spectrum; B_n is the neutron binding energy; E_{is} is the energy of the isomeric level; and E_{max} is the endpoint energy of the bremsstrahlung spectrum. In [8, 9], it was indicated that, in a number of reactions, the threshold energy exceeds the sum $B_n + E_{\text{is}}$ and corresponds to the population of isomers through some activation states lying 1 to 2 MeV above the isomeric state. Information about the relationship between the ratios of the yields and of the cross sections at a given photon energy can be deduced from the shapes of the excitation function (they are given in [10] for the ground states of nuclei and in [8, 9] for a number of isomers) and of the bremsstrahlung spectrum (its calculation for the present conditions of irradiation is given in [11]). From these data, it follows that, at the maximum of the excitation function (it is close to the energy of the giant dipole resonance), the ratio of the cross sections is 10 to 15% greater than the ratio of the yields, the uncertainty in determining the threshold for the isomer-formation reaction having but a slight effect on the isomeric ratios.

The isomeric ratios obtained in this way according to Eqs. (2) and (3) are given in Table 3. They agree with known data (which are also presented in Table 3) within the common errors, but, as a rule, the former have a higher accuracy.

CALCULATION OF ISOMERIC RATIOS

The isomeric ratios were calculated within the statistical model [16, 17] on the basis of the method proposed for the first time by Huizenga and Vandebosch [18] and subsequently improved by a number of authors (see, for example, [19–21]). This method

involves calculating the distributions of nuclei with respect to the excitation energy and angular momentum at each step of the reaction. In (γ, n) reactions, the formation of a compound nucleus, the evaporation of a neutron, and the emission of a photon cascade are such steps. In $(n, 2n)$ reactions, there is yet another step, that of the evaporation of one more neutron from a nucleus whose mass number is greater by unity.

In the case of a $(n, 2n)$ reaction, the compound nucleus is formed at a single value of the excitation energy, while, in a (γ, n) reaction, a distribution of the excitation energy is observed because of the bremsstrahlung spectrum of γ radiation. At the same time, the angular-momentum distribution in (γ, n) reactions is significantly narrower because a photon introduces an angular momentum of unity in the target nucleus (the contribution from the capture of γ rays having higher multiplicities can be neglected). Examples of these distributions at various reaction steps are shown in Figs. 1 and 2.

Neutron evaporation from a compound nucleus (second step of the reaction) leads to the smearing of the distributions with respect to the excitation energy and angular momentum. In order to obtain these distributions, we calculated the transmission coefficients for neutrons having various orbital angular momenta (in these calculations, we used the parameters of the optical model [22]). These transmission coefficients determine the probability of neutron evaporation from a compound nucleus having preset values of the kinetic energy and angular momentum; therefore, they make it possible to derive the excitation-energy and angular-momentum distributions of a product nucleus. In $(n, 2n)$ reactions, this operation was performed twice.

The calculation of the last reaction step (photon cascade) reduced to obtaining the energy and

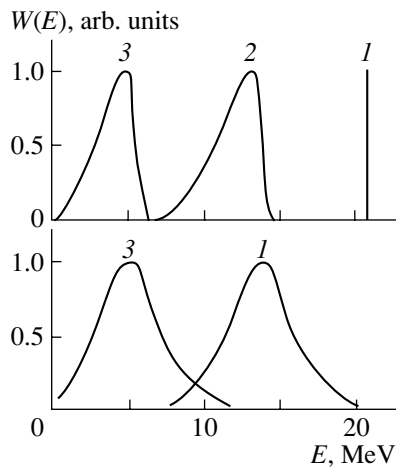


Fig. 1. Excitation-energy distributions of Ir nuclei in (upper panel) $(n, 2n)$ and (lower panel) (γ, n) reactions at various steps: (1) compound nucleus, (2) after the emission of the first neutron in $(n, 2n)$ reactions, and (3) final nucleus prior to the photon cascade.

angular-momentum distributions after the emission of every photon of the cascade. Every time, we computed the probability of a transition to the ground or isomeric state or to a known intermediate level from which the only radiative transition to the ground or isomeric state proceeded. This step of the reaction is the most sensitive to variations in the statistical-model parameters that determine the dependence of the level density on the energy (a) and the angular momentum (σ), especially in the case of (γ, n) reactions, which involve a smaller number of steps and narrower distributions with respect to angular momenta. A detailed description of this method for calculating isomeric ratios and examples of such calculations are given in [23].

Using the approach outlined above, we have calculated the isomeric ratios for all of the nuclei under investigation and all reactions for both isomeric states. Naturally, the isomeric ratios depend on the statistical-model parameters a and σ . The calculated isomeric ratios are listed in Table 3 for these parameters set to values typical of the nuclear region under investigation ($a = 20 \text{ MeV}^{-1}$, $\sigma = 4.9$) [24].

DISCUSSION OF THE RESULTS

From a comparison of the data in Table 3, one can see that the results of the calculations faithfully reproduce the behavior of the isomeric ratios in the nuclear region under investigation—in particular, their dependences on the isomer spin and the angular momentum introduced in the target nucleus. By way of example, we indicate that, in all cases, the isomeric ratios are lower for high-spin isomers than for low-spin ones and that they are higher in $(n, 2n)$ than

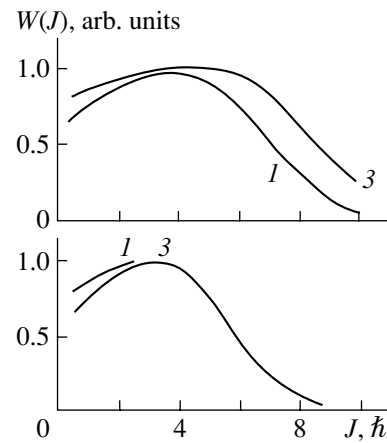


Fig. 2. As in Fig. 1, but for angular momenta.

in (γ, n) reactions. At the same time, the distinction between the measured and calculated isomeric-ratio values is beyond the experimental errors for both reactions and levels in a number of cases [the $J^\pi = 7^+$ and 11^- levels in ^{190}Ir for the $(n, 2n)$ reactions and the $J^\pi = 5^+$ level in ^{196}Au for (γ, n) and $(n, 2n)$ reactions]. This distinction can be explained by the approximate character of the model used in the calculation, the uncertainty in the choice of parameters, and the effect of the nuclear structure on the population of the isomers.

However, agreement between the calculated and experimental isomeric ratios can be attained by varying the parameters a and σ within rather narrow intervals. For the same nucleus, the resulting values of these parameters appear to be slightly different for different isomers and reactions. By way of example, we indicate that, for the $J^\pi = 5^+$ isomer in ^{196}Au , the values of σ at the fixed value of $a = 20 \text{ MeV}^{-1}$ in the (γ, n) and $(n, 2n)$ reactions prove to be 3.3 and 3.7, which are appreciably lower than those for the $J^\pi = 12^-$ isomer ($\sigma = 4.9$). A similar distinction is also observed for the ^{190}Ir nucleus in the (γ, n) and $(n, 2n)$ reactions; for the latter, the agreement between the experimental and calculated isomeric ratios is reached at $\sigma = 8$. In all probability, the reason behind this distinction is that the above factors responsible for the deviations of the calculated isomeric ratios from their experimental counterparts manifest themselves differently in different cases.

Such a scatter of the values of σ that are necessary for describing the isomeric ratios when the entire body of information is used for each of the nuclei under investigation gives no way to establish unambiguously the variation of this parameter (and, consequently, the dependence of the level density on the angular momentum) in the transition nuclear region. It seems that a more refined model that takes

into account the effect of the nuclear structure on the population of isomeric states is required here. This could be the quasiparticle–phonon model proposed by V.G. Soloviev and his coauthors [25, 26] and successfully used, for example, in describing the dependence of isomeric ratios for $1h_{11/2}$ states on the atomic number of a nucleus in the vicinity of the $N = 82$ closed neutron shell [27].

ACKNOWLEDGMENTS

We are grateful to Yu.Ts. Oganessian, M.G. Itkis, and Yu.E. Penionzhkevich for interest in this study and support. Thanks are also due to A.G. Belov for irradiating the samples used and to V.A. Zubkov and M.N. Kirsanov for assistance in the measurements.

REFERENCES

1. Yu. P. Gangrsky, A. P. Tonchev, and N. P. Balabanov, *Fiz. Élem. Chastits At. Yadra* **27**, 1043 (1996) [*Phys. Part. Nucl.* **27**, 428 (1996)].
2. V. M. Mazur, *Fiz. Élem. Chastits At. Yadra* **28**, 1297 (1997).
3. V. M. Bychkov, V. N. Manokhin, A. B. Pashchenko, and V. I. Plyaskin, *Cross Sections for Threshold Reactions Induced by Neutrons: A Handbook* (Énergoizdat, Moscow, 1982) [in Russian].
4. M. A. Blokhin, *X-Ray Physics* (Gostekhzdat, Moscow, 1953) [in Russian].
5. M. J. Martin and P. H. Stelson, *Nucl. Data Sheets* **21**, 1 (1972).
6. B. Singh, *Nucl. Data Sheets* **61**, 299 (1990).
7. Zhou Chunmei, Wang Congqing, and Tao Zhenlan, *Nucl. Data Sheets* **83**, 145 (1998).
8. V. M. Mazur, V. A. Zheltonozhskii, and Z. M. Bigan, *Yad. Fiz.* **58**, 970 (1995) [*Phys. At. Nucl.* **58**, 898 (1995)].
9. I. N. Vishnevsky, V. A. Zheltonozhsky, V. M. Mazur, and M. V. Hoshovsky, *Yad. Fiz.* **62**, 941 (1999) [*Phys. At. Nucl.* **62**, 880 (1999)].
10. S. S. Dietrich and B. L. Berman, *At. Data Nucl. Data Tables* **38**, 199 (1988).
11. Ph. G. Kondev, A. P. Tonchev, Kh. G. Khristov, and V. E. Zhuchko, *Nucl. Instrum. Methods Phys. Res. B* **71**, 126 (1992).
12. G. Gursio and P. Sona, *Nuovo Cimento B* **54**, 719 (1968).
13. S. M. Qaim, *Nucl. Phys. A* **185**, 614 (1972).
14. L. Z. Dzhilavyan, L. E. Lazareva, V. N. Ponomarev, and A. A. Sorokin, *Yad. Fiz.* **33**, 591 (1981) [*Sov. J. Nucl. Phys.* **33**, 308 (1981)].
15. G. N. Flerov, Yu. P. Gangrskii, B. N. Markov, *et al.*, *Yad. Fiz.* **6**, 17 (1967) [*Sov. J. Nucl. Phys.* **6**, 12 (1967)].
16. H. Bethe, *Phys. Rev.* **50**, 332 (1936).
17. T. Ericsson, *Adv. Phys.* **9**, 245 (1969).
18. J. R. Huizenga and R. Vandenbosch, *Phys. Rev.* **120**, 1305 (1960).
19. N. N. Kolesnikov and V. B. Gubin, *Izv. Vyssh. Uchebn. Zaved., Ser. Fiz.*, No. 8, 77 (1984).
20. L. Ya. Arifov, B. S. Mazitov, and V. G. Ulanov, *Yad. Fiz.* **34**, 1028 (1981) [*Sov. J. Nucl. Phys.* **34**, 572 (1981)].
21. O. G. Grudzevich, *Yad. Fiz.* **61**, 29 (1998) [*Phys. At. Nucl.* **61**, 24 (1998)].
22. C. M. Perey and F. C. Perey, *At. Data Nucl. Data Tables* **17**, 2 (1976).
23. Yu. P. Gangrsky, P. Zuzaan, N. N. Kolesnikov, *et al.*, *Izv. Vyssh. Uchebn. Zaved., Ser. Fiz.* **65**, 111 (2001).
24. A. Gilbert and A. C. W. Kameron, *Can. J. Phys.* **43**, 1446 (1965).
25. A. I. Vdovin and V. G. Soloviev, *Fiz. Élem. Chastits At. Yadra* **14**, 99 (1983) [*Sov. J. Part. Nucl.* **14**, 237 (1983)].
26. V. V. Voronov and V. G. Soloviev, *Fiz. Élem. Chastits At. Yadra* **14**, 583 (1983) [*Sov. J. Part. Nucl.* **14**, 583 (1983)].
27. A. G. Belov, Yu. P. Gangrsky, L. M. Melnikova, *et al.*, *Yad. Fiz.* **64**, 1987 (2001) [*Phys. At. Nucl.* **64**, 1901 (2001)].

Translated by V. Bukhanov

NUCLEI Experiment

Nature of Parity Violation in Neutron Interaction with Lead

J. Andrzejewski¹⁾, N. A. Gundorin²⁾, I. L. Karpikhin³⁾,
L. Lason¹⁾, G. A. Lobov³⁾, D. V. Matveev²⁾, and L. B. Pikelner²⁾*

Received July 3, 2003; in final form, October 7, 2003

Abstract—The effect of parity violation in the interaction of thermal neutrons with lead was discovered in a number of studies. According to the existing theory, this effect is explained by the mixing of compound states characterized by different parities (*s*- and *p*-wave resonances). In view of the absence of a *p*-wave resonance in the region of thermal neutron energies, it is of importance to reveal a level below the neutron binding energy, a so-called negative resonance. The energy dependence of the cross section for radiative neutron capture on lead was measured in the present study, and it is shown that, for the ²⁰⁷Pb isotope, the results of this measurement deviate from the $1/\sqrt{E}$ law, thereby suggesting the presence of a strong negative resonance. The parameters of this resonance are estimated. © 2004 MAIK “Nauka/Interperiodica”.

INTRODUCTION

In the early 1980s, enhanced parity-violation effects in slow-neutron interaction with nuclei were predicted theoretically [1–3] and discovered experimentally [4, 5]. It was shown that the mechanism responsible for the enhancement of such effects is associated with the structure and properties of target nuclei. The effects in question are maximal in the region of *p*-wave resonances. By way of example, we indicate that, for ¹³⁹La, the total cross section at the *p*-wave resonance of energy 0.75 eV changes by 10% upon going over from unpolarized to polarized neutrons.

A detailed investigation of such effects for a number of nuclei was later performed at Los Alamos [6], where total neutron cross sections were measured as functions of the neutron helicity. All of the results obtained in this way were matched with a theory where these effects were explained in terms of mixing of compound states that have different parities, *s*- and *p*-wave resonances in the case being considered.

In addition to parity violation in the total cross section, there is yet another effect, the rotation of the spin of a neutron having a polarization orthogonal to the momentum vector and traversing the target being studied, and this effect was measured experimentally. Both effects were described on the basis of a unified theoretical model.

The range of nuclei for which the rotation of the thermal-neutron spin was measured includes lead nuclei. The result obtained for this case in [7] is

$$\Delta\varphi = (2.24 \pm 0.33) \times 10^{-6} \text{ rad/cm.}$$

The target used was manufactured from natural lead containing four isotopes. Since lead features no resonances in the vicinity of thermal neutron energies, it was interesting to find out which isotope is responsible for the effect. An experiment performed anew with natural lead [8] confirmed the existence of the effect. The value obtained for spin-rotation angle was

$$\Delta\varphi = (3.53 \pm 0.79) \times 10^{-6} \text{ rad/cm.}$$

A measurement performed with the ²⁰⁷Pb isotope, whose concentration in the natural mixture of lead isotopes is 22%, revealed that this isotope makes no contribution to the effect being studied [8].

Later on, a measurement was performed with the ²⁰⁴Pb isotope [9], whose concentration in natural lead is as low as 1.4%, and the value obtained for the spin-rotation angle was

$$\Delta\varphi = (8 \pm 2) \times 10^{-5} \text{ rad/cm.}$$

This value is somewhat smaller than that which is required for reproducing the effect in natural lead, but it could qualitatively account for it.

Within the simplified two-level model where one *s*-wave resonance is mixed with one *p*-wave resonance, the expression for the spin-rotation angle can be represented in the form [10]

$$\Delta\varphi = \frac{4\pi\lambda^2(1 \text{ eV})\rho W_{sp} \sqrt{\Gamma_n^s(1 \text{ eV})\Gamma_n^p(1 \text{ eV})}}{(E - E_s)(E - E_p)} \text{ [rad/cm]}. \quad (1)$$

¹⁾University of Lodz, Lodz, Poland.

²⁾Neutron Physics Laboratory, Joint Institute for Nuclear Research, Dubna, Moscow oblast, 141980 Russia.

³⁾Institute of Theoretical and Experimental Physics, Bol'shaya Chermushkinskaya ul. 25, Moscow, 117259 Russia.

* e-mail: plb@nf.jinr.ru

Here, λ is the neutron wavelength divided by 2π ; ρ is the number of nuclei per unit volume (in cm^3) of the target; W_{sp} is the matrix element of the weak-interaction-induced mixing of states having opposite parities; Γ_n^s and Γ_n^p are the neutronic widths of, respectively, the s - and the p -wave resonance; and E_s and E_p are their energies. The symbol “1 eV” in parentheses indicates that a given quantity is rescaled to 1 eV. For the total resonance widths, it is assumed in expression (1) that $\Gamma_s \ll E - E_s$ and $\Gamma_p \ll E - E_p$.

By using in (1) the known parameters of s - and p -wave resonances in ^{204}Pb [11], one can show that $\Delta\varphi$ appears to be a few orders of magnitude smaller than its experimental counterpart. It is possible that the compound state corresponding to the p -wave resonance lies below the neutron binding energy (this is the case of a so-called negative resonance). From (1), it can be seen that the effect in the thermal region for $E < 0.1$ eV is proportional to $\sqrt{\Gamma_n^{s,p}}/E_{s,p}$. Choosing, for the s -wave resonance, the maximum value of this ratio from [11] [$E_s = -3$ keV and $\Gamma_n^s(1 \text{ eV}) = 1.3$ eV] and assuming, for the p -wave resonance, the mean values of $\Gamma_n^p(1 \text{ eV}) = 3 \times 10^{-7}$ eV and $E_p = D/10 = 100$ eV (D is the mean level spacing, which is about 1 keV for ^{204}Pb), we obtain $\Delta\varphi = 9 \times 10^{-7}$ rad/cm, which is two orders of magnitude smaller than the corresponding experimental value. The value of $W_{sp} = 5 \times 10^{-3}$ eV, which was used here, is somewhat overestimated with respect to the relevant mean value. A greater effect can be obtained by considerably increasing Γ_n^p and by lowering E_p . By way of example, we indicate that, increasing Γ_n^p by an order of magnitude and placing the resonance at an energy of 5 eV below the neutron binding energy, we would arrive at $\Delta\varphi = 6 \times 10^{-5}$ rad/cm. This value is already close to the experimental result for ^{204}Pb , but it is sizably smaller than that which was obtained in the measurements with natural lead.

Thus, the explanation of the parity-violation effect in lead may be associated with the presence of a strong p -wave resonance in the vicinity of the neutron binding energy. Therefore, it would be of paramount importance to discover such a negative resonance.

FORMULATION OF THE EXPERIMENTAL PROBLEM AND ESTIMATION OF THE EXPECTED RESULT

As a method for seeking a negative resonance, we proposed studying the cross section for radiative neutron capture as a function of neutron energy. This

cross section is described by the Breit–Wigner formula

$$\sigma_\gamma(E) = \frac{\pi\lambda^2 g\Gamma_n\Gamma_\gamma}{(E - E_0)^2 + \Gamma^2/4}. \quad (2)$$

For $E \ll E_0$ and $\Gamma \ll E_0$, expression (2) can be reduced to the form

$$\sigma_\gamma^s(E) = \frac{\pi\lambda^2(1 \text{ eV})\Gamma_n^{(0)}\Gamma_\gamma}{E_s^2\sqrt{E}} \quad (3)$$

for s -wave interaction and to the form

$$\sigma_\gamma^p(E) = \frac{\pi\lambda^2(1 \text{ eV})g\Gamma_n^{(1)}\Gamma_\gamma V_1}{E_p^2\sqrt{E}} \quad (4)$$

for p -wave interaction.

In expressions (3) and (4), $\Gamma_n^{(0)}$ and $\Gamma_n^{(1)}$ are the neutron-energy-independent reduced neutronic widths of the s - and p -wave resonances at the energies E_s and E_p , respectively. The centrifugal attenuation factor

$$V_1 = \frac{(kR)^2}{1 + (kR)^2}, \quad (5)$$

where $k = 1/\lambda$ is the neutron wave number and R is the nuclear radius, plays an important role in the p -wave cross section.

The quantity V_1 for lead is $V_1 = 3 \times 10^{-6}E$. It follows that the neutron-capture cross section as a function of energy behaves differently for s and p waves; that is,

$$\sigma_\gamma^s(E) \sim 1/\sqrt{E} \quad \text{and} \quad \sigma_\gamma^p(E) \sim \sqrt{E}.$$

Let us now estimate σ_γ^p for the strong negative resonance considered above: $E_p = -5$ eV, $\Gamma_n^{(1)} = 1$ eV, and $\Gamma_\gamma = 0.5$ eV. At an energy of 0.025 eV, we then have $\sigma_\gamma^p = 6.3 \times 10^{-3}$ b, which is about 1% of the total capture cross section at the thermal point: $\sigma_\gamma^s(0.025 \text{ eV}) = 660 \times 10^{-3}$ b [11]. Even at a neutron energy of 1 eV, however, the relationship in question changes significantly: $\sigma_\gamma^s = 104$ mb and $\sigma_\gamma^p = 40$ mb.

Figure 1 displays (dashed curve) σ_γ^s and (solid curve) $\sigma_\gamma^s + \sigma_\gamma^p$ versus the neutron energy. It can be seen that, by measuring the energy dependence of the cross section for radiative neutron capture over the range between the thermal point and 2 to 3 eV, we can estimate the contribution of the p wave or set an upper limit on this contribution.

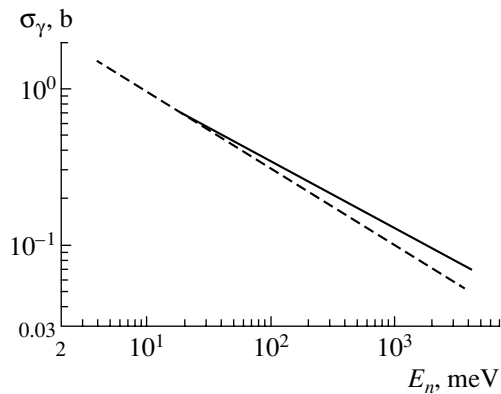


Fig. 1. Cross sections for radiative neutron capture on a ^{204}Pb nucleus versus (dashed curve) σ_γ^s and (solid curve) $\sigma_\gamma^s + \sigma_\gamma^p$ [$(\sigma_\gamma^s)^T = 660$ mb, and $(\sigma_\gamma^p)^T = 6.3$ mb].

EXPERIMENTAL PROCEDURE AND DESCRIPTION OF THE EXPERIMENT

The experiment was performed in a neutron beam from the IBR-2 pulsed reactor installed at the Neutron Physics Laboratory (Joint Institute for Nuclear Research, Dubna). The well-developed time-of-flight procedure was used in the spectrometry of neutrons. As follows from the results mentioned in the Introduction, the discovery of a negative resonance in radiative neutron capture on the lead isotope of mass number 204 was expected to be the most probable. For the target being studied, we therefore used a cylindrical sample from lead enriched in this isotope: it contained 36.6% ^{204}Pb , 30.6% ^{206}Pb , 13.2% ^{207}Pb , and 19.6% ^{208}Pb versus 1.43, 24.15, 22.4, and 52.4% in a natural mixture of isotopes. The total weight of the sample was 4.7 g. In order to reduce the probability of various systematic effects in performing the experiment in question, it was thought to be the most convenient to measure the spectra of gamma rays from two targets simultaneously, the target being studied and a reference one such that the neutron-capture cross section for it obeys the standard $1/\sqrt{E}$ law. If the relationship between the relevant intensities is favorable for the purposes pursued here and if the energy resolution is sufficiently high for separating the chosen gamma lines from the two components of such a target, the results would make it possible to draw an unambiguous conclusion on whether the energy dependence of the cross section for radiative neutron capture deviates from the $1/\sqrt{E}$ law for the target being studied. In the present study, the spectrum of gamma radiation in radiative neutron capture was measured with the aid of the HPGe detector entering into the composition of the COmbined COrrelative Spectrometer (COCOS). The application of this spectrometer in neutron beams

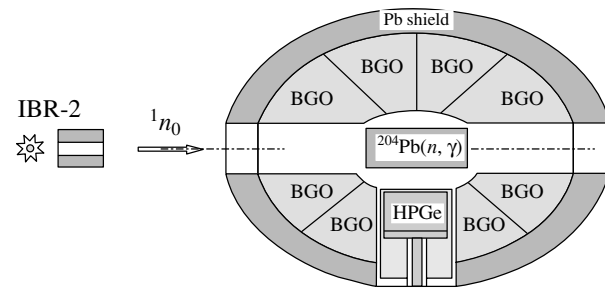


Fig. 2. Layout of the COCOS gamma spectrometer.

is motivated by the need for suppressing the background to the maximum possible degree in order to improve the accuracy of the analysis of the spectrum of gamma rays accompanying the neutron–nucleus interactions being studied. The concept of the spectrometer is based on the cascade nature of gamma radiation from an excited nucleus. It is characterized by a combined application of a semiconductor Ge detector, which possesses a high energy resolution, and scintillation crystal detectors, which have a high photon-detection efficiency, and by a compact geometry of the multichannel detector system, a correlation analysis of multidimensional experimental data being involved. The layout of the spectrometer is shown in Fig. 2.

A collimated neutron beam 1n_0 of diameter 1 cm is incident on the target of dimensions $\varnothing 0.6 \times 2$ cm. Crystal BGO scintillators surrounding the target and the HPGe detector are intended for recording gamma rays with an energy resolution of 15 to 20% (at the energy of $E_\gamma = 511$ keV) and an absolute efficiency close to 50%. The semiconductor HPGe detector of 1 to 2% absolute efficiency records cascade gamma rays in a 200- to 300-ns time window of coincidences. A high energy resolution of this detector (0.1–0.4%) makes it possible to single out in the spectrum and to identify individual lines associated with the deexcitation of excited compound nuclei formed in the target. The recorded-photon energies lie in the interval between 200 keV and 8 MeV.

In our measurements, information about $\gamma\gamma$ coincidences is recorded on magnetic carriers. The software of the spectrometer makes it possible to monitor basic parameters in the on-line mode and to perform subsequently a full treatment of experimental data in the off-line mode.

In processing data obtained in our experiment, we sorted them with the aim of selecting the required events with respect to the energy of neutrons captured by the sample and with respect to the energy of accompanying gamma radiation. For one measurement series of duration 156 h, Fig. 3 shows the integrated

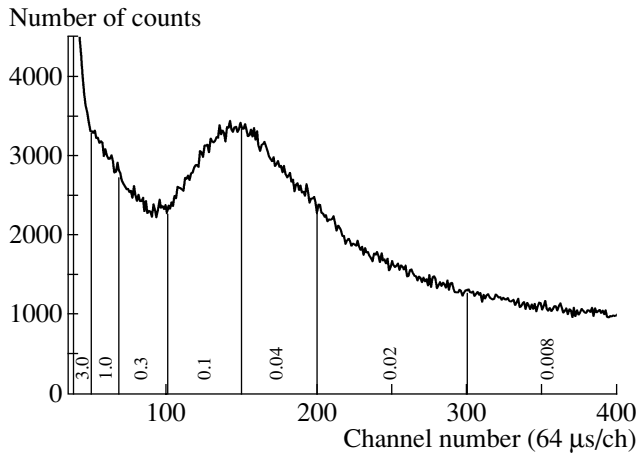


Fig. 3. Integrated time-of-flight spectrum for the full energy interval of $\gamma\gamma$ coincidences (the mean neutron energy is indicated in eV).

time-of-flight spectrum—that is, the spectrum corresponding to HPGe–BGO $\gamma\gamma$ coincidences over the full range of photon energies. The spectrum was partitioned into seven segments, and the mean neutron energy is indicated within each of these. For each segment, we constructed the spectrum of gamma rays recorded by the HPGe detector in coincidence with the detection of annihilation photons in the energy range 511 ± 100 keV by the BGO scintillators.

Figure 4 displays the gamma-spectrum section corresponding to that part of the time-of-flight spectrum where the mean neutron energy is 0.04 eV. In the measurement series being discussed, a copper foil served as a reference sample. For photons from a direct transition to the ground state, a selection of coincidences with the 511-keV line ensures a distinct separation of the peaks associated with the single (S) and double (D) emission of annihilation photons for both the lead isotope being studied and the copper isotope used.

The spectrum also features the analogous S and D peaks that clearly stand out against the background and which correspond to radiative neutron capture by the ^{207}Pb isotope, which was present in the sample along with the ^{204}Pb isotope. With the aim of reducing the counting rate in the spectrometer, we therefore conducted further measurements without a copper foil and compared the intensities of the relevant gamma radiation for the ^{207}Pb and ^{204}Pb isotopes. In the gamma spectra corresponding to each of the seven intervals of the neutron energy, we determined the areas of the S and D peaks for both isotopes and calculated the ratio of the sums of these areas corresponding to the number of recorded photons

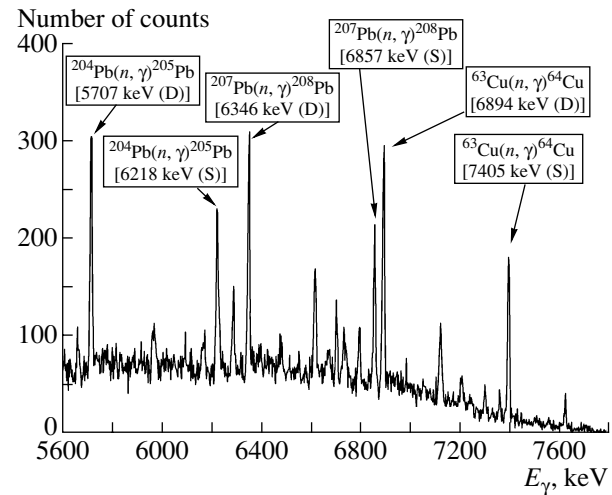


Fig. 4. High-energy section of the gamma spectrum from the HPGe detector for a mean neutron energy of 0.04 eV ($t_{\text{meas}} = 156$ h).

associated with a direct transition in compound nuclei upon neutron capture.

For the isotope being studied, the number of events recorded by the spectrometer over the measurement time that contribute to the peak area is generally given by

$$N_i(E_n) = \phi(E_n)n_i\sigma_{E_\gamma}(E_n)\varepsilon(E_\gamma), \quad (6)$$

where $\phi(E_n)$ is the number of neutrons that hit the sample, n_i is the number of nuclei per 1 cm^2 in the isotope being studied, $\sigma_{E_\gamma}(E_n)$ is the partial radiative-capture cross section for a gamma transition of energy E_γ , and $\varepsilon(E_\gamma)$ is the absolute efficiency of the detection of a photon with energy E_γ .

In our case, the ratio of the areas of the peaks for the sample being studied (1) and the reference sample (2) then corresponds to the ratio $K(1/2)$ of the intensities of direct transitions in them and has the form

$$\begin{aligned} \frac{N_1(E_n)}{N_2(E_n)} &= \frac{n_1\varepsilon_{E_\gamma 1}[\sigma_{E_\gamma}^s(E_n) + \sigma_{E_\gamma}^p(E_n)]_1}{n_2\varepsilon_{E_\gamma 2}[\sigma_{E_\gamma}^s(E_n)]_2} \quad (7) \\ &= K(1/2)(E_n). \end{aligned}$$

This expression does not involve the neutron flux since both isotopes are exposed to the same beam simultaneously. The ratio $(n_1\varepsilon_{E_\gamma 1})/(n_2\varepsilon_{E_\gamma 2})$ is independent of the neutron energy; only the ratio of the cross sections changes. If the numerator of the expression on the right-hand side of (7) does not involve the p -wave cross section for the sample being studied, then the ratio $K(1/2)$ will be identical for all values of the neutron energy. Thus, we can see that the existence of the energy dependence of this

Table 1. Normalized ratios of the intensities of direct transitions in the ^{207}Pb , ^{204}Pb , and ^{63}Cu isotopes

E_n , eV	$K(^{207}\text{Pb}/^{204}\text{Pb})$	$K(^{207}\text{Pb}/^{63}\text{Cu})$
0.008	1.00 ± 0.05	1.03 ± 0.05
0.02	1.02 ± 0.06	0.96 ± 0.04
0.04	1.01 ± 0.06	1.02 ± 0.04
0.10	1.02 ± 0.07	1.04 ± 0.06
0.30	1.23 ± 0.09	1.19 ± 0.08
1.0	1.60 ± 0.16	1.42 ± 0.17
3.0	2.30 ± 0.38	1.84 ± 0.30

Table 2. Cross sections for radiative neutron capture by the ^{207}Pb isotope for the s and p waves

E_n , eV	σ_γ^s , mb	σ_γ^p , mb	$(\sigma_\gamma^s + \sigma_\gamma^p)/\sigma_\gamma^s$
0.008	1120	5.5	1.00
0.02	707	9	1.01
0.04	500	12	1.02
0.10	316	20	1.06
0.30	183	33	1.18
1.0	100	56	1.56
3.0	58	82	2.41

ratio suggests the presence of the sought resonance in the nucleus being studied and makes it possible to estimate its parameters.

EXPERIMENTAL RESULTS AND THEIR DISCUSSION

Upon processing experimental data from a few series of measurements with samples enriched in the ^{204}Pb isotope (the total duration of the measurements was 575 h), it turned out that, with increasing neutron energy, the ratio of the intensities of direct transitions, $K(^{204}\text{Pb}/^{207}\text{Pb})$, decreases instead of increasing (as might have been expected). The values obtained in this experiment for the inverse ratio $K(^{207}\text{Pb}/^{204}\text{Pb})$ are given in Table 1 for seven groups of neutrons in energy. These values were obtained after a normalization where the mean value of the ratio $K(^{207}\text{Pb}/^{204}\text{Pb})$ for two groups in which the neutron energies are 8 and 20 meV and for which the p -wave contribution is negligible is taken as unity. According to our experimental data, it is the ^{207}Pb isotope rather than ^{204}Pb that has a negative resonance.

In order to confirm this surprising experimental result, we performed additional measurements with a different sample that was enriched in ^{207}Pb to 88.3%. For a reference sample, we took, instead of the ^{204}Pb lead isotope, the ^{63}Cu copper isotope from a natural composition. The results obtained by processing data from the additional experiment of duration 125 h are given in Table 1 and in Fig. 5 in the form of the ratio $K(^{207}\text{Pb}/^{63}\text{Cu})$. These values were also obtained after a normalization to neutron groups where the mean neutron energies are 8 and 20 meV. The results of the additional experiment exhibit a similar dependence: the ratio of the intensities of direct transitions in compound nuclei upon radiative neutron capture by the ^{207}Pb and ^{63}Cu isotopes grows with increasing neutron energy.

The results of these two experiments lead to the conclusion that, in the vicinity of the neutron binding energy, there is a strong p -wave resonance in the ^{207}Pb (and not in ^{204}Pb) isotope.

We will now address the question of which negative p -wave resonance in ^{207}Pb may explain the observed parity-violation effect in natural lead, assuming, in accordance with the conclusion drawn in the present study, that this effect is caused by precisely this isotope. Taking, for the spin-rotation angle in natural lead, the average value in two experiments [7, 8], $\Delta\varphi = 2.5 \times 10^{-6}$ rad/cm, we find, for the ^{207}Pb isotope (its concentration in natural lead is 22%), that $\Delta\varphi = 1.14 \times 10^{-5}$ rad/cm. Further, we use expression (1) to describe this spin rotation and substitute all known values into it. In the denominator, we can concurrently discard E , since thermal and cold neutrons, for which $E \ll E_s, E_p$, were employed in measuring $\Delta\varphi$. For the s -wave resonance, we take the maximum value of $\sqrt{g\Gamma_n^s(1\text{ eV})}/E_s$. From [11], we have $E_s = -36$ keV and $g\Gamma_n^s = 4.7$ eV, and the relative matrix element is $W_{sp} \approx 5 \times 10^{-3}$ eV. We then have $\sqrt{g\Gamma_n^p(1\text{ eV})}/E_p = 4.4 \times 10^{-4}$. This ratio can be used to calculate the p -wave cross section for radiative capture. It is obvious that this calculation will yield only a rough estimate, since one has to use a few quantities for which there are no precise data. This concerns the matrix element W_{sp} , the radiative width Γ_γ^p in (4), and the partial gamma widths $\Gamma_{\gamma i}$ of the s and p resonances (in the experiment, we have examined only the ratio for specific transitions rather than the ratio of the total cross sections for radiative neutron capture). However, even such a rough estimate is sufficient for comparing the values calculated by formula (7) with experimental data. The square of the ratio $\sqrt{g\Gamma_n^p(1\text{ eV})}/E_p$, which was estimated above, directly appears in expression (4); however, we use not only thermal neutrons, for which one can

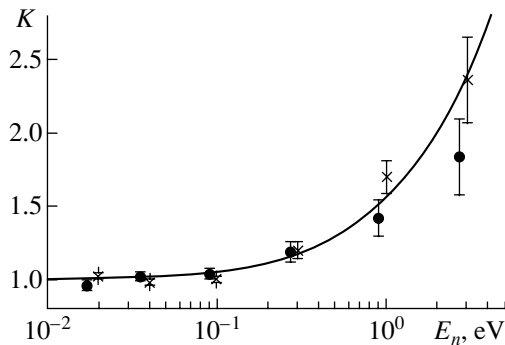


Fig. 5. Energy dependence of the experimental values of K along with the results of the calculation. The points represent the results for (\times) $^{207}\text{Pb}/^{204}\text{Pb}$ and (\bullet) $^{207}\text{Pb}/^{63}\text{Cu}$. The solid curve corresponds to $(\sigma_\gamma^s + \sigma_\gamma^p)/\sigma_\gamma^s$.

discard E in the denominator of the expression on the right-hand side of (2), but also neutrons of energy up to 3 eV. In view of this, we assume that $E_p = -20$ eV, whence we derive $\Gamma_n^p(1 \text{ eV})$. This choice does not have a significant effect on the ensuing estimations. For the total radiative width Γ_γ^p , we take the value of 0.5 eV, which lies within the region of the strongly scattered values of Γ_γ^p for known p -wave resonances [11]. On the basis of values adopted for the parameters of p -wave resonances, we can calculate the cross section for p -wave radiative neutron capture and compare it with the calculated s -wave cross section, which receives the main contribution from the negative resonance with the above parameters. The results of these calculations are presented in Table 2. The ratios $(\sigma_\gamma^s + \sigma_\gamma^p)/\sigma_\gamma^s$ are also given there for the neutron energies being considered.

Since, in neutron capture by ^{207}Pb nuclei, a direct gamma transition to the ground state of the compound nucleus ^{208}Pb nearly exhausts the radiative-capture process, it is reasonable to compare the ratios from Table 2 with the experimental values of $K(E_n)$. The curve in Fig. 5 was constructed on the basis of the results of the calculations from Table 2. One can see that it is in fairly good agreement with experimental data.

CONCLUSION

The results of our experiments and calculations give sufficient grounds to conclude that the ^{207}Pb iso-

tope has a strong negative resonance, which can explain the parity-violation effect consisting in neutron-spin rotation as polarized neutrons traverse a sample of natural lead [7, 8]. However, this is at odds with the experimental results reported in [8, 9], where such an effect was not found in ^{207}Pb , but it was observed in ^{204}Pb . In this connection, it is highly desirable to measure anew the effect of parity violation for ^{207}Pb . In addition, it is of interest to make an attempt at revealing parity violation in the correlation $\mathbf{s} \cdot \mathbf{k}$ (between the neutron spin and the photon momentum). The expected magnitude of the effect is about 10^{-5} ; that is, it is accessible to measurement.

ACKNOWLEDGMENTS

This work was supported by the Russian Foundation for Basic Research (project nos. 01-02-16024-a and 02-02-16935-a) and INTAS (project no. 00-00043).

REFERENCES

1. V. A. Karmanov and G. A. Lobov, *Pis'ma Zh. Éksp. Teor. Fiz.* **10**, 332 (1969)[*JETP Lett.* **10**, 212 (1969)].
2. O. P. Sushkov and V. V. Flambaum, *Pis'ma Zh. Éksp. Teor. Fiz.* **32**, 377 (1980)[*JETP Lett.* **32**, 352 (1980)].
3. V. E. Bunakov and V. P. Gudkov, *Z. Phys. A* **303**, 285 (1981).
4. M. Forte, B. R. Heckel, *et al.*, *Phys. Rev. Lett.* **45**, 2088 (1980).
5. V. P. Afimenkov, S. B. Borzakov, *et al.*, *Pis'ma Zh. Éksp. Teor. Fiz.* **34**, 308 (1981)[*JETP Lett.* **34**, 295 (1981)]; *Pis'ma Zh. Éksp. Teor. Fiz.* **35**, 42 (1982)[*JETP Lett.* **35**, 51 (1982)].
6. G. E. Mitchell *et al.*, *Phys. Rep.* **354**, 157 (2001).
7. B. R. Heckel, N. F. Ramsey, *et al.*, *Phys. Lett. B* **119B**, 298 (1982).
8. V. P. Bolotsky, O. N. Ermakov, R. Golub, *et al.*, *Yad. Fiz.* **59**, 1873 (1996) [*Phys. At. Nucl.* **59**, 1808 (1996)].
9. R. Golub, I. L. Karpikhin, *et al.*, in *Proceedings of the IX International Seminar on Interaction of Neutron with Nuclei, Dubna, 2001*, p. 33.
10. V. E. Bunakov and L. B. Pikelner, *Prog. Part. Nucl. Phys.* **39**, 337 (1997).
11. S. F. Mughabghab, *Neutron Cross Sections* (Academic, New York, 1984), Vol. 1, Part B.

Translated by A. Isaakyan

NUCLEI
Experiment

Measurement of the Probability of ^{232}Th Ternary Fission Induced by Fast Neutrons

V. A. Khriachkov*, M. V. Dunaev, I. V. Dunaeva, N. N. Semenova, and A. I. Sergachev

Institute of Physics and Power Engineering, pl. Bondarenko 1, Obninsk, Kaluga oblast, 249020 Russia

Received May 20, 2003; in final form, August 18, 2003

Abstract—Results obtained by measuring the energy dependence of the probability of ^{232}Th ternary fission in the region of vibrational resonances are presented. The measurements were performed by using a double ionization chamber with Frisch grids and a CsI(Tl) scintillation detector. The use of digital methods for pulse processing made it possible to obtain highly reliable results. The data analysis reveals that our value of the ternary-fission probability is compatible with existing systematics, which nevertheless need some correction. The results of our measurements unambiguously indicate that local variations in the total kinetic energy of fission fragments in the region of the individual vibrational resonances cannot be explained by corresponding variations in the ternary-fission probability. © 2004 MAIK “Nauka/Interperiodica”.

INTRODUCTION

Almost all fission events are known to be accompanied by the emission of light particles, including neutrons evaporated from fission fragments. However, light particles emitted in the vicinity of the scission point of a fissile nucleus within periods considerably shorter than the evaporation time are of major interest for understanding of the dynamics of the fission process.

Upon formation, a light particle moves under the effect of the Coulomb repulsion of two fragments moving apart. Calculations by the trajectory method allow one to reconstruct the angular and energy distributions of light particles for various initial conditions. The calculations show that the angular and energy distributions of third particles emitted in the process of nuclear fission are highly sensitive to the initial position of the charged particle and to the velocity of fission fragments at the instant of emission. Thus, the final angular and energy distributions of third particles provide the most direct way of determining the properties of a fissile system at the instant of scission. At present, the probability of ternary fission has been studied in detail for almost all spontaneously fissile nuclei and a set of nuclei in fission induced by fast neutrons. Fission channels involving the emission of protons, deuterons, tritons, alpha particles, and other heavier nuclei have been revealed [1].

At the same time, a number of nuclei that can undergo fission only under the effect of fast neutrons have not yet received adequate study. Investigation of the ternary-fission probability for these nuclei can

contribute to the development of systematics owing to the extension of the range of the fissility parameter (Z^2/A). Also, of particular interest is the dependence of the ternary-fission yield on the excitation energy of a fissile nucleus, and this dependence can be studied only with fast neutrons. For example, the observed effect of a local decrease in the total kinetic energy of fission fragments in the vicinity of some vibrational resonances [2] cannot be explained either by variations in the mass distribution or by the behavior of the prompt-neutron multiplicity [3]. It was assumed that the ternary-fission probability may increase in the vicinity of these resonances, thereby causing a decrease in the total kinetic energy of fission fragments [4].

The breakup of a nucleus into three particles is improbable and can justifiably be classified with rare events. By way of example, we indicate that, in the spontaneous fission of ^{252}Cf , the probabilities of alpha-particle, triton, and proton emission are about 3×10^{-3} , 2×10^{-4} , and 6×10^{-5} , respectively. Systems of two or more ($\Delta E + E$) semiconductor detectors are usually used to study ternary fission [5, 6]. This experimental scheme of low luminosity is widely applied in studying spontaneous fission and fission induced by thermal neutrons since the statistical accuracy needed for analysis can be obtained with it. A high threshold of light-particle detection—it is determined by the total particle absorption in a ΔE detector—is an obvious drawback of this system. Complex multidetector setups characterized by a high efficiency of light-charged-particle detection [7] provide yet another example of setups used to study ternary fission. Detectors of this type were

* e-mail: hva@ippe.obninsk.ru

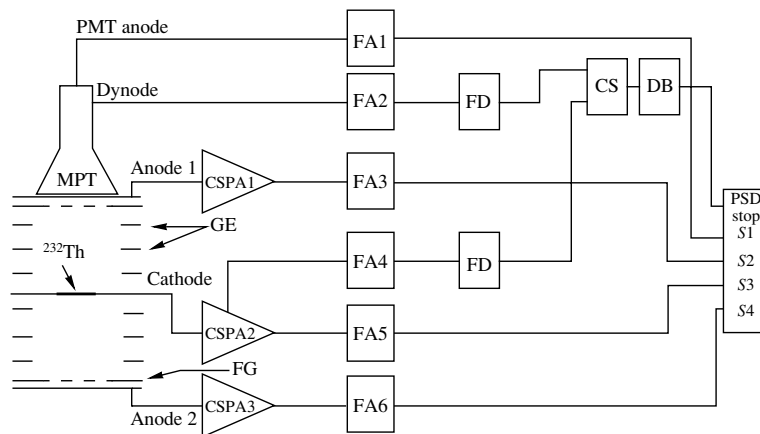


Fig. 1. Layout of the experimental setup: (PMT) photomultiplier tube, (PSD) pulse-shape digitizer, (CSPA) charge-sensitive preamplifier, (FA) fast amplifier, (CS) coincidences scheme, (DB) delay block, (FD) fast discriminator, (S1–S4) digitizer inputs, (GE) guard electrodes, and (FG) Frisch grid.

successfully applied in investigating spontaneous ternary fission. However, they cannot be used in beams of fast and even thermal neutrons because of their large dimensions and complexity.

The cross section for fission induced by fast neutrons is two orders of magnitude smaller than that induced by thermal neutrons. A high gamma-ray background from a neutron target and stringent geometric constraints arising in operation at an accelerator cause additional difficulties. In order to solve the problem efficiently, a novel detector system satisfying our specific conditions was designed.

EXPERIMENTAL SETUP

The spectrometer used incorporates a double pulsed ionization chamber (PIC) with Frisch grids for recording pair fission fragments and a thin scintillation screen with photomultiplier tube (PMT) for recording light particles. Figure 1 shows the layout of the setup. The ionization chamber consisted of two anodes, two Frisch grids, and a common cathode. A ^{232}Th spectrometric layer 3 cm in diameter and $200 \mu\text{g}/\text{cm}^2$ in thickness on an Al_2O_3 substrate transparent to fission fragments was placed at the center of the cathode. The whole surface of the spectrometric layer was covered with gold (of thickness about $50 \mu\text{g}/\text{cm}^2$) in order to ensure the electrical conductivity of the cathode.

The electrodes are 120 mm in diameter. In order to ensure the uniformity of the electric field, three guard electrodes were placed in between the cathode and the grid. The distance between the cathode and the Frisch grid is 40 mm, and the distance between the grid and the anode is 2 mm. The ring-shaped upper anode of the chamber was manufactured from stainless steel and was covered with a metallized

polypropylene film $100 \mu\text{m}$ thick glued onto it in order to ensure the accumulation of electrons from the ionization chamber. This film is transparent to long-range particles produced within the layer of the isotope under study. The chamber was filled with a gas mixture (90%Ar + 10%CH₄) at a pressure of 0.75 atm, and a -4-kV bias voltage was applied to the cathode. A system of dividers between the cathode and the ground ensured the application of the required potentials to the guard electrodes and the Frisch grids. The anodes were grounded.

A scintillation detector based on a thin CsI(Tl) crystal and equipped with an PMT-110 photomultiplier tube was used as a detector of light particles. The crystal, 1 mm thick, can fully absorb alpha particles of energy up to 50 MeV, tritons of energy up to 20 MeV, and protons of energy up to 14 MeV. The scintillator diameter is 70 mm.

The pulses from the spectrometer—that is, a cathode pulse, two anode pulses from the chamber, and one anode pulse from the photomultiplier tubes—were supplied to the input of a pulse-shape digitizer (Le Croy 2262). These four pulses were recast into a digital code and were saved in computer memory for further processing. Figure 2 displays an example of digital oscillograms corresponding to an event of ^{233}Th ternary fission. This structure of the spectrometer tract made it possible to improve the accuracy and the reliability of the measurements substantially. A pulse-shape analysis based on well-developed powerful mathematical methods—such as Fourier analysis and the method of least squares—permitted obtaining information that is inaccessible by present-day analog methods for pulse processing.

An analysis of digital oscillograms by digital methods of pulse processing enabled us to obtain the kinetic energy, the mass, and the emission angle

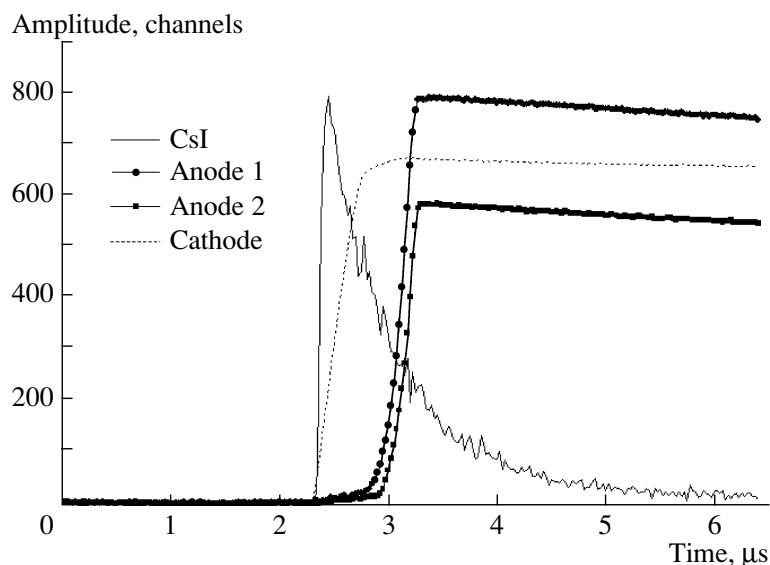


Fig. 2. Example of spectrometer pulses.

[8] and to study the behavior of specific ionization losses [9] for each of the complementary fission fragments simultaneously. The fragment energies were corrected for the inefficiency of the Frisch grid [10], the energy losses within the target [11], and the pulse-height defect [8]. Additionally, each of the pulses was tested carefully for a pileup caused by alpha particles and scattered protons. The following main features of the fission-fragment detector were obtained: the energy resolution for alpha particles was 36 keV at $E_\alpha = 6$ MeV; the energy resolution for fission fragments was about 1 MeV; the mass resolution was about 1 amu; and the angular resolution was 0.067 in units of the cosine of the emission angle.

Pulses from the long-range-particle detector were analyzed for possible overlaps. The particle energy was determined from the pulse area. The energy resolution estimated by using alpha particles from ^{226}Ra decays was 180 keV. The tail of the pulse was approximated by a superposition of two exponential functions by the method of least squares. For each pulse, this fit yielded the contributions of the individual exponentials and their decay times. The resulting area of the fast component was used as a criterion for sorting the particles according to their types. Methods for processing CsI(Tl) pulses were described in more detail elsewhere [12]. The method based on an analysis of the contribution of the fast component provides a resolution that is 1.5 to 2 times higher than the resolution of the conventional ΔE method. This difference in the resolution can be explained by the fact that the former method makes it possible to analyze the total contribution of the fast component over the entire time interval and, in contrast to the analog method

of pulse processing, does not admit any admixture of the slow component. It is of importance that the new method ensures a clear separation of electrons from other charged particles (there is no fast component for electrons at all). In studying ternary nuclear fission induced by fast neutrons, gamma rays, beta particles, and neutrons are the main source of the background, which can be efficiently suppressed by using this method of particle separation.

An analysis of the correlation between the times of arrival of pulses from the cathode of the ionization chamber and the anode of the photomultiplier tube offers wide possibilities for estimating the contribution of random backgrounds and for investigating their structure.

To test the spectrometer, we choose the spontaneous ternary fission of ^{252}Cf . The choice was motivated by the fact that this reaction was thoroughly studied, so that the data published in the literature can be used to test the operating properties of the setup. We employed a ^{252}Cf layer of diameter 5 mm whose activity was 15 Bq. Figure 3 displays the two-dimensional spectrum of scintillation pulses that was obtained in coincidence with the production of fragments. In addition to alpha particles, the spectrum involves tritons, protons, and electrons. Figure 4 shows the measured energy distribution of alpha particles. The yields of tritons and protons with respect to the yield of alpha particles were 6.96% and 1.4%, respectively; in [14], these yields were reported to be 7.1% and 1.6%. The yields of particles and their angular and energy distributions are in good agreement with data obtained by other researchers [13, 15].

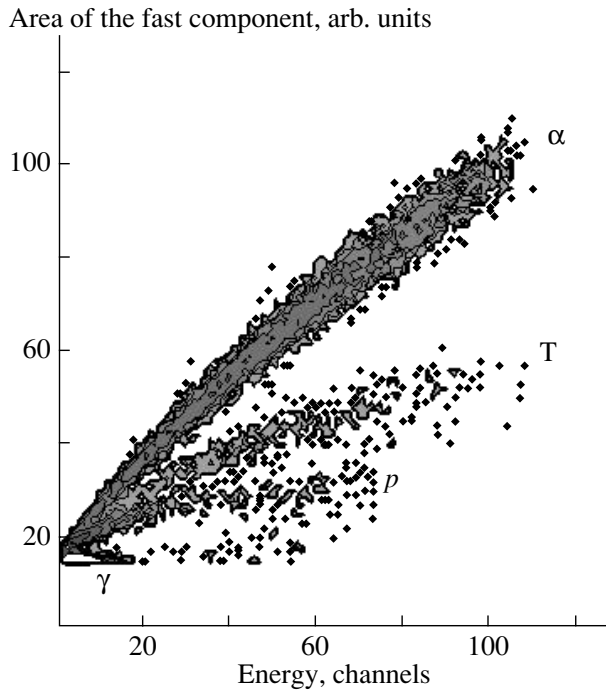


Fig. 3. Two-dimensional spectrum of light particles accompanying ^{252}Cf spontaneous fission in terms of the area of anode pulses and the area of the fast component (coordinate axes).

The detector design, the structure of the accumulation system, and the algorithms of data processing were described in more detail elsewhere [16].

DESCRIPTION OF THE EXPERIMENT

The measurements were performed in a beam from the EG-1 accelerator at the Institute of Physics and Power Engineering (Obninsk). The reaction $T(p, n)^3\text{He}$ was used to obtain fast neutrons. The mean current at the target was $10\ \mu\text{A}$. The yields from ^{232}Th ternary fission induced by fast neutrons of energy 1.6, 1.8, and 2.2 MeV were measured for the first time. Since the detector of light particles covered only part of the solid angle, it was necessary to determine its detection efficiency. The geometric efficiency ε was obtained by three independent methods.

(i) A Monte Carlo calculation of ε was performed for the actual dimensions of the ionization chamber, the fissile layer, the scintillator, and the Frisch grid. The result was $\varepsilon = 10.5\%$.

(ii) The absolute alpha-particle activity was determined for the ^{252}Cf layer within the ionization chamber. After that, the working gas of the chamber was evacuated, and 6-MeV alpha particles from ^{252}Cf spontaneous fission had the possibility of reaching the scintillator. The ratio of the scintillator counting

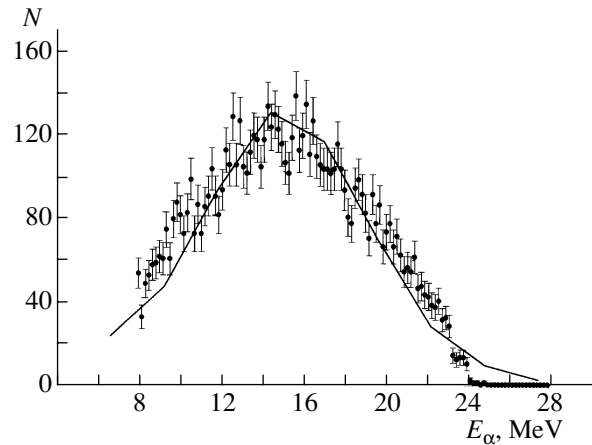


Fig. 4. Energy distribution of alpha particles produced in ternary fission: (points) data obtained in this study and (solid curve) data from [13].

rates to the absolute activity of the layer served as an estimate of the geometric efficiency, which appeared to be 10.8%.

(iii) In measuring ^{252}Cf ternary fission, the geometric efficiency was determined by using the well-known value of the ratio of the ternary-fission yield to the binary-fission yield for this element ($T/B = 3.77 \pm 0.11$ [5]). The resulting efficiency appeared to be $\varepsilon = 10.6\%$.

Three independent methods for determining the efficiency allowed us to estimate it to a precision of 4%—that is, $\varepsilon = 10.6 \pm 0.4$. A special feature of the geometry of the spectrometer is that it records alpha particles traveling in the forward direction. In turn, long-range alpha particles are emitted with the highest probability in the direction orthogonal to the axis along which fission fragments fly apart. It follows, among other things, that the maximum probability of the detection of long-range alpha particles is observed in the situation where fission fragments fly apart along the layer ($\cos\theta = 0$), while the minimum detection probability is realized for $\cos\theta = 1$. This effect is absent if the angular distribution of fission fragments is isotropic, in which case the geometric efficiency can be used to determine the probability of ternary fission correctly. In fact, the angular distributions of fragments originating from ^{232}Th fission can have considerable anisotropy and can fluctuate strongly in the vicinity of vibrational resonances [17]. For each fission fragment, the angles of escape from the target were measured throughout the experimental time. The total angular distributions were reconstructed at the stage of data processing. In Fig. 5, the angular distributions obtained in our study are displayed along with those from [17], where the measurements were performed with tracking detectors. Some discrepancy

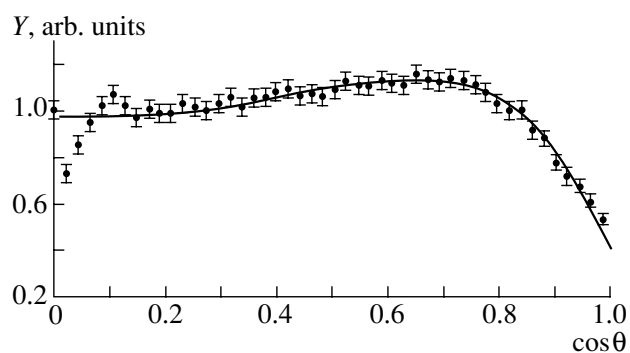


Fig. 5. Angular distribution of fragments originating from ^{232}Th fission induced by 1.6-MeV neutrons: (points) our data and (curve) data from [17].

between the angular distributions in the region of cosine values close to zero can be explained by fragment scattering within the target. An additional correction to the detection efficiency was calculated by the Monte Carlo method. This was done on the basis of a specially developed algorithm by using the known shape of the angular distributions of fragments, the geometry of the spectrometer, and the angular distribution of the long-range particles with respect to the fragment emission angle. This correction did not exceed 15% of the geometric efficiency throughout the neutron-energy range being studied, this value being less than the statistical accuracy attained in the experiment.

Figure 6 shows the resulting probability of ^{233}Th ternary fission as a function of the incident-neutron energy. The mean value of the ternary-fission probability over the range between 1.6 and 2.2 MeV is $(1.7 \pm 0.3) \times 10^{-3}$. The experimental values of the probability of ternary nuclear fission that were obtained for both spontaneous and thermal-neutron-induced fission [1, 7, 18, 19] are displayed in Fig. 7 versus the fissility parameter Z^2/A . It is evident that a fissile system has different values of the excitation energy, depending on the fission type. However, a simple analysis of the displayed data reveals that the effect of the excitation energy on the ternary-fission probability is modest at low excitation energies. By way of example, we indicate that, according to available data on the spontaneous fission of ^{240}Pu and ^{242}Pu and on ^{239}Pu and ^{241}Pu fission induced by thermal neutrons, these fissile systems are similar apart from the excitation energy associated with the neutron binding energy (about 5 MeV). Figure 7 demonstrates that the difference of the ternary-fission yields is within the experimental uncertainties in this case. This fact permits performing a global analysis of our result obtained for ^{233}Th and the data available

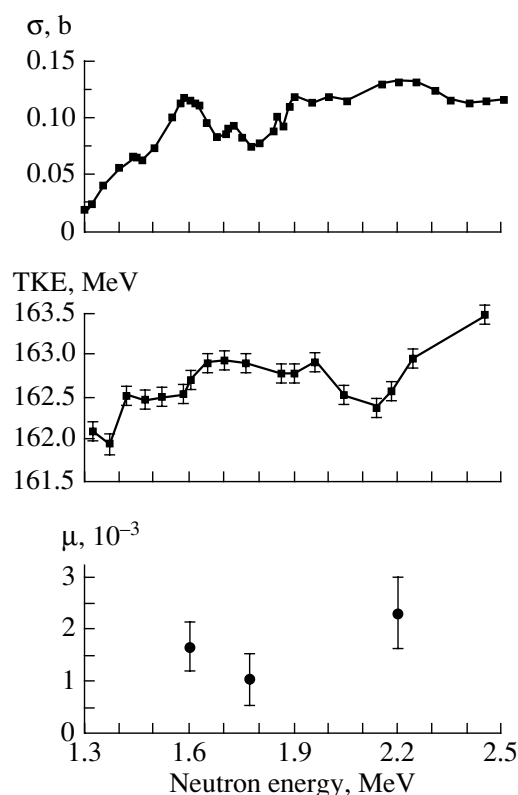


Fig. 6. Cross section for ^{232}Th fission, total kinetic energy of fission fragments [2], and probability of ^{232}Th ternary fission versus the energy of incident neutrons.

from the literature. The fissility-parameter range between 35.69 and 39 has been investigated quite comprehensively (see Fig. 7). However, the data sample presented here can be described, at the same confidence level, in terms of a wide variety of functions, so that it is hardly possible to draw an unambiguous conclusion concerning the behavior of the ternary-fission probability. The fissility parameter for ^{233}Th is 34.76, which is considerably smaller than the lowest value obtained previously (^{232}Pa , $Z^2/A = 35.69$). This allows us to assess the behavior of the ternary-fission probability over a wider region of fissility-parameter values. The dash-dotted line in Fig. 7 represents the ternary-fission probabilities predicted by the semiempirical formula [20]

$$T/B = 1.081 \times 10^{-7} A^{2/3} (Z^2/A - 26.12) \quad (1) \\ \times (Z^2/A^{2/3} - 178.13),$$

which was obtained within the model assuming a random rupture of the fissile-nucleus neck.

On the whole, this dependence describes fairly well the behavior of the ternary-fission probability, although the predicted values are systematically below the experimental data. The value predicted for ^{233}Th

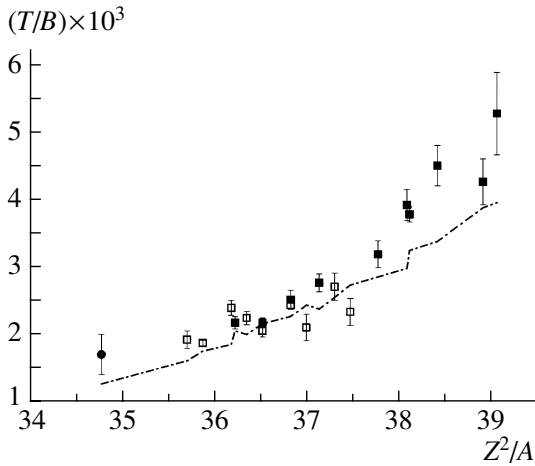


Fig. 7. Ratio of the yields of ternary and binary fission for a set of nuclei as a function of the fissility parameter Z^2/A : (■) spontaneous fission, (□) fission induced by thermal neutrons, and (●) data obtained in this study. The dash-dotted line corresponds to the prediction from [20].

is also somewhat below that which was obtained in our study; probably, a correction of the empirical coefficients in (1) is necessary.

Let us consider in more detail the behavior of the energy dependence of the ternary-fission probability. In the region of the 2.2-MeV vibrational resonance, the total kinetic energy of fission fragments decreases locally by $\Delta\text{TKE} \sim 0.5$ MeV with respect to nonresonance fission. As was mentioned above, a fluctuation of the ternary-fission yields in nuclear fission via vibrational resonances was hypothesized as one of the possible explanations of this effect. One of our objectives here was to test the validity of this hypothesis.

The measurements performed previously by Mehta *et al.* [21] showed that the total kinetic energy of ternary-fission fragments is 12 MeV lower than that for ordinary binary fission. This fact permits estimating the ternary-fission-probability value that is necessary for explaining the observed decrease in the total kinetic energy,

$$\overline{\text{TKE}} = (1 - \mu)\text{TKE}_B + \mu\text{TKE}_T, \quad (2)$$

where $\overline{\text{TKE}}$ is the mean total kinetic energy determined for a given neutron energy, TKE_B is the mean total kinetic energy in binary fission, TKE_T is the mean total kinetic energy in ternary fission, and μ is the ternary-fission probability. Considering that $\text{TKE}_B - \text{TKE}_T = 12$ MeV, we can easily express the expected difference in the ternary-fission probability ($\Delta\mu$) in terms of the difference of the mean total kinetic energies in fission induced by neutrons of different energies (ΔTKE),

$$\Delta\mu = \Delta\text{TKE}/12. \quad (3)$$

Using (3), we can easily find that the observed difference in TKE (about 0.5 MeV) could be explained by an increase in the ternary-fission probability by 0.042. The experimentally observed variation in the ternary-fission probability is 0.0012, which is about 40 times less than the expected value. It follows that, despite the meager available statistics of ternary-fission events, experimental data unambiguously lead to the conclusion that the local decrease in the total kinetic energy in the region of vibrational resonances cannot be explained in terms of a local increase in the ternary-fission probability.

ACKNOWLEDGMENTS

This work was supported by the Russian Foundation for Basic Research and the administration of the Kaluga oblast (project no. 03-02-96358).

REFERENCES

1. *The Nuclear Fission Process*, Ed. by C. Wagemans (CRC Press, London, 1989).
2. B. D. Kuzminov, A. I. Sergachev, V. F. Mitrofanov, *et al.*, in *Proceedings of the IX International Symposium on the Interaction of Fast Neutrons with Nuclei, Gaussig, 1982*, p. 145.
3. V. V. Malinovskii, B. D. Kuz'minov, and N. N. Semenova, *At. Énergiya* **54**, 209 (1983).
4. A. A. Goverdovskii, B. D. Kuzminov, V. F. Mitrofanov, and A. I. Sergachev, in *Proceedings of the International Conference the Fiftieth Anniversary of Nuclear Fission, Leningrad, 1989*, p. 360.
5. J. F. Wild, P. A. Baisden, R. J. Dougan, *et al.*, *Phys. Rev. C* **32**, 488 (1985).
6. C. Wagemans, E. Alleart, F. Caitucoli, *et al.*, *Nucl. Phys. A* **369**, 1 (1981).
7. R. A. Nobles, *Phys. Rev.* **126**, 1508 (1962).
8. C. Budtz-Jorgensen, H.-H. Knitter, Ch. Straede, *et al.*, *Nucl. Instrum. Methods Phys. Res. A* **258**, 209 (1987).
9. V. A. Khriatchkov, I. V. Gubareva, M. V. Dunaev, and N. N. Semenova, Preprint No. 2740, FÉI (Inst. Phys. Power Eng., Obninsk, 1998).
10. V. A. Khriatchkov, A. A. Goverdovski, V. V. Ketlerov, *et al.*, *Nucl. Instrum. Methods Phys. Res. A* **394**, 261 (1997).
11. M. V. Dunaev, I. V. Dunaeva, V. A. Khriatchkov, and N. N. Semenova, in *Proceedings of the VIII International Seminar on Interaction of Neutrons with Nuclei, Dubna, 2000*, p. 363.
12. V. A. Khryachkov, M. V. Dunaev, V. V. Ketlerov, *et al.*, *Prib. Tekh. Éksp.*, No. 3, 29 (2000).
13. W. Loveland, *Phys. Rev. C* **9**, 395 (1974).
14. C. Wagemans, in *Particle Emission from Nuclei* (CRC Press, Boca Raton, FL, 1988), Vol. III.
15. S. W. Cospers, J. Cerny, and R. C. Gatti, *Phys. Rev.* **154**, 1193 (1967).

16. V. A. Khryachkov, A. I. Sergachev, M. V. Dunaev, *et al.*, Prib. Tekh. Éksp., No. 5, 34 (2002).
17. S. B. Ermagambetov, L. D. Smirenkina, and G. N. Smirenkin, At. Énergiya **23**, 20 (1967).
18. C. Wagemans, M. Asghar, P. D'hondt, *et al.*, Nucl. Phys. A **285**, 32 (1977).
19. C. Wagemans and O. Serot, in *Proceedings of the II International Workshop on Nuclear Fission and Fission-Product Spectroscopy, Seyssins, France, 1988*, p. 299.
20. V. Rubchenya and S. Yavshits, Z. Phys. A **329**, 217 (1988).
21. G. K. Mehta, J. Poitou, M. Ribrag, and C. Signarbieux, Phys. Rev. C **7**, 373 (1973).

Translated by E. Kozlovsky

NUCLEI
Experiment

Spectra and Mean Energies of Prompt Neutrons from ^{238}U Fission Induced by Primary Neutrons of Energy in the Region $E_n < 20$ MeV

G. N. Lovchikova, A. M. Trufanov, M. I. Svirin*, V. A. Vinogradov, and A. V. Polyakov

Institute of Physics and Power Engineering, pl. Bondarenko 1, Obninsk, Kaluga oblast, 249020 Russia

Received February 2, 2004

Abstract—The time-of-flight technique is used to measure the ratios $R(E, E_n) = N(E, E_n)/N_{\text{Cf}}(E)$ of the normalized (to unity) spectra $N(E, E_n)$ of neutrons accompanying the neutron-induced fission of ^{238}U at primary-neutron energies of $E_n = 6.0$ and 7.0 MeV to the spectrum $N_{\text{Cf}}(E)$ neutrons from the spontaneous fission of ^{252}Cf . These experimental data and the results of their analysis are discussed together with data that were previously obtained for the neutron-induced fission of ^{238}U at the primary energies of $E_n = 2.9, 5.0, 13.2, 14.7, 16.0,$ and 17.7 MeV. © 2004 MAIK “Nauka/Interperiodica”.

INTRODUCTION

During the evolution of a fissile nucleus from the equilibrium to the saddle-point configuration, neutron emission is the main channel among those that compete with the fission process. It is common practice to assume that the time of the transition from the saddle to the scission point is so short that a significant number of particles cannot be emitted within it.

Up to the threshold of emission fission, there is no preequilibrium component either in the measured spectra of prompt fission neutrons or in their mean multiplicity. Secondary neutrons are emitted predominantly from fully accelerated fragments originating from the fission of the primary compound nucleus A . When all directions in which fission fragments may fly apart are equiprobable, the shape of the spectra of prompt fission neutrons is identical at any angle and is the simplest, being close to that of a Maxwell distribution. This case is realized in nuclear fission induced by thermal neutrons or in the spontaneous fission of nuclei. The emission of postfission neutrons has but a small effect on the observables of the fission process, and one can take this effect into account by means of the corresponding corrections. The emission of prefission neutrons leads to more far-reaching consequences. It forms new possibilities for fission—new reactions in which nuclei of lower mass undergo fission come into play. This causes serious difficulties for studying the properties of the fission process as functions of energy.

In emission fission, the shape of the spectra of prompt fission neutrons differs significantly from the shape of the postfission component because of the

contribution from prefission neutrons. The spectrum of neutrons from fully accelerated fragments serves as a reference of shape, and it is against this reference that one observes effects associated with the emission of prefission neutrons. A comparison of the experimentally measured ratios $R(E, E_n) = N(E, E_n)/N_{\text{Cf}}(E)$ of the normalized (to unity) spectra of neutrons from the neutron-induced fission of the nuclides under study, $N(E, E_n)$, at the primary-neutron energies of $E_n = 2.9$ and 14.7 MeV to the spectrum $N_{\text{Cf}}(E)$ of neutrons from the spontaneous fission of ^{252}Cf [1–3] demonstrates clearly, for ^{232}Th , $^{235,238}\text{U}$, and ^{237}Np target nuclei, the distinctions between the shapes of the measured distributions below and well above the threshold for emission fission. The calculated curves that were obtained on the basis of the model of two neutron sources reproduce satisfactorily the shape of the observed distributions at $E_n = 14.7$ MeV over a broad region of secondary-neutron energies ($E \geq 2$ MeV). In the “soft” section of the spectrum ($E < 2$ MeV), however, the calculated curves lie considerably lower than the corresponding experimental values [1, 2, 4]. An anomalously high yield of soft neutrons was also observed in the distributions $R(E, E_n)$ measured at different energies for ^{238}U (at $E_n = 13.2$ MeV [5] and at 16.0 and 17.7 MeV [6, 7]) and for ^{232}Th (at 14.6 and 17.7 MeV [8]).

In order to remove the discrepancy between the results of the calculations and experimental data for $E_n > 13$ MeV, one can assume that, at high excitation energies of the primary compound nucleus, a third source of neutrons, that which produces soft neutrons, comes into play. In [7–9], the system of well-developed fragments prior to their separation—

* e-mail: svirin@ippe.obninsk.ru

that is, the system of nonaccelerated fragments—was considered as a third source. It was assumed that this dinuclear system is in a statistical equilibrium with respect to all degrees of freedom and that its lifetime is sufficiently long for neutron emission to occur, provided that this is energetically possible. With allowance for three neutron sources, it proved to be possible to describe the experimental behavior of the distributions $R(E, E_n)$ for $E_n > 13$ MeV over the entire measured range of prompt-fission-neutron energies, including the anomalous segment $E < 2$ MeV.

The entire body of accumulated data on the spectra of fission neutrons in the region of emission fission is insufficient for pinpointing primary-neutron energies (E_n) at which the traditional model of two neutron sources describes experimental results adequately. Alternatively, the question is that of determining the energy value E_n above which the third source of neutrons comes into play. In order to answer this question, we must have at our disposal experimental information about the spectra of prompt neutrons from ^{238}U fission over the range between the emission-fission threshold of $E_n = 6$ MeV and $E_n = 13$ MeV. In order to supplement the data obtained previously, we have measured and analyzed the energy distributions $R(E, E_n)$ at the emission-fission threshold of $E_n = 6$ MeV and at the beginning of the second plateau in the fission cross section (at $E_n = 7$ MeV). We present here the respective results and assess the mean multiplicity and the mean energy of prompt fission neutrons within the models of two and three neutron sources.

1. DESCRIPTION OF THE EXPERIMENT

The spectra of neutrons from the fission of ^{238}U nuclei were measured over the energy range $E = 0.14$ – 15 MeV. The measurements relied on the time-of-flight method and employed a fast-neutron spectrometer created at the Institute of Physics and Power Engineering (Obninsk) on the basis of the EGP-10M electrostatic charge-exchange accelerator. The most important units of the spectrometer included a source that produced fast neutrons via the reaction $\text{T}(p, n)^3\text{He}$ occurring on a gaseous tritium target, a neutron detector, a fission-fragment detector in the form of a multilayer flow-type ionization chamber, a system for monitoring primary neutrons, and electronics.

In choosing a source of neutrons, we tried primarily to obtain a reasonably high neutron flux at a high energy resolution and a low background from structural materials. As a source of monoenergetic neutrons, a gaseous tritium source [10] bombarded with protons from the EGP-10M accelerator satisfies these requirements. A gaseous-tritium-containing

target chamber in the form of a thin-wall (0.2-mm-thick) steel cylinder 40 mm in length and 10 mm in diameter was mounted in the ion guide of the accelerator. Two windows between which a cooling helium flux circulated separated tritium from the vacuum system of the proton accelerator. The windows were made from rolled ^{58}Ni foils of thickness $10\ \mu\text{m}$, which were tightened with ring indium gaskets. The geometric dimensions of the proton beam incident on the target were bounded by bars having a straight-through hole of diameter 6 mm, which were located at a distance of 10 cm upstream of the target. The inner surfaces of the target and of the cooling cell, as well as the side of the bars that faces the beam, were covered with a layer of the ^{58}Ni isotope (its degree of enrichment was 96%) 0.1 to 0.3 mm thick. This was done in order to reduce the yield of background neutrons from the reaction (p, n) on the structural materials of the target—the threshold for the reaction $^{58}\text{Ni}(p, n)$ is rather high (9.5 MeV). A detailed comparison of the parameters of solid-state and gaseous tritium targets as neutron sources was performed in [11]. It was shown there that, in the case of a gaseous tritium target, the contribution of nonmonoenergetic neutrons did not exceed 1% at proton energies in the region $E_p < 9$ MeV; at the same time, it turned out that, with solid-state tritium targets, it was very difficult to obtain monoenergetic neutrons of energy in excess of 5 MeV.

In order to determine the sought energy of neutrons emitted at zero angle with respect to the incident proton beam (in this direction the neutron energy and yield are maximal), it is necessary to know the energy of bombarding protons. In the present study, the accelerated-proton energies of $E_p = 7.7$ and 8.5 MeV were used to obtain the neutron energies of $E_n = 6$ and 7 , respectively.

The neutron detector consisted of a paraterphenyl crystal 5 cm in diameter and 5 cm in thickness and a FEU-143 photomultiplier tube (Kren) produced in Russia. An anode signal from the photomultiplier tube served for forming a “start” label and for identifying a pulse in shape with the aim of suppressing photons.

A scintillator from paraterphenyl has a higher neutron-detection efficiency than a stilbene crystal. This enables us to create a neutron detector having a lower energy threshold for recording neutrons, about 100 keV, and an absolute efficiency of about 50%. These are features of paramount importance for performing a thorough investigation into the low-energy section of neutron spectra ($E < 2$ MeV), which is of greatest interest for revealing the mechanism of neutron emission in spontaneous fission. For the first time, such a detector was created and applied in [12].

Our neutron detector had the following properties: the time resolution was about 2.5 ns; the energy threshold for neutron detection was about 80 keV; and the photon-suppression factor was about 10. The detector was placed within a special, combined, massive shielding in the form of a tank filled with a mixture of lithium hydride and paraffin. A truncated steel pyramid of length 70 cm was arranged in front of the tank. In order to suppress the photon background, the detector was surrounded on all sides by lead of thickness 10 cm; the end face of the crystal was closed with lead 0.5 cm thick. Thereby, we ensured an efficient shielding of the neutron detector, and this led to a considerable reduction of the background from photons and neutrons scattered by the walls and the floor of the experimental hall.

The fission-fragment detector has already been repeatedly described in the literature (see, for example, [1, 2]); in view of this, only a brief characterization of its structure and operation is given here. A multilayer flow-type ionization chamber containing fissile-substance (^{238}U) layers of total weight 5.61 g served as the fission-fragment detector. In order to reduce the electrical capacitance, the chamber was divided into three sections. Each section was connected to a specially developed small-size, wideband preamplifier. One of the sections contained layers of the substance under study, with the ^{252}Cf isotope being uniformly distributed over its thickness. This made it possible to determine the neutron-detector efficiency and to measure the fission-neutron spectra in question with respect to the spectrum of neutrons from the spontaneous fission of ^{252}Cf . A simultaneous measurement of the fission-neutron spectrum being studied and the respective spectrum for the reference nucleus ^{252}Cf under identical conditions makes it possible to get rid of many experimental errors. The efficiency of fission-fragment detection was about 70%. Pure methane (99.9%) was used as a flowing gas. Special attention was given to the identity of the features of the cross sections for ^{238}U and the reference nucleus ^{252}Cf .

The electronic system that was part of the fast-neutron spectrometer was implemented within the CAMAC standard. It included equipment connected to the detectors in the experimental hall; equipment for separating, selecting, and sorting events and for coding, processing, and counting events; electronics involved in the detection, on-line accumulation, control, and graphical representation of relevant information; and equipment for saving, storing, and processing information, as well as for recasting it into a convenient form. A dedicated package of codes was developed for accomplishing a computer-aided control of the experiment. A more detailed description

of the electronic equipment used was given in [13]. In order to record the time-of-flight spectra of neutrons from four sections of the chamber simultaneously, one time analog-to-digital converter was used in the spectrometer, whereby it was possible to reduce considerably systematic errors associated with the differential nonlinearity and temperature drift of the converter. This enables us to use the accelerator in the continuous mode. The stability of operation of the electronics and detectors was monitored by tracing, on the time scale, the shape and the position of the photon peak from the spontaneous fission of ^{252}Cf nuclei occurring in the ionization chamber.

The procedure of measurements (accumulation of information) consisted in repeating measurements of neutron spectra many times for each section of the ionization fission chamber, which was arranged at an angle of 45° with respect to the proton-beam axis at a distance of 15 cm from the target center. In order to monitor the flux of neutrons emitted from the target, use was made of an all-wave counter oriented at an angle of 90° and positioned at a distance of about 3 m.

The accumulated single experimental spectra were summed, but, preliminarily, they were shifted along the time scale in order to compensate for the time drift of the equipment used. For this, we calculated, for each single spectrum associated with each section, the position of the centroid of the photon peak and determined the shift in terms of channel fractions. Upon performing data treatment in this way, we obtained the total time spectra for each of the four sections of the fission chamber. After that, a correction for different flight-path lengths for each section was introduced in these total time spectra. The spectra corrected in this way were summed and converted into energy spectra.

In Fig. 1, the results of our present experiment are given in the form of the directly measured ratios of the prompt-neutron spectrum $N(E, E_n)$ for ^{238}U fission induced by neutrons of energy $E_n = 6$ and 7 MeV to the neutron spectrum $N_{\text{Cf}}(E)$ for the spontaneous fission of ^{252}Cf ; that is,

$$R(E, E_n) = N(E, E_n)/N_{\text{Cf}}(E).$$

The experimental data in question were treated in such a way that, with allowance for the contribution from neutrons of energy in the region $E \leq E_{\text{min}} = 0.14$ MeV, both spectra were normalized as

$$\int_0^\infty N(E, E_n)dE = \int_0^\infty N_{\text{Cf}}(E)dE = 1.$$

The error in the experimental data was determined primarily by the statistical accuracy of the measurements (1.5–25%). The mean energy of neutrons was

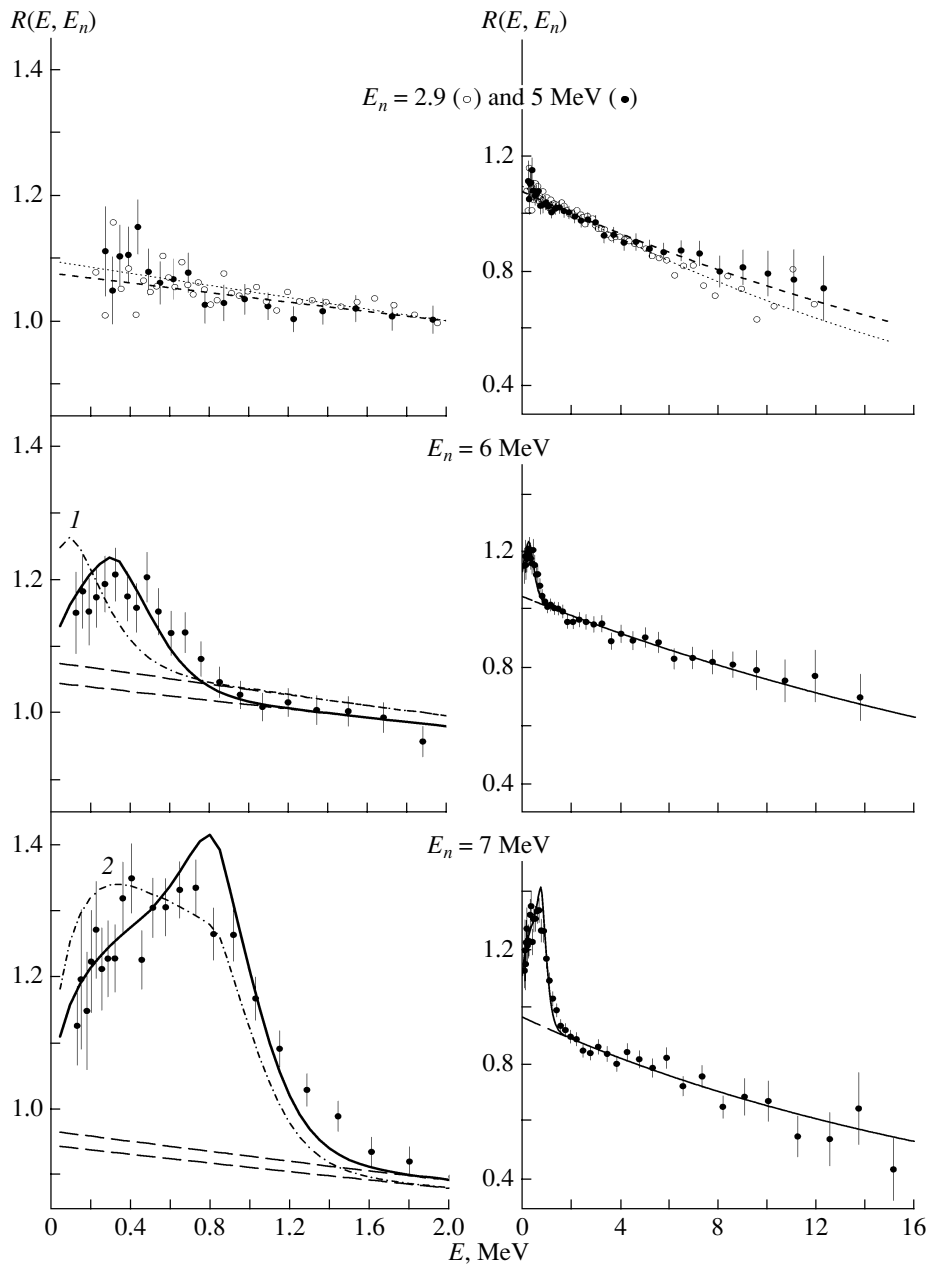


Fig. 1. Ratios $R(E, E_n)$ of the spectra of neutrons from the $^{238}\text{U} + n$ fission process to the spectrum of neutrons from the spontaneous fission of ^{252}Ci . The points represent experimental values. The dotted (for $E_n = 2.9$ MeV) and the dashed (for 5 MeV) curves correspond to the ratios of the Maxwell distributions in (22). The solid and dash-dotted curves illustrate various versions of the description of experimental distributions for $E_n = 6$ and 7 MeV (see main body of the text). The dashed lines show the level of the postfission component.

evaluated by means of integration over the normalized observed spectrum $N(E, E_n)$,

$$\bar{E}(E_n) = \int_0^{\infty} EN(E, E_n)dE.$$

This yielded $\bar{E}(E_n) = 1.99 \pm 0.03$ MeV at $E_n = 6$ MeV and $\bar{E}(E_n) = 1.87 \pm 0.03$ MeV at $E_n = 7$ MeV.

2. EMISSION OF POST- AND PREFISSION NEUTRONS

2.1. Basic Relations

The emission of neutrons from an excited fissile nucleus prior to its disintegration is the main channel that competes with fission. If the excitation energy E^* of the primary parent nucleus A is less than some threshold value, $E^* < E_{\text{thr}} = B_n^A + B_f^{A-1}$ (where B_n^A

and B_f^{A-1} are respectively, the neutron binding energy in the nucleus A and the height of the fission barrier in the nucleus $A - 1$, then, upon the emission of a first-chance neutron, the residual nucleus $A - 1$ cannot undergo fission. In the case of this, single-chance fission, the excited fragments originating from the fission of the nucleus A , which are accelerated owing to their mutual Coulomb repulsion, will be the only source of neutrons. As to the emission of neutrons, it is governed by the evaporation model, in which case the angular distribution is nearly isotropic in the c.m. frame of a fragment of mass number M , while their energy spectrum has the form [14]

$$n(\varepsilon, M)d\varepsilon = \frac{1}{\Gamma(k+1)\theta^{k+1}}\varepsilon^k \exp\left(-\frac{\varepsilon}{\theta}\right) d\varepsilon, \quad (1)$$

where $k = 1$ and $\theta = \tau_1(M - 1)$ for single-chance emission, $k = 5/11 \approx 1/2$ and $\theta = (11/12)\tau_1(M - 1)$ for multichance emission, and $\tau_1(M - 1)$ is the temperature of the residual nucleus $M - 1$ after the emission of the first neutron.

In rescaling the distribution in (1) from the c.m. to the laboratory frame, we use the relation $\varepsilon = E + \omega - 2\sqrt{\omega E} \cos \psi$ between the energies involved [the transition Jacobian is $J(\varepsilon, E) = \sqrt{E/\varepsilon}$]; taking into account the contribution from the complementary fragment (under the assumption that the two fragments are identical, $M = A - M = A/2$), we obtain the expression at $k = 1/2$ for describing the spectrum of neutrons at different angles ψ with respect to the direction along which the fragments fly apart:

$$N_W(E, \psi)dEd\Omega = (2\pi)^{-1} \left(\frac{E}{\pi\theta^3}\right)^{1/2} \times \exp\left(-\frac{\omega + E}{\theta}\right) \cosh\left(\frac{2\sqrt{\omega E}}{\theta} \cos \psi\right) dEd\Omega. \quad (2)$$

The angular distributions of neutrons in the laboratory frame are highly anisotropic, having the shape of rather narrow rosettes along the direction of fragment motion. Expression (2) can easily be generalized to the case of fragments whose parameters are different. For example, one can readily take into account the difference of the mean kinetic energies ω per nucleon for two groups of fragments, light and complementary heavy ones.

Integration of expression (2) over the solid angle $d\Omega = 2\pi \sin \psi d\psi$ leads to the well-known Watt formula

$$N_W(E, \theta, \omega) = (\pi\omega\theta)^{-1/2} \times \exp\left(-\frac{\omega + E}{\theta}\right) \sinh\left(\frac{2\sqrt{\omega E}}{\theta}\right) \quad (3)$$

with the mean energy given by

$$\bar{E}_W = 3\theta/2 + \omega. \quad (4)$$

Expression (3) describes integrated spectra, which are identical at different angles if all directions at which fragments fly apart are equiprobable. This case is realized in spontaneous fission and in fission induced by thermal and fast neutrons—for example, in the experiments of our group at $E_n = 2.9$ MeV [2, 3] and at 5.0 MeV [5]. The parameters θ and ω , which are to be determined from experimental results, are averages over a broad distribution of excitation energies of fission fragments and over their mass distribution. Expression (3), which depends on two parameters, is not convenient in constructing a systematics of mean energies and in simulating the spectrum of postfission neutrons in emission (multichance) fission.

For fission events characterized by $\omega \rightarrow 0$, which are not realized in experiments, the Watt formula reduces to a Maxwell distribution; that is,

$$N_M(E, T) = 2 \left(\frac{E}{\pi T^3}\right)^{1/2} \exp\left(-\frac{E}{T}\right). \quad (5)$$

Although there is no physical validation of the application of relation (5) to describing the spectra of fission neutrons, it is widely used to parametrize the results of measurements. In this parametrization, there is only one parameter (T), which is determined from the least squares fit to experimental spectra $N(E, E_n)$ and which is related to the mean energy as

$$\bar{E}_M = 3T/2. \quad (6)$$

Experimental results revealed that the spectra of prompt neutrons from spontaneous fission [15, 16], fission induced by thermal neutrons [17, 18], and fission induced by fast neutrons in the case of single-chance fission ($E_n < B_f^{A-1}$) have a shape close to that of a Maxwell distribution. Deviations from it can be taken into account quite correctly in terms of the shape function $\mu(E)$,

$$N(E) = N_M(E, T)\mu(E). \quad (7)$$

This function has received the most detailed study for the spontaneous fission of ^{252}Cf [19]. The features of this fission process have the status of a neutron reference [20].

An analytic estimate of the shape function can be obtained with the aid of the relation [21]

$$\tilde{\mu}(E) = N_W(E, \theta, \omega)/N_M(E, T) \quad (8)$$

if the parameters θ and T are eliminated from (3) and (5) by using the assumption that the mean energies involved are equal, $\bar{E}_W = \bar{E}_M = \bar{E}$. The result

is

$$\tilde{\mu}(E) = \frac{1}{3} \left[\frac{E}{\bar{E}^3} \omega(\bar{E} - \omega) \right]^{-1/2} \times \exp \left[-\frac{3\omega(E + \bar{E})}{2(\bar{E} - \omega)} \right] \sinh \left[\frac{3(E\omega)^{1/2}}{\bar{E} - \omega} \right]; \tag{9}$$

for $\omega \rightarrow 0$, we have $\tilde{\mu}(E) \rightarrow 1$. An expression that approximates the thoroughly studied shape function for the ²⁵²Cf nucleus is given in [5].

As soon as the excitation energy of the primary compound nucleus A is increased above the threshold for the respective $(n, n'f)$ reaction, $E^* > E_{thr} (E_n > B_f^{A-1})$, the fission process appears to be of an emission character. In this case, each of the $(n, xn'f)$ reactions [where $x = 0, 1, \dots, x_{max}(E_n)$ is the number of neutrons emitted prior to the fission of, respectively, $A, A - 1, \dots, A - x_{max}(E_n)$ isotopes] makes a contribution $\sigma_{fA-x}(E_n)$ to the total fission cross section:

$$\sigma_f(E_n) = \sum_{x=0}^{x_{max}(E_n)} \sigma_{fA-x}(E_n). \tag{10}$$

The first chance of fission corresponds to $x = 0$, and the $(x_{max} + 1)$ th chance corresponds to $x = x_{max}$; here, $x_{max}(E_n)$ is the maximum number of prefission neutrons that is possible for a given value of the primary neutron energy E_n .

Within traditional concepts, one considers two sources of neutrons accompanying the emission fission of nuclei. These are (i) the source of postfission neutrons, which originate from the fully accelerated fragments formed in the fission of $A, A - 1, \dots, A - x_{max}(E_n)$ isotopes, and (ii) the source of prefission neutrons, which originate from fissile nuclei themselves prior to their disintegration. Accordingly, the

differential yield of secondary neutrons can be represented as the sum of two components; that is,

$$\frac{d\bar{\nu}(E, E_n)}{dE} = \frac{d\bar{\nu}_{iaf}(E, E_n)}{dE} + \frac{d\bar{\nu}_{pre}(E, E_n)}{dE}. \tag{11}$$

The energy distribution of postfission neutrons from fully accelerated fragments can be represented as a superposition of Maxwell distributions:

$$\frac{d\bar{\nu}_{iaf}(E, E_n)}{dE} = \alpha \sum_{x=0}^{x_{max}(E_n)} \bar{\nu}_{fA-x}(\bar{E}_{nx}) \times \mu(E) N_M(E, T_x) \frac{\sigma_{fA-x}(E_n)}{\sigma_f(E_n)}. \tag{12}$$

In contrast to the primary compound nucleus A (²³⁹U, $x = 0, \bar{E}_{n0} = E_n$), which is characterized by a single value of the excitation energy, $E^* = E_n + B_{nA}$, the residual nuclei $A - x (x \geq 1)$ formed upon the emission of x neutrons are characterized by a distribution of excitation energies $U = E^* - \sum_{i=0}^x B_{nA-i} - E$,

$$F_{A-x}(U) = d\sigma_{nx} \left(E^* - \sum_{i=0}^x B_{nA-i} - U \right) / dE, \tag{13}$$

where $d\sigma_{nx}(E)/dE$ is the spectrum of neutrons emitted from the excited nucleus $A + 1 - x$ (the main channel that competes with the fission of the nucleus $A + 1 - x$). The primary-neutron energy $\bar{E}_{nx} = \bar{U}_{A-x} - \bar{B}_{nA-x}$ and the mean multiplicity $\bar{\nu}_{fA-x}(\bar{E}_{nx})$ of prompt neutrons from fully accelerated fragments correspond to the mean excitation energy

$$\bar{U}_{A-x} = \frac{\int_{B_{fA-x}}^{E^* - \sum_{i=0}^x B_{nA-x}} U F_{A-x}(U) dU}{\int_{B_{fA-x}}^{E^* - \sum_{i=0}^x B_{nA-x}} F_{A-x}(U) dU} \tag{14}$$

of the nucleus $A - x$.

The estimate of the mean neutron multiplicity $\bar{\nu}_{fA-x}(\bar{E}_{nx})$ in (12) was based on the use of the systematics of $\bar{\nu}_f(E_n)$ in [22] and its extrapolation to the region $E_n \geq B_{fA-1}$ of emission-fission energies,

$$\begin{aligned} \bar{\nu}_{fA-x}(\bar{E}_{nx}) &= 2.33 \tag{15} \\ &+ 0.06 [2 - (-1)^{A-x-Z} - (-1)^Z] \\ &+ 0.15(Z - 92) + 0.02(A - x - 236) \\ &+ [0.130 + 0.006(A - x - 236)](\bar{E}_{nx} - E_{tx}), \end{aligned}$$

$$\begin{aligned} E_{tx} &= 18.6 - 0.36Z^2/(A - x) \\ &+ 0.2 [2 - (-1)^{A-x-Z} - (-1)^Z] - B_{nA-x} \end{aligned}$$

[in (15), A is a compound nucleus—that is, a target nucleus plus one neutron], while the estimate $T_x = 2\bar{E}_{fx}/3$ was based on the Terrell semiempirical formula [23]

$$\bar{E}_{fx} = a + b\sqrt{\bar{\nu}_{fA-x} + 1}, \tag{16}$$

where the parameters take the values of $a = 0.75$ MeV and $b = 0.65$ MeV [24], which are universal for all

nuclei. The constant α in (12) was introduced to fit experimental data and to compensate for the inevitable error in the description of $\bar{\nu}_{fA-x}(E_n)$ on the basis of the systematics of $\bar{\nu}_f(E_n)$. A similar uncertainty is also inherent in the use of the systematics of T_x ; in view of this, the quantity $T_x = 2\beta\bar{E}_{fx}/3$ was varied within 3% with the aid of the constant β .

The differential yield of pre-fission neutrons in emission fission can be represented in the form

$$\frac{d\bar{\nu}_{\text{pre}}(E, E_n)}{dE} \quad (17)$$

$$= \sum_{x=1}^{x_{\text{max}}(E_n)} \left(\sum_{i=x}^{x_{\text{max}}(E_n)} N_{xi}(E, E_n) \frac{\sigma_{fA-i}(E_n)}{\sigma_f(E_n)} \right).$$

In expression (17),

$$N_{xi}(E, E_n) = \frac{d\sigma_{nx}(E, E_n)}{dE} \times f_i(E, E_n) \Big/ \int_E \frac{d\sigma_{nx}(E, E_n)}{dE} f_i(E, E_n) dE \quad (18)$$

is the normalized (to unity) spectrum of neutrons emitted by nuclei $A + 1 - x$ (at a fixed value of $x = 1, 2, 3, \dots$) whose energies E are such that the subsequent fission of residual nuclei $A - i$ formed upon the sequential emission of i neutrons ($i \geq x$) is energetically possible. The cutoff function $f_i(E, E_n)$ is the probability of the fission of nuclei $A - i$ as a function of the emitted-neutron energy E :

$$f_i(E, E_n) \quad (19)$$

$$= P_{fA-i} \left(U_i = E^* - \sum_{x=1}^i B_{nA-x+1} - E \right).$$

If one disregards effects associated with tunnel penetrability of the fission barrier, nuclei $A - i$ cannot undergo fission at energies satisfying the condition $U_i \leq B_{fA-i}$. The neutron spectrum $d\sigma_{nx}(E, E_n)/dE$ ($1 \leq x \leq i$) is cut off by the function $f_i(E, E_n)$ at the threshold energy

$$E = E_i^{\text{thr}} = E^* - \sum_{x=1}^i B_{nA-x+1} - B_{fA-i}.$$

The neutron spectra studied here refer to the primary-neutron-energy region $E_n < 20$ MeV, where there can occur the one-, two-, and three-chance fission reactions $^{238}\text{U}(n, xn'f)$, $x = 0, 1, 2$. In the energy region $E_n < B_{fA-1}$ of the one-chance reaction ($x = 0$), we have $d\bar{\nu}_{\text{pre}}/dE = 0$. The expression for the spectrum of pre-fission neutrons in the energy

range $B_{fA-1} \leq E_n < B_{nA-1} + B_{fA-2}$ of the two-chance reaction [$x_{\text{max}}(E_n) = 1$ in (17)] has the form

$$\frac{d\bar{\nu}_{\text{pre}}(E, E_n)}{dE} = N_{11}(E, E_n) \frac{\sigma_{fA-1}(E_n)}{\sigma_f(E_n)}. \quad (20)$$

In the energy range $B_{nA-1} + B_{fA-2} \leq E_n < B_{nA-1} + B_{nA-2} + B_{fA-3}$ of the three-chance reaction [$x_{\text{max}}(E_n) = 2$ in (17)], the spectrum in question is given by

$$\frac{d\bar{\nu}_{\text{pre}}(E, E_n)}{dE} = N_{11}(E, E_n) \frac{\sigma_{fA-1}(E_n)}{\sigma_f(E_n)} \quad (21)$$

$$+ N_{12}(E, E_n) \frac{\sigma_{fA-2}(E_n)}{\sigma_f(E_n)}$$

$$+ N_{22}(E, E_n) \frac{\sigma_{fA-2}(E_n)}{\sigma_f(E_n)}.$$

2.2. On the Shape of the Fission-Neutron Spectra in the Reaction $^{238}\text{U}(n, f)$ at $E_n = 2.9$ and 5 MeV

In the studies of our group, the shape of the fission-neutron spectra from (n, f) reactions was investigated in detail at $E_n = 2.9$ MeV for target nuclei ^{232}Th , $^{235,238}\text{U}$ [1, 2], and ^{237}Np [3] and at 5 MeV for ^{238}U [5]. For these energy values ($E_n = 2.9$ and 5 MeV), the measured spectra of neutrons from ^{238}U fission are given in Fig. 1, along with their description. As was mentioned above, the data are presented in the form of the ratios $R(E, E_n) = N(E, E_n)/N_{\text{Cf}}(E)$ of the normalized (to unity) quantities

$$N(E, E_n) = \frac{d\bar{\nu}(E, E_n)}{dE} / \bar{\nu}(E_n)$$

for the induced fission of ^{238}U and the quantity

$$N_{\text{Cf}}(E) = \frac{d\bar{\nu}_{\text{Cf}}(E)}{dE} / \bar{\nu}_{\text{Cf}}$$

for the spontaneous fission of ^{252}Cf . The experimental ratios $R(E, E_n)$ are described satisfactorily by the smooth energy dependences

$$R_M(E, E_n) = \frac{N_M[E, T(E_n)]}{N_M(E, T_{\text{Cf}})} \quad (22)$$

$$= \left(\frac{T_{\text{Cf}}}{T(E_n)} \right)^{3/2} \exp \left[\frac{T_{\text{Cf}} - T(E_n)}{T_{\text{Cf}} T(E_n)} E \right],$$

which are obtained as the ratios of the Maxwell distributions in (5) at the temperatures of $T_{\text{Cf}} = 1.42$ MeV and $T(E_n = 2.9 \text{ MeV}) = 1.332$ MeV (dotted curve) and $T(E_n = 5 \text{ MeV}) = 1.352$ MeV (dashed curve).

At a rather high precision achieved to date in measuring $R(E, E_n)$, these functions carry virtually no information about the deviations of the shape of

the spectra $N(E, E_n)$ under study from (5). If, in reconstructing the spectra $N(E, E_n)$ on the basis of the experimental ratios $R(E, E_n)$, one takes the Maxwell distribution in (5), the resulting description of the spectra in question will have the same form. From the estimate presented in [19] and based on a vast body of experimental data and from the results of theoretical calculations, it follows, however, that the spectrum $N_{Cf}(E)$ for the spontaneous fission of californium features quite significant deviations from a Maxwell distribution. These deviations can be taken into account in terms of the shape function in (7). This means that the deviations of the fission spectra $N(E, E_n)$ being studied from the Maxwell distribution in (5) are similar to the deviations $\mu(E)$ exhibited by the shape of the reference spectrum. The foregoing is valid for other actinide nuclei as well; therefore, the statement that the shape function is “universal” [3] is quite plausible. Thus, we can say that, at actual errors in measuring $R(E, E_n)$, information about the shape of the spectra $N(E, E_n)$ under study is correct inasmuch as the estimate of $\mu(E)$ for the reference spectrum is reliable—that is, the situation here is typical of what we usually have for the results of relative measurements.

2.3. Spectra of Prompt Fission Neutrons at $E_n = 6$ and 7 MeV (at the Emission-Fission Threshold and above It)

Let us discuss the data presented in Fig. 1 and obtained by measuring anew the energy dependences for $R(E, E_n)$ at the primary-neutron energies of $E_n = 6$ and 7 MeV. A specific feature in the soft section of the experimental distributions in the form of a bell stands out clearly against the background of a nearly linear dependence of $R(E, E_n)$ at $E_n = 2.9$ and 5 MeV in the same region of secondary-neutron energies. At higher energies, $E \geq 1$ MeV at $E_n = 6$ MeV and $E \geq 2$ MeV at $E_n = 7$ MeV, all four distributions have the same form peculiar to postfission neutrons.

The feature in the shape of the distributions at $E_n = 6$ and 7 MeV is a manifestation of the contribution of postfission neutrons, which appear as soon as the relevant $(n, n'f)$ reaction becomes possible. Figure 2a shows the prefission-neutron spectrum $d\bar{\nu}_{pre}(E, E_n)/dE$ calculated at $E_n = 7$ MeV according to (20) for two versions of the cutoff function, (which is given in Fig. 2b): (curve 1) the function $f_1(E, E_n)$ simulated in the form of a step function with a smoothed edge and (curve 2) the function $f_1(E, E_n) = P_{fA-1}(U = E_n - E)$ [see (19)]. If one disregards the tunnel penetrability of the fission barrier, the threshold for the relevant $(n, n'f)$ reaction cuts off the spectrum $d\sigma_{n1}(E, E_n)/dE$ of first neutrons (Fig. 2c) at the secondary-neutron energy $E =$

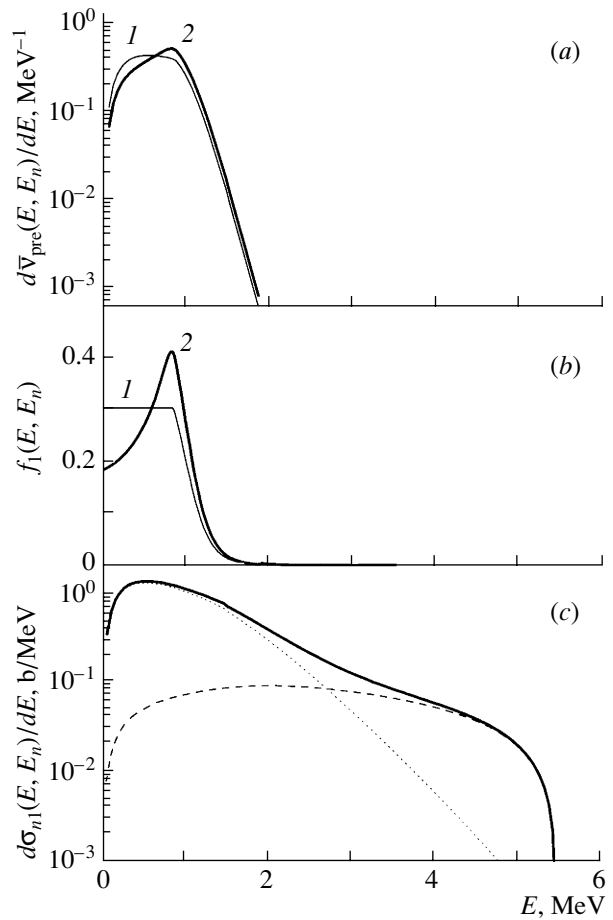


Fig. 2. (a) Spectrum of prefission neutrons at $E_n = 7$ MeV according to our calculations for two versions of the cutoff function $f_1(E, E_n)$: (curve 1) that which is simulated in the form of a step function with a smoothed edge and (curve 2) that which is defined by (19); (b) cutoff function (the notation for the curves is identical to that in Fig. 2a); (c) spectrum of first neutrons (solid curve) and its components: (dotted curve) compound component and (dashed curve) preequilibrium component.

$E_1^{thr} = E_n - B_{fA-1}$. From Fig. 2, it can be seen that the spectrum of prefission neutrons (Fig. 2a) is determined primarily by the compound component of the spectrum of first neutrons (Fig. 2c). In this prefission-neutron spectrum, the fraction of preequilibrium neutrons of energy in the region $E \leq 1.5$ MeV is more than one order of magnitude less than the fraction of the compound component.

Various versions of the description of the experimental data at $E_n = 6$ and 7 MeV in terms of expression (11)—that is, in terms of a linear combination of the contributions from post- and prefission neutrons [$d\bar{\nu}_{faf}(E, E_n)/dE$ (12) and $d\bar{\nu}_{pre}(E, E_n)/dE$ (17), respectively] for $x_{max}(E_n) = 1$ —are illustrated in Fig. 1, where the respective results are given in the form of the ratios $R(E, E_n)$. The mean yields $\bar{\nu}_i$ and

Calculated mean yields, mean energies (in MeV) for the components of the neutron spectra, and cross sections for individual chances (in barns)

Cutoff function	$\bar{\nu}$	$\bar{\nu}_{\text{faf}}$	$\bar{\nu}_{\text{pre}}$	\bar{E}	\bar{E}_{faf}	\bar{E}_{pre}	σ_{f239}	σ_{f238}	χ^2_N/N
$E_n = 6 \text{ MeV}$									
$f_1(E, E_n = 6 \text{ MeV})$	3.201	3.155	0.046	1.995	2.020	0.261	0.536*	0.026**	1.42
$f_1(E, E_n = 6.5 \text{ MeV})$	3.201	3.115	0.086	1.994	2.038	0.391	0.536*	0.051*	0.50
$E_n = 7 \text{ MeV}$									
$f_1(E, E_n = 7 \text{ MeV})$	3.374	2.980	0.394	1.861	2.018	0.676	0.582*	0.379*	1.16
Steplike f_1	3.374	2.980	0.394	1.859	2.026	0.600	0.582*	0.379*	2.07

Note: Given in the table are the mean yields and mean energies for ($\bar{\nu}_{\text{faf}}, \bar{E}_{\text{faf}}$) postfission neutrons from fully accelerated fragments and ($\bar{\nu}_{\text{pre}} = \sigma_{f238}/\sigma_f, \bar{E}_{\text{pre}}$) for prefission neutrons; also given are the sum $\bar{\nu} = \bar{\nu}_{\text{faf}} + \bar{\nu}_{\text{pre}}$ and the quantity \bar{E} determined according to (30) (see below).

* Values obtained from a description of the standard cross section for ^{238}U fission by means of its decomposition into individual chances.

** The second-chance-fission cross section σ_{f238} was obtained from the best fit to the fission-neutron spectrum with the cutoff function $f_1(E, E_n = 6 \text{ MeV})$.

the mean energies \bar{E}_i ($i = \text{faf, pre}$) for the components of the neutron spectra and the fission cross sections for various chances, σ_{fA-x} , are presented in the table for various versions of the calculation.

The best description of the experimental data at $E_n = 6 \text{ MeV}$ is achieved with the cutoff function $f_1(E, E_n) = P_{fA-1}(U = E_n - E)$ calculated at $E_n = 6.5 \text{ MeV}$ (and not at 6 MeV , as would be more natural). In this version of the calculation, the fission cross section $\sigma_f = \sigma_{f239} + \sigma_{f238}$ and its first- and second-chance components (σ_{f239} and σ_{f238} , respectively) were taken from a self-consistent description of the standard cross section for the fission of a ^{238}U target nucleus by means of its decomposition into individual chances [7]. In describing the experimental distribution $R(E, E_n)$ at $E_n = 6 \text{ MeV}$ with the relevant cutoff function $f_1(E, E_n = 6 \text{ MeV})$, the best fit to experimental data was obtained upon reducing the second-chance-fission cross section σ_{f238} nearly by a factor of 2 (see table). In Fig. 1, one can see that, for this version of the calculation, curve 1 does not lie in the region of experimental points at low energies ($E < 0.8 \text{ MeV}$). [For the presentation in Fig. 1 to be clearer, the soft sections of the spectra ($E \leq 2 \text{ MeV}$) at $E_n = 6$ and 7 MeV are shown on the left, while the spectra for the entire range of measured energies E are displayed on the right.] The calculated spectrum of prefission neutrons appears to be softer than the spectrum observed experimentally. The description of the spectrum with the function $f_1(E, E_n = 6.5 \text{ MeV})$ (solid curve in Fig. 1 for $E_n = 6 \text{ MeV}$) leads to satisfactory agreement with the experimental results.

In contrast to what we have in the case of $E_n = 6 \text{ MeV}$, the description of the experimental distribution $R(E, E_n)$ at 7 MeV with the relevant function $f_1(E, E_n = 7 \text{ MeV})$ reproduces the shape of the observed distribution over the entire range $E = 0.14\text{--}15 \text{ MeV}$ of measured energies (solid curve), this being indicative of an adequate interpretation of features that are associated with the emission of prefission neutrons. In the low-energy region ($E < 1.8 \text{ MeV}$), these features are especially pronounced against the background of a nearly linear dependence for postfission neutrons from fully accelerated fragments. Curve 2 in Fig. 1 for $E_n = 7 \text{ MeV}$ —it was calculated with the cutoff function in the form of a step whose edge is smoothed [a simplified version of the simulation of $f_1(E, E_n)$ —reproduces the shape of the spectrum somewhat worse in the energy region of prefission neutrons.

Additional experimental investigations are required for establishing the reason why the description with the relevant cutoff function $f_1(E, E_n = 6 \text{ MeV})$ is unable to reproduce experimental results at $E_n = 6 \text{ MeV}$. Detailed measurements and a detailed analysis of the fission-neutron spectrum on the two sides of the emission-fission threshold $E_n = B_{fA-1}$ —for example, over the range of primary-neutron energies E_n between 5.6 and 6.6 MeV with a step of $\Delta E = 0.2 \text{ MeV}$ —could contribute to clarifying this point. At energies in the region $E_n < B_{fA-1}$, the probability for a nucleus $A - 1$ (^{238}U) to undergo fission is determined by the tunnel penetrability, which is sensitive to the shape of the fission barrier. The distinction between the barrier shape used in the calculation and that which actually exists may be the reason why it

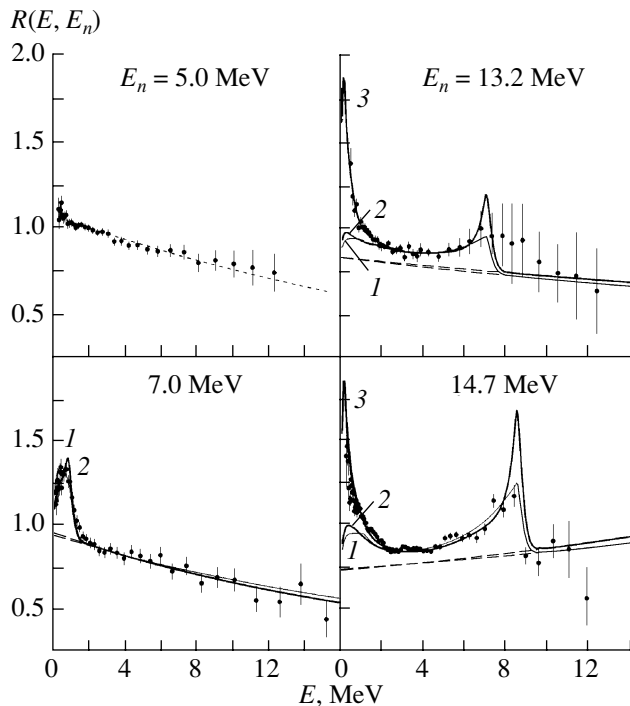


Fig. 3. Ratios $R(E, E_n)$ of the spectra of fission neutrons from the reaction $^{238}\text{U}(n, xn'f)$ to the spectrum of neutrons from the spontaneous fission of ^{252}Cf . The points represent experimental data. The solid curves 1 and 2 show the results of the calculation disregarding the contribution of neutrons from nonaccelerated fragments [see (11)] and employing (1) $f_i(E, E_n)$ in the form of a step function with a smoothed edge or (2) that taken according to (19); curve 3 corresponds to the calculation allowing for the contribution of neutrons from nonaccelerated fragments [see (25)] and employing $f_i(E, E_n)$ in the form (19). The dashed lines show the level of the postfission component.

is necessary to select $f_1(E, E_n)$. At $E_n = 7$ MeV, the excitation energy of the fissile nucleus $A - 1$ (^{238}U) is 1 MeV above the barrier height, with the result that the function $f_1(E, E_n)$ is virtually insensitive to the barrier shape. In principle, the true reason can be different, however.

Thus, we can see that, within the model of two sources, the experimental distributions of neutrons from the emission-fission process induced in ^{238}U target nuclei by incident neutrons of energy 6 or 7 MeV can be described in terms of relations (11). The change in the shape of the distribution of the neutron yield at low energies in relation to the shape of $R(E, E_n)$ at $E_n = 2.9$ and 5 MeV is adequately described by the contribution of prefission neutrons. A sharp decrease in the yield of prefission neutrons at higher energies E owing to the cutoff of the spectrum of first neutrons by the function $f_1(E, E_n)$ and

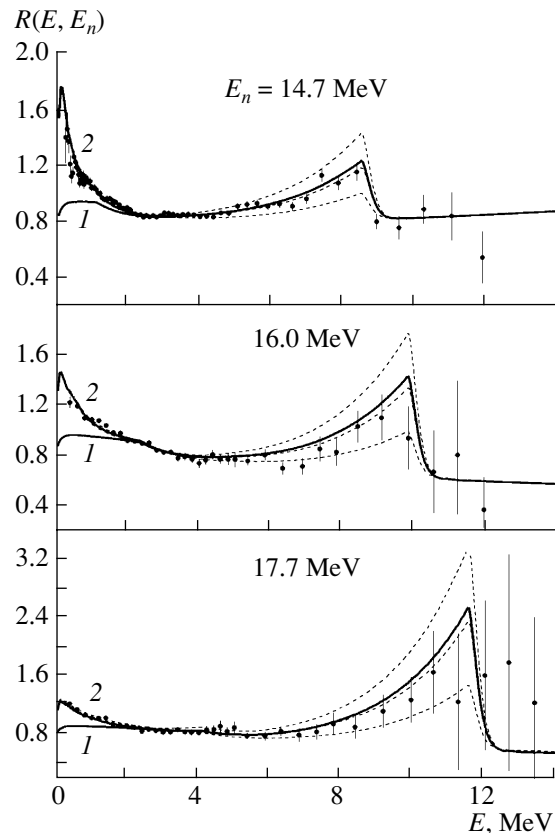


Fig. 4. Ratios $R(E, E_n)$ and their angular dependence. The points represent experimental data. The solid curves show the results of the calculation (1) without and (2) with allowance for the contribution of neutrons from nonaccelerated fragments [see Eqs. (11) and (25), respectively], the cutoff function $f_i(E, E_n)$ being parametrized in the form of a step function with a smoothed edge. The dashed curves were calculated for angles of (upper curve) 30° , (middle curve) 90° , and (lower curve) 150° .

the softness of their spectra in relation to the harder spectrum of postfission neutrons make it possible to observe it against the background of the postfission component in the measured dependences $R(E, E_n)$.

2.4. Features of the Shape of the Spectrum of Neutrons Accompanying Emission Fission for $E_n > 13$ MeV

The “family” of single-type distributions $R(E, E_n)$ for the emission fission of ^{238}U target nuclei that is induced by neutrons of energy $E_n = 13.2, 14.7, 16.0,$ and 17.7 MeV is displayed in Figs. 3 and 4. For the sake of comparison, the distributions $R(E, E_n)$ at $E_n = 5$ and 7 MeV are also presented in Fig. 3; the shape of the last two was discussed above (see Fig. 1). A detailed analysis of the shape of $R(E, E_n)$ for $E_n > 13$ MeV is given in [5, 7]. Here, we will dwell only on

its basic points in connection with the emergence of new experimental information at $E_n = 6$ and 7 MeV.

In the region $E_n > 13$ MeV, a manifestation of the cutoff of the spectrum of first neutrons by the threshold of the reaction $(n, n'f)$ at the energy $E = E_1^{\text{thr}} = E_n - B_{fA-1}$ is associated with the preequilibrium component of neutrons; at $E_n = 6$ and 7 MeV, this is associated with the compound (evaporation) component. If the spectrum of first neutrons for $E_n > 13$ MeV were of a purely evaporative origin, then the number of neutrons of such energy would be negligible at $E = E_1^{\text{thr}}$; for this reason and because of an exponential decrease in the yield of postfission neutrons with increasing E , the effect being discussed would not be observable. An admixture of a hard component (because of a nonequilibrium mechanism of the emission of first neutrons, the yield here being a few orders of magnitude higher than in the case of the evaporation mechanism) renders possible a visual observation of a sharp upper boundary and of a high-energy maximum that is associated with prefission neutrons. In accord with the results of a theoretical calculation that employed the exciton model of preequilibrium decay to describe the hard component of first neutrons, they are seen most clearly in the experimental distribution for $E_n = 14.7$ MeV (this distribution was measured to a fairly high statistical accuracy). From Figs. 3 and 4, it is obvious that, in response to a change in the bombarding-neutron energy E_n , the upper boundary and the maximum of prefission neutrons in the distribution are shifted on the energy scale according to the relation $E = E_1^{\text{thr}} = E_n - B_{fA-1}$, this corroborating the correctness of the present interpretation of the observed effect.

In contrast to what we have in the energy range $E_n = 7-10$ MeV, it is rather difficult to measure, at higher energies, the shape of the distribution $R(E, E_n)$ in the region of the high-energy maximum that is caused by the emission of prefission neutrons; the higher the energy E_n , the greater the difficulties to be overcome here because of low statistics and background conditions of the experiment. For $E_n = 13.2$ and 14.7 MeV, Fig. 3 illustrates the description of the data with the cutoff function simulated in the form of a step having a smoothed edge (curves 1) and with that which is defined in terms of the fission probability according to (19) (curves 2). For $E_n > 13$ MeV, the agreement between the calculated and measured values in comparing them in the region of the high-energy maximum associated with prefission neutrons is therefore qualitative rather than quantitative. An answer to the question of which of the two versions of the cutoff function $f_i(E, E_n)$ that are used in our calculations leads to better agreement with experimental data can be obtained more readily at lower

energies ($E_n = 7-10$ MeV). Previously, this was demonstrated in Subsection 2.3 for the example of the distribution $R(E, E_n)$ measured at $E_n = 7$ MeV. In our calculation, we did not introduce a correction for the smearing of the upper boundary of the function $f_i(E, E_n)$ due to the energy resolution; its inclusion would lead to the broadening of the high-energy maximum and to a decrease in its amplitude.

A second special feature that was first discovered in the spectra of neutrons accompanying the fission of actinide nuclei ^{232}Th , $^{235,238}\text{U}$, and ^{237}Np [1-4] that is induced by neutrons of energy $E_n = 14.7$ MeV is associated with an anomalously high yield of soft neutrons ($E < 2$ MeV) in experimental distributions as contrasted against the results of a theoretical description within the traditional approach that takes into account two sources of secondary neutrons. Measurements at different values of the primary-neutron energy—at $E_n = 13.2$ MeV [5] and 16.0, 17.7 MeV [6, 7] for ^{238}U target nuclei and at 14.6 and 17.7 MeV [8] for ^{232}Th target nuclei—confirmed the presence of such an excess in new experimental information. In Fig. 3, two versions of the description of the experimental distributions $R(E, E_n)$ for $E_n = 13.2$ and 14.7 MeV in terms of two neutron sources are shown by curves 1 and 2. In Fig. 4, the results of the calculation for 16.0 and 17.7 MeV in the version that employs $f_i(E, E_n)$ in the form of a step function are represented by curves 1. Thus, an analysis of the experimental distributions $R(E, E_n)$ within the two-source model leads to a contradictory situation. On one hand, the distribution $R(E, E_n)$ measured in the two-chance fission reaction at the primary-neutron energy of $E_n = 7$ MeV, which corresponds to the beginning of the second plateau in the fission cross section, has a shape that complies well with its calculated counterpart. On the other hand, an excess yield of soft neutrons ($E < 2$ MeV) in relation to theoretical results is observed in the experimental distribution $R(E, E_n)$ for the same two-chance reaction $E_n = 13.2$ MeV and in the distribution $R(E, E_n)$ measured for the three-chance reaction at 14.7, 16.0, and 17.7 MeV. It is natural to assume, in the energy range between 7 and 13.2 MeV, a third source that emits neutrons having a soft energy spectrum comes into play.

The statistical model taken in a conventional formulation disregards the possibility of particle emission during the evolution of the system from the saddle configuration to the scission point. As was indicated above, it is common practice to assume that this time is so short (in relation to particle-emission time) that no significant number of particles can be emitted within it. In principle, the observed excess in the distributions $R(E, E_n)$ at high values

of the primary-neutron energy E_n may be due to an increase in the lifetime of the system in the transition from the saddle to the scission point. The additional emission of particles alone would not result in the inapplicability of the relations of the statistical model that are used here and would not change the calculated partial cross sections σ_{fA-x} . The spectrum of additional neutrons can be calculated on the basis of the statistical model, but, within this model, it is difficult to determine thermal excitation energies in the process of a dynamical transition of the system from the saddle to the scission configuration. The problem can be simplified by reducing it to determining the spectrum of neutrons emitted by the system of fragments at the scission point that have already been formed. For example, the theoretical analysis of Brunner and Paul in [25], who studied the dinuclear system of fragments, made it possible to assess the mean kinetic energy of fragments as a function of the fragment-mass ratio, the resulting dependence being in surprisingly good agreement with experimental data. In considering neutron emission, it is necessary to assume that, in the system of fragments that have already been formed, there is statistical equilibrium with respect to all degrees of freedom, the lifetime of the system being such that the fragment A_i ($i = 1, 2$) can emit a neutron, provided that the fragment excitation energy satisfies the condition

$$E_{i0}^* = C(E_n + B_{nA}) \frac{A_i}{A} > B_{nA_i}. \quad (23)$$

The coefficient C indicates which fraction of the excitation energy $E^* = E_n + B_{nA}$ of the compound nucleus A was converted into the thermal excitation energy of the dinuclear system of already formed fragments at the instant of their separation.

Although a physical validation of the existence of a long-lived system of fragments that are in contact presents considerable difficulties, the spectrum of neutrons emitted from such a system of nonaccelerated fragments can be calculated on the basis of the statistical model. The result is [7]

$$\begin{aligned} \frac{d\bar{\nu}_{\text{naf}}(E, E_n)}{dE} &= \frac{\sigma_{fA}}{\sigma_f} \sum_{A_i} Y(A_i) \quad (24) \\ &\times \int_{E_{i0}^*} G(E_{i0}^*, \langle E_{i0}^* \rangle) \\ &\times \left[\sum_{Z_j} P(A_i, Z_j) N(E, A_i, Z_j, E_{i0}^*) \right] dE_{i0}^*, \end{aligned}$$

where $Y(A_i)$ is the mass distribution of fission fragments that is normalized to two; $G(E_{i0}^*, \langle E_{i0}^* \rangle)$ is the excitation-energy distribution normalized to unity;

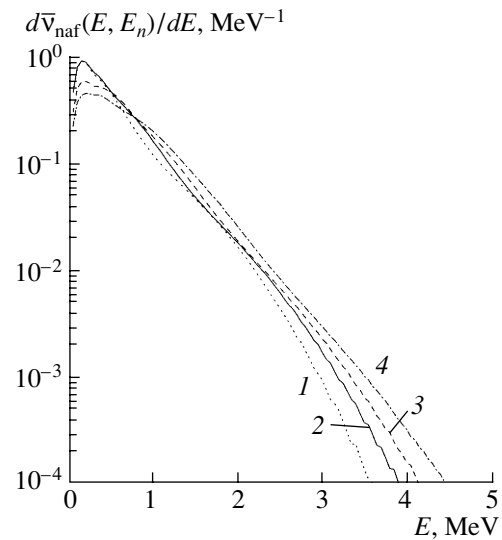


Fig. 5. Differential yield (24) of neutrons from nonaccelerated fragments produced in the fission of a ^{239}U compound nucleus at the primary-neutron energies of $E_n =$ (curve 1) 13.2, (2) 14.7, (3) 16.0, and (4) 17.7 MeV.

$P(A_i, Z_j)$ is the charge distribution of fixed- A_i fragments that is normalized to unity (as a rule, a few isobaric nuclei correspond to such fragments); and $N(E, A_i, Z_j, E_{i0}^*)$ is the spectrum of neutrons from fragments having fixed values of A_i , Z_j , and E_{i0}^* that is normalized to unity (for more details, see [7]). With allowance for the third neutron source in (24), the differential yield of fission neutrons can be represented in the form

$$\begin{aligned} \frac{d\bar{\nu}(E, E_n)}{dE} &= \frac{d\bar{\nu}_{\text{iai}}(E, E_n)}{dE} \quad (25) \\ &+ \frac{d\bar{\nu}_{\text{pre}}(E, E_n)}{dE} + \frac{d\bar{\nu}_{\text{naf}}(E, E_n)}{dE}. \end{aligned}$$

The first two terms in (25) are given by the same relations (12) and (17) as in the two-source model specified by Eq. (11). In describing the experimental distributions $R(E, E_n)$ for $E_n > 13$ MeV with allowance for all three neutron sources in (25), the coefficient C in (23) [recall that the hardness of the spectrum in (24) depends on this coefficient] was used as an adjustable parameter. For ^{238}U , satisfactory agreement between the measured and calculated distributions $R(E, E_n)$ at $E_n = 13.2, 14.7, 16.0,$ and 17.7 MeV over the entire range of energies E under study, including the low-energy region $E < 2$ MeV, can be obtained at a single value of the coefficient C , $C = 0.53$. The results obtained by describing the experimental values of $R(E, E_n)$ with allowance for all three sources are represented by curves 3 in Fig. 3 and by curves 2 in Fig. 4. For four values of E_n , the neutron spectra (24) from nonaccelerated frag-

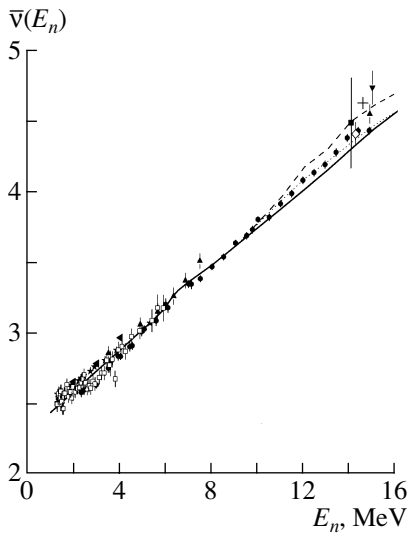


Fig. 6. Mean multiplicity of prompt neutrons from the neutron-induced fission of ^{238}U target nuclei as a function of the primary-neutron energy E_n . The displayed experimental values were borrowed from (●) [26], (■) [27], (▼) [28], (▲) [29], (◄) [30], (◇) [31], (□) [32], (★) [33], and (+) [34]. The solid curve in the region of emission fission ($E_n \geq 6$ MeV) represents the results of the calculation allowing two neutron sources. The dashed and dotted curves correspond to the calculation performed under the assumption of three neutron sources (see main body of the text).

ments produced in the fission of the compound nucleus $A = ^{239}\text{U}$ are given separately in Fig. 5.

3. ESTIMATING THE MEAN MULTIPLICITY $\bar{\nu}(E_n)$ AND THE MEAN ENERGY $\bar{E}(E_n)$ OF NEUTRONS FROM ^{238}U FISSION INDUCED BY FAST NEUTRONS VERSUS THEIR PRIMARY ENERGY E_n

3.1. Mean Multiplicity of Neutrons

Since there is presently no experimental information about the distributions $R(E, E_n)$ for energies in the range $7 < E_n < 13.2$ MeV, we are unable to establish the exact value of the threshold energy $E_n^{\text{thr}3}$ above which a third source of neutrons having a soft spectrum comes into play. An attempt can be made to estimate $E_n^{\text{thr}3}$ by invoking the mean neutron multiplicity $\bar{\nu}(E_n)$ per fission event, which is an integrated feature of the fission process. Unfortunately, there is only one experimental study, that reported in [26], where the dependence $\bar{\nu}(E_n)$ was measured over the energy range $E_n = 7\text{--}13$ MeV, which is of interest for our purposes. The overwhelming majority of the experiments devoted to determining $\bar{\nu}(E_n)$ were performed at primary-neutron energies below 7 MeV and in the vicinity of the value of 14 MeV. For ^{238}U

target nuclei, Fig. 6 displays a sample of experimental data on $\bar{\nu}(E_n)$ [26–34] measured up to an energy of $E_n = 15$ MeV.

The integrated counterpart of the differential relation (11) has the form

$$\bar{\nu}(E_n) = \bar{\nu}_{\text{iaf}}(E_n) + \bar{\nu}_{\text{pre}}(E_n). \quad (26)$$

In expression (26), which determines the mean multiplicity of neutrons per fission event under the assumption of two neutron sources, the first term

$$\bar{\nu}_{\text{iaf}}(E_n) = \sum_{x=0}^{x_{\text{max}}(E_n)} \bar{\nu}_{fA-x}(\bar{E}_{nx}) \frac{\sigma_{fA-x}(E_n)}{\sigma_f(E_n)} \quad (27)$$

determines the mean multiplicity of postfission neutrons from fully accelerated fragments, while the second term

$$\begin{aligned} \bar{\nu}_{\text{pre}}(E_n) &= \sum_{x=1}^{x_{\text{max}}(E_n)} x \frac{\sigma_{fA-x}(E_n)}{\sigma_f(E_n)} \quad (28) \\ &= \sum_{x=0}^{x_{\text{max}}(E_n)} x \frac{\sigma_{fA-x}(E_n)}{\sigma_f(E_n)} \end{aligned}$$

represents that for prefission neutrons.

For the one-chance (n, f) reaction [$E_n < B_{fA-1} \approx 6$ MeV, $x_{\text{max}}(E_n) = 0$], we must set $\bar{\nu}_{\text{pre}}(E_n) = 0$ in relation (26). In this case, the mean yield of neutrons is determined by neutron emission from fully accelerated fragments produced in the fission of the nucleus A : $\bar{\nu}(E_n) = \bar{\nu}_{\text{iaf}}(E_n) = \bar{\nu}_{fA}(E_n)$.

The description of the observed feature $\bar{\nu}(E_n)$ is based on Howerton's systematics [22] [formula (15) above]. It is used to estimate the postfission-neutron yield $\bar{\nu}_{\text{iaf}}(E_n)$. In the energy region $E_n > B_{fA-1} \approx 6$ MeV of emission fission, the yield $\bar{\nu}_{\text{iaf}}(E_n)$ is supplemented with the prefission-neutron contribution $\bar{\nu}_{\text{pre}}(E_n)$. The quantities $\bar{\nu}_{\text{iaf}}(E_n)$ and $\bar{\nu}_{\text{pre}}(E_n)$ were calculated by using the cross sections σ_f and σ_{fA-x} obtained from the description of the standard cross section for ^{238}U fission and its decomposition into individual chances. The cross section for ^{238}U fission and its components are displayed in Fig. 7a.

In Fig. 6, the calculated mean multiplicity of neutrons per fission event as a function of the primary-neutron energy E_n is shown by the solid curve. A change in the slope of $\bar{\nu}(E_n)$ as a function of energy is clearly seen at $E_n = 6$ MeV, this structure being due to the prefission-neutron contribution that emerges as soon as the second source becomes operative. In the distribution $R(E, E_n)$ measured for $E_n = 6$ MeV, the soft spectrum of prefission neutrons ($E < 1$ MeV) stands out distinctly in Fig. 1 against the background of the hard postfission component.

Above 6 MeV, the experimental data and the values estimated on the basis of expression (26), which takes into account two neutron sources, agree up to $E_n = 9\text{--}9.5$ MeV. At still higher energies, the experimental values of $\bar{\nu}(E_n)$ lie somewhat above the calculated curve.

In Fig. 6, the dashed curve for $E_n > 9$ MeV represents the mean neutron multiplicity estimated according to the relation

$$\bar{\nu}(E_n) = \bar{\nu}_{\text{taf}}(E_n) + \bar{\nu}_{\text{pre}}(E_n) + \bar{\nu}_{\text{naf}}(E_n), \quad (29)$$

which takes into account the contribution $\bar{\nu}_{\text{naf}}(E_n)$ of neutrons from nonaccelerated fragments (third source). It can be seen that the calculated dashed curve goes somewhat higher than the experimental values quoted in [26]. In a close vicinity of the energy $E_n = 14$ MeV, where there is a set of data from different measurements, the estimate based on (29) agrees with the experimental results from [27, 29] and even lies below the values obtained in [28]. In principle, the system of nonaccelerated fragments can lose part of its thermal energy via gamma radiation. Assuming that the mean photon energy is $\bar{E}_\gamma = \bar{B}_{nA_i}/2$ and taking it into account in the total energy balance, we obtain an estimate of $\bar{\nu}(E_n)$ (dotted curve in Fig. 6), which agrees with experimental data from [26]. One can see that the experimental data reported in [26] for $\bar{\nu}(E_n)$ in the range $E_n = 7\text{--}14$ MeV (the only source of such information) are obviously insufficient for testing relations (26) and (29). On the basis of an analysis of the mean neutron multiplicity, the threshold energy $E_n^{\text{thr}3}$ above which there appears a third source of neutrons having a soft energy spectrum can be taken to be about 9 MeV for a first approximation. A more accurate estimate of $E_n^{\text{thr}3}$ can be obtained by additionally measuring and analyzing the distribution $R(E, E_n)$ in the energy range $E_n = 7\text{--}14$ MeV.

3.2. Mean-Energy of Fission Neutrons

For the ^{238}U target nucleus, the number of measured and analyzed distributions $R(E, E_n)$ for $E_n < 20$ MeV makes it possible to determine the dependence of the mean energy of fission neutrons on the primary-neutron energy E_n , $\bar{E}(E_n)$. It has the simplest form in the region of energies below the threshold for emission fission, $E_n < B_{fA-1} \approx 6$ MeV. Here, one can make use of the well-known systematics developed by Terrell [23], who proposed parametrizing the mean energy in the form (16). Within this systematics, three quantities E_n , Z , and A , which are of interest for the nuclear-fission process, are replaced by one quantity that is dependent on them—this is the mean yield of postfission neutrons from fully accelerated fragments. In Fig. 7b,

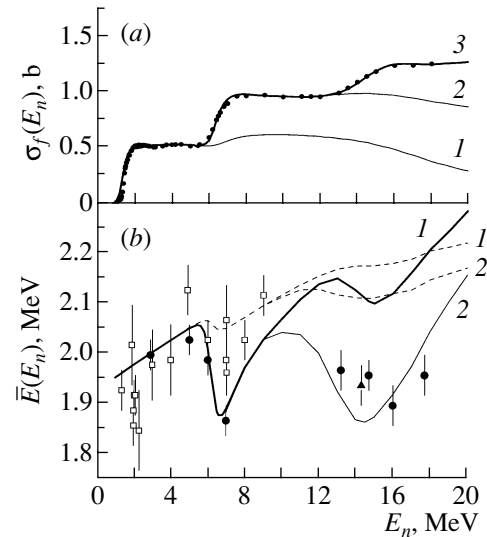


Fig. 7. (a) Cross section for ^{238}U fission. The points correspond to the standard values, while the calculated curves represent the cross sections (1) σ_{fA} , (2) $\sigma_{fA} + \sigma_{fA-1}$, and (3) $\sigma_{fA} + \sigma_{fA-1} + \sigma_{fA-2}$. (b) Mean energy of neutrons accompanying the fission of ^{238}U target nuclei as a function of the primary-neutron energy E_n . The points represent the experimental values (\bullet) for $E_n = 2.9$ MeV from [2], 5 MeV from [5], 6 and 7 MeV from the present study, 13.2 MeV from [5], 14.7 MeV from [2], and 16.0 and 17.7 MeV from [6]; (\blacktriangle) for $E_n = 14.3$ MeV from [36]; and (\square) for $E_n = 1.35\text{--}9$ MeV from [35]. The solid and dashed curves show the results of the calculations for, respectively, $\bar{E}(E_n)$ and $\bar{E}_{\text{taf}}(E_n)$ with allowance for (curves 1) two and (curves 2) three neutron sources.

one can see that, in the energy region of the first plateau of the fission cross section ($E_n < 6$ MeV), the mean energy $\bar{E}(E_n)$ increases monotonically with increasing E_n . Our experimental values of $\bar{E}(E_n)$, as determined from the fission-neutron spectrum $N(E, E_n) = R(E, E_n)N_{\text{Cf}}(E)$ measured at $E_n = 2.9$ and 5 MeV, comply well with the systematics specified by Eq. (16). The experimental values taken from [35] and from other earlier studies are characterized by large uncertainties and are widely scattered around the calculated curve.

The prefission-neutron component appears above the threshold for emission fission—for example, in the distributions measured at $E_n = 6$ and 7 MeV (see Fig. 1). In this case, the fission-neutron energy averaged over the two-component spectrum (11) is given by the expression

$$\bar{E}(E_n) = (\bar{\nu}_{\text{taf}}(E_n)\bar{E}_{\text{taf}}(E_n) + \bar{\nu}_{\text{pre}}(E_n)\bar{E}_{\text{pre}}(E_n))/\bar{\nu}(E_n), \quad (30)$$

which is represented by the solid curve 1 in Fig. 7b. The dashed curve 1 shows the primary-neutron-energy dependence of the mean energy for the post-

fission component (neutrons from fully accelerated fragments), $\bar{E}_{\text{fai}}(E_n)$. Upon going over from the primary-neutron energy E_n of 5.8 to 7 MeV, the second source of neutrons (prefission ones) becomes operative, which is manifested in a sharp decrease in $\bar{E}(E_n)$, this corresponding to a transition from the first to the second plateau in the fission cross section (see Fig. 7a). Concurrently, the mean prefission-neutron yield $\bar{\nu}_{\text{pre}}(E_n) = \sigma_{fA-1}(E_n)/\sigma_f(E_n)$ increases from zero to a maximum value. The mean energy $\bar{E}(E_n)$ (30) decreases because of the contribution of the soft prefission-neutron component, which is concentrated in the energy range $0 \leq E \leq E_n - B_{fA-1}$. A modest decrease in the mean energy $\bar{E}_{\text{fai}}(E_n)$ of postfission neutrons in this case is associated with the contribution of neutrons from fully accelerated fragments produced in second-chance fission—that is, the fission of ^{238}U nuclei. Within the second-plateau range $7 \leq E_n \leq 13$ MeV, the function $\bar{\nu}_{\text{pre}}(E_n)$ changes with energy only slightly. With increasing E_n , the mean energies of pre- and postfission neutrons [$\bar{E}_{\text{pre}}(E_n)$ and $\bar{E}_{\text{fai}}(E_n)$, respectively] grow. The dependence $\bar{E}(E_n)$ (solid curve 1 in Fig. 7b) reaches a maximum at 13 MeV (at the end of the second plateau). A second decrease in $\bar{E}(E_n)$, but with a smaller amplitude than in the range $5.8 \leq E_n \leq 7$ MeV, is observed in going over from the second to the third plateau in the fission cross section—that is, in the range $13 \leq E_n \leq 15$ MeV. In the region $E_n > 15$ MeV, the mean energy grows again. One can see that prefission-neutron emission, which generates new possibilities (chances) for fission complicates considerably the energy dependence of the mean energy of prompt fission neutrons in relation to the simple Terrell systematics for postfission neutrons as given by Eq. (16).

The systematics of $\bar{E}(E_n)$ as obtained within the traditional approach of two sources of neutrons [see Eq. (26)] accompanying the fission of actinide nuclei is in good agreement with our experimental data for $E_n = 6$ and 7 MeV,¹⁾ but it gives mean-energy values (solid curve 1 in Fig. 7b) that are much greater than their experimental counterparts for $E_n = 13.2$ [5], 14.3 [36], 14.7 [2], and 16.0, 17.7 MeV [6].

In Fig. 7b, the solid curve 2 represents the mean energy

$$\bar{E}(E_n) = (\bar{\nu}_{\text{fai}}(E_n)\bar{E}_{\text{fai}}(E_n) + \bar{\nu}_{\text{pre}}(E_n)\bar{E}_{\text{pre}}(E_n)) \quad (31)$$

¹⁾The experimental values of $\bar{E}(E_n)$ for $E_n = 7, 8,$ and 9 MeV from other studies were obtained in terms of temperature [see Eq. (6)] determined by using that section of the spectrum where there are no prefission neutrons. These values must be compared with the estimate of the mean energy for the postfission component (dashed curve 2 in Fig. 7b).

$$+ \bar{\nu}_{\text{fai}}(E_n)\bar{E}_{\text{fai}}(E_n))/\bar{\nu}(E_n),$$

which was estimated with allowance for the contribution of neutrons from nonaccelerated fragments. Owing to the fact that the third source of neutrons having a soft spectrum [see Eq. (24)] is operative in the primary-neutron-energy region $E_n > E_n^{\text{thr3}} = 9$ MeV, the mean energy there is lower than that which is given by (30) (solid curve 1). In this case, the experimental data for $E_n > 13$ MeV in Fig. 7b lie rather close to the calculated solid curve 2. Because of the loss of thermal energy via neutron emission from the system of nonaccelerated fragments, the mean energy $\bar{E}_{\text{fai}}(E_n)$ of postfission neutrons from fully accelerated fragments in (31) (dashed curve 2) will be somewhat less than that in the case of (30) (dashed curve 1).

4. ANGULAR DEPENDENCE OF FISSION-NEUTRON SPECTRA

Our experiment consisted in directly measuring the ratios $R(E, E_n)$ at an angle of $\vartheta = 90^\circ$ with respect to the momentum of primary neutrons [1, 2]. This corresponds to the double-differential neutron yield $d^2\bar{\nu}(E, E_n, \vartheta)/dEd\Omega$. In analyzing experimental information, the quantity

$$N(E, E_n, \vartheta) = 4\pi \frac{d^2\bar{\nu}(E, E_n, \vartheta)}{dEd\Omega} / \bar{\nu}(E_n) \quad (32)$$

for the angle $\vartheta = 90^\circ$ was taken for an integrated yield of fission neutrons. The experimental spectrum in (32) may be different from the actual spectrum that is obtained upon integration over the solid angle,

$$\begin{aligned} \tilde{N}(E, E_n) & \quad (33) \\ &= 2\pi \int_0^{2\pi} \frac{d^2\bar{\nu}(E, E_n, \vartheta)}{dEd\Omega} d(\cos \vartheta) / \bar{\nu}(E_n), \end{aligned}$$

since it is rather difficult to obtain a complete set of data on the spectrum $d^2\bar{\nu}(E, E_n, \vartheta)/dEd\Omega$ at different angles. First, this would consume much time. (A measurement of the fission-neutron spectrum at one angle to an acceptable statistical accuracy takes about a month of continuous accelerator operation.) Second, unacceptable background conditions at forward angles ($\vartheta \leq 60^\circ$) give no way to obtain reliable experimental information there.

At different angles ϑ , the change in the spectrum given by (32) in relation to the spectrum in (33) integrated with respect to angles can be estimated as follows. Under the assumption of two sources, we represent the double-differential yield of fission neutrons as the sum of three components; that is,

$$\frac{d^2\bar{\nu}(E, E_n, \vartheta)}{dEd\Omega} = \frac{d^2\bar{\nu}_{\text{fai}}(E, E_n, \vartheta)}{dEd\Omega} \quad (34)$$

$$+ \frac{d^2 \bar{\nu}_{\text{pre}}^{\text{com}}(E, E_n, \vartheta)}{dE d\Omega} + \frac{d^2 \bar{\nu}_{\text{pre}}^{\text{dir}}(E, E_n, \vartheta)}{dE d\Omega}.$$

The first term in (34) determines the yield of post-fission neutrons, which are directly related to the energy released upon the disintegration of fully accelerated fragments. Since all directions along which fission fragments may fly apart are equiprobable in the laboratory frame, the angular distribution of neutrons is isotropic there, so that expressions (32) and (33) yield the same integrated postfission-neutron spectrum, $N_{\text{fai}}(E, E_n, \vartheta) = \tilde{N}_{\text{fai}}(E, E_n)$. The same is true for the angular distribution of neutrons emitted from nonaccelerated fragments. In describing experimental distributions, this, third, source of neutrons is included to match the calculated and measured results in the low-energy region $E < 2$ MeV (curve 3 in Fig. 3 and curve 2 in Fig. 4). In emission fission ($E_n > B_{fA-1}$), the angular distribution of the compound component of pfission neutrons [second term in (34)] in the primary-neutron-energy region $E_n < 20$ MeV, which is studied here, is nearly isotropic, so that $N_{\text{pre}}^{\text{com}}(E, E_n, \vartheta) = \tilde{N}_{\text{pre}}^{\text{com}}(E, E_n)$.

The anisotropic component in the angular distribution of neutrons accompanying emission fission is due to the contribution of the prompt (nonequilibrium) mechanism of the emission of first neutrons, whose angular distribution

$$\frac{d\bar{\nu}_{\text{pre}}^{\text{dir}}(\vartheta)}{d\Omega} = \int_E \frac{d^2 \nu_{\text{pre}}^{\text{dir}}(E, E_n, \vartheta)}{dE d\Omega} dE \quad (35)$$

is stretched in the forward direction (the yield is maximal at an angle of $\vartheta = 0^\circ$ and is minimal at an angle of 180°).

The exciton model of preequilibrium decay has been successfully used to simulate the integrated (over a solid angle of 4π) spectrum of secondary particles emitted upon the multistep direct interaction of a bombarding particle with target nuclei in various (n, n') , (p, n) , (p, p') , etc., reactions, but it cannot predict the angular dependence of the yield of emitted particles. The general idea behind the treatment of multistep statistical and multistep compound processes can be used in a phenomenological approach to parametrize the angular dependence of the cross section for the emission of secondary particles within the exciton model and traditional statistical theory as [37]

$$\frac{d^2 \sigma(E, \vartheta)}{dE d\Omega} = \frac{1}{4\pi} \left[\frac{d\sigma_{\text{preeq}}}{dE} \sum_{l=0}^{l_{\text{max}}} b_l P_l(\cos \vartheta) + \frac{d\sigma_{\text{com}}}{dE} \sum_{\substack{l=0 \\ \Delta l=2}}^{l_{\text{max}}} b_l P_l(\cos \vartheta) \right], \quad (36)$$

where $d\sigma_{\text{preeq}}/dE$ and $d\sigma_{\text{com}}/dE$ are, respectively, the preequilibrium and the compound spectrum within a solid angle of 4π , while $P_l(\cos \vartheta)$ are Legendre polynomials. In [37], it was proposed to take the coefficients b_l in the general form

$$b_l = \frac{2l + 1}{1 + \exp[A_l(B_l - E)]} \quad (37)$$

by analogy with the weighted penetrability factors for a parabolic barrier. This resulted in deriving the systematics

$$A_l = k_1 + k_2 [l(l + 1)]^{m_1/2}, \quad (38)$$

$$B_l = k_3 + k_4 [l(l + 1)]^{m_2/2},$$

where m_i are integers. A fit to experimental data on (p, p') reactions yields

$$A_l = 0.036 \text{ MeV}^{-1} \quad (39)$$

$$+ l(l + 1) \times 0.0039 \text{ MeV}^{-1},$$

$$B_l = 92 \text{ MeV} - [l(l + 1)]^{-1/2} \times 90 \text{ MeV}.$$

In [37], the proposed angular dependence was tested by using the experimental angular distributions measured for secondary particles $b = n, p, d, t, {}^3\text{He}$, and ${}^4\text{He}$ over the energy range $E_b = 4\text{--}60$ MeV in $A(a, b)$ reactions for a broad range of nuclei from $A = {}^{12}\text{C}$ to ${}^{232}\text{Th}$ and bombarding particles $a = p, d, {}^3\text{He}$, and ${}^4\text{He}$ of energy in the interval $E_a = 18\text{--}80$ MeV. It was found that the above semiempirical parametrization has a high predictive power. This makes it possible to estimate the double-differential cross sections (yields) (36) for secondary particles by combining the systematics of angular distributions from [37] with the existing models of preequilibrium decay and with statistical theory.

Such an estimate of the angular dependence of the spectra of neutrons accompanying the spontaneous fission of ²³⁸U nuclei that is induced by neutrons of energy $E_n = 14.7, 16.0, \text{ and } 17.7$ MeV is given in Fig. 4 in the form of the ratio of the spectrum in (33) under study for three angles of $30^\circ, 90^\circ, \text{ and } 150^\circ$ to the spectrum for the spontaneous fission of ²⁵²Cf (respectively, the upper, the middle, and the lower dashed curve). It can be seen that the middle dashed curve corresponding to the calculated spectrum (32) for an angle of 90° and the solid curve corresponding to the calculated spectrum (33), which is integrated with respect to angles, differ only slightly and only at the end of the ascent toward the apex in the hard section of the distributions. The experimental fission-neutron spectrum (32) taken over a solid angle of 4π and obtained from a measurement at an angle of $\vartheta =$

90° can be refined by multiplying it by the calculated correction factor

$$\eta(E) = \tilde{N}(E, E_n)/N(E, E_n, \vartheta = 90^\circ). \quad (40)$$

The maximum value of this factor is $\max[\eta(E)] = 1.04$ for $E_n = 14.7$ MeV and 1.10 for 17.7 MeV.

CONCLUSION

The ratios $R(E, E_n)$ of the spectra of prompt neutrons originating from the neutron-induced fission of ^{238}U to the spectrum of neutrons from the spontaneous fission of ^{252}Cf have been measured over the range of secondary-neutron energies between 0.14 and 15 MeV, the energy of bombarding neutrons being either at the emission-fission threshold, $E_n = 6$ MeV, or somewhat above, $E_n = 7$ MeV.

The shape of the observed energy distributions has been reproduced by the calculations based on the traditional approach of two neutron sources in emission fission, this indicating that interpretations in terms of the emission of prefission neutrons are correct.

At the same time, the investigation of the spectra of prompt neutrons from ^{238}U fission induced by neutrons of energy $E_n = 13.2, 14.7, 16.0,$ and 17.7 MeV revealed that, in the low-energy section ($E < 2$ MeV), the shape of the experimental distributions cannot be reproduced within the same model of two sources.

The values of $E_n = 7$ and 13.2 MeV belong to the same energy region, that of the two-chance fission reaction, and correspond to the beginning and the end of the second plateau in the fission cross section. The calculated shape of the fission-neutron distribution for the first energy value is consistent with its experimental counterpart, while that for the second one is not. At the energy of $E_n = 13.2$ MeV and above, there is an excess yield of soft neutrons (those of energy in the region $E < 2$ MeV) in the experimental distributions in relation to the results of the calculations. This discrepancy can be removed by introducing, at an energy between 7 and 13.2 MeV ($E_n \simeq 9$ MeV according to a rough estimation), a third source that produces neutrons having a soft spectrum. In explaining the shape of the energy distributions observed for $E_n > 13.2$ MeV in the low-energy region $E < 2$ MeV, the assumption that the third source is associated with neutron emission from nonaccelerated fragments has led to encouraging results.

In the case of emission fission, the systematics of the mean energies of prompt fission neutrons that is based on the relations of the traditional model assuming that there are two sources of neutrons complies with experimental data on $\bar{E}(E_n)$ for $E_n = 6$ and 7 MeV, but it leads to values exceeding experimental

data for $E_n > 13.2$ MeV. By including, in the systematics of $\bar{E}(E_n)$ for $E_n > 9$ MeV, additional neutron emission from a third source that has a soft spectrum, one can reduce the calculated values of the mean energy to a level of their experimental counterparts.

Measurements and analysis of the spectra of prompt fission neutrons at primary-neutron energies in the range $E_n = 8\text{--}13$ MeV are of considerable interest for precisely determining the threshold energy above which the contribution from a third source appears in experimental distributions.

REFERENCES

1. G. S. Boykov, V. D. Dmitriev, G. A. Kudyaev, *et al.*, *Z. Phys. A* **340**, 79 (1991).
2. G. S. Boikov, V. D. Dmitriev, G. A. Kudyaev, *et al.*, *Yad. Fiz.* **53**, 628 (1991) [*Sov. J. Nucl. Phys.* **53**, 392 (1991)].
3. G. S. Boikov, V. D. Dmitriev, M. I. Svirin, and G. N. Smirenkin, *Yad. Fiz.* **57**, 2126 (1994) [*Phys. At. Nucl.* **57**, 2047 (1994)].
4. G. S. Boykov, V. D. Dmitriev, G. A. Kudyaev, *et al.*, *Ann. Nucl. Energy* **21**, 585 (1994).
5. A. M. Trufanov, G. N. Lovchikova, M. I. Svirin, *et al.*, *Yad. Fiz.* **64**, 3 (2001) [*Phys. At. Nucl.* **64**, 1 (2001)].
6. G. N. Smirenkin, G. N. Lovchikova, A. M. Trufanov, *et al.*, *Yad. Fiz.* **59**, 1934 (1996) [*Phys. At. Nucl.* **59**, 1865 (1996)].
7. M. I. Svirin, G. N. Lovchikova, and A. M. Trufanov, *Yad. Fiz.* **60**, 818 (1997) [*Phys. At. Nucl.* **60**, 727 (1997)].
8. G. N. Lovchikova, A. M. Trufanov, M. I. Svirin, and V. A. Vinogradov, *Yad. Fiz.* **67**, 914 (2004) [*Phys. At. Nucl.* **67**, 890 (2004)].
9. G. N. Lovchikova, A. M. Trufanov, M. I. Svirin, *et al.*, in *Proceedings of the XIV International Workshop on Nuclear Fission Physics, Obninsk, 1998* (Obninsk, 2000), p. 72.
10. N. I. Fetisov, S. P. Simakov, A. M. Trufanov, *et al.*, *Prib. Tekh. Éksp.*, No. 6, 22 (1980).
11. G. N. Lovchikova, O. A. Salmikov, S. P. Simakov, *et al.*, IAEA-TECDOC-410 (IAEA, Vienna, 1987), p. 290.
12. V. A. Talalaev, S. P. Simakov, *et al.*, *Acta Universitatis Debreceniensis* (1991), p. 13.
13. V. G. Demenkov, V. S. Nesterenko, A. M. Trufanov, *et al.*, Preprint No. 2013, FÉI (Inst. Phys. Power Eng., Obninsk, 1989).
14. K. J. Le Couteur and D. W. Lang, *Nucl. Phys.* **13**, 32 (1959).
15. C. Budtz-Jørgensen and H.-H. Knitter, *Nucl. Phys. A* **490**, 307 (1988).
16. H. Marten, D. Richter, D. Seeliger, *et al.*, *Nucl. Instrum. Methods Phys. Res. A* **264**, 375 (1988).
17. M. V. Blinov, N. M. Kazarinov, A. N. Protopopov, *et al.*, *Zh. Éksp. Teor. Fiz.* **42**, 1017 (1962) [*Sov. Phys. JETP* **15**, 704 (1962)].
18. M. S. Samant, R. P. Anand, R. K. Choudhury, *et al.*, INDC(NDS)-251 (IAEA, Vienna, 1991), p. 95.

19. W. Mannhart, IAEA-TECDOC-410 (IAEA, Vienna, 1987), p. 158.
20. *Nuclear Data Standards for Nuclear Measurements*, NEANDC-311 "U," INDC(SEC)-101 (OECD, Paris, 1992).
21. G. N. Lovchikova, G. N. Smirenkin, A. M. Trufanov, *et al.*, *Yad. Fiz.* **62**, 1551 (1999) [*Phys. At. Nucl.* **62**, 1460 (1999)].
22. R. J. Howerton, *Nucl. Sci. Eng.* **62**, 438 (1977).
23. J. Terrell, *Phys. Rev.* **113**, 527 (1959).
24. J. Terrell, in *Proceedings of the Symposium on Physics and Chemistry of Fission, Salzburg, 1965* (IAEA, Vienna, 1965), Vol. II, p. 3.
25. W. Brunner and H. Paul, *Physics of Nuclear Fission* (Gosatomizdat, Moscow, 1963).
26. J. Frehaut, G. Mosinski, and M. Soleilhac, EXFOR-II/ACCESS-97, IAEA, V-0.6B-Test March-2000.
27. N. N. Flerov and V. N. Talyzin, *At. Énergiya* **5**, 653 (1958).
28. H. Conde and N. Starfelt, *Nucl. Sci. Eng.* **11**, 397 (1961).
29. I. Asplund-Nilsson, H. Conde, and N. Starfelt, *Nucl. Sci. Eng.* **20**, 527 (1964).
30. D. S. Mather, P. Fieldhouse, and A. Moat, *Nucl. Phys.* **66**, 149 (1965).
31. P. Fieldhouse, E. R. Culliford, D. S. Mather, *et al.*, *J. Nucl. Energy* **20**, 549 (1966).
32. M. V. Savin, Yu. A. Khokhlov, I. N. Paramonova, *et al.*, *At. Énergiya* **32**, 408 (1972).
33. V. G. Vorob'eva, N. P. D'yachenko, B. D. Kuz'minov, *et al.*, *Vestn. At. Nauki Tekh., Ser. Yad. Konst.*, No. 15, 3 (1974).
34. H. Yamamota, Y. Mori, Y. Wakuta, *et al.*, *J. Nucl. Sci. Tech.* **16**, 779 (1979).
35. I. Doring, H. Marten, A. Ruben, and D. Seeliger, INDC(NDS)-251/L (IAEA, Vienna, 1991), p. 159.
36. Yu. A. Vasil'ev, Yu. S. Zamyatnin, E. I. Sirotinin, *et al.*, *Physics of Nuclear Fission* (Gosatomizdat, Moscow, 1962), p. 121 [in Russian]; Yu. A. Vasil'ev, Yu. S. Zamyatnin, Yu. A. Il'in, *et al.*, *Zh. Éksp. Teor. Fiz.* **38**, 671 (1960) [*Sov. Phys. JETP* **11**, 483 (1960)].
37. C. Kalbach and F. M. Mann, *Phys. Rev. C* **23**, 112 (1981).

Translated by A. Isaakyan

Scission Neutrons in the General Systematics of the Yields of Light Particles from Ternary Nuclear Fission

G. V. Val'sky*

Petersburg Nuclear Physics Institute, Russian Academy of Sciences, Gatchina, 188350 Russia

Received February 5, 2003; in final form, July 17, 2003

Abstract—An interpolation formula that was previously obtained on the basis of a statistical approach is applied to experimental data quoted in the literature over the past few years for light-particle yields from the ternary fission of nuclei. Arguments are adduced in favor of this approach, and an analysis of errors inherent in it is given. Tables are presented in which experimental light-particle yields for eight cases of fission are given along with those that were obtained from the interpolation formula. The applicability of this formula to estimating the yields of so-called scission neutrons is analyzed. © 2004 MAIK “Nauka/Interperiodica”.

INTRODUCTION

The first systematic measurements of the yields of light nuclides from ternary nuclear fission induced by thermal neutrons were performed in 1969–1975 at the Leningrad Nuclear Physics Institute (presently Petersburg Nuclear Physics Institute) by a group of researchers headed by A.A. Vorobyov [1–4]. This group explored the ternary fission of ^{233}U , ^{235}U , ^{239}Pu , and ^{242m}Am nuclei that was induced by thermal neutrons. The measurements in those studies were performed with the aid of a magnetic time-of-flight mass spectrometer (MTOFMS) installed in a horizontal channel of a PWR-M reactor. For the case of the spontaneously fissile nucleus ^{252}Cf , the measurements had been performed since 1967 by means of a ΔE – E telescope (see, for example, [5]). That method of investigations, which, of course, has a lower potential than the MTOFMS method, is advantageous in that it is characterized by a high efficiency of particle detection in the case of relatively weak sources of spontaneous fission.

Over the past few years, the yields of light particles in ternary fission have intensively been studied with the aid of the Lohengrin mass separator at the Laue–Langevin Institute (Grenoble, France). In addition to the aforementioned cases, the ternary fission of ^{229}Th [6], ^{241}Pu [7], ^{245}Cm [7, 8], and ^{249}Cf [9] nuclei that is induced by thermal neutrons was explored there among other things. High neutron fluxes from the Grenoble reactor and high qualities of the Lohengrin mass separator made it possible to reach, in some cases, silicon isotopes in measuring the yields in question. Thus, a vast body of experimental data

on the yields and energy spectra of “third” particles has been accumulated at the present time.

Attempts at describing the yields of light nuclei in ternary fission in terms of a single mathematical expression that would reflect, at the same time, the physics behind the phenomenon being studied have been made many times (see, for example, [10–14]). A survey of basic models used in calculating the yields and spectra of particles originating from ternary fission is given in [7]. None of the formulas for describing the yields in question was derived on the basis of underlying principles of quantum mechanics. As a matter of fact, the ternary-fission process is treated in terms of classical mechanics, the quantum-mechanical features of this process being in the background. The formulas used are semiempirical and involve parameters that are determined from experimental data. In the course of the fission process, a fissile system passes through a state in which the production of a third particle requires minimum expenditures of energy. A state where three fission fragments have already undergone separation but still have quite modest initial velocities is considered in the majority of ternary-fission models as an input state for trajectory calculations. A comparison of the ultimate results obtained in such calculations for the angular and energy distributions of third fragments with respective distributions found from experiments makes it possible to correct the choice of input configuration. The difference of the energies of the input configurations for different versions of ternary fission permits applying the methods of statistical physics to estimating the relative yields of different third particles.

We will dwell at some length on the approach adopted in [11], where it is assumed that the problem

* e-mail: pleva@npni.spb.ru

of yields from ternary fission can be solved on the basis of applying general principles of statistical physics to the emission of light nuclides in the ternary fission of nuclei without invoking any parameters that determine a specific configuration at the instant of scission.

1. PARTICLE YIELDS IN TERNARY FISSION IN TERMS OF STATISTICAL PHYSICS

Upon passing the saddle point owing to a decrease in the potential energy at the initial stage, a fissile nucleus, which is a complex system, begins a collective motion toward scission, simultaneously evolving, according to the laws of statistical physics, toward an increase in the density of its possible quantum states—that is, toward an increase in the internal excitation. Upon scission, the excitation energy of fragments is removed by neutron and photon emission. In much more rare cases, moving fragments may emit an alpha particle or a proton (so-called polar emission).

As to the emission of a third particle in the “scission” of the nucleus undergoing fission, the prevalent concept is that, in the fission process, the configuration of the nucleus passes through the stage within which two main fragments that have not yet undergone separation are connected by a comparatively thin neck formed by a few nucleons. It is precisely the place where particle fluxes associated with the formation of stationary nucleon orbits in would-be fragments have the highest density and where the collective energy of the fluxes can go over with the highest probability to the excitation energy of individual quasiparticles, increasing the temperature in the region of the neck. The “thermal emission” of neutrons, alpha particles, and other light nuclei from this region of an elevated temperature becomes possible for a short time (less than 10^{-20} s). This emission is facilitated for a particle that, at the instant of separation—that is, at the saddle of the potential barrier surrounding the nucleus—possesses the lowest energy, thereby ensuring the highest level density in the residual nuclear system. A decrease in the density of quantum states in a system that has a rather large number of degrees of freedom and a rather high excitation energy is characterized by the factor $e^{-\Delta E/\Theta}$, where ΔE is the decrease in the energy of the residual system due to the arrival of the particle at the potential barrier and Θ is a temperature parameter. The main contribution to the energy ΔE that the emitted particle of mass number A and charge number Z removes from the fissile system comes from the sum of the separation energies of Z protons and $N = A - Z$ neutrons minus their binding energy in the particle. The Coulomb energy of the particle at the barrier makes a contribution of equally

great importance. We note that the increase in the kinetic energy of a charged light particle owing to its acceleration upon scission does not coincide with its Coulomb energy at the instant of scission because of the simultaneous motion of two main fragments. It is the Coulomb energy at the barrier top that affects the probability of the emission of one particle or another. The initial kinetic energy at the instant of separation has no effect on the relative probability of particle emission, since, according to statistical mechanics, it must be identical (and equal to 2Θ) for any particle, with the exception of two main fragments.

The above concepts served as a basis for attempts at deriving an interpolation formula that would make it possible to estimate as-yet-unknown integrated yields of some particles by using only data on the measured yields of other particles. In particular, such a formula could be applied to those nuclides for which a direct measurement of the yields is complicated for one reason or another. This refers not only to unstable nuclei—that is, to those that are able to decay in flight to lighter nuclides—but also to protons, for which yield measurements are impeded by the background associated, at least partly, with (n, p) , (d, p) , and (α, p) reactions on the structural elements of the instruments used, and, finally, to neutrons, for which it is difficult to measure yields against the background of neutrons from fully accelerated fragments. Such a formula was proposed in [11], and the first results obtained by applying it to experimental data were also presented there. As a matter of fact, this formula involves four parameters, whose values are to be determined from a comparison with experimental data. These are (see [11]) the proton work function ε_p taken, together with the proton energy, at the Coulomb barrier; the neutron work function ε_n ; a temperature parameter (Θ); and a scale parameter (η). For the sake of simplicity, it was assumed that the particle that removes energy from the original system does not possess internal degrees of freedom, since it would be necessary otherwise to include in the respective calculation the energy expended into them with allowance for the probability of their excitation. Since this probability is low in view of a large spacing between the ground and the first excited state in the majority of light nuclei, it was assumed that the use of the expression $2I + 1$, where I is the ground-state spin of the emitted light nuclide, for a statistical factor would not lead to significant errors.

Flaws in this approach to the ternary-fission phenomenon are obvious. First and foremost, we note that, in traditional applications of statistical physics, one deals with an equilibrium system characterized by a uniform distribution of energy over degrees of freedom. But in our case, the system being considered undergoes such quick variations that the energy

released in processes proceeding predominantly in the neck region hardly has time, before particle emission, to be distributed uniformly over the entire volume of the system and, accordingly, over degrees of freedom. Therefore, the temperature parameter Θ in the above formula may only have the meaning of a local temperature that characterizes the emission zone. (The approach being considered can be justified to some extent by considering that, on one hand, energy is continuously supplied to the emission zone owing to a decrease in the deformation energy and that, on the other hand, it is transferred from this zone to the region of lower energies in large fragments, whereby there arises some kind of a dynamical equilibrium.) Second, the assumption that the proton work function ε_p and the neutron work function ε_n remain unchanged irrespective of the number of nucleons separated from the system in the formation of the emitted particle underlies formula (1) from [11]. This property is inherent in a classical equilibrium system that consists of a "heat bath" having a high level density (and containing a large number of various particles interacting with one another) and a small "subsystem" (that is, a "gas" formed by emitted particles) that is in equilibrium with the heat bath. Concurrently, it is assumed that the exchange of nuclides between the two parts of the system can occur without inducing any changes in the parameters of the heat bath. In this case, ε_p and ε_n are constant quantities (proton and neutron "chemical" potentials). But our system is in fact only part of a fissile nucleus, where the number of nucleons is finite. It can hardly be expected that the second, the third, etc., neutron or proton would have the same work function as the first one. It is more probable that the work function of a specific nucleon depends on how many nucleons and which ones were separated within previous time intervals.

In view of the above comments, the applicability of the formulas proposed in [11] has a limited range. At least, it can be expected that the yields of particles having a rather large mass number would be overestimated, since, in this case, the reserve of our heat bath in energy and the number of particles approaches the limit beyond which it would be incorrect to treat Θ , ε_p , and ε_n as constant quantities, even approximately. This was confirmed in a comparison of the results of calculations based on the interpolation formula with experimental results.

In the review part of Köster's dissertation [7] (see pp. 35, 37, 38), a comparison of the results obtained by calculating light-particle yields in ternary fission on the basis of various models and experimental data is given in a graphical form. It was indicated there that all of these models reproduce quite correctly the yields of particles emitted with rather high intensities, but they describe poorly the yields of particles for

which the ratio N/Z deviates from the mean value strongly. For the example of ^{233}U and ^{235}U fission, it was shown that the model proposed in [11] reproduces fairly well the yields in the region of the lightest particles originating from ternary fission and, in contrast to other models, describes quite accurately a large jump of the yields of ^4He and ^3He ; however, it overestimates the yields in the region of high mass numbers significantly.

The next section of the present article is devoted to a detailed consideration of special features of the approach proposed in [11]. It is assumed that the advantages that this approach possesses in the region of the lightest particles will make it possible to assess neutron emission in the ternary-fission process.

2. ANALYSIS OF THE RESULTS OBTAINED BY PROCESSING EXPERIMENTAL DATA ON THE BASIS OF THE INTERPOLATION FORMULA

Tables 1–5 give experimental data from [1–3, 6–8, 15–23] and the results of fitting the interpolation formula to various sets of experimental data. Some of the results quoted here were already presented in a graphical form in [11]. In the tables, the symbol # labels those experimental data that were used in the equations for determining the parameters of the interpolation formula. Yields that do not possess a high reliability, since they were calculated for nuclides whose charge and mass numbers, Z and A , are far beyond the region where the parameters were determined, are enclosed in brackets (as a matter of fact, it is extrapolation rather than interpolation that was applied to these nuclides). The term "unstable" was used in the sense specified in the preceding section. In examining these tables, one can easily see that the result of fitting depends on the range (in A and Z) to which those light nuclei belong whose yields were used to derive equations for determining the parameters of the interpolation formula.

Two fits were constructed for the case of the fission process $^{233}\text{U}(n_{\text{th}}, f)$: one was based on data from [1] (Table 1), while the other was based on the same data supplemented with new data from [6] (Table 4). The first fit, in which use was made of the yields of nuclides belonging to the range from ^4He to ^9Be , is satisfactory for elements from hydrogen to beryllium, only the calculated yield of ^{10}Be being underestimated in relation to experimental data by a factor approximately equal to two. The fit quality is characterized by the criterion value of $\chi^2/(N - n) = 0.38$. (Here, $N = 6$ is the number of equations used and $n = 4$ is the number of parameters in the interpolation formula. The values of the agreement criterion are given in the last column of Table 6.) The second fit, in which use

Table 1. Comparison of experimental and interpolated yields of light nuclides in the ternary fission of nuclei (normalized to 10^4 nuclei of ^4He)

No.	Z	N	Nuclide	Unstable nuclides	$^{235}\text{U} + n_{\text{th}}$ [2]		$^{233}\text{U} + n_{\text{th}}$ [1]	
					experiment	interpolation	experiment	interpolation
1	0	1	n		—	$[5.99(64) \times 10^6]$	—	$[2.13(37) \times 10^6]$
2	1	0	^1H		115(15)*	[160(17)]	—	[38(13)]
3	1	1	^2H		50(2)	[204(17)]	41(2)	[48(15)]
4	1	2	^3H		720(30)	[1920(90)]	460(20)	[630(130)]
5	2	1	^3He		<0.01	$2.87(57) \times 10^{-2}$	—	$5.8(24) \times 10^{-3}$
6	2	2	^4He		10 000(190)#	10 020(190)	10 000(270) #	10 000(270)
7	2	3	^5He	$^4\text{He} + n + 0.89 \text{ MeV}$	—	1980(45)	—	1500(60)
8	2	4	^6He		191(9)#	193(8)	137(7)#	140(70)
9	2	5	^7He	$^6\text{He} + n + 0.44 \text{ MeV}$	—	50.0(32)	—	28(3)
10	2	6	^8He		8.2(6)	8.0(7)	3.6(4)	4.6(5)
11	3	2	^5Li	$^4\text{He} + ^1\text{H} + 1.97 \text{ MeV}$	—	$2.4(5) \times 10^{-2}$	—	$11(3) \times 10^{-3}$
12	3	3	^6Li		0.05(2)	0.13(2)	—	$7.6(14) \times 10^{-2}$
13	3	4	^7Li		4.1(3)#	3.8(3)	3.7(2)#	3.6(2)
14	3	5	^8Li		1.8(3)#	2.0(1)	1.8(2)#	1.9(1)
15	3	6	^9Li		3.0(4)#	3.2(2)	3.6(5)#	3.4(3)
16	4	3	^7Be		$<10^{-2}$	$2.9(8) \times 10^{-5}$	$<10^{-2}$	$1.6(5) \times 10^{-5}$
17	4	4	^8Be	$2(^4\text{He}) + 0.092 \text{ MeV}$	0.5(2)**	1.2(1)	—	2.8(4)
18	4	5	^9Be		2.9(3)	1.5(1)	3.7(8)#	3.3(5)
19	4	6	^{10}Be		32(2)	6.1(3)	43(3)	19.7(53)
20	4	7	^{11}Be		2.0(3)#	1.53(9)	—	[4.3(11)]
21	4	8	^{12}Be		1.5(3)	0.76(6)	—	[2.1(5)]
22	5	5	^{10}B		<0.02	$0.96(19) \times 10^{-3}$	—	$[2.0(3) \times 10^{-3}]$
23	5	6	^{11}B		0.25(13)#	0.29(3)	—	[1.4(4)]
24	5	7	^{12}B		0.17(5)#	0.25(2)	—	$[6.9(27) \times 10^{-2}]$
25	5	8	^{13}B		0.20(6)	1.17(9)	—	[7.4(32)]
26	5	9	^{14}B		0.10(5)	0.15(1)	—	[0.85(37)]
27	6	7	^{13}C		0.5(3)	0.25(3)	—	[3.1(15)]
28	6	8	^{14}C		5.4(6)#	5.4(6)	—	[110(74)]
29	6	9	^{15}C		1.5(10)#	1.3(1)	—	[44(29)]
30	6	10	^{16}C		0.2(1)	2.4(3)	—	[59(43)]
31	7	9	^{16}N		<0.05	$8.3(13) \times 10^{-2}$	—	—
32	8	10	^{18}O		<0.05	[0.10(2)]	—	—
33	8	12	^{20}O		0.5(2)	[2.4(5)]	—	—
34	9	11	^{20}F		—	$[3.3(6) \times 10^{-3}]$	—	—
35	10	14	^{24}Ne		—	[2.1(20)]	—	—
36	10	16	^{26}Ne		—	[38(13)]	—	—

Note: Data labeled with * and ** were borrowed from [15] and [16], respectively.

Table 2. Comparison of experimental and interpolated yields of light nuclides in the ternary fission of nuclei (normalized to 10^4 nuclei of ^4He)

No.	Z	N	Nuclide	Unstable nuclides	$^{239}\text{Pu} + n_{\text{th}} [3]$		$^{242m}\text{Am} + n_{\text{th}} [3]$	
					experiment	interpolation	experiment	interpolation
1	0	1	n		—	$[2.8(2) \times 10^6]$	—	$[2.17(27) \times 10^6]$
2	1	0	^1H		190(10)*	[164(9)]	—	[213(27)]
3	1	1	^2H		69(2)	[205(10)]	—	[256(30)]
4	1	2	^3H		720(30)	[1620(50)]	620(60)	[1720(70)]
5	2	1	^3He		<0.01	$5.5(5) \times 10^{-2}$	—	0.10(2)
6	2	2	^4He		$10^4(200)\#$	9900(200)	$10^4(150)\#$	10 020(230)
7	2	3	^5He	$^4\text{He} + n + 0.89 \text{ MeV}$	—	2100(40)	—	2270(50)
8	2	4	^6He		192(5)#	205(10)	214(6)#	212(7)
9	2	5	^7He	$^6\text{He} + n + 0.44 \text{ MeV}$	—	56.5(25)	—	62(3)
10	2	6	^8He		8.8(4)	8.7(6)	—	9.0(6)
11	3	2	^5Li	$^4\text{He} + ^1\text{H} + 1.966 \text{ MeV}$	—	$5.5(5) \times 10^{-2}$	—	0.10(3)
12	3	3	^6Li		<0.05	0.26(2)	—	0.42(8)
13	3	4	^7Li		6.5(2)#	6.6(3)	8.2(26)#	8.8(10)
14	3	5	^8Li		3.2(3)#	3.4(1)	3.6(4)#	4.4(4)
15	3	6	^9Li		5.3(3)#	4.9(2)	6.4(13)#	5.8(3)
16	4	3	^7Be		<0.01	$1.2(2) \times 10^{-4}$	—	$2.8(10) \times 10^{-4}$
17	4	4	^8Be	$2(^4\text{He}) + 0.092 \text{ MeV}$	—	2.7(2)	—	3.7(5)
18	4	5	^9Be		5.1(6)	3.35(60)	7.5(15)#	4.5(5)
19	4	6	^{10}Be		49(1)	11.0(3)	57(6)	12.3(6)
20	4	7	^{11}Be		3.5(3)#	2.9(1)	—	—
21	4	8	^{12}Be		2.2(5)	1.35(5)	—	—
22	5	6	^{11}B		0.9(3)#	0.85(5)	—	—
23	5	7	^{12}B		1.0(4)#	0.66(3)	—	—
24	5	8	^{13}B		1.3(4)	2.8(1)	—	—
25	5	9	^{14}B		0.2(1)	0.38(2)	—	—
26	6	7	^{13}C		<1	0.85(5)	—	—
27	6	8	^{14}C		14.0(6)#	14.4(7)	14.5(15)	15.1(15)
28	6	9	^{15}C		3.5(13)#	6.2(3)	—	—
29	6	10	^{16}C		3.5(16)	6.0(4)	—	[5.7(8)]
30	7	9	^{16}N		<0.02	[0.34(20)]	—	—
31	7	10	^{17}N		—	[0.90(5)]	—	—
32	7	11	^{18}N		—	[1.5(1)]	—	—
33	8	10	^{18}O		—	[0.50(5)]	—	—
34	8	12	^{20}O		0.8(4)	[8.7(8)]	—	—

* Data borrowed from [17].

Table 3. Comparison of experimental and interpolated yields of light nuclides in the ternary fission of nuclei (normalized to 10^4 nuclei of ^4He)

No.	Z	N	Nuclide	Unstable nuclides	$^{241}\text{Pu} + n_{\text{th}}$ [7]		$^{245}\text{Am} + n_{\text{th}}$ [7]	
					experiment	interpolation	experiment	interpolation
1	0	1	n		—	$[4.3(7) \times 10^6]$	—	$[1.73(22) \times 10^6]$
2	1	0	^1H		—	$[162(18)]$	—	$[233(25)]$
3	1	1	^2H		42(4)	$[240(38)]$	—	—
4	1	2	^3H		786(42)	$[2.23(15) \times 10^3]$	679(44)	$[689(35)]$
5	2	1	^3He		—	—	<0.6	0.17(3)
6	2	2	^4He		$10^4(700)\#$	$9.81(65) \times 10^3$	$10^4(600)\#$	9680(540)
7	2	3	^5He	$^4\text{He} + n + 0.89 \text{ MeV}$	—	$2.5(1) \times 10^3$	—	—
8	2	4	^6He		260(30)#	288(19)	286(16)#	294(14)
9	2	6	^8He		15(1)	17.9(22)	19(4)	17.5(18)
10	3	2	^5Li	$^4\text{He} + ^1\text{H} + 1.97 \text{ MeV}$	—	$4.4(10) \times 10^{-2}$	—	—
11	3	3	^6Li		—	0.24(4)	<0.3	0.73(11)
12	3	4	^7Li		6.7(6)#	7.0(6)	13.6(13)#	14.4(11)
13	3	5	^8Li		4.2(6)#	4.4(3)	5.6(18)#	8.2(5)
14	3	6	^9Li		8.3(6)#	7.4(5)	13.6(17)#	11.3(6)
15	4	3	^7Be		<0.2	$8(2) \times 10^{-5}$	—	—
16	4	4	^8Be	$2(^4\text{He}) + 0.092 \text{ MeV}$	—	2.1(20)	—	—
17	4	5	^9Be		4.4(5)	3.1(3)	9.1(11)	7.5(6)
18	4	6	^{10}Be		46(6)	11.8(4)	66(5)	19.6(6)
19	4	7	^{11}Be		5.9(17)#	3.7(2)	8.1(10)#	6.2(3)
20	4	8	^{12}Be		2.8(13)	2.1(2)	5.5(17)	3.0(2)
21	4	10	^{14}Be		$2.7(10) \times 10^{-3}$	$2.7(4) \times 10^{-2}$	0.018(12)	0.043(6)
22	5	5	^{10}B		<0.03	$2.6(1) \times 10^{-3}$	<0.3	0.016(3)
23	5	6	^{11}B		1.6(10)#	0.67(8)	2.4(13)#	0.72(7)
24	5	7	^{12}B		1.0(4)#	0.62(5)	2.3(4)#	2.05(13)
25	5	8	^{13}B		—	—	2.2(6)	6.15(30)
26	6	6	^{12}C		—	—	<4.8	0.30(6)
27	6	7	^{13}C		—	—	1.1(5)	1.8(2)
28	6	8	^{14}C		12.6(8)#	11.3(7)	23.3(16)#	22.8(13)
29	6	9	^{15}C		4.3(4)#	5.8(4)	7.7(11)#	11.4(7)
30	6	10	^{16}C		5.0(9)	6.7(7)	9.5(13)	10.5(10)
31	6	12	^{18}C		0.28(5)	$[1.9(3)]$	0.32(11)	$[2.4(4)]$
32	7	8	^{15}N		<0.044	$[0.15(9)]$	0.17(7)	$[0.59(7)]$
33	7	9	^{16}N		$7.9(32) \times 10^{-2}$	$[0.24(11)]$	0.27(8)*	$[0.85(7)]$
34	7	10	^{17}N		0.34(10)	$[0.72(6)]$	0.77(31)	$[1.85(13)]$
35	7	11	^{18}N		0.16(4)	$[1.48(14)]$	0.47(21)	$[3.37(29)]$
36	8	8	^{16}O		—	—	<47	$[0.014(3)]$
37	8	9	^{17}O		—	—	<0.2	$[0.14(2)]$
38	8	10	^{18}O		—	—	1.0(4)	$[0.53(5)]$
39	8	11	^{19}O		0.26(12)	$[1.66(16)]$	0.77(47)	$[4.78(42)]$
40	8	12	^{20}O		1.10(12)	$[7.2(9)]$	2.7(4)	$[13.4(17)]$
41	8	14	^{22}O		0.12(4)	$[152(36)]$	0.39(19)	$[161(36)]$

* Data borrowed from [8].

Table 4. Comparison of experimental and interpolated yields of light nuclides in the ternary fission of nuclei (normalized to 10^4 nuclei of ^4He)

No.	Z	N	Nuclide	$^{233}\text{U} + n_{\text{th}} [1, 6]$		$^{245}\text{Cm} + n_{\text{th}} [7]$	
				experiment	interpolation	experiment	interpolation
1	0	1	n	—	$[3.4(3) \times 10^6]$	—	$[9.3(11) \times 10^5]$
2	1	0	^1H	—	$[124(8)]$	—	$[40(5)]$
3	1	1	^2H	41(2)	$[139(7)]$	—	—
4	1	2	^3H	463(23)	$[1.22(5) \times 10^3]$	679(44)#	739(37)
5	2	1	^3He	<0.1	$2.5(4) \times 10^{-2}$	<0.6	$1.7(4) \times 10^{-2}$
6	2	2	^4He	$10^4(266)\#$	$9.76(26) \times 10^3$	$10^4(600)\#$	9880(540)
7	2	4	^6He	137(8)#	140(7)	286(16)#	264(11)
8	2	6	^8He	3.6(4)	4.4(4)	19(4)#	15.8(15)
9	3	3	^6Li	<0.05	$4.3(5) \times 10^{-2}$	<0.3	0.29(5)
10	3	4	^7Li	3.7(2)#	3.8(2)	13.6(13)#	11.6(9)
11	3	5	^8Li	1.81(20)#	1.75(8)	5.6(18)#	7.4(5)
12	3	6	^9Li	3.56(48)#	2.49(14)	13.6(17)#	14.6(8)
13	4	5	^9Be	3.7(8)	1.9(1)	9.1(11)	13.6(12)
14	4	6	^{10}Be	43(3)	7.2(2)	66(5)#	70(4)
15	4	7	^{11}Be	<0.3	0.86(4)	8.1(10)	21.0(15)
16	4	8	^{12}Be	1.1(2)#	0.70(5)	5.5(7)	$[13.0(13)]$
17	4	10	^{14}Be	—	—	0.018(12)	$[0.15(2)]$
18	5	5	^{10}B	—	—	<0.3	$[0.018(4)]$
19	5	6	^{11}B	—	—	2.4(13)	$[7.6(8)]$
20	5	7	^{12}B	$3.7(6) \times 10^{-1}\#$	$3.6(2) \times 10^{-1}$	2.3(4)	$[7.9(7)]$
21	5	8	^{13}B	$6.2(13) \times 10^{-1}\#$	1.55(6)	2.2(6)	$[47(5)]$
22	5	9	^{14}B	$1.4(8) \times 10^{-2}$	0.30(2)	0.21(6)	$[12.5(14)]$
23	6	6	^{12}C	—	—	<4.8	$[2.0(3)]$
24	6	7	^{13}C	—	—	1.1(5)	$[19(2)]$
25	6	8	^{14}C	11.4(4)#	11.0(4)	23.3(16)	$[560(80)]$
26	6	9	^{15}C	2.4(3)#	4.1(2)	7.7(11)	$[280(40)]$
27	6	10	^{16}C	2.1(3)	4.0(3)	9.5(33)	$[380(70)]$
28	6	12	^{18}C	—	—	0.32(11)	$[118(27)]$
29	7	8	^{15}N	—	—	0.17(7)	—
30	7	9	^{16}N	$2.6(11) \times 10^{-2}$	$[0.20(1)]$	0.27(8)*	—
31	7	10	^{17}N	—	—	0.77(31)	—
32	7	11	^{18}N	—	—	0.47(21)	—
33	8	8	^{16}O	—	—	<47	—
34	8	9	^{17}O	—	—	<0.2	—
35	8	10	^{18}O	—	—	1.0(4)	—
36	8	11	^{19}O	—	—	0.77(47)	—
37	8	12	^{20}O	0.71(8)	6.9(5)	2.7(4)	—
38	8	14	^{22}O	—	—	0.39(19)	—
39	9	11	^{20}F	—	—	<0.08	—
40	10	14	^{24}Ne	—	—	0.23(6)*	—
41	12	18	^{30}Mg	—	—	0.060(27)*	—

Note: Data labeled with * were borrowed from [8]. In the "Experiment" column for the case of ^{233}U , data on the yields of nuclides from ^{12}Be were taken from [6], while the remaining data were taken from [1].

Table 5. Comparison of experimental and interpolated yields of light nuclides in the ternary fission of nuclei (normalized to 10^4 nuclei of ^4He)

No.	Z	N	Nuclide	Unstable nuclides	^{248}Cm (spont. fis.) [18]		^{252}Cf (spont. fis.) [19–23]	
					experiment	interpolation	experiment	interpolation
1	0	1	n		–	$[2.3(6) \times 10^6]$	–	$[0.65(14) \times 10^6]$
2	1	0	^1H		160(20)	$[26.6(35)]$	160(20)*	$[19.4(36)]$
3	1	1	^2H		50(5)#	51(5)	63(3)*	37(5)
4	1	2	^3H		922(18)#	921(18)	590(20)*#	591(19)
5	2	1	^3He		–	–	<9*	$0.95(39) \times 10^{-2}$
6	2	2	^4He		$10^4(500)\#$	10 100(500)	$10^4(350)\#$	10 028(540)
7	2	3	^5He	$^4\text{He} + n + 0.89 \text{ MeV}$	–	–	$2.1(5) \times 10^{3**}$	$2.6(2) \times 10^3$
8	2	4	^6He		354(31)#	335(21)	403(26)#	369(15)
9	2	5	^7He	$^6\text{He} + n + 0.44 \text{ MeV}$	–	–	85(21)**	128(8)
10	2	6	^8He		24(4)#	26(3)	25(4)#	30.6(31)
11	3	2	^5Li	$^4\text{He} + ^1\text{H} + 1.966 \text{ MeV}$	–	$1.1(5) \times 10^{-2}$	–	$3.3(14) \times 10^{-2}$
12	3	3	^6Li		–	0.11(4)	–	0.29(9)
13	3	4	^7Li		–	7.2(16)	17(4)#	16.3(27)
14	3	5	^8Li		–	5.6(2)	10(5)#	12.7(17)
15	3	6	^9Li		–	14.7(2)	25(11)#	31.5(26)
Sum of Z = 3 yields					26(9)	27.6(16)	52(5)***	61(4)
16	4	3	^7Be		–	$2.1(13) \times 10^{-5}$	–	$1.3(8) \times 10^{-4}$
17	4	4	^8Be	$2(^4\text{He}) + 0.092 \text{ MeV}$	–	4.0(11)	10(6)****	15.2(32)
18	4	5	^9Be		–	7.2(20)	–	28(5)
19	4	6	^{10}Be		–	58(11)	185(20)	193(16)
20	4	7	^{11}Be		–	$[19.3(42)]$	–	$[67.5(61)]$
21	4	8	^{12}Be		–	$[15.3(32)]$	–	$[52(6)]$
22	4	10	^{14}Be		–	$[0.21(2)]$	–	$[0.80(12)]$
Sum of Z = 4 yields					49(24)	$[104(12)]$	126(30)***	$[340(20)]$
23	5	5	^{10}B		–	–	–	$[3.4(15) \times 10^{-2}]$
24	5	6	^{11}B		–	–	–	$[22(5)]$
25	5	7	^{12}B		–	–	–	$[28.6(46)]$
26	5	8	^{13}B		–	–	–	$[220(25)]$
sum of Z = 5 yields					–	–	6.3(4)***	$[271(26)]$

Note: Data on the light-nuclide yields labeled with * and ** were borrowed from [19] and [21], respectively; *** data on the integrated yields of elements from [22] and **** data on the yield of ^8Be from [23]; the remaining data were taken from [20].

was made of nuclides from ^4He to ^{15}C , resulted in $\chi^2/(N - n) = 8.6$ for $N = 10$, this suggesting that its quality is much poorer. Nonetheless, it faithfully reproduces the yields of light nuclei from helium to

carbon, with the exception of ^{10}Be , whose yield calculated by the interpolation formula is underestimated by a factor of 6, and ^{14}B , whose yield is overestimated by a factor of 20. The yields of the hydrogen isotopes

Table 6. Some features of ternary fission according to calculations on the basis of some fits (for comments to this table, see main body of the text)

Reaction	N	$w_\alpha \times 10^3$	Θ , MeV	$w_p \times 10^5$	w_n	ε_p , MeV	ε_n , MeV	τ_0 , 10^{-21} s	$\frac{\chi^2}{N-n}$
$^{235}\text{U} + n_{\text{th}}$	$10; 4 \leq A \leq 15$	1.57(3)	1.31(2)	2.52(26)	0.94(10)	17.1(5)	3.3(4)	8.2(10)	0.97
$^{233}\text{U} + n_{\text{th}}$	$6; 4 \leq A \leq 10$	1.88(5)	1.17(3)	0.71(24)	0.40(7)	16.0(3)	3.2(3)	5.3(7)	0.37
$^{233}\text{U} + n_{\text{th}}$	$10; 4 \leq A \leq 15$	1.88(5)	1.29(1)	2.33(16)	0.64(6)	16.6(2)	3.4(2)	6.7(7)	8.6
$^{239}\text{Pu} + n_{\text{th}}$	$10; 4 \leq A \leq 15$	2.00(4)	1.37(1)	3.28(18)	0.56(4)	16.8(2)	3.4(1)	4.0(3)	2.1
$^{241}\text{Pu} + n_{\text{th}}$	$10; 4 \leq A \leq 15$	1.98(13)*	1.38(3)	3.25(35)	0.87(14)	17.2(5)	3.2(3)	4.2(8)	3.8
$^{242m}\text{Am} + n_{\text{th}}$	$6; 4 \leq A \leq 9$	2.21(5)	1.43(3)	4.71(62)	0.48(12)	16.7(3)	3.5(3)	2.5(3)	4.3
$^{245}\text{Cm} + n_{\text{th}}$	$8; 3 \leq A \leq 10$	2.8(4)**	1.28(2)	1.11(14)	0.26(3)	16.9(4)	3.4(3)	1.5(2)	3.0
$^{245}\text{Cm} + n_{\text{th}}$	$10; 4 \leq A \leq 15$	2.8(4)**	1.51(2)	6.51(71)	0.48(6)	16.7(3)	3.6(3)	3.3(5)	4.4
^{248}Cm , sp.f.	$5; 2 \leq A \leq 8$	2.35(12)*	1.20(3)	6.24(81)	0.54(13)	16.5(6)	2.3(6)	3.4(11)	0.78
^{252}Cf , sp.f.	$8; 3 \leq A \leq 10$	2.84(10)	1.25(3)	0.55(10)	0.18(4)	15.8(6)	2.8(4)	1.0(3)	1.1

^2H and ^3H also proved to be overestimated, by a factor of 3.5 and by a factor of 2.5, respectively. In relation to the first fit, the results are overestimated for the neutron yield as well, approximately by a factor of 1.5 (there are presently no experimental data on this yield). Since the first fit was constructed by using experimental data for a lighter group of nuclides (we refer to this as an “interpolation on the basis of a short series”) and has a much better value of the agreement criterion, the results of its application to the yields of the lightest particles, including neutrons, deserve more confidence. (It should be noted that, in comparing different models, Köster [7] calculated the yields of nuclides having relatively high values of A for the case of ^{233}U fission by the formula from [11], where, in all probability, he used the parameters determined on the basis of the short series, and this could result in a considerable excess of the calculated yields above their experimental counterparts in Fig. 1.6.5 in [7]).

Two different fits were constructed for the case of the fission process $^{245}\text{Cm}(n_{\text{th}}, f)$ as well: one on the basis of a short series from ^3H to ^{10}Be inclusive (Table 4) and the other on the basis of a heavier group of nuclides belonging to a long series from ^4He to ^{15}C (Table 3). The first exhibits good agreement with experimental data within the interpolation region (up to ^{10}Be), but it overestimates the yields of nuclides having higher values of Z and A . The second is in satisfactory agreement with experimental data up to ^{16}C , but it underestimates the yields of ^{10}Be and ^{11}B , albeit leading to severalfold overestimated results for the yields of ^{13}B and for the yields of almost all isotopes of $Z \geq 7$ nuclei. In relation to the first fit, the second one gives higher values for the yields of single nucleons—for example, by a factor of two for neutrons.

Our fits for the fission processes $^{235}\text{U} + n_{\text{th}}$, $^{239}\text{Pu} + n_{\text{th}}$, and $^{241}\text{Pu} + n_{\text{th}}$ (Tables 1–3) overestimate the yields of ^2H and ^3H nuclei and, probably, the yield of neutrons. Since the fits in question were based on a “long series,” as in the case of the second fits for $^{245}\text{Cm}(n_{\text{th}}, f)$ and $^{233}\text{U}(n_{\text{th}}, f)$, where, in relation to the fits based on the groups of lighter nuclides, the neutron yield was overestimated by a factor of 2 and by a factor of 1.5, respectively, it can be assumed that the overestimation here is within a factor of 1.5 to 2 as well. In relation to experimental data, the yield of ^{10}Be is underestimated by a factor of about 5, while the yields of ^{13}B , ^{16}C , and ^{20}O are significantly overestimated, as a rule.

For the yields in the ternary-fission process $^{242m}\text{Am}(n_{\text{th}}, f)$ (Table 2), the interpolation formula was fitted to data on the same nuclides as in the first version of the fit for the reaction $^{233}\text{U}(n_{\text{th}}, f)$. As before, the yield of ^{10}Be proved to be underestimated (by a factor greater than 4 here), but, in contrast to the case of $^{233}\text{U}(n_{\text{th}}, f)$, the yield of ^3H is overestimated nearly by a factor of 3 here. In all probability, the neutron yield is also overestimated, whereas the yield of the comparatively heavy nuclide ^{14}C proved to be in agreement with the experimental value. In this respect, the case of $^{242m}\text{Am}(n_{\text{th}}, f)$ is rather close to the fits based on long series.

The next two fits refer to the spontaneous fission of the ^{248}Cm and ^{252}Cf isotopes (Table 5; use was made here of data from [18–23]). The first of these was constructed on the basis of data on the yields of two hydrogen and three helium isotopes. In the second, use was made of data on the yield of three helium and three lithium isotopes. Both fits underestimate the proton yield (by a factor of 6 in the first and by

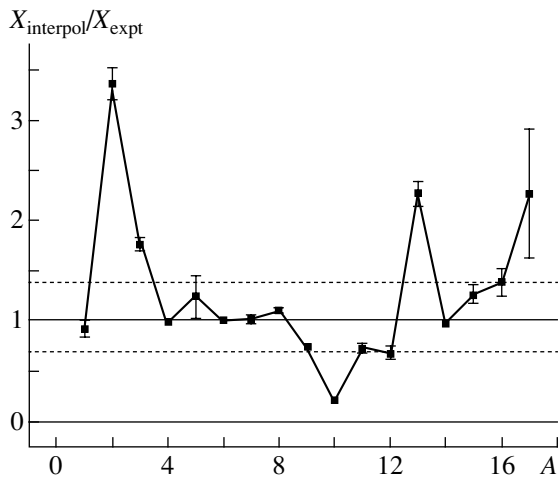


Fig. 1. Ratio of the sum of the yields calculated by the interpolation formula for all light nuclei of mass number A to the sum of the yields found experimentally for the same nuclei versus A . Use was made of the weighted mean of data on the thermal-neutron-induced fission of ^{233}U , ^{235}U , ^{239}Pu , ^{241}Pu , ^{242m}Am , and ^{245}Cm nuclei. With the exception of the case of ^{242m}Am , interpolation was performed on the basis of a long series of nuclides.

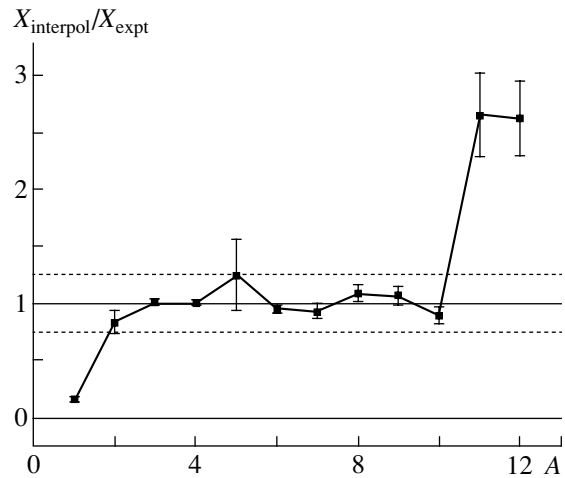


Fig. 2. As in Fig. 1. Use was made of the weighted mean data on the thermal-neutron-induced fission of ^{233}U and ^{245}Cm nuclei and on the spontaneous fission of ^{248}Cm and ^{252}Cf nuclei. The interpolation here was performed on the basis of a “short series.”

a factor of 8 in the second case), but they faithfully reproduce the total yield of lithium isotopes. The first overestimates the total yield of beryllium isotopes by a factor of about two [18], while the second faithfully reproduces the ^{10}Be yield [20], which, however, proved to be in excess of the total experimental yield of Be from [22]. As to the calculated yields of neutrons from these two reactions, it can hardly be expected that they are sizably overestimated, since the values of the parameters in the respective formulas were calculated on the basis of equations for isotopes of the lightest three elements.

One can easily see that a fit on the basis of a “long series” overestimates, as a rule, the yields of nuclei having low values of A and Z and the yields of nuclei having high values of A and Z , while a fit on the basis of a “short series” overestimates, almost exclusively, the yields of nuclei having high values of A and Z . These features of the fits are demonstrated in Fig. 1 (fit on the basis of a “long series”) and Fig. 2 (fit on the basis of a “short series”). For the aforementioned reasons, the case of $^{242m}\text{Am}(n_{\text{th}}, f)$ was included in Fig. 1.

In Figs. 1 and 2, the nuclide atomic weight and the ratio of the sum of the yields calculated by the interpolation formula for all nuclei of given A to the sum of the experimentally measured yields of the same nuclei are plotted along the abscissa and the ordinate, respectively. The weighted mean values of such ratios for six and four fits are shown in Figs. 1 and 2, respectively. From Fig. 1, one can see that,

within the atomic-weight range being considered, the majority of the ratios lie between 0.7 and 1.4. In Fig. 2, the points are grouped closer to the straight line on which the ratio in question is equal to unity. However, the points corresponding to $A > 17$ for Fig. 1 and to $A > 12$ for Fig. 2 were not plotted in the figures, since they lie far beyond the boundaries adopted here for the figures, thereby indicating the limit above which the formulas used become inapplicable.

If the interpolation formula were correct, the graph would lie horizontally around the mean ordinate ($X_{\text{interpol}}/X_{\text{expt}} = 1$, with the scatter of points being within the statistical errors; however, it can be seen from the figures that this is not so. If we eliminate, in Fig. 1, the points at $A = 1$ (protons) and $A = 13$ (predominantly ^{13}B) from consideration, it can be seen there that the points are rather grouped around a parabola. It follows that our interpolation formula, which involves four parameters, is unable to ensure the required accuracy over so wide a range of argument values ($2 < A < 17$).

In fitting on the basis of a short series (Fig. 2), the situation is better. Here, we see nine points lying (within the errors) on the expected horizontal line. Therefore, there are reasons to believe that, for nuclides whose atomic weights satisfy the condition $A \leq 10$, the interpolation formula reproduces their yields quite precisely. Yet, the point $A = 1$ does not fit in the general graph, in just the same way as in Fig. 1. The number of protons recorded experimentally is nearly an order of magnitude greater than that which is expected on the basis of the interpolation formula. One possible reason for this was already indicated in Section 1. It should be noted that all data on protons

Table 7. Estimates of the yields of scission neutrons per nuclear-fission event

Nucleus	^{235}U	^{233}U	^{239}Pu	^{241}Pu	^{242m}Am	^{245}Cm	^{248}Cm (sp.f.)	^{252}Cf (sp.f.)
w_n	0.55	0.40	0.33	0.51	0.48	0.26	0.54	0.18
Δw_n	0.09	0.07	0.05	0.10	0.12	0.03	0.13	0.04

were obtained with the aid of $\Delta E-E$ telescopes. As usual, thin foils used for filtering beams can be a source of secondary protons in this case.

Summarizing the above comments on the content of Tables 1–5 and relying on the data of the graph in Fig. 2, we have to recognize that the interpolating formula from [11] leads to satisfactory results only in the case where it is applied to the range of light nuclei ($A \leq 10$).

Table 6 lists the main parameters of the interpolation formula and some quantities that were calculated on the basis of these parameters and which have clear physical meaning. The quantity N in the second column is the number of equations used to determine the parameters; there, we also give the intervals of atomic weights for those nuclides whose yields were taken into account.

In the third column, we quote the yields of alpha particles per fission event. These values, which were measured in individual experiments, serve for a normalization of other yields. They were taken predominantly from [4]. An asterisk labels values obtained by interpolating the dependence $w_\alpha(Z^2/A)$, which was also presented in [4]. A number of w_α values for ^{245}Cm are quoted in [7]. The data labeled with two asterisks correspond to the last publication cited in [7] (1998).

In the columns from the fourth to the ninth one, we give successively the temperature parameter Θ , the proton yield w_p and the neutron yield w_n per fission event, the partial (or “chemical”) potentials for protons (ε_p) and neutrons (ε_n), and the mean emission time τ_0 .

The quantities quoted in the tenth column characterize the quality of the fits in terms of the interpolation formula to experimental data for those nuclides whose yields were employed in these fits. From Tables 1–5, one can see how great the distinctions between the yields obtained on the basis of the interpolation formula and their experimental counterparts can be for those nuclides whose A and Z values are beyond the boundaries of the interpolation region.

The possibility of estimating the yields of neutrons that are emitted via the same mechanism (as a matter of fact, the evaporation mechanism) as charged particles and within the same time interval and which are therefore identified here as scission neutrons is

the most interesting consequence of the applications of the interpolation formula. [Various authors refer to such neutrons as “pre-scission” or “breakup” neutrons because of their main special feature: the energy spectrum and the angular distribution of these neutrons differ from the corresponding distributions of neutrons emitted by fully accelerated fragments. There is no generally accepted terminology for this kind of neutron emission in nuclear fission; nor is there a clear understanding of whether the emission of such a neutron occurs prior to the scission of the nucleus (that is, before the instant after which the short-range nuclear interaction between main fragments virtually disappears), after it, or both prior to and after it.]

As was indicated above, the estimate of the neutron yield depends on whether interpolation was based on a long or a short group of nucleons. Approximate values of scission-neutron yields in nuclear fission are given in Table 7. The estimates obtained on the basis of data on a short group (including those for the case of ^{242m}Am) were taken from Table 6 without any changes. In order to arrive at unified normalization, the estimates in Table 6 for ^{235}U , ^{239}Pu , and ^{241}Pu , in which case the interpolation was performed on the basis of a long series, were multiplied by 0.57 ± 0.07 . This coefficient was obtained as the mean ratio of the data on the neutron yields in the second and third lines for ^{233}U and in the seventh and eighth lines for ^{245}Cm (Table 6).

A nearly horizontal plateau of the ratios ($X_{\text{interpol}}/X_{\text{expt}} \approx 1$ in Fig. 2 from $A = 2$ to $A = 10$) provides an additional argument in favor of the correctness of estimating the neutron yield by means of a fit based on a short series. An extrapolation of this plateau to the point $A = 1$ corresponding to neutrons will hardly lead to a large deviation from unity. The point $A = 1$ in the figures corresponds to protons exclusively, since we do not have experimental data on neutron yields at our disposal. According to measurements (see Tables 1, 2, 5), the proton yield in ternary fission is only $(1-2) \times 10^{-2}$ of the alpha-particle yield; therefore, it can be distorted by the contributions from possible background reactions, especially (n, p), as was indicated above, while the neutron yield, which, according to interpolations,

is two orders of magnitude higher than the alpha-particle yield, is nearly unaffected by such distortions.

Despite a broad, nearly isotropic angular distribution of scission neutrons, their expected high yield renders them appropriate, along with charged particles, for studying the T -odd triple correlation that was discovered quite recently (see, for example, [24–27]) and which arouses great interest. It should be noted that, at an angle of 90° with respect to the axes along which fission fragments fly apart—recall that this is precisely the angle at which a counter for recording a third particle in measurements of the triple correlation is arranged—the background of neutrons emitted from fully accelerated fragments is relatively small. In one of the recent investigations devoted to examining precission neutrons [28], it was established that the excess of neutrons at an angle of about 90° (this excess cannot be explained within the model of emission from fully accelerated fragments) is about 30% for the spontaneously fissile nucleus ^{252}Cf and about 60% for the fission process $^{235}\text{U}(n_{\text{th}}, f)$. Our data on neutron yields in Table 7 are in qualitative agreement with the results presented in [28], but this fact alone does not give sufficient grounds to believe that the emission of all precission neutrons proceeds via the same mechanism as that which governs the emission of light charged particles.

The data in Tables 6 and 7 make it possible to disclose some special features of ternary fission that are unlikely to have been seen previously. By way of example, we indicate that, in the fission of nuclei characterized by identical values of Z , a heavier isotope emits a greater number of scission neutrons. Further, there is a distinct anticorrelation, with a coefficient $K \approx -0.7$, between the yields of alpha particles (third column in Table 6) and neutrons (Table 7), this being indicative of a strong competition between the emission of these two types of particles. It is interesting to note that the neutron and proton work functions (with allowance for the Coulomb barrier in the case of protons) as calculated for various fissile nuclei with the parameters of the interpolation formula proved to be constant within the statistical errors. A fit of all values in the seventh and the eighth column of Table 6 to constant values leads to $\langle \varepsilon_p \rangle = 16.64 \pm 0.31$ MeV at $\chi^2/(N - n) = 1.09$ and $\langle \varepsilon_n \rangle = 3.36 \pm 0.18$ MeV at $\chi^2/(N - n) = 0.75$ (in the table, the root-mean-square scatter is indicated parenthetically near the corresponding results). The neutron work function is much smaller than its ordinary values for nonexcited nuclear fragments, but this may probably be explained by the excitation of nucleons in the neck above the ground-state level under nonstationary conditions before their emission.

From Table 6, one can see that, in just the same way as the neutron and proton yields, the fitted temperature depends on the group of nuclides used in a fit. In relation to ε_p and ε_n , the quantity Θ undergoes wider variations from one fit to another. The emission time τ_0 changes within a still wider interval, also showing a strong dependence on the interpolation region. As the main trend for it, we can indicate the reduction of τ_0 , with increasing nuclear-fissility parameter Z^2/A .

CONCLUSION

An analysis of the results obtained with aid of the interpolation formula has revealed that the evaporation model provides a rather sound basis for describing the emission of light particles in ternary fission. From a detailed consideration, it has become clear, however, that the interpolation formula used, which involves only four adjustable parameters, is unable to reflect correctly the probabilities of the emission of light nuclides for any A and Z values encountered in ternary fission. It the parameters were fitted to the known yields of the lightest third fragments—for example, from ^3H to ^9Li —then the extrapolation of the formula to the isotopes of $Z \geq 5$ nuclei leads to overestimated results, the excess above the experimental values growing sharply with increasing Z . If a fit is constructed on the basis of the known yields of light nuclides belonging to the intermediate range—say, from helium to carbon—the resulting yields will be overestimated for $Z \geq 7$ nuclei, on one hand, and for ^2H and ^3H , on the other hand. Probably, the formula can be “corrected” by introducing one to two adjustable parameters, but this would lead to a complication of respective calculations and would mean a deviation from a simple evaporation concept.

As to the predictive power of the interpolation formula in what is concerned with the yield of scission neutrons, we can hope that this yield will be determined correctly if the parameters in this formula are chosen in such a way as to reproduce the yields of the isotopes of hydrogen (with the exception of ^1H), helium, and lithium correctly. The expected relatively high yields of scission neutrons open new possibilities for studying the dynamics of fission. In particular, I think that, in addition to the already known values of the triple-correlation coefficient for alpha particles in the fission of ^{235}U and ^{233}U , it would be desirable to measure this coefficient for such neutrons in the fission of the same nuclei [29]. A comparison of the results obtained in this way would make it possible to draw some conclusions on the effect of the charge and mass of a light particle on the phenomenon being studied.

ACKNOWLEDGMENTS

I am grateful to Prof. F. Gönnenwein (Tübingen, Germany) for stimulating interest in this study and for acquainting me with U. Köster's dissertation [7], which contains a comprehensive review on various issues of ternary nuclear fission. Thanks are also due to Prof. G. A. Petrov for permanent attention to this study and enlightening discussions on the problems considered there.

This work was supported by the Russian Foundation for Basic Research (project no. 02-02-17051) and INTAS (grant no. 99-0229).

REFERENCES*

1. A. A. Vorobyov, D. M. Seliverstov, V. T. Grachev, *et al.*, Phys. Lett. B **30B**, 332 (1969).
2. A. A. Vorobyov, D. M. Seliverstov, V. T. Grachev, *et al.*, Phys. Lett. B **40B**, 102 (1972).
3. A. A. Vorob'ev, V. T. Grachev, I. A. Kondurov, *et al.*, Yad. Fiz. **20**, 461 (1974) [Sov. J. Nucl. Phys. **20**, 248 (1975)].
4. I. A. Kondurov, A. M. Nikitin, and D. M. Seliverstov, Byull. Tsentra Dannyykh LIYaF, No. 6, 11 (1977).
5. S. W. Casper, J. Cerny, and R. S. Gatti, Phys. Rev. **154**, 1193 (1967).
6. M. Wostheinrich *et al.*, in *Proceedings of the Second International Workshop on Nuclear Fission and Fission-Product Spectroscopy, Seyssins, France*, Ed. by G. Fioni *et al.*; AIP Conf. Proc. **447**, 330 (1998).
7. U. Köster, Dissertation (Physik-Department der Technischen Universität München, 1999).
8. M. Hesse, Ph.D. Thesis (Eberhard-Karls-Universität, Tübingen, 1997).
9. M. Davi, Ph.D. Thesis (Universität Mainz, 1997).
10. I. Halpern, Annu. Rev. Nucl. Sci. **21**, 245 (1971).
11. G. V. Val'skiĭ, Yad. Fiz. **24**, 270 (1976) [Sov. J. Nucl. Phys. **24**, 140 (1976)].
12. V. A. Rubchenya and S. G. Yavshitz, Z. Phys. A **329**, 217 (1988).
13. G. A. Pik-Pichak, Yad. Fiz. **57**, 966 (1994) [Phys. At. Nucl. **57**, 906 (1994)].
14. H. Faust and Z. Bao, in *Proceedings of the Seminar on Fission, Pont d'Oye III, Castle of Pont d'Oye, Habay-la-Neuve, Belgium, 1995*, Ed. by C. Wage-mans, p. 220.
15. M. Dakowski, J. Chwaszczewska, T. Krogulski, *et al.*, Phys. Lett. B **25B**, 213 (1967).
16. V. N. Andreev, V. T. Nedopekin, and V. I. Rogov, Yad. Fiz. **8**, 38 (1968) [Sov. J. Nucl. Phys. **8**, 22 (1969)].
17. T. Krogulski, J. Chwaszczewska, M. Dakowski, *et al.*, Nucl. Phys. A **128**, 219 (1969).
18. M. P. Ivanov *et al.*, Yad. Fiz. **60**, 399 (1997) [Phys. At. Nucl. **60**, 329 (1997)].
19. S. L. Whetstone and T. D. Thomas, Phys. Rev. **154**, 1174 (1967).
20. Z. Dlouhy, J. Švanda, *et al.*, in *Proceedings of the 6th International Conf. on Nuclei far from Stability and 9th International Conf. on Atomic Masses and Fundamental Constants*, Bernkastel-Kues, Ed. by R. Neugart and A. Wöhr, Inst. Phys. Conf. Ser., No. 132 (IOP, Bristol, 1992), p. 481.
21. Yu. N. Kopatch, M. Mutterer, D. Schwalm, *et al.*, Phys. Rev. C **65**, 044614 (2002).
22. P. Singer, Ph.D. Thesis (TH Darmstadt, 1997).
23. M. Mutterer, Yu. N. Kopatch, P. Jesinger, and F. Gönnenwein, submitted to World Sci.
24. P. Jesinger, A. Kötzle, A. M. Gagarski, *et al.*, in *Proceedings of the Second International Workshop on Nuclear Fission and Fission-Product Spectroscopy, Seyssins, France, 1998*, Ed. by G. Fioni *et al.*; AIP Conf. Proc. **447**, 395 (1998).
25. P. Jesinger, F. Gönnenwein, A. Kötzle, *et al.*, in *Proceedings of the Second International Conference on Fission and Neutron-Rich Nuclei, St. Andrews, Scotland, 1999*, Ed. by J. Hamilton *et al.*, p. 306.
26. P. Jesinger, F. Gönnenwein, A. Kötzle, *et al.*, in *Proceedings of the Seminar on Fission, Pont d'Oye IV, Castle of Pont d'Oye, Habay-la-Neuve, Belgium, 1999*, p. 111.
27. V. E. Bunakov and F. Goennenwein, Yad. Fiz. **65**, 2096 (2002) [Phys. At. Nucl. **65**, 2036 (2002)].
28. N. V. Kornilov, A. B. Kagalenko, and F.-J. Hambsch, Yad. Fiz. **64**, 1451 (2001) [Phys. At. Nucl. **64**, 1373 (2001)].
29. G. A. Petrov, V. E. Bunakov, F. Goennenwein, *et al.*, Project INTAS 99-0229.

Translated by A. Isaakyan

*The references to the articles quoted in [6, 8, 9, 14, 18–20, 22] and [15, 17] are given according to [7] and [4], respectively.

Doorway States for One-Nucleon-Transfer Reactions and Nuclear Correlation Energy*

B. L. Birbrair** and V. I. Ryazanov

Petersburg Nuclear Physics Institute, Russian Academy of Sciences, Gatchina, 188350 Russia

Received July 25, 2003; in final form, November 10, 2003

Abstract—The correlation effects are found to provide a dominant contribution to the nuclear binding energies. This result is obtained within a simple renormalizable model for the multiparticle forces between nucleons. © 2004 MAIK “Nauka/Interperiodica”.

1. INTRODUCTION

The correlation energy of nuclear matter remains one of the most important problems of nuclear theory in view of applications to astrophysics and high-density QCD. As discussed in our previous work [1], quantitative information about the correlation energies of finite nuclei can be obtained within the framework of the theory of doorway states for one-nucleon-transfer reactions [2] by calculating the nuclear static energy, arising from the motion of nucleons in the nuclear static field. But we found that the results seem to be ambiguous because only the three- and four-particle forces were taken into account in addition to the two-particle ones (the estimated effect of the finite range of the multiparticle forces is found to be small). Accounting for the fact that the ultimate origin of the multiparticle forces is the nonlinearity of strong interaction, we proposed a simple model of nonlinearity that includes both the forces of all multiplicities and the finite range [3] (see also the Appendix in [2]).

In this model, the multiparticle forces are taken into account by introducing an additional scalar–isoscalar field with the Lagrangian density

$$L = \frac{1}{2} \partial_\mu \phi \partial^\mu \phi - \frac{1}{2} \Lambda^2 \phi^2 - \frac{1}{3} \lambda_3 \phi^3 - \frac{1}{4} \lambda_4 \phi^4 - g \bar{\psi} \psi \phi, \quad (1)$$

the corresponding classical static field thus obeying the equation

$$\Lambda^2 \phi + \lambda_3 \phi^2 + \lambda_4 \phi^3 = -g\rho_s + \Delta\phi, \quad (2)$$

where Δ is the Laplacian and ρ_s is the scalar density distribution of nucleons in the nucleus [4]. The last term on the right-hand side of (1) describes the

coupling of the field ϕ to the nucleon one ψ ; g is the coupling constant.

The field ϕ contains the “two-particle” component ϕ_2 obeying the equation

$$\Lambda^2 \phi_2 = -g\rho_s + \Delta\phi_2. \quad (3)$$

It must be subtracted, because this part of the nuclear scalar field results from the observed free-space two-particle forces as described in [2]. Thus, the contribution of multiparticle forces to the nuclear static field is

$$W(r) = g[\phi(r) - \phi_2(r)]. \quad (4)$$

2. ANALYSIS

As shown in [2], the multiparticle field $W(r)$ is repulsive in the nuclear surface region and attractive in the nuclear interior (Fig. 1a). Let us analyze the situation in the local density approximation $W(r) = W[\rho_s(r)]$. Since the scalar density ρ_s is a decreasing function of r , the field W is positive at $0 < \rho_s < \rho_1$ with the maximum W_m in this region and negative at $\rho_s > \rho_1$, $\rho_1 = \rho_s(r_1)$ (Fig. 1b). Let us neglect for a moment the Laplacian terms of Eqs. (2) and (3) (they are taken into account in the actual calculations; see Section 3). In this case,

$$W = g(\phi - \phi_2) = -\frac{g\lambda_4}{\Lambda^2} \left(\frac{\lambda_3}{\lambda_4} + \phi \right) \phi^2. \quad (5)$$

At $\rho_s = \rho_1$ [see Fig. 1b and Eq. (3) without the Laplacian term],

$$g \left(\phi + \frac{g\rho_1}{\Lambda^2} \right) = -\frac{g\lambda_4}{\Lambda^2} \phi^2 \left(\frac{\lambda_3}{\lambda_4} + \phi \right) = 0 \quad (6)$$

and therefore

$$\frac{\lambda_3}{\lambda_4} = \frac{g\rho_1}{\Lambda^2}. \quad (7)$$

*This article was submitted by the authors in English.

** e-mail: birbrair@thd.pnpi.spb.ru

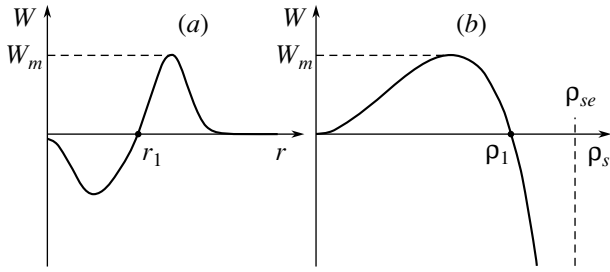


Fig. 1. Contribution of multiparticle forces to the nuclear static field as a function of (a) radial distance r and (b) scalar density ρ_s .

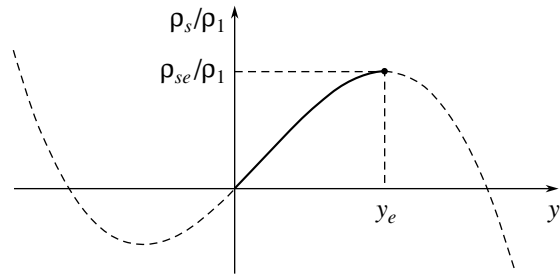


Fig. 2. The ratio ρ_s/ρ_1 as a function of y . The solid curve is for the physical branch of the solution of Eq. (12).

Introducing the dimensionless quantities y and y_2 [3],

$$\phi = -\frac{g\rho_1}{\Lambda^2}y, \quad \phi_2 = -\frac{g\rho_1}{\Lambda^2}y_2, \quad (8)$$

we get

$$W = -\frac{g^4\rho_1^3}{\Lambda^8}\lambda_4y^2(1-y). \quad (9)$$

The maximum W_m occurs at $y = 2/3$, so

$$\lambda_3 = -\frac{27\Lambda^6W_m}{4g^3\rho_1^2}, \quad \lambda_4 = -\frac{27\Lambda^8W_m}{4g^4\rho_1^3} \quad (10)$$

and therefore

$$W = -\frac{g}{\Lambda^2}(\lambda_3\phi^2 + \lambda_4\phi^3) = \frac{27}{4}W_my^2(1-y). \quad (11)$$

Thus, both the ϕ^3 and ϕ^4 terms of the Lagrangian density (1) must be included to get the required form of the “multiparticle” field (Fig. 1). It should be mentioned in this connection that the condition of the renormalizability requires the absence of higher power terms in (1). According to the contemporary point of view, the renormalizability is not obligatory at the meson–baryon level, but in our opinion it is highly desirable, because otherwise the theory has no predictive power. It is also important that the renormalizability allows only a restricted number of phenomenological parameters, in contrast to the effective theories, where the above number can be arbitrary (the only restriction in this case is the so-called “naturalness” [5, 6], which is not confirmed by the experimental data on the doorway states [3, 7]).

From Eqs. (2), (8), and (10), we get the following equation for the quantity y :

$$y + \frac{3}{x}y^2(1-y) = \frac{\rho_s}{\rho_1}, \quad x = \frac{4g^2\rho_1}{9\Lambda^2W_m}. \quad (12)$$

The ratio ρ_s/ρ_1 is plotted in Fig. 2. As seen from the plot, the solution $y = y(\rho_s)$ has three branches: the physical one

$$0 \leq y \leq y_e = \frac{1}{3}(\sqrt{1+x} + 1) \quad (13)$$

in the region

$$0 \leq \rho_s \leq \rho_{se} = \frac{1}{9}\rho_1 \left(1 + \frac{2(1+x)}{\sqrt{1+x}-1} \right) \quad (14)$$

and two unphysical ones with (i) $y < 0$ and (ii) $y > y_e$. Indeed, branch $y < 0$ begins at negative densities, which is obviously nonsense, whereas branch $y > y_e$ has a nonzero value at $\rho_s = 0$, thus existing without the source.

Therefore, the physical solution of Eq. (12) has the endpoint with the coordinates (13) and (14). As follows from above, this is the consequence of nonlinearity and renormalizability. The physical significance of this result will be discussed in the next section.

3. RESULTS

In the case of finite nuclei, the quantities $y(r)$ and $y_2(r)$ obey the equations

$$y(r) + \frac{3}{x}y^2(r)[1-y(r)] = \frac{\rho_s(r)}{\rho_1} + \frac{1}{\Lambda^2}\Delta y(r), \quad (15)$$

$$y_2(r) = \frac{\rho_s(r)}{\rho_1} + \frac{1}{\Lambda^2}\Delta y_2(r). \quad (16)$$

Equation (15) is solved by iteration starting from the physical solution of Eq. (12). Both Eqs. (15) and (16) are solved jointly with the relations for the neutron and proton scalar densities $\rho_{s\tau}(r)$, $\tau = n, p$, in the local density approximation [4]:

$$\rho_{s\tau}(r) = \frac{M_\tau(r)}{2\pi^2} \left[k_{F\tau}(r) \sqrt{M_\tau^2(r) + k_{F\tau}^2(r)} - M_\tau^2(r) \ln \frac{\sqrt{M_\tau^2(r) + k_{F\tau}^2(r)} + k_{F\tau}(r)}{M_\tau(r)} \right] \quad (17)$$

with $(k_{F\tau}(r) = (3\pi^2\rho_\tau(r))^{1/3}$ is the local Fermi momentum)

$$M_\tau(r) = m + S_\tau(r), \quad (18)$$

$$\begin{aligned}
S_\tau(r) = S_2(r) - \frac{9xW_m}{4} [y(r) - y_2(r)] \\
+ \frac{1}{2}\beta[\rho_s^-(r)]^2 - \tau_3 [S_2^-(r) + \beta\rho_s(r)\rho_s^-(r)], \\
\rho_s(r) = \rho_{sn}(r) + \rho_{sp}(r), \\
\rho_s^-(r) = \rho_{sn}(r) - \rho_{sp}(r), \\
\tau_3 = \begin{cases} -1, \tau = n, \\ +1, \tau = p, \end{cases}
\end{aligned}$$

and m being the free nucleon mass. The “two-particle” scalar–isoscalar and scalar–isovector fields $S_2(r)$ and $S_2^-(r)$, as well as the vector–isoscalar and vector–isovector ones, are expressed through the free-space two-particle forces as described in [2] (in the present work, the Bonn B potential [8] is used for the two-particle forces).

As shown in [2], the dominant part of the isovector nuclear potential results from the multiparticle forces. But in contrast to the isoscalar term $W(r)$, the isovector one $W^-(r)$ is positive in the whole nuclear region, and, therefore, its multiparticle structure cannot be safely determined. For this reason, we assumed $W^-(r)$ to be of three-particle origin:

$$W^-(r) = \beta\rho_s(r)\rho_s^-(r). \quad (19)$$

It is a functional derivative of the multiparticle symmetry energy

$$\mathcal{E}_{m,\text{symm}} = \frac{1}{2}\beta \int \rho_s(r') [\rho_s^-(r')]^2 d\mathbf{r}' \quad (20)$$

with respect to the isovector–scalar density $\rho_s^-(r)$. But $\mathcal{E}_{m,\text{symm}}$ also has a functional derivative with respect to the isoscalar–scalar density $\rho_s(r)$, and this is just the third term on the right-hand side of the second equation in (18).

The parameters of the nonlinearity are determined by performing the procedure of [2], i.e., solving the Dirac equation with the scalar and vector fields for the doorway-state energies and comparing the calculations with the experimental data. The results are practically the same as those in Fig. 4 of [2]. In this way, we found

$$\begin{aligned}
W_m = 11.5 \text{ MeV}, \quad \rho_1 = 0.146 \text{ fm}^{-3}, \quad (21) \\
x = 16.127, \quad \beta = 5.604 \text{ fm}^5, \quad \Lambda = 986.64 \text{ MeV}.
\end{aligned}$$

As follows from [1] and the present work, the nuclear static energy is

$$\begin{aligned}
\mathcal{E}_{\text{st}} = \sum_{\tau=n}^p \left(\sum_{\lambda} \theta(\varepsilon_{F\tau} - \varepsilon_{\lambda\tau}) n_{\lambda\tau} \varepsilon_{\lambda\tau} \right. \\
\left. + \varepsilon_{F\tau} N_{\tau,\text{out}} \right) - \frac{1}{2} \int \left\{ \left[S_2(r) - \frac{9xW_m}{4} (y(r) \right. \right.
\end{aligned}$$

$$\begin{aligned}
\left. - y_2(r) \right) + 2\beta(\rho_s^-(r))^2 \Big] \rho_s(r) + \frac{27W_m\rho_1}{8} y^3(r) \\
\times \left(\frac{2}{3} - y(r) \right) + S_2^-(r)\rho_s^-(r) + V(r)\rho(r) \\
\left. + V^-(r)\rho^-(r) + C(r)\rho_{\text{ch}}(r) \right\} d\mathbf{r},
\end{aligned}$$

where $V(r)$ and $V^-(r)$ are vector–isoscalar and vector–isovector nuclear fields, $C(r)$ is the Coulomb one, $\rho(r)$ and $\rho^-(r)$ are isoscalar and isovector density distributions, $\rho_{\text{ch}}(r)$ is the charge-density one, $\varepsilon_{\lambda\tau}$ are the doorway-state energies, $\varepsilon_{F\tau}$ is the Fermi level, $n_{\lambda\tau}$ are the occupation numbers, and

$$N_{\tau,\text{out}} = \sum_{\lambda} \theta(\varepsilon_{\lambda\tau} - \varepsilon_{F\tau}) n_{\lambda\tau}. \quad (23)$$

We used the following ansatz for the occupation numbers:

$$\begin{aligned}
n_{\lambda\tau} = x_{\lambda\tau} A_{\tau} \left(\sum_{\nu} x_{\nu\tau} \right)^{-1}, \quad (24) \\
x_{\lambda\tau} = \frac{1}{2} \left(1 - \frac{\varepsilon_{\lambda\tau} - F_{\tau}}{\sqrt{(\varepsilon_{\lambda\tau} - F_{\tau})^2 + D^2}} \right), \\
A_{\tau} = \begin{cases} N, \tau = n, \\ Z, \tau = p, \end{cases}
\end{aligned}$$

with $D = 10$ MeV, i.e., the half-spreading width of the doorway states [2]. The energy F_{τ} is between the Fermi one $\varepsilon_{F\tau}$ and that of the first unoccupied state. The F_{τ} value is chosen to minimize the quantity

$$\int \left(\rho_{\tau,\text{exp}}(r) - \sum_{\lambda} n_{\lambda\tau} \psi_{\lambda\tau}^+(x) \psi_{\lambda\tau}(x) \right)^2 d\mathbf{r}. \quad (25)$$

Here, $\psi_{\lambda\tau}(x)$ are the doorway-state wave functions, $x = \{\mathbf{r}, \alpha\}$, α is the spin variable, and $\rho_{\tau,\text{exp}}(r)$ are the experimentally observed density distributions of neutrons and protons in nuclei. The sum in the integrand is only the diagonal part of the nucleon-density distribution: the latter also has the nondiagonal one

$$\sum_{\lambda\nu(\lambda\neq\nu)} \rho_{\lambda\nu;\tau} \psi_{\lambda\tau}^+(x) \psi_{\nu\tau}(x), \quad \rho_{\lambda\nu;\tau} < \sqrt{n_{\lambda\tau} n_{\nu\tau}}, \quad (26)$$

but, as shown in [1], the nondiagonal elements $\rho_{\lambda\nu;\tau}$ of the density matrix do not enter the static energy. In the calculations, we included the positive-energy states up to 100 MeV, discretizing the continuum by introducing the infinite potential well

$$U_{\tau}(r) = \begin{cases} S_{\tau}(r) + V_{\tau}(r), & r \leq R_{\text{ch}}, \\ \infty, & r > R_{\text{ch}}, \end{cases} \quad (27)$$

Static, binding, and correlation energies (in MeV)

	\mathcal{E}_{st}		$\mathcal{E}_{\text{bind}}$	$\mathcal{E}_{\text{corr}}$
	[1]	present work		
^{16}O	-47.0	-86.2	-127.6	-41.4
^{40}Ca	-120.7	-121.2	-342.0	-220.8
^{90}Zr	-234.2	-107.7	-783.9	-676.2
^{208}Pb	-233.3	+154.6	-1636.5	-1791.1

where the interval $0 < r < R_{\text{ch}}$ is the region in which the nuclear-charge densities are determined in [9].

The correlation energy of nuclei is the difference between the binding and static ones, the former being the experimental quantity. The results of the calculations are shown in the table. As seen from the table, the correlation energy becomes of increasing importance with increasing mass number. The reason for which the static energy changes sign between ^{90}Zr and ^{208}Pb is the increase in positive energy contributions from the multiparticle terms $[9xW_m/8](y(r) - y_2(r))\rho_s(r)$ and $[27W_m\rho_1/16]y^3(r)(y(r) - 2/3)$ with increasing nuclear size.

It is instructive to compare the present results for the static energy with those of [1], where only three- and four-particle forces are taken into account together with the two-particle ones. In this case, the static energy is negative throughout the periodic system, whereas it changes sign between ^{90}Zr and ^{208}Pb when the higher multiparticle forces are included via the nonlinearity of strong interaction.

According to Eqs. (13), (14), (18), and (21), the endpoint values of the scalar density and the scalar field in isosymmetric nuclear matter are

$$\rho_{se} = 0.1933 \text{ fm}^{-3}, \quad y_e = 1.7128, \quad (28)$$

$$S_e = S_{2e} + W_e = -b\rho_{se} - \frac{9xW_m}{4} \left(y_e - \frac{\rho_{se}}{\rho_1} \right) = -497.22 \text{ MeV},$$

where

$$b = \frac{3g_{\sigma 1}^2}{4\mu_{\sigma 1}^2} \left(\frac{\Lambda_{\sigma 1}^2 - \mu_{\sigma 1}^2}{\Lambda_{\sigma 1}^2} \right)^2 + \frac{g_{\sigma 0}^2}{4\mu_{\sigma 0}^2} \left(\frac{\Lambda_{\sigma 0}^2 - \mu_{\sigma 0}^2}{\Lambda_{\sigma 0}^2} \right)^2 = 11.62 \text{ fm}^2, \quad (29)$$

and

$$\frac{g_{\sigma 1}^2}{4\pi} = 8.2797, \quad \frac{g_{\sigma 0}^2}{4\pi} = 16.9822, \quad (30)$$

$$\mu_{\sigma 1} = 550 \text{ MeV}, \quad \mu_{\sigma 0} = 720 \text{ MeV},$$

$$\Lambda_{\sigma 1} = \Lambda_{\sigma 0} = 2000 \text{ MeV}$$

are the Bonn- B -potential parameters [8]. The corresponding endpoint density ρ_e is obtained by solving the equation [4]

$$\rho_{se} = \frac{M_e}{\pi^2} \left(k_{\text{Fe}} \sqrt{M_e^2 + k_{\text{Fe}}^2} - M_e^2 \ln \frac{\sqrt{M_e^2 + k_{\text{Fe}}^2} + k_{\text{Fe}}}{M_e} \right), \quad (31)$$

$$M_e = m + S_e$$

for the endpoint Fermi momentum k_{Fe} . In this way, we get

$$k_{\text{Fe}} = 1.4739 \text{ fm}^{-1}, \quad (32)$$

$$\rho_e = \frac{2k_{\text{Fe}}^3}{3\pi^2} = 0.2213 \text{ fm}^{-3} = 1.3\rho_0,$$

where $\rho_0 = 0.17 \text{ fm}^{-3}$ is the equilibrium density of nuclear matter. Thus, the nuclear static field does not exist at higher densities than the endpoint one. But this result is hardly of any practical significance because (i) there are no stable nuclei with such density values, and (ii) as follows from our results for the static energies, the properties of finite nuclei and nuclear matter are governed by the correlation effects.

4. CONCLUSIONS

Until very recently, it was assumed that nucleons in nuclei interact mainly via the two-particle forces. For this reason, the conventional logic of textbooks on nuclear theory was as follows: "Let us first study deuteron and elastic NN scattering; deduce the NN potential from the relevant experimental data; and use it for few-nucleon systems, complex nuclei, and nuclear matter." But as unambiguously follows from our investigation of the doorway states [1–3, 7], this is the "way nowhere." Indeed:

(i) The three- and four-particle forces are found to be of the same magnitude as the two-particle ones. For this reason, the Faddeev and Faddeev–Jakubowsky equations as well as the Hartree–Fock–Brueckner and Dirac–Hartree–Fock–Brueckner methods are irrelevant approaches, since they are based on the two-particle forces only.

(ii) The seeming success of the above approaches is due to the fact that the three- and four-particle forces nearly compensate each other at observed nucleon density values. But such a near compensation hardly occurs at higher densities, and therefore the contemporary results for the equation of state of nuclear matter are at least doubtful.

(iii) As seen from our results for nuclear static energies, the nonlinearity of strong interaction is of importance, and therefore it must be taken into account to the full extent in nuclear theory.

ACKNOWLEDGMENTS

We are greatly indebted to Prof. M.G. Ryskin and Dr. M.B. Zhalov for permanent attention to our work and helpful discussions.

REFERENCES

1. B. L. Birbrair and V. I. Ryazanov, *Yad. Fiz.* **64**, 471 (2001)[*Phys. At. Nucl.* **64**, 416 (2001)].
2. B. L. Birbrair and V. I. Ryazanov, *Yad. Fiz.* **63**, 1842 (2000)[*Phys. At. Nucl.* **63**, 1753 (2000)].
3. B. L. Birbrair and V. I. Ryazanov, *Yad. Fiz.* **65**, 1491 (2002)[*Phys. At. Nucl.* **65**, 1456 (2002)].
4. J. D. Walecka, *Ann. Phys. (N.Y.)* **83**, 491 (1974).
5. H. Georgi, *Phys. Lett. B* **298**, 187 (1993).
6. R. J. Furnstahl, B. D. Serot, and H. B. Tang, *Nucl. Phys. A* **618**, 446 (1997).
7. B. L. Birbrair and V. I. Ryazanov, *Eur. Phys. J. A* **15**, 343 (2002).
8. R. Machleidt, K. Holinde, and Ch. Elster, *Phys. Rep.* **149**, 1 (1987).
9. H. de Vries *et al.*, *At. Data Nucl. Data Tables* **36**, 495 (1987).

Total Cross Sections for Nucleus–Nucleus Reactions within the Glauber–Sitenko Approach for Realistic Distributions of Nuclear Matter

V. K. Lukyanov^{1)*}, E. V. Zemlyanaya¹⁾, and B. Słowiński^{2),3)}

Received October 17, 2003

Abstract—The microscopic eikonal phase shifts for nucleus–nucleus collisions and total reaction cross sections are calculated by using the expression previously derived for the profile (thickness) of a realistic distribution of nucleons in the form of a symmetrized Fermi function. If, in addition, the density of the projectile nucleus is approximated by a Gaussian function and if a density profile of arbitrary form is taken for the target nucleus, the phase shift in question reduces to a one-dimensional integral. Questions are considered that are associated with the derivation of density parameters for “pointlike” nucleons in nuclei, with the possibility of approximating realistic densities by Gaussian functions in the region of the nuclear surface, with the dependence of the cross section on the range of nucleon–nucleon interaction and on the nuclear-medium density, and with the role of the distortion of the trajectory. Conclusions on the physics of the process are drawn, and the cross sections calculated on the basis of the present approach without using free parameters are compared with available experimental data. © 2004 MAIK “Nauka/Interperiodica”.

1. INTRODUCTION

In nuclear physics, the Glauber–Sitenko approach [1, 2], with allowance for some modifications, is used to study nucleus–nucleus collisions at energies of about 10 to 100 MeV per projectile nucleon. Within this conceptual framework, the eikonal phase shift can be determined either by specifying a phenomenological optical potential or by calculating it within a microscopic approach, where it is expressed in terms of nuclear-density distributions and the amplitude for nucleon–nucleon scattering.

Usually, the parameters of a phenomenological potential $U_{\text{opt}}(r) = V(r) + iW(r)$ are fitted on the basis of a comparison of the results of calculations with experimental data on elastic-scattering cross sections and on total reaction cross sections. However, there remain here questions concerning ambiguities in the resulting parameters [3]. To illustrate this statement, we note that, for the total reaction cross section obtained analytically in [4] for the Woods–Saxon potential, it was shown there that this cross section is determined primarily by two combinations RW_0 and R/a of three parameters of the potential—its range R , its diffuseness a , and its depth

W_0 ; naturally, this makes it possible to vary these parameters within broad ranges of their possible values. As to the microscopic approach, it is absolutely free from adjustable parameters and enables one to calculate the eikonal phase shifts themselves instead of scattering potentials. Owing to this, it is possible to perform predictive calculations—in particular, calculations of total cross sections for reactions involving radioactive nuclei. The latter is of importance for solving problems of radioactive-waste transmutation [5, 6].

Since the early study of Fernbach *et al.* [7], the microscopic approach has been used to calculate proton–nucleus cross sections. Later on, it was generalized in [8, 9] to the case of nuclear–nuclear scattering on the basis of the theory of multiple nucleon scattering by nuclei [1, 2]. It has been extensively employed in analyzing total cross sections for the interaction of beams of light nuclei with nuclei. Among other things, this made it possible to discover a neutron halo in the ${}^6\text{He}$ and ${}^9\text{Li}$ nuclei and a proton halo in the ${}^{11}\text{Be}$ nucleus and to find neutron- and proton-rich nuclei (see, for example, [10]; see also the review articles of Bertulani *et al.* [11] and Knyazkov *et al.* [12]). Much attention has also been given to studying the mechanism of nuclear scattering—namely, to taking into account the deviations of true trajectories from a straight-line one [13, 14], the role of higher order corrections to the eikonal phase shift [15], the clustering of nuclei [16], and other effects.

¹⁾Joint Institute for Nuclear Research, Dubna, Moscow oblast, 141980 Russia.

²⁾Faculty of Physics, Warsaw University of Technology, Warsaw, Poland.

³⁾Institute of Atomic Energy, Otwock–Swierk, Poland.

* e-mail: lukyanov@thsun1.jinr.ru

In the majority of such studies, use is made of Gaussian functions for nuclear densities, since it is possible in this case to perform a separation of variables in multidimensional integrals for eikonal phase shifts and to obtain relevant results in an analytic form. This is the main reason why such functions and their modifications are used in calculating cross sections even for heavy-ion scattering, although physical considerations obviously require taking, in this case, functions of an extended shape as a basis. Fermi functions of the form $u_F(r) = [1 + \exp(r - R/a)]^{-1}$, which provide the most realistic representations for the distributions of the densities and potentials in medium-mass and heavy nuclei, are employed most often in nuclear physics. Unfortunately, it is difficult to perform analytic calculations with Fermi functions—for example, it is impossible to separate variables in the aforementioned multidimensional integrals for the phase shifts. Nevertheless, it has become ever more common to resort to them not only in numerical but also in analytic calculations. In contrast to Gaussian functions, Fermi functions have a correct, exponential, behavior at the periphery of nucleus–nucleus collisions, which is a region that, in such processes, makes a dominant contribution to differential cross sections for scattering and to total reaction cross sections. Therefore, it is highly desirable to develop analytic methods for calculating cross sections within a microscopic approach that would employ realistic shapes of nuclear densities. The parameters of such densities can be borrowed from tabular data obtained, for example, from an analysis of information about electron–nucleus scattering. This would provide sufficient grounds to believe that basic structural features of nuclei participating in the scattering of nuclei are taken correctly into account and would make it possible to study the true mechanism of their interaction and to perform reliable predictive calculations of respective cross sections. This is precisely the objective of the present study.

The ensuing exposition is organized as follows. In Section 2, we present some modifications to the basic formula for the phase shift in the microscopic approach, this being of importance both for obtaining deeper insight into the mechanism of nucleus–nucleus scattering and for performing calculations without resort to assumptions adopted in a number of studies. In Section 3, we give explicit expressions for so-called nuclear-density profile functions specified in the form of a Gaussian, a uniform, and a symmetrized Fermi function. It is shown how the four-dimensional convolution integral for the phase shift can be reduced to a one-dimensional integral if the density of the projectile (light) nucleus is taken in the form of a Gaussian function, while the density of the target nucleus is taken in the form of a symmetrized

Fermi function. In the case of densities having an arbitrary form, this integral can be represented in the form of a one-dimensional integral of the Fourier–Bessel transforms of their profiles. An explicit form of such a transform is given for the profile of a nuclear density represented by a symmetrized Fermi function. Conclusions on the applicability of so-called modified Gaussian density functions are drawn. In Section 4, we examine problems concerning the use of nuclear densities as obtained from nuclear form factors in electron–nucleus scattering, the effect of the choice of range for nucleon–nucleon forces and the effect of distortions of scattering trajectories, and the role of a nuclear medium. In Section 5, we perform a comparison with experimental data and draw conclusions.

2. BASIC FORMULAS OF THE MICROSCOPIC APPROACH

Within the eikonal approximation and the microscopic approach [1, 2], the total reaction cross section has the form

$$\sigma_R = 2\pi \int_0^\infty db b \left(1 - e^{-\chi(b)}\right), \quad (2.1)$$

where the phase shift

$$\chi(b) = \bar{\sigma}_{NN} \mathcal{I}(b) \quad (2.2)$$

is expressed in terms of the isospin-averaged total cross section for nucleon–nucleon scattering,

$$\bar{\sigma}_{NN} = \frac{Z_p Z_t \sigma_{pp} + N_p N_t \sigma_{nn} + (Z_p N_t + N_p Z_t) \sigma_{np}}{A_p A_t}, \quad (2.3)$$

and the convolution integral, which, in the case of nucleus–nucleus scattering, has the form [8]

$$\mathcal{I}(b) = \int d^2 s_p d^2 s_t \rho_p^0(s_p) \rho_t^0(s_t) f(\xi), \quad (2.4)$$

$$\xi = \mathbf{b} - \mathbf{s}_p + \mathbf{s}_t.$$

Here, \mathbf{s} and ξ lie in the impact-parameter (b) plane, which is orthogonal to the z axis aligned with the projectile momentum \mathbf{k}_i ,⁴⁾ and $\rho^0(s)$ stands for the so-called thicknesses (profiles) of the density distributions $\rho^0(r)$ of the centers of mass of nucleons (“pointlike nucleons”) in the projectile and target nuclei (their mass numbers being denoted by A_p and A_t , respectively).⁵⁾ The densities themselves are defined

⁴⁾ A similar expression was obtained in [17] within the model of the flux tubes of nucleons of colliding nuclei.

⁵⁾ We denote by \mathbf{s} and \mathbf{r} the coordinates in, respectively, two- and three-dimensional spaces, the relation $r^2 = s^2 + z^2$ being valid in our case. Accordingly, $\rho(r)$ and $\rho^0(r)$ stand for the density distributions, while $\rho(s)$ and $\rho^0(s)$ are their profiles.

as follows:

$$\rho(s) = \int_{-\infty}^{\infty} dz \rho \left(\sqrt{s^2 + z^2} \right). \quad (2.5)$$

The pointlike densities $\rho^0(r)$ differ from the matter-density distributions $\rho(r)$ in nuclei that consist of actual, “dressed,” nucleons. There is a vast body of tabular data for $\rho(r)$ that were obtained from an analysis of the form factors for electron–nucleus scattering,⁶⁾ and our objective is to develop an approach that would be free from adjustable parameters. However, it is not convenient that, here, pointlike densities $\rho^0(r)$ must be determined each time on the basis of known experimental nuclear densities $\rho(r)$.

The function $f(\xi)$ determines the form of the amplitude for nucleon–nucleon interaction; that is,

$$f(\xi) = (\sqrt{\pi} a_N)^{-2} e^{-\xi^2/a_N^2}, \quad a_N^2 = \frac{2}{3} r_{N\text{rms}}^2, \quad (2.6)$$

where $r_{N\text{rms}}^2$ is the mean-square range of nucleon–nucleon interaction. It can be determined if one considers that the parameter a_N is expressed with the aid of the relation $a_N^2 = 2\beta$ in terms of the slope parameter β of the amplitude for nucleon–nucleon scattering⁷⁾ in the form $\exp(-q^2\beta/2)$. According to [18], values of β at an energy of about 1 GeV lie within the range 0.21–0.23 fm⁻², which corresponds to $r_{N\text{rms}}^2 = 0.63$ –0.69 fm². In our case, nucleon–nucleon forces act in a nuclear medium. In order to take into account its effect, an extra factor f_m is usually introduced in the integrand in (2.4). In the following, we will consider this issue in greater detail.

The convolution integral in (2.4) is close in form to the six-dimensional double-folding integral in the calculations of a nucleus–nucleus potential [19]. In either case, one has to seek methods for separating

⁶⁾In general, the densities $\rho(r)$ appearing here depend on coordinates in the c.m. frame of the corresponding nucleus. However, the center-of-mass-motion factor $\exp(q^2\langle r^2 \rangle/6A)$, where q is the momentum transfer, $\langle r^2 \rangle$ is the mean-square radius of the nucleus being considered, and A is its mass number, is not isolated in them, as a rule, in analyzing experimental form factors. In view of this, tabular $\rho(r)$ provide nuclear-charge or nuclear-matter distributions in the field of a fixed potential. At low q and high A , the densities in the two systems coincide.

⁷⁾The amplitude is $f_N(q) = f_N(0)f(q)$, where $f_N(0) = (k_N/4\pi)\bar{\sigma}_{NN}(i + \alpha_{NN})$, with k_N and α_{NN} being, respectively, the relative momentum of colliding nucleons and the ratio of the real part of the amplitude to its imaginary part. For $f(q) = \exp(-q^2 a_N^2/4)$, the Fourier–Bessel transformation $f(\xi) = (2\pi)^{-2} \int \exp(-i\mathbf{q} \cdot \boldsymbol{\xi}) f(q) d^2q$ then yields expression (2.6); in the zero-range approximation ($a_N = 0$), in which case $f(q) = 1$, we obtain $f(\xi) = \delta^{(2)}(\xi)$.

variables in relevant integrands. In Section 3, it will be shown that this integral can be calculated explicitly if both densities are specified in the form of Gaussian functions or can be reduced to a one-dimensional integral if one of the densities is taken in the Gaussian form. At the same time, there is a standard method for reducing such integrals to one-dimensional integrals via a transition to the momentum representation. For this, we make two-dimensional Fourier–Bessel transformations of the integrands in (2.4) as

$$\begin{aligned} u(s) &= \frac{1}{(2\pi)^2} \int e^{-i\mathbf{k} \cdot \mathbf{s}} \tilde{u}(k) d^2k \quad (2.7) \\ &= \frac{1}{2\pi} \int_0^\infty J_0(ks) \tilde{u}(k) k dk, \end{aligned}$$

where

$$\tilde{u}(k) = \int e^{i\mathbf{k} \cdot \mathbf{s}} u(s) d^2s = 2\pi \int_0^\infty J_0(ks) u(s) s ds. \quad (2.8)$$

Expression (2.4) then takes the form

$$\mathcal{I}(b) = \frac{1}{2\pi} \int_0^\infty k dk J_0(kb) \tilde{\rho}_p^0(k) \tilde{\rho}_t^0(k) \tilde{f}(k), \quad (2.9)$$

where

$$\tilde{f}(k) = \exp(-k^2 r_{N\text{rms}}^2/6). \quad (2.10)$$

For the nuclear-density profile, we further use the convolution

$$\rho_i(s) = \int d^2s_N \rho_N(s_N) \rho_i^0(|\mathbf{s} - \mathbf{s}_N|), \quad (2.11)$$

where $\rho_N(s_N)$ is the nucleon-density function. With the aid of (2.7), we then obtain

$$\tilde{\rho}_i(k) = \tilde{\rho}_N(k) \tilde{\rho}_i^0(k). \quad (2.12)$$

For a Gaussian nucleon density of mean-square radius $r_{0\text{rms}}^2$, we have

$$\tilde{\rho}_N(k) = \exp\left(-\frac{k^2 r_{0\text{rms}}^2}{6}\right). \quad (2.13)$$

From (2.9), it then follows that

$$\mathcal{I}(b) = \frac{1}{2\pi} \int_0^\infty k dk J_0(kb) \tilde{\rho}_p^0(k) \tilde{\rho}_t^0(k) \exp\left(-\frac{k^2 \tau^2}{6}\right), \quad (2.14)$$

$$\tau^2 = r_{N\text{rms}}^2 - r_{0\text{rms}}^2. \quad (2.15)$$

If we assume that $r_{N_{\text{rms}}}^2$ and $r_{0_{\text{rms}}}^2$ coincide, then $\tau^2 = 0$; therefore, we have

$$\mathcal{I}(b) = \frac{1}{2\pi} \int_0^\infty k dk J_0(kb) \tilde{\rho}_p^0(k) \tilde{\rho}_t(k). \quad (2.16)$$

Accordingly, the following relation holds in the coordinate representation:

$$\mathcal{I}(b) = \int_0^\infty d^2s \rho_p^0(|\mathbf{b} - \mathbf{s}|) \rho_t(s). \quad (2.17)$$

Thus, we have derived expressions for the convolution integrals in the form of (2.14), (2.16), and (2.17). Instead of the profile functions for the pointlike target-nucleus density, these expressions involve the profiles of the nuclear-matter density, $\rho_t(s)$ or $\tilde{\rho}_t(k)$. It is the corresponding densities $\rho(r)$ that are known from an analysis of nuclear form factors and are presented in tables; for medium-mass and heavy nuclei, it is common practice to parametrize them in the form of Fermi functions. In principle, relations (2.12) and (2.13) can be used for the projectile nucleus as well, in which case it is necessary to set $\tilde{\rho}_p^0 = \tilde{\rho}_p / \tilde{\rho}_N$. But in the integrands in (2.14) and (2.16), there will then appear a growing Gaussian function, and the integrals in question will be divergent at the upper limit if realistic functions having exponential asymptotic behavior are taken for the profiles of both densities. Of course, one can proceed in a formal way that consists either in cutting off the integrals at a point where the integrands begin to grow or in replacing the Gaussian nucleon form factor $\tilde{\rho}_N(k)$ (2.13) by the dipole expression [see Eq. (4.2) below]. On the other hand, no divergence appears if the profile of the density of one of the nuclei is also taken in the Gaussian form.

Finally, we note that, frequently, phase shifts are calculated in the zero-range approximation ($r_{N_{\text{rms}}}^2 = 0$), this leading to the convolution integral (2.9) with $\tilde{f}(k) = 1$ or, in the coordinate representation, to an expression that is analogous to (2.17), but which involves $\rho_t^0(s)$ instead of $\rho_t(s)$. The replacement of the pointlike densities ρ^0 by the nuclear densities ρ is an even rougher approximation. It can now be seen that such approximations are not necessary and that they distort the true mechanism of nucleus–nucleus scattering.

3. EIKONAL PHASE SHIFTS FOR REALISTIC NUCLEAR-DENSITY DISTRIBUTIONS

It has already been indicated that, in order to obtain analytic expressions for phase shifts and cross

sections, many authors use Gaussian distributions of the densities and their profiles; that is,

$$\rho_G(r) = \rho_G(0) e^{-r^2/a_G^2}, \quad \rho_G(0) = A/(\sqrt{\pi}a_G)^3, \quad (3.1)$$

$$\rho_G(s) = (\sqrt{\pi}a_G) \rho_G(0) e^{-s^2/a_G^2}, \quad a_G^2 = \frac{2}{3} R_{\text{rms}}^2, \quad (3.2)$$

where the only parameter a_G is determined by the root-mean-square radius R_{rms} of the nucleus being considered.⁸⁾

Since uniform density distributions are sometimes used for medium-mass and heavy nuclei, we also present the corresponding distributions and their profiles:

$$\rho_u(r) = \rho_u(0) \Theta(R_u - r), \quad \rho_u(0) = 3A/(4\pi R_u^3), \quad (3.3)$$

$$\rho_u(s) = \rho_u(0) \sqrt{R_u^2 - s^2} \Theta(R_u - s), \quad (3.4)$$

$$R_u^2 = \frac{5}{3} R_{\text{rms}}^2.$$

In a number of cases, a realistic density in the form of a Fermi function is approximated as a linear combination of Gaussian functions with adjustable weight coefficients and the adjustable parameters a_G . This was done in [20]; in [21], a similar fit to the profile of a Fermi function was constructed directly. Unfortunately, one has to repeat this procedure for each new set of parameters R and a of the original Fermi function. However, one can use the fact that, for heavy ions, scattering cross sections and total reaction cross sections are determined primarily by the behavior of phase shifts at the periphery of the collision process. In all probability, this was first taken into account in [22], where the Fermi distribution $\rho_F(r)$ was simulated only in the region of its tail by using one Gaussian function. Later on, Charagi and Gupta [23] employed this procedure to simulate the profile $\rho_F(s)$ of the Fermi function rather than the Fermi function itself. In doing this, they matched, at the periphery, the profile of a Gaussian function [see Eq. (3.2)] to the profile $\rho_F(s)$ at two points, thereby determining both parameters $a_{\bar{G}}$ and $\rho_{\bar{G}}(0)$ of the modified Gaussian function

$$\rho_{\bar{G}}(s) = (\sqrt{\pi}a_{\bar{G}}) \rho_{\bar{G}}(0) e^{-s^2/a_{\bar{G}}^2}. \quad (3.5)$$

This function is not normalized since, in contrast to what we had in (3.1), its parameters are not related to each other. In general, the matching of the profile

⁸⁾In those cases where it is necessary to take the pointlike distributions $\rho_G^0(r)$, the parameter $(a_G^0)^2 = \frac{2}{3} R_{\text{rms}}^2$ can be determined in terms of the root-mean-square radius of the distribution of pointlike nucleons in the nucleus, $R_{\text{rms}}^2 = R_{\text{rms}}^2 - r_{0_{\text{rms}}}^2$.

$\rho_{\bar{G}}(s)$ with any smooth and extended function $\rho(s)$ at two points s_1 and s_2 leads to determining the two parameters of this profile function $\rho_{\bar{G}}(s)$; that is,

$$\rho_{\bar{G}}(0) = (\sqrt{\pi}a_{\bar{G}})^{-1} \rho(s_1) \exp(s_1^2/a_{\bar{G}}^2), \quad (3.6)$$

$$a_{\bar{G}} = \left[\frac{s_2^2 - s_1^2}{\ln \rho(s_1) - \ln \rho(s_2)} \right]^{1/2}. \quad (3.7)$$

In [23], this matching of profiles in the form of modified Gaussian functions with the profiles $\rho_F^0(s)$ of pointlike nuclear Fermi distributions was performed at the points $s_1 = c$ and $s_2 = c + 4d$, where c and d are, respectively, the radius and the diffuseness parameter of the density $\rho_F^0(r)$. The profile functions $\rho_F^0(s)$ themselves were found by means of a numerical integration in (2.5); the diffuseness parameter was taken to be identical for all nuclei, $d = 0.53$ fm; and the radius c was determined on the basis of known data on the root-mean-square charge radii of nuclei and the nucleon (R_{rms} and $r_{0\text{rms}}$, respectively) with the aid of the formula

$$R_{\text{rms}}^2 = R_{\text{rms}}^2 - r_{0\text{rms}}^2 = \frac{3}{5}c^2 \left[1 + \frac{7}{3} \left(\frac{\pi d}{c} \right)^2 \right]. \quad (3.8)$$

In general, the accuracy of this matching must be tested each time when the diffuseness parameter a of the nuclear Fermi densities $\rho_F(r)$ have different values for different nuclei; therefore, the values of the diffuseness parameter d in the calculation of the profiles $\rho_F^0(s)$ are also different. Moreover, the parameters of modified Gaussian functions depend on the choice of matching functions as well.

Since the study reported in [24], the symmetrized Fermi function

$$\begin{aligned} u_{\text{SF}}(r) &= \frac{\sinh(R/a)}{\cosh(R/a) + \cosh(r/a)} \\ &= \frac{1}{1 + \exp \frac{r-R}{a}} - \frac{1}{1 + \exp \frac{r+R}{a}} \end{aligned} \quad (3.9)$$

has been used first in calculating nuclear form factors in electron–nucleus scattering and then in other nuclear-physics problems. It possesses a number of advantages over the Fermi function, this also concerning the case of analytic calculations [25, 26]. Its universality in applications consists in that it faithfully simulates the density distribution in nuclei from light to heavy ones [27]. From (3.9), it can be seen that, for medium-mass and heavy nuclei ($R \gg a$), this function is virtually coincident with the usual Fermi function $u_F(r) = 1/(1 + \exp[(r-R)/a])$. For the symmetrized Fermi density, one can therefore use tabulated data on the Fermi distributions of both nuclear densities [28] and pointlike-nucleon densities [29]. For our problem, it is of importance that the profile

for precisely the symmetrized Fermi function could be found explicitly [30], whereby the ensuing calculations are significantly simplified. The symmetrized Fermi distribution and its profile have the form

$$\rho_{\text{SF}}(r) = \rho_{\text{SF}}(0) \frac{\sinh(R/a)}{\cosh(R/a) + \cosh(r/a)}, \quad (3.10)$$

$$\rho_{\text{SF}}(0) = \frac{3A}{4\pi R^3} \left[1 + \left(\frac{\pi a}{R} \right)^2 \right]^{-1},$$

$$\rho_{\text{SF}}(s) = 2R\rho_{\text{SF}}(0) \frac{\sinh(R/a)}{\cosh(R/a) + \sinh(s/a)} P(s). \quad (3.11)$$

Here, the main dependence of the profile on s is determined by the symmetrized Fermi function having the same parameters as the density $\rho_{\text{SF}}(r)$. The correction function $P(s)$ is given in [30] and is defined in terms of the auxiliary function $x(s)$, which satisfies the condition $x(s) \ll 1$. This makes it possible to simplify the function $P(s)$ in such a way that

$$P(s) = \frac{a}{R} \ln(4/x(s)), \quad (3.12)$$

$$x(s) = \frac{2}{\kappa} \frac{\cosh(s/a)}{\cosh(s/a) + \cosh(R/a)} \left\{ 1 + \frac{\kappa - 1}{\cosh(s/a)} \right\},$$

where κ is expressed in terms of the radius R and the diffuseness parameter a as

$$\kappa = e^{\delta}, \quad (3.13)$$

$$\delta = 1.10315 + 0.34597(R/a) - 0.00446(R/a)^2.$$

The numerical coefficients in (3.13) were found in [30] by fitting the profile in (3.11) to the numerical values of the profile integral (2.5) of the function $\rho_{\text{SF}}(r)$ (3.10) in the parameter region $5 \leq R/a \leq 20$. At the center of the nucleus, the correction function assumes the value of $P(0) = 1$, while, in the region of the main contribution between $s = R$ and ∞ , it changes only slightly, by about $0.4(a/R)$. This makes it possible to use the approximation where $P(s)$ is taken at one point—for example, at $s = R$ or at the point $s = s_{1/3} = R + a \ln 2$, where the density is one-third as great as its value at the origin.⁹⁾ Under the condition $\cosh(R/a) \gg \kappa$, we then have

$$P_a(R) \simeq \frac{a}{R} [\ln 4\kappa] \quad (3.14)$$

$$= \frac{a}{R} \left[2.48945 + 0.34597 \frac{R}{a} - 0.00446 \left(\frac{R}{a} \right)^2 \right]$$

⁹⁾In [19], it was found that the behavior of the cross sections for nucleus–nucleus scattering is determined primarily by the overlap region of the densities at their periphery for $s \geq s_{1/3}$, where $\rho(s_{1/3}) = (1/3)\rho(0)$.

and, accordingly,

$$\rho_{\text{SF}}(s) \simeq 2R\rho_{\text{SF}}(0) \frac{\sinh(R/a)}{\cosh(R/a) + \cosh(s/a)} P_a(R). \quad (3.15)$$

For the ^{16}O , ^{40}Ca , and ^{208}Pb nuclei, the profile functions for the densities in the form of the symmetrized Fermi function are shown in Fig. 1 according to a numerical calculation by formula (2.5) (points), along with the corresponding profiles for a modified Gaussian function that were obtained by formulas (3.6) and (3.7) at $s_1 = R$ and $s_2 = R + 4a$. The solid curves there represent the results of the calculation of $\rho_{\text{SF}}(s)$ by the analytic formula (3.11). The parameters of the density in the form of the symmetrized Fermi function were borrowed from [27] and are quoted in Table 1. It can be seen that, in the internal region, there is a strong discrepancy between the profiles for a modified Gaussian function and the profiles of the density in the form of the symmetrized Fermi function (for example, by nearly two orders of magnitude for ^{208}Pb). There is also a discrepancy in the region where the densities themselves decreased by not less than two orders of magnitude. The profiles of a uniform and a Gaussian form of the density distribution will differ from the profile of the Fermi functions even more pronouncedly. In Fig. 2, the profiles $\rho_{\text{SF}}(s)$ are shown for the same nuclei, but according to the calculation by (solid curves) the analytic formula (3.11) with the exact correction function $P(s)$ and (dashed curves) the analytic formula (3.15) with the approximate correction function $P_a(s = R)$. It turns out that the use of the correction function at the radius value introduces virtually no changes in the behavior of the profile function in the peripheral region. A modest distinction within a factor of 2 for the ^{208}Pb nucleus appears only in the nuclear interior, this being much less than the distinction between the profile functions for the symmetrized Fermi and modified Gaussian functions (see Fig. 1).

Thus, we have the possibility of choosing, in the following, the profiles $\rho(s)$ of an explicit analytic form for a Gaussian, a uniform, and a symmetrized Fermi function. Below, these three types of functions will be employed in calculating the microscopic eikonal phase shifts $\chi(b)$ and total reaction cross sections.

First, we consider the convolution integral (2.17) for the case where the Gaussian function (3.5) is taken for the profile $\rho_p^0(\zeta)$ of the projectile-nucleus density. Substituting in it

$$\rho_{\text{G},p}^0(|\mathbf{b} - \mathbf{s}|) = (\sqrt{\pi}a_{\text{G},p}^0)\rho_{\text{G},p}^0(0) \times \exp\left[-\frac{1}{(a_{\text{G},p}^0)^2}(b^2 - 2bs \cos \varphi + s^2)\right] \quad (3.16)$$

and employing, in performing integration with respect to the variable φ , the definition of the zeroth-order Bessel function of an imaginary argument, $I_0(x)$ [31], we obtain

$$\mathcal{I}_{\text{G},t}(b) = 2\pi(\sqrt{\pi}a_{\text{G},p}^0)\rho_{\text{G},p}^0(0) \exp\left(-\frac{b^2}{(a_{\text{G},p}^0)^2}\right) \times \int_0^\infty ds s \rho_t(s) \exp\left(-\frac{s^2}{(a_{\text{G},p}^0)^2}\right) I_0\left(\frac{2bs}{(a_{\text{G},p}^0)^2}\right). \quad (3.17)$$

In a more general case where the root-mean-square radius of the nucleon differs from the range of nucleon–nucleon interaction, it is convenient to use the convolution integral (2.4) featuring the profiles of pointlike densities for both nuclei. It can then be shown that, in the case of a modified Gaussian profile function for the projectile nucleus [see Eq. (3.5)], the convolution integral takes the form

$$\mathcal{I}_{\text{G},N,t}(b) = 2\pi \frac{(a_{\text{G},p}^0)^2}{(a_{\text{G},p}^0)^2 + a_N^2} \times (\sqrt{\pi}a_{\text{G},p}^0)\rho_{\text{G},p}^0(0) \exp\left(-\frac{b^2}{(a_{\text{G},p}^0)^2 + a_N^2}\right) \times \int_0^\infty ds s \rho_t^0(s) \exp\left(-\frac{s^2}{(a_{\text{G},p}^0)^2 + a_N^2}\right) \times I_0\left(\frac{2bs}{(a_{\text{G},p}^0)^2 + a_N^2}\right). \quad (3.18)$$

Table 1. Parameters of the symmetrized Fermi nuclear-density distributions $\rho_{\text{SF}}(r, R, a)^*$

Nucleus	R , fm	a , fm	R_{rms} , fm	References
^{12}C	2.214	0.488	2.496	[27]
^{16}O	2.562	0.497	2.711	[27]
^{20}Ne	2.74	0.572	3.004	[28]
^{24}Mg	2.934	0.569	3.105	[27]
^{27}Al	3.07	0.519	3.06	[28]
^{28}Si	3.085	0.563	3.175	[27]
^{32}S	3.255	0.601	3.370	[27]
^{40}Ca	3.556	0.578	3.493	[27]
^{66}Zn	4.340	0.559	3.952	[28]
^{89}Y	4.86	0.542	4.27	[28]
^{208}Pb	6.557	0.515	5.427	[27]

* The parameters taken from [28] were given there for the Fermi distributions $\rho_F(r, R, a)$, which are close to $\rho_{\text{SF}}(r, R, a)$ for the four nuclei indicated there.

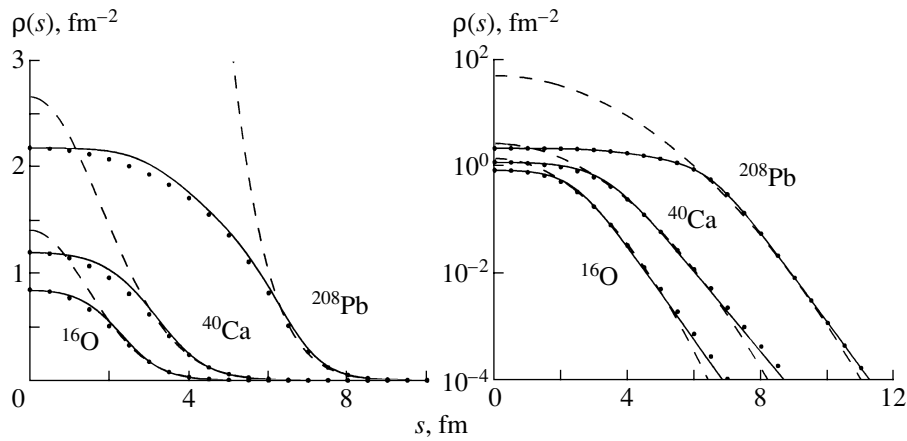


Fig. 1. Thickness functions for the density in the form of the symmetrized Fermi function: (points) results of a numerical integration by formula (2.5), (dashed curves) profiles in the form of a modified Gaussian function that are matched with them, and (solid curves) results of the calculation by the analytic formula (3.11). The parameters of the density were borrowed from Table 1.

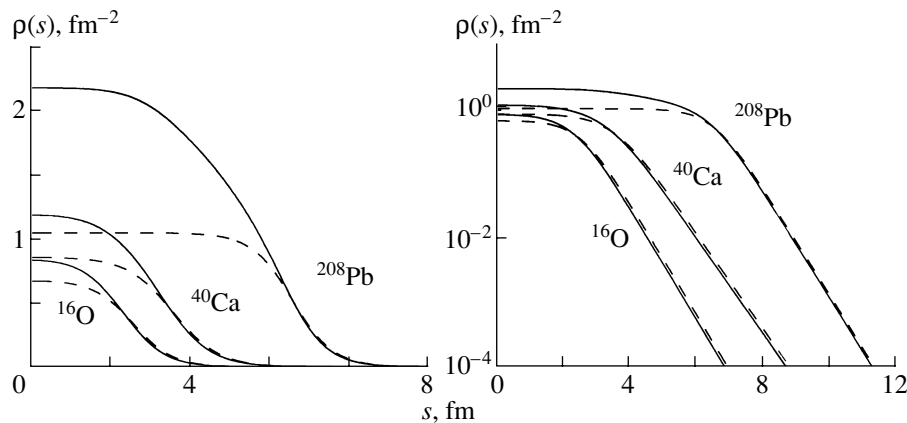


Fig. 2. Thickness functions for the densities in the form of the symmetrized Fermi function according to the calculation by (solid curves) the analytic formula (3.11) with the exact correction function $P(s)$ and (dashed curves) formula (3.15) with the approximate correcting function $P_a(s = R)$. The parameters here are identical to those used for Fig. 1.

If the Gaussian profile function for the target nucleus is substituted in this expression, the integral in (3.18) is taken explicitly [31]. The result is [22]

$$\mathcal{I}_{\bar{G},N,t}(b) = \frac{1}{\pi} \frac{(\sqrt{\pi}a_{\bar{G},p}^0)^3 (\sqrt{\pi}a_{\bar{G},t}^0)^3}{(a_{\bar{G},p}^0)^2 + (a_{\bar{G},t}^0)^2 + a_N^2} \rho_{\bar{G},p}^0(0) \times \rho_{\bar{G},t}^0(0) \exp\left(-\frac{b^2}{(a_{\bar{G},p}^0)^2 + (a_{\bar{G},t}^0)^2 + a_N^2}\right). \quad (3.19)$$

We note that the substitutions $\bar{G} \rightarrow G$ and $(\sqrt{\pi}a_i^0)^3 \rho_{\bar{G},i}^0(0) \rightarrow A_i$ are necessary in (3.17)–(3.19) if use is made of the normalized Gaussian functions (3.1).

We take it for granted that symmetrized Fermi functions provide realistic density distributions in

medium-mass and heavy nuclei. The corresponding profile functions are given explicitly by Eq. (3.10) or (3.15). The Bessel functions $I_0(x)$ and $J_0(x)$ are also known explicitly in the form of approximations in terms of polynomials [32]. Thus, all functions in the convolution integrals (3.17) and (3.18) are specified explicitly, which is very convenient for a numerical integration.

In the case where, for both nuclei, the density distribution is specified in the form of symmetrized Fermi functions, it is advisable to use the convolution integrals in the momentum representation (2.9), (2.14), or (2.16), a convenient form of the profiles for such distributions being that in the approximation specified by Eq. (3.15). The respective Fourier transform can then be calculated explicitly. Indeed, the substitution of the density function (3.15) as $u(s)$ into (2.8) makes

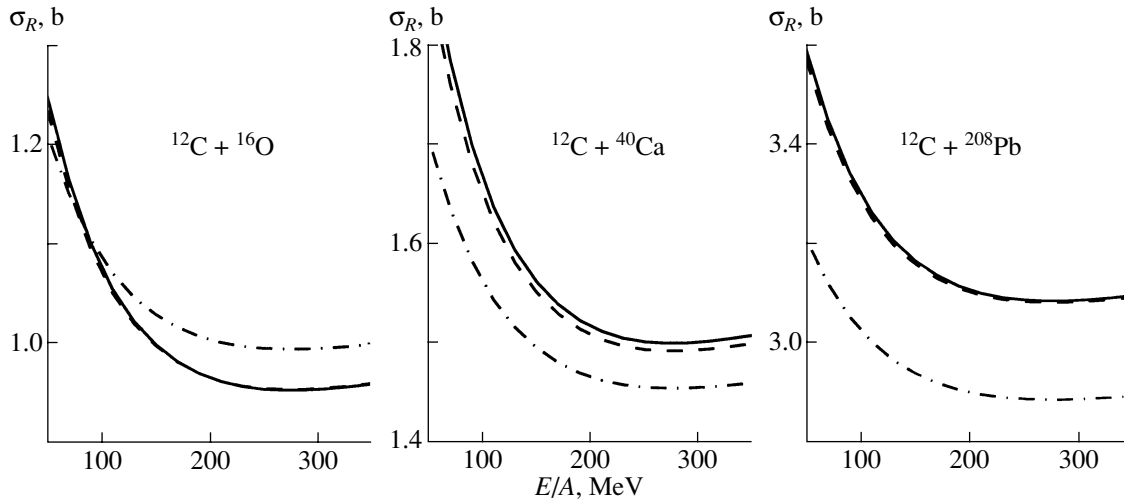


Fig. 3. Total reaction cross sections obtained by using various models of the density–thickness functions. For the projectile nucleus ^{12}C , use was made of a profile taken in the form of a modified Gaussian function and fitted to the profile of the pointlike–nucleon density in the form of a symmetrized Fermi function (the values of the relevant parameters are quoted in Table 2). For target nuclei, the density profiles corresponded to nuclear densities in the form of symmetrized Fermi functions (the parameter values are quoted in Table 1), uniform nuclear densities [see Eq. (3.4)], or nuclear densities simulated in the same way as for the target nucleus [model of modified Gaussian functions—see Eq. (3.5)]. The results for these three cases are represented by the solid, dash-dotted, and dashed curves, respectively.

it possible to write

$$\tilde{\rho}_{\text{SF}}(k) = 4\pi R \rho_{\text{SF}}(0) P_a(R) \mathcal{F}_{\text{SF}}(k, a, R), \quad (3.20)$$

where

$$\begin{aligned} \mathcal{F}_{\text{SF}}(k, a, R) &\equiv \mathcal{F}_{\text{SF}}(k) \\ &= \int_0^\infty s ds J_0(ks) \frac{\sinh(R/a)}{\cosh(R/a) + \cosh(s/a)}. \end{aligned} \quad (3.21)$$

Taking into account the peripheral character of nuclear collisions, we can assume that the main contribution comes from the region $ks \gg 1$. We then have the following approximate expression (see, for example, [33]):

$$\mathcal{F}_{\text{SF}}(k) = \frac{\pi a R}{\sinh(\pi a k)} J_1(kR). \quad (3.22)$$

Sprung and Martorell [25] obtained corrections to it, but these corrections are immaterial in the above calculations of the total cross sections.

In Fig. 3, the total reaction cross sections calculated for collisions between ^{12}C projectile nuclei of energy 50 to 350 MeV per nucleon and ^{16}O , ^{40}Ca , and ^{208}Pb target nuclei are shown for three cases where the nuclear densities in the target nuclei were chosen in the form of symmetrized Fermi functions, modified Gaussian functions, or uniform-distribution functions. In calculating the phase shift χ , use was made of the convolution integral in the form (3.17). For the projectile nucleus ^{12}C , we took the density profile in the form of a modified Gaussian function

matched at the points $s_1 = c$ and $s_2 = c + 4a$ [see Eqs. (3.5)–(3.7)] with the profile of the pointlike–nucleon density in the form of a symmetrized Fermi function (the parameter values are given in Table 2). The profile functions for the target nuclei in the form of modified Gaussian functions were matched in the same way, the parameters of ρ_{SF} being taken from Table 1. This table also presents the values of the root-mean-square radius R_{rms} that were used to calculate the radius R_u of the uniform-distribution density (3.4). The total cross sections σ_{NN} for nucleon–nucleon scattering as functions of energy were parametrized as in [23]. One can see that, for the density in the form of a step (dash-dotted curves), the behavior of the total reaction cross section differs significantly from that which is obtained in the case

Table 2. Parameters of the symmetrized Fermi distributions $\rho_{\text{SF}}^0(r, c, d)$ of the pointlike–nucleon density in nuclei [29]

Nucleus	c , fm	d , fm
^{12}C	2.275	0.393
^{16}O	2.624	0.404
^{24}Mg	2.984	0.484
^{28}Si	3.134	0.477
^{32}S	3.291	0.520
^{40}Ca	3.593	0.493

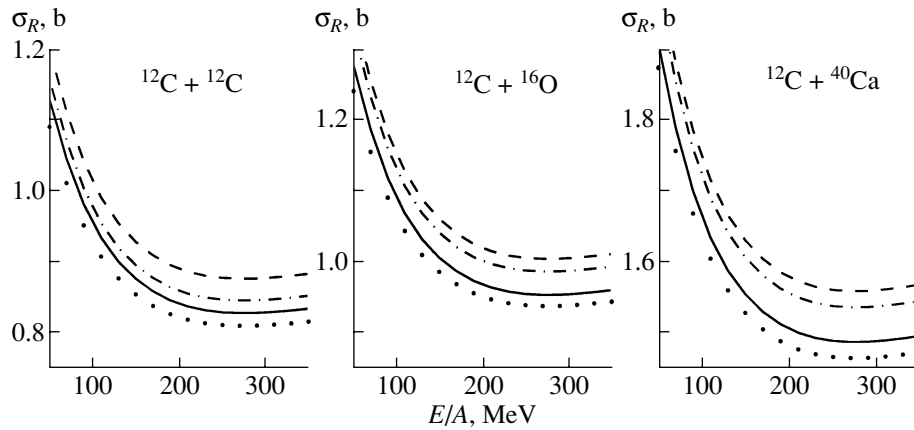


Fig. 4. Illustration of the dependence of the calculated cross sections on the parameters of the pointlike-nucleon density that were determined from an analysis of data on electron–nucleus scattering: (solid curves) results of the calculations with the parameter values from Table 2, (dashed curves) results obtained with the parameters determined by using Eqs. (4.3), (dash-dotted curves) results of the calculations with the parameters borrowed from [37], and (points) results of the calculation in the momentum representation with the aid of Eq. (3.20) (see main body of the text).

of the physically validated density in the form of a symmetrized Fermi function (solid curves). The calculations of the cross sections on the basis of the models of a symmetrized Fermi function (solid curves) and a modified Gaussian function (dashed curves) are in satisfactory agreement with each other. That, at low energies, the cross sections calculated with symmetrized Fermi functions exceed slightly those calculated with modified Gaussian functions is due to an extended tail of the densities in the form of a symmetrized Fermi function. A weak growth of the cross sections calculated with modified Gaussian functions for target nuclei at higher energies in relation to the case of symmetrized Fermi functions is associated with the greater values of the modified Gaussian functions in the nuclear interior, this resulting in that absorption is switched on earlier.

The calculation of the cross sections in the momentum representation for the case where realistic symmetrized Fermi distributions ρ_{SF} are taken for both nuclei with an approximate correcting function $P_a(R)$ in the form (3.14) and, accordingly, approximate profiles in the form (3.20) leads (see Fig. 4) to results (points) that differ slightly (by about 2%) from the results of precise calculations (solid curves).

4. RESULTS OF THE CALCULATIONS AND DISCUSSION

4.1. On the Use of Nuclear Densities from Electron–Nucleus Scattering

The convolution integrals (2.4) and (2.9) involve the profiles of the pointlike-nucleon densities $\rho^0(s)$ of both nuclei. At the same time, one of the densities in the transformed integrals (2.16) and (2.17) remains a pointlike one, while the other is a nuclear density

$[\rho(s)]$. Thus, the problem of determining pointlike-nucleon densities is not removed, so that it is necessary to address the question of how they can be derived. In general, they can be constructed on the basis of nuclear models. However, we were inclined from the outset to rely on data from independent experiments—for example, on densities as obtained from nuclear form factors. As before, we will assume that $\rho_{(S)F}^0(r)$ provides a realistic form of pointlike-nucleon density.

The first method was developed in [29] and is based on isolating, in the experimental nuclear form factor $F(q)$, the form factor $F^0(q)$ for a nucleus formed by pointlike nucleons and on extracting, from the latter, the density distribution of pointlike nucleons. In just the same way as in (2.12), the nuclear form factor is then represented in the form

$$F(q) = F_P(q)F^0(q); \quad (4.1)$$

for the proton form factor, use was made of the dipole formula, which, at low momentum transfers, can be approximated by a Gaussian function as

$$F_P(q) = \left(1 + \frac{q^2 r_{0rms}^2}{12}\right)^{-2} \simeq \exp(-q^2 r_{0rms}^2/6). \quad (4.2)$$

Further, the method of a model-independent analysis was used to reconstruct the density $\rho^0(r)$ from $F^0(q)$, a trial density function being chosen as a linear combination of the function $\rho_{SF}^0(r)$ and its radial variations in the form of the derivatives $\rho_{SF}^{0(n)}(r)$ with adjustable weight coefficients. For these trial densities, the calculations of $F^0(q)$ were performed in the high-energy approximation [34, 35] (rather than in

the Born approximation), which yields results that are close to numerical solutions to the Dirac equation. Table 2 presents part of these data [29]—namely, the radius c and the diffuseness parameter d of the density $\rho_{\text{SF}}^0(r, c, d)$. We disregarded the contribution of the radial variations to the total cross sections, since they manifest themselves only in differential cross sections at high momentum transfers. We note that the value of $r_{0\text{rms}}^2 = 0.658 \text{ fm}^2$, which was used in the analysis in [29] for the proton mean-square radius, is close to the nucleon mean-square radius of $r_{0\text{rms}}^2 = 0.65 \text{ fm}^2$ in the calculation of the double-folding potential in [19]. Therefore, it is quite legitimate to identify the pointlike-nucleon densities obtained in [29] with the density distributions $\rho_{\text{SF}}^0(r)$ of pointlike nucleons.¹⁰⁾

An alternative method was developed in [36] and is based on deriving the parameters c and d of the density $\rho^0(r, c, d)$ from data on the nuclear densities $\rho(r, R, a)$ with the aid of a comparison of r^n moments calculated analytically, on one hand, for the density $\rho_{\text{F}}(r, R, a)$ having an explicit form and, on the other hand, for the same density specified by the folding formula, which is similar to (2.11). If only terms of order $(\pi a/R)^2$ and $r_{0\text{rms}}^2/(9c^2)$ are retained in the expansions of the corresponding integrals, it then turns out that

$$c = R \left[1 + \frac{1}{3} \left(\frac{r_{0\text{rms}}}{R} \right)^2 \right], \quad (4.3)$$

$$d = a \left[1 - \frac{1}{2} \left(\frac{r_{0\text{rms}}}{\pi a} \right)^2 \right].$$

If one employs the parameters of the nuclear density $\rho_{\text{SF}}(r, R, a)$ from Table 1 and sets $r_{0\text{rms}}^2 = 0.658 \text{ fm}^2$, then the calculations by formulas (4.3) yield results for the radius c of the pointlike-nucleon density that are slightly underestimated (by less than 1%) in relation to the data in Table 2 and results for the diffuseness parameter d that are overestimated (by not more than 10%) in relation to the respective data there. In order to assess the degree to which the accuracy in determining them is of importance in calculating total cross sections, we examine the data in Fig. 4. For that case, pointlike-nucleon densities in the form of

¹⁰⁾Assuming that the neutron and proton components of the nuclear density are related by the equation $\rho_N^0(r) = (N/Z)\rho_Z^0(r)$ and specifying the root-mean-square radii of the nuclear density (R_{rms}^2) and of the pointlike-nucleon distribution ($\mathcal{R}_{\text{rms}}^2$), as well the mean-square radii of protons ($\langle r^2 \rangle_p = 0.76 \text{ fm}^2$) and neutrons ($\langle r^2 \rangle_n = -0.11 \text{ fm}^2$) (see [19]), we find from the relation $R_{\text{rms}}^2 = \mathcal{R}_{\text{rms}}^2 + \langle r^2 \rangle_p + \langle r^2 \rangle_n = \mathcal{R}_{\text{rms}}^2 + \langle r^2 \rangle$ that the mean-square radius of nucleons is $\langle r^2 \rangle = \langle r^2 \rangle_p + \langle r^2 \rangle_n = 0.65 \text{ fm}^2$.

symmetrized Fermi functions were taken for both nuclei in the convolution integral (2.9). The solid curves there show the results obtained for the case where the parameters c and d were set to the values from Table 2. The dashed curves correspond to the calculations with the parameters c and d determined by formulas (4.3) on the basis of the R and a values from Table 1. The dash-dotted curves represent the results of the calculations with the parameters c and d of pointlike-nucleon distributions from [37], where they are given (in femtometers) for ^{12}C (2.1545, 0.425), ^{16}O (2.525, 0.45), and ^{40}Ca (3.60, 0.523). In that study, they were used in calculating the real part of the double-folding potentials for nucleus–nucleus interaction, and this made it possible to explain data on the elastic scattering of nuclei at energies of about 10 MeV per nucleon. In all cases, we set $r_{N\text{rms}}^2 = 0.658 \text{ fm}^2$. It can be seen that the distinction between the cross sections is within about 6 to 10%. We believe that the method of deriving the pointlike-nucleon densities from an analysis of nuclear form factors $F^0(q)$ is the most justified, and it is of importance to compose tables of such densities.

4.2. On the Choice of Range for Nucleon–Nucleon Interaction

In Section 2, it was shown that, in the case where the root-mean-square nucleon radius is assumed to be equal to the range of nucleon–nucleon interaction ($r_{0\text{rms}}^2 = r_{N\text{rms}}^2$), the convolution integral is simplified, taking the form (2.17), where only two functions overlap, the profile of the nuclear-density distribution in the target nucleus and the profile of the pointlike-nucleon density in the projectile nucleus. In general, the above radius and range may be different, however. As to the shape parameter of the nucleon–nucleon interaction, $a_N^2 = (2/3)r_{N\text{rms}}^2$, it can be found from data on free-nucleon scattering that $r_{N\text{rms}}^2$ takes values in the range 0.63–0.69 fm^2 . At the same time, $r_{0\text{rms}}^2$ was taken to be 0.658 fm^2 in the dipole formula (4.2) [29] and 0.650 fm^2 in calculating the double-folding potential for the nucleus–nucleus interaction [19]. We have calculated the total reaction cross sections with $r_{N\text{rms}}^2 = 0.63, 0.658, 0.69 \text{ fm}^2$ (Fig. 5), employing the more general expression for the convolution integral in the form (3.18). For the ^{12}C , ^{16}O , and ^{40}Ca nuclei, the parameters c and d of the pointlike-nucleon densities are given in Table 2, while, for the ^{208}Pb nucleus, they were calculated by formulas (4.3). As in Fig. 3, the profile for the ^{12}C projectile nucleus was taken in the form of a modified Gaussian function and was matched with the profile in the form of a symmetrized Fermi function. In Fig. 5,

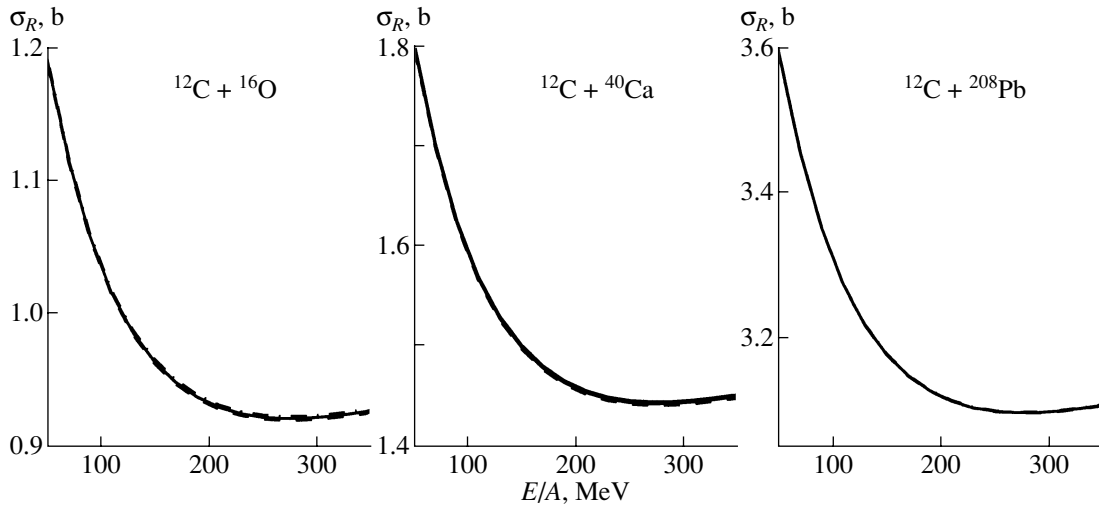


Fig. 5. Effect of the choice of range for nucleon–nucleon interaction on the total cross sections for nuclear–nuclear reactions: $r_{N_{rms}}^2 =$ (solid curves) 0.658, (dashed curves) 0.630, and (dash-dotted curves) 0.69 fm². The values of the parameters c and d were taken from Table 2 for the ¹⁶O and ⁴⁰Ca nuclei and were determined for the ²⁰⁸Pb nucleus by formulas (4.3) on the basis of the R and a values from Table 1. For the ¹²C nucleus, the profile in the form of a modified Gaussian function is identical to that in Fig. 3.

it can be seen that, in all of the examples considered here, the cross sections are nearly identical, especially for heavy target nuclei. Thus, investigation of total cross sections for nucleus–nucleus reactions does not highlight distinctions between the root-mean-square nucleon radius and the range of nucleon–nucleon interaction. Moreover, it should be borne in mind that the parameter a_N of the amplitude for the nucleon–nucleon interaction in a nuclear medium can differ from its value in the case of free-nucleon scattering.

4.3. Effect of the Distortion of Trajectories

In the repulsive Coulomb field of the target nucleus, the trajectory of the projectile nucleus is deflected from the scattering center, this naturally leading to a decrease in the total reaction cross section. In [38], this effect was taken into account by replacing, in the phase shift $\chi(b)$, the impact parameter b by the distance b_c of the closest approach of colliding nuclei in the Coulomb field; that is,

$$b \rightarrow b_c = \bar{a} + \sqrt{\bar{a}^2 + b^2}, \quad (4.4)$$

where $\bar{a} = Z_p Z_t e^2 / (2E_{c.m.})$ is half the distance of the closest approach in the field $Z_p Z_t e^2 / r$ at $b = 0$, with $E_{c.m.}$ being the kinetic energy in the c.m. frame of colliding nuclei. The substitution of b_c for b in the nuclear part $\Phi_N(b)$ of the phase shift has come into use in calculating differential cross sections for elastic scattering as well (see [13]); in general, this procedure proved to be quite justified (see, for example, [39]).

At the periphery of the collision process, the contribution to the distortion from the real part $V(r)$ of the attractive nuclear potential can also be taken into account, in principle, which would bring the Coulomb trajectory closer to the target nucleus. If the region $b \geq R_s = R_p + R_t + (a_p + a_t) \ln 2$, where the overlapping nuclear densities are less than one-third of their values at the center [19], is assumed to be the main region of elastic collisions, then the effect of the tail of the nuclear potential can be qualitatively taken into account by means of the substitution

$$b \rightarrow \tilde{b}_c = \tilde{a} + \sqrt{\tilde{a}^2 + b^2}, \quad (4.5)$$

where $\tilde{a} = (Z_p Z_t e^2 - R_s |V(R_s)|) / (2E_{c.m.})$. A more refined method for taking into account nuclear distortions was formulated in [40] and was applied in a number of studies (see, for example, [14]). If, however, the optical potential $V_{opt}(r)$ itself is constructed by means of a numerical fit to experimental data, then the use of its real part for taking into account the distortion of the trajectory in calculating total reaction cross sections σ_R is meaningless. Indeed, data on σ_R , if any, are included themselves in such cases in the fitting procedure. If, on the contrary, there are no such data, then they are calculated on the basis of the S_l matrix obtained by using data on only elastic scattering, and these “calculated” σ_R are frequently considered as “experimental data” on total cross sections. Thus, the inclusion of nuclear distortions of trajectories is likely to be meaningful only in constructing the eikonal phase shifts for distorted waves in calculating inelastic scattering and nucleon-transfer reactions within

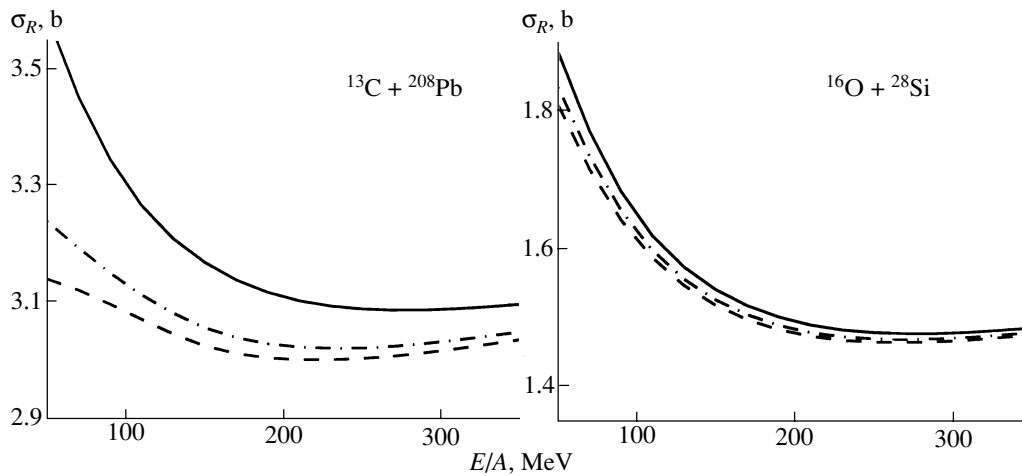


Fig. 6. Illustration of the role of the distortion of trajectories in calculating total reaction cross sections. The solid curves correspond to cross sections obtained without allowance for distortions, while the dashed and dash-dotted curves represent the results of the calculations allowing, respectively, for only the Coulomb distortion and for the Coulomb and nuclear distortions. The choice of parameter values for these data is discussed in the main body of the text.

the theory of direct reactions. In principle, the real part of the nucleus–nucleus potential can be calculated—for example, by the folding method. In this case, it is meaningful to calculate both differential and total cross sections on the basis of the Glauber–Sitenko approach with allowance for the distortion of the trajectory by both the Coulomb and the nuclear field.

Figure 6 presents the results obtained by calculating the total cross sections for $^{13}\text{C} + ^{208}\text{Pb}$ and $^{16}\text{O} + ^{28}\text{Si}$ reactions by using the convolution integral in the form (3.17). The calculations were performed either without allowance for distortions of trajectories (solid curves) or with allowance for such distortion by only the Coulomb field according to (4.4) (dashed curves) or by both the Coulomb and the nuclear potential according to (4.5) (dash-dotted curves). In the last case, it was necessary to specify the parameters of the real part of the optical potential, and we took them from [41] for $^{13}\text{C} + ^{208}\text{Pb}$ (potential C at 390 MeV) and from [42] for $^{16}\text{O} + ^{28}\text{Si}$ (potential E-18 at 215.2 MeV). In calculating phase shifts, we used, for the ^{13}C nucleus, the parameters of the pointlike-nucleon density in the ^{12}C nucleus and took them from Table 2, together with the density parameters of the ^{16}O nucleus. For the ^{208}Pb and ^{28}Si nuclei, such parameters were calculated by formulas (4.3) on the basis of the R and a values from Table 1. As might have been expected, the inclusion of the Coulomb distortion generates sizable corrections (about 10%) in the total cross sections for reactions on heavy nuclei at energies below 100 MeV per nucleon, these corrections being beyond the experimental errors. With increasing collision energy, the corrections in question decrease; for lighter target nuclei (right panel in

Fig. 6), they are about 2%, which can be disregarded. The contribution of the nuclear distortion is small in relation to its Coulomb counterpart for ^{208}Pb and is commensurate with it for the reaction on ^{28}Si , but both effects are small in the latter case. Moreover, it should be borne in mind that the real part of the nuclear potential decreases with increasing energy. In view of this, the contribution of the nuclear distortion decreases at higher energies, but we disregarded this in our estimate.

4.4. Role of a Nuclear Medium

The microscopic approach involves the energy-dependent cross section $\sigma_{NN}(\varepsilon_{\text{lab}})$ for free-nucleon scattering, and this is precisely what determines primarily the dependence of the nuclear cross section on the collision energy $E_{\text{lab}} = \varepsilon_{\text{lab}} A_p$. We take $\sigma_{NN}(\varepsilon_{\text{lab}})$ in the form of the parametrization obtained in [23] within the energy range $\varepsilon_{\text{lab}} = 0.01\text{--}1$ GeV. In a more general case, the effect of a nuclear medium is taken into account by introducing this cross section in the integrand of the convolution integral and by making the substitutions

$$\begin{aligned}\sigma_{np} &\rightarrow \sigma_{np} f_m(np), \\ \sigma_{pp} = \sigma_{nn} &\rightarrow \sigma_{nn} f_m(nn),\end{aligned}\quad (4.6)$$

where the factors $f_m(np)$ and $f_m(nn)$ depend on the nucleon energy $\varepsilon_{\text{lab}} = E_{\text{lab}}/A_p$ and on the nuclear-matter density. The problem of the nuclear-medium effect on the nucleon–nucleon interaction has been examined by many authors. For example, numerical calculations of the total cross sections for nucleon–nucleon interaction in nuclear matter were performed in [43] on the basis of the Dirac–Brueckner approach,

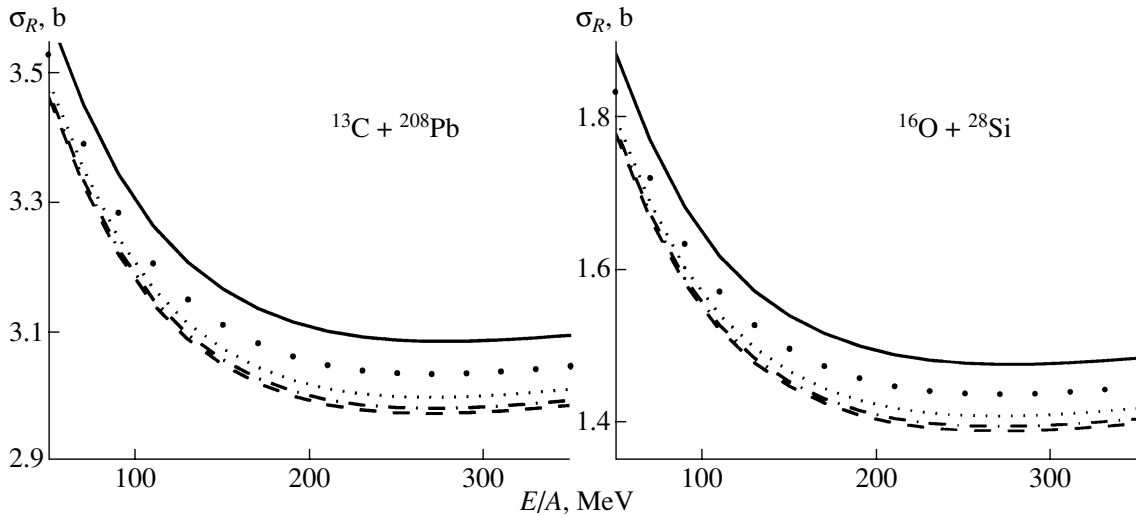


Fig. 7. Illustration of the role of a nuclear medium in calculating total reaction cross sections: results obtained (solid curves) without allowance for the factor of the medium effect ($\bar{\rho} = 0$), (points) at the density value in the overlap region at $1/20$ of the density $\rho_0 = \rho_p(0) + \rho_t(0)$ at the center of either nucleus, (dotted curves) at the density value $(1/6)\rho_0$, (dash-dotted curves) at the density value $(1/3)\rho_0$, and (dashed curves) for the case of the density overlap at the centers of the nuclei involved (at ρ_0).

while the parametrization of these cross sections was given in [44] by means of introducing the correction factors

$$f_m(np) = \frac{1 + 20.88\varepsilon_{\text{lab}}^{0.04} \rho^{2.02}}{1 + 35.86\rho^{1.90}}, \quad (4.7)$$

$$f_m(nn) = \frac{1 + 7.772\varepsilon_{\text{lab}}^{0.06} \rho^{1.48}}{1 + 18.01\rho^{1.46}},$$

where the energy and density are given in MeV and fm^{-3} units. It can be seen that, in the particular case of free nucleons, where $\rho = 0$, we have $f_m(np) = f_m(nn) = 1$; with increasing density, the factors in question and, hence, the effective cross sections decrease.¹¹⁾ It is difficult to calculate the convolution integrals with the correction factors in the above form and with allowance for the dependence of the density on r ; therefore, we restrict ourselves to deriving qualitative estimates of the nuclear-medium effect on total cross sections for nucleus–nucleus reactions. In Fig. 7, the results of such calculations are illustrated for the case where the nuclear densities in (4.7) are assumed to be constant ($\rho = \bar{\rho} = \bar{\rho}_p + \bar{\rho}_t$) for any region of location of an interacting-nucleon pair. Denoting by $\rho_0 = \rho_p(0) + \rho_t(0)$ the total density at the

centers of colliding nuclei, we then present the results obtained by calculating the cross section for (solid curves) free-nucleon scattering (at $\bar{\rho} = 0$), as well as for (points) $\bar{\rho} = (1/20)\rho_0$, (dotted curves) $(1/6)\rho_0$, (dash-dotted curves) $(1/3)\rho_0$, and (dashed curves) ρ_0 . One can see that the inclusion of the medium factor may lead to the reduction of the cross section by 4 to 7%, the nuclear-matter dependence appearing to be highly nonlinear.

5. CONCLUSION AND COMPARISON WITH EXPERIMENTAL DATA

(i) It has been shown that the original expression for the eikonal phase shift within the microscopic approach can be represented in a form that is convenient for use—namely, one of the two profile functions there for the pointlike-nucleon density in nuclei has been transformed into the nuclear-density profile in that expression. This is convenient since the latter can be directly obtained from independent experiments—for example, from data on nuclear form factors.

(ii) The microscopic approach is based on the calculation of eikonal phase shifts. These have been significantly simplified—namely, the original four-dimensional integrals for them have been reduced to one-dimensional integrals. In contrast to the existing practice of calculating phase shifts by means of representing nuclear densities in the form of Gaussian functions, we have also demonstrated here wide possibilities for employing realistic density distributions in the form of (symmetrized) Fermi functions, whose parameters for the majority of the nuclei can be found

¹¹⁾In microscopic approaches where nucleus–nucleus potentials are constructed on the basis of the double-folding procedure, there arise similar problems of taking into account the dependence of nucleon–nucleon potentials on energy and nuclear densities. However, the Glauber–Sitenko approach possesses the advantage that the main energy dependence has already been taken into account in parametrizing the cross section σ_{NN} for free-nucleon scattering.

in existing tables. Moreover, all of the functions appearing in the one-dimensional integrals for eikonal phase shifts are specified explicitly, which simplifies the relevant calculations significantly.

(iii) Two methods have been presented for deriving the parameters c and d of the pointlike-nucleon density $\rho_{\text{SF}}^0(r, c, d)$ in nuclei: one relies on experimental information about nuclear form factors, while the other consists in rescaling on the basis of the parameters of the nuclear density $\rho_{\text{SF}}(r, R, a)$. It has turned out that the distinction between these two methods may lead to a distinction between the calculated cross sections that exceeds characteristic errors in their experimental measurements. We believe that the derivation of the infolded densities $\rho_{\text{SF}}^0(r)$ from the respective form factors obtained by dividing nuclear form factors by the nucleon form factor and, if necessary, by taking into account the factor associated with center-of-mass motion (as was done, for example, in [29]) would be a more justified method.

(iv) In the course of methodological calculations, it has been shown that the root-mean-square value of the range of nucleon–nucleon interaction and the root-mean-square nucleon radius can be taken to be identical ($r_{N\text{rms}}^2 = r_{0\text{rms}}^2$). Slight distinctions between them are within the accuracy of their determination, this introducing virtually no changes in the calculated total reaction cross sections. At the same time, the rather simple expressions (2.16) and (2.17) can be used for the convolution integral if $r_{N\text{rms}}^2 = r_{0\text{rms}}^2$, the convolution integral (2.17) of two density–thickness functions, the nuclear and the pointlike one, reduces to a rather simple one-dimensional integral.

(v) In many cases, the Coulomb distortion of the trajectory must be taken into account in calculating cross sections. This may be done by formally replacing, in the phase shift $\chi(b)$, the impact parameter b by b_c according to (4.4). It does not seem reasonable to take additionally into account the nuclear distortion, since the parameters of the nuclear potential itself must be determined from a numerical fit to experimental data with allowance, in general, for the same total cross sections that are to be explained within the Glauber–Sitenko approach.

(vi) We have not been able to obtain a definitive answer to the question of whether it is necessary to introduce the factor f_m correcting the dependence of nucleon–nucleon cross sections on the nuclear-medium density. Estimations have revealed that, in the region of intermediate energies, this factor does not generate significant corrections to total cross sections. Moreover, the use of the factors $f_m(np)$ and $f_m(nn)$ presented in [44] is rather difficult in calculations usually performed in practice. This difficulty arose, for example, in the simpler problem of

analyzing data on proton–nucleus scattering [45]. Moreover, Gaussian functions were taken for basic nuclear densities both in [44] and in [45], and the replacement of these functions by realistic ones may change conclusions on the form of f_m themselves. For example, the agreement between the results of the calculations and experimental data on the total cross sections for reactions induced by the interaction between protons and nuclei, alpha particles and nuclei, and ^{12}C nuclei at intermediate energies was attained in [46] with realistic densities $\rho_{\text{F}}(r)$ and a factor f_m that differs in form from that which was presented above.¹²⁾

(vii) Our calculations revealed that, in the case of comparatively light projectile nuclei, it is more advisable to use the convolution integral in the form (3.17), where the profile function $\rho_p^0(s)$ for the pointlike-nucleon density in the projectile nucleus is simulated by a modified Gaussian function ρ_{G}^0 , which is determined with the aid of (3.6) and (3.7) in terms of the parameters of a realistic symmetrized Fermi function, these parameters being taken, for example, from Table 2. In the case of heavier projectile nuclei, it is more reasonable to employ the convolution integral in the form (2.16), where, for both nuclei, one can substitute the explicit expressions known for the Fourier–Bessel profiles of the realistic densities in the form of a symmetrized Fermi function [see Eq. (3.22)]. In all calculations, we have taken into account the Coulomb distortion of the trajectories.

(viii) We note that the problem of correctly employing the input formula (2.4) for computing the convolution integral has not been properly discussed in the available literature. If a finite range of nucleon–nucleon interaction ($a_N^2 \neq 0$) is taken explicitly into account, it involves both densities for pointlike intranuclear nucleons. If, however, the root-mean-square nucleon radius is taken to be identical to the range of nucleon–nucleon interaction, then the nucleon–nucleon factor $f(\xi)$ disappears from this integral; concurrently, one of the pointlike-nucleon densities transforms into the distribution of the nuclear-matter density. At the same time, by no means does the absence of the factor $f(\xi)$ in such an integral imply that use was made of the zero-range approximation for the nucleon–nucleon interaction. Confusion arises if one speaks about the zero-range approximation, setting, in fact, $a_N^2 = (2/3)r_{N\text{rms}}^2 = 0$

¹²⁾In the calculations of the real part of the double-folding nucleus–nucleus potential, the nuclear-medium effect on the nucleon–nucleon potential is parametrized in terms of simpler dependences of f_m in the form of power-law and exponential functions of the density $\rho(r)$ (see, for example, [47]).

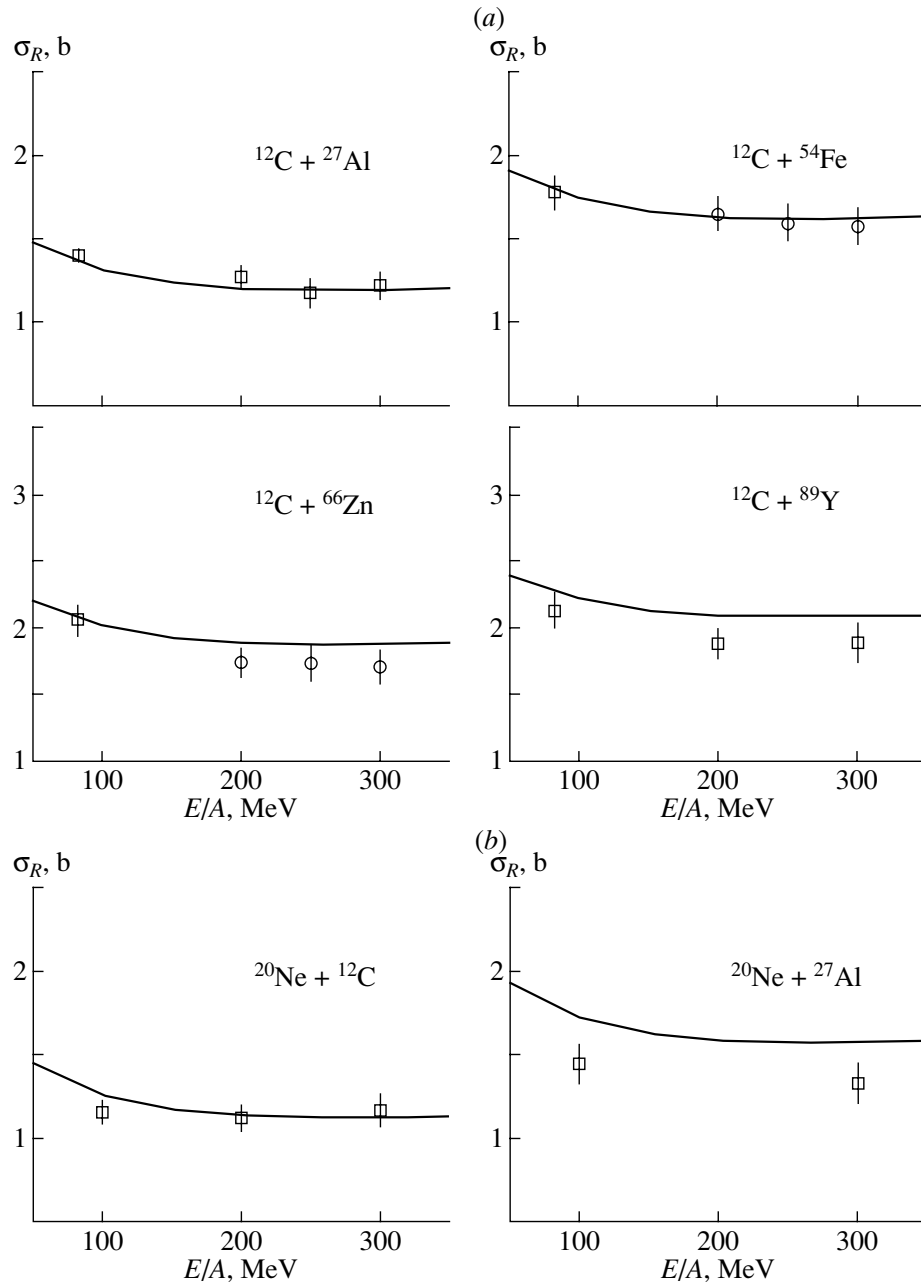


Fig. 8. Results of the calculations for the total cross sections along with experimental data from [48]. For the parameters of nuclear densities, use was made of data known from experiments on electron–nucleus scattering (see main body of the text). The Coulomb distortion of the trajectories was taken into account.

in the original integral (2.4) and employing, at the same time, tabular data for both densities (that is, nuclear densities instead of pointlike–nucleon densities).

In Figs. 8a and 8b, the results of our calculations are given along with experimental data from [48]. The parameters of the density distributions in the form of a symmetrized Fermi function were taken from Table 1. For the ^{12}C projectile nucleus, the

parameters c and d of the density ρ_{SF}^0 are given in Table. 2, while, for the ^{20}Ne nucleus, they were calculated by formula (4.3) on the basis of data given in Table 1. The convolution integral was used in the form (3.17). Only the Coulomb distortion of the trajectories was taken into account. Thus, no free parameters were introduced. One can see that, in all cases, with the exception of those of

$^{12}\text{C} + ^{89}\text{Y}$ and $^{20}\text{Ne} + ^{27}\text{Al}$ reactions, there is good agreement with experimental data. The discrepancies in the aforementioned cases may be due to determining the density parameters for the odd nuclei ^{89}Y and ^{27}Al from form factors in electron–nucleus scattering (see the respective references in [28]) by formulas for spinless nuclei. This discrepancy can be removed by taking into account the medium factor f_m in the calculations. However, we believe that, first of all, it is necessary to refine data on the densities of these nuclei. It is also worth noting that the calculations in [48], which employed Gaussian functions [22] and which reproduced the tails of the density distributions, yielded, for the reactions indicated in Figs. 8a and 8b, overestimated cross-section values beyond the experimental errors. Possibly, this was due to the use of nuclear densities instead of pointlike-nucleon ones (see above). At the same time, the calculations in [49] with uniform distributions for target nuclei and Gaussian distributions for projectile nuclei led to underestimated cross sections for $^{20}\text{Ne} + ^{12}\text{C}$ and $^{12}\text{C} + ^{27}\text{Al}$ reactions, although nuclear root-mean-square radii (rather than those for pointlike-nucleon distributions) were used there to determine the “step” radius R_u in (3.3). This result complies with what is shown in Fig. 3 for the calculation of cross sections with unrealistic density functions.

ACKNOWLEDGMENTS

We are grateful to the fund of the Infeld–Bogolyubov Program for support. The work of E.V. Zemlyanaya was supported by the Russian Foundation for Basic Research (project no. 03-01-00657).

REFERENCES

1. R. J. Glauber, *Lectures on Theoretical Physics* (Interscience, New York, 1959), Vol. 1.
2. A. G. Sitenko, *Ukr. Fiz. Zh.* **4**, 152 (1959).
3. G. D. Satchler, *Direct Nuclear Reactions* (Clarendon, Oxford, 1983).
4. V. K. Lukyanov, B. Słowiński, and E. V. Zemlyanaya, *Yad. Fiz.* **64**, 1349 (2001) [*Phys. At. Nucl.* **64**, 1273 (2001)].
5. J.-S. Wan *et al.*, *Kerntechnik* **63**, 167 (1998).
6. L. W. Townsend and J. W. Wilson, *Radiat. Res.* **106**, 283 (1986).
7. S. Fernbach, R. Serber, and T. B. Teylor, *Phys. Rev.* **75**, 1352 (1949).
8. W. Czyz and L. C. Maximon, *Ann. Phys. (N.Y.)* **52**, 59 (1969).
9. J. Formanek, *Nucl. Phys. B* **12**, 441 (1969).
10. I. Tanihata, *J. Phys. G* **22**, 157 (1996).
11. C. A. Bertulani, L. F. Cano, and M. S. Hussein, *Phys. Rep.* **226**, 281 (1993).
12. O. M. Knyaz'kov, I. N. Kukhtina, and S. A. Fayans, *Fiz. Élem. Chastits At. Yadra* **30**, 870 (1999) [*Phys. Part. Nucl.* **30**, 369 (1999)].
13. A. Vitturi and F. Zardi, *Phys. Rev. C* **36**, 1404 (1987).
14. Moon Hoe Cha, *Phys. Rev. C* **46**, 1026 (1992).
15. C. E. Aguiar, F. Zardi, and A. Vitturi, *Phys. Rev. C* **56**, 1511 (1997).
16. J. A. Tostevin, R. C. Johnson, and J. S. Al-Khalili, *Nucl. Phys. A* **630**, 340c (1998).
17. G. F. Bertsch, B. A. Brown, and H. Sagava, *Phys. Rev. C* **39**, 1154 (1989).
18. G. D. Alkhozov, V. V. Anisovich, and P. E. Volkovitsky, *High-Energy Diffractive Interaction of Hadrons with Nuclei at High Energies* (Nauka, Leningrad, 1991) [in Russian].
19. G. R. Satchler and W. G. Love, *Phys. Rep.* **55**, 183 (1979).
20. O. D. Dalkarov and V. A. Karmanov, *Nucl. Phys. A* **445**, 579 (1985).
21. H. M. Fayyad, T. H. Rihan, and A. M. Awini, *Phys. Rev. C* **53**, 2334 (1996).
22. P. J. Karol, *Phys. Rev. C* **11**, 1203 (1975).
23. S. Charagi and S. Gupta, *Phys. Rev. C* **41**, 1610 (1990).
24. Yu. N. Eldyshev, V. K. Luk'yanov, and Yu. S. Pol', *Yad. Fiz.* **16**, 506 (1972) [*Sov. J. Nucl. Phys.* **16**, 282 (1973)].
25. D. W. L. Sprung and J. Martorell, *J. Phys. A* **30**, 6525 (1997).
26. M. Grypeos, C. Koutroulos, V. Lukyanov, and A. Shebeko, *J. Phys. G* **24**, 1913 (1998).
27. V. V. Burov, D. N. Kadrev, V. K. Lukyanov, and Yu. S. Pol', *Yad. Fiz.* **61**, 595 (1998) [*Phys. At. Nucl.* **61**, 525 (1998)].
28. H. de Vries, C. W. de Jager, and C. de Vries, *At. Data Nucl. Data Tables* **36**, 495 (1987).
29. V. V. Burov and V. K. Luk'yanov, Preprint No. P4-11098, OIYaI (Joint Inst. Nucl. Res., Dubna, 1977).
30. V. K. Lukyanov and E. V. Zemlyanaya, *J. Phys. G* **26**, 357 (2000).
31. I. S. Gradshteyn and I. M. Ryzhik, *Tables of Integrals, Sums, Series, and Products*, 5th ed. (Fizmatgiz, Moscow, 1971; Academic, New York, 1980).
32. *Handbook of Mathematical Functions*, Ed. by M. Abramowitz and I. A. Stegun (Dover, New York, 1971; Nauka, Moscow, 1979).
33. M. E. Grypeos, C. G. Koutroulos, V. K. Lukyanov, and A. V. Shebeko, *Fiz. Élem. Chastits At. Yadra* **32**, 1494 (2001) [*Phys. Part. Nucl.* **32**, 779 (2001)].
34. I. Zh. Petkov, V. K. Luk'yanov, and Yu. S. Pol', *Yad. Fiz.* **4**, 57 (1966) [*Sov. J. Nucl. Phys.* **4**, 41 (1967)].
35. V. K. Luk'yanov, I. Zh. Petkov, and Yu. S. Pol', *Yad. Fiz.* **9**, 349 (1969) [*Sov. J. Nucl. Phys.* **9**, 204 (1969)].
36. S. Fäldt and A. Ingemarssen, *J. Phys. G* **9**, 261 (1983).
37. M. El-Azab Farid and G. R. Satchler, *Nucl. Phys. A* **438**, 525 (1985).
38. R. M. De Vries and J. C. Peng, *Phys. Rev. C* **22**, 1055 (1980).

39. V. K. Lukyanov and E. V. Zemlyanaya, *Int. J. Mod. Phys. E* **10**, 169 (2001).
40. D. M. Brink and G. R. Satchler, *J. Phys. G* **7**, 43 (1981).
41. M. Buenerd *et al.*, *Nucl. Phys. A* **424**, 313 (1984).
42. G. R. Satchler, *Nucl. Phys. A* **279**, 493 (1977).
43. G. Q. Li and R. Machleidt, *Phys. Rev. C* **48**, 1702 (1993); **49**, 566 (1994).
44. Cai Xiangzhou, Feng Jun, Shen Wenqing, *et al.*, *Phys. Rev. C* **58**, 572 (1998).
45. A. de Vismes, P. Roussel-Chomaz, and R. Carstoiu, *Phys. Rev. C* **62**, 064612 (2000).
46. R. K. Tripathi, J. W. Wilson, and F. A. Cucinotta, *Nucl. Instrum. Methods Phys. Res. B* **145**, 277 (1998).
47. Dao T. Khoa, G. R. Satchler, and W. von Oertzen, *Phys. Rev. C* **56**, 954 (1997).
48. S. Kox *et al.*, *Phys. Rev. C* **35**, 1678 (1987).
49. A. Y. Abul-Magd and M. Talib Ali-Alhinai, *Nuovo Cimento A* **110**, 1281 (1997).

Translated by A. Isaakyan

NUCLEI
Theory

On Physics at Planck Distances: Quantum Mechanics¹⁾

L. V. Prokhorov*

St. Petersburg State University, St. Petersburg, Russia

Received June 19, 2003

Abstract—The nature of quantum description is clarified. It is shown that complex-valued probability amplitudes are admissible within classical Hamiltonian mechanics. According to standard probability theory, such a description is always possible. The case of a spherical phase space is considered. It is shown that, in such a classical theory, there appears a universal constant that has dimensions of action (h), as well as Fock space and all attributes of quantum mechanics. Excitations of a chain of such systems are described by the equations of quantum mechanics with a correct normalization condition. It is shown that an answer to the question of what a particle and its wave function are is provided by quantum field theory (these are a single-particle field excitation and a function that describes it). Experiments are proposed that would make it possible to solve the problem of the physical nature of the wave function.

© 2004 MAIK “Nauka/Interperiodica”.

1. INTRODUCTION

In getting acquainted with quantum mechanics, there arise a number of questions. These include the following: Why is a wave associated with a particle, and what is the nature of this wave? Why is this wave complex-valued? Why is this a “probability wave”? As one obtains deeper insights into this theory, the main problem comes to the fore: quantum mechanics is a probabilistic theory, but a quantity that appears to be its main object is a complex function ψ (a probability amplitude, also referred to as a “complex probability”) rather than a probability. This brings about new questions:

(i) Why is it necessary to harness complex-valued probabilities and why is standard probability theory (its main object being a probability density $w \geq 0$) not applicable?

(ii) What are connections between a theory featuring complex-valued probabilities and a standard theory—is the former a generalization of the latter, or, on the contrary, can it be obtained as a particular case?

(iii) Does a quantum-mechanical description not impose constraints on a probabilistic description of processes in spacetime?

There are reasons to believe that other problems and paradoxes—namely, the particle-wave duality (uncertainty relation), the integrity of the photon (an

extended particle in a theory involving a local interaction), the origin of the Planck constant h , paradoxes associated with the description of macroscopic bodies in terms of a wave function (for example, Schrödinger’s paradox concerning a superposition of states of “a living and a dead cat” [1], and the Einstein–Podolsky–Rosen paradox [2])—are of a subordinate character and will be clarified upon resolving the question of why it is necessary to invoke complex-valued probabilities.

In this study, we consider the question of the nature of a quantum-mechanical description and of its place in standard probability theory. The ensuing exposition is organized as follows.

First of all, we find out (Section 2) whether it is possible—and if so, in which cases—to construct, within classical probability theory, a description in terms of auxiliary functions whose bilinear combinations yield probability densities (distributions) (see also [3]). It turns out that one can easily indicate examples of such systems. Their basic properties are the following: factorability of the distribution in phase space (that is, $W(q, p) = w_1(q)w_2(p)$; this property is desirable, but it is not necessary) and finiteness of the motion in it (the requirement that the probability be normalizable). A transition to complex-valued canonical variables ($q, p \rightarrow z, \bar{z}$, $z = (q + ip)/\sqrt{2}$) highlights the similarity of the mathematical formalism of original classical Hamiltonian theory to the formalism of quantum mechanics (the role of the complex variable z is analogous to the role of the probability amplitude).

In Section 3, it is shown that classical probability theory [4] admits the existence of a theory relying

* e-mail: lev.prokhorov@pobox.spbu.ru

¹⁾ Extended version of the report presented at the session of the Department of Nuclear Physics, Russian Academy of Sciences, on November 29, 2000, at the Institute of Theoretical and Experimental Physics (ITEP, Moscow).

on the concept of a probability amplitude (albeit this theory does not specify rules according to which one should treat such amplitudes). Moreover, the representation of the probability density in terms of the squared modulus of some complex-valued function is a necessary and sufficient condition for the existence of an absolutely continuous probability distribution. In connection with the requirement that the motion be finite in phase space, we will examine the simplest case where the phase space is a sphere (Section 4). As a result, it turns out that (a) in the theory, there appears a universal constant that has dimensions of action (volume of the two-dimensional phase space)—it is natural to associate it with the Planck constant h ; (b) there exists a transformation that maps a sphere onto a complex plane and which proves that a system whose phase space is spherical is equivalent to a Hamiltonian system specified by the canonical variables z and \bar{z} that possesses a non-trivial symplectic structure, which can be interpreted as a Gibbs distribution for a harmonic oscillator; (c) random variables of this system (entire functions) form a Fock space; (d) the random variables $z^n/\sqrt{n!}$ are eigenfunctions of the harmonic-oscillator-energy operator; and (e) energy is quantized, $E = \hbar\omega$. As a matter of fact, a probabilistic theory in such a phase space contains the entire mathematical formalism of quantum mechanics, including the Planck constant and commutation relations for canonical variables. It should be emphasized that we imply a description within classical probability theory.

It can easily be shown (see Section 5) that, in the continuous limit, a chain of such systems characterized by an oscillatory interaction between the nearest neighbors leads to one-dimensional relativistic quantum mechanics and that, in the nonrelativistic limit, we arrive at the Schrödinger equation and at the formula $w \sim \psi^*\psi$ for the probability density. It is natural to set the spacing between neighboring systems, a , to a value about the Planck length $l_p = 1.6 \times 10^{-33}$ cm. Thus, we see that, in the model being discussed, a quantum theory on the real axis is obtained as a limiting case of a classical structure that is discrete at short distances and which is described within standard probability theory. Similar results arise in more intricate cases as well (such as those featuring a potential, an arbitrary dimensionality of relevant spaces, and a multicomponent wave function).

In Section 6, we emphasize that quantum field theory does indeed unambiguously solve the problem of an “elementary particle” and of its wave function: a particle is a quantum (that is, a single-particle excitation) of the corresponding field, while its wave function is a function that describes a single-particle excitation of the field, this being fully consistent with

the proposed model. In Section 7, we discuss experiments that would make it possible to clarify the nature of the wave function. In Section 8, which concludes the present article, we give a summary of our analysis. The Appendix contains some points of a purely mathematical character (various cases of bilinear expressions for the probability density and the proof of some formulas given in Section 4).

It should be noted that attempts at exploring profound connections between classical (“deterministic”) and quantum theories were made in the recent studies of ‘t Hooft [5] and Man’ko and Marmo [6] (the former was motivated by the problem of a quantum-mechanical description of a gravitational field—see references quoted in [5]).

Problems discussed in this article were formulated rather long ago, but they have recently become quite urgent. First of all, this is explained by the accumulation of new experimental data concerning the most important statements of quantum mechanics (Bell’s inequalities [7, 8], Bose–Einstein condensation [9], Schrödinger’s paradox of “a living and a dead cat” [10], quantum mechanics of particles in a gravitational field [11]). Second, this is associated with the perception of the gravity of problems that arise in quantizing a gravitational field [5, 12]. The point here is not even that the gravitational Lagrangian is nonrenormalizable, which prevents a calculation of corrections to the main process. Anyway, this is nothing but a kind of flaw common to all local field theories. A more serious problem is associated with the existence of black holes, where there occurs a loss of information. According to [13], a black hole radiates as a blackbody, but, within a theory specified by a self-conjugate Hamiltonian, the evolution operator is unitary, in which case no dissipative processes are possible [12].

All of this caused enormous and quite justified interest in the foundations of quantum mechanics. The present study gives an answer to the question of how quantum mechanics employing probability amplitudes and containing a fundamental constant that has dimensions of action (h) may appear within classical theory. Of course, this is impossible in Euclidean physical space. In order to accomplish this goal, it is necessary to go beyond it by representing, say, a one-dimensional space by a chain of oscillators. A probabilistic theory is obtained if such a chain is placed in a heat bath. By identifying the Gibbs distribution for an oscillator with the measure of the phase-space volume, one can then equate this volume to the Planck constant h . As a result, the evolution of perturbations of the chain in the continuous limit, where the spacings between oscillators tend to zero, is described by one-dimensional quantum theory. The fundamental structure (chain) is now discrete, which

removes the problem of ultraviolet divergences; as to the heat bath, not only does its presence explain the appearance of probabilities in the theory, but this also provides the possibility of dissipative processes in the system.

By no means is the present consideration aimed at questioning the validity of quantum mechanics in the microcosm or its corollaries. The objective of this study is to seek a more general theory that is free from the aforementioned difficulties. The proposed model faithfully reproduces standard quantum mechanics in the continuous limit.

2. PRELIMINARY DISCUSSION

We will now address the question of whether the probability distribution (probability density) can be given by a bilinear function of dynamical variables within standard probability theory. Suppose that a state of a matter point is characterized by a probability density $W(q, p)$, where q and p fix the point in two-dimensional phase space [W can also be the probability of finding the particle within a rectangle that is specified by the vertex coordinates $(\pm q, \pm p)$]. If the probability densities $w_1(q)$ and $w_2(p)$ on the q and p axes are independent, then $W(q, p) = w_1(q)w_2(p)$. This circumstance can be represented in different forms. If, for example, $\mathbf{w}(w_1, w_2)$ is the two-dimensional vector formed by the components w_1 and w_2 , we have $W = \mathbf{w}\hat{g}\mathbf{w}/2 \equiv (\mathbf{w}, \mathbf{w})/2$, where $\hat{g} = \sigma_1$ is a metric tensor, $\sigma_{1,2,3}$ being the Pauli matrices. We emphasize that the dependence of W on the two-dimensional vector \mathbf{w} has a bilinear form: such dependences, which are characteristic of quantum mechanics, are not alien to classical probability theory.

Different forms of presentation are also possible. Along with \mathbf{w} , we introduce the conjugate vector $\bar{\mathbf{w}} = \mathbf{w}\sigma_3$. We then have $\mathbf{W} = \bar{\mathbf{w}} \wedge \mathbf{w}/2$, where \wedge symbolizes the external product of vectors and the density is the bivector measure $|\mathbf{W}|$ (area specified by the bivector). There is yet another form of presentation that is more appropriate for our purposes.

Hamilton's equations of motion $\dot{q} = \partial H/\partial p = \{q, H\}$ and $\dot{p} = -\partial H/\partial q = \{p, H\}$, where H is a Hamiltonian function and $\{, \}$ is a Poisson bracket, can be written in terms of the complex numbers $z = (q + ip)/\sqrt{2}$ and $\bar{z} = (q - ip)/\sqrt{2}$, $\{z, \bar{z}\} = -i$: $\dot{z} = -i\partial H(z, \bar{z})/\partial \bar{z}$ (see, for example, [14]). If, by using the functions $w_{1,2}$, one forms the complex number

$$w(q, p) = w_1(q) + iw_2(p), \tag{2.1}$$

then

$$W = |\bar{w} \wedge w/2i| = w_1w_2 \tag{2.2}$$

(we treat w_1 and iw_2 as the components of a 2-vector). But in this case, we have to restrict ourselves to the positive quadrant of the complex plane, since the physical domain is specified by the inequalities $w_{1,2} \geq 0$. The entire plane spanned by w_1 and w_2 can be used only upon unambiguously defining w beyond the physical domain. Yet, one could assume w to be arbitrary in intermediate calculations, setting $w_{1,2} \geq 0$ only in the ultimate expressions. For example, w may be an analytic function of z ; that is,

$$w = w_1(q) + iw_2(p) = w(q + ip). \tag{2.3}$$

The last equality is a functional equation. Its solution is given by a linear function $w(z) = bz + c$, where $\text{Im } b = 0$. Without loss of generality, we set $b = 1$ and $c = 0$ in the following. If the Hamiltonian is invariant under rotations in the complex plane, that is, if $H(z', \bar{z}') = H(z, \bar{z})$, where

$$z' = \exp(i\alpha)z, \tag{2.4}$$

then a "coordinate axis" can be chosen arbitrarily (we will need this circumstance).

Thus, a description in terms of complex numbers that is extended to the entire complex plane is appropriate only for distributions of quite a particular form. The "complex probability" $w(z)$ is proportional to the canonical variable z ; therefore, it follows from the normalizability of probabilities that motion in phase space must be finite (as motion on a Riemann sphere or on a torus). There is the following duality: the variable z plays two roles—it is a dynamical variable, on one hand, and a "complex probability," on the other hand; that is,

$$\begin{aligned} &\text{canonical variable} \leftarrow z \\ &\rightarrow \text{probability amplitude.} \end{aligned}$$

To the best of my knowledge, Strocchi [14] was the first who paid attention to the fact that, upon a transition to complex-valued canonical variables, the mathematical formalism of classical theory becomes closer to the quantum-mechanical formalism. A construction of specific models belonging to the type in question is given in Sections 4 and 5, along with the discussion of reasons behind the probabilistic description of a particle.

If phase space is compact (or if motion in it is finite for one reason or another), the meaning of the Planck constant h becomes clear—it relates the probability P to the area of the phase space ($P \sim |qp|/h$). If, further, z is a dimensionless quantity, it is necessary that there exist yet another world constant (l), having dimensions of length; we then have $z = (q/l + ilp/h)/\sqrt{2}$. It is natural to identify the constant l with the Planck length: $l \sim l_p$. It should also be noted that one can

render the formalism fully real by making the substitution $i \rightarrow -i\sigma_2$.

In order to define the probability in a general case featuring a “complex” coordinate axis—that is, in the case where q and p are complex numbers—we introduce the vector $\mathbf{z}(z_q, z_p) = z_q \mathbf{e}_q + z_p \mathbf{e}_p$, where z_q and z_p are complex numbers and $\mathbf{e}_{q,p}$ are basis vectors in phase space. We then have

$$\mathbf{W} = i\bar{\mathbf{z}} \wedge \mathbf{z} = i(z_q^* z_p - z_p^* z_q) \mathbf{e}, \quad (2.5)$$

where $\mathbf{e} = \mathbf{e}_q \wedge \mathbf{e}_p$ is a unit bivector. The probability is then given by the coefficient of \mathbf{e} .

Finally, one can go over from the measure $w_1(q)w_2(p)dqdp$ in the phase space to the trivial measure $dQdP$ by making the *noncanonical transformation* specified by the relations (see [15]) $dQ = w_1(q)dq$ and $dP = w_2(p)dp$. It can easily be proven that the ultimate formalism will be canonical and will feature a nontrivial symplectic form. Upon going over to the complex variables $Z = (Q + iP)/\sqrt{2}$, we arrive at a theory characterized by a nontrivial symplectic manifold. In the Appendix, we present various generalizations of expressions (2.2) and (2.5), including those for arbitrary distributions $w(q, p)$ and for Grassmann variables.

3. THEOREM ABOUT A CHARACTERISTIC FUNCTION

We will now find out whether standard probability theory admits a description in terms of probability amplitudes. The following theorem is proven in probability theory [4, p. 100].

A complex-valued function $f(t)$ of a real-valued variable t is a characteristic function for an absolutely continuous distribution if and only if it admits the representation

$$f(t) = \int_{-\infty}^{\infty} g(t + \theta) \overline{g(\theta)} d\theta, \quad (3.1)$$

where $g(\theta)$ is a complex-valued function of a real-valued variable θ such that

$$\int_{-\infty}^{\infty} |g(\theta)|^2 d\theta = 1.$$

A distribution is absolutely continuous if it is specified by the probability density $p(x) \geq 0$. The characteristic function $f(t)$ is the Fourier transform of the function $p(x)$; that is,

$$f(t) = \int_{-\infty}^{\infty} dx e^{itx} p(x).$$

Going over to a new function $\psi(x)$ as

$$g(\theta) = (2\pi)^{-1/2} \int_{-\infty}^{\infty} dx \psi(x) e^{i\theta x},$$

we recast expression (3.1) into the form

$$p(x) = |\psi(x)|^2. \quad (3.2)$$

The equality in (3.2) establishes a relationship between the mathematical formalism of quantum mechanics and the formalism of probability theory. From (3.2), it follows that, for any absolutely continuous distribution on the real axis, the probability density can always be represented as the squared modulus of a complex-valued function from L^2 (that is, a function belonging to a Hilbert space), and vice versa: $|\psi(x)|^2$, where $\psi \in L^2$, always specifies some absolutely continuous probability distribution. But these are functions that are used in quantum mechanics. From here, it follows that a quantum-mechanical probabilistic description is within the standard conceptual framework of probability theory as specified by Kolmogorov’s axioms [16]. It does not constrict standard probability theory.

However, the aforesaid does not mean that nothing new appears upon going over to complex-valued functions $\psi(x)$ (probability amplitudes). If one assumes that the function $\psi(x)$ corresponds to some “physical reality” [2] and takes it as a basis for a physical theory, it is necessary to specify rules according to which one would treat probability amplitudes. Obviously, they must be such that the rules according to which one treats probability distributions and which follow from them will be consistent with Kolmogorov’s axioms [16]. The axioms of a theory that is based on the concept of a probability amplitude are formulated in [17]. In the following, a theory that employs probability amplitudes will be referred to as a quantum theory.

4. HAMILTONIAN MECHANICS OF A SYSTEM WHOSE PHASE SPACE IS COMPACT

Spherical phase space. Suppose that the phase space of a particle is a sphere S^2 of radius R . The area 2-form is then $\omega_2 = R^2 \sin \theta d\varphi \wedge d\theta$, and the respective Poisson bracket is given by

$$\{f, g\} = \frac{1}{R^2 \sin \theta} \left(\frac{\partial f}{\partial \varphi} \frac{\partial g}{\partial \theta} - \frac{\partial f}{\partial \theta} \frac{\partial g}{\partial \varphi} \right).$$

It is well known that, with the aid of a stereographic projection, a sphere can be mapped onto the

complex plane Z , $|Z| = 2R \cot \theta/2$ and $\arg Z = \varphi$, a 2-form being defined there as

$$\omega_2 = \frac{1}{2i} \left(1 + \frac{\bar{Z}Z}{4R^2} \right)^{-2} d\bar{Z} \wedge dZ.$$

This is an example of a noncanonical transformation to the new canonical variables Z and \bar{Z} (transition to a Riemann sphere) with a new Poisson bracket,

$$\{f, g\} = 2i \left(1 + \frac{\bar{Z}Z}{4R^2} \right)^2 \left(\frac{\partial f}{\partial \bar{Z}} \frac{\partial g}{\partial Z} - \frac{\partial f}{\partial Z} \frac{\partial g}{\partial \bar{Z}} \right).$$

The following mapping of a sphere onto a complex plane admits a clear physical interpretation:

$$|z|^2 = \frac{1}{\beta} \ln \frac{1}{2\beta R^2 \sin^2 \theta/2}, \quad \arg z = \varphi, \quad (4.1)$$

$$\omega_2 = \frac{d\bar{z} \wedge dz}{i} e^{-\beta \bar{z}z}. \quad (4.2)$$

Setting $z = (q + ip)/\sqrt{2}$ and $1/\beta = kT$ in (4.2), we arrive at the Gibbs distribution for an oscillator,

$$G(q, p) = e^{-H/kT}, \quad (4.3)$$

where $H = (p^2 + q^2)/2$. Thus, a dynamical system that has one degree of freedom and whose phase space is spherical is equivalent to an oscillator in a heat bath. Going over to a new Hamiltonian according to the relation $H \rightarrow \tilde{H} = p^2/2m + \gamma q^2/2$ and equating the area of the phase space to h , we obtain

$$\int dqdp e^{-\beta \tilde{H}} = \frac{2\pi}{\omega} \frac{1}{\beta} = h (= 4\pi R^2), \quad (4.4)$$

$$\omega = \sqrt{\frac{\gamma}{m}}.$$

The mean energy of an oscillator is

$$\bar{E} = h^{-1} \int dqdp \tilde{H} e^{-\beta \tilde{H}} = \frac{1}{\beta}. \quad (4.5)$$

With allowance for (4.4), this yields

$$\bar{E} = \hbar\omega \quad (\hbar = h/2\pi). \quad (4.6)$$

It is natural to identify the constant h with the Planck constant. Considering further that $G(q, p)dqdp/h$, which is proportional to an element of the phase-space area, specifies the probability distribution in the phase space, we can represent the probability $P(A)$ corresponding to an event A in the form

$$P(A) = \int_A e^{-\beta H} dqdp/h = \frac{S(A)}{h}, \quad (4.7)$$

where $S(A)$ is the area of the region A of the phase space.

Fock space. Surprisingly, a system whose phase space Γ is compact (suppose that Γ is a sphere)

opens the way to a probabilistic description. Indeed, there is a natural measure (area) on a sphere—that is, there appears, in a natural way, the probability space (Ω, \mathcal{A}, P) [18], where Ω (set of elementary events) is the set of points on the sphere, \mathcal{A} is the Borel set (algebra) of all subsets of Ω , and P is a nonnegative function (probability distribution) specified on \mathcal{A} (for example, it can be specified by the condition requiring that the probability density p be constant on the sphere, $p(\theta, \varphi) = 1/4\pi R^2$). There is a fact that is still more important: it was established above that a sphere admits such a mapping onto a complex sphere that a *particle on a sphere* system can be interpreted as a *harmonic oscillator in a heat bath* system. This circumstance introduces radically new elements in the theory. An oscillator whose state is controlled by the Gibbs distribution characterized by some temperature is an object described within probability theory. Concurrently, there appears, however, temperature and the possibility of dissipative processes, the temperature being expressed in terms of h and being a world constant. A fact that is even more noteworthy is that random complex quantities form a Fock space.

Let us first discuss an ordinary case. In a one-dimensional space R^1 , one can consider three different constructions: classical Hamiltonian mechanics, statistical mechanics for a phase space in the form of a plane, and quantum mechanics. It is only necessary to specify a Hamiltonian (and a temperature in the second case; the Poisson bracket is assumed to have a conventional form, since the phase space in question is a plane).

In the case of a spherical phase space, the Poisson bracket is determined by the measure of the sphere's surface area—that is, by a nontrivial symplectic form. Concurrently, it turns out that (i) the problem of a "free" particle is equivalent to the problem of a particle in a plane phase space with a nontrivial symplectic form; (ii) a *harmonic oscillator in a heat bath* system is obtained upon going over to a statistical description; and (iii) random orthogonal variables of the system form a basis in the respective Fock space. The first two statements were validated above. We will now prove the third one.

We denote

$$\begin{aligned} d\mu(\bar{z}, z) &= \frac{d\bar{z} \wedge dz}{2\pi i} e^{-\bar{z}z} \\ &= \frac{dq \wedge dp}{2\pi} e^{-(q^2+p^2)/2} \\ &\quad \left(z = \frac{q + ip}{\sqrt{2}} \right). \end{aligned} \quad (4.8)$$

The measure in (4.8) is normalized to unity. Entire complex-valued functions $f(z)$ of order $\rho \leq 2$ form a set of random complex-valued quantities [18,

Chapter X]; also, $\langle |f(z)|^2 \rangle = \int d\mu |f(z)|^2$. They form a Hilbert space where the scalar product is defined as [18, Chapter X]:

$$(f, g) = \int d\mu(\bar{z}, z) f(z) g^*(\bar{z}) \quad (4.9)$$

$$(g^*(\bar{z}) = \overline{g(z)}).$$

The Hilbert space where the scalar product is specified by Eq. (4.9) is a Fock space [19, page 72] ["scalar field in $(0+1)$ spacetime"—only one oscillator remains from the field]. Indeed, it can easily be shown that the functions $Z_n(z) = z^n/\sqrt{n!}$ form an orthonormalized basis in this space (see Appendix); that is,

$$(Z_n, Z_m) = \delta_{nm}.$$

Further, we have

$$\bar{z} Z_n(\bar{z}) = \sqrt{n+1} Z_{n+1}(\bar{z}),$$

$$\frac{d}{d\bar{z}} Z_n(\bar{z}) = \sqrt{n} Z_{n-1}(\bar{z}); \quad (4.10)$$

that is, the multiplication of the functions $Z_n(\bar{z})$ by \bar{z} and their differentiation with respect to \bar{z} are identical to the action of the operators \hat{a}^+ and \hat{a} on the state $|n\rangle$ of a harmonic oscillator. That the operator $\hat{a} = d/d\bar{z}$ is the Hermitian conjugate of the operator of multiplication by \bar{z} (that is, \hat{a}^+) follows from the definition of the scalar product in (4.9) with allowance for (4.8) (see Appendix); therefore, the notation $Z_n(\bar{z}) = \langle \bar{z}|n\rangle$ is appropriate. The random complex-valued quantities $Z_n(\bar{z})$ are eigenfunctions of the harmonic-oscillator-energy operator $\hat{H} = \hat{a}^+ \hat{a} + 1/2 = \bar{z} d/d\bar{z} + 1/2$. The commutator of the operators \hat{a} and \hat{a}^+ is equal to unity ($[\hat{a}, \hat{a}^+] = 1$); in view of the relation $\bar{z} = (q - ip)/\sqrt{2}$, which is equivalent to $\hat{q} = (\hat{a} + \hat{a}^+)/\sqrt{2}$ and $\hat{p} = (\hat{a} - \hat{a}^+)/i\sqrt{2}$, it follows that $[\hat{q}, \hat{p}] = i$ and $\hat{H} = (\hat{q}^2 + \hat{p}^2)/2$. In the Appendix, we derive the corresponding commutation relations that take explicitly into account the reduced Planck constant \hbar ($[\hat{a}, \hat{a}^+] = \hbar$ and $[\hat{q}, \hat{p}] = i\hbar$). Thereby, we reproduce the quantum-mechanical formalism of a harmonic oscillator. Within this model, the classical equations of motion are modified. According to (4.2), the Poisson bracket assumes the form

$$\{f, g\} = \omega(\bar{z}, z) \left(\frac{\partial f}{\partial \bar{z}} \frac{\partial g}{\partial z} - \frac{\partial f}{\partial z} \frac{\partial g}{\partial \bar{z}} \right), \quad (4.11)$$

$$\omega(\bar{z}, z) = ie^{\beta \bar{z} z}.$$

From the above, we derive $\dot{z} = \{z, H\} = ie^{\beta \bar{z} z}(-z)$, which leads to

$$z(t) = e^{-i\omega^* t} z(0),$$

since $\{e^{\beta \bar{z} z}, H\} = 0$; here, $\omega^* = e^{\beta \bar{z} z}$ (see Appendix for details).

Since analytic functions are determined by their values on the boundary of their analyticity domain, one can go over to an equivalent description in terms of complex-valued random variables on the real axis, $\psi_n(q)$. Introducing eigenfunctions of the operator \hat{H} on the q axis, $\langle q|n\rangle = \mathcal{H}_n(q)$, where

$$\mathcal{H}_n(q) = (2^n n! \sqrt{\pi})^{-1/2} H_n(q) e^{-q^2/2}$$

is an orthonormalized set of Hermite functions, we can construct the kernel of the unitary operator $U(\bar{z}, q)$ relating the entire complex-valued functions $f(z)$ of the Fock space to the functions $\psi(q)$ from L^2 on R^1 ; that is,

$$U(\bar{z}, q) = \sum_n \langle \bar{z}|n\rangle \langle n|q\rangle \quad (4.12)$$

$$= \sum_n Z_n(\bar{z}) \mathcal{H}_n(q) = \pi^{-1/4} e^{-\frac{\bar{z}^2 + q^2}{2} + \sqrt{2} q \bar{z}}.$$

The function $U(\bar{z}, q)$ possesses the property (see Appendix)

$$\int_{-\infty}^{\infty} dq U(z, q) U(\bar{z}, q) = e^{\bar{z} z},$$

where the exponential function $e^{\bar{z} z}$ is the kernel of the identity operator for the scalar product specified by the measure in (4.8) ("complex delta function"). Further, we have

$$\int d\mu(\bar{z}, z) U(z, q) U(\bar{z}, q') = \delta(q - q')$$

and

$$\int_{-\infty}^{\infty} dq U(\bar{z}, q) \mathcal{H}_n(q) = Z_n(\bar{z}),$$

$$\int d\mu(\bar{z}, z) Z_n(z) U(\bar{z}, q) = \mathcal{H}_n(q);$$

that is, the functions $Z_n(z)$ correspond to eigenfunctions of a harmonic oscillator on the q axis.

We note that, here, a transition from a statistical description (Gibbs distribution) to a quantum-mechanical description (Fock space) does not involve any "quantization procedure." There only occurs here a transition from a probabilistic Gibbs distribution to a set of the distributions

$$|Z_n(z)|^2 \exp(-|z|^2)$$

fully in accordance with standard probability theory (see Section 3). Thus, a Hilbert space appears here as one of the possible schemes of description that are compatible with classical probability theory. The recognition of a superposition of random quantities as admissible (physical) states—that is, the inclusion of the superposition principle in the scheme—would appear to be an actual quantization.

5. QUANTUM MECHANICS

Chain of oscillators. Within the model formulated in Section 4, there was only a possibility of a quantum description. We will now construct a classical probabilistic model in which states and processes are described in terms of quantum mechanics. We will consider a chain of N oscillators introduced in Section 4, the corresponding Lagrangian being ($\tilde{\gamma} \gg \gamma > 0$)

$$L = \frac{1}{2} \sum_i [\dot{q}_i^2 - \tilde{\gamma}(q_i - q_{i+1})^2 - m^2 q_i^2], \quad (5.1)$$

$$\dot{q}_i = \frac{dq_i}{dt}.$$

Perturbations propagate along the chain, so that, if only one oscillator was excited at the initial instant t_0 , then the excitation wave will reach the other ones with time. According to the Poincaré [20] theorem, the integral

$$P(S) = \frac{1}{h} \int_S \sum_i dq_i \wedge dp_i \quad (5.2)$$

over an arbitrary surface S in $2N$ -dimensional phase space $R_q^N \times R_p^N$ does not change with time. On the other hand, the integral in (5.2) can be interpreted, according to (4.7), as the probability distribution on a $2D$ surface in $2N$ -dimensional space, that is, as the probability of recording an event either in the $2D$ region $\int_S dq_1 \wedge dp_1$, or in the region $\int_S dq_2 \wedge dp_2$, etc; therefore, the conservation of the integral in (5.2) is equivalent to probability conservation. It should be emphasized that probability conservation follows from the laws of classical Hamiltonian mechanics. In the continuous limit, where the spacing a between the oscillators tends to zero ($a \rightarrow 0, i \rightarrow \infty, ai \rightarrow x, q_i/\sqrt{a} \rightarrow \varphi(x), \tilde{\gamma}a^2 \rightarrow 1$), expression (5.1) reduces to the Lagrangian for a massive scalar field; that is,

$$L = \frac{1}{2} \int dx (\dot{\varphi}^2 - \varphi'^2 - m^2 \varphi^2). \quad (5.3)$$

From (5.3), one readily obtains the Klein–Fock–Gordon equation of motion

$$(\square - m^2)\varphi = 0.$$

We now recall that φ can be treated as the probability amplitude; that is, the propagation of the field $\varphi(x, t)$ along the chain can be treated as the propagation of a “complex-probability” wave. However, the field φ is real-valued; in order to extract a probability amplitude (wave function) from solutions to the equation of motion, it is therefore necessary to make use of its general solution,

$$\varphi(x, t) = \int d^2k \delta(k_0^2 - k^2 - m^2) \quad (5.4)$$

$$\times f(k_0, k) \exp[-i(k_0 t - kx)].$$

In view of manifest relativistic invariance of the theory, the probability density on the x axis must transform as the zero component of a conserved 2-vector. Such a vector cannot be constructed from the real-valued solution in (5.4). However, the function in (5.4) can be broken down, in a relativistically invariant way, into positive-frequency and negative-frequency solutions [those featuring, respectively, the exponentials $\exp(iE_k t)$ and the exponentials $\exp(-iE_k t)$, where $E_k = \sqrt{k^2 + m^2}$]. From them, we construct the conserved vectors

$$j_\mu = i\varepsilon(E)(\varphi_\pm^* \partial_\mu \varphi_\pm - \partial_\mu \varphi_\pm^* \varphi_\pm), \quad (5.5)$$

where the functions

$$\varphi_\pm(x, t) = \int \frac{dk}{4\pi E_k} f(\pm E_k, \pm k) \exp[\mp i(E_k t - kx)]$$

correspond to “positive”-energy ($\varphi_+ \sim \exp(-iE_k t)$) and “negative”-energy ($\varphi_- \sim \exp(iE_k t)$) solutions. The appearance of the sign $\varepsilon(E)$ of energy in (5.5) is associated with the requirement that the Lorentz-invariant integral $\int dx j_0$ be positive, $\int dx j_0 > 0$. The condition $\int dx j_0 = 1$ is the normalization condition for probabilities. It is the, expression in (5.5) for $E > 0$ that is used in the relativistic quantum mechanics of bosons, although the density j_0 is not positive definite. In order to verify that this expression for the probability density on the x axis is in accord with the above definition of the probability in (2.5), we recall that z and \bar{z} are canonically conjugate quantities. Here, φ and $\pi = \partial\mathcal{L}/\partial\dot{\varphi} = \dot{\varphi}$ are canonically conjugate; introducing the complex 2-vector $\Phi(\varphi_+, \pi_+)$ and using (2.5), we therefore find that the probability density on the x axis is given by $j_0 \mathbf{e} = i\Phi \wedge \Phi$, so that

$$j_0 = i(\varphi_+^* \pi_+ - \pi_+^* \varphi_+) = i(\varphi_+^* \dot{\varphi}_+ - \dot{\varphi}_+^* \varphi_+),$$

which is fully consistent with (5.5). For monochromatic waves, this is the invariant normalization of “ $2E$ particles in a unit volume.” Setting now $\varphi = \exp(-imt)\psi$, we arrive, in the nonrelativistic limit, at the Schrödinger equation for a free particle,

$$i\dot{\psi} = -\psi''/2m,$$

with $j_0 \sim \psi^* \psi$. This example demonstrates how, within classical probability theory, one can obtain a quantum description, including the superposition principle, since the sum of solutions is also a solution.

The model in question is a chain of coupled oscillators that are placed in a heat bath and which are described statistically. There arises the question of how the concept of a wave function can appear in such a system, since each oscillator is described by the Gibbs distribution (4.3). The answer is nearly obvious. First, the particles here, in contrast to what

occurs in the case of N particles in a heat bath, form an ordered chain where only the nearest neighbors interact. In other words, this is not a standard case considered in statistical physics. Second, a particle affects its neighbors only through one of the two canonical variables (namely, through q). The Lagrange equations of motion are formulated only for one of the two variables appearing in the probability distribution. Of the canonical variables, the second half, which are necessary for calculating probabilities, are reconstructed from Hamilton's equations of motion. Herein lies the reason behind the appearance of quantities whose bilinear combinations yield probabilities; these quantities carry probabilistic information, but they are not probabilities themselves.

Schrödinger equation for a particle in a force field specified by a potential $U(x)$ is obtained in the following way. Instead of the Lagrangian in (5.1), we take

$$L = \frac{1}{2} \sum_i [\dot{q}_i^2 - \tilde{\gamma}(q_i - q_{i+1})^2 - m^2 q_i^2 - 2mU_0(i)q_i^2].$$

Going over to the continuous limit, where $a \rightarrow 0$, $i \rightarrow \infty$, $ai \rightarrow x$, $q_i/\sqrt{a} \rightarrow \varphi(x)$, etc., under the conditions $\tilde{\gamma}a^2 \rightarrow 1$ and $U_0(i) \rightarrow U(x)$, we obtain the Lagrangian density

$$\mathcal{L} = \frac{1}{2}(\dot{\varphi}^2 - \varphi'^2 - m^2\varphi^2 - 2mU(x)\varphi^2), \quad (5.6)$$

which yields, in the nonrelativistic limit, the Schrödinger equation with the potential $U(x)$. It is now straightforward to construct the entire formalism of one-dimensional quantum mechanics—that is, to introduce the operators \hat{x} and \hat{p} satisfying the appropriate commutation relation, the Hilbert space of state vectors, uncertainty relations, the superposition principle, etc. We note, however, that only the formalism of quantum mechanics will be reproduced in this way; at the moment, it does not follow from anywhere that all of this concerns the description of a particle, since the concept of a “particle” has yet to be specified. Only upon constructing a quantum field theory can one speak about particles.

Quantum mechanics in k -dimensional space.

The above construction can easily be generalized to the case of a space having an arbitrary number of dimensions. For this, we choose a Cartesian system of coordinates in a k -dimensional Euclidean space and place oscillators (elementary systems) at integral-valued points. Each oscillator is then characterized by k integers $\mathbf{n}(n_1, \dots, n_k)$; its coordinate q is denoted by $\varphi(\mathbf{n})$. The interaction of the neighbors is specified by the function $V(\Delta\varphi_1(\mathbf{n}), \dots, \Delta\varphi_k(\mathbf{n})) \approx V(0) + V_{,i}(0)\Delta\varphi_i(\mathbf{n}) + V_{,ij}(0)\Delta\varphi_i(\mathbf{n})\Delta\varphi_j(\mathbf{n})/2 + m^2\varphi^2(\mathbf{n})/2$, where $\Delta\varphi_i(\mathbf{n}) = \varphi(\mathbf{n}) - \varphi(\mathbf{n}_i)$, $\mathbf{n}_i =$

$\mathbf{n}(n_1, \dots, n_i - 1, \dots, n_k)$, and $V_{,i} = \partial V/\partial \Delta\varphi_i(\mathbf{n})$. Setting $V_{,i}(0) = 0$ and $V_{,ij}(0) = \tilde{\gamma}\delta_{ij}$, we find that, in the limit where $a_i \rightarrow a \rightarrow 0$, $n_i \rightarrow \infty$, $n_i a \rightarrow x^i$, and $\tilde{\gamma}a^2 \rightarrow 1$, the Lagrangian

$$L = \frac{1}{2} \sum_{(n)} [\dot{\varphi}^2(\mathbf{n}, t) - \tilde{\gamma}(\Delta\varphi_i(\mathbf{n}, t))^2 - m^2\varphi^2(\mathbf{n}, t)] = \frac{1}{2} \sum_{(n)} \Pi a_i \left[\left(\frac{\dot{\varphi}(\mathbf{n}, t)}{(\Pi a_i)^{1/2}} \right)^2 - \tilde{\gamma} \sum_i a_i^2 \left(\frac{\Delta\varphi_i(\mathbf{n}, t)}{a_i(\Pi a_i)^{1/2}} \right)^2 - m^2 \frac{\varphi^2(\mathbf{n}, t)}{\Pi a_i} \right] \quad (5.7)$$

[here, $\Pi a_i = \prod_{i=1}^k a_i$, and summation is performed over the set (n_1, \dots, n_k)] takes a familiar form,

$$L = \frac{1}{2} \int d^k x [\dot{\varphi}^2 - (\partial_i \varphi)^2 - m^2 \varphi^2]. \quad (5.8)$$

In the nonrelativistic limit, we arrive at the Schrödinger equation in k -dimensional space. Following the same line of reasoning as in the above one-dimensional model, we can straightforwardly obtain the Schrödinger equation for a particle in a potential field.

Quantum mechanics featuring a multicomponent wave function. It is straightforward to construct a theory that describes an “isospin” state of a particle as well. The “isospin” indices j number the components φ^j and π^j of the canonical variables of an elementary system. Thus, it is assumed that the elementary system is multidimensional and that the quantities φ^j realize a representation of some simple group—that is, the sublimiting Lagrangian is invariant under this group.

While the description of “intrinsic” degrees of freedom of a particle does not present any serious difficulties, it is impossible to introduce spin variables in so straightforward a way. This is because “spacetime” appears only upon going over to a continuous limit, whence it follows that relativistic tensor indices (that is, spin variables) cannot be introduced in a natural way in an elementary system. Since the result is known from the outset, this can be done, of course; however, the resulting construction will be quite artificial. In this respect, fields of half-integer spin will cause still greater difficulties. Their inclusion in the scheme being considered is associated with an even more serious question—a simulation of supersymmetry. This problem is of importance in and of itself, irrespective of the origin of a quantum description; it is related to the fundamental properties of the physical object referred to as “spacetime.” Spin variables appear in a natural way in constructing a theory involving superstrings.

6. WAVE FUNCTION AND PLANCK CONSTANT

Wave function and “wave–particle” duality.

According to [2], each element of physical reality must be reflected in a physical theory. What physical reality corresponds to a wave function? It is obvious that the answer to this question will clarify the problem of “particle–wave” duality.

The question of how a “wave” (wave function) is related to a “particle” (matter point) has arisen since the beginning of the quantum era. Originally, Schrödinger assumed that a particle is a wave packet. However, a wave packet spreads with time, while a particle is not. De Broglie assumed that linear quantum mechanics is a limit of some nonlinear theory admitting singular solutions that are identified with particles (double–solution theory), but linear quantum mechanics reproduces experimental data to an extremely high degree of precision. That the problem in question was considered in its original formulation dating back to the 1920s, when present-day quantum field theory had yet to be developed, was a weak point of all subsequent attempts at interpreting quantum mechanics.

According to Sections 2, 4, and 5, a wave function describes a state of the chain of excited oscillators [correspondence $q_i(t)/\sqrt{a} \leftrightarrow \varphi(x, t)$ in Section 5]. This is fully consistent with quantum field theory, which provides a clear answer to the question of what a particle (for example, the electron) is: a particle is a quantum (single-particle excitation) of the corresponding field. This excitation is inevitably nonlocal (inasmuch as its energy is finite), and the very concept of a “pointlike particle” is inapplicable to such an object. Nonetheless, the electron is considered as the quintessence of a pointlike particle and, according to quantum mechanics, can be recorded within an arbitrarily small region of space. This also seems to be fully consistent with the obvious fact that the interaction of fields is local. We will show that not only does quantum field theory remove the problem of wave–particle duality, but it also resolves the problem of physical reality behind the concept of a wave function.

In quantum field theory, a single-particle excitation is described by the state vector

$$\hat{A}(f)|0\rangle, \quad (6.1)$$

where $\hat{A}(f) = -i \int d^3x \hat{A}(x) \overleftrightarrow{\partial}_0 f(x)$, $\hat{A}(x)$ is the operator of the scalar field $A(x)$, and $|0\rangle$ is the vacuum vector. The function $f(x)$ characterizes a field excitation. On the other hand, $f(x)$ is the wave function for the single-particle excitation being considered—that is, for a particle; therefore, one can give the following answers to above questions.

(i) The wave function for a particle is a function that describes a single-particle excitation of the corresponding field, which is precisely the physical reality behind the wave function.

(ii) A single-particle nonlocal field excitation behaves as a pointlike particle; that is, it is produced and absorbed as a discrete unit in an arbitrarily small region of space.

This gives an answer to questions concerning the nature of wave–particle duality and solves the problem of “photon integrity” (a photon is emitted and absorbed as a discrete unit). Indeed, a field (for example, an electromagnetic field) is a set of coupled oscillators. Fields interact locally—that is, each oscillator interacts with the corresponding oscillator of another field (for example, of an electron–positron field). A given oscillator cannot lose the entire amount of its energy without affecting neighboring oscillators, since this would lead to a discontinuity of the function that describes the corresponding field. However, such states are impossible since they correspond to infinite energies. Indeed, the Hamiltonian of any boson field involves a $(\nabla\varphi)^2$ term, and a discontinuity in φ would mean the emergence of a nonintegrable singularity of the form $[\delta(x)]^2$ in this term. Therefore, the process of field interaction is not completed until neighboring oscillators transfer their energy to a given and, ultimately, different field. This explains, on one hand, why a particle can be found at any spatial point where $\psi(x) \neq 0$ (any excited oscillator can interact with any other field) and, on the other hand, why particles behave as discrete units in quantum mechanics (a single-particle excitation is produced and absorbed entirely by virtue of the continuity of fields). The meaning of uncertainty relations also becomes clearer. The uncertainty in the coordinate of a particle is a property inherent in the object (nonlocal field excitation) that is associated with the particle. We emphasize once again that, within quantum field theory, the answer to the question of what the nature of a wave function is appears to be fully consistent with the results presented in Sections 2 and 5: the field φ is a dynamical variable, while a function that characterizes an excitation of this field is, according to (6.1), a wave function—that is, *dynamical variable–probability amplitude* duality indicated in Section 2 holds.

This, at first glance obvious, statement on the essence of the wave function has far-reaching corollaries. The simplest of these is the possibility of breaking down or composing quanta—for example, the possibility of breaking down a photon or an electron into two, three, etc., parts. It seems that this is impossible for the reasons listed immediately above. However, the prohibition is removed by resorting to

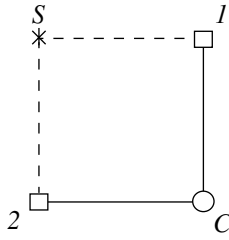


Fig. 1.

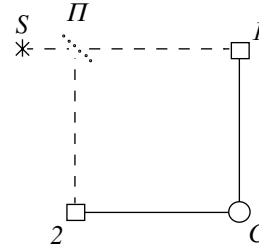


Fig. 2.

macroscopic bodies, which, on the scale of the microcosm, possess an indefinitely great energy. Indeed, the possibility of partitioning an electron was demonstrated about twenty years ago through the observation of the fractional quantum Hall effect [21] (the authors of that study were awarded a Nobel prize of 1998 in physics for their discovery). Recently, there appeared articles [22] reporting on a direct observation of objects with charges of $e/3$ and $e/5$, where e is the electron charge.

Thus, the problem of the meaning of the wave function is solved within quantum field theory. Concurrently, answers are given to a number of important questions, such as wave—particle duality, the integrity of the photon (and of other quanta), and uncertainty relations. However, the question of why field theory invokes probability amplitudes remains open, and this is one of the fundamental questions. Moreover, there arise new questions. The most important of these is the following: If a field excitation is indeed a wave function, why is the equation for the wave function linear? Is it not true that fields are described by non-linear equations?

In order to answer the first question, one has to address physics at Planck distances (it is necessary to construct a quantized-field model). It turns out that the reason behind the appearance of probabilities in it is identical to the reason behind the appearance of a probabilistic description in quantum mechanics (Sections 4, 5). These issues will be discussed in a dedicated publication. The answer to the last question is simple: field theory is linear in the corresponding Fock space.

Planck constant \hbar . The appearance of the Planck constant \hbar in a theory is usually thought to be a signal of a transition to quantum theory. That this is not so follows from a simple example. This is a mechanical system having one degree of freedom and a compact phase space Γ . Suppose that this is a sphere of radius R . The classical Hamiltonian mechanics of such a particle will then inevitably contain, from the outset, a constant that is fundamental for this theory and which has the same dimensionality as \hbar —this is the phase-space area ($4\pi R^2$). Thus, we see that, within classical

Hamiltonian mechanics, one can construct dynamical systems involving a quantum of the action functional. From the aforesaid, it does not follow, however, that such systems have no bearing on quantum mechanics. Although the appearance of \hbar in a theory does not mean an automatic transition to a quantum description, one can construct, from such systems, whose phase space is compact, a structure (chain) whose excitations are described in terms of quantum mechanics (see Section 5). It is natural to expect that such structures appear at Planck distances.

7. SOME EXPERIMENTAL CONSEQUENCES

The following experiment will enable us to give an answer to the fundamental question of whether it is possible to break down a photon.

In Fig. 1, light from a source S finds its way to photomultiplier tubes (I , 2). In the experiment being discussed, one records (i) the number N_c of events in which both photomultiplier tubes are actuated (the counter C records only coincidences) and (ii) the number N_n of events in which only one of the photomultiplier tubes is actuated (the counter C now records only such events).

In Fig. 2, light from a source is incident on a semi-transparent mirror (Π) and then goes to photomultiplier tubes (I , 2). There is the following alternative:

(i) In accordance with the generally accepted interpretation of quantum mechanics, the number of simultaneous actuations of the photomultiplier tubes in the experiment depicted in Fig. 2 is $N_c/2$ (since the probability that two photons hit the mirror Π simultaneously is equal to the probability that they hit photomultiplier tubes I and 2 simultaneously in Fig. 1).

(ii) In accordance with [3] and with the results presented in Sections 2, 5, and 6, the number of simultaneous actuations of photomultiplier tubes in the scheme depicted in Fig. 2 is $N_c/2 + N_n/4$ because the number of single photons hitting the mirror Π is one-half as great as the total number of photons hitting the photomultiplier tubes I and 2 in Fig. 1 and because, in half of the cases, part of the wave goes

toward the photomultiplier tube 1, while its remaining part goes toward the photomultiplier tube 2, both parts being recorded.

It is desirable that the experiment depicted in Fig. 2 be implemented in two versions: (1) the distance between the photomultiplier tubes 1 and 2 is longer than the photon coherence length and (2) the distance between them is shorter than the photon coherence length. Since $N_n > N_c$ for nondegenerate light, the effect in question can be discovered even with instruments whose sensitivity is moderate.

A similar experiment is possible for electrons as well. In a branched quantum wire, an electron can break down into two or more parts (depending on the number of lines at the branch point of the wire). This would yield an independent (and more direct in relation to that in [22]) piece of evidence for the partitioning of an electron.

8. CONCLUSIONS

The facts that have been established in the present study and which are of importance for obtaining deeper insights into the nature of a quantum description are the following:

(i) Theories are possible in which there is a duality in the sense that complex canonical variables are simultaneously probability amplitudes (Sections 2, 4).

(ii) Standard probability theory admits a description of stochastic processes in terms of complex-valued probability amplitudes (Section 3).

(iii) In a classical theory whose phase space is compact, there is a fundamental constant (\hbar), the phase-space area, having the dimensionality of action (Section 4).

(iv) A *particle whose phase space is spherical* system is equivalent to a *particle whose phase space is a plane and has a nontrivial symplectic structure* system. Here, (a) the resulting distribution is identical to the Gibbs distribution for an oscillator in a heat bath and (b) random variables in such a phase space form a Fock space.

(v) In the case of a spherical phase space, the time evolution of a particle state can be described by (a) classical mechanics featuring a nontrivial Poisson bracket, (b) classical statistical mechanics with a Gibbs distribution for a harmonic oscillator, or (c) probability theory involving distributions in the phase space that are specified by orthonormalized (oscillator) functions in the corresponding Fock space (that is, $|Z_n(z)|^2 \exp(-\bar{z}z)$; see Section 4).

(vi) Quantum mechanics on the real axis arises in the classical system of linearly ordered oscillators in a heat bath (Section 5).

This approach is characterized by the following features: recourse to physics at Planck distances, discreteness of the fundamental structure, determinism (classical mechanics), and possibility of dissipative processes. The reason behind the emergence of probabilities in quantum mechanics (even for a free particle in Euclidean space) becomes clear. The fact that the wave function, which is an object of a theory where there is no determinism, obeys a causal equation of motion is also explained.

't Hooft [5], who studied the possibility of a quantum description of gravitation (it was indicated above that, in the quantum theory of gravitation, there is loss of information in black holes in addition to the obvious difficulty associated with the nonrenormalizability of the theory), formulated similar requirements on the theory.

Let us consider the classical limit $\hbar \rightarrow 0$ in (4.4). It corresponds to zero temperature of the heat bath: $T = \hbar\omega/k \rightarrow 0$. Since, according to (4.4), the radius R of the Riemann sphere then tends to zero, the concept of a probability distribution on it loses meaning; therefore, the possibility of dissipative processes disappears, so that the theory becomes deterministic in accordance with 't Hooft's hypothesis that quantization appears as the result of dissipative processes at Planck distances [5] (see also [23]).

Finally, it should be noted that the idea of a curved momentum space of the Universe (see, for example, [24, p. 52] and references therein) proved to be useful for physics at Planck distances.

As will be shown in a dedicated publication, the proposed approach makes it possible to construct, in a natural way, a string model (chain of oscillators on a segment) and a superstring model (for example, a Ramon–Neveu–Schwarz superstring). This leads to the appearance of noncommuting (Grassmann) variables and of excitations featuring an angular momentum of $\hbar/2$ and to a clarification of the nature of the Dirac sea. Moreover, a model that unifies all interactions, including gravitational interaction, is obtained if one assumes that space is a network formed by superstrings (this unification is due to the fact that superstring excitations contain all fields). By construction, the resulting theory will be supersymmetric (by virtue of the supersymmetry of the Lagrangian) and will not contain ultraviolet divergences (by virtue of the original discreteness of the model).

Note added in proof. A subsequent analysis has revealed that quantum mechanics is a statistical theory of nonequilibrium states of ordered structures (chains of oscillators in a heat bath) characterized by a long relaxation time.

APPENDIX

Generalization of the Formulas Presented in Section 2

Arbitrary dimensions. The results given in Section 2 can easily be generalized to the case of space having an arbitrary number n of dimensions. Indeed, we assume that

$$W(x_1, \dots, x_n) = w_1(x_1) \dots w_n(x_n). \quad (A.1)$$

Further, we form the vectors

$$\mathbf{w}_i = \sum_{j=1}^n \alpha_{ij} w_j \mathbf{e}_j, \quad (A.2)$$

where α_{ij} are elements of some nondegenerate matrix, $\det \alpha \neq 0$. We then have

$$\begin{aligned} \mathbf{W} &= \frac{1}{\det \alpha} \mathbf{w}_1 \wedge \dots \wedge \mathbf{w}_n \quad (A.3) \\ &= w_1(x_1) \dots w_n(x_n) \mathbf{e}_1 \wedge \dots \wedge \mathbf{e}_n \equiv W \mathbf{e}. \end{aligned}$$

Arbitrary densities. The factorability requirement (A.1) is not necessary. We assume that

$$W(x, y) = \sum_k w_1^{(k)}(x) w_2^{(k)}(y). \quad (A.4)$$

Instead of (A.2), we can then form the vector

$$\mathbf{w} = \sum_{i=1,2} \sum_k w_i^{(k)} \mathbf{e}_i^{(k)}, \quad (A.5)$$

where

$$\begin{aligned} \mathbf{e}_i^{(k)} &\equiv \mathbf{e}_i \otimes \boldsymbol{\varepsilon}^{(k)}, \quad (A.6) \\ \mathbf{e}_i^{(k)} \wedge \mathbf{e}_j^{(k')} &\equiv \mathbf{e}_i \wedge \mathbf{e}_j \boldsymbol{\varepsilon}^{(k)} \cdot \boldsymbol{\varepsilon}^{(k')}, \\ \mathbf{e}_i \wedge \mathbf{e}_j &= \varepsilon_{ij} \mathbf{e}, \quad \boldsymbol{\varepsilon}^{(k)} \cdot \boldsymbol{\varepsilon}^{(k')} = \delta^{kk'}, \\ \varepsilon_{12} &= 1 \end{aligned}$$

[the vectors $\boldsymbol{\varepsilon}^{(k)}$ form an orthonormalized basis in a space whose dimensionality is determined by the number of terms in the sum on the right-hand side of (A.4)], and the conjugate vector

$$\bar{\mathbf{w}} = \sum_{i=1,2} \sum_k (-1)^{\delta_{i2}} w_i^{(k)} \mathbf{e}_i^{(k)}. \quad (A.7)$$

By analogy with (A.3), we have

$$\mathbf{W} = \frac{1}{2} \bar{\mathbf{w}} \wedge \mathbf{w} = \sum_k w_1^{(k)} w_2^{(k)} \mathbf{e} = W \mathbf{e}; \quad (A.8)$$

that is, probabilities are given by bilinear forms of auxiliary quantities in the present case as well. A generalization of formulas (A.4)–(A.8) to the case of a space having an arbitrary number of dimensions is trivial.

Complex variables. If the variables q and p are complex-valued from the outset (that is, if q describes a system having two degrees of freedom), then we have $q^{(\pm)} = (q_1 \pm iq_2)/\sqrt{2}$, $p^{(\pm)} = (p_1 \mp ip_2)/\sqrt{2}$, $\{q^{(\pm)}, p^{(\pm)}\} = 1$, $\mathbf{z}^{(+)} = q^{(+)} \mathbf{e}_q + p^{(+)} \mathbf{e}_p$, and

$$\begin{aligned} \mathbf{W}^{(+)} &= i \mathbf{z}^{(+)*} \wedge \mathbf{z}^{(+)} \\ &\equiv i [q^{(+)*} \wedge p^{(+)} \mathbf{e}_q \wedge \mathbf{e}_p + p^{(+)*} \wedge q^{(+)} \mathbf{e}_p \wedge \mathbf{e}_q]. \end{aligned}$$

Here, the external product $q^{(+)*} \wedge p^{(+)}$ is the product of the 2-vectors $q^{(+)*}$ and $p^{(+)}$ whose components are $(q_1^*/\sqrt{2}, -iq_2^*/\sqrt{2})$ and $(p_1/\sqrt{2}, -ip_2/\sqrt{2})$; that is, $q^{(+)*} \wedge p^{(+)} = -i(q_1^* p_2 - q_2^* p_1)/2$.

Fermions. We introduce $\psi = q\theta/\sqrt{2}$ and $\psi^+ = q^* \bar{\theta}/\sqrt{2}$, where q is a complex number; $\theta = \theta_1 + i\theta_2$; and $\bar{\theta} = \theta_1 - i\theta_2$, with θ_1 and θ_2 being real-valued generators of the Grassmann algebra, $[\theta_1, \theta_2]_+ = 0$. In this case, the Lagrangian is linear in velocities ($\mathcal{L} \sim \psi^+ \dot{\psi}$), so that $p_\psi = \psi^+$. For \mathbf{z} , we take $\mathbf{z} = \psi \mathbf{e}_q + \psi^+ \mathbf{e}_p$. We define

$$\begin{aligned} \mathbf{W} &= \mathbf{z} \wedge \mathbf{z} = \psi \cdot \psi^+ \mathbf{e}_q \wedge \mathbf{e}_p \\ &+ \psi^+ \cdot \psi \mathbf{e}_p \wedge \mathbf{e}_q = qq^* \theta \cdot \bar{\theta} \mathbf{e}, \end{aligned}$$

where $\theta \cdot \bar{\theta} = \theta \bar{\theta} = 2i\theta_2 \theta_1$; the probability is then the factor in front of $\theta \bar{\theta} \mathbf{e}$.

Proof of the Formulas Presented in Section 4

The orthonormality of the functions $Z_n(z)$ is proven by performing integration by parts in the scalar product

$$\begin{aligned} (z^n, z^m) &= \int \frac{d\bar{z} \wedge dz}{2\pi i} e^{-\bar{z}z} z^n \bar{z}^m \\ &= \int \frac{d\bar{z} \wedge dz}{2\pi i} z^n \left(-\frac{d}{dz}\right)^m e^{-\bar{z}z} = n! \delta_{nm} \quad (m \geq n); \end{aligned}$$

for $n \geq m$, it is necessary to perform differentiation with respect to \bar{z} . Formula (4.12) follows from the expansion

$$e^{-z^2+2zq} = \sum_{n=0}^{\infty} H_n(q) \frac{z^n}{n!}$$

(the exponential here is the generating function for Hermite polynomials). We will now present the proof of the fact that $\exp(\bar{z}z)$ is the kernel of the identity operator:

$$\begin{aligned} \int d\mu(\bar{\zeta}, \zeta) e^{z\bar{\zeta}} f(\zeta) &= \int \frac{d\bar{\zeta} \wedge d\zeta}{2\pi i} e^{-\bar{\zeta}\zeta+z\bar{\zeta}} f(\zeta) \\ &= \int \frac{d\bar{\zeta} \wedge d\zeta}{2\pi i} e^{-\bar{\zeta}\zeta} f(\zeta+z) = f(z); \end{aligned}$$

in the last equality, we have used the expansion of the function $f(\zeta+z)$ in a Taylor series in ζ . The

derivation of other formulas that are associated with $U(\bar{z}, q)$ does not involve any difficulties either.

In order to take \hbar into account explicitly, we go over to the Hamiltonian

$$\tilde{H} = \frac{1}{2} \sqrt{\frac{\gamma}{m}} \left(\frac{p^2}{\sqrt{\gamma m}} + \sqrt{\gamma m} q^2 \right) = \omega \tilde{z} \bar{z},$$

$$\tilde{z} = \frac{\tilde{q} + i\tilde{p}}{\sqrt{2}}, \quad \tilde{q} = q(\gamma m)^{1/4}, \quad \tilde{p} = p(\gamma m)^{-1/4}.$$

We then have

$$\frac{d\bar{z} \wedge dz}{i} e^{-\beta \bar{z} z} \rightarrow \frac{d\tilde{z} \wedge d\bar{z}}{i} e^{-\beta \omega \tilde{z} \bar{z}} \equiv d\tilde{\mu}, \quad \beta \omega = 1/\hbar$$

(instead of \tilde{z} , we will write z in the following). Further, if $\hat{a}^+ \leftrightarrow \bar{z}$, then

$$\int d\tilde{\mu} f(z) \bar{z} g^*(\bar{z}) = \int d\tilde{\mu} \hbar \frac{d}{dz} f(z) g^*(\bar{z});$$

that is, $\hat{a} \leftrightarrow \hbar \frac{d}{d\bar{z}}$, whence it follows that $[\hat{a}, \hat{a}^+] = \hbar$ and $[\hat{q}, \hat{p}] = i\hbar$.

According to (4.11), the classical equations of motion have the form

$$\dot{z} = \{z, \tilde{H}\} = ie^{\bar{z}z/\hbar}(-\omega z);$$

that is, $z(t) = \exp(-i\omega^* t)z(0) = \exp(-i\bar{E}^* t/\hbar)z(0)$, where $\omega^* = \omega \exp(\bar{z}z/\hbar)$.

Obviously, $\dot{Z}_n(z) = -i\omega n \exp(\bar{z}z/\hbar)Z_n(z)$; that is, $\bar{E}_n^* = \hbar\omega^* n$. This is precisely the equation for the state vector of a harmonic oscillator with energy \bar{E}_n^* in the corresponding Fock space.

REFERENCES

1. E. Schrödinger, *Naturwissenschaften* **23**, 803 (1935).
2. A. Einstein, B. Podolsky, and N. Rosen, *Phys. Rev.* **47**, 777 (1935).
3. L. V. Prokhorov, *Vestn. St.-Peterb. Gos. Univ., Ser. 4*, No. 25, 136 (1999).
4. E. Lukach, *Characteristic Functions* (Nauka, Moscow, 1979).
5. G. 't Hooft, *Class. Quantum Grav.* **16**, 3263 (1999).
6. V. I. Man'ko and G. Marmo, *Phys. Scripta* **60**, 111 (1999).
7. W. Tittel *et al.*, *Europhys. Lett.* **40**, 595 (1997).
8. G. Weihs *et al.*, *Phys. Rev. Lett.* **81**, 5039 (1998).
9. E. A. Cornell and C. E. Wiemann, *Sci. Am.* **278**, 26 (1998).
10. J. R. Friedman *et al.*, *Nature (London)* **406**, 43 (2000).
11. V. V. Nesvizhevsky *et al.*, *Nature (London)* **415**, 297 (2002).
12. G. 't Hooft, *Nucl. Phys. B (Proc. Suppl.)* **43**, 1 (1995).
13. S. W. Hawking, *Phys. Rev. D* **14**, 2460 (1976).
14. F. Strocchi, *Rev. Mod. Phys.* **38**, 36 (1966).
15. L. V. Prokhorov and S. V. Shabanov, *Hamiltonian Mechanics of Gauge Systems* (Izd. St.-Peterburg. Gos. Univ., St. Petersburg, 1997), Ch. 1.
16. A. N. Kolmogorov, *Foundations of the Theory of Probabilities*, 2nd ed. (Nauka, Moscow, 1974; Chelsea, New York, 1956).
17. L. V. Prokhorov, *Vestn. Leningrad. Gos. Univ., Ser. 4*, No. 16, 130 (1975).
18. M. Loève, *Probability Theory* (Princeton, 1960; Inostr. Lit., Moscow, 1962).
19. N. Hurt, *Geometric Quantization in Action* (Reidel, Dordrecht, 1983; Mir, Moscow, 1985).
20. H. Goldstein, *Classical Mechanics*, 2nd ed. (Addison-Wesley, Reading, Mass., 1980; Nauka, Moscow, 1975).
21. D. C. Tsui, H. L. Störmer, and A. C. Gossard, *Phys. Rev. Lett.* **48**, 1559 (1982).
22. R. de Picciotto *et al.*, *Nature (London)* **389**, 162 (1997); M. Reznikov *et al.*, *Nature (London)* **399**, 238 (1999).
23. M. Blasone, P. Jizba, and G. Vitiello, *Phys. Lett. A* **287**, 205 (2001).
24. V. G. Kadyshevsky, in *Problems of Theoretical Physics* (Nauka, Moscow, 1972).

Translated by A. Isaakyan

ELEMENTARY PARTICLES AND FIELDS
Experiment

Signals of the Abelian Z' Boson within the Analysis of the LEP2 Data*

V. I. Demchik, A. V. Gulov**, V. V. Skalozub***, and A. Yu. Tishchenko

Dnepropetrovsk National University, Dnepropetrovsk, Ukraine

Received April 9, 2003; in final form, September 9, 2003

Abstract—The preliminary LEP2 data on $e^+e^- \rightarrow l^+l^-$ scattering are analyzed to establish a model-independent search for the signals of virtual states of the Abelian Z' boson. The recently introduced observables make it possible to pick up uniquely the Abelian Z' signals in these processes. The mean values of the observables are in accordance with the Z' existence. However, the accuracy of the experimental data is deficient to detect the signal at more than a 1σ C.L. The results of other model-independent fits and further prospects are discussed. © 2004 MAIK “Nauka/Interperiodica”.

1. INTRODUCTION

The recently stopped LEP2 experiments have accumulated a huge amount of data on four-fermion processes at the c.m. energies $\sqrt{s} \sim 130\text{--}207$ GeV [1, 2]. Besides the precision tests of the Standard Model (SM) of elementary particles, these data allow the estimation of the energy scale of a new physics beyond the SM.

Various approaches to detect manifestations of physics beyond the SM have been proposed in the literature. They can be subdivided into model-dependent and model-independent methods. The former usually means the comparison of experimental data with the predictions of some specific models which extend the SM at high energies. In this way, some popular grand unified theories, the supersymmetry models, as well as the theories of technicolor or extra dimensions, are intensively discussed and the values of couplings, mixing angles, and particle masses are constrained. In particular, model-dependent bounds are widely presented in the LEP reports [1, 2].

In the model-independent approach, one fits some effective low-energy parameters such as four-fermion contact couplings. Below the scale of the heavy particle decoupling, various theories beyond the SM can be described by the same set of effective contact interactions between the SM particles. The only difference is in the values of the corresponding coefficients, which can be fitted by experimental data. This idea is elaborated in the effective Lagrangian method [3] as well as in the helicity “models” introduced by the LEP

collaborations (LL, RR, ...) [1, 2]. An advantage of the approach is the restricted set of parameters which describe the low-energy phenomenology of any model beyond the SM for a specified scattering process. Unfortunately, each effective model-independent parameter conceals a number of different scenarios of new physics. As a consequence, the model-independent approach makes it possible to detect a signal of new physics, but it cannot distinguish the particle (defined by specific quantum numbers) responsible for the signal.

It seems to us that it is reasonable to develop model-independent searches for the manifestations of heavy particles with specific quantum numbers. Such an approach is intended to detect the signal of some heavy particle (for example, the heavy neutral vector boson) by means of the data of the LEP2 or other experiments without specifying a model beyond the SM. In this way, it is also possible to derive model-independent constraints on the mass and the couplings of the considered heavy particle. To develop this approach, one has to take into account some model-independent relations between the couplings of the heavy particle as well as some features of the kinematics of the considered scattering processes.

In the present paper, we focus on the problem of model-independent searches for signals of the heavy Abelian Z' boson [4] by means of the analysis of the LEP2 data on the lepton processes $e^+e^- \rightarrow \mu^+\mu^-$ and $e^+e^- \rightarrow \tau^+\tau^-$. This particle is a necessary element of different models extending the SM. The low limits on its mass estimated for a variety of popular models (χ , ψ , η , L–R models [5] and the Sequential Standard Model (SSM) [6]) are found to be in the wide energy interval 600–2000 GeV [1, 2]. In what follows, we assume that the Z' boson is heavy enough to be decoupled at the LEP2 energies.

* This article was submitted by the authors in English.

** e-mail: gulov@ff.dsu.dp.ua

*** e-mail: skalozub@ff.dsu.dp.ua

In the previous papers [7], we argued that the low-energy Z' couplings to the SM particles satisfy some model-independent relations, which are the consequences of renormalizability of a theory beyond the SM, remaining in other respects unspecified. These relations, called the renormalization-group (RG) relations, predict two possible types of low-energy Z' interactions with the SM fields, namely, the chiral and the Abelian Z' bosons. Each Z' type is described by a few couplings to the SM fields. Therefore, it is possible to introduce observables which uniquely pick up the Z' virtual state [7].

The Z' signal in the four-lepton scattering process $e^+e^- \rightarrow l^+l^-$ can be detected with a sign-definite observable, which is ruled by the c.m. energy and an additional kinematic parameter. The incorporation of the next-to-leading terms in $m_{Z'}^{-2}$ allows one to consider the Z' effects beyond the approach of four-fermion contact interactions [8]. As a consequence, the four-fermion contact couplings and the Z' mass can be fitted separately.

The introduced observable can be computed directly from the differential cross sections. However, the statistical errors of the available differential cross sections of LEP2 experiments are one order of magnitude larger than the accuracy of the corresponding total cross sections and the forward–backward asymmetries. Fortunately, the differential cross sections of the $e^+e^- \rightarrow l^+l^-$ processes at the LEP2 energies (including the one-loop radiative corrections) can be successfully approximated by a two-parametric polynomial of the cosine of the scattering angle. This makes it possible to recalculate the observable from the total cross sections and the forward–backward asymmetries, reducing noticeably the experimental uncertainty.

Thus, the outlined analysis has to answer whether or not one could detect the model-independent signal of the Abelian Z' boson by treating the LEP2 data. As will be shown, the LEP2 data on the scattering into μ and τ pairs lead to the Abelian Z' signal at about a 1σ confidence level.

The paper is organized as follows. In Section 2, the necessary information on the model-independent description of the Z' interactions at low energies and the RG relations are given. In Section 3, the observables to pick up the Z' boson uniquely are introduced. In the last section, the results on the LEP data fit and the conclusions as well as further prospects are discussed.

2. Z' COUPLINGS TO THE SM PARTICLES

The Abelian Z' boson can be introduced in a model-independent (phenomenological) way by defining its effective low-energy couplings to the SM particles. Such a parametrization is well known in the literature [4]. Since we are going to take account of the Z' effects in the $e^+e^- \rightarrow l^+l^-$ process at LEP2 energies $\sqrt{s} \ll m_{Z'}$, we parametrize the Z' interactions induced at the tree level only. As the decoupling theorem [9] guarantees, they are of renormalizable type, since the nonrenormalizable interactions are generated at higher energies due to radiation corrections and suppressed by the inverse heavy mass ($m_{Z'}$ in our case). The SM gauge group $SU(2)_L \times U(1)_Y$ is considered as a subgroup of the underlying theory group. Thus, the mixing interactions of the types $Z'W^+W^-$, $Z'ZZ$, ... are absent at the tree level. Under these assumptions, the Z' couplings to the fermion and scalar fields are described by the Lagrangian

$$\mathcal{L} = \left| \left(D_\mu^{\text{ew},\phi} - \frac{i\tilde{g}}{2} \tilde{Y}(\phi) \tilde{B}_\mu \right) \phi \right|^2 \quad (1)$$

$$+ i \sum_{f=f_L, f_R} \bar{f} \gamma^\mu \left(D_\mu^{\text{ew},f} - \frac{i\tilde{g}}{2} \tilde{Y}(f) \tilde{B}_\mu \right) f,$$

where ϕ is the SM scalar doublet, \tilde{B}_μ denotes the massive Z' field before the spontaneous breaking of the electroweak symmetry, and the summation over all SM left-handed fermion doublets $f_L = \{(f_u)_L, (f_d)_L\}$ and the right-handed singlets $f_R = \{(f_u)_R, (f_d)_R\}$ is understood. The notation \tilde{g} stands for the charge corresponding to the Z' gauge group, and $D_\mu^{\text{ew},\phi}$ and $D_\mu^{\text{ew},f}$ are the electroweak covariant derivatives. Diagonal 2×2 matrices $\tilde{Y}(\phi) = \text{diag}(\tilde{Y}_{\phi,1}, \tilde{Y}_{\phi,2})$, $\tilde{Y}(f_L) = \text{diag}(\tilde{Y}_{L,f_u}, \tilde{Y}_{L,f_d})$ and numbers $\tilde{Y}(f_R) = \tilde{Y}_{R,f}$ mean the unknown Z' generators characterizing the model beyond the SM.

In particular, the Lagrangian (1) generally leads to the $Z-Z'$ mixing of order $m_Z^2/m_{Z'}^2$, which is proportional to $\tilde{Y}_{\phi,2}$ and originated from the diagonalization of the neutral vector-boson states. The mixing contributes to the scattering amplitudes and cannot be neglected at the LEP2 energies [10].

The Z' couplings to a fermion f are parametrized by two numbers $\tilde{Y}_{L,f}$ and $\tilde{Y}_{R,f}$. Alternatively, the couplings to the axial-vector and vector fermion currents, $a_{Z'}^l \equiv (\tilde{Y}_{R,l} - \tilde{Y}_{L,l})/2$ and $v_{Z'}^l \equiv (\tilde{Y}_{L,l} + \tilde{Y}_{R,l})/2$, can be used. Their values are determined by an unknown model beyond the SM. Assuming an arbitrary underlying theory, one usually supposes that the parameters a_f and v_f are independent numbers. However,

if a theory beyond the SM is renormalizable, these parameters satisfy some relations. For the Z' boson, this is reflected in the correlations between a_f and v_f [7]. These correlations are model-independent in a sense that they do not depend on the underlying model. A detailed discussion of this point and the derivation of the RG relations are given in [7]. Therein, it is shown that two types of Z' -boson interactions are admitted—the chiral and the Abelian ones. In the present paper, we are interested in the Abelian Z' couplings, which are described by the relations

$$v_f - a_f = v_{f^*} - a_{f^*}, \quad a_f = T_{3,f} \tilde{Y}_\phi, \quad (2)$$

$$\tilde{Y}_{\phi,1} = \tilde{Y}_{\phi,2} \equiv \tilde{Y}_\phi,$$

where $T_{3,f}$ is the third component of the fermion weak isospin, and f^* means the isopartner of f (namely, $l^* = \nu_l, \nu_l^* = l, \dots$).

The relations (2) ensure, in particular, the invariance of the Yukawa terms with respect to the effective low-energy subgroup $\tilde{U}(1)$ corresponding to the Abelian Z' boson. As follows from the relations, the couplings of the Abelian Z' to the axial-vector fermion currents have a universal absolute value proportional to the Z' coupling to the scalar doublet. So, in what follows, we will use the short notation $a = a_l = -\tilde{Y}_\phi/2$. Note also that the Z - Z' mixing is expressed in terms of the axial-vector coupling a .

An important benefit of the relations (2) is the possibility of reducing the number of independent parameters of new physics. For example, they can be used to relate the coefficients of the effective Lagrangians [11]. Due to a fewer number of independent Z' couplings, the amplitudes and cross sections of different scattering processes are also related. As a result, one is able to pick up the characteristic signal of the Abelian Z' boson in these processes and to fit successfully the corresponding Z' couplings. In the present paper, we take into account the RG relations (2) in order to introduce the observables convenient for uniquely detecting the Abelian Z' signals in LEP experiments and to obtain the corresponding experimental constraints on the signal.

3. OBSERVABLES

3.1. The Differential Cross Section

Let us consider the processes $e^+e^- \rightarrow l^+l^-$ ($l = \mu, \tau$) with nonpolarized initial- and final-state fermions. In order to introduce the observable which selects the signal of the Abelian Z' boson, we need to compute the differential cross sections of the processes up to the one-loop level.

The lower order diagrams describe the neutral vector-boson exchange in the s channel ($e^+e^- \rightarrow$

$V^* \rightarrow l^+l^-, V = A, Z, Z'$). As for the one-loop corrections, two classes of diagrams are taken into account. The first one includes the pure SM graphs (the mass operators, the vertex corrections, and the boxes). The second set of one-loop diagrams improves the Born level Z' -exchange amplitude by “dressing” the Z' propagator and the Z' -fermion vertices. We assume that Z' states are not excited inside loops. Such an approximation means that the Z' boson is completely decoupled. Then, the differential cross section consists of the squared tree-level amplitude and the term from the interference of the tree-level and one-loop amplitudes. To obtain an infrared-finite result, we also take into account the processes with the soft-photon emission in the initial and final states.

Various computational software programs for calculation of amplitudes and cross sections have been developed. For example, the SM cross sections in the LEP fits are usually generated with ZFITTER. However, ZFITTER requires severe modifications to incorporate the effects of heavy particles beyond the SM. Therefore, we perform the necessary calculations with other software programs. The Feynman diagrams and the amplitudes are generated with FEYNARTS. The algebraic reduction of the one-loop tensor integrals to scalar integrals as well as the cross-section construction are carried out with FORMCALC. The scalar one-loop integrals are evaluated with the LOOPTOOLS library within the \overline{MS} renormalization scheme. The unknown Higgs boson mass is set to 125 GeV in accordance with the present-day bounds.

In the lower order in $m_{Z'}^{-2}$, the Z' contributions to the differential cross section of the process $e^+e^- \rightarrow l^+l^-$ are expressed in terms of four-fermion contact couplings only. If one takes into consideration the higher order corrections in $m_{Z'}^{-2}$, it becomes possible to estimate separately the Z' -induced contact couplings and the Z' mass [8]. In the present analysis, we keep the terms of order $O(m_{Z'}^{-4})$ to fit both of these parameters.

Expanding the differential cross section in the inverse Z' mass and neglecting the terms of order $O(m_{Z'}^{-6})$, we have

$$\frac{d\sigma_l(s)}{dz} = \frac{d\sigma_l^{\text{SM}}(s)}{dz} \quad (3)$$

$$+ \sum_{i=1}^7 \sum_{j=1}^i \left[A_{ij}^l(s, z) + B_{ij}^l(s, z) \zeta \right] a_i a_j$$

$$+ \sum_{i=1}^7 \sum_{j=1}^i \sum_{k=1}^j \sum_{n=1}^k C_{ijkn}^l(s, z) a_i a_j a_k a_n,$$

where the dimensionless quantities

$$\zeta = \frac{m_Z^2}{m_{Z'}^2}, \quad \epsilon = \frac{\tilde{g}^2 m_Z^2 a^2}{4\pi m_{Z'}^2}, \quad (4)$$

$$(a_1, a_2, a_3, a_4, a_5, a_6, a_7)$$

$$= \sqrt{\frac{\tilde{g}^2 m_Z^2}{4\pi m_{Z'}^2}} (a, v_e, v_\mu, v_\tau, v_d, v_s, v_b)$$

are introduced. In what follows, the index $l = \mu, \tau$ denotes the final-state lepton.

The coefficients A, B, C are determined by the SM couplings and masses. Each factor may include the tree-level contribution, the one-loop correction, and the term describing the soft-photon emission. The factors A describe the leading-order contribution, whereas others correspond to the higher order corrections in $m_{Z'}^{-2}$.

3.2. The Observable

To take into consideration the correlations (2), we introduce the observable $\sigma_l(z)$ defined as the difference of cross sections integrated over some ranges of the scattering angle θ [12]:

$$\sigma_l(z) \equiv \int_z^1 \frac{d\sigma_l}{d\cos\theta} d\cos\theta - \int_{-1}^z \frac{d\sigma_l}{d\cos\theta} d\cos\theta, \quad (5)$$

where z stands for the cosine of the boundary angle. The idea of introducing the z -dependent observable (5) is to choose the value of the kinematic parameter z in such a way as to pick up the characteristic features of the Abelian Z' signals.

The deviation of the observable from its SM value can be derived by the angular integration of the differential cross section and has the form

$$\Delta\sigma_l(z) = \sigma_l(z) - \sigma_l^{\text{SM}}(z) \quad (6)$$

$$= \sum_{i=1}^7 \sum_{j=1}^i \left[\tilde{A}_{ij}^l(s, z) + \tilde{B}_{ij}^l(s, z)\zeta \right] a_i a_j$$

$$+ \sum_{i=1}^7 \sum_{j=1}^i \sum_{k=1}^j \sum_{n=1}^k \tilde{C}_{ijkn}^l(s, z) a_i a_j a_k a_n.$$

There is an interval of values of the boundary angle at which the factors $\tilde{A}_{11}^l, \tilde{B}_{11}^l$, and \tilde{C}_{1111}^l at the sign-definite parameters $\epsilon, \epsilon\zeta$, and ϵ^2 contribute more than 95% of the observable value. This makes it possible to construct the sign-definite observable $\Delta\sigma_l(z^*) < 0$ by specifying the proper value of z^* .

In general, one could choose the boundary angle z^* in different schemes. In the previous papers [10,

12], we considered just a small number of tree-level four-fermion contact couplings and specified z^* in order to cancel the factor at the vector–vector coupling. However, if one-loop corrections are taken into account, there are a large number of additional contact couplings. Thus, we have to define some quantitative criterion $F(z)$ to estimate the contributions from sign-definite factors at a given value of the boundary angle z . Maximizing the criterion, one could derive the value z^* , which corresponds to the sign-definite observable $\Delta\sigma_l(z^*)$. Since the observable is linear in the coefficients A, B , and C , we introduce the following criterion:

$$F = \frac{|\tilde{A}_{11}| + \omega_B |\tilde{B}_{11}| + \omega_C |\tilde{C}_{1111}|}{\sum_{\text{all } \tilde{A}} |\tilde{A}_{ij}| + \omega_B \sum_{\text{all } \tilde{B}} |\tilde{B}_{ij}| + \omega_C \sum_{\text{all } \tilde{C}} |\tilde{C}_{ijkn}|}, \quad (7)$$

where the positive “weights” $\omega_B \sim \zeta$ and $\omega_C \sim \epsilon$ take into account the order of each term in the inverse Z' mass.

The numeric values of the “weights” ω_B and ω_C can be taken from the present-day bounds on the contact couplings [1, 2] or [13]. As the computation shows, the value of z^* with an accuracy of 10^{-3} depends only on the order of the “weight” magnitudes. So, in what follows, we take $\omega_B \sim 0.004$ and $\omega_C \sim 0.00004$.

The function $z^*(s)$ is a decreasing function of the c.m. energy. It is tabulated for the LEP2 energies in Tables 1 and 2. The corresponding values of the maximized function F are within the interval $0.95 < F < 0.96$.

Since $\tilde{A}_{11}^l(s, z^*) < 0, \tilde{B}_{11}^l(s, z^*) < 0,$ and $\tilde{C}_{1111}^l(s, z^*) < 0$, the observable

$$\Delta\sigma_l(z^*) = \left[\tilde{A}_{11}^l(s, z^*) + \zeta \tilde{B}_{11}^l(s, z^*) \right] \epsilon \quad (8)$$

$$+ \tilde{C}_{1111}^l(s, z^*) \epsilon^2$$

is negative with an accuracy of 4–5%. Since this property follows from the RG relations (2) for the Abelian Z' boson, the observable $\Delta\sigma_l(z^*)$ selects the model-independent signal of this particle in the processes $e^+e^- \rightarrow l^+l^-$. This allows one to use the data on scattering into $\mu\mu$ and $\tau\tau$ pairs in order to estimate the Abelian Z' coupling to the axial-vector lepton currents.

Although the observable can be computed from the differential cross sections directly, it is also possible to recalculate it from the total cross sections and the forward–backward asymmetries. The recalculation procedure has the proper theoretical accuracy. Nevertheless, it allows one to reduce the experimental errors on the observable, since the published data on

Table 1. The boundary angle and the observable for the scattering into μ pairs at the one-loop level

\sqrt{s} , GeV	z^*	F_{\max}	$\Delta\sigma_\mu(z^*)$
130	0.450	0.89	$-729\epsilon - 1792\epsilon\zeta - 19\,636\epsilon^2$
136	0.439	0.91	$-709\epsilon - 1859\epsilon\zeta - 16\,880\epsilon^2$
161	0.400	0.94	$-643\epsilon - 2183\epsilon\zeta - 6890\epsilon^2$
172	0.390	0.95	$-619\epsilon - 4099\epsilon\zeta - 4099\epsilon^2$
183	0.383	0.95	$-599\epsilon - 2545\epsilon\zeta - 1334\epsilon^2$
189	0.380	0.96	$-586\epsilon - 2635\epsilon\zeta - 495\epsilon^2$
192	0.380	0.96	$-579\epsilon - 2681\epsilon\zeta - 63\epsilon^2$
196	0.380	0.96	$-571\epsilon - 2745\epsilon\zeta - 528\epsilon^2$
200	0.378	0.95	$-564\epsilon - 2811\epsilon\zeta - 1137\epsilon^2$
202	0.376	0.96	$-560\epsilon - 2845\epsilon\zeta - 1448\epsilon^2$
205	0.374	0.96	$-555\epsilon - 2897\epsilon\zeta - 1923\epsilon^2$
207	0.372	0.96	$-552\epsilon - 2932\epsilon\zeta - 2245\epsilon^2$

Table 2. The boundary angle and the observable for the scattering into τ pairs at the one-loop level

\sqrt{s} , GeV	z^*	$\Delta\sigma_\tau(z^*)$
130	0.460	$-687\epsilon - 1664\epsilon\zeta - 25\,782\epsilon^2$
136	0.442	$-688\epsilon - 1779\epsilon\zeta - 20\,784\epsilon^2$
161	0.400	$-625\epsilon - 2097\epsilon\zeta - 10\,993\epsilon^2$
172	0.391	$-601\epsilon - 2263\epsilon\zeta - 8382\epsilon^2$
183	0.385	$-571\epsilon - 2402\epsilon\zeta - 7580\epsilon^2$
189	0.380	$-568\epsilon - 2533\epsilon\zeta - 5135\epsilon^2$
192	0.380	$-562\epsilon - 2578\epsilon\zeta - 4769\epsilon^2$
196	0.379	$-554\epsilon - 2640\epsilon\zeta - 4272\epsilon^2$
200	0.378	$-547\epsilon - 2704\epsilon\zeta - 3761\epsilon^2$
202	0.377	$-543\epsilon - 2736\epsilon\zeta - 3501\epsilon^2$
205	0.374	$-548\epsilon - 2834\epsilon\zeta - 1292\epsilon^2$
207	0.372	$-544\epsilon - 2868\epsilon\zeta - 1010\epsilon^2$

the total cross sections and the forward–backward asymmetries are still more precise than the data on the differential cross sections.

The recalculation is based on the fact that the differential cross section can be approximated with a good accuracy by a two-parametric polynomial in the cosine of the scattering angle z :

$$\frac{d\sigma_l(s)}{dz} = \frac{d\sigma_l^{\text{SM}}(s)}{dz} + (1+z^2)\beta_l + z\eta_l + \delta_l(z), \quad (9)$$

where $\delta_l(z)$ measures the difference between the exact and the approximated cross sections. The approximated cross section reproduces the exact one in the limit of the massless initial- and final-state leptons and if one neglects the contributions of the box diagrams.

Performing angular integration, it is easy to obtain the expression for the observable,

$$\begin{aligned} \Delta\sigma_l(z^*) &= \sigma_l(z^*) - \sigma_l^{\text{SM}}(z^*) \\ &= (1-z^{*2})\eta_l - \frac{2\beta_l}{9}z^*(3+z^{*2}) + \tilde{\delta}_l(z^*), \end{aligned} \quad (10)$$

and for the total and forward–backward cross sections,

$$\begin{aligned} \Delta\sigma_l^T &= \sigma_l^T - \sigma_l^{T,\text{SM}} = \frac{8\beta_l}{9} + \tilde{\delta}_l(-1), \\ \Delta\sigma_l^{\text{FB}} &= \sigma_l^{\text{FB}} - \sigma_l^{\text{FB,SM}} = \eta_l + \tilde{\delta}_l(0). \end{aligned} \quad (11)$$

Then, the factors β_l and η_l can be eliminated from the observable:

$$\Delta\sigma_l(z^*) = (1-z^{*2})\Delta\sigma_l^{\text{FB}} \quad (12)$$

$$- \frac{3}{12}z^*(3+z^{*2})\Delta\sigma_l^T + \xi_l.$$

The quantity ξ_l ,

$$\xi_l = \tilde{\delta}_l(z^*) - (1-z^{*2})\tilde{\delta}_l(0) + \frac{3}{12}z^*(3+z^{*2})\tilde{\delta}_l(-1), \quad (13)$$

measures the theoretical accuracy of the approximation.

The forward–backward cross section is related to the total cross section and the forward–backward asymmetry by means of the following expression:

$$\Delta\sigma_l^{\text{FB}} = \Delta\sigma_l^T A_l^{\text{FB}} + \sigma_l^{T,\text{SM}} \Delta A_l^{\text{FB}}. \quad (14)$$

As the computation shows, $\tilde{\delta}_l(z^*) \simeq 0.01\Delta\sigma_l(z^*)$, $\tilde{\delta}_l(0) \simeq 0.007\Delta\sigma_l^{\text{FB}}$, and $\tilde{\delta}_l(-1) \simeq -0.07\Delta\sigma_l^T$ at the LEP2 energies. Taking into account the experimental values of the total cross sections and the forward–backward asymmetries at the LEP2 energies ($\Delta\sigma_l^T \simeq 0.1$ pb, $\sigma_l^{T,\text{SM}} \simeq 2.7$ pb, $\Delta A_l^{\text{FB}} \simeq 0.04$, $A_l^{\text{FB}} \simeq 0.5$), one can estimate the theoretical error as $\xi_l \simeq 0.003$ pb. At the same time, the corresponding statistical uncertainties on the observable are larger than 0.06 pb. Thus, the proposed approximation is quite good and can be successfully used to obtain more accurate experimental values of the observable.

4. DATA FIT AND CONCLUSIONS

To search for the model-independent signals of the Abelian Z' boson, we will analyze the introduced observable $\Delta\sigma_l(z^*)$ on the basis of the LEP2 data set.

In the lower order in $m_{Z'}^{-2}$, the observable (8) depends on one flavor-independent parameter ϵ ,

$$\Delta\sigma_l^{\text{th}}(z^*) = \tilde{A}_{11}^l(s, z^*)\epsilon + \tilde{C}_{1111}^l(s, z^*)\epsilon^2, \quad (15)$$

which can be fitted from the experimental values of $\Delta\sigma_\mu(z^*)$ and $\Delta\sigma_\tau(z^*)$. As we noted above, the sign of the fitted parameter ($\epsilon > 0$) is a characteristic feature of the Abelian Z' signal.

In what follows, we will apply the usual fit method based on the likelihood function. The central value of ϵ is obtained by the minimization of the χ^2 function:

$$\chi^2(\epsilon) = \sum_n \frac{[\Delta\sigma_{\mu,n}^{\text{exp}}(z^*) - \Delta\sigma_\mu^{\text{th}}(z^*)]^2}{(\delta\sigma_{\mu,n}^{\text{exp}}(z^*))^2}, \quad (16)$$

where the sum runs over the experimental points entering a chosen data set. The 1σ C.L. interval (b_1, b_2) for the fitted parameter is derived by means of the likelihood function $L(\epsilon) \propto \exp[-\chi^2(\epsilon)/2]$. It is determined by the equations

$$\int_{b_1}^{b_2} L(\epsilon') d\epsilon' = 0.68, \quad L(b_1) = L(b_2). \quad (17)$$

To compare our results with those of [1, 2], we introduce the contact interaction scale

$$\Lambda^2 = 4m_{Z'}^2\epsilon^{-1}. \quad (18)$$

This normalization of contact couplings is admitted in [1, 2]. We use again the likelihood method to determine a one-sided lower limit on the scale Λ at the 95% C.L. It is derived by the integration of the likelihood function over the physically allowed region $\epsilon > 0$. The exact definition is

$$\Lambda = 2m_{Z'}(\epsilon^*)^{-1/2}, \quad (19)$$

$$\int_0^{\epsilon^*} L(\epsilon') d\epsilon' = 0.95 \int_0^\infty L(\epsilon') d\epsilon'.$$

We also introduce the probability of the Abelian Z' signal as the integral of the likelihood function over the positive values of ϵ :

$$P = \int_0^\infty L(\epsilon') d\epsilon'. \quad (20)$$

Actually, the fitted value of the contact coupling ϵ originates mainly from the leading-order term in the inverse Z' mass in Eq. (8). The analysis of the higher order terms allows one to estimate the constraints on the Z' mass alone. Replacing ϵ in the observable (8) with its fitted central value $\bar{\epsilon}$, one obtains the expression

$$\Delta\sigma_l(z^*) = [\tilde{A}_{11}^l(s, z^*) + \zeta\tilde{B}_{11}^l(s, z^*)] \bar{\epsilon} \quad (21)$$

$$+ \tilde{C}_{1111}^l(s, z^*)\bar{\epsilon}^2,$$

which depends on the parameter $\zeta = m_Z^2/m_{Z'}^2$. Then, the central value on this parameter and the corresponding 1σ C.L. interval are derived in the same way as those for ϵ .

To fit the parameters ϵ and ζ , we start with the LEP2 data on the total cross sections and the forward–backward asymmetries [1, 2]. Those data are converted into the experimental values of the observable $\Delta\sigma_l(z^*)$ with the corresponding errors $\delta\sigma_l(z^*)$ by means of the following relations:

$$\Delta\sigma_l(z^*) = \left[A_l^{\text{FB}}(1 - z^{*2}) - \frac{z^*}{4}(3 + z^{*2}) \right] \Delta\sigma_l^T \quad (22)$$

$$+ (1 - z^{*2}) \sigma_l^{T, \text{SM}} \Delta A_l^{\text{FB}},$$

$$(\delta\sigma_l(z^*))^2 = \left[A_l^{\text{FB}}(1 - z^{*2}) - \frac{z^*}{4}(3 + z^{*2}) \right]^2 (\delta\sigma_l^T)^2$$

$$+ \left[(1 - z^{*2}) \sigma_l^{T, \text{SM}} \right]^2 (\delta A_l^{\text{FB}})^2.$$

We perform the fits assuming several data sets, including the $\mu\mu$, $\tau\tau$, and the complete $\mu\mu$ and $\tau\tau$ data, respectively. The results are presented in Table 3. As one can see, the more precise $\mu\mu$ data demonstrate the signal of about 1σ level. It corresponds to the Abelian Z' boson with a mass of the order of 1.2–1.5 TeV if one assumes the value of $\tilde{\alpha} = \tilde{g}^2/4\pi$ to be in the interval 0.01–0.02. No signal is found by the analysis of the $\tau\tau$ cross sections. The combined fit of the $\mu\mu$ and $\tau\tau$ data leads to the signal below the 1σ C.L.

Note that the mean values of ϵ have changed by 20% in comparison with the winter 2002 data, whereas the uncertainties remain approximately the same. Thus, the Abelian Z' signal will probably be picked up at no more than 1σ C.L. when the final LEP2 data on $e^+e^- \rightarrow \mu^+\mu^-, \tau^+\tau^-$ are completed.

Being governed by the next-to-leading contributions in $m_{Z'}^{-2}$, the fitted values of ζ are characterized by significant errors. The $\mu\mu$ data set gives the central value which corresponds to $m_{Z'} \simeq 1.1$ TeV.

We also perform a separate fit of the parameters based on the direct calculation of the observable from the differential cross sections. The complete set of available data [14] is used (see Table 4). The results are given in Table 5. As one can see, the experimental uncertainties of the data on the differential cross sections are one order of magnitude larger than the

Table 3. The contact coupling ϵ with a 68% C.L. uncertainty, a 95% C.L. lower limit on the scale Λ , the probability of the Z' signal P , and the value of $\zeta = m_Z^2/m_{Z'}^2$, as a result of the fit of the observable recalculated from the total cross sections and the forward–backward asymmetries

Data set	ϵ	Λ , TeV	P	ζ
Winter 2002				
$\mu\mu$	$0.0000482_{-0.0000493}^{+0.0000496}$	15.7	0.83	0.007 ± 0.215
$\tau\tau$	$0.0000016_{-0.0000656}^{+0.0000661}$	16.0	0.51	-0.052 ± 8.463
$\mu\mu$ and $\tau\tau$	$0.0000313_{-0.0000395}^{+0.0000396}$	18.1	0.78	0.006 ± 0.264
Summer 2002				
$\mu\mu$	$0.0000366_{-0.0000486}^{+0.0000489}$	16.4	0.77	0.009 ± 0.278
$\tau\tau$	$-0.0000266_{-0.0000639}^{+0.0000643}$	17.4	0.34	-0.001 ± 0.501
$\mu\mu$ and $\tau\tau$	$0.0000133_{-0.0000387}^{+0.0000389}$	19.7	0.63	0.017 ± 0.609

corresponding errors of the total cross sections and the forward–backward asymmetries. These data also provide the larger values of the contact coupling ϵ . As for the more precise $\mu\mu$ data, three of the LEP2 collaborations demonstrate positive values of ϵ . The combined ϵ is also positive and remains practically unchanged by the incorporation of the $\tau\tau$ data.

Now, we compare the fits based on the differential cross sections and the total cross sections. As was mentioned in the previous section, the indirect computation of the observable from the total cross sections and the forward–backward asymmetries inspires some insufficient theoretical uncertainty about

Table 4. The differential cross sections used for fitting (the letters F and P mark the final and the preliminary data, respectively)

\sqrt{s} , GeV	ALEPH	DELPHI	L3	OPAL
130				F
136				F
161				F
172				F
183		F	F	F
189	P	F	F	F
192	P	P		P
196	P	P		P
200	P	P		P
202	P	P		P
205	P	P		P
207	P	P		P

2% of the statistical one. It also increases the statistical error because of the recalculation procedure. Nevertheless, the uncertainty of the fitted parameter ϵ within the recalculation scheme is one order of magnitude less than that for the direct computation from the differential cross sections. This difference is explained by the different accuracy of the available experimental data on the differential and the total cross sections. If the final LEP2 differential cross sections are as accurate as the present data on the total cross sections, the direct computation of the observable will be able to reduce, in principle, the uncertainty of the fitted coupling ϵ .

To compare our results with the fits of the contact couplings presented by the LEP collaborations in [1, 2], let us briefly describe the approach used therein. Since only one parameter of new physics can be successfully fitted, the LEP collaborations usually discuss eight “models” (LL, RR, LR, RL, VV, AA, A0, V0) which assume specific helicity couplings between the initial-state and final-state fermion currents. Each model is described by only one nonzero four-fermion coupling, while the others are set to zero. For example, in the LL model, the nonzero coupling of left-handed fermions is taken into account. The signal of new physics is fitted by considering the interference of the SM amplitude with the contact four-fermion term. Whatever physics exists beyond the SM, it has to manifest itself in some contact coupling mentioned. Hence, it is possible to find the low limit on the masses of the states responsible for the interactions considered. In principle, a number of states may contribute to each of the models. Therefore, the purpose of the fit described by these models is to find any signal of new physics. No specific types of new particles are considered in this analysis.

As has been shown, the characteristic signal of the Abelian Z' boson is related to the flavor-independent

Table 5. The contact coupling ϵ with 68% C.L. uncertainties computed from the differential cross sections

	μ data	τ data	μ and τ data
ALEPH	$0.00014^{+0.00068}_{-0.00069}$	$-0.00007^{+0.00120}_{-0.00120}$	$0.00009^{+0.00059}_{-0.00060}$
DELPHI	$-0.00010^{+0.00070}_{-0.00070}$	$0.00000^{+0.00140}_{-0.00140}$	$-0.00008^{+0.00062}_{-0.00063}$
L3	$0.00013^{+0.00043}_{-0.00043}$	$0.00024^{+0.00053}_{-0.00054}$	$0.00018^{+0.00033}_{-0.00033}$
OPAL	$0.00028^{+0.00074}_{-0.00075}$	$-0.00017^{+0.00120}_{-0.00120}$	$0.00015^{+0.00063}_{-0.00063}$
Combined	$0.00012^{+0.00028}_{-0.00030}$	$0.00012^{+0.00043}_{-0.00043}$	$0.00012^{+0.00024}_{-0.00024}$

couplings to the axial-vector currents. To pick up the signal, we construct the observable which is dominated by the axial-vector couplings. The contributions of the remaining couplings are suppressed in the observable by the special choice of the kinematic parameters. In this regard, let us turn to the helicity “models” [1, 2] and compare our results with the fit for the axial model (AA). As it follows from the present analysis, this model could be sensitive to the signals of the Abelian Z' boson. Of course, the parameters ϵ [1, 2] (in what follows, we will mark it as ϵ_{EWWG}) and ϵ in the present paper are not the same quantity. First, they are normalized by different factors and related as $\epsilon_{\text{EWWG}} = -\epsilon m_{Z'}^{-2}/4$. Second, as we have already noted, in the AA model the Z' couplings to the vector fermion currents are set to zero; therefore, it is possible to describe only some particular case of the Abelian Z' boson. Moreover, in this model, both the positive and the negative values of ϵ_{EWWG} are considered, whereas in our approach only the positive ϵ values (which correspond to the negative ϵ_{EWWG}) are permissible. As the value of the four-fermion contact coupling in the AA model is dependent on the lepton flavor, the Abelian Z' induces the axial-vector coupling which is universal for all lepton types. Considering the winter 2002 data [1], it is interesting to note that the fitted value of ϵ_{EWWG} in the AA model for the $\mu^+\mu^-$ final states ($-0.0025^{+0.0018}_{-0.0023}$ TeV^{-2}) and the value derived under the assumption of lepton universality ($-0.0018^{+0.0016}_{-0.0019}$ TeV^{-2}) are similar to our results, which correspond to -0.0015 ± 0.0015 TeV^{-2} and -0.0009 ± 0.0012 TeV^{-2} , respectively. As for the summer 2002 data [2], only the value of ϵ_{EWWG} under the assumption of lepton universality is available (-0.0013 ± 0.0017 TeV^{-2}). It is close to our result for the $\mu\mu$ process (-0.0011 ± 0.0015 TeV^{-2}). However, the central value of ϵ_{EWWG} is about three times greater than the corresponding one for the combined μ and τ data (-0.0004 ± 0.0012 TeV^{-2}). Thus, the signs of the central values in the AA model agree with our results, and the uncertainties are of the same order. The fitted values of the 95% C.L. lower limit

on the scale Λ are again in good accordance with the corresponding values of Λ^- for the AA model of [2]. Thus, we come to a conclusion that the AA model is mainly responsible for signals of the Abelian Z' gauge boson, although a lot of details concerning its interactions are not accounted for within this fit.

It is worth mentioning the recent paper by Chivukula and Simmons [15], who derived model-dependent bounds on the mass of the Z' boson for flavor-changing technicolor models. It has been found that, in these models, $m_{Z'}$ is heavier than about 1 TeV. It is interesting to note that this value is very close to our model-independent result which corresponds to the flavor-conserved case.

As follows from the present analysis, the Abelian Z' boson has to be light enough to be discovered at the LHC. On the other hand, the LEP2 data on the processes $e^+e^- \rightarrow \mu^+\mu^-, \tau^+\tau^-$ do not provide the necessary statistics for the detection of the model-independent signal of the Abelian Z' boson at more than 1σ C.L. Thus, it is of interest to find the observables for other scattering processes in order to increase the data set. In this regard, let us note the paper [16], where the helicity “models” were applied to the Bhabha scattering $e^+e^- \rightarrow e^+e^-(\gamma)$. As was shown therein, the AA model demonstrates a 2σ -level deviation from the SM. However, these deviations could not be interpreted directly as the signal of the Abelian Z' boson because of the reasons mentioned above. Therefore, it seems appropriate to us to find the observable for the Abelian Z' search in the process $e^+e^- \rightarrow e^+e^-$.

ACKNOWLEDGMENTS

This work was supported in part by the State Foundation for Fundamental Research of Ukraine (grant no. F7/296-2001).

REFERENCES

1. ALEPH Collab., DELPHI Collab., L3 Collab., OPAL Collab., LEP Electroweak Working Group, SLD Heavy Flavour, Electroweak Working Group, hep-ex/0112021.

2. LEP Electroweak Working Group, LEP2FF/02-03.
3. J. Wudka, *Int. J. Mod. Phys. A* **9**, 2301 (1994).
4. A. Leike, *Phys. Rep.* **317**, 143 (1999).
5. P. Langacker, R. W. Robinett, and J. L. Rosner, *Phys. Rev. D* **30**, 1470 (1984); D. London and J. L. Rosner, *Phys. Rev. D* **34**, 1530 (1986); J. C. Pati and A. Salam, *Phys. Rev. D* **10**, 275 (1974); R. N. Mohapatra and J. C. Pati, *Phys. Rev. D* **11**, 566 (1975).
6. G. Altarelli *et al.*, *Z. Phys. C* **45**, 109 (1989).
7. A. Gulov and V. Skalozub, *Eur. Phys. J. C* **17**, 685 (2000).
8. T. G. Rizzo, *Phys. Rev. D* **55**, 5483 (1997).
9. T. Appelquist and J. Carazzone, *Phys. Rev. D* **11**, 2856 (1975).
10. A. Gulov and V. Skalozub, *Nucl. Phys. B (Proc. Suppl.)* **102**, 363 (2001).
11. A. Gulov and V. Skalozub, *Int. J. Mod. Phys. A* **16**, 179 (2001).
12. A. Gulov and V. Skalozub, *Phys. Rev. D* **61**, 055007 (2000).
13. A. Gulov and V. Skalozub, hep-ph/0107236.
14. ALEPH Collab., Preprint ALEPH 2000-047; Preprint ALEPH 2001-019; DELPHI Collab., *Phys. Lett. B* **485**, 45 (2000); Preprint DELPHI 2000-128; Preprint DELPHI 2001-094; L3 Collab., *Phys. Lett. B* **479**, 101 (2000); OPAL Collab., *Eur. Phys. J. C* **2**, 441 (1998); **6**, 1 (1999); **13**, 553 (2000); Preprint OPAL Physics Note PN424 (2000); Preprint OPAL Physics Note PN469 (2001).
15. R. Chivukula and E. Simmons, hep-ph/0205064.
16. D. Bourilkov, *Phys. Rev. D* **64**, 071701 (2001).

ELEMENTARY PARTICLES AND FIELDS
Experiment

Single-Spin Asymmetry of Inclusive γ Production in $p\uparrow p$ Interactions at 200 GeV/c*

Yu. V. Kharlov, D. A. Morozov, S. B. Nurushev, and A. N. Vasiliev

Institute for High Energy Physics, Protvino, Moscow oblast, 142284 Russia

Received September 17, 2003

Abstract—From the data of Fermilab polarization experiment E704, the analyzing power A_N^γ of inclusively produced photons was extracted. It is small, of the order of 2–4%. The analyzing power of “leading” photons (the fastest in $\pi^0 \rightarrow \gamma\gamma$ decay) is a factor of 2 higher than A_N^γ assuming a definite model for x_F dependence of A_N^γ . A Monte Carlo simulation is performed in order to see effects at higher statistics than in the E704 experiment. This simulation showed that the process of inclusive photons may be used as a basis for future polarimetry at polarized colliders. The example of one local photon polarimeter at RHIC is discussed. © 2004 MAIK “Nauka/Interperiodica”.

INTRODUCTION

The powerfully polarized RHIC is becoming available for spin physics study in the highest ever reached beam energy range ($50 \leq \sqrt{s} \leq 500$ GeV) [1]. One of the important problems in making RHIC an efficient tool is to build a local polarimeter for measuring the beam polarization at the interaction region. There are several proposals to use for such a goal the inclusive neutral pion polarimeter [2–4]. But space limitation and several other experimental conditions may require a polarimeter placement far away from the interaction point. In this case, inclusive photon production becomes attractive and it was proposed in [5]. Due to an absence of experimental data on $A_N^\gamma(x_F^\gamma, p_T^\gamma)$, the authors of [5] used the phenomenological model for estimation of $A_N^\gamma(x_F^\gamma, p_T^\gamma)$. In the present paper, we aim to reconstruct $A_N^\gamma(x_F^\gamma, p_T^\gamma)$ from the Fermilab polarization experiment E704 [6, 7] making use of experimental data and Monte Carlo simulation. The consistency of two such approaches is also considered.

This paper is organized in the following way. Section 1 is dedicated to analysis of experimental data in E704 and offers the extracted asymmetries $A_N^\gamma(x_F^\gamma, p_T^\gamma)$. Section 2 describes a simulation procedure by the Monte Carlo technique and presents the estimated values of $A_N^\gamma(x_F^\gamma, p_T^\gamma)$. In Section 3, we discuss a photon polarimeter in the E704 environment at 200 GeV. Section 4 presents the estimates of parameters for one inclusive photon polarimeter which is under test at RHIC [8]. In the Conclusion, the main results of our study are summarized.

1. EXTRACTION OF $A_N^\gamma(x_F^\gamma, p_T^\gamma)$ FROM E704 DATA

In the previous papers [6, 7], the analyzing power for inclusive π^0 production $A_N^{\pi^0}(x_F, p_T)$ in the reaction

$$p\uparrow + p \rightarrow \pi^0 + X \quad (1)$$

was extracted at 200-GeV/c initial momentum by detecting both photons from π^0 decay. In the present paper, we have a goal to perform an extraction of the photon analyzing power $A_N^\gamma(x_F^\gamma, p_T^\gamma)$ in the reaction

$$p\uparrow + p \rightarrow \gamma + X$$

under various conditions.

First of all, one needs to know the analyzing power of all inclusively produced photons. A shower in the calorimeter which is well fitted by the electromagnetic shower shape is accepted as a photon. To select the electromagnetic shower, we follow the criterion developed in [9] (see also [10]). Table 1 contains the reconstructed analyzing power $A_N^\gamma(x_F^\gamma, p_T^\gamma)$ for such photons at threshold $p_T^c = 0.5$ GeV/c. Analyzing power is defined as a relative difference of the cross sections with different beam polarization. Figure 1a shows small but nonzero asymmetries of the order of 2–4% at $x_F^\gamma = 0.3–0.5$. False asymmetry is determined similarly to the analyzing power, but the event samples are not correlated with the beam polarization. These uncorrelated samples can be defined in different ways: (i) on the basis of the same statistics which were used for $A_N^\gamma(x_F^\gamma, p_T^\gamma)$ estimates mixing all directions of the beam polarizations, (ii) using the unpolarized beam, and (iii) for whole statistics. All

*This article was submitted by the authors in English.

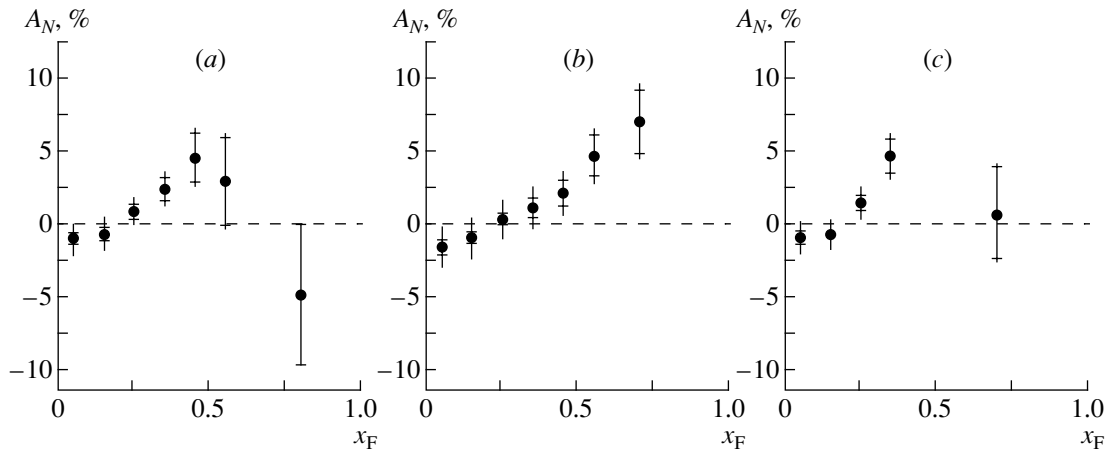


Fig. 1. The analyzing power in E704 experiment for (a) all inclusively produced photons, (b) “raw” neutral pions, and (c) “leading” photons. The inner error bars are the statistical uncertainties, and the outer error bars are the statistical and systematic uncertainties added in quadrature.

cases give us a value of false asymmetry of the order of 1% on average and it has been added as systematic error in Fig. 1. There is an indication that the inclusively produced photons might have small but nonzero analyzing power A_N^γ . The statistics of E704 are poor for making an unambiguous statement.

Keeping in mind that the reaction (1) has $A_N^{\pi^0}$ much higher than A_N^γ estimated above for inclusively produced photons, we decided to restrict sources of photon pairs to the mass region $0.07 < m_{\gamma\gamma} < 0.2 \text{ GeV}/c^2$. Not being able to identify a decay photon from π^0 , we called such a source of photon pairs as “raw” π^0 . The analyzing power of such “raw” neutral pions is presented in Table 2 and Fig. 1b. The false asymmetries calculated in a similar way as in Fig. 1a give 1% values as well. Asymmetry $A_N^\gamma(x_F, p_T)$ in this case is a little bit higher than in Fig. 1a for $A_N^\gamma(x_F, p_T)$ but approximately a factor of 2 smaller

than for true π^0 . Such a difference can be explained by an unpolarized combinatorial background which was estimated strictly in [7].

To improve the situation, we selected the leading photons (i.e., the photons with a higher energy) for each π^0 decay. The corresponding analyzing powers for “leading” photons are presented in Table 3 and in Fig. 1c. Again, the systematic errors connected with false asymmetry are of the order of 1%. The analyzing power of leading photons is approximately a factor of 2 higher than that of inclusive photons (see Tables 1 and 3 in x_F intervals 0.2–0.3 and 0.3–0.4).

So somehow our expectation is justified. The conclusions from analysis of E704 data are the following:

The inclusively produced photons have an asymmetry of the order of 2% at $x_F = 0.35$ and about 4% at $x_F = 0.45$.

The leading photons have an analyzing power of the order of 4% at $x_F = 0.35$.

Table 1. The analyzing power of reaction $p_\uparrow + p \rightarrow \gamma + X$ at 200 GeV/c

x_F	$A_N^\gamma, \%$
0.0–0.1	-1.0 ± 0.4
0.1–0.2	-0.7 ± 0.4
0.2–0.3	0.8 ± 0.5
0.3–0.4	2.4 ± 0.8
0.4–0.5	4.6 ± 1.7
0.5–0.6	2.9 ± 3.1
0.6–1.0	-4.9 ± 4.8

Table 2. The analyzing power of reaction $p_\uparrow + p \rightarrow \pi^0 + X$ at 200 GeV/c

x_F	$A_N, \%$
0.0–0.1	-1.6 ± 0.5
0.1–0.2	-1.0 ± 0.4
0.2–0.3	0.3 ± 0.4
0.3–0.4	1.1 ± 0.7
0.4–0.5	2.1 ± 0.9
0.5–0.6	4.7 ± 1.4
0.6–0.8	7.1 ± 2.2

The asymmetry of photons is smaller than the asymmetry of π^0 (by approximately 2–3 times), but in the case of photons one can work at smaller x_F^γ .

The statistics of the E704 experiment are scarce for more detailed analysis. For this reason, in the following sections, we will describe a Monte Carlo simulation procedure which we made in order to see asymmetries at much higher statistics.

2. SIMULATION OF A SINGLE-SPIN ASYMMETRY BASED ON THE E704 DATA

In the E704 experiment, the single-spin asymmetry of π^0 mesons in the reaction $p_\uparrow p \rightarrow \pi^0 X$ was studied. We simulated a π^0 production with the single-spin asymmetry defined by the experimental measurements [6, 7]. Expecting that the decay photons (from $\pi^0 \rightarrow \gamma\gamma$) have nonzero asymmetry, we have analyzed the following dependences:

$A_N^\gamma(x_F^\gamma)$ for leading photon in the decay $\pi^0 \rightarrow \gamma\gamma$ (it means that x_F^γ of this photon is the highest in π^0 decay) for every π^0 having nonzero asymmetry (“useful” pion [5]),

$A_N^\gamma(x_F^\gamma)$ for all photons produced by $p_\uparrow p$ interaction versus cuts in p_T^γ : 0.3, 0.4, 0.5, 0.6, and 0.7 GeV/c.

2.1. Event-Generation Algorithm

In the E704 experiment, the following results for single-spin π^0 asymmetry were obtained [see Fig. 2 (circles)] [6].

The following algorithm was constructed for generation of such events for the reactions $p_\uparrow p \rightarrow aX$ at $E(p_\uparrow) = 200$ GeV, where

$$a = \begin{cases} \text{“useful” } \pi^0, \\ \gamma \text{ from “useful” } \pi^0, \\ \gamma \text{ from all sources.} \end{cases} \quad (2)$$

(i) Minimum-bias pp events are generated by PYTHIA-5.72 [11]. The decay $\pi^0 \rightarrow \gamma\gamma$ is forbidden.

(ii) Assuming that $A_N(x_F)$ depends on x_F linearly (from Fig. 2),

$$A_N = b + cx, \quad (3)$$

the factors b and c are determined: $b = -0.082 \pm 0.032$, $c = 0.341 \pm 0.070$ with $\chi^2/\text{ndf} = 1.76/2$.

(iii) For each generated “useful” π^0 meson (in correspondence with Fig. 2), the $A_N^\pi(x_F)$ value was assigned according to relation (3). The other π^0 have been left in the events without asymmetry.

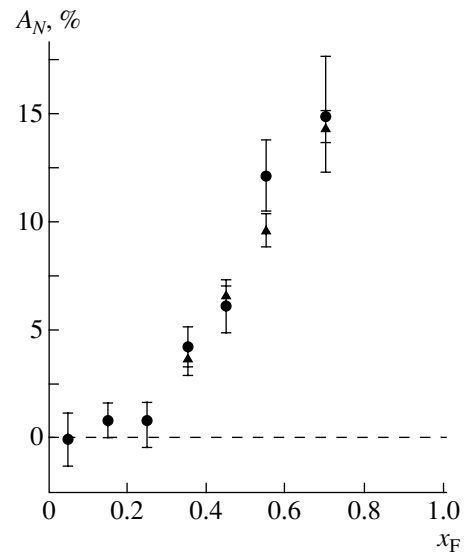


Fig. 2. The asymmetry parameters A_N for inclusive π^0 production by 200-GeV polarized protons. Points: (●) experimental values, (▲) Monte Carlo results.

(iv) The azimuthal angle of π^0 was generated by the following dependence of the π^0 yield:

$$I(x_F, p_T) = I_0(x_F, p_T)[1 + A_N(x_F, p_T)P_b \cos \phi], \quad (4)$$

where I is the invariant cross section of π^0 production, I_0 is the same cross section for an unpolarized beam, and $P_b = 0.456$ is beam polarization in E704.

(v) All π^0 decays are allowed.

After proceeding through this algorithm, we have the same set of events as in E704 with the only difference that polarization asymmetry (spin \uparrow and \downarrow) is converted to azimuthal asymmetry (left–right), and we assume zero asymmetry in all other channels of γ production in the $p_\uparrow p$ interaction.

2.2. An Approach to Estimate the Asymmetry

The asymmetry of inclusively produced particle a [see (2)] in the interaction of interest was calculated in the following way.

Table 3. The analyzing power of reaction $p_\uparrow + p \rightarrow$ “leading” $\gamma + X$ at 200 GeV/c

x_F	A_N , %
0.0–0.1	-0.9 ± 0.4
0.1–0.2	-0.7 ± 0.3
0.2–0.3	1.4 ± 0.5
0.3–0.4	4.6 ± 1.2
0.4–1.0	0.7 ± 3.1

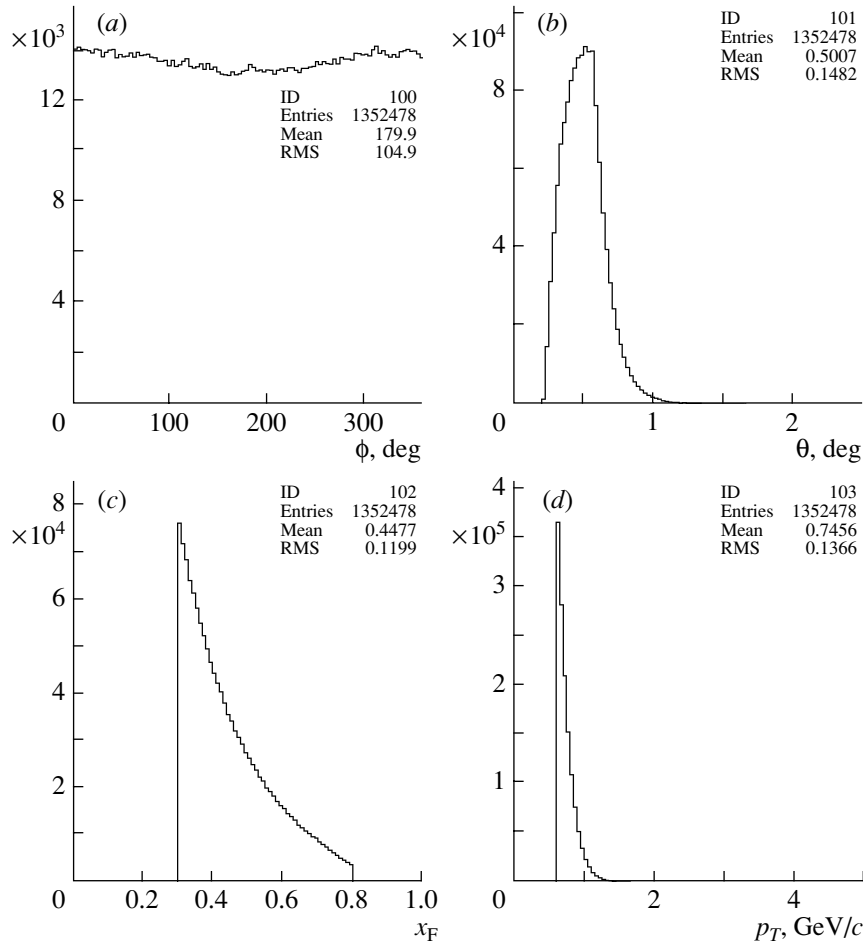


Fig. 3. The distributions of “useful” π^0 mesons on (a) the azimuthal angle ϕ , (b) the polar angle θ , (c) x_F , and (d) p_T .

With fixed value of x_F , the asymmetry $A_N(p_T)$ is determined from (4) via the equation

$$A_N(p_T) = \frac{1}{P_b} \frac{I^L(p_T) - I^R(p_T)}{I^L(p_T) + I^R(p_T)} = \frac{1}{P_b} \frac{N^L(p_T) - N^R(p_T)}{N^L(p_T) + N^R(p_T)},$$

where $N^L(p_T)$ and $N^R(p_T)$ are the numbers of particles a with positive and negative directions of beam polarization (i.e., in our terminology flying, respectively, to the left and to the right relative to the beam direction) normalized by the flux of incident protons hitting the target and having on average zero polarization.

For normalized events $N^{L,R}$, one may write

$$N^{L,R}(p_T, \phi) = N^0(p_T)(1 \pm \epsilon(p_T) \cos \phi),$$

where N^0 means events averaged over beam polarization. A raw asymmetry $\epsilon(p_T)$ was determined as a

result of a fit versus $\cos \phi$:

$$\epsilon(p_T) \cos \phi = \frac{N^L(p_T) - N^R(p_T)}{N^L(p_T) + N^R(p_T)}.$$

After the calculation of the raw asymmetry $\epsilon(p_T)$, an unknown quantity $A_N(p_T)$ was reconstructed as

$$A_N(p_T) = \frac{\epsilon(p_T)}{P_b}.$$

2.3. Results of Asymmetry Estimate

As a test of the algorithm, the generated results for $A_N^{\pi^0}(x_F)$ for π^0 mesons (the acceptance of the E704 calorimeter was taken into account) are compared to their experimental values (see Fig. 2).

There is good consistency between the simulated $A_N^{\pi^0}(x_F)$ and their experimental values: $\chi^2/\text{ndf} = 2.3/4$. Kinematical variables of “useful” π^0 mesons are shown at Fig. 3.

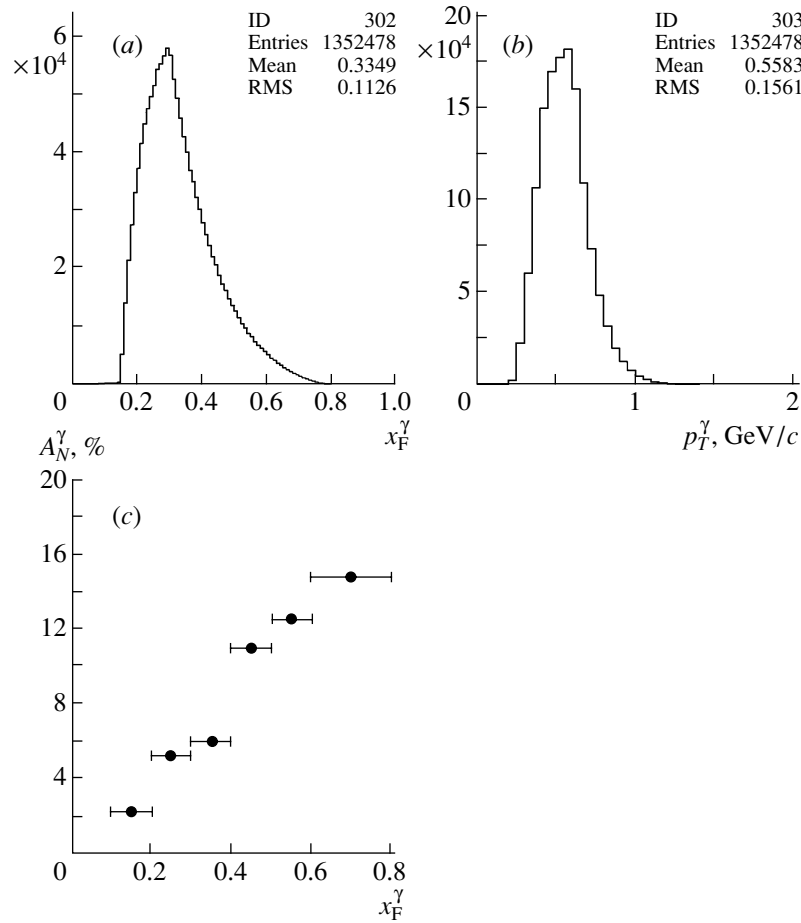


Fig. 4. The “leading”-photon distributions over (a) x_F^γ , (b) p_T^γ ; (c) analyzing power of the “leading” photons (see error values in Table 4).

These results convinced us that this algorithm may be applied to study $A_N^\gamma(x_F)$ of inclusive γ production.

Firstly, we assume that the only source of γ production is a π^0 decay. It is known that η mesons may add around 10% additional photons. Since A_N for η production is the same as A_N for π^0 [10], we can take the η source as a π^0 source. In this case, only “useful” π^0 were chosen; i.e., in some sense, this is the ideal version for our polarimeter, which may not be reached in the experiment. Photon distributions over x_F^γ , p_T^γ , and $A_N^\gamma(x_F^\gamma)$ are shown in Table 4 and Fig. 4.

Figure 3a reflects the distribution (4) for approximate value of $\epsilon = A_N P_b \simeq 0.07$. Since the electromagnetic calorimeter has a full azimuthal acceptance, one does not need to make corrections for the detector acceptance. Figure 3b illustrates the limited acceptance of the electromagnetic calorimeter used in the E704 experiment. Figure 3c demonstrates the importance of making the cut at $x_F = 0.3$ in order to suppress a contribution of “harmful” π^0 mesons

to the analyzing power. Figure 3d stems from the distributions presented in Figs. 3b and 3c. For example, taking the position of the distribution maxima $\theta = 0.5^\circ$, $x_F = 0.4$, one gets an expected position of the maximum in the p_T distribution, $p_T = 8.5 \times 10^{-3} \cdot 0.4 \cdot 200 \text{ GeV}/c = 0.7 \text{ GeV}/c$, which is consistent with Fig. 3d. Table 4 shows that $A_N^\gamma(x_F)$ is higher than $A_N^{\pi^0}(x_F)$ at lower x_F values. This can be easily understood in the following way. The photons with low x_F^γ are produced by π^0 of higher $x_F^{\pi^0}$. Since these π^0 have a higher analyzing power $A_N^{\pi^0}(x_F)$, they transfer them to photons with lower x_F^γ (on average $x_F^\gamma \simeq x_F^{\pi^0}/2$).

Figure 4a presents the energy spectrum of the “leading” photons coming from π^0 decays. As expected, this spectrum is softer than the spectrum of the parent π^0 (see Fig. 3c). According to Fig. 4a, one must put a cut at $x_F^\gamma \simeq 0.2$ in order to select practically all “useful” photons (having nonzero analyzing power) and, at the same time, to suppress back-

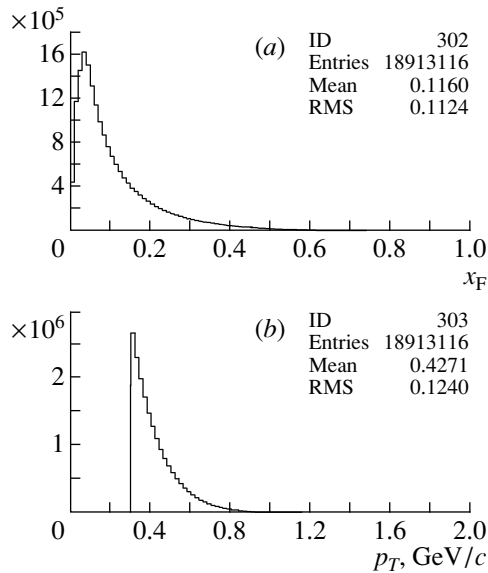
Table 4. The MC parameter A_N for “leading” γ from π^0 decay

x_F^γ	$A_N^\gamma, \%$
0.1–0.2	2.23 ± 0.97
0.2–0.3	5.16 ± 0.44
0.3–0.4	5.98 ± 0.48
0.4–0.5	10.94 ± 0.70
0.5–0.6	12.48 ± 1.06
0.6–0.8	14.75 ± 1.57

grounds essentially. The p_T^γ distribution presented in Fig. 4b gives a hint to the necessary p_T threshold for keeping the “useful” photons and decreasing the background contributions. Figure 4c is our main goal. It demonstrates that the $A_N^\gamma(x_F)$ for “leading” photons behaves practically in the same way as $A_N^{\pi^0}(x_F)$ does. Therefore, assuming that backgrounds may be essentially suppressed, one can use the “leading”-photon production as a basis of a new type of polarimeter.

3. THE POSSIBLE PHOTON POLARIMETER IN THE E704 EXPERIMENT

In this section, we make an estimate of the possible photon polarimeter in the E704 environments. We calculated the photon distributions on x_F and p_T (see Figs. 5a and 5b) and also analyzing power $A_N^\gamma(x_F)$ for

**Fig. 5.** The distributions on (a) x_F and (b) p_T of photons from all sources with $p_T^c = 0.3$ GeV/c.

different p_T threshold (see Fig. 6). All photons were taken into account.

The results for photon yield and analyzing power in the reaction $p\uparrow p \rightarrow \gamma X$ at 200 GeV/c are presented in Table 5. The typical distributions are shown in Fig. 5 for the cut $p_T^c = 0.3$ GeV/c. The steps of these distributions decrease on x_F and p_T reflect the yield of photons. The analyzing power $A_N^\gamma(x_F)$ increases with x_F at fixed p_T . With increasing threshold in p_T (see Table 5), $A_N^\gamma(x_F)$ steadily increases with x_F . At the same time, the increase of threshold on p_T suppresses the yield of photons and the so-called a factor of merit

$$M = \langle A_N^\gamma \rangle^2 N$$

varies with the cut on p_T , where N is the number of photons integrated over x_F and p_T , and $\langle A_N^\gamma \rangle$ is the analyzing power integrated over p_T and averaged over x_F . The precision in beam polarization measurement $\delta P_b = \Delta P_b / P_b$ depends on this factor in the following way:

$$\delta P_b^2 = \frac{1}{M d^2},$$

where d is a dilution factor defined as

$$d = \frac{S}{B + S},$$

S is a signal (number of γ from “useful” π^0), and B is a background (number of γ from all other sources).

Another important parameter is geometrical efficiency of the detector, which is defined as

$$E = \frac{N_{\text{acc}\gamma}}{N_{\text{ev}}},$$

where $N_{\text{acc}\gamma}$ is the number of photons accepted by the detector and N_{ev} is the number of generated events in $p\uparrow p$ collisions. The parameter of interest is time T for accumulation of necessary statistics N at the luminosity of experiment L , which is given by

$$T = \frac{N}{L\sigma E},$$

where $\sigma = 40$ mb is the total cross section of pp interaction at 200 GeV. For the E704 experiment, the luminosity was estimated in the following way. From [12], it follows that the intensity of tagged protons with polarization magnitude $>35\%$ and average polarization 45% is 3×10^6 polarized protons per spill (at incident flux of 10^{12} protons per 20-s spill). Since the duty factor is 3, the intensity of a polarized proton beam is $I = 3 \times 10^6 / (20 \cdot 3) = 5 \times 10^4$ polarized protons/s. In the E704 experiment, a liquid hydrogen target was used with a length of $l = 100$ cm and a density of $\rho = 0.07$ g/cm³. Therefore, the luminosity L is $L = I N_A \rho l = 5 \times 10^4 \cdot 6 \times 10^{23} \cdot$

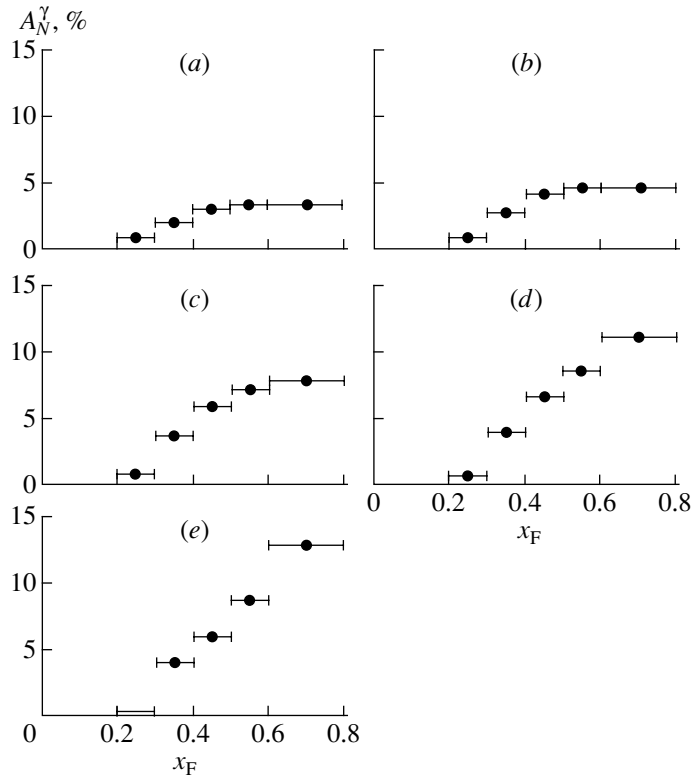


Fig. 6. Dependences $A_N^\gamma(x_F)$ for different p_T thresholds for photons from all sources: (a) $p_T^c = 0.3$ GeV/c, (b) $p_T^c = 0.4$ GeV/c, (c) $p_T^c = 0.5$ GeV/c, (d) $p_T^c = 0.6$ GeV/c, (e) $p_T^c = 0.7$ GeV/c (see error values in Table 5).

$0.07 \times 100 \text{ cm}^{-2} \text{ s}^{-1} = 2.1 \times 10^{29} \text{ cm}^{-2} \text{ s}^{-1}$. This is consistent with [13]. In Table 6 and Fig. 7, these parameters are shown for different p_T cuts.

4. THE LOCAL INCLUSIVE PHOTON POLARIMETER AT RHIC

The main RHIC detectors, PHENIX and STAR, occupy practically all free space around the interaction region (IR) with length of about ± 10 m. The only spot where one can install the local inclusive photon polarimeter (LIPP) is about 18 m from the interaction point (IP), just in front of the zero-degree calorimeter (ZDC) [14]. Such an approach was discussed earlier in [5], where only the top energy, $\sqrt{s} = 500$ GeV, was taken into account. Additionally, it was assumed that the analyzing power of leading photons from π^0 and η decays is the same as for parent particles. On the other hand, in this paper, we put the results of the E704 experiment (see above) as a basis for the photon analyzing power A_N^γ . We assume that A_N^γ does not depend on the initial energy.

We analyze three cases:

- the initial colliding protons having a total energy $\sqrt{s} = 500$ GeV;
- $\sqrt{s} = 200$ GeV;

the fixed target mode (FTM) with initial laboratory momentum $p_L = 200$ GeV/c (similar to E704) but with the internal jet target.

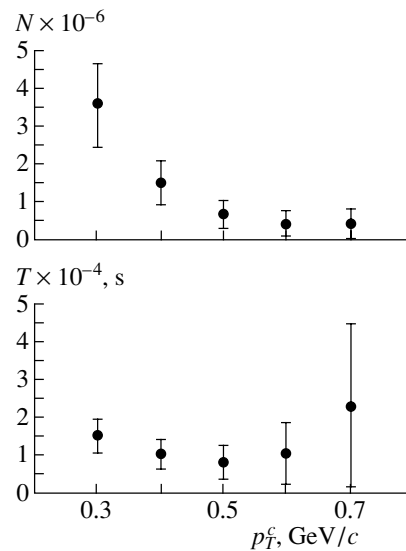


Fig. 7. Dependences of necessary statistics $N(p_T^c)$ and time $T(p_T^c)$ of accumulation of these statistics to obtain the value of beam polarization with 5% accuracy in E704 environment.

Table 5. The MC estimates for $A_N^\gamma(x_F)$ (in percent) taking into account all sources of photons in reaction $p\uparrow p \rightarrow \gamma X$ at 200 GeV/c in E704 environment

x_F	$p_T^c, \text{ GeV}/c$				
	0.3	0.4	0.5	0.6	0.7
0.1–0.2	0.06 ± 0.05	0.05 ± 0.07	0.00 ± 0.10	0.02 ± 0.14	-0.28 ± 0.21
0.2–0.3	0.82 ± 0.07	0.85 ± 0.10	0.78 ± 0.14	0.69 ± 0.21	0.31 ± 0.32
0.3–0.4	1.95 ± 0.11	2.83 ± 0.14	3.62 ± 0.20	3.88 ± 0.29	3.95 ± 0.43
0.4–0.5	2.95 ± 0.16	4.19 ± 0.20	5.87 ± 0.27	6.64 ± 0.39	5.90 ± 0.57
0.5–0.6	3.26 ± 0.24	4.71 ± 0.29	7.10 ± 0.38	8.51 ± 0.53	8.72 ± 0.76
0.6–0.8	3.28 ± 0.32	4.67 ± 0.38	7.85 ± 0.49	11.06 ± 0.66	12.83 ± 0.94

Table 6. Main parameters of the photon polarimeter in E704 environment

$p_T^c, \text{ GeV}/c$	$N_{ev}, 10^8$	$S, 10^7$	$S + B, 10^7$	d	$\langle A_N \rangle, \%$	$N, 10^6$	$E, 10^{-2}$	$T, 10^4 \text{ s}$
0.3	5	3.25	7.58	0.43	2.5 ± 0.4	3.57 ± 1.11	2.84	1.50 ± 0.46
0.4	5	1.81	4.03	0.45	3.6 ± 0.7	1.52 ± 0.59	1.75	1.03 ± 0.37
0.5	5	0.98	2.00	0.48	5.1 ± 1.4	0.67 ± 0.37	0.97	0.82 ± 0.45
0.6	5	0.49	0.94	0.51	6.0 ± 2.3	0.43 ± 0.33	0.48	1.06 ± 0.81
0.7	5	0.21	0.43	0.50	6.1 ± 2.8	0.43 ± 0.40	0.22	2.33 ± 2.14

The parameters of a proton beam and a proton jet target are taken as close as possible to the RHIC ones [14, 15]. The electromagnetic calorimeter is taken as it was made for the PHENIX collaborators and recently tested at a RHIC polarized run [8]. So it has a rectangular shape with a width of 10 cm and a height of 24 cm and is installed at a distance of 18 m from the IP.

The Monte Carlo results for A_N^γ are presented in Fig. 8 and Table 7 at a p_T cut of 0.5 GeV/c. 2×10^9 , 5×10^8 , and 2×10^9 events were generated at

Table 7. Analyzing power $A_N^\gamma(x_F)$ (in percent) for two RHIC modes

x_F	$\sqrt{s} = 500 \text{ GeV}$	FTM $p_L = 200 \text{ GeV}/c$
0.3–0.4	0.00 ± 0.00	3.41 ± 2.20
0.4–0.5	6.08 ± 1.35	5.27 ± 0.87
0.5–0.6	7.11 ± 1.41	5.77 ± 0.80
0.6–0.8	5.41 ± 1.28	6.21 ± 0.72

$\sqrt{s} = 200, 500 \text{ GeV}$, and FTM at $p_L = 200 \text{ GeV}/c$, respectively.

Figure 8a (for $\sqrt{s} = 500 \text{ GeV}$ case) shows an analyzing power of $\sim 6\%$ at $x_F > 0.4$. At $x_F = 0.35$, A_N is practically zero. Due to a correlation between p_T and x_F , at our cut $p_T^c = 0.5 \text{ GeV}/c$, there are no statistics for $x_F < 0.3$. The same comments are applicable to FTM at $p_L = 200 \text{ GeV}/c$ (Fig. 8b): only A_N varies in range 3–6% for $x_F > 0.3$ and also there are no statistics at $x_F < 0.3$. We do not show in Fig. 8 and Table 7 results for $\sqrt{s} = 200 \text{ GeV}$ due to the small acceptance of the detector and a cut $p_T^c = 0.5 \text{ GeV}/c$. There are no statistics from “useful” π^0 , while the background contribution prevails over signal and makes A_N close to zero.

Table 8 (analog of Table 6) presents the main parameters of the local inclusive photon polarimeter for RHIC in different modes of RHIC operation. For time estimates for reaching 5% precision in beam polarization measurement, the following luminosities were used: $L = 2 \times 10^{32} \text{ cm}^{-2} \text{ s}^{-1}$ at $\sqrt{s} = 500 \text{ GeV}$ [16], $L = 10^{31} \text{ cm}^{-2} \text{ s}^{-1}$ at $\sqrt{s} = 200 \text{ GeV}$ [16], $L = 10^{31} \text{ cm}^{-2} \text{ s}^{-1}$ at FTM [15]. Since at $\sqrt{s} = 200 \text{ GeV}$

Table 8. Main parameters of the RHIC local inclusive polarimeter at different modes of operation

Regime	$N_{ev}, 10^9$	$S, 10^6$	$S + B, 10^6$	d	$\langle A_N \rangle, \%$	$N, 10^6$	$E, 10^{-3}$	T, min
$\sqrt{s} = 500 \text{ GeV}$	0.5	0.43	1.24	0.35	4.2 ± 3.1	1.80 ± 2.59	1.61	2.0 ± 2.8
FTM $p_L = 200 \text{ GeV}/c$	2	1.45	3.82	0.38	5.5 ± 0.8	0.97 ± 0.28	1.19	33.5 ± 9.7

in the actual configuration a local inclusive photon polarimeter cannot serve as a useful tool (see explanation above), we omitted it from Table 8.

CONCLUSION

Single-spin asymmetry of inclusively produced photons has been obtained from the E704 experimental data. However, the statistics in the experiment were not appropriate to achieve an accuracy in the asymmetry needed for polarimetry. A Monte Carlo algorithm based on π^0 asymmetry from E704 [10] has been developed with a goal to estimate the expected parameters of a local inclusive photon polarimeter at RHIC.

In the Monte Carlo study, it has been shown that the asymmetry of leading photons from decays of π^0 with Feynman variable $x_F^\gamma > 0.3$ and $p_T^\gamma > 0.6 \text{ GeV}/c$ increases linearly with x_F and approaches 15% at $x_F^\gamma \simeq 0.7$. The asymmetry of all inclusive photons in $p \uparrow p$ interactions is significant as well. It is in the range 4–6% for moderate transverse momenta thresholds for photon detection. This asymmetry can be considered as an analyzing power for polarimetry.

The idea to create a polarimeter based on the analyzing power of single inclusive photons in $p \uparrow p$

interactions has been checked by numerical calculations. No time-consuming π^0 reconstruction algorithm is needed for this polarimeter. As an example, it is shown for the E704 environment that this polarimeter can measure the beam polarization with an accuracy of 5% at transverse momentum threshold $p_T^c = 0.5 \text{ GeV}/c$ in approximately 2 h. In the RHIC environment with the same p_T^c cut, it takes $\sim 5 \text{ min}$ at $\sqrt{s} = 500 \text{ GeV}$ and $\sim 30 \text{ min}$ in FTM. And we cannot measure the beam polarization at $\sqrt{s} = 200 \text{ GeV}$.

ACKNOWLEDGMENTS

We are deeply grateful to Y. Goto, K. Imai, and N. Saito for valuable discussion and useful information.

REFERENCES

1. T. Roser, in *Proceedings of 14th International Spin Physics Symposium, Osaka, Japan, 2000*, p. 312.
2. E. A. Andreeva *et al.*, Preprint No. 97-61, IHEP (Inst. High Energy Phys., Protvino, 1997).
3. A. A. Bogdanov *et al.*, Preprint No. 98-54, IHEP (Inst. High Energy Phys., Protvino, 1998).
4. K. Imai, in *Proceedings of Workshop on RHIC Spin, RIKEN BNL Research Center, 1999*, p. 251.
5. A. A. Bogdanov *et al.*, Preprint No. 2000-42, IHEP (Inst. High Energy Phys., Protvino, 2000).
6. B. E. Bonner *et al.*, *Phys. Rev. Lett.* **61**, 1918 (1988).
7. D. L. Adams *et al.*, *Z. Phys. C* **56**, 181 (1992).
8. Y. Fukao *et al.*, in *Proceedings of the XV International Symposium on High Energy Spin Physics*, BNL, USA, 2002.
9. D. L. Adams *et al.*, Preprint No. 1991-99, IHEP (Inst. High Energy Phys., Protvino, 1991).
10. D. L. Adams *et al.*, *Nucl. Phys. B* **510**, 3 (1998).
11. T. Sjöstrand, *Comput. Phys. Commun.* **82**, 74 (1994).
12. D. P. Grosnick *et al.*, *Nucl. Instrum. Methods Phys. Res. A* **290**, 269 (1990).
13. S. B. Nurushev *et al.*, Preprint No. 12-97, MEPHI (Moscow Eng.-Phys. Inst., 1997).
14. C. Adler *et al.*, *Nucl. Instrum. Methods Phys. Res. A* **470**, 488 (2001).
15. M. Conte *et al.*, in *Proceedings of Workshop on High Energy Polarimetry*, BNL, USA, 1999, p. 47.
16. M. Beddo *et al.*, RHIC Proposal R5 (Aug. 1992).

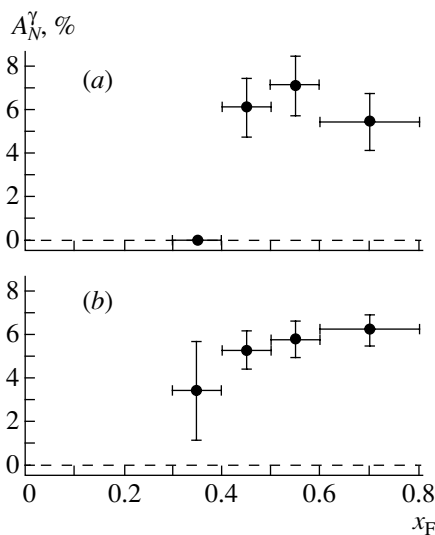


Fig. 8. Analyzing power $A_N^\gamma(x_F)$ for two RHIC modes: (a) $\sqrt{s} = 500 \text{ GeV}$, (b) FTM $p_L = 200 \text{ GeV}/c$.

ELEMENTARY PARTICLES AND FIELDS
Experiment

The Analysis of π^- -Meson Spectra in Semicentral CC and CTa Collisions at a Momentum of 4.2 GeV/c per Nucleon in Terms of Light-Front Variables*

L. V. Chkhaidze^{1)**}, T. D. Djobava¹⁾, V. R. Garsevanishvili²⁾, L. L. Kharkhelauri¹⁾,
E. N. Kladnitskaya³⁾, A. A. Kuznetsov³⁾, and G. O. Kuratashvili¹⁾

Received April 24, 2003; in final form, September 15, 2003

Abstract—The inclusive spectra of pions produced in CC and CTa collisions at a momentum of 4.2 GeV/c per nucleon are analyzed in terms of light-front variables ξ and ζ . The phase space of the secondary pions is divided into two parts with very different angular and momentum distributions. In one of these parts, the thermal equilibrium assumption seems to be in good agreement with the data. Corresponding temperatures T are extracted, and their dependence on $(A_P A_T)^{1/2}$ is studied: T decreases linearly with increasing $(A_P A_T)^{1/2}$. The results are compared with the predictions of the quark–gluon string model (QGSM). The QGSM satisfactorily reproduces the experimental data. © 2004 MAIK “Nauka/Interperiodica”.

1. INTRODUCTION

The study of single-particle inclusive processes [1] remains one of the simplest and effective tools for the investigation of multiple production of secondaries at high energies. The consequences of the limiting fragmentation hypothesis [2] and those of the parton model [3] and the principle of automodelity for strong interactions [4] have been formulated in this way.

At high energies, different dynamical mechanisms contribute to the spectra of secondaries. Among them, “pionization” and fragmentation mechanisms have been widely discussed. Pionization means the existence of secondary pions with relatively low momenta and a flat (almost isotropic) angular distribution in the c.m. frame of colliding objects. The fragmentation component has a sharply anisotropic angular distribution in the c.m. frame. One of the main problems in this direction is the separation of these two components. Currently, there exists no unique way to separate these mechanisms. Different authors propose different ways and none of them seems to be satisfactory. It will be shown that the presentation of inclusive spectra in terms of light-front

variables provides a unique possibility of separating these two components.

An important role in establishing the properties of multiple particle production is played by the choice of kinematic variables in terms of which the observable quantities are presented (see, e.g., [5–7]).

In this paper, we continue the study of π mesons produced in relativistic nucleus–nucleus collisions in terms of light-front variables. The choice of light-front variables is due to the fact that these variables seem to be more sensitive to the interaction dynamics as compared to the well-known Feynman variables x_F and rapidity y .

The light-front analysis of π^- mesons produced in He(Li,C), CNe, CCu, CPb, and MgMg collisions at a momentum of 4.5 GeV/c per nucleon has been performed in previous publications [8, 9]. The data were obtained on the SKM-200-GIBS facility of the Joint Institute for Nuclear Research in Dubna. On the basis of this analysis, we were able to separate the phase-space region, where thermal equilibrium seems to be achieved. The same analysis was performed on a part of inelastic CC and CTa collisions at a momentum of 4.2 GeV/c per nucleon registered in the 2-m Propane Bubble Chamber of JINR [10]. In this paper, the spectra of pions from semicentral CC and CTa collisions at a momentum of 4.2 GeV/c per nucleon are studied in terms of light-front variables. Semicentral collisions were separated from the whole ensemble of inelastic CC and CTa interactions identified unambiguously.

*This article was submitted by the authors in English.

¹⁾High Energy Physics Institute, Tbilisi State University, Georgia.

²⁾Mathematical Institute, Georgian Academy of Sciences, Tbilisi.

³⁾Joint Institute for Nuclear Research, Dubna, Moscow oblast, 141980 Russia.

** e-mail: ida@sun20.hepi.edu.ge; ichkhaidze@yahoo.com

2. EXPERIMENT

The data were obtained on the 2-m Propane Bubble Chamber of JINR. The chamber was placed in a magnetic field of 1.5 T. Three Ta plates $140 \times 70 \times 1$ mm in size mounted in the fiducial volume of the chamber at a distance of 93 mm from each other served as a nuclear target. The separation method of CC collisions in propane, data processing, identification of particles, and discussion of corrections are described in detail in [11]. Apart from the unambiguously identified CC collisions with the we probability equal to one, the experimental data also contain the sample of CC events with $we = 0.21$. When studying the inclusive characteristics of CC collisions, the distributions are obtained for the whole ensemble of CC collisions taking into account the weight factor we .

The subsample of “semicentral” events with the number of participant protons $N_{\text{part}} \geq 4$ was selected for the analysis from the whole ensemble of CC and CTa collisions. With this aim, the target fragments ($p < 0.3$ GeV/c for CC and $p < 0.2$ GeV/c for CTa), projectile stripping ($p > 3$ GeV/c and angle $\theta < 4^\circ$) fragments, and also light projectile fragments with $Z > 1$ (^3He , ^4He) identified by ionization visually and π^+ mesons were excluded from the whole ensemble of secondary particles.

An additional identification of π^+ mesons was performed [12] in order to separate participant protons since π^+ mesons were identified in a narrow interval of momenta up to 0.5 GeV/c in the propane chamber. For the particles with $p > 0.5$ GeV/c in all CC collisions, special statistical weights were introduced for π^+ meson and proton hypothesis separately. The separation of the group of CC collisions with $we = 1$ and the necessity of unambiguous separation of protons and π^+ mesons led to the difference in the momentum distributions of π^- and π^+ mesons. To remove this difference, the correction of π^+ meson identification was made. The procedure was performed for CC and CTa events statistically with the assumption that the distributions of π^- and π^+ mesons must be similar.

In consequence, the group of semicentral 9500 (20 477 π^- mesons) CC and 1620 CTa (11 318 π^\pm mesons) collisions was separated from inelastic 15 965 CC (25 409 π^- mesons) and 2469 CTa (12 160 π^\pm mesons) collisions.

3. LIGHT-FRONT PRESENTATION OF INCLUSIVE DISTRIBUTIONS

Here, we propose unified scale-invariant variables for the presentation of single-particle inclusive distributions, the properties of which are described below.

Consider an arbitrary 4-momentum $p_\mu(p_0, \mathbf{p})$ and introduce light-front combinations [13]:

$$p_\pm = p_0 \pm p_3. \quad (1)$$

If the 4-momentum p_μ is on the mass shell ($p^2 = m^2$), the combinations p_\pm, \mathbf{p}_T (where $\mathbf{p}_T = (p_1, p_2)$) define the so-called horospherical coordinate system (see, e.g., [14]) on the corresponding mass-shell hyperboloid $p_0^2 - \mathbf{p}^2 = m^2$.

Let us construct the scale-invariant variables [15]

$$\xi^\pm = \pm \frac{p_\pm^c}{p_\pm^a + p_\pm^b} \quad (2)$$

in terms of the 4-momenta $p_\mu^a, p_\mu^b, p_\mu^c$ of particles a, b, c , entering from the inclusive reaction $a + b \rightarrow c + X$. The z axis is taken to be the collision axis, i.e., $p_z = p_3 = p_L$. Particles a and b can be hadrons, heavy ions, and leptons. The light-front variables ξ^\pm in the c.m. frame are defined as follows [15]:

$$\xi^\pm = \pm \frac{E \pm p_z}{\sqrt{s}} = \pm \frac{E + |p_z|}{\sqrt{s}}, \quad (3)$$

where s is the usual Mandelstam variable, and $E = \sqrt{p_z^2 + p_T^2 + m^2}$ and p_z are the energy and the z component of the momentum of the produced particle. The upper sign in Eq. (3) is used for the right-hand-side hemisphere, and the lower sign is used for the left-hand-side one. It is also convenient to introduce the variables

$$\zeta^\pm = \mp \ln|\xi^\pm| \quad (4)$$

in order to enlarge the scale in the region of small ξ^\pm . The invariant differential cross section in terms of these variables looks as follows:

$$E \frac{d\sigma}{d\mathbf{p}} = \frac{|\xi^\pm|}{\pi} \frac{d\sigma}{d\xi^\pm dp_T^2} = \frac{1}{\pi} \frac{d\sigma}{d\zeta^\pm dp_T^2}. \quad (5)$$

In the limits of high p_z ($|p_z| \gg p_T$) and high p_T ($p_T \gg |p_z|$), the ξ^\pm variables go over to the well-known variables $x_F = 2p_z/\sqrt{s}$ and $x_T = 2p_T/\sqrt{s}$, respectively, which are intensively used in high-energy physics. The ξ^\pm variables are related to x_F, x_T , and rapidity y as follows:

$$\xi^\pm = \frac{1}{2} \left(x_F \pm \sqrt{x_F^2 + x_T^2} \right), \quad (6)$$

$$x_T = \frac{2m_T}{\sqrt{s}},$$

$$y = \pm \frac{1}{2} \ln \frac{(\xi^\pm \sqrt{s})^2}{m_T^2}, \quad (7)$$

$$m_T = \sqrt{p_T^2 + m^2}.$$

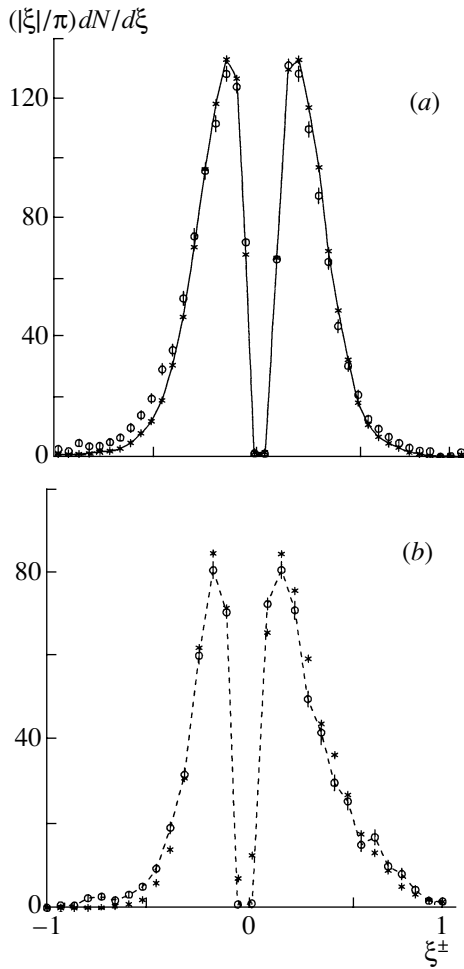


Fig. 1. The ξ^\pm distribution of pions from (a) CC collisions and (b) CTA collisions. Points: (o) experimental data, (*) QGSM data. (The curves are the result of spline approximation of experimental data in order to guide the eye.)

These variables are widely used in the treatment of many theoretical problems (see, e.g., the original and review papers [16–21]).

4. THE ANALYSIS OF PION DISTRIBUTIONS IN TERMS OF LIGHT-FRONT VARIABLES

The analysis in CC collisions has been carried out for the π^- mesons. To increase small statistics of CTA collisions, the data on π^- and π^+ mesons have been combined. Figure 1 presents the ξ^\pm distributions of π^- mesons in CC and π^- and π^+ mesons in CTA interactions. The main differences of the ξ^\pm distributions and x_F distributions (Fig. 2) are the following: (i) the existence of a forbidden region around the point $\xi^\pm = 0$; (ii) the existence of maxima at some $\tilde{\xi}^\pm$ in the region of relatively small $|\xi^\pm|$; (iii) the existence of the limits for $|\xi^\pm| \leq m/\sqrt{s}$.

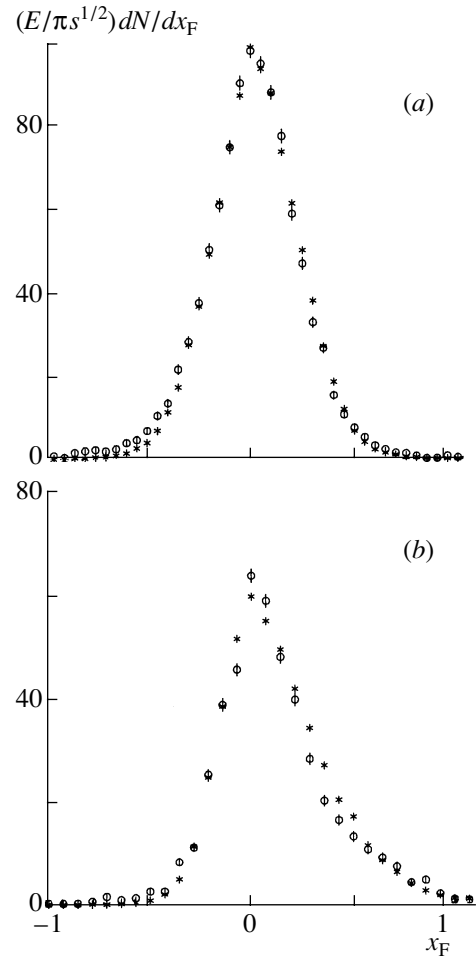


Fig. 2. The x_F distribution of pions from (a) CC collisions and (b) CTA collisions. Points: (o) experimental data, (*) QGSM data.

The experimental data for the invariant distributions $(1/\pi)dN/d\zeta^\pm$ are shown in Fig. 3. As the ξ and ζ distributions for CC collisions are symmetric, the data have been analyzed over the whole range (ξ^\pm , ζ^\pm) of the ξ and ζ variables. The CTA data have been analyzed only in the forward hemisphere (ξ^+ , ζ^+). The maxima at $\tilde{\zeta}^\pm$ are also observed in the invariant distributions $(1/\pi)dN/d\zeta^\pm$. However, the region $|\xi^\pm| > |\tilde{\xi}^\pm|$ goes over to the region $|\zeta^\pm| < |\tilde{\zeta}^\pm|$ and vice versa [see Eqs. (3) and (4)]. Maxima are observed at $|\tilde{\zeta}^\pm| = 1.95 \pm 0.05$ for CC and $|\tilde{\zeta}^\pm| = 2.00 \pm 0.05$ for CTA. $\tilde{\zeta}^\pm$ is a function of energy [see Eqs. (3), (4)] and does not depend on the projectile (A_P) and target (A_T) masses.

In order to study the nature of these maxima, we have divided the phase space into two regions $|\zeta^\pm| > |\tilde{\zeta}^\pm|$ and $|\zeta^\pm| < |\tilde{\zeta}^\pm|$ and studied the p_T^2 and angular distributions of π mesons in these regions separately. For example, the number of pions in CTA interactions

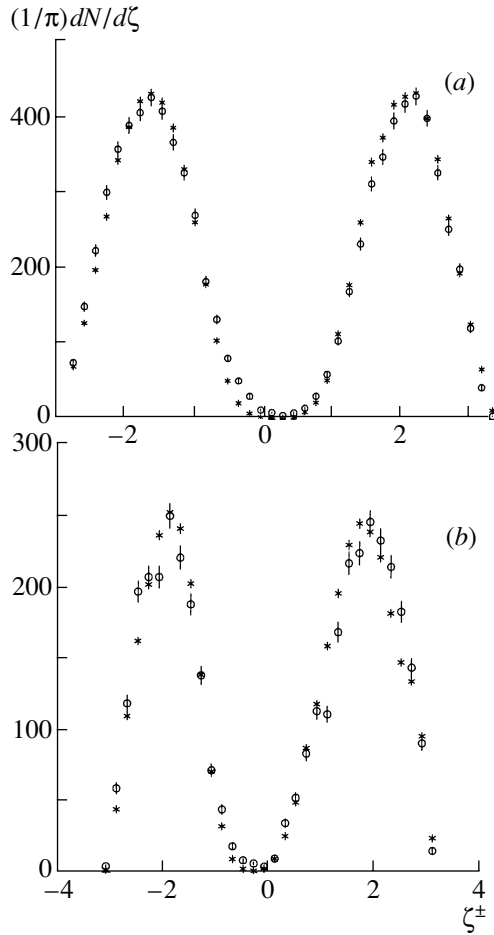


Fig. 3. The ζ^\pm distribution of pions from (a) CC collisions and (b) CTa collisions. Points: (o) experimental data, (*) QGSM data.

is equal to 2770 in the region $\zeta^+ > \tilde{\zeta}^+$ and 3904 in $\zeta^+ < \tilde{\zeta}^+$. The angular and p_T^2 distributions of π mesons from CC and CTa interactions in different regions of ζ^\pm are presented in Figs. 4 and 5.

From Figs. 4 and 5, one can see that the angular and p_T^2 distributions of pions in CC and CTa differ significantly in the $|\zeta^\pm| > |\tilde{\zeta}^\pm|$ and $|\zeta^\pm| < |\tilde{\zeta}^\pm|$ regions. The angular distribution of pions in the region $|\zeta^\pm| < |\tilde{\zeta}^\pm|$ is sharply anisotropic in contrast to an almost flat distribution in the region $|\zeta^\pm| > |\tilde{\zeta}^\pm|$ (Figs. 4a and 4b). A flat behavior of the angular distribution allows one to think that a partial thermal equilibrium is observed in the region $|\zeta^\pm| > |\tilde{\zeta}^\pm|$ ($|\zeta^\pm| < |\tilde{\zeta}^\pm|$) of phase space. The slopes of the p_T^2 distributions differ greatly in different regions of ζ^\pm (Figs. 5a and 5b). Thus, the values of $\tilde{\zeta}^\pm$ are the boundaries of two regions with significantly different characteristics of pions. The validity of this statement can be seen from the momentum distributions of π^-

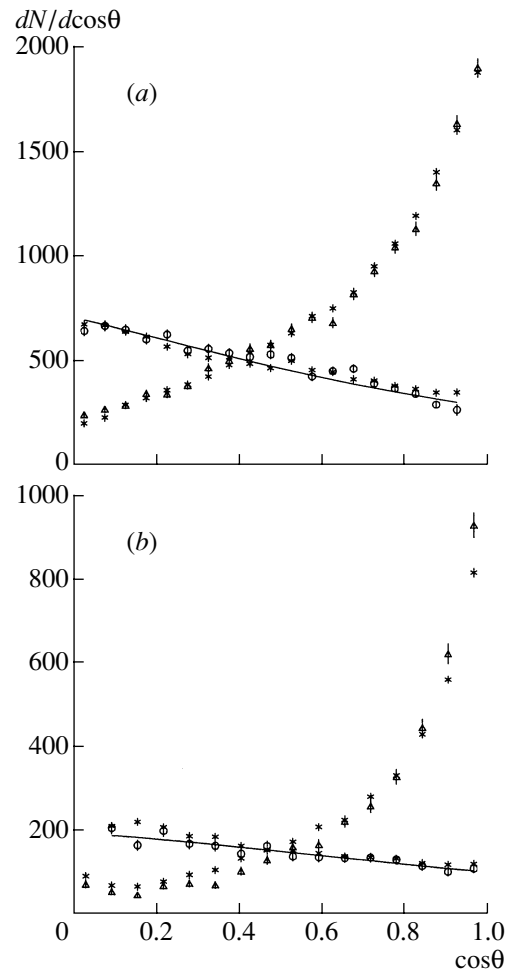


Fig. 4. The $\cos \theta$ distribution of pions from (a) CC collisions and (b) CTa collisions. Points: (o) experimental data for $|\zeta^\pm| > |\tilde{\zeta}^\pm|$, (Δ) experimental data for $|\zeta^\pm| < |\tilde{\zeta}^\pm|$, (*) QGSM data in both regions. The solid lines are the fit of the experimental data in the region $|\zeta^\pm| > |\tilde{\zeta}^\pm|$ by Eq. (10).

mesons in the laboratory frame. Figure 6 presents the momentum distribution of pions from CC (Fig. 6a) and CTa (Fig. 6b) collisions in the laboratory frame. The shaded area corresponds to the region $\zeta^+ > \tilde{\zeta}^+$ and the nonshaded one to the region $0 < \zeta^+ < \tilde{\zeta}^+$. As can be seen from Fig. 6, these two regions have almost no overlap in the momentum space. Pions from the region $\zeta^+ > \tilde{\zeta}^+$ have a small momentum, up to 0.5 GeV/c. The pions from $\zeta^+ < \tilde{\zeta}^+$ region have the momentum from ~ 0.5 to 3 GeV/c. Figure 7 presents the $\langle p_{\text{lab}} \rangle$ dependence on θ_{lab} for both pairs of nuclei in the $\zeta^+ > \tilde{\zeta}^+$ and $\zeta^+ < \tilde{\zeta}^+$ regions. The shapes of these dependences are different. It is necessary to say that with increasing A_P and A_T , $\langle p_{\text{lab}} \rangle$ decreases and $\langle \theta_{\text{lab}} \rangle$ increases.

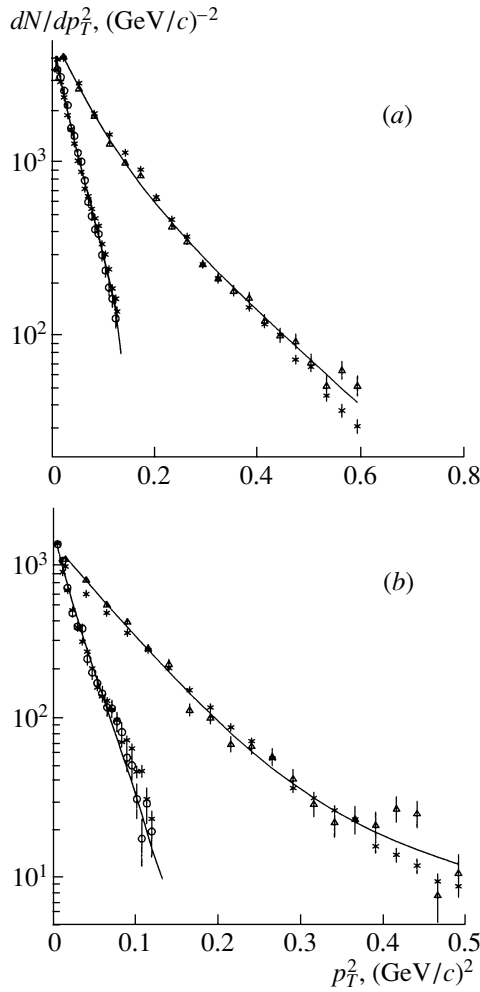


Fig. 5. The p_T^2 distribution of pions from (a) CC collisions and (b) CTa collisions. Points: (o) experimental data for $|\zeta^\pm| > |\tilde{\zeta}^\pm|$, (Δ) experimental data for $|\zeta^\pm| < |\tilde{\zeta}^\pm|$, (*) QGSM data in both regions. The solid curves are the fit of the experimental data in the regions $|\zeta^\pm| > |\tilde{\zeta}^\pm|$ and $|\zeta^\pm| < |\tilde{\zeta}^\pm|$ by Eqs. (9) and (12), respectively.

To describe the spectra in the region $|\zeta^\pm| > |\tilde{\zeta}^\pm|$, the Boltzmann distribution $f(E) \sim e^{-E/T}$ has been used.

The $(1/\pi)dN/d\zeta^\pm$, dN/dp_T^2 , and $dN/d\cos\theta$ distributions in this region look as follows:

$$\frac{1}{\pi} \frac{dN}{d\zeta^\pm} \sim \int_0^{p_{T,\max}^2} E f(E) dp_T^2, \quad (8)$$

$$\frac{dN}{dp_T^2} \sim \int_0^{p_{z,\max}} f(E) dp_z, \quad (9)$$

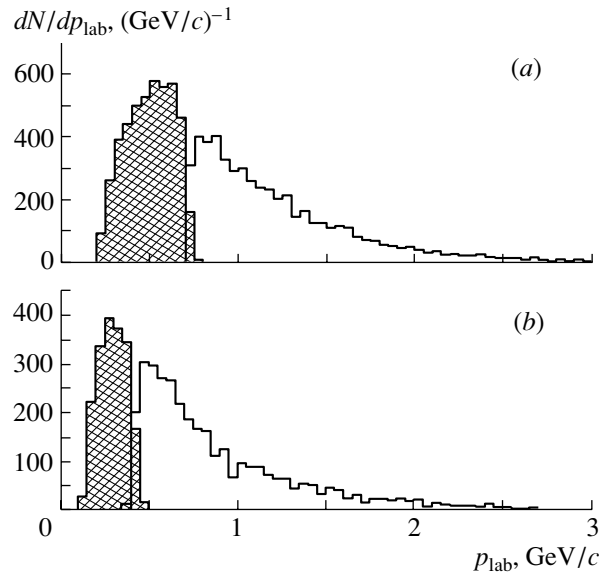


Fig. 6. The momentum distribution of pions in the laboratory frame from (a) CC collisions and (b) CTa collisions. The shaded areas correspond to the region of $|\zeta^+| > |\tilde{\zeta}^+|$.

$$\frac{dN}{d\cos\theta} \sim \int_0^{p_{\max}} f(E) p^2 dp, \quad (10)$$

$$E = \sqrt{\mathbf{p}^2 + m_\pi^2}, \quad \mathbf{p}^2 = p_z^2 + p_T^2, \quad (11)$$

where

$$p_{T,\max}^2 = (\tilde{\xi}^\pm \sqrt{s})^2 - m_\pi^2,$$

$$p_{z,\max} = [p_T^2 + m^2 - (\tilde{\xi}^\pm \sqrt{s})^2] / (-2\tilde{\xi}^\pm \sqrt{s}),$$

$$p_{\max} = \left(-\tilde{\xi}^\pm \sqrt{s} \cos\theta + \sqrt{(\tilde{\xi}^\pm \sqrt{s})^2 - m_\pi^2 \sin^2\theta} \right) / \sin^2\theta.$$

The experimental distributions in the region $|\zeta^\pm| > |\tilde{\zeta}^\pm|$ have been fitted by expressions (8)–(10), respectively. The results of the fit of the $dN/d\cos\theta$, dN/dp_T^2 , and $(1/\pi)dN/d\zeta^\pm$ distributions are given in Table 1 and Figs. 4 and 5. They show good agreement with experiment. The values of the parameter T obtained by fitting the data with the Boltzmann distribution are presented in Table 1.

The spectra of π^- mesons in the region $|\zeta^\pm| > |\tilde{\zeta}^\pm|$ are satisfactorily described by the formulas which follow from thermal equilibrium. The same formulas extrapolated to the region $|\zeta^\pm| < |\tilde{\zeta}^\pm|$ deviate significantly from the data. Therefore, in the region $|\zeta^\pm| < |\tilde{\zeta}^\pm|$, the p_T^2 distributions have been fitted by the formula

$$\frac{dN}{dp_T^2} \sim \alpha e^{-\beta_1 p_T^2} + (1 - \alpha) e^{-\beta_2 p_T^2} \quad (12)$$

Table 1. The results of fitting the distributions of pions in the region $|\zeta^\pm| > |\tilde{\zeta}^\pm|$ by Eqs. (8)–(10)

Reaction	$ \tilde{\zeta}^\pm $	Type of event	T, MeV		
			$(1/\pi)dN/d\zeta^\pm$	$dN/d\cos\theta$	dN/dp_T^2
$\text{CC} \rightarrow \pi^- + X$	1.95 ± 0.05	Experiment	86 ± 2	67 ± 3	79 ± 1
		QGSM	88 ± 1	62 ± 1	81 ± 1
$\text{CTa} \rightarrow \pi^\pm + X$	2.00 ± 0.05	Experiment	63 ± 2	59 ± 5	64 ± 2
		QGSM	66 ± 1	66 ± 2	70 ± 1

and the ζ^+ distributions by the formula

$$\frac{1}{\pi} \frac{dN}{d\zeta^+} \sim (1 - \xi^+)^n = (1 - e^{-|\zeta^+|})^n. \quad (13)$$

The latter is an analog of the $(1 - x_F)^n$ dependence—the result of the well-known quark–parton model consideration (see, e.g., [22]) which gives $n = 3$ for π^- mesons. The dependence $(1 - e^{-|\zeta^\pm|})^n$ is in good agreement with experiment in the region $|\zeta^\pm| < |\tilde{\zeta}^\pm|$ and deviates from it in the region $|\zeta^\pm| > |\tilde{\zeta}^\pm|$. The results of the fit are given in Table 2 and Fig. 5.

Thus, in the ζ^\pm (ξ^\pm) distributions, we have singled out points $\tilde{\zeta}^\pm$ ($\tilde{\xi}^\pm$) which separate in the phase space two regions with significantly different characteristics. There are no such points in the x_F and y distributions.

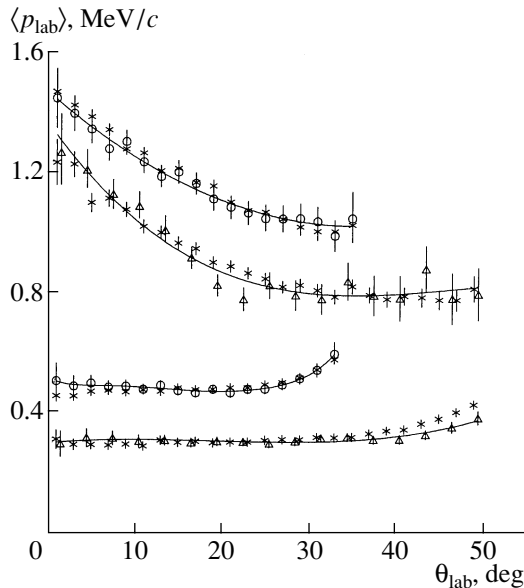


Fig. 7. The $\langle p_{\text{lab}} \rangle$ dependence on θ_{lab} in the regions $\zeta^+ > \tilde{\zeta}^+$ (bottom data) and $0 < \zeta^+ < \tilde{\zeta}^+$ (top data). Points: (o) CC collisions, (Δ) CTa collisions, (*) QGSM data in both regions for both pairs of nuclei. The curves are the result of polynomial approximation.

In this paper, the quark–gluon string model (QGSM) [23] is used for comparison with the experimental data.

A detailed description and comparison of the QGSM with experimental data over a wide energy range can be found in [8, 9, 24]. The model yields a generally good overall fit to most experimental data [24, 25].

We have generated CC and CTa interactions using the Monte Carlo generator COLLI [26] based on the QGSM.

In the COLLI generator, there are two ways to generate events: (i) at unfixed impact parameter \tilde{b} and (ii) at fixed b .

At the first step, the version of the generation program with unfixed impact parameter \tilde{b} has been used; 50 000 CC and 10 000 CTa inelastic collisions at a momentum of 4.2 GeV/c have been generated. Then, similarly as for the experimental data, the selection criteria of participant protons have been applied on these events; namely, the target fragments ($p < 0.3$ GeV/c for CC and $p < 0.2$ GeV/c for CTa) and the projectile strippings ($p > 3$ GeV/c and angle $\theta < 4^\circ$) have been excluded. From the analysis of generated events, the protons with deep angles greater than 60° have been excluded additionally, because such vertical tracks are registered with less efficiency in the experiment. After selection of events with the number of participant protons $N_{\text{part}} \geq 4$, the group of semicentral collisions remains for analysis. For these events from the impact parameter distribution, the mean values of $\langle b \rangle = 2.65 \pm 0.02$ fm for CC and $\langle b \rangle = 5.65 \pm 0.03$ fm for CTa semicentral interactions have been obtained.

At the second step, 50 000 CC and 10 000 CTa semicentral collisions have been generated at a fixed impact parameter equal to $\langle b \rangle$. The average physical characteristics and analyzing distributions generated for fixed and unfixed impact parameter coincide within the errors.

Table 2. The results of the fit of the distributions of π^- mesons in the region $\zeta^+ < \tilde{\zeta}^+$ by Eqs. (12) and (13)

Reaction	Type of event	dN/dp_T^2			$(1/\pi)dN/d\zeta^+$
		α	$\beta_1, (\text{GeV}/c)^{-2}$	$\beta_2, (\text{GeV}/c)^{-2}$	n
$\text{CC} \rightarrow \pi^- + X$	Experiment	0.71 ± 0.06	16.2 ± 1.4	5.9 ± 0.5	3.4 ± 0.6
	QGSM	0.69 ± 0.03	24.0 ± 3.0	8.7 ± 0.1	4.1 ± 0.1
$\text{CTa} \rightarrow \pi^\pm + X$	Experiment	0.76 ± 0.03	24.6 ± 2.0	7.1 ± 0.4	2.8 ± 0.1
	QGSM	0.66 ± 0.10	22.5 ± 3.0	8.1 ± 0.2	2.5 ± 0.3

The experimental results have been compared with the QGSM generated events for values of $\langle b \rangle$. Figures 1 and 3 present the ξ^\pm and ζ^\pm distributions of π mesons from the QGSM calculations together with the experimental ones for CC and CTa interactions. One can see that the QGSM reproduces experimental distributions well. The QGSM also reproduces the x_F , $\cos\theta$, and p_T^2 distributions (Figs. 2, 4, and 5). The QGSM data show similar characteristics in different regions of ζ as experimental data: sharply anisotropic angular distributions in the region $|\zeta^\pm| < |\tilde{\zeta}^\pm|$ and almost flat distribution in the region $|\zeta^\pm| > |\tilde{\zeta}^\pm|$; the slopes of the p_T^2 distributions differ greatly in

different regions of ζ^\pm ; the momentum distributions of pions in the laboratory frame in different regions of ζ^\pm have a similarly different shape of spectra as the experimental ones (Fig. 6). The momentum distributions of the QGSM data reproduce the corresponding experimental spectra in both regions of ζ^\pm . The distributions obtained by the QGSM in the region $|\zeta^\pm| > |\tilde{\zeta}^\pm|$ have been fitted by expressions (8)–(10). The results of the fit are given in Table 1 and Figs. 4 and 5. In the region $|\zeta^\pm| < |\tilde{\zeta}^\pm|$, the p_T^2 and ζ^\pm distributions have been fitted by Eqs. (12) and (13), respectively. The results of the fit are given in Table 2 and Fig. 5. One can see from Table 1 that the values of T extracted from the experimental and QGSM data agree within the errors for CC and CTa collisions.

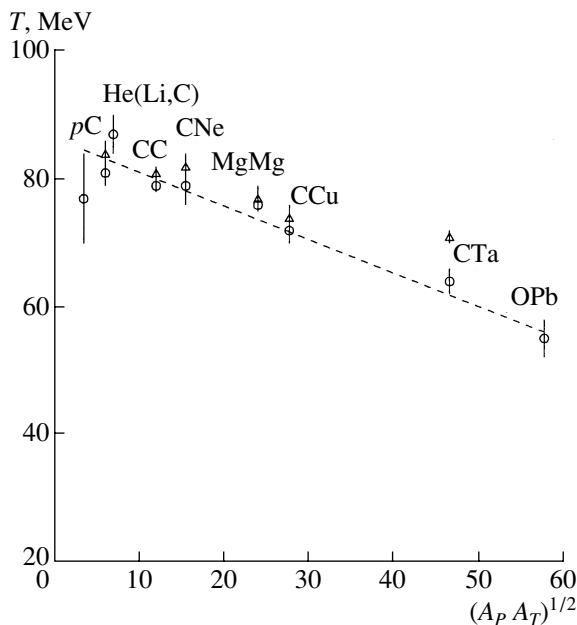


Fig. 8. The dependence of the parameter T on $(A_P A_T)^{1/2}$ for He(Li,C), CNe, MgMg, CCu, OPb [8, 9], pC , HeC [10], and our results for semicentral CC and CTa. Points: (o) experimental data, (Δ) QGSM data. The dashed line is the result of linear approximation of the experimental data.

Figure 8 shows the dependence of the parameter T from Table 1 on $(A_P A_T)^{1/2}$, obtained from the experimental and QGSM data together with our previous results [8, 9] for He(Li, C), CNe, CCu, MgMg, and OPb interactions obtained on the SKM-200-GIBS setup and pC and HeC obtained by the Propane Collaboration in [10]. One can see that T decreases linearly with increasing $(A_P A_T)^{1/2}$, i.e., with increasing the number of participating nucleons. A similar behavior is predicted by the QGSM. It is worth mentioning that the values of T obtained for semicentral CC and CTa collisions in this paper agree within the errors with the results for inelastic CC and CTa obtained in [10]. Thus, the values of T seem to depend on the centrality degree very slightly.

5. CONCLUSIONS

The inclusive spectra of pions produced in CC and CTa collisions at a momentum of 4.2 GeV/c per nucleon are analyzed in terms of light-front variables ξ and ζ .

(i) The results of this paper confirm the conclusions of the previous publications [8, 9] that the phase space of secondary π mesons is divided into two regions with respect to the maximum value of $\tilde{\zeta}^\pm$ ($\tilde{\xi}^\pm$).

The angular and momentum distributions of pions in these regions are very different.

(ii) In one of these kinematical regions $|\zeta^\pm| > |\tilde{\zeta}^\pm|$, the $dN/d\cos\theta$, dN/dp_T^2 , and $(1/\pi)dN/d\zeta^\pm$ distributions are fitted by statistical model predictions. Thus, thermal equilibrium seems to be reached and corresponding temperatures were obtained.

(iii) The T dependence on $(A_P A_T)^{1/2}$ is studied. The temperature decreases with increasing $(A_P A_T)^{1/2}$.

(iv) The experimental results are compared with the QGSM. The model seems to be in a good agreement with the data.

ACKNOWLEDGMENTS

We express our deep gratitude to N. Amaglobeli for his continuous support. We are very grateful to N. Amelin for providing us with the QGSM code program COLLI. One of us (L.Ch.) would like to thank the Board of Directors of the Laboratory of High Energies of JINR for their warm hospitality and also J. Lukstins and O. Rogachevsky for their help during the preparation of the manuscript.

REFERENCES

1. A. A. Logunov, M. A. Mestvirishvili, and Nguen van Hieu, *Phys. Lett. B* **25B**, 611 (1967).
2. J. Benecke *et al.*, *Phys. Rev.* **188**, 2159 (1969).
3. R. Feynman, *Phys. Rev. Lett.* **23**, 1415 (1969).
4. V. A. Matveev, R. M. Muradyan, and A. N. Tavkhelidze, *Lett. Nuovo Cimento* **5**, 907 (1972).
5. A. M. Baldin, *Nucl. Phys. A* **447**, 203 (1985).
6. A. A. Baldin, *Yad. Fiz.* **56**, 174 (1993) [*Phys. At. Nucl.* **56**, 385 (1993)].
7. A. M. Baldin and L. A. Didenko, *Fortschr. Phys.* **38**, 261 (1994).
8. M. Anikina *et al.*, *Nucl. Phys. A* **640**, 111 (1998).
9. M. Anikina *et al.*, *Eur. Phys. J. A* **7**, 139 (2000).
10. L. T. Akhobadze *et al.*, *Phys. At. Nucl.* **63**, 1584 (2000).
11. A. Bondarenko *et al.*, JINR-P1-98-292 (Dubna, 1998).
12. L. V. Chkhaidze *et al.*, Preprint No. E1-2002-255, JINR (Joint Inst. Nucl. Res., Dubna, 2002).
13. P. A. M. Dirac, *Rev. Mod. Phys.* **21**, 392 (1949).
14. N. Ya. Vilenkin and Ya. A. Smorodinsky, *Zh. Éksp. Teor. Fiz.* **46**, 1793 (1964) [*Sov. Phys. JETP* **19**, 1209 (1964)]; V. R. Garsevanishvili *et al.*, *Teor. Mat. Fiz.* **7**, 203 (1971).
15. N. S. Amaglobeli *et al.*, *Eur. Phys. J. C* **8**, 603 (1999).
16. V. R. Garsevanishvili *et al.*, *Teor. Mat. Fiz.* **23**, 310 (1975).
17. S. J. Chang, R. G. Root, and T. M. Yan, *Phys. Rev. D* **7**, 1133 (1973).
18. H. Leutwyler, *Nucl. Phys. B* **76**, 413 (1974).
19. S. J. Brodsky *et al.*, *Particle World* **3**, 109 (1993).
20. K. G. Wilson *et al.*, *Phys. Rev. D* **49**, 6720 (1994).
21. B. Desplanques, V. A. Karmanov, and J. F. Mathiot, *Nucl. Phys. A* **589**, 697 (1995); J. Carbonell *et al.*, *Phys. Rep.* **300**, 215 (1998).
22. J. Gunion, SLAC-PUB-2607 (Sept. 1980).
23. N. Amelin *et al.*, *Phys. Rev. Lett.* **67**, 1523 (1991).
24. N. Amelin and L. Csernai, in *Proceedings of the International Workshop on Correlations and Multiparticle Production (CAMP), Marburg, Germany, 1990* (World Sci., Singapore, 1990); N. S. Amelin, K. K. Gudima, and V. D. Toneev, *Yad. Fiz.* **51**, 512 (1990) [*Sov. J. Nucl. Phys.* **51**, 327 (1990)].
25. N. S. Amelin *et al.*, *Yad. Fiz.* **51**, 841 (1990) [*Sov. J. Nucl. Phys.* **51**, 535 (1990)]; **52**, 272 (1990) [**52**, 172 (1990)].
26. N. S. Amelin, Preprint No. P2-86-837, JINR (Joint Inst. Nucl. Res., Dubna, 1986).

Double Vector-Charmonium Production in Electron–Positron Annihilation into Two Photons at $\sqrt{s} = 10.6$ GeV

A. V. Luchinsky*

Institute for High Energy Physics, Protvino, Moscow oblast, 142284 Russia

Received April 1, 2003

Abstract—In experimentally studying the exclusive production of two $c\bar{c}$ mesons in electron–positron annihilation, the BELLE Collaboration obtained results that differ substantially from theoretical predictions. Recently, it was assumed that a significant part of this discrepancy can be explained by the process $e^+e^- \rightarrow 2\gamma^* \rightarrow 2J/\psi$, and its cross section was published. It is shown here that these results are incorrect (the cross sections are overestimated). The correct values of the cross sections for the double production of various vector charmonia are given. © 2004 MAIK “Nauka/Interperiodica”.

Charmonium states (such as J/ψ , $\psi(2S)$, or η_c) are of great interest both from the theoretical and from the experimental point of view. First, they have a clear experimental signature. Second, their theoretical description is simplified significantly owing to their nonrelativistic nature. Of special interest is the exclusive production of various charmonium states in e^+e^- annihilation since all nonperturbative constants involved in such processes can be determined phenomenologically from $V \rightarrow e^+e^-$ decay widths, where V stands for one of the $c\bar{c}$ vector–charmonium states, $V = J/\psi$, $\psi(2S)$, $\psi(3770)$, $\psi(4040)$, $\psi(4160)$ or $\psi(4415)$.

Recently, the BELLE Collaboration investigated double charmonium production in e^+e^- annihilation at the c.m. energy of $\sqrt{s} = 10.6$ GeV [1]. Its results differ significantly from the predictions based on nonrelativistic QCD (NRQCD) [2–4]. For example, the measured cross section for the process $e^+e^- \rightarrow J/\psi\eta_c$ is about one order of magnitude larger than the results obtained in [3–5]. This difference is a challenge to our current understanding of charmonium-production processes.

A possible explanation of this discrepancy was proposed by Bodwin, Braaten, and Lepage (BBL) [6], who assumed that some of the events considered by the BELLE Collaboration like those of $J/\psi\eta_c$ production in fact involve the production of a J/ψ pair in electron–positron annihilation into two photons. They obtained the following values:

$$\begin{aligned}\sigma_{\text{BBL}}[e^+e^- \rightarrow J/\psi + J/\psi] &= 8.70 \pm 2.94 \text{ fb}, \\ \sigma_{\text{BBL}}[e^+e^- \rightarrow J/\psi + \psi(2S)] &= 7.22 \pm 2.44 \text{ fb},\end{aligned}$$

* e-mail: Alexey.Luchinsky@ihep.ru

$$\sigma_{\text{BBL}}[e^+e^- \rightarrow \psi(2S) + \psi(2S)] = 1.50 \pm 0.51 \text{ fb}.$$

However, these results have some drawbacks that follow from the approximations used in [6].

(i) The calculations in [6] were performed with the aid of NRQCD, and the values of $M_{J/\psi} = M_{\psi(2S)} = 2m_c = 2.8$ GeV were used there instead of the physical masses of vector mesons. Since the reaction in the experiment proceeded at a c.m. energy close to the threshold, the cross section depends strongly on the final-particle masses, so that this approximation may lead to large errors.

(ii) All QCD corrections were neglected in [6]. As was shown in [2], the effect of these corrections may be significant. By way of example, we indicate that, in the zeroth order in α_s , the matrix element $\langle O_1 \rangle_{J/\psi}$, which was used in [6] and which is proportional to the J/ψ -meson width with respect to decay through the electron mode, is

$$[\langle O_1 \rangle_{J/\psi}]_{\text{LO}} = 0.208 \text{ GeV}^3,$$

but that, upon taking into account the first-order QCD corrections, it becomes

$$[\langle O_1 \rangle_{J/\psi}]_{\text{NLO}} = 0.335 \text{ GeV}^3.$$

Both of these disadvantages can be remedied by using physical values of input parameters (vector-meson masses and couplings of vector mesons to electrons) rather than model ones.

Four diagrams for the process $e^+e^- \rightarrow V_1V_2$ are shown in Fig. 1. Two additional diagrams can be obtained from the diagrams in Figs. 1c and 1d by interchanging the final vector mesons. First of all, it worth noting that the diagrams in Figs. 1c and 1d are suppressed with respect to the first two diagrams

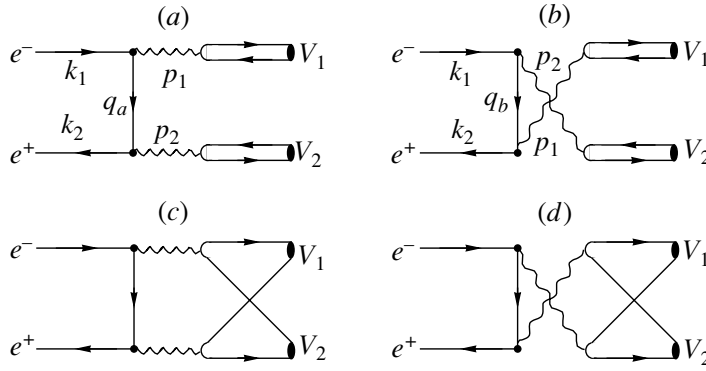


Fig. 1. Diagrams for the process $e^+e^- \rightarrow 2\gamma^* \rightarrow V_1V_2$.

by a factor of $(4M_V^2/s)^2 \sim 0.1$, which arises from the virtual-photon propagators. The QCD corrections caused by a gluon emitted and captured by the same quark or by the quarks of a vector meson are taken into account in the effective coupling of the vector meson to an electron. An additional suppression arises owing to the gluon propagator and color when a gluon line connects quarks from different vector mesons. For these reasons, we consider below only the diagrams in Figs. 1a and 1b, which lead to a sizable peak in the angular distribution for the case where vector mesons travel in directions very close to the beam axis. At the same time, the diagrams in Figs. 1c and 1d produce a nearly isotropic distribution.

The amplitude corresponding to the diagrams in Figs. 1a and 1b is given by

$$\mathcal{M} = e^2 g_1 g_2 \phi_1^\mu \phi_2^\nu \times \left[\frac{\bar{v}(k_2) \gamma_\nu \hat{q}_a \gamma_\mu u(k_1)}{q_a^2} + \frac{\bar{v}(k_2) \gamma_\mu \hat{q}_b \gamma_\nu u(k_1)}{q_b^2} \right],$$

where $u(k_1)$ and $\bar{v}(k_2)$ are, respectively, the electron and the positron spinor wave function; ϕ_i^α is the polarization vector of the i th meson; and g_i is the coupling constant in the eeV_i vertex. This coupling can be obtained from the vector-meson width with respect to decay via the electron mode:

$$g_i^2 = 12\pi \frac{\Gamma_i^{ee}}{M_i}.$$

Here, M_i is the mass of the V_i particle and Γ_i^{ee} is its width with respect to decay into electrons.

The differential cross section has the form

$$\begin{aligned} \frac{d\sigma}{dx} &= \frac{1}{64\pi} \frac{2b}{s^2} \sum |\mathcal{M}|^2 \\ &= \frac{g_1^2 g_2^2 b}{32\pi s^2} \left[\frac{6s(M_1^2 + M_2^2)}{M_1^2 M_2^2} - 6 + \frac{4a^2}{M_1^2 M_2^2} \right. \\ &\quad \left. - \frac{3M_1^2}{M_2^2} - \frac{3M_2^2}{M_1^2} - \frac{s^2}{M_1^2 M_2^2} + 12 \frac{a^2 + b^2 x^2}{a^2 - b^2 x^2} \right] \end{aligned} \quad (1)$$

$$\begin{aligned} &- 8M_1^2 M_2^2 \frac{a^2 + b^2 x^2}{(a^2 - b^2 x^2)^2} + 2s \left(\frac{M_1^2}{M_2^2} \frac{1}{a - bx} \right. \\ &\quad \left. + \frac{M_2^2}{M_1^2} \frac{1}{a + bx} \right) + 2 \left(\frac{M_1^2}{M_2^2} \frac{a + bx}{a - bx} + \frac{M_2^2}{M_1^2} \frac{a - bx}{a + bx} \right) \\ &\quad + 2 \left(\frac{1}{M_1^2} \frac{(a - bx)^2}{a + bx} + \frac{1}{M_2^2} \frac{(a + bx)^2}{a - bx} \right) \\ &\quad - 2 \left(\frac{a - bx}{M_2^2} + \frac{a + bx}{M_1^2} \right) - 2s^2 \left(\frac{1}{M_2^2(a - bx)} \right. \\ &\quad \left. + \frac{1}{M_1^2(a + bx)} \right) + \frac{4sa}{a^2 - b^2 x^2} \Big], \end{aligned}$$

where summation is performed over the polarizations of all particles, $x = \cos \theta$ is the cosine of the angle between the e^- and V_1 momenta in the c.m. frame,

$$a = \frac{s - M_1^2 - M_2^2}{2},$$

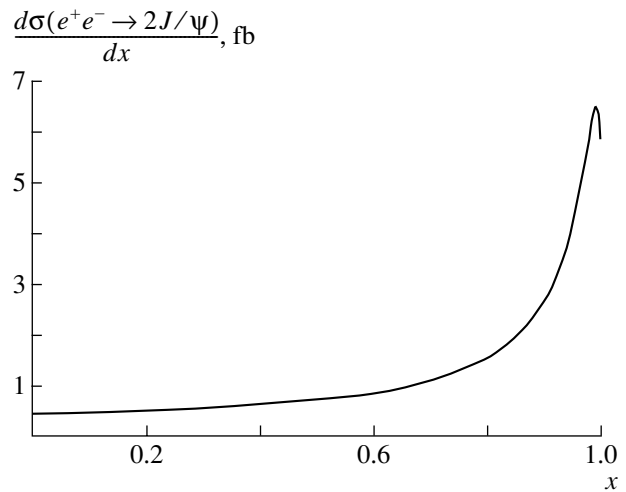


Fig. 2. Angular distribution for the process $e^+e^- \rightarrow 2J/\psi$.

Table 1. Masses of vector mesons and their widths with respect to decay into electrons

i	$J/\psi(1S)$	$\psi(2S)$	$\psi(3770)$	$\psi(4040)$	$\psi(4160)$	$\psi(4415)$
M_i [GeV]	3.097	3.685	3.77	4.04	4.159	4.415
Γ_i^{ee} [eV]	5.26	2.12	0.26	0.75	0.77	0.47

Table 2. Values of $\sigma(e^+e^- \rightarrow V_1V_2)$ (in fb)

V_2	V_1					
	$J/\psi(1S)$	$\psi(2S)$	$\psi(3770)$	$\psi(4040)$	$\psi(4160)$	$\psi(4415)$
$J/\psi(1S)$	2.26	1.46	0.17	0.46	0.46	0.26
$\psi(2S)$	1.46	0.23	0.06	0.15	0.15	0.08
$\psi(3770)$	0.17	0.06	0.003	0.02	0.02	0.01
$\psi(4040)$	0.46	0.15	0.02	0.02	0.05	0.03
$\psi(4160)$	0.46	0.15	0.02	0.05	0.02	0.02
$\psi(4415)$	0.26	0.08	0.01	0.03	0.02	0.01

$$b = \frac{1}{2} \sqrt{s - (M_1 + M_2)^2} \sqrt{s - (M_1 - M_2)^2}.$$

For the case of $V_1 = V_2 = J/\psi$, Fig. 2 presents the differential cross section as a function of the cosine of the scattering angle (since the differential cross section is an even function of the cosine of the scattering angle, only the region of positive x is shown). One can easily see the aforementioned peak in the vicinity of the point $x = 1$.

The total cross section can be obtained from expression (1) by integrating it with respect to x from -1 to 1 :

$$\sigma = \int_{-1}^1 \frac{d\sigma}{dx} dx = \frac{g_1^2 g_2^2}{8\pi a s^2} \quad (2)$$

$$\times \left((s^2 + (M_1^2 + M_2^2)^2) \ln \frac{a+b}{a-b} - 8ab \right).$$

In the case of identical final particles, the result in (2) must be divided by 2 to avoid the double counting of identical states.

Using the experimental values given in Table 1 for the masses of vector mesons and their widths with respect to decay into electrons, we obtain the total-cross-section values presented in Table 2. These re-

sults differ significantly from those quoted in [6].¹⁾ By way of example, we indicate that, for $V_1 = V_2 = J/\psi$,

$$\frac{\sigma_{\text{BBL}}(e^+e^- \rightarrow 2J/\psi)}{\sigma(e^+e^- \rightarrow 2J/\psi)} \approx 3.8.$$

This is because the QCD corrections were not taken into account in [6]. Here, these corrections are included in the effective coupling of vector mesons to an electron.

Thus, I would like to note that the explanation proposed in [6] is not adequate, so that the question of the discrepancy between the results of the BELLE experiment and the respective theoretical predictions remains unsolved.

ACKNOWLEDGMENTS

I am grateful to A.K. Likhoded and S.S. Gerstein for stimulating discussions and enlightening comments.

This work was supported by the Russian Foundation for Basic Research (project nos. 01-02-16558, 00-15-96645).

¹⁾The authors of [6] informed me that they corrected the aforementioned disadvantages in their new publication [7]. Nevertheless, the present article is of interest since it reports on an independent confirmation of their results.

REFERENCES

1. K. Abe *et al.* (BELLE Collab.), Phys. Rev. Lett. **89**, 142001 (2002).
2. G. T. Bodwin, E. Braaten, and G. P. Lepage, Phys. Rev. D **51**, 1125 (1995); **55**, 5853 (1997).
3. E. Braaten and J. Lee, Phys. Rev. D **67**, 054007 (2003); hep-ph/0211085.
4. K.-Y. Liu, Z.-G. He, and K.-T. Chao, Phys. Lett. B **557**, 45 (2003).
5. A. V. Berezhnoy and A. K. Likhoded, hep-ph/0303145.
6. G. T. Bodwin, E. Braaten, and J. Lee, Phys. Rev. Lett. **90**, 162001 (2003).
7. G. T. Bodwin, E. Braaten, and J. Lee, Phys. Rev. D **67**, 054023 (2003).

Translated by S. Slabospitsky

ELEMENTARY PARTICLES AND FIELDS
Theory

Electroweak Radiative Effects in the Møller Scattering of Polarized Particles

V. A. Zykunov*

Gomel State Technical University, Gomel, Belarus

Received January 8, 2003; in final form, September 1, 2003

Abstract—Bremsstrahlung-induced electroweak radiative corrections to observables of the Møller scattering of polarized particles are calculated. The covariant method is used to remove infrared divergences. Owing to this, the ultimate result does not involve unphysical parameters. The electroweak corrections being considered are shown to reduce the polarization asymmetry in the region studied in the E-158 experiment at SLAC. For example, the asymmetry is shifted by approximately -11% at $E = 48$ GeV and $y = 0.5$. © 2004 MAIK “Nauka/Interperiodica”.

1. INTRODUCTION

Among experiments that are being presently performed at SLAC, the E-158 experiment [1], which is devoted to studying the Møller scattering of a polarized 45- to 48-GeV electron beam on unpolarized electrons of a hydrogen target, is of particular interest because of an unprecedented precision to which the experimentalists involved in this project are going to measure the parity-violating polarization asymmetry $A_{LR}^{(1)}$ of this process (it is assumed that the relative error in determining this asymmetry will be about 8%), whereby they hope to obtain the squared sine of the Weinberg angle, s_W^2 (this is one of the most important parameters of the Standard Model), to a precision of $\delta s_W^2 \approx \pm 0.0008$.

In order to extract reliable information from experimental data, it is necessary to take into account higher order effects—that is, to allow for processes that are more intricate than that under study, but which are indistinguishable from it experimentally. This procedure (the inclusion of radiative corrections) is inherent in any modern experiment, especially that which is as precise as E-158.

Naturally, interest in the Møller scattering of polarized particles is not caused exclusively by its potential for determining s_W^2 . For example, the scattering of two identical polarized fermions has long since been used in determining, to a high degree of precision, the polarization of an electron beam (see [2] and references therein), as well as in monitoring luminosities (in particular, at DESY). Electromagnetic radiative corrections and the degree of their influence on measurement of beam polarizations in a Møller

polarimeter were assessed in [3]; also, the history of the calculation of radiative corrections in the process considered here was expounded there. It is natural that, at energies applied in polarimetry, electroweak effects are negligible in relation to electromagnetic effects.

Yet another reason that stimulates interest in Møller scattering is that it enables one to test the Standard Model and to reveal traces of new physics. By way of example, we indicate that, in the intensively discussed projects of the TESLA collider and e^-e^- and $\mu^-\mu^-$ colliders [4], high hopes for the discovery of Higgs bosons, manifestations of contact interactions, the compositeness of the electron, new gauge bosons, etc., are pinned on the scattering of identical polarized fermions. It is quite obvious that, since the projects being discussed are characterized by energies in the TeV region, radiative corrections will play an extremely important role in relevant experiments, the electroweak component there being on the same order of magnitude as the electromagnetic component.

Having said this, we return to low-energy experiments that study the Møller scattering of polarized particles, but which nevertheless require calculating electroweak corrections. For the first time, radiative corrections to the observables of Møller scattering (under the kinematical conditions of the E-158 experiment) were calculated by Czarnecki and Marciano [5]. According to their calculations, the asymmetry measured in the kinematical region of the E-158 experiment is approximately 40% lower than its theoretical value calculated at the tree level. Approximately the same value was obtained by Denner and Pozzorini [6], who studied radiative corrections in the Møller scattering of polarized particles at arbitrary energies. It should be noted

* e-mail: zykunov@gstu.gomel.by

that different renormalization schemes were used in those two studies—these were the modified minimal-subtraction (\overline{MS}) scheme in [5] and the scheme of on-shell renormalization in [6]—so that the good agreement between those results indicates that the calculations were quite reliable. However, all radiative contributions to observables were not consistently taken into account in [5] or in [6]. For example, Czarnecki and Marciano [5] disregarded completely the bremsstrahlung contribution, assuming that it is small and is dependent on specific experimental conditions.

The next step was due to Petriello [7], who calculated the total set of $O(\alpha)$ electroweak radiative corrections. As to the contribution of virtual particles, which was calculated in [7] by applying the scheme of on-shell renormalization, the result was fully in accord with that presented by Denner and Pozzorini [6]. In addition, Petriello [7] investigated the contribution of hard bremsstrahlung under the E-158 experimental conditions. He found that the sensitivity of the cross sections and polarization asymmetry to this part of radiative corrections becomes much lower upon imposing the respective experimental cuts.

The use of an unphysical parameter ΔE that separates the region of soft photons is a feature peculiar to the calculation performed in [7]. The introduction of ΔE makes it possible to avoid difficulties associated with the contribution of real photons, but one can dispense with this under conditions of the E-158 experiment. Since the problem being discussed is of great topical interest, an attempt is made here to calculate and to estimate numerically, within the Standard Model, electroweak radiative corrections caused by internal bremsstrahlung in the process $e^-e^- \rightarrow e^-e^- \gamma$ under experimental conditions where the emitted photon is not recorded. The last circumstance plays a key role in our approach to the problem—we can apply the procedure that ensures a covariant separation and cancellation of an infrared divergence (so-called Bardin–Shumeiko method [8]); owing to this, our result for radiative corrections will not be dependent on any unphysical parameters (including ΔE).

The ensuing exposition is organized as follows. In Section 2, we give the result for the Born process and explain its kinematics. In Section 3, we present infrared-divergent contributions that are caused by additional virtual particles and which were calculated in the Feynman gauge within the scheme of on-shell renormalization; also, we calculate there internal bremsstrahlung and demonstrate how the infrared divergence cancels. A numerical analysis and conclusions are given in Section 4. The Appendix contains the list of integrals that are involved in the calculation

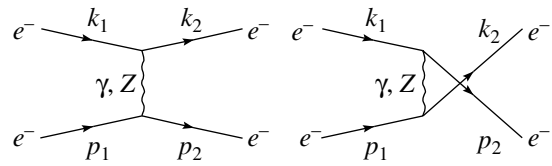


Fig. 1. Diagrams describing radiationless Møller scattering in the t and in the u channel (left and right figures, respectively).

of bremsstrahlung, but which were not determined in previous studies.

2. BORN CROSS SECTION AND BASIC NOTATION

Within the Standard Model, the Born cross section for Møller scattering can be represented in the form

$$\frac{d\sigma^0}{dy} = \frac{\pi\alpha^2}{s} \sum_{l=1}^4 (M_l^0 + \hat{M}_l^0). \quad (1)$$

We denote by k_1 and p_1 the 4-momenta of initial electrons and by k_2 and p_2 their counterparts for final electrons (see Fig. 1). In terms of these 4-momenta, the standard set of Mandelstam invariant quantities can be written as

$$s = (k_1 + p_1)^2, \quad t = (k_1 - k_2)^2, \quad u = (k_2 - p_1)^2. \quad (2)$$

The variable y is given by

$$y = -t/s. \quad (3)$$

We note that, in the Born approximation, $y = (1 - \cos\theta)/2$, where θ is the scattering angle of the recorded electron with the 4-momentum k_2 in the c.m. frame of initial electrons, since, in the c.m. frame, the energy of the initial electron (E^*) is equal to the energy of the recorded electron (E'^*). The “hat” operator in expression (1) and below denotes the substitution $t \leftrightarrow u$. Its origin in (1) is obvious—this is crossing symmetry. We also note that, where possible, we disregard the electron mass m .

The squares of the matrix elements in the Born cross sections are expressed in terms of the propagators

$$D^{ik} = \frac{1}{k - m_i^2} \quad (i = \gamma, Z) \quad (4)$$

and the functions M_{ev} and M_{odd} as

$$\begin{aligned} M_1^0 &= D^{\gamma t} (D^{\gamma t} M_{\text{ev}}^{\gamma\gamma\gamma\gamma} - D^{\gamma u} M_{\text{odd}}^{\gamma\gamma\gamma\gamma}), \\ M_2^0 &= D^{\gamma t} (D^{Zt} M_{\text{ev}}^{\gamma Z\gamma Z} - D^{Zu} M_{\text{odd}}^{\gamma Z\gamma Z}), \\ M_3^0 &= D^{Zt} (D^{\gamma t} M_{\text{ev}}^{Z\gamma Z\gamma} - D^{\gamma u} M_{\text{odd}}^{Z\gamma Z\gamma}), \end{aligned} \quad (5)$$

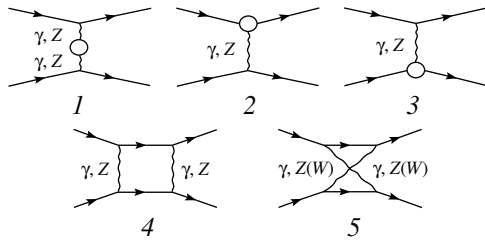


Fig. 2. One-loop t -channel diagrams for the process $e^- e^- \rightarrow e^- e^-$. The self-energy and vertex-function contributions are represented by circles; their exact representation can be found in [9, 10]. Five u -channel diagrams are obtained from those that are displayed here by means of the substitution $k_2 \leftrightarrow p_2$.

$$M_4^0 = D^{Zt}(D^{Zt}M_{ev}^{ZZZZ} - D^{Zu}M_{odd}^{ZZZZ}).$$

The functions M_{ev} and M_{odd} were chosen in a form that is convenient for representing not only the Born cross section but also radiative contributions; that is,

$$M_{ev}^{ijkl} = 2(s^2 + u^2)\lambda_{1B}^{ij}\lambda_{1T}^{kl} + 2(s^2 - u^2)\lambda_{2B}^{ij}\lambda_{2T}^{kl}, \tag{6}$$

$$M_{odd}^{ijkl} = -2s^2(\lambda_{1B}^{ij}\lambda_{1T}^{kl} + \lambda_{2B}^{ij}\lambda_{2T}^{kl}). \tag{7}$$

In taking the squares of the matrix elements, we made use of the equation

$$\begin{aligned} \rho^{ij}(k_1) &= (v^i - a^i\gamma_5)\rho(k_1)(v^j + a^j\gamma_5) \\ &= \frac{1}{2}(\lambda_{1B}^{ij}\hat{k}_1 - \lambda_{2B}^{ij}\gamma_5\hat{k}_1) + O(m) \end{aligned} \tag{8}$$

[and of the analogous equation for $\rho^{ij}(p_1)$], which relate the γ matrices, the density matrices $\rho(k_1)$ and $\rho(p_1)$ for the initial particles, and the couplings and the polarizations $p_{B(T)}$ of beam (target) electrons. The cross sections involve these couplings and polarizations only in specific combinations; that is,

$$\lambda_{1B(T)}^{ij} = \lambda_V^{ij} - p_{B(T)}\lambda_A^{ij}, \tag{9}$$

$$\lambda_{2B(T)}^{ij} = \lambda_A^{ij} - p_{B(T)}\lambda_V^{ij},$$

$$\lambda_V^{ij} = v^i v^j + a^i a^j, \quad \lambda_A^{ij} = v^i a^j + a^i v^j, \tag{10}$$

where

$$v^\gamma = 1, \quad a^\gamma = 0, \quad v^Z = (I_e^3 + 2s_W^2)/(2s_W c_W), \tag{11}$$

$$a^Z = I_e^3/(2s_W c_W).$$

We recall that $I_e^3 = -1/2$ and that s_W (c_W) is the sine (cosine) of the Weinberg angle.

It should be noted that, in the cross section (1), the contribution corresponding to photon exchange is coincident with the result presented in [3]; also, agreement with the results quoted in [5] for the cross sections $d\sigma_{LL}/dy$, $d\sigma_{RR}/dy$, and $d\sigma_{RL}/dy = d\sigma_{LR}/dy$

is achieved. The subscripts L and R on the cross sections mean that $p_{B(T)} = -1$ and $p_{B(T)} = +1$, respectively.

3. ELECTROWEAK RADIATIVE EFFECTS

It is meaningless to consider “internal”-bremsstrahlung effects (which we are going to investigate) without simultaneously taking into account one-loop radiative corrections caused by the presence of additional virtual particles (so-called V contribution). Under the conditions of the E-158 experiment, this part has received quite an adequate study (see Introduction); therefore, a complete calculation will not be reproduced here. Nevertheless, we will need that part of the V contribution which contains an infrared divergence. The isolation of this part is ambiguous—the only thing that must be strictly respected is that the isolated term must be proportional to the Born cross section. In our situation, where the correction to the polarization asymmetry is of interest (this is the ratio of the cross sections), this contribution alone cannot change the asymmetry and is very small against the background of the remaining terms (as will become clear from a numerical analysis). Thus, the isolation of the divergent part will be performed here by using the results obtained in [9, 10], where the self-energies of gauge bosons (in the renormalization scheme used in [9], there are no contributions from electron self-energies) and vertex functions were calculated. We will also need expressions for the contributions of box diagrams from [11].

3.1. Isolation of the Infrared Divergence from the Contribution of Virtual Particles

The contribution of virtual particles to the observables of Møller scattering can be represented by three classes of diagrams: boson “self-energies,” vertices, and “boxes” (see Fig. 2). The corresponding cross section is given by

$$\frac{d\sigma^V}{dy} = \frac{d\sigma^S}{dy} + \frac{d\sigma^{Ver}}{dy} + \frac{d\sigma^B}{dy}. \tag{12}$$

(i) The contributions of the photon and Z -boson self-energies (diagram 1 in Fig. 2) are free from infrared divergences and are not considered here.

(ii) In order to calculate the required part of the electron vertex corrections (diagrams 2 and 3 in Fig. 2), we have used the form factors $\delta F_{V,A}^{je}$ from [9] (pp. 722, 723) at $k^2 = t, u$. Replacing the coupling constants v and a by these form factors (for example, $v^\gamma \rightarrow \delta F_V^{\gamma e}$) in the corresponding terms of the Born

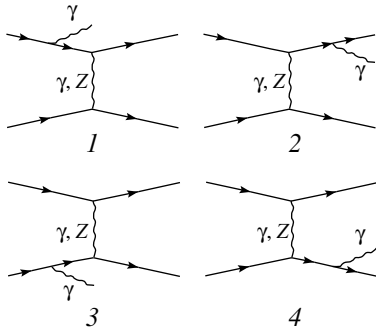


Fig. 3. Diagrams for the bremsstrahlung process $e^-e^- \rightarrow e^-e^-\gamma$ in the t channel. Four u -channel diagrams are obtained from those displayed in this figure by means of the substitution $k_2 \leftrightarrow p_2$.

functions $M_{\text{ev,odd}}$, we obtain the vertex component of the cross section in the form

$$\frac{d\sigma^{\text{Ver}}}{dy} = \frac{2\pi\alpha^2}{s} \text{Re} \sum_{l=1}^4 (M_l^V + \hat{M}_l^V), \quad (13)$$

where

$$\begin{aligned} M_1^V &= D^{\gamma t} (D^{\gamma t} (M_{\text{ev}}^{F\gamma\gamma\gamma\gamma} + M_{\text{ev}}^{\gamma\gamma F\gamma\gamma}) \\ &\quad - D^{\gamma u} (M_{\text{odd}}^{F\gamma\gamma\gamma\gamma} + M_{\text{odd}}^{\gamma\gamma F\gamma\gamma})), \\ M_2^V &= D^{\gamma t} (D^{Zt} (M_{\text{ev}}^{F\gamma Z\gamma Z} + M_{\text{ev}}^{\gamma Z F\gamma Z}) \\ &\quad - D^{Zu} (M_{\text{odd}}^{F\gamma Z\gamma Z} + M_{\text{odd}}^{\gamma Z F\gamma Z})), \\ M_3^V &= D^{Zt} (D^{\gamma t} (M_{\text{ev}}^{FZ\gamma Z\gamma} + M_{\text{ev}}^{Z\gamma FZ\gamma}) \\ &\quad - D^{\gamma u} (M_{\text{odd}}^{FZ\gamma Z\gamma} + M_{\text{odd}}^{Z\gamma FZ\gamma})), \\ M_4^V &= D^{Zt} (D^{Zt} (M_{\text{ev}}^{FZZZZ} + M_{\text{ev}}^{ZZFZZ}) \\ &\quad - D^{Zu} (M_{\text{odd}}^{FZZZZ} + M_{\text{odd}}^{ZZFZZ})). \end{aligned} \quad (14)$$

(iii) As to the box component of the cross section (diagrams 4 and 5 in Fig. 2), we are interested in the contributions of those boxes that involve at least one virtual photon; diagrams containing two Z bosons and two W bosons are infrared-finite and are not considered here for this reason. Thus, the required cross-section component, written with the aid of the results presented in [11], has the form

$$\begin{aligned} \frac{d\sigma^B}{dy} &= \frac{2\pi\alpha^2}{s} \text{Re}((M_1^0 + M_2^0)(C_{\gamma\gamma}(t, s) \\ &\quad - C_{\gamma\gamma}^5(t, s)) + (M_3^0 + M_4^0)(C_{\gamma Z}(t, s) \\ &\quad - C_{\gamma Z}^5(t, s))) + (t \leftrightarrow u). \end{aligned} \quad (15)$$

The explicit expressions for the functions C and C^5 are given in [11] (p. 1088).

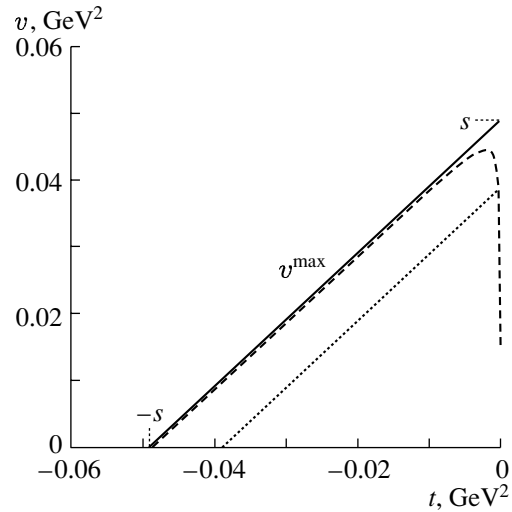


Fig. 4. Chew–Low diagram at $s \approx 0.05 \text{ GeV}^2$ for (solid line) the actual electron mass and (dashed line) that which is artificially magnified by a factor of 20. The dotted line corresponds to v^{max} under the conditions of the E-158 experiment.

We represent the V contribution as the sum of an infrared-divergent and an infrared-finite part. Further, we use the identity transformation

$$\frac{d\sigma^V}{dy} = \frac{d\sigma_{\text{IR}}^V}{dy} + \frac{d\sigma^V}{dy}(\lambda^2 \rightarrow s), \quad (16)$$

where λ is the photon mass regularizing the infrared divergence. For the infrared-divergent part, we obtained an expression that is proportional to the Born cross section; that is,

$$\frac{d\sigma_{\text{IR}}^V}{dy} = -\frac{2\alpha}{\pi} \ln \frac{s}{\lambda^2} \left(\ln \frac{tu}{m^2 s} - 1 \right) \frac{d\sigma^0}{dy}. \quad (17)$$

3.2. Contribution of Real-Photon Emission (R Contribution)

Let us consider Møller scattering process involving the emission of one bremsstrahlung photon of 4-momentum k : $e^-e^- \rightarrow e^-e^-\gamma$. Eight diagrams correspond to it: these are four t -channel diagrams (see Fig. 3) and four u -channel diagrams, which can be obtained by means of the substitution $k_2 \leftrightarrow p_2$. The differential cross section for the process in question has the form

$$\begin{aligned} \frac{d\sigma^R}{dy} &= -\frac{\alpha^3}{4s\pi} \int_0^{v^{\text{max}}} dv \\ &\quad \times \int \frac{d^3k}{k_0} \delta[(k_1 + p_1 - k_2 - k)^2 - m^2] \end{aligned} \quad (18)$$

$$\times \sum_{j,i=1}^4 (-1)^{i+j} M_{ij}^R,$$

where, for the kinematical variables (the square of the matrix element M_{ij}^R depends on them—see below), we use the standard set

$$\begin{aligned} z &= 2kk_2, & z_1 &= 2kk_1, & t_1 &= (p_2 - p_1)^2, & (19) \\ v_1 &= 2kp_1 = s + u + t_1 - 4m^2, \\ v &= 2kp_2 = s + u + t - 4m^2, \end{aligned}$$

which satisfies the equalities

$$v_1 - v = z - z_1 = t_1 - t. \quad (20)$$

We note that, as before, s , t , and u are given by the expressions in (2). In a number of cases (see Appendix), it is advisable to use the nonstandard variable

$$z_2 = (k_1 - p_2)^2 = u - v + z_1. \quad (21)$$

The domain of v was investigated in [12] and is described by the Chew–Low diagram in Fig. 4. The solid line represents an upper bound on v at $s \approx 0.05 \text{ GeV}^2$. It can be seen that, within the segment $t \ll 0$, the hyperbola degenerates into the straight line $v^{\max} = s + t$. This is due to the smallness of the

square of the electron mass in relation to other invariant quantities. The dashed line represents v^{\max} at the same value of s , but for the electron mass artificially magnified by a factor of 20. Here, the shape of a hyperbola is clearly seen (the straight lines $v = s + t$ and $t = 0$ are asymptotes to it). Further, we emphasize that, since the upper bound $v = v^{\max}$ corresponds to the point $u = 0$ (collinear singularity), we must cut off the integration domain at a value that corresponds to the possibilities of the E-158 experiment—the energy of the detected particle lies in the region $E^L \geq 10 \text{ GeV}$. We then have $u^{\max} = 2m(m - E^L)$ and $v^{\max} = s + t + u^{\max} - 4m^2$. The last equation yields a straight line lying below $v^{\max} \approx s + t$ (dotted line in Fig. 4).

The indices i and j in expression (18) denote the type of diagram (in Fig. 3) that contributes to the cross section; both i and j can take four values (their meaning is obvious—the indices label the intermediate boson and the channel through which the reaction proceeds):

$$i, j = (1, 2, 3, 4) = (\gamma t, \gamma u, Zt, Zu). \quad (22)$$

By employing the standard Feynman rules for calculating the matrix elements M_{ij}^R , we obtain

$$M_{ij}^R = \begin{cases} (M_{ij}^R)_{zz} + (M_{ij}^R)_{zv} + (M_{ij}^R)_{vz} + (M_{ij}^R)_{vv} & \text{for } ij = 13, 31, 11, 33 \\ (M_{ij}^R)_f + (M_{ij}^R)_l + (M_{ij}^R)_{tu} + (M_{ij}^R)_s & \text{for } ij = 12, 14, 32, 34. \end{cases}$$

The terms in this formula are the traces of the products of combinations of the γ matrices and density matrices, these traces being multiplied by the corresponding propagators; that is,

$$\begin{aligned} (M_{ij}^R)_{zz} &= \text{tr}[G_1^{\mu\alpha} \rho^{ij}(k_1) G_1^{\nu\alpha T} \Lambda(k_2)] & (23) \\ &\times \text{tr}[\gamma_\mu \rho^{ij}(p_1) \gamma_\nu \Lambda(p_2)] D^{it_1} D^{jt_1}, \\ (M_{ij}^R)_{zv} &= \text{tr}[G_1^{\mu\alpha} \rho^{ij}(k_1) \gamma_\nu \Lambda(k_2)] \\ &\times \text{tr}[\gamma_\mu \rho^{ij}(p_1) G_2^{\nu\alpha T} \Lambda(p_2)] D^{it_1} D^{jt}, \\ (M_{ij}^R)_{vz} &= \text{tr}[G_2^{\mu\alpha} \rho^{ij}(p_1) \gamma_\nu \Lambda(p_2)] \\ &\times \text{tr}[\gamma_\mu \rho^{ij}(k_1) G_1^{\nu\alpha T} \Lambda(k_2)] D^{it} D^{jt_1}, \\ (M_{ij}^R)_{vv} &= \text{tr}[G_2^{\mu\alpha} \rho^{ij}(p_1) G_2^{\nu\alpha T} \Lambda(p_2)] \\ &\times \text{tr}[\gamma_\mu \rho^{ij}(k_1) \gamma_\nu \Lambda(k_2)] D^{it} D^{jt}, \\ (M_{ij}^R)_f &= \text{tr}[G_1^{\mu\alpha} \rho^{ij}(k_1) G_3^{\nu\alpha} \Lambda(p_2)] \\ &\times \gamma_\mu \rho^{ij}(p_1) \gamma_\nu \Lambda(k_2) D^{it_1} D^{ju}, \\ (M_{ij}^R)_l &= \text{tr}[G_1^{\mu\alpha} \rho^{ij}(k_1) \gamma_\nu \Lambda(p_2)] \\ &\times \gamma_\mu \rho^{ij}(p_1) G_4^{\nu\alpha} \Lambda(k_2) D^{it_1} D^{jz_2}, \end{aligned}$$

$$\begin{aligned} (M_{ij}^R)_{tu} &= \text{tr}[\gamma_\mu \rho^{ij}(k_1) \\ &\times G_3^{\nu\alpha} \Lambda(p_2) G_2^{\mu\alpha} \rho^{ij}(p_1) \gamma_\nu \Lambda(k_2)] D^{it} D^{ju}, \\ (M_{ij}^R)_s &= \text{tr}[\gamma_\mu \rho^{ij}(k_1) \gamma_\nu \Lambda(p_2) \\ &\times G_2^{\mu\alpha} \rho^{ij}(p_1) G_4^{\nu\alpha} \Lambda(k_2)] D^{it} D^{jz_2}, \end{aligned}$$

where

$$\Lambda(p) = \hat{p} + m, \quad \hat{p} = \gamma^\mu p_\mu, \quad (24)$$

$$G_1^{\mu\alpha} = \gamma^\mu \frac{2k_1^\alpha - \hat{k}\gamma^\alpha}{-z_1} + \frac{2k_2^\alpha + \gamma^\alpha \hat{k}}{z} \gamma^\mu, \quad (25)$$

$$G_2^{\mu\alpha} = \gamma^\mu \frac{2p_1^\alpha - \hat{k}\gamma^\alpha}{-v_1} + \frac{2p_2^\alpha + \gamma^\alpha \hat{k}}{v} \gamma^\mu, \quad (26)$$

$$G_3^{\nu\alpha} = \frac{2k_1^\alpha - \gamma^\alpha \hat{k}}{-z_1} \gamma^\nu + \gamma^\nu \frac{2p_2^\alpha + \hat{k}\gamma^\alpha}{v}, \quad (27)$$

$$G_4^{\nu\alpha} = \frac{2p_1^\alpha - \gamma^\alpha \hat{k}}{-v_1} \gamma^\nu + \gamma^\nu \frac{2k_2^\alpha + \hat{k}\gamma^\alpha}{z}. \quad (28)$$

In order to obtain the expressions for M_{ij}^R at other values of i and j (22, 44, 24, 42, etc.), we can use a peculiar symmetry of the expressions in (23):

$$\begin{aligned} (M_{24}^R)_{zz} &= (M_{13}^R)_{zz} \Big|_{k_2 \leftrightarrow p_2} \quad (29) \\ &= \left[(M_{13}^R)_{zz} \Big|_{k_2 \leftrightarrow p_2, k_1 \leftrightarrow p_1} \right] \Big|_{k_1 \leftrightarrow p_1} \\ &= (M_{13}^R)_{vv} \Big|_{k_1 \leftrightarrow p_1} = (M_{13}^R)_{vv} \Big|_{t \leftrightarrow u} \end{aligned}$$

and

$$(M_{24}^R)_{vv} = (M_{13}^R)_{zz} \Big|_{t \leftrightarrow u}. \quad (30)$$

For the cases of 22 and 44, we obtain the analogous result, while, for the interference part (the indices zv and vz), the symmetry is somewhat more complicated:

$$(M_{24}^R)_{zv} + (M_{42}^R)_{vz} = \left[(M_{13}^R)_{vz} + (M_{31}^R)_{zv} \right] \Big|_{t \leftrightarrow u}; \quad (31)$$

similar relations hold for other terms in expression (18). As a result, we can represent the sum in the bremsstrahlung cross section as

$$\begin{aligned} \sum_{j,i=1}^4 (-1)^{i+j} M_{ij}^R &= (M_{11}^R + M_{13}^R + M_{31}^R + M_{33}^R \\ &\quad - M_{12}^R - M_{14}^R - M_{32}^R - M_{34}^R) + (t \leftrightarrow u). \end{aligned} \quad (32)$$

3.3. Isolation of the Infrared Divergence in the R Contribution

Our next task is to isolate the infrared divergence in the bremsstrahlung cross section. For this purpose, we will make use of the method proposed in [8]: first of all, we will find the infrared-divergent parts of the squares of the matrix elements in (23); naturally, they must be proportional to the corresponding Born expressions. On the basis of these results, we will then construct the infrared-divergent part of the R contribution $d\sigma_{IR}^R/dy$ by formula (18). The finite expressions that are obtained from this infrared-divergent part by subtracting divergences,

$$(M_{ij}^R)^F = M_{ij}^R - (M_{ij}^R)^{IR}, \quad (33)$$

will then form [naturally, according to (18) as well] the infrared-finite cross section $d\sigma_F^R/dy$. Thus, the cross section in (18) breaks down into two terms

$$\frac{d\sigma^R}{dy} = \frac{d\sigma_{IR}^R}{dy} + \frac{d\sigma_F^R}{dy}. \quad (34)$$

Upon integration with respect to the variables k and v and upon λ parametrization (the details of

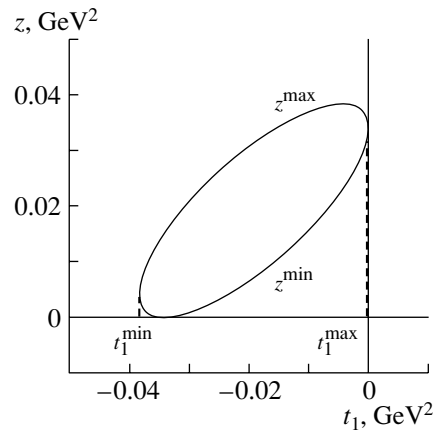


Fig. 5. Domain of integration over the entire phase space of the bremsstrahlung photon ($E = 48$ GeV, $v = s/4$, $y = 0.5$).

this procedure are described in [13]), the infrared-divergent part in expression (34) (the first term there) can be represented in the form

$$\frac{d\sigma_{IR}^R}{dy} = \frac{2\alpha}{\pi} \ln \frac{(v^{\max})^2}{s\lambda^2} \left(\ln \frac{tu}{m^2s} - 1 \right) \frac{d\sigma^0}{dy}. \quad (35)$$

The integrals involved in the bremsstrahlung cross sections will be calculated analytically over the phase space of the bremsstrahlung photon and numerically (since the resulting expressions are very complicated) with respect to the variable v . The integral over the photon phase space can be represented in the form [14]

$$\begin{aligned} I[A] &= \frac{1}{\pi} \int \frac{d^3k}{k_0} \delta[(k_1 + p_1 - k_2 - k)^2 - m^2] [A] \\ &= \frac{1}{\pi} \int_{t_1^{\min}}^{t_1^{\max}} dt_1 \int_{z^{\min}}^{z^{\max}} \frac{dz}{\sqrt{R_z}} [A], \end{aligned} \quad (36)$$

where R_z is a Gram determinant multiplied by -1 ; it can be represented as a polynomial of second degree in z ,

$$R_z = A_z z^2 + 2B_z z + C_z, \quad (37)$$

with the coefficients being given by

$$A_z = 4m^2 t - (v - t)^2, \quad (38)$$

$$B_z = E t_1 + F,$$

$$E = v(u - 2m^2) - st, F = t(2m^2 v + st - sv),$$

$$C_z = -(A t_1^2 + 2B t_1 + C),$$

$$A = (s - v)^2 - 4m^2 s,$$

$$B = -st(s - v - 4m^2) - 2m^2 v^2,$$

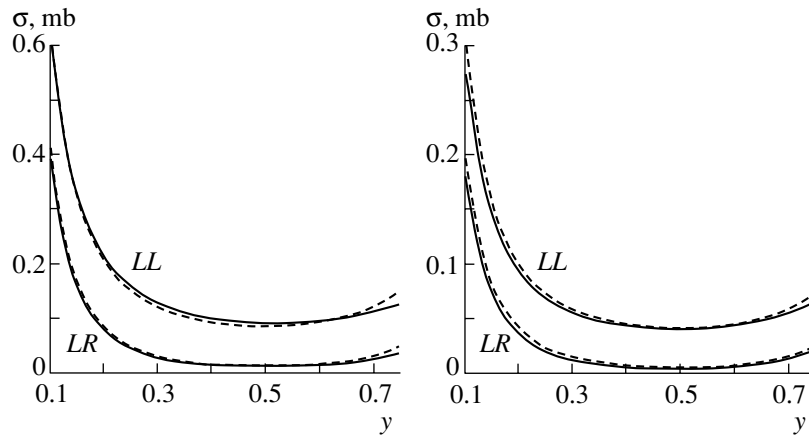


Fig. 6. Cross sections σ_{LL} and σ_{LR} versus y at (left panel) $E = 48$ GeV and (right panel) $E = 100$ GeV: (dashed lines) Born cross sections and (solid lines) cross sections with allowance for radiative corrections.

$$C = st^2(s - 4m^2).$$

The integration limits $z^{\min/\max}$ and $t_1^{\min/\max}$ (see Fig. 5), which are necessary for the calculations, can be found by solving the equations $R_z = 0$ and $z^{\min} = z^{\max}$, respectively. The results are

$$z^{\min/\max} = (-B_z \pm \sqrt{B_z^2 - A_z C_z}) / A_z (A_z < 0), \quad (39)$$

$$t_1^{\min/\max} = \frac{1}{2\tau} (v(t - v) + 2m^2 t \mp v\sqrt{-A_z}), \quad (40)$$

$$\tau = v + m^2,$$

where the upper (lower) sign is for min (max). It should be noted that, here, there is some arbitrariness in choosing variables to which one can go over in performing integration over the phase space of the bremsstrahlung photon (see Appendix).

The expression for $(M_{ij}^R)^F$ was calculated by means of the REDUCE system for analytic calculations [15]. Its role amounted to (a) evaluating the trace in (23), (b) subtracting the infrared divergence according to (33) and (c) summing similar terms. Since the results are rather cumbersome, they are not presented here. In order to reduce the probability of an error in rewriting them, the data obtained as an output of the application of the REDUCE system were transferred, without editing, to the FORTRAN code RCORR2A1¹⁾ (Radiative CORRections TO asymmetry A1) as a set of subroutine functions [for example, the function $\text{MRZ}(p_B, p_T, i, j, s, v, t, t_1, z, 0)$ corresponds to $(M_{ij}^R)_{zz}^F$]. The integrals involved in the calculation are presented in the Appendix. They are

¹⁾This code can be obtained from the present author by e-mail.

also introduced in RCORR2A1 as individual subroutine functions and are tested there for correctness of analytic integration.

3.4. Result of the Cancellation of the Infrared Divergence

Summing the infrared-divergent parts of the V and R contributions [formulas (17) and (35)],

$$\frac{d\sigma^C}{dy} = \frac{d\sigma_{\text{IR}}^V}{dy} + \frac{d\sigma_{\text{IR}}^R}{dy} \quad (41)$$

$$= \frac{4\alpha}{\pi} \ln \frac{v^{\max}}{s} \left(\ln \frac{tu}{m^2 s} - 1 \right) \frac{d\sigma^0}{dy},$$

we arrive at a result that is completely free from infrared divergences and which does not involve unphysical parameters; the index “ C ” on this part of the cross section means the cancellation of the infrared divergence.

4. NUMERICAL ESTIMATES AND CONCLUSIONS

Here, we present the results obtained by numerically estimating the radiative effects considered above. Particular attention will be given to the bremsstrahlung effect on the observed polarization asymmetry $A_{LR}^{(1)}$ in the scattering of longitudinally polarized 45- and 48-GeV electron beams on an unpolarized electron target, this corresponding to the E-158 experiment (SLAC) [1]. We also consider the case corresponding to an electron energy of 100 GeV. In the present study, we take into account only one experimental cut, that which is associated with cutting off the integration domain in the variable v , and construct the FORTRAN code RCORR2A1 in such a way that the resulting formulas are readily

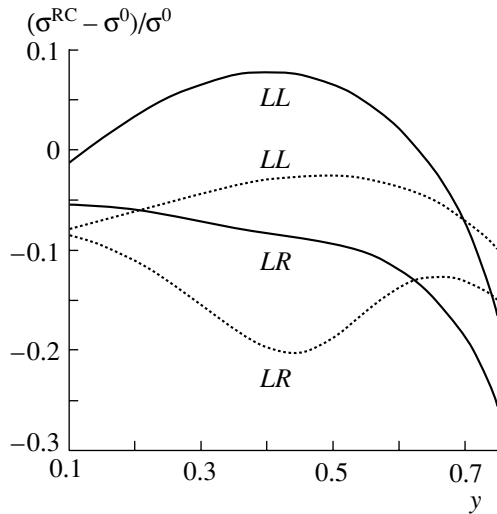


Fig. 7. Corrections to the cross sections: $(\sigma_{LL}^{RC} - \sigma_{LL}^0)/\sigma_{LL}^0$ and $(\sigma_{LR}^{RC} - \sigma_{LR}^0)/\sigma_{LR}^0$. The dotted and solid curves were calculated at $E=100$ GeV and $E=48$ GeV, respectively.

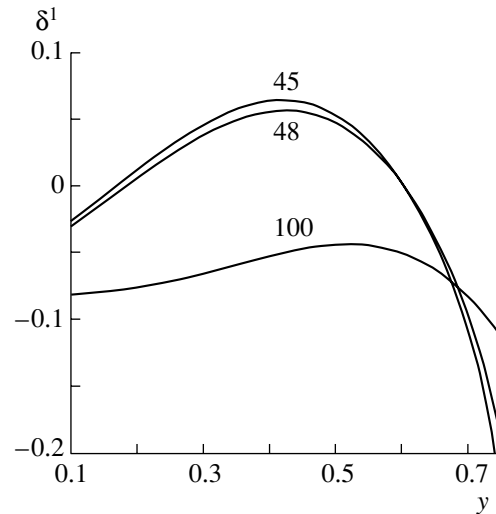


Fig. 8. Corrections δ^1 versus y . The numbers on the curves indicate the values of E in GeV units.

applicable to estimating the correction in question under any experimental conditions. All estimates are given at the electroweak-parameter values of $m_W = 80.451$ GeV, $m_Z = 91.1863$ GeV, and

$$c_W = m_W/m_Z, s_W = \sqrt{1 - c_W^2}. \quad (42)$$

The polarization asymmetry $A_{LR}^{(1)}$ is defined in a standard way:

$$A_{LR}^{(1)} \equiv A = \frac{\sigma_{LL} + \sigma_{LR} - \sigma_{RL} - \sigma_{RR}}{\sigma_{LL} + \sigma_{LR} + \sigma_{RL} + \sigma_{RR}}. \quad (43)$$

Here and below, we use the condensed notation $\sigma \equiv d\sigma/dy$. We define the correction to the asymmetry as the ratio

$$\delta A_{LR}^{(1)} = \frac{A^{RC} - A^0}{A^0}, \quad (44)$$

where A^0 is the Born asymmetry and A^{RC} is the asymmetry with allowance for radiative corrections. Further, the cross section that takes into account electroweak radiative corrections is defined here as the sum

$$\sigma^{RC} = \sigma^0 + \sigma^C + \sigma_F^R. \quad (45)$$

We begin our analysis by considering the Born cross sections σ_{LL}^0 and σ_{LR}^0 and the cross sections allowing for the corrections σ_{LL}^{RC} and σ_{LR}^{RC} . They are displayed in Fig. 6 for the electron-beam energies of $E = 48$ and 100 GeV. It should be noted that, both for the Born cross sections and for the cross section allowing for the corrections, σ_{LL} is close to σ_{RR} (by virtue of the smallness of electroweak effects) and $\sigma_{LR} \equiv$

σ_{RL} . The cross-section ratios $(\sigma_{LL}^{RC} - \sigma_{LL}^0)/\sigma_{LL}^0$ and $(\sigma_{LR}^{RC} - \sigma_{LR}^0)/\sigma_{LR}^0$, which are shown in Fig. 7 at the energies of $E = 48$ and 100 GeV, are also determined almost completely by the electromagnetic component.

Further, we proceed to analyze the effect of radiative corrections on the cross-section components forming the polarization asymmetry. For example, the correction δ^1 defined as

$$\delta^1 = \frac{\sigma_{LL}^{RC} + \sigma_{LR}^{RC}}{\sigma_{LL}^0 + \sigma_{LR}^0} \quad (46)$$

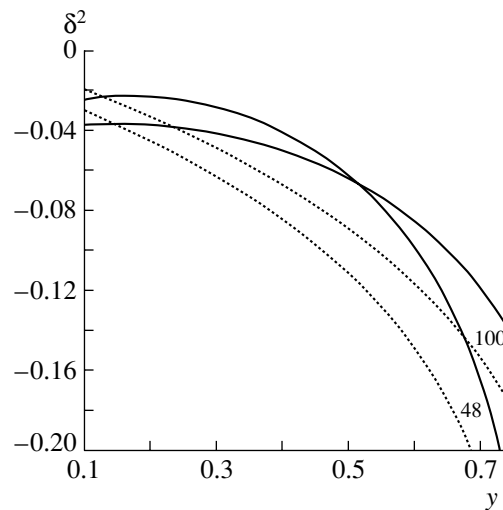


Fig. 9. Corrections δ^2 versus y : (dotted curves) corrections allowing only for electromagnetic effects and (solid curves) corrections allowing for all radiative effects. The numbers on the curves indicate the values of E in GeV units.

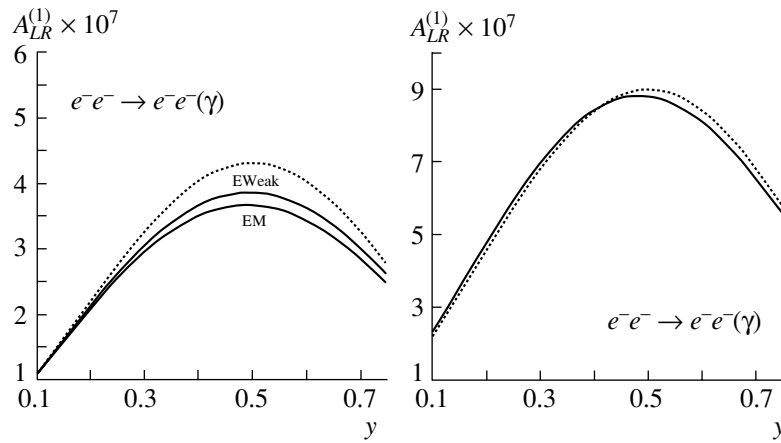


Fig. 10. Polarization asymmetries in Møller scattering versus y : (dotted curves) Born result and (solid curves) asymmetries allowing for radiative corrections (the curves labeled with EM and EWeak in the left panel represent the results including, respectively, only electromagnetic corrections and the total electroweak corrections). The left panel corresponds to the kinematics of the E-158 experiment and the beam energy of $E = 48$ GeV, while the right panel corresponds to the beam energy of $E = 100$ GeV.

and shown in Fig. 8 is virtually independent of electroweak-physics effects. On the contrary, the correction composed from a drastically different combination present in the asymmetry,

$$\delta^2 = \frac{\sigma_{LL}^{RC} - \sigma_{RR}^{RC}}{\sigma_{LL}^0 - \sigma_{RR}^0} \quad (47)$$

(see Fig. 9), depends greatly on the electroweak contribution.

The scale and the behavior of the asymmetry $A_{LR}^{(1)}$ are shown in Fig. 10 (a maximum in the asymmetry at $y = 0.5$ is quite distinct). It can be seen that the inclusion of radiative effects leads to a result below the value in the Born approximation, their influence

becoming more pronounced with increasing y . Since, owing to the structure of the asymmetry in (43), the purely electromagnetic component contributes only to the denominator of the asymmetry in the form of the term $2\sigma_{\gamma\gamma}^{RC,unpol}$ (the indices “unpol” and “ $\gamma\gamma$ ” mean that, in the cross section σ^{RC} , one takes terms corresponding to the scattering of only unpolarized electrons and only via the exchange of photons; it is obvious that $\sigma_{\gamma\gamma}^{RC,unpol} > 0$), this part of the correction reduces the asymmetry, as it must. This effect is partly compensated by “weak” effects (that is, by the contributions to the cross section from the diagrams involving Z -boson exchange and from the interference of the γ and Z diagrams; at comparatively low energies of the E-158 experiment, the effects of weak physics are not expected to exceed purely electromagnetic effects), which increase the asymmetry slightly. Nevertheless, the total effect remains negative at E-158 energies, but, even upon increasing the energy only up to $E = 100$ GeV, the electromagnetic and the “weak” effect compensate each other in the region of small y . It should be noted that the result quoted for the correction in [7] is positive (+4%), which is difficult to explain on the basis of qualitative arguments similar to those presented above. The regularities of the influence of electroweak corrections on the asymmetry are reflected in Fig. 11, which displays the behavior of the correction to the asymmetry $\delta A_{LR}^{(1)}$ versus y at various electron energies. For example, it can be seen that, at the energy of $E = 48$ GeV and at $y = 0.5$ (0.75), the correction is about -11% (-6%); this correction is minimal in the region of intermediate values of y , and it can also clearly be seen that, with

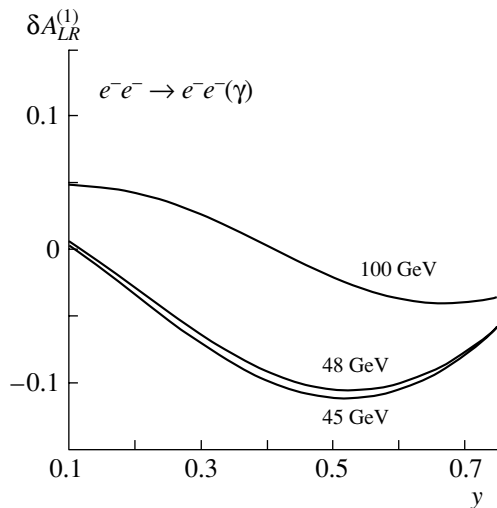


Fig. 11. Corrections to the polarization asymmetry versus y at various beam energies.

increasing energy, this minimum is shifted toward greater values of y .

In summary, electroweak effects of bremsstrahlung in the Møller scattering of polarized particles have been calculated in the present study. Particular attention has been given to investigating the observables of the E-158 experiment (SLAC), where it is planned to measure, with an unprecedented precision, the polarization asymmetry $A_{LR}^{(1)}$. The Bardin–Shumeiko method has been used to remove the infrared divergence. Owing to this, the result does not contain unphysical parameters. The calculations have revealed that, in the region studied by the E-158 experiment, the effects of internal bremsstrahlung reduce the polarization asymmetry $A_{LR}^{(1)}$ significantly; for example, the asymmetry is shifted by about -11% (-6%) at $y = 0.5$ (0.75). The FORTRAN code RCORR2A1 has been written, which makes it possible to apply the formulas quoted above to estimating corrections to the polarization asymmetry measured in the E-158 experiment.

ACKNOWLEDGMENTS

I am grateful to the directorate of SLAC for the kind hospitality extended to me there and for the opportunity of presenting my report at the workshop of the E-158 group. Special thanks are due to Yu. Kolomensky and J. Suarez for the formulation of the problem and to K. Kumar and P. Bosted for stimulating discussions and enlightening comments.

Note added in proof. At present time, the estimates given above changed owing to the removal of inaccuracies in the numerical calculation based on the RCORR2A1 code, the refinement of the kinematical region of the E-158 experiment, and the addition of box diagrams involving a photon that were calculated anew. For example, the correction to the asymmetry in Fig. 11 is about 7% at a beam energy of 48 GeV and $y = 0.5$.

APPENDIX

Scalar Integrals

Here, we present scalar integrals that must be evaluated in calculating the bremsstrahlung cross section. The expressions that are integrated are grouped in such a way that the result is free from infrared divergences. Thereby, we achieve, first, a more compact form of the resulting expressions and, second, the preservation of the required accuracy at the end of the domain of integration with respect to the variable v ($v^{\min} = 0$). Where possible, we

used the approximation motivated by the kinematical conditions of the E-158 experiment; that is,

$$m^2 \ll s, |t|, |u|, v, z, z_1, v_1, |t_1|, |z_2| \ll m_Z^2.$$

The asterisk symbol denotes the substitution $z \rightarrow z_1$ —for example, $I[f(z^n)]^* = I[f(z_1^n)]$. The meaning of the indices i and j is determined here by the first symbol in expression (22)—that is, we have $i = \gamma, Z$ and $j = \gamma, Z$.

First, we present the list of integrals with respect to z that were involved in the calculations:

$$\begin{aligned} J_0 &= \int_{z^{\min}}^{z^{\max}} \frac{dz}{\sqrt{R_z}} = \frac{\pi}{\sqrt{-A_z}}, \\ J_1 &= \int_{z^{\min}}^{z^{\max}} \frac{dz}{z\sqrt{R_z}} = \frac{\pi}{\sqrt{-C_z}}, \\ J_1^* &= \int_{z^{\min}}^{z^{\max}} \frac{dz}{z_1\sqrt{R_z}} = \frac{\pi}{\sqrt{-C_z}} \Big|_{s \leftrightarrow u}, \\ J_2 &= \int_{z^{\min}}^{z^{\max}} \frac{dz}{z^2\sqrt{R_z}} = \frac{\pi B_z}{(-C_z)^{3/2}}, \\ J_2^* &= \int_{z^{\min}}^{z^{\max}} \frac{dz}{z_1^2\sqrt{R_z}} = \frac{\pi B_z}{(-C_z)^{3/2}} \Big|_{s \leftrightarrow u}, \\ J_3 &= \int_{z^{\min}}^{z^{\max}} \frac{z dz}{\sqrt{R_z}} = \frac{\pi B_z}{(-A_z)^{3/2}}, \\ J_4 &= \int_{z^{\min}}^{z^{\max}} \frac{z^2 dz}{\sqrt{R_z}} = \pi \frac{(3B_z^2 - A_z C_z)}{2(-A_z)^{5/2}}, \\ J_5^j &= \int_{z^{\min}}^{z^{\max}} \frac{D^{jz_2} dz}{\sqrt{R_z}} = -\frac{\pi}{\sqrt{-R_p}}, \end{aligned}$$

$$R_p = A_z p^2 - 2B_z p + C_z, \quad p = u - v_1 - m_j^2.$$

Further, we present the lists of expressions integrated with respect to both variables (z and t_1). We arrange them in the same order as they appear in the text of our FORTRAN code. Thus, the integrals evaluated in calculating the term $(M_{ij}^R)_{zz}$ in the bremsstrahlung cross section (the part caused exclusively by photon emission from electrons of 4-momentum k_1 and k_2 —the “upper” electron in Fig. 3) are labeled with the index z and are given by

$$I_{z,1}^{ij} = I \left[\frac{m^2}{z^2} (D^{it} D^{jt} - D^{it_1} D^{jt_1}) \right] = \frac{1}{s} D_v^{it} D_v^{jt}$$

$$\times \left(m_i^2 D^{it} + m_j^2 D^{jt} + \frac{v}{s} (m_i^2 m_j^2 D^{it} D^{jt} - 1) + 2 \right) \quad (i \neq j),$$

$$I_{z,1}^{\gamma\gamma} = \frac{2s - v}{t^2 s^2} - \frac{v(v - t)^2}{t^4 s^2}, \quad I_{z,1}^{ZZ} \approx 0;$$

$$D_v^{it} = \frac{1}{t - m_i^2(1 - v/s)};$$

$$I_{z,2}^{ij} = I \left[\frac{m^2}{z^2} (t D^{it} D^{jt} - t_1 D^{it_1} D^{jt_1}) \right] = \frac{t}{s} D_v^{it} D_v^{jt} \times \left(1 + m_i^2 D^{it} + m_j^2 D^{jt} + \frac{v}{s} m_i^2 m_j^2 D^{it} D^{jt} \right) \quad (i \neq j),$$

$$I_{z,2}^{\gamma\gamma} = \frac{1}{st}, \quad I_{z,2}^{ZZ} \approx 0;$$

$$I_{z,3}^{ij} = I \left[\frac{m^2}{z^2} (t^2 D^{it} D^{jt} - t_1^2 D^{it_1} D^{jt_1}) \right]$$

$$= \frac{t^2}{s} D_v^{it} D_v^{jt} (m_i^2 D^{it} + m_j^2 D^{jt} + \frac{v}{s} m_i^2 m_j^2 D^{it} D^{jt});$$

$$I_{z,4}^{ij} = I \left[\frac{D^{it} D^{jt} - D^{it_1} D^{jt_1}}{zz_1} \right],$$

$$I_{z,4}^{\gamma Z} \equiv I_{z,4}^{Z\gamma} \approx \frac{1}{tm_Z^2} (I_{z,10}^\gamma - I_{z,10}^{\gamma*});$$

$$I_{z,6}^{ij} = I \left[\frac{D^{it_1} D^{jt_1}}{z} \right],$$

$$I_{z,6}^{\gamma Z} \equiv I_{z,6}^{Z\gamma} \approx -\frac{1}{m_Z^2} I_{z,10}^\gamma;$$

$$I_{z,7}^{ij} = I \left[\frac{t_1 D^{it_1} D^{jt_1}}{z} \right],$$

$$I_{z,7}^{\gamma\gamma} = I_{z,10}^\gamma, \quad I_{z,7}^{Z\gamma} \equiv I_{z,7}^{Z\gamma} \equiv I_{z,10}^Z \approx -\frac{1}{m_Z^2} I_{z,12};$$

$$I_{z,8}^{ij} = I \left[\frac{t_1^2 D^{it_1} D^{jt_1}}{z} \right],$$

$$I_{z,8}^{\gamma\gamma} = I_{z,12}, \quad I_{z,8}^{Z\gamma} \equiv I_{z,8}^{Z\gamma} \approx -\frac{1}{m_Z^2} I \left[\frac{t_1}{z} \right];$$

$$I_{z,9}^{ij} = I [t_1 D^{it_1} D^{jt_1}],$$

$$I_{z,9}^{\gamma\gamma} = \frac{1}{\sqrt{-A_z}} \ln \frac{m^2 t^2}{\tau(t - v)^2},$$

$$I_{z,9}^{\gamma Z} \equiv I_{z,9}^{Z\gamma} = \frac{1}{\sqrt{-A_z}} \ln \frac{m_Z^2}{m_Z^2 + v - t};$$

$$I_{z,10}^i = I \left[\frac{D^{it_1}}{z} \right]$$

$$= -\frac{1}{\sqrt{c}} \ln \frac{(st + m_i^2(v - s))^2}{m^2(m^2(m_i^2 - t)^2 - m_i^2 v p_z)},$$

$$c = Am_i^4 + 2Bm_i^2 + C, \quad p_z = t - v - m_i^2;$$

$$I_{z,11} = I \left[\frac{1}{zz_1} \right] = \frac{2}{v\sqrt{t(t - 4m^2)}} L_m,$$

$$L_m = \ln \frac{|t|}{m^2};$$

$$I_{z,12} = I \left[\frac{1}{z} \right] = \frac{1}{\sqrt{A}} L_A, \quad L_A = \ln \frac{(s - v)^2}{m^2 \tau}.$$

The integrals from the terms $(M_{ij}^R)_{zv}$ and $(M_{ij}^R)_{vz}$ (these are the parts corresponding to the interference between photon emission from electrons of 4-momentum k_1 and k_2 and emission from electrons of 4-momenta p_1 and p_2 —the “lower” electron in Fig. 3) are labeled with the index zv and can be written as

$$I_{zv,1}^i = I \left[\frac{D^{it} - D^{it_1}}{zv} \right] = (D^{it} I_{z,12} - I_{z,10}^i)/v;$$

$$I_{zv,2}^i = I \left[\frac{t D^{it} - t_1 D^{it_1}}{zv} \right] = m_i^2 I_{zv,1}^i;$$

$$I_{zv,3}^i = I \left[\frac{t^2 D^{it} - t_1^2 D^{it_1}}{zv} \right],$$

$$I_{zv,3}^\gamma = \frac{t}{v - s} I_{z,12} - \frac{-st + uv}{\tau A},$$

$$I_{zv,3}^Z = -\frac{1}{2m_Z^2 A} \left(2t^2(v - 2s)I_{z,12} - (v - t)|u| - \frac{3B(|u|v - s|t|)}{\tau A} \right);$$

$$I_{zv,4}^i = I \left[\frac{D^{it} - D^{it_1}}{zv_1} \right]$$

$$= -\frac{D^{it}}{|4m^2 - u|p_z} \ln \frac{(4m^2 - u)^2}{m^4} + \frac{1}{p_z} I_{z,10}^i;$$

$$I_{zv,5} = I \left[\frac{v}{zv_1} \right] = \frac{1}{|4m^2 - u|} \ln \frac{(4m^2 - u)^2}{m^4};$$

$$I_{zv,7}^i = I \left[\frac{t_1 D^{it_1}}{z} \right] = I_{z,12} + m_i^2 I_{z,10}^i;$$

$$I_{zv,8}^i = I \left[\frac{t_1^2 D^{it_1}}{z} \right],$$

$$I_{zv,8}^\gamma \equiv I \left[\frac{t_1}{z} \right] = -\frac{v}{\tau} \frac{|u|v - s|t|}{A} - \frac{B}{A} I_{z,12},$$

$$I_{zv,8}^Z \approx -\frac{1}{m_Z^2} I \left[\frac{t_1^2}{z} \right] = -\frac{1}{2m_Z^2 A^2}$$

$$\times (-3B|st| - (A(t - v) - 3B)|uv| + 2B^2 I_{z,12});$$

$$I_{zv,10}^i = I \left[\frac{D^{it_1}}{v_1} \right] = -\frac{1}{(v - t)p_z}$$

$$\times \ln \frac{(m^2(t - m_i^2)^2 - m_i^2 v p_z)m^2}{p_z^2(t - v)^2};$$

$$\begin{aligned}
 I_{zv,11}^i &= I \left[\frac{zD^{it_1}}{v_1} \right] \\
 &= -\frac{1}{p_z} \left(vI_{zv,14}^i - \frac{vE}{(v-t)^2\tau} + \frac{vu}{(v-t)^2}L_u \right), \\
 L_u &= \ln \frac{(t-v)^2}{m^2v}; \\
 I_{zv,12}^i &= I \left[\frac{D^{it_1}}{v} \right] = \frac{1}{v(v-t)}L_t^i, \\
 L_t^i &= \ln \left| \frac{m^2(t-m_i^2)^2 - m_i^2vp_z}{\tau p_z^2} \right|; \\
 I_{zv,13}^i &= I \left[\frac{t_1D^{it_1}}{v} \right], \\
 I_{zv,13}^\gamma &= \frac{1}{\tau}, \quad I_{zv,13}^Z \approx \frac{v-t}{2m_Z^2\tau}; \\
 I_{zv,14}^i &= I \left[\frac{zD^{it_1}}{v} \right], \\
 I_{zv,14}^\gamma &= \frac{E}{(v-t)^2\tau} + \frac{F}{(v-t)^3v}L_t^\gamma, \\
 I_{zv,14}^Z &\approx \frac{st+vu}{2\tau m_Z^2(v-t)}.
 \end{aligned}$$

The integrals that had to be evaluated in calculating the term $(M_{ij}^R)_{vv}$ (this is the part corresponding to photon emission from the “lower” electron) are labeled with the index v . Since these integrals do not involve propagators, they are independent of the intermediate-vector-boson mass and, hence, coincide with the expressions from the calculation of the R contribution for the case where only photons are exchanged [3]. The same is true for the cross-section component $(M_{ij}^R)_{tu}$, which corresponds to the interference between emission from the “lower” electron in the t channel and emission from the “lower” electron in the u channel. Thus, the integrals I_v and I_{tu} are not presented here.

Further, we consider the integrals corresponding to the interference between emission from the “upper” t -channel electron and emission from the “lower” u -channel electron. They are contained in the component $(M_{ij}^R)_f$ and are labeled with the index f . We have

$$\begin{aligned}
 I_{f,2}^i &= I \left[\frac{D^{it} - D^{it_1}}{zz_1} \right] = D^{it}(I_{z,10}^{i*} - I_{z,10}^i); \\
 I_{f,3}^i &= I \left[\frac{tD^{it} - t_1D^{it_1}}{zz_1} \right] \\
 &= D^{it}(-I_{z,12}^{i*} + I_{z,12} + I_{zv,7}^{i*} - I_{zv,7}^i); \\
 I_{f,4}^i &= I \left[\frac{t^2D^{it} - t_1^2D^{it_1}}{zz_1} \right]
 \end{aligned}$$

$$\begin{aligned}
 &= D^{it}(-I_{zv,8}^{\gamma*} \\
 &+ I_{zv,8}^\gamma - tI_{z,12}^{i*} + tI_{z,12} + I_{zv,8}^{i*} - I_{zv,8}^i); \\
 I_{f,5}^i &= I \left[\frac{v}{zz_1} \right] = vI_{z,11}; \\
 I_{f,8}^i &\equiv I_{zv,1}^{i*}; \quad I_{f,9}^i \equiv I_{zv,2}^{i*}; \\
 I_{f,10}^i &\equiv I_{zv,3}^{i*}; \\
 I_{f,14}^i &= I \left[\frac{m^2(D^{it} - D^{it_1})}{z_1^2} \right] \\
 &= \left(\frac{D_v^{it}}{s} \right) \Big|_{s \leftrightarrow u} tD^{it}; \\
 I_{f,15}^i &= I \left[\frac{m^2(tD^{it} - t_1D^{it_1})}{z_1^2} \right] \\
 &= \left(\frac{m_i^2 D_v^{it}}{s} \right) \Big|_{s \leftrightarrow u} tD^{it}; \\
 I_{f,16}^i &= I \left[\frac{m^2(t^2D^{it} - t_1^2D^{it_1})}{z_1^2} \right] \\
 &= \left(\frac{m_i^2 D_v^{it} - 1}{s-v} \right) \Big|_{s \leftrightarrow u} t^2D^{it}; \\
 I_{f,17}^i &\equiv I_{zv,8}^{i*}; \quad I_{f,18}^i \equiv I_{zv,7}^{i*}; \\
 I_{f,19}^i &\equiv I_{z,10}^{i*}; \quad I_{f,20}^i \equiv vI_{zv,14}^i; \\
 I_{f,21}^i &\equiv vI_{zv,13}^i; \quad I_{f,22}^i \equiv vI_{zv,12}^i; \\
 I_{f,23} &\equiv I_{z,12}^{i*}; \quad I_{f,24} = I \left[\frac{m^2v}{z_1^2} \right] = 1.
 \end{aligned}$$

The integrals corresponding to the interference between emission from the “lower” t -channel electron and emission from the “lower” u -channel electron are contained in the component $(M_{ij}^R)_s$ and are labeled with the index s (the specific invariant quantity z_2 manifests itself in it; therefore, it is more convenient, in a number of cases, to perform integration with respect to the variables v_1 and z_1 or with respect to the variables z and z_1). The results are

$$\begin{aligned}
 I_{s,1}^j &= I \left[\frac{D^{ju} - D^{jz_2}}{zv} \right] = \left(D^{ju}I_{z,12} + \frac{1}{d_{z_2}}L_{s_1} \right) / v, \\
 d_{z_2} &= -su + m_j^2(s-v), \quad p_s = u-v-m_j^2, \\
 L_{s_1} &= \ln \frac{d_{z_2}^2}{m^2p_s(m^2p_s - m_j^2v)}; \\
 I_{s,3}^j &= I \left[\frac{D^{jz_2}}{z} \right] = -\frac{1}{d_{z_2}}L_{s_1}; \\
 I_{s,4}^j &= I \left[\frac{D^{ju} - D^{jz_2}}{v_1v} \right] \\
 &= \left(D^{ju} \frac{1}{\sqrt{-A_z}}L_u + \frac{1}{d_{z_1}}L_{s_4} \right) / v,
 \end{aligned}$$

$$\begin{aligned}
d_{z_1} &= tu + m_j^2(v - t), \\
L_{s_4} &= \ln \frac{d_{z_1}^2 \tau}{m^2 v p_s (m^2 p_s - m_j^2 v)}; \\
I_{s,7}^j &= I \left[\frac{D^{jz_2}}{v_1} \right] = -\frac{1}{d_{z_1}} L_{s_4}; \\
I_{s,10}^j &= I \left[\frac{D^{jz_2}}{v} \right] = \frac{1}{(s+t)v} \ln \left| 1 + \frac{v(s+t)}{\tau p_s} \right|; \\
I_{s,11}^j &= I \left[\frac{D^{jz_2 z}}{v} \right] = \frac{E_s}{\tau(s+t)^2} \\
&\quad + \frac{F_s - E_s p_s}{(s+t)^3 v} \ln \left| 1 + \frac{v(s+t)}{\tau p_s} \right|, \\
E_s &= s(s+t) - v(s-t), \quad F_s = -vt(s+t); \\
I_{s,12}^j &\equiv v I_{s,10}^j; \\
I_{s,13}^j &= I \left[\frac{m^2(D^{ju} - D^{jz_2})}{v_1^2} \right] = \frac{u}{d_{z_1}} D^{ju}.
\end{aligned}$$

The integrals corresponding to the interference of emission from the “upper” t -channel electron and emission from the “upper” u -channel electron—these are contained in the component $(M_{ij}^R)_l$ and are labeled with the index l (for the sake of simplicity and in order to improve the accuracy of the calculations, some of these integrals were brought together into combinations labeled with the index ll)—can be written as

$$\begin{aligned}
I_{l,1}^{ij} &= I \left[\frac{m^2}{z^2} (D^{it} D^{ju} - D^{it_1} D^{jz_2}) \right], \\
I_{l,1}^{\gamma\gamma} &= \frac{2s-v}{s^2 t u}, \quad I_{l,1}^{Z\gamma} \approx -\frac{1}{m_Z^2 s t}, \\
I_{l,1}^{Z\gamma} &\approx -\frac{1}{m_Z^2 s u}, \quad I_{l,1}^{ZZ} \approx 0; \\
I_{l,2}^{ij} &= I \left[\frac{1}{z z_1} (D^{it} D^{ju} - D^{it_1} D^{juv}) \right] \\
&= D^{it} D^{juv} (-D^{ju} I_{f,5} + I_{z,10}^{i*} - I_{z,10}^i), \\
D^{juv} &= \frac{1}{u-v-m_j^2}; \\
I_{l,4}^i &= I \left[\frac{1}{z v_1} (D^{it} - D^{itv}) \right] = -D^{it} D^{itv} I_{z v,5}^i, \\
D^{itv} &= \frac{1}{t-v-m_i^2}; \\
I_{l,6}^{ij} &= I \left[\frac{1}{z} D^{it_1} D^{jz_2} \right], \\
I_{l,6}^{\gamma\gamma} &= -\frac{1}{s} \left(I_{z,10}^\gamma - I_{l,13}^{\gamma\gamma} + \frac{2}{s u} \ln \frac{s}{m^2} \right),
\end{aligned}$$

$$\begin{aligned}
I_{l,6}^{Z\gamma} &\approx -\frac{1}{m_Z^2} I_{z,10}^\gamma, \quad I_{l,6}^{Z\gamma} \approx -\frac{1}{m_Z^2} I_{s,3}^\gamma, \quad I_{l,6}^{ZZ} \approx 0; \\
I_{l,8}^{ij} &= I \left[\frac{1}{z_1 v_1} (D^{it} D^{ju} - D^{itv} D^{juv}) \right] \\
&= \frac{s+m_i^2+m_j^2}{s} D^{it} D^{ju} D^{itv} D^{juv} \ln \frac{s^2}{m^4}; \\
I_{l,9}^i &\equiv I_{z,10}^{i*}; \quad I_{l,10} \equiv I_{z,12}^*; \\
I_{l,13}^{ij} &= I [D^{it_1} D^{jz_2}], \\
I_{l,13}^{\gamma\gamma} &= \frac{2}{\sqrt{s^2 v^2 - 4st(s+t)m^2}} \ln \frac{sv^2}{m^2 ut}, \\
I_{l,13}^{Z\gamma} &\approx -\frac{1}{m_Z^2 (v-t)} \ln \frac{m^2 t^2}{\tau(t-v)^2}, \\
I_{l,13}^{Z\gamma} &\approx -\frac{1}{m_Z^2 (s+t)} \ln \frac{m^2}{\tau}, \quad I_{l,13}^{ZZ} \approx 0; \\
I_{ll,1}^i &= I \left[\frac{v D^{it_1}}{z z_1} \right] = D^{it} (I_{f,5} - v I_{z,10}^{i*} + v I_{z,10}^i); \\
I_{ll,2} &= I \left[\frac{D^{\gamma t} - D^{\gamma tv}}{z_1 v_1} \right] = -\frac{1}{st(t-v)} \ln \frac{s^2}{m^4}.
\end{aligned}$$

REFERENCES

1. K. S. Kumar *et al.*, Mod. Phys. Lett. A **10**, 2979 (1995); R. Carr *et al.*, SLAC-PROPOSAL-E-158.
2. G. Alexander and I. Cohen, hep-ex/0006007.
3. N. M. Shumeiko and J. G. Suarez, J. Phys. G **26**, 113 (2000).
4. C. A. Heush, Int. J. Mod. Phys. A **15**, 2347 (2000).
5. A. Czarnecki and W. Marciano, Phys. Rev. D **53**, 1066 (1996).
6. A. Denner and S. Pozzorini, Eur. Phys. J. C **7**, 185 (1999).
7. F. J. Petriello, SLAC-PUB-9532 (Oct. 2002); hep-ph/0210259.
8. D. Yu. Bardin and N. M. Shumeiko, Nucl. Phys. B **127**, 242 (1977); Yad. Fiz. **29**, 969 (1979) [Sov. J. Nucl. Phys. **29**, 499 (1979)].
9. M. Böhm *et al.*, Fortsch. Phys. **34**, 687 (1986).
10. W. Hollik, Fortsch. Phys. **38**, 165 (1990).
11. M. Böhm and H. Spiesberger, Nucl. Phys. B **294**, 1081 (1987).
12. G. F. Chew and F. E. Low, Phys. Rev. **113**, 1640 (1959).
13. N. M. Shumeiko, S. I. Timoshin, and V. A. Zykunov, J. Phys. G **23**, 1593 (1997).
14. E. Byckling and K. Kajantie, *Particle Kinematics* (Macmillan, London, 1973; Mir, Moscow, 1975).
15. A. C. Hearn, *REDUCE User's Manual for Version 3.4.1*, RAND Santa Monica, CA 90407-2138 (1992).

Translated by A. Isaakyan

ELEMENTARY PARTICLES AND FIELDS
Theory

S Wave of Pion–Pion Scattering from Data on the Reaction $\pi^-p \rightarrow \pi^0\pi^0n$

N. N. Achasov* and G. N. Shestakov**

*Institute of Mathematics, Siberian Division, Russian Academy of Sciences,
pr. Akademika Koptyuga 4, Novosibirsk, 630090 Russia*

Received March 17, 2003

Abstract—The results of recent experiments performed at KEK, Brookhaven National Laboratory, the Institute for High-Energy Physics (Protvino), and CERN to study the reaction $\pi^-p \rightarrow \pi^0\pi^0n$ are analyzed in detail. For S -wave pion–pion scattering in the channel of isospin $I = 0$, new data are obtained for the phase shift δ_0^0 and the inelasticity parameter η_0^0 . Difficulties that arise in using, for the amplitudes of the S and D waves of the final $\pi^0\pi^0$ system, physical solutions selected on the basis of partial-wave analyses are discussed. It is noteworthy that other solutions are preferable in principle in the region of the invariant mass m of the $\pi^0\pi^0$ system above 1 GeV. With the aim of clarifying the situation and further studying the properties of the $f_0(980)$ resonance, it is proposed to perform, in the reaction $\pi^-p \rightarrow \pi^0\pi^0n$, an especially careful examination of the m region in the vicinity of the $K\bar{K}$ threshold.

© 2004 MAIK “Nauka/Interperiodica”.

1. INTRODUCTION

Reactions of the $\pi N \rightarrow \pi\pi N$ type, which, at high energies and low values of the square of the 4-momentum transfer from the incident pion to the final dipion system ($0 < -t < 0.2 \text{ GeV}^2$), are dominated by the one-pion-exchange mechanism, are one of the main sources of information about $\pi\pi \rightarrow \pi\pi$ processes. The method of partial-wave analysis is used to treat data on these reactions. As a rule, a number of possible solutions are obtained for the amplitudes of partial waves of the final dipion system. In some cases, the only solution is selected on the basis of additional physical arguments. In general, vast statistics, the use of polarized targets, and precise measurements of absolute cross-section values for $\pi N \rightarrow \pi\pi N$ reactions at various energies are required for obtaining reliable and unambiguous results over a broad range of m values. Relevant surveys and detailed discussions on the results of experimental investigations performed for $\pi N \rightarrow \pi\pi N$ reactions and pion–pion scattering over the region $2m_\pi < m < 2 \text{ GeV}$ by the beginning of 1999 can be found in [1, 2].

In the present study, we analyze the latest data on the intensities and the relative phase of the S and D waves of the $\pi^0\pi^0$ system produced in the reaction $\pi^-p \rightarrow \pi^0\pi^0n$ over the range of m values between 0.32 and 1.64 GeV. These data were obtained at KEK [3], Brookhaven National Laboratory

(BNL) [4], the Institute for High Energy Physics (IHEP, Protvino) [5], and CERN [6] at incident-pion energies of 8.9, 18.3, 38, and 100 GeV, respectively. The main objective of our analysis is to determine the phase shift δ_0^0 and the inelasticity parameter η_0^0 for S -wave pion–pion scattering through the channel of isotopic spin $I = 0$; these new results would be supplementary to old “canonical” data extracted from experiments that studied the reaction $\pi^-p \rightarrow \pi^+\pi^-n$ at an energy of 17.2 GeV [7–12]. We pay special attention to a similarity of physical solutions selected as the result of partial-wave analyses for all four experiments that studied the production of $\pi^0\pi^0$ systems and to common difficulties arising in attempts at interpreting these data and at comparing them with data on the production of $\pi^+\pi^-$ systems. It turns out, among other things, that some of these solutions lead to strong violations of the unitarity condition for the $\pi\pi$ -scattering amplitude under study. Moreover, it can be concluded that, for the branching fraction of the decay process $f_2(1270) \rightarrow \pi\pi$, data on the production of $\pi^0\pi^0$ systems suggest a value that is considerably smaller than that which is quoted by the Particle Data Group (PDG) [13]. In view of great interest in the sector of light scalar resonances (see, for example, the review articles in [1, 2, 13–15]), we propose performing especially thorough measurements of the reaction $\pi^-p \rightarrow \pi^0\pi^0n$ in the range of m values between 0.9 and 1.1 GeV—that is, in the region of the $K\bar{K}$ threshold—because this would make it possible to determine more reliably the coupling of the $f_0(980)$ resonance to the $K\bar{K}$ channel and to solve the long-

* e-mail: achasov@math.nsc.ru

** e-mail: shestako@math.nsc.ru

standing question [16] of a possible ambiguity in the behavior of the phase shift δ_0^0 above the $K\bar{K}$ threshold.

The ensuing exposition is organized as follows. In Section 2, we analyze the results of the KEK experiments [3], in which data on the phase shift δ_0^0 were obtained in the region of m values between 0.36 and 1 GeV. The δ_0^0 values that we found by a different method over the m range between 0.68 and 1 GeV agree with the data from [3] within the errors. We also quote new results for δ_0^0 and η_0^0 in the range $1 < m < 1.64$ GeV. In Section 3, the S - and D -wave mass distributions obtained in the BNL experiment [4] are extrapolated from the physical region of the reaction $\pi^-p \rightarrow \pi^0\pi^0n$ to the pion-pole point ($t = m_\pi^2$). Considering various solutions found in [4] for these distributions, we determine a few sets of values for δ_0^0 and η_0^0 in the range of m values between 0.32 and 1.52 GeV. The results of the GAMS Collaboration [5, 6] for the reaction $\pi^-p \rightarrow \pi^0\pi^0n$ are discussed in Section 4. There, we also summarize all difficulties indicated in the course of our consideration that are associated with the physical solutions presented in [3–6] and with the normalization of data on the production of $\pi^0\pi^0$ systems. In the Conclusions, we briefly formulate a few specific proposals concerning a further investigation of the reaction $\pi^-p \rightarrow \pi^0\pi^0n$. We hope that they will be used to clarify the current experimental situation.

2. ANALYSIS OF THE KEK DATA

In the KEK experiments [3], data on the intensities of the S and D waves in the process $\pi^+\pi^- \rightarrow \pi^0\pi^0$ and on the relative phase of the respective amplitudes were obtained over the interval of m values between 0.36 and 1.64 GeV. With the aid of the Chew–Low linear extrapolation and a partial-wave analysis, these data were extracted from experiments that studied the reaction $\pi^-p \rightarrow \pi^0\pi^0n$. Since the absolute value of the cross section for the production of the $\pi^0\pi^0$ system was not determined in [3], the intensities of the S and D waves ($|A_S|^2$ and $|A_D|^2$, respectively) were initially presented in identical arbitrary units. No alternative solutions for $|A_S|^2$ and $|A_D|^2$ were discussed in [3]. The intensity of the S wave is related to the phase shifts δ_0^I and the inelasticity parameters η_0^I in a standard way; that is, $|A_S|^2 \sim |a_0^0 - a_0^2|^2$, where $a_0^I = (\eta_0^I \exp(2i\delta_0^I) - 1)/(2i)$. Similarly, we have $|A_D|^2 \sim |a_2^0 - a_2^2|^2$, where $a_2^I = (\eta_2^I \exp(2i\delta_2^I) - 1)/(2i)$. In order to find the phase shift δ_0^0 , it was assumed in [3] that the relation $\eta_0^0 = \eta_0^2 = 1$ holds below the $K\bar{K}$ threshold, in which case $|A_S|^2 \sim \sin^2(\delta_0^0 - \delta_0^2)$. Since it is well-known from many previous experiments

that, with increasing m , the phase shift δ_0^0 , which increases smoothly, passes through the value of 90° in the range $0.7 < m < 0.9$ GeV and that the phase shift $\delta_0^2 < 0$ is smooth and is modest in magnitude (see, for example, [2, 7, 8, 17]), the normalization condition $\max(|A_S|^2) = 1$ was adopted in [3] in order to evaluate the difference $\delta_0^0 - \delta_0^2$. The KEK data normalized in this way that were obtained in [3] for the intensities of the S and D waves are displayed in Fig. 1, along with data on the relative phase $\delta = \phi_S - \phi_D$ of the amplitudes $A_S = |A_S| \exp(i\phi_S)$ and $A_D = |A_D| \exp(i\phi_D)$. In [3], the parametrization $\delta_0^2 = -0.87q$ (where $q = (m^2/4 - m_\pi^2)^{1/2}$ and δ_0^2 are taken in GeV and radians, respectively) was employed for the $I = 2$ phase shift of the S wave, and data for δ_0^0 in the m range between 0.36 and 1 GeV were obtained in this way. In the following, we will use, for δ_0^2 , the fit to data from [17, 18] in Fig. 2.¹⁾ Using this fit and the data on $|A_S|^2$ in Fig. 1a, we have also evaluated the phase shift δ_0^0 for $m < 1$ GeV (see Fig. 1d), and the results proved to be nearly coincident with those presented in [3].

We will now determine simultaneously the phase shift δ_0^0 and the inelasticity parameter η_0^0 in the range of m values between 0.68 and 1.64 GeV, invoking data on the relative phase δ and the intensity $|A_S|^2$ (see Figs. 1c and 1a). Taking into account the present-day accuracy of data on the D wave (see Fig. 1b), we can disregard the small amplitude a_2^2 [17, 18] in estimating the phase shift ϕ_D and assume that the D -wave amplitude is saturated by the contribution of the $f_2(1270)$ resonance and is given by

$$A_D = \frac{m_{f_2} B_{f_2\pi\pi} \Gamma}{m_{f_2}^2 - m^2 - im_{f_2} \Gamma}, \quad (1)$$

where m_{f_2} is the mass of the $f_2(1270)$ resonance, $B_{f_2\pi\pi}$ is the branching fraction of its decay into the $\pi\pi$ system, and $\Gamma = (m_{f_2}/m) \Gamma_{f_2}(q/q_{f_2})^5 \times D(q_{f_2} R_{f_2})/D(q R_{f_2})$. In the last expression, $D(x) = 9 + 3x^2 + x^4$, $q_{f_2} = (m_{f_2}^2/4 - m_\pi^2)^{1/2}$, R_{f_2} is the interaction range, and Γ_{f_2} is the width of the $f_2(1270)$ resonance. The fit in Fig. 1b corresponds to the

¹⁾This fit was constructed by means of the parametrization $\delta_0^2 = aq/(1 + bm^2 + cm^4 + dm^6)$, where a , b , c , and d are adjustable parameters. For want of reliable data on the deviation of η_0^2 from unity, we set $\eta_0^2 = 1$ for all values of m . Upon obtaining more or less reliable data on η_0^2 , it would be of interest to take into account possible inelastic effects as well. It is natural to expect sizable manifestations of inelasticity in the $I = 2$ pion–pion channel only for $m > 1.54$ GeV—that is, above the actual $\rho\rho$ threshold rather than above the $K\bar{K}$ threshold, as in the case of the $I = 0$ pion–pion channel.

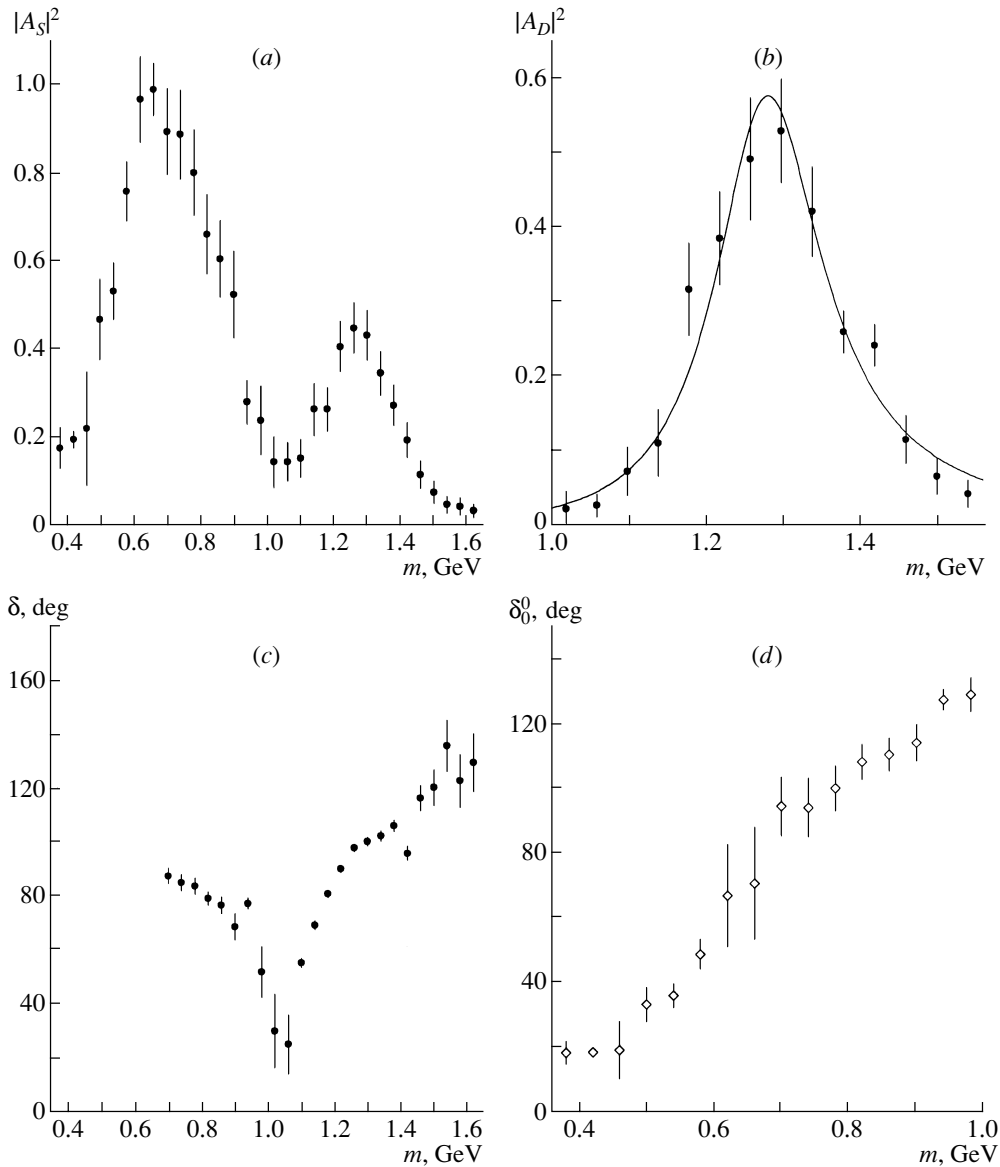


Fig. 1. KEK data [3] on the reaction $\pi^+\pi^- \rightarrow \pi^0\pi^0$: (a) normalized intensity $|A_S|^2$ of the S wave; (b) normalized intensity $|A_D|^2$ of the D wave [the curve represents a fit to the data in terms of the form in (1) with the parameters of the $f_2(1270)$ resonance that are set to those in (2)]; (c) relative phase δ of the amplitudes of the S and D waves; and (d) phase shift δ_0^0 in the S wave of pion-pion scattering through the $I = 0$ channel according to data on $|A_S|^2$ under the assumption that $\eta_0^0 = 1$.

following values of the parameters of this resonance:

$$\begin{aligned}
 m_{f_2} &= 1.283 \pm 0.008 \text{ GeV}, \\
 \Gamma_{f_2} &= 0.170 \pm 0.014 \text{ GeV}, \\
 R_{f_2} &= 3.59 \pm 0.71 \text{ GeV}^{-1}, \\
 B_{f_2\pi\pi} &= 0.760 \pm 0.034.
 \end{aligned}
 \tag{2}$$

Thus, ϕ_D is specified as the phase of the Breit-Wigner amplitude (1). In order to express the sought parameters δ_0^0 and η_0^0 in terms of the known values of δ , $|A_S|^2$, δ_0^2 , and ϕ_D , it is convenient to represent the

amplitude A_S in the form (see footnote 1))

$$\begin{aligned}
 A_S &= e^{2i\delta_0^2} \eta_0^0 \frac{e^{2i(\delta_0^0 - \delta_0^2)} - 1}{2i} \\
 &= e^{2i\delta_0^2} \tilde{A}_S = e^{i(2\delta_0^2 + \phi)} |\tilde{A}_S|,
 \end{aligned}
 \tag{3}$$

where ϕ is the phase of the amplitude \tilde{A}_S , which is characterized by the fact that, for it, the relationships between $\delta_0^0 - \delta_0^2$, ϕ , η_0^0 , and $|\tilde{A}_S|$ in the Argand diagram have the same form as the relationships between the corresponding parameters of any unitary partial-wave amplitude of specific isospin—for example, the phase ϕ lies within the interval $0^\circ - 180^\circ$, since

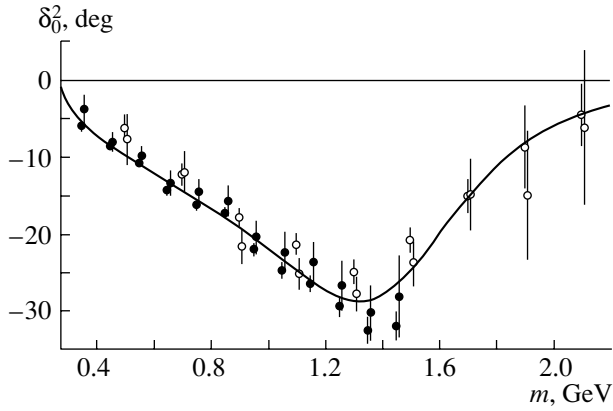


Fig. 2. Phase shift in the S wave of pion–pion scattering through the $I = 2$ channel. The displayed data were borrowed from (closed circles) [17] and (open circles) [18]. The curve represents the fit to the data that was constructed on the basis of the procedure described in the main body of the text.

$\text{Im}(\tilde{A}_S) > 0$. Thus, we obtain

$$\phi = \delta - 2\delta_0^2 + \phi_D, \quad (4)$$

$$\eta_0^0 = \sqrt{1 - 4|A_S| \sin \phi + 4|A_S|^2},$$

$$\sin[2(\delta_0^0 - \delta_0^2)] = \frac{2|A_S| \cos \phi}{\eta_0^0}, \quad (5)$$

$$\cos[2(\delta_0^0 - \delta_0^2)] = \frac{1 - 2|A_S| \sin \phi}{\eta_0^0}.$$

Since information about δ is extracted from data on the product $|A_S||A_D| \cos \delta$ and since $\cos \delta$ does not determine the sign of the relative phase of the S and D waves, there are also two solutions for δ , one in which $\delta > 0$ and the other in which $\delta < 0$. This is not the whole story, however: if $\cos \delta$ is close to unity in some region of m , there can occur a transition from one solution to the other. The KEK data from [3] in Fig. 1c indicate that the phase shift δ undergoes the sharpest variations in the vicinity of the $K\bar{K}$ threshold [this is a manifestation of the $f_0(980)$ resonance] and that $\cos \delta \approx 1$ at $m \approx 1$ GeV. Thus, we have in principle four possible versions: (i) $\delta > 0$ for $m < 1$ GeV and $\delta < 0$ for $m > 1$ GeV, (ii) $\delta > 0$ for all m , (iii) $\delta < 0$ for all m , and (iv) $\delta < 0$ for $m < 1$ GeV and $\delta > 0$ for $m > 1$ GeV. However, versions (iii) and (iv), where $\delta < 0$ for $m < 1$ GeV, can be discarded from the outset. Indeed, an estimation of δ for $m < 1$ GeV by means of the relation $\delta = \delta_0^0 + \delta_0^2 - \phi_D$ readily demonstrates that, in this region of m , the phase shift δ will inevitably be positive for the generally accepted definition of the signs of the phase shifts δ_0^0 , δ_0^2 , and ϕ_D [see Figs. 1d and 2 and formula (1)]. In the following, we will therefore consider only versions (i) and (ii).

For the above two versions of the behavior of the phase shift δ , Fig. 3 shows δ_0^0 and η_0^0 values in the interval $0.68 < m < 1.64$ GeV that were extracted from the KEK data (see Figs. 1a–1c) by using formulas (4) and (5). For the sake of comparison and completeness, the values of δ_0^0 that were obtained from data on $|A_S|^2$, which have already been given individually in Fig. 1d, are also displayed in Fig. 3 within the range $0.36 < m < 1$ GeV. As can be seen, for example, from Fig. 3a, the sets of δ_0^0 values obtained in the region $0.68 < m < 1$ GeV by two different methods are in reasonable agreement with each other. We note that, in extracting δ_0^0 and η_0^0 values, an individual Argand diagram for the amplitude \tilde{A}_S (3) was constructed for each version, whereupon the $2(\delta_0^0 - \delta_0^2)$ values found by formulas (4) and (5) were extrapolated by requiring that changes in the phase shift δ_0^0 as a function of m be smooth. That a strong violation of unitarity occurs in the second version for $m > 1.16$ GeV (see Fig. 3d) can easily be understood on the basis of the first equation in (4): $\phi = \delta - 2\delta_0^2 + \phi_D$. For this version, the values of ϕ for $1.16 < m < 1.64$ GeV appear to be within the range between 180° and 360° , but this is forbidden for the phase of a formally unitary amplitude \tilde{A}_S . Moreover, the phase shift δ_0^0 for $m > 1$ GeV in the second version (see Fig. 3c) proves to be strongly different from that which is expected on the basis of $\pi^+\pi^-$ -production data [7–12], according to which the phase shift δ_0^0 taken, say, at m in the vicinity of 1.3 GeV must be about 270° . Thus, the second version, which corresponds to $\delta > 0$ for all values of m , has been disproved. As to the first version, its characteristic features are the following (see Figs. 3a, 3b): a sizable deviation of η_0^0 from unity for $m < 1$ GeV, an approximate equality of η_0^0 to unity for $1 < m < 1.12$ GeV, a violation of unitarity in the region around 1.2 GeV, and rather sharp variations in δ_0^0 and η_0^0 at still higher values of m . The resulting pattern agrees poorly with data from [7–12] on the production of $\pi^+\pi^-$ systems and is hardly anything more than an artifact of a partial-wave analysis of data on the reaction $\pi^-p \rightarrow \pi^0\pi^0n$.

We would like to highlight yet another difficulty. The normalization adopted for $|A_S|^2$ results in that the branching fraction of the decay process $f_2(1270) \rightarrow \pi\pi$ is $B_{f_2\pi\pi} = 0.760 \pm 0.034$ [see Eq. (2)]. But according to the PDG data [13], it is $B_{f_2\pi\pi} = 0.847_{-0.013}^{+0.024}$. These values differ from each other by about the doubled sum of their errors, whence one can in principle draw the following conclusion. The KEK data from [3] indicate that, at least for $m \approx m_{f_2}$, the absolute value of the cross section for the production of the $f_2(1270)$ resonance

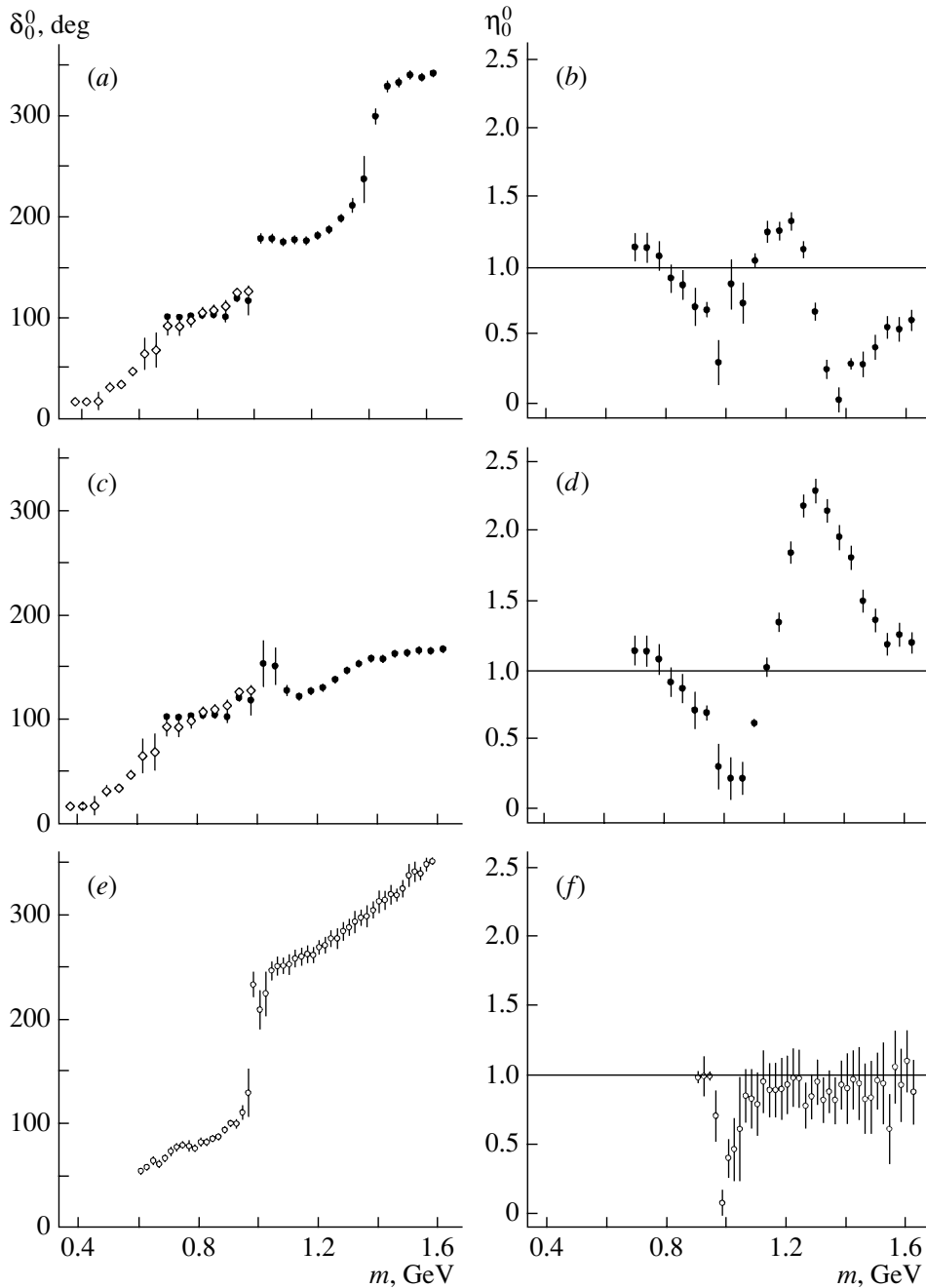


Fig. 3. Phase shift δ_0^0 and inelasticity parameter η_0^0 as extracted from KEK data on the reaction $\pi^+\pi^-\rightarrow\pi^0\pi^0$ (closed circles) for the (a, b) first and (c, d) second versions of the behavior of the phase shift δ . Open diamonds represent the phase shift δ_0^0 corresponding to Fig. 1d. One of the first sets of detailed data on δ_0^0 and η_0^0 from the investigation of the reaction $\pi^-p\rightarrow\pi^+\pi^-n$ [7] (e, f) is shown for the sake of comparison.

in the reaction $\pi^-p\rightarrow\pi^0\pi^0n$ through the one-pion-exchange mechanism may prove to be about 20% smaller than that which is expected on the basis of the PDG data [13]. On the other hand, it is clear that the normalization of m distributions obtained in [3] to the known value of $B_{f_2\pi\pi}$ [13] with the aid of the relation $\max|A_D|^2=(1+\eta_2^0)^2/4=B_{f_2\pi\pi}^2$ will

lead to a result that is approximately 25% above the unitary limit for $|A_S|^2$ in the most interesting region of m —namely, in the region of the lightest scalar resonance $\sigma(600)$ [3, 13, 19].

In the following, we will see that all of the aforementioned difficulties also arise in the analysis of

data from other experiments that studied the reaction $\pi^- p \rightarrow \pi^0 \pi^0 n$.

3. ANALYSIS OF THE BNL DATA

Vast statistics of $\pi^- p \rightarrow \pi^0 \pi^0 n$ events were accumulated in the BNL experiment [4], and a partial-wave analysis of the angular distributions of $\pi^0 \pi^0$ distributions in these events was performed in the same study. This analysis, which scanned ten consecutive intervals of $-t$ that cover the range $0 < -t < 1.5 \text{ GeV}^2$ and a broad range of m values (between 0.32 and 2.2 GeV) with a step of 0.04 GeV, resulted in deriving two possible solutions for the nonnormalized intensities of S and D_0 partial waves and, accordingly, four possible solutions for their relative phase. In just the same way as in [4], we will use here the notation $|S|^2$ and $|D_0|^2$ for the intensities of the S and D_0 waves, respectively, and the notation φ_{S-D_0} for their relative phase. Also, we denote by D_0 the $L_z = 0$ D wave, where L_z is the projection of the relative orbital angular momentum of the $\pi^0 \pi^0$ system onto the z axis in the Gottfried–Jackson frame [4]. A solution such that it corresponds to a large value of $|S|^2$ and a small value of $|D_0|^2$ for $m < 1 \text{ GeV}$ and extends smoothly to the region $m > 1 \text{ GeV}$, where the $f_2(1270)$ resonance is dominant in the D_0 wave, was singled out in [4], together with two corresponding solutions for the phase shift φ_{S-D_0} , as a physical solution. It should be noted that a different solution intersects the physical solution at $m \approx 1 \text{ GeV}$. We agree with the arguments used in [4] to reject this different solution in the region $m < 1 \text{ GeV}$. For $m > 1 \text{ GeV}$, however, we will analyze both solutions, along with the case where the relative phase goes over from one solution to the other.

For our analysis, we take the BNL data from [4] on $|S|^2$, $|D_0|^2$, and φ_{S-D_0} for five intervals of $-t$, $0.01 < -t < 0.03 \text{ GeV}^2$, $0.03 < -t < 0.06 \text{ GeV}^2$, $0.06 < -t < 0.1 \text{ GeV}^2$, $0.1 < -t < 0.15 \text{ GeV}^2$, and $0.15 < -t < 0.2 \text{ GeV}^2$, and the region $m < 1.6 \text{ GeV}$. We note that data on φ_{S-D_0} are available only for $m > 0.8 \text{ GeV}$. In order to evaluate the m dependence of the quantities $|A_S|^2$, $|A_D|^2$, and δ (see Section 2), which characterize the reaction $\pi^+ \pi^- \rightarrow \pi^0 \pi^0$ on the mass shell, we parametrize the t dependences of $|S|^2$, $|D_0|^2$, and φ_{S-D_0} as

$$|S|^2 = \frac{m^2}{q} |A_S|^2 \frac{-t \exp[b_S(t - m_\pi^2)]}{(t - m_\pi^2)^2}, \quad (6)$$

$$|D_0|^2 = 5 \frac{m^2}{q} |A_D|^2 \frac{-t \exp[b_{D_0}(t - m_\pi^2)]}{(t - m_\pi^2)^2},$$

$$\varphi_{S-D_0} = \delta + \alpha(t/m_\pi^2 - 1) \quad (7)$$

and, for each m interval of width 0.04 GeV, determine, from a fit to the data from [4], the nonnormalized intensities $|A_S|^2$ and $|A_D|^2$ and the phase shift δ , along with the slope parameters b_S , b_{D_0} , and α in the corresponding extrapolating functions.²⁾ In the region $m < 1 \text{ GeV}$, we concurrently accepted, in each interval of $-t$, only one solution for $|S|^2$ and $|D_0|^2$ —namely, the physical solution that was singled out in [4]—and the two solutions for φ_{S-D_0} that correspond to it. For $m > 1 \text{ GeV}$, we took the physical and the aforementioned different solution for $|S|^2$ and $|D_0|^2$ and, accordingly, four solutions for φ_{S-D_0} . Since the absolute value of the cross section for the reaction $\pi^- p \rightarrow \pi^0 \pi^0 n$ was not determined in [4], we use here the same procedure as in Section 2 in order to normalize $|A_S|^2$ and $|A_D|^2$. After the extrapolation to the point $t = m_\pi^2$ in the way outlined above and normalization, the data corresponding to the physical and the different solution are represented by, respectively, closed and open symbols in Figs. 4a, 4c, and 4e. It is interesting to note that, for the different solution, two branches of the phase shift φ_{S-D_0} —that where $\varphi_{S-D_0} > 0$ for all values of m and that where $\varphi_{S-D_0} < 0$ for all values of m —intertwine in the region $m > 1.24 \text{ GeV}$ upon the extrapolation, so that there arise (as can clearly be seen in Fig. 4e) two new branches of the phase shift δ , which depend

²⁾This two-parameter fit to the experimentally measured off-shell intensities of partial waves, which is aimed at obtaining data extrapolated to the pion pole, has been extensively used in the literature (see, for example, [9, 17, 20, 21]). A determination of the phase shift δ by means of a direct extrapolation of the data from [4] on φ_{S-D_0} [see Eq. (7)] is questionable. The problem would not have arisen if direct data on the contribution of the interference between the S and D_0 waves had been presented in [4]. A fit to such data with the aid of the two-parameter form $-2ta \exp[b(t - m_\pi^2)] / (t - m_\pi^2)^2$, which is similar to that in (6), and an identification of the parameter a with $\sqrt{5}(m^2/q)|A_S||A_D| \cos \delta$ would have made it possible to determine $|\delta|$ according to a conventional scheme. For want of such data, we have performed an indirect verification of the results for the phase shift δ that were obtained with the aid of formula (7). We evaluated $2|S||D_0| \cos \varphi_{S-D_0}$ on the basis of data from [4] on $|S|^2$, $|D_0|^2$, and φ_{S-D_0} and found the interference contribution on the mass shell with the aid of the aforementioned extrapolation, whereupon, knowing $|A_S|^2$ and $|A_D|^2$ from independent sources, we determined δ . The values of δ that were obtained by the above two independent methods proved to be nearly coincident. Because of the inevitable double rescaling of errors in the above indirect verification, the errors in δ of course proved to be larger than those in the fit on the basis of expression (7). On the other hand, the error in the δ values determined with the aid of (7) are virtually identical to the errors in the data from [4] on φ_{S-D_0} that are used here. All of the aforesaid gave us sufficient grounds for adopting the above method for determining δ .

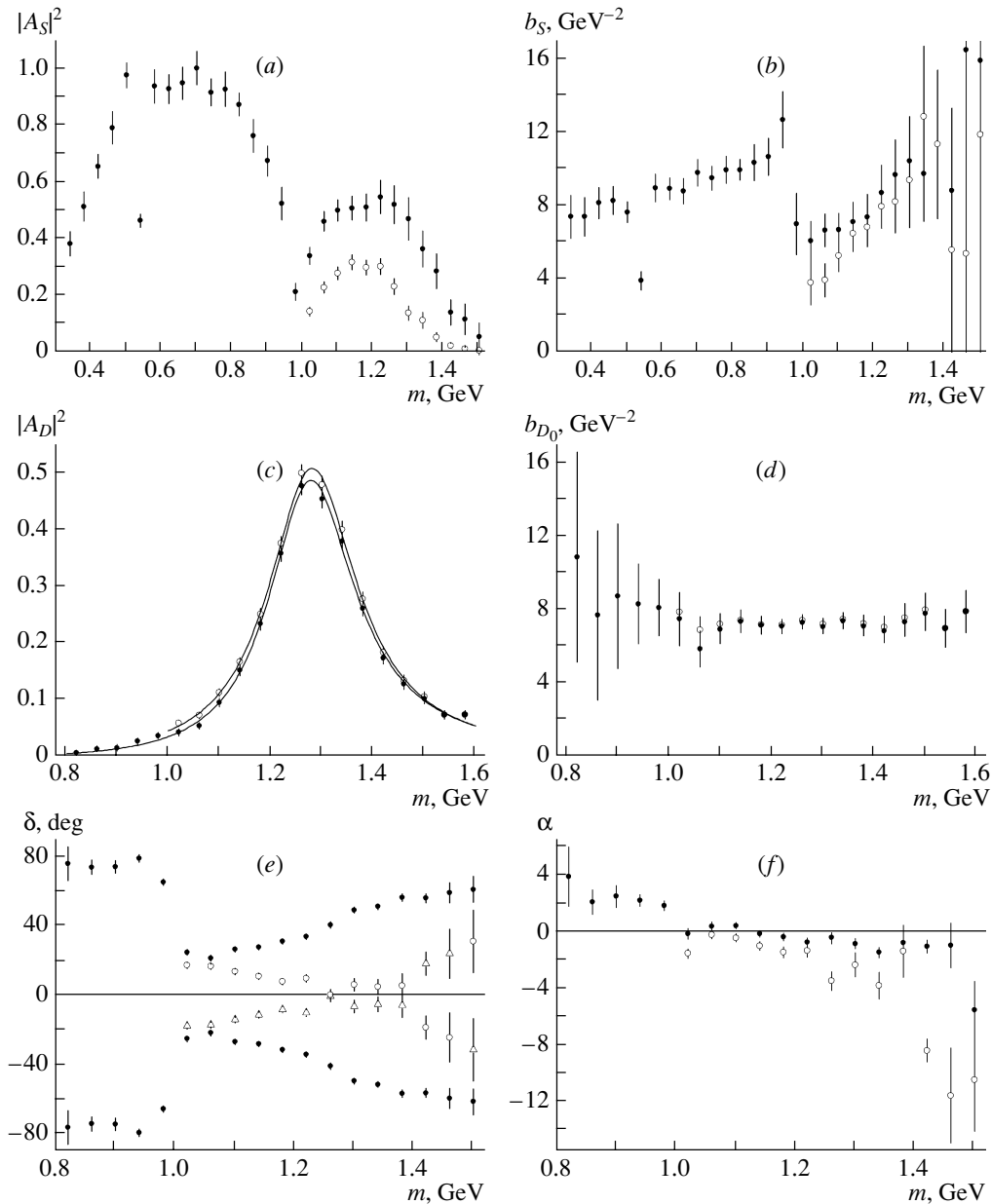


Fig. 4. Results obtained by extrapolating the BNL data: (a, c) extrapolated and normalized intensities of the S and D waves and (e) relative phase δ of the amplitudes of the S and D waves. Figures 4b, 4d, and 4f display the slope parameters b_S , b_{D_0} , and α versus m . Everywhere, closed symbols represent a physical solution. Open circles (and triangles in Fig. 4e for δ) correspond to a different solution. The upper and lower curves in Fig. 4c, which were obtained with the aid of the formula (1), correspond to the parameters of the $f_2(1270)$ resonance that were set to the values in (8) and (9), respectively.

on m smoothly and which are either intersecting or touching at $m \approx 1.26$ GeV.

As in Section 2, we will first determine δ_0^0 for $m < 1$ GeV on the basis of data on $|A_S|^2$ (see Fig. 4a), setting $\eta_0^0 = 1$ in this region. The values of δ_0^0 that were obtained in this way are represented by the open circles in Fig. 5a. We note that a couple of points in the region around $m \approx m_K$, where there are distortions associated with events of the decay $K_S^0 \rightarrow \pi^0\pi^0$ [4],

were discarded. Having at our disposal data on $|A_S|^2$, $|A_D|^2$, and δ in the region $m > 0.8$ GeV (see Fig. 4), we will further determine the values of δ_0^0 and η_0^0 on the basis of the general formulas (3)–(5) and (1). For solutions preliminarily selected among those given in Fig. 4 and for some of their combinations, the results are represented by the closed symbols in Fig. 5. As a matter of fact, this selection reduced, first of all, to discarding, for $m < 1$ GeV, the physical solution

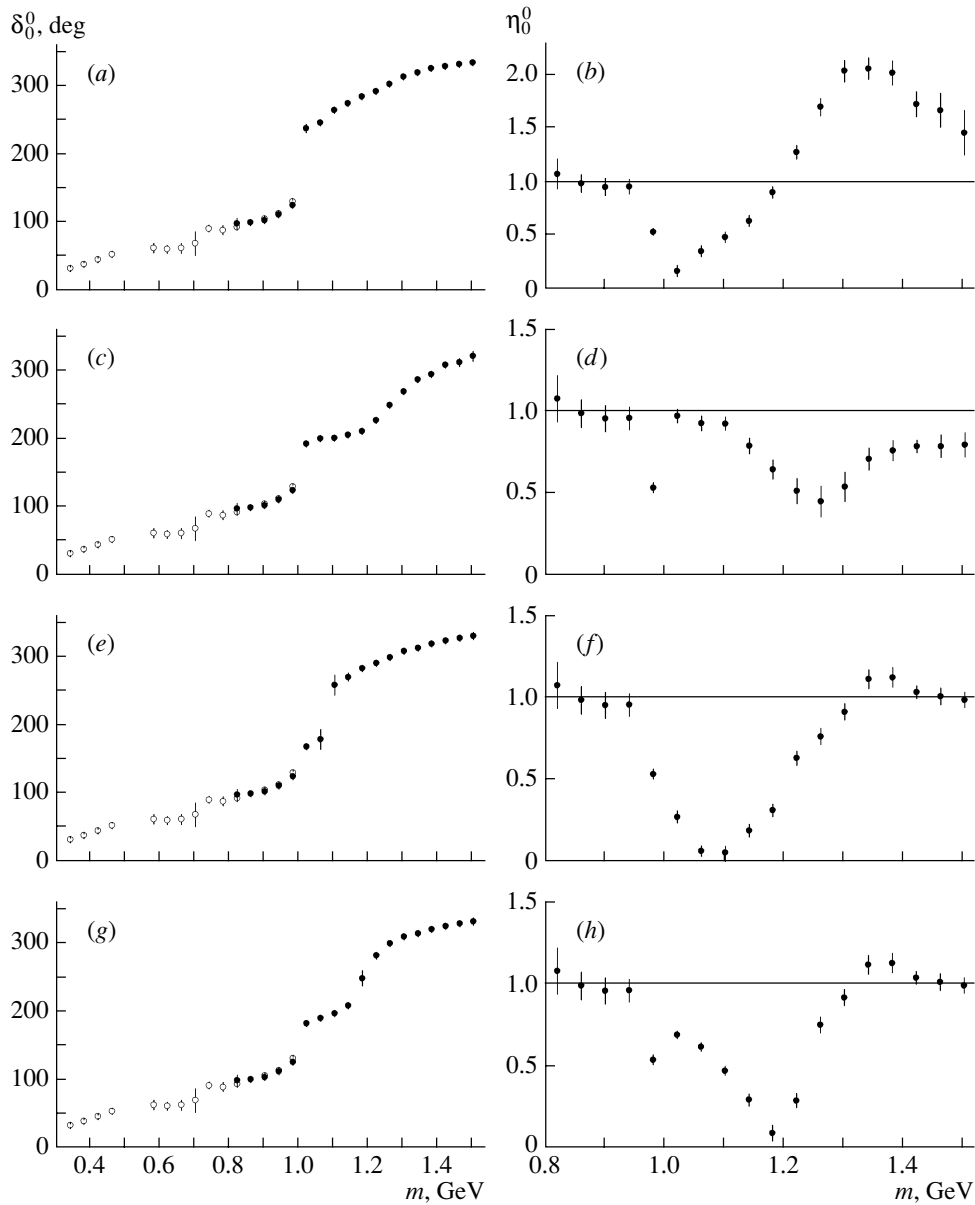


Fig. 5. Phase shift δ_0^0 and inelasticity parameter η_0^0 extracted from the BNL data [4]: (a, b) results corresponding to the physical solution (see Fig. 4) where $\delta > 0$ for all values of m ; (c, d) results corresponding to the physical solution for the case where, at $m \approx 1$ GeV, the phase shift δ goes over from the branch of its positive values to the branch of its negative values (see Fig. 4e); (e, f) results corresponding to a combination (see Figs. 4a, 4e) of a physical solution where $\delta > 0$ for $m < 1$ GeV and the different solution for $m > 1$ GeV where $\delta > 0$ for $1 < m < 1.28$ GeV and $\delta < 0$ for $1.28 < m < 1.52$ GeV; (g, h) results corresponding to a combination of the physical solution where $\delta > 0$ for $m < 1$ GeV and the different solution for $m > 1$ GeV where $\delta < 0$ for $1 < m < 1.52$ GeV (see Fig. 4e). The open circles represent the phase shift δ_0^0 obtained from data on $|A_S|^2$ for $m < 1$ GeV (see Fig. 4a) under the assumption that $\eta_0^0 = 1$.

in which $\delta < 0$ (see Fig. 4e), since, according to the simple estimate $\delta_0^0 = \delta - \delta_0^2 + \phi_D$ (see Section 2), the phase shift δ_0^0 for this solution in the range between 0.8 and 1 GeV proves to be about $-(25^\circ - 40^\circ)$, which is of course unsatisfactory. From Figs. 5a and 5b, which correspond to the physical solution where $\delta > 0$ for all values of m , it can further be seen that this solution must also be discarded because of a strong

violation of the unitarity condition for $m > 1.2$ GeV. Figures 5c and 5d correspond to the physical solution for $|A_S|^2$, $|A_D|^2$, and δ , but, at $m \approx 1$ GeV, the phase shift δ in this solution goes over from the branch of its positive values to the branch of its negative values (see Fig. 4e). This solution does not violate unitarity, but it corresponds to a weak coupling between the $\pi\pi$ and $K\bar{K}$ channels in the vicinity of the

$K\bar{K}$ threshold, since, in this solution, η_0^0 is close to unity in the region $1 < m < 1.15$ GeV. The latter does not agree with data on the reactions $\pi^-p \rightarrow \pi^+\pi^-n$, $\pi^+p \rightarrow \pi^+\pi^-\Delta^{++}$, and $\pi N \rightarrow K\bar{K}(N, \Delta)$ (see, for example, [7, 9, 10, 16, 22, 23]). Figures 5e and 5f correspond to a combination of the physical solution where $\delta > 0$ for $m < 1$ GeV and the different solution for $m > 1$ GeV where $\delta > 0$ for $1 < m < 1.28$ GeV and $\delta < 0$ for $1.28 < m < 1.52$ GeV (see Figs. 4a, 4e). Figures 5g and 5h correspond to a similar combination of the physical solution and the different solution where $\delta < 0$ for $1 < m < 1.52$ GeV (see also Fig. 4e). The versions that differ from the last two only in that, for them, $\delta > 0$ for $m > 1.28$ GeV lead to a sizable violation of the unitarity condition for $m > 1.32$ GeV. For this reason, they are not illustrated here. Thus, we can conclude that only the version depicted in Figs. 5e and 5f agrees qualitatively in many respects with the results obtained from analyses of data on the production of $\pi^+\pi^-$ systems [1, 7, 9, 11]. It was indicated above that, in this version, the relative phase $\delta = \phi_S - \phi_D$ goes through zero in the vicinity of the $f_2(1270)$ resonance, being positive below the $f_2(1270)$ resonance and negative above it. It is of importance to emphasize here that precisely this type of behavior of the relative phase δ as a function of m is confirmed by the data of the experiment that studied the reaction $\pi^-p \rightarrow \pi^+\pi^-n$ at 17.2 GeV on a polarized target and which was reported in [11].

In comparing Figs. 5 and 3, it is worth noting that, for $m < 0.5$ GeV, the BNL data lead to values of the relative phase δ_0^0 that are considerably greater than those from the analysis of the KEK data.

In extracting information about δ_0^0 and η_0^0 , the phase shift ϕ_D was determined from a fit to data on $|A_D|^2$ with the aid of expression (1) that are given in Fig. 4c. As a result, the parameters of the $f_2(1270)$ resonance proved to be (see also the curves in Fig. 4c)

$$\begin{aligned} m_{f_2} &= 1.279 \pm 0.002 \text{ GeV}, & (8) \\ \Gamma_{f_2} &= 0.205 \pm 0.005 \text{ GeV}, \\ R_{f_2} &= 3.96 \pm 0.24 \text{ GeV}^{-1}, \\ B_{f_2\pi\pi} &= 0.697 \pm 0.008 \end{aligned}$$

for the physical solution and

$$\begin{aligned} m_{f_2} &= 1.281 \pm 0.002 \text{ GeV}, & (9) \\ \Gamma_{f_2} &= 0.211 \pm 0.005 \text{ GeV}, \\ R_{f_2} &= 4.65 \pm 0.33 \text{ GeV}^{-1}, \\ B_{f_2\pi\pi} &= 0.712 \pm 0.007 \end{aligned}$$

for the different solution. Thus, the BNL data indicate that $B_{f_2\pi\pi}$ may be about 84% of the value presented by the PDG [13]. The possible implications of this discrepancy have already been discussed at the end of

Section 2, which is devoted to the analysis of the KEK data (recall that the analogous ratio for the KEK data was 90%).

4. DISCUSSION OF THE GAMS DATA

The experiments of the GAMS Collaboration, which were performed at energies of 38 GeV [5] and 100 GeV [6], accumulated the vastest statistics of events of the reaction $\pi^-p \rightarrow \pi^0\pi^0n$. Despite this, the range of low $-t$ between 0 and 0.2 GeV did not receive adequate study in [5, 6]. Only data averaged over this region were presented in [5] for $|S|^2$ and φ_{S-D_0} and in [6] for $|S|^2$, $|D_0|^2$, and φ_{S-D_0} . On this basis, nothing can therefore be said about the corresponding quantities extrapolated to the pion pole. Nonetheless, we will discuss some special features of these data. A physical and a different solution are quoted in [5] for $|S|^2$ over the range $0.8 < m < 1.6$ GeV, and only one physical solution for φ_{S-D_0} is given there, only its branch where $\varphi_{S-D_0} > 0$ being presented (supposedly, the reader is tacitly assumed to guess himself that there exists a branch where $\varphi_{S-D_0} = -|\varphi_{S-D_0}|$). The results established in [5] for the m dependences of $|S|^2$ and φ_{S-D_0} comply well with the corresponding BNL data [4]. In the case of the physical solution, for example, the m dependences of $|S|^2$ and φ_{S-D_0} from [5] behave in nearly the same way as the those for the quantities $|A_S|^2$ and δ in the corresponding case (closed symbols in Figs. 4a and 4e). As was shown above, however, this physical solution for $|A_S|^2$ and δ (where $\delta > 0$ for all values of m) is unsatisfactory because of a strong violation of the unitarity condition in the region $m > 1.2$ GeV (see Figs. 5a, 5b). We also note that, for $|S|^2$, $|D_0|^2$, and φ_{S-D_0} measured at an energy of 100 GeV, only one solution was singled out and presented in [6] as the result of their analysis. Unfortunately, this single solution is similar to the physical solution obtained in the GAMS experiment for the reaction $\pi^-p \rightarrow \pi^0\pi^0n$ at 38 GeV [5].

It is of paramount importance that the GAMS experiment performed to study the reaction $\pi^-p \rightarrow \pi^0\pi^0n$ at an energy of 38 GeV resulted in establishing the absolute value of the cross section for the D_0 -wave production of the $f_2(1270)$ resonance in the $-t$ range between 0 and 0.2 GeV²: $\sigma_{D_0}(\pi^-p \rightarrow f_2(1270)n \rightarrow \pi^0\pi^0n) = 2.3 \pm 0.2 \mu\text{b}$ [24]. Later on, this result was used to normalize data obtained at 100 GeV [6]. Although the above cross-section value is about 1.5 to 2 times larger than that in previous experiments [24, 25], it is 1.57 times smaller than the estimate based on the one-pion-exchange model (for details of the history concerning the production

of the $f_2(1270)$ resonance, see [25]). Indeed, the estimate obtained on the basis of the one-pion-exchange model with allowance for the PDG data [13] on m_{f_2} , Γ_{f_2} , and $B_{f_2\pi\pi}$ yields

$$\begin{aligned} & \sigma_{D_0}(\pi^- p \rightarrow f_2(1270)n \rightarrow \pi^0\pi^0 n) \quad (10) \\ & \approx \sigma^{\text{OPE}}(\pi^- p \rightarrow f_2(1270)n \rightarrow \pi^0\pi^0 n) \\ & \approx \frac{g_{\pi^-pn}^2}{4\pi} \frac{5\pi}{m_p^2 P_{\pi^-}^2} m_{f_2} \Gamma_{f_2} \frac{2}{9} B_{f_2\pi\pi}^2 \\ & \times \int_{-0.2 \text{ GeV}^2}^0 \frac{-t \exp[b_{f_2}(t - m_\pi^2)]}{(t - m_\pi^2)^2} dt \approx 3.6 \text{ } \mu\text{b}, \end{aligned}$$

where $P_{\pi^-} = 38 \text{ GeV}$, $g_{\pi^-pn}^2/4\pi \approx 2 \times 14.3$, and the slope parameter is $b_{f_2} \approx 7.5 + 2 \times 0.8 \ln(38/18.3) \approx 8.68 \text{ GeV}^{-2}$ (the Regge energy dependence and the results for the slope parameter b_{D_0} in the region of the $f_2(1270)$ peak in Fig. 4d were taken into account in estimating it). The cross-section value obtained in [24] is smaller by approximately the same factor than the estimate obtained in [25] from an extrapolation of available data on the reaction $\pi^- p \rightarrow f_2(1270)n \rightarrow \pi^+\pi^- n$ at energies of 17.2 GeV [8], and 100 and 175 GeV [26] to the GAMS energy of 38 GeV. Thus, the GAMS data from [24] indicate that $B_{f_2\pi\pi}$ may be about 80% of the value presented by the PDG [13].

We will now briefly summarize the main difficulties that we encountered in analyzing data from four different experiments that studied the reaction $\pi^- p \rightarrow \pi^0\pi^0 n$. First, physical solutions selected as the result of partial-wave analyses of data on the production of $\pi^0\pi^0$ systems yield, for δ_0^0 and η_0^0 , values that are in poor agreement with known results that were obtained from data on the production of $\pi^+\pi^-$ systems, at least for $m > 1 \text{ GeV}$, some of these solutions leading to a strong violation of the unitarity condition. At the same time, preferable solutions can be found among other solutions in the region $m > 1 \text{ GeV}$. Second, all data on the production of $\pi^0\pi^0$ systems astonishingly suggest a sizably smaller value of $B_{f_2\pi\pi}$ in relation to that which is adopted at the present time [13]. This difficulty seems serious and interesting. We recall that experiments studying the production of dipion systems on unpolarized targets—in particular, the experiments discussed here, which were reported in [3–6]—are unable in principle, even in the case of enormously vast statistics, to separate the contributions of amplitudes having the quantum numbers of π and a_1 exchanges in the t channels, because these contributions to the unpolarized cross sections are incoherent [27]. In other words, there

is no model-independent method here for performing such a separation. In our opinion, the difficulty concerning $B_{f_2\pi\pi}$ is therefore yet another piece of evidence that a partial-wave analysis of the experiments discussed here, which were aimed at studying the production of dipion systems on unpolarized targets, can determine the intensities and phases of the S , D , etc., waves of pion-pion scattering only approximately, irrespective of the extrapolation method used. The degree to which this determination is approximate depends on the relative contribution of a nondominant a_1 exchange. In the case of a rather high statistical accuracy, its presence in events corresponding to $|S|^2$ can manifest itself, in experiments with unpolarized targets, precisely as the aforementioned difficulty. As a matter of fact, this statement follows, in quite a natural way, from an analysis of the nonnormalized KEK and BNL data (see the discussion at the end of Section 2). As to the GAMS data [24], they are rather indicative of the existence of the general problem of reliably measuring the absolute value of the cross section for the reaction $\pi^- p \rightarrow \pi^0\pi^0 n$ (in the above consideration, we have already pointed to the evolution of data on the cross section for the production of $\pi^0\pi^0$ systems). Detailed discussions on additional assumptions that are necessary in analyzing data from experiments with unpolarized targets and on the contribution of a_1 exchange can be found, for example, in [1, 2, 11, 12, 27–29].

5. CONCLUSIONS

By using the simplest possible procedure, we have extracted, from data on the reaction $\pi^- p \rightarrow \pi^0\pi^0 n$, the phase shift and the inelasticity parameter for S -wave pion-pion scattering through the $I = 0$ channel.

Obviously, further experimental investigations of the reaction $\pi^- p \rightarrow \pi^0\pi^0 n$ are required both for refining our knowledge of its mechanism and for obtaining more detailed information about pion-pion scattering and about light scalar resonances in this channel. Setting aside the general recommendation to study the reaction $\pi^- p \rightarrow \pi^0\pi^0 n$ on a polarized target, we will now briefly formulate a number of specific proposals aimed at clarifying the situation currently prevalent in this realm:

(i) It is highly desirable to measure the absolute value of the cross section for this reaction at various energies—for example, at KEK, BNL, IHEP, and CERN—and to obtain detailed data on m and t distributions for the S and D waves of the $\pi^0\pi^0$ system, especially in the region $-t < 0.2 \text{ GeV}^2$, which is dominated by the one-pion-exchange mechanism. The relative accuracy of such measurements must be

on the same order as or higher than that to which $(B_{f_2\pi\pi})^2$ is known at the present time [13]. This would immediately make it possible to obtain a reliable description of the differential cross section for the production of the $f_2(1270)$ resonance within the standard model of one-pion exchange and to assess the degree to which the cross section for the production of the $\pi^0\pi^0$ system in the S wave at its absolute maximum occurring within the range $0.6 < m < 0.8$ GeV is consistent with this model under the standard assumption (which is incorporated in the model) that the normalization is performed in such a way that $|A_S|^2 = 1$ (or $\delta_0^0 - \delta_0^2 = 90^\circ$ and $\eta_0^0 = \eta_0^2 = 1$) at the point of the maximum. An experimental value in excess of the estimate within the one-pion-exchange model would be a good piece of evidence, from an experiment with an unpolarized target, that the a_1 -exchange amplitude is present in the region of the absolute maximum of the S -wave cross section. But if the experimental value proved to be less than the value that is expected within the one-pion-exchange model, this would lead to a complete disorganization of the currently prevalent concepts of the behavior of the phase shift δ_0^0 in the region $m < 1$ GeV, but this is improbable.

(ii) We propose that, for low values of $-t$, especially thorough measurements of the production of $\pi^0\pi^0$ systems in the S wave be performed over the region of m values between 0.9 and 1.1 GeV—that is, over the region of the well-known interference minimum in $|S|^2$ in the vicinity of the $K\bar{K}$ threshold. Such measurements would furnish additional important information about the coupling of the $f_0(980)$ resonance to the $K\bar{K}$ channel (the corresponding coupling constant is denoted by $g_{f_0K\bar{K}}$) and would make it possible to resolve the long-standing question [16] of the possible ambiguity in the behavior of the phase shift δ_0^0 above the $K\bar{K}$ threshold for $g_{f_0K+K^-}^2/(4\pi) > 4\pi m_K^2 \approx 3.1$ GeV². Moreover, the cross-section value in the immediate vicinity of the

minimum (if it occurs below the K^+K^- threshold) can be used to set a presumably rather stringent upper bound on the contribution of a_1 exchange at low $-t$ in this region of m .

(iii) Among the requirements that make it possible to single out a physical solution, there is the assumption of the phase coherence of the amplitudes of the D_0 and D_- waves (see, for example, [4, 6, 9, 30]), where D_- is the D wave in which $|L_z| = 1$ in the Gottfried–Jackson frame and which is caused by unnatural-parity exchanges in the t channel of the reaction $\pi N \rightarrow \pi\pi N$. In this connection, we would like to highlight a new alarming circumstance: according to the observations reported in [6], the ratio of the cross sections for the production of the $f_2(1270)$ resonance in the D_- and D_0 waves depends sizably on energy, its value at 100 GeV being one-half as great as that at 38 GeV. This may suggest that the contributions of the πP and $a_2 P$ Regge cuts (P stands for Pomeron exchange), which determine the amplitude of the production of the D_- wave in the reference frame being considered, begin to compensate each other with increasing energy, the phase coherence of the amplitudes of the production of D_0 and D_- waves therefore being destroyed.

(iv) We also propose that, for the contribution associated with the interference between the S and D_0 waves and extracted from experiments with unpolarized targets, use be made in the following not of the frequently employed simplified notation $|S||D_0|\cos\varphi_{S-D_0}$ but of a notation that carries information about the coherence factor (see, for example, [31]) and which is more adequate to the actually observed quantity. In an experiment, one simultaneously measures the intensities $|S|^2$ and $|D_0|^2$ and the interference contribution $\xi|S||D_0|\cos\tilde{\varphi}$. As a matter of fact, the intensities are given by $|S| \equiv [|S_\pi|^2 + |S_{a_1}|^2]^{1/2}$ and $|D_0| \equiv [|D_{0\pi}|^2 + |D_{0a_1}|^2]^{1/2}$, while the coherence factor ξ ($0 \leq \xi \leq 1$) and the phase shift $\tilde{\varphi}$ can be represented as

$$\xi = \left| \frac{\sum_{i=\pi, a_1} S_i D_{0i}^*}{\left[\left(\sum_{i=\pi, a_1} |S_i|^2 \right) \left(\sum_{i=\pi, a_1} |D_{0i}|^2 \right) \right]^{1/2}} \right|,$$

$$\tilde{\varphi} = \arctan \left[\frac{\left(\sum_{i=\pi, a_1} |S_i||D_{0i}|\sin\varphi_i \right)}{\left(\sum_{i=\pi, a_1} |S_i||D_{0i}|\cos\varphi_i \right)} \right],$$

where S_π ($D_{0\pi}$) and S_{a_1} (D_{0a_1}) are the amplitudes of the production of the S (D_0) wave through the mechanisms of, respectively, π and a_1 exchanges

(these amplitudes correspond to two independent configurations of the nucleon helicities in the reaction $\pi N \rightarrow \pi\pi N$) and φ_i is the relative phase of

the amplitudes of the S_i and D_{0i} waves. We will now consider the case where the amplitude of the D_{0a_1} wave can be disregarded. Denoting $\tilde{\varphi} = \varphi_\pi$ by φ_{S-D_0} , we can then see that, even in this case, the interference contributions differ from the simplified expression $|S||D_0| \cos \varphi_{S-D_0}$ by the coherence factor $\xi = 1/\sqrt{1 + |S_{a_1}|^2/|S_\pi|^2}$. But if we set $\xi = 1$ for all values of m , then we will always be dealing with the effectively reduced value $|\cos \varphi_{S-D_0}|$.

ACKNOWLEDGMENTS

We are grateful to the E852 Collaboration for providing free access to detailed BNL data (<http://dustbunny.physics.indiana.edu/pi0pi0pwa/>).

This work was supported in part by a joint grant from INTAS and the Russian Foundation for Basic Research (RFBR), no. IR-97-232, by the RFBR, project no. 02-02-16061, and by the Presidential grant no. 2339.2003.2 for support of leading scientific schools.

REFERENCES

1. P. Minkovski and W. Ochs, *Eur. Phys. J. C* **9**, 283 (1999).
2. V. V. Vereshchagin, K. N. Mukhin, and O. O. Patarakin, *Usp. Fiz. Nauk* **170**, 353 (2000).
3. K. Takamatsu *et al.*, in *Proceedings of the International Workshop on e^+e^- Collisions from ϕ to J/ψ , Novosibirsk, 1999*, Ed. by G. V. Fedotovich and S. I. Redin (BINP, Novosibirsk, 2000), p. 163; *Nucl. Phys. A* **675**, 312c (2000); *Prog. Theor. Phys.* **102**, E52 (2001).
4. J. Gunter, A. R. Dzierba, *et al.*, *Phys. Rev. D* **64**, 072003 (2001).
5. D. Alde *et al.*, *Z. Phys. C* **66**, 375 (1995).
6. D. Alde *et al.*, *Eur. Phys. J. A* **3**, 361 (1998); *Yad. Fiz.* **62**, 446 (1999) [*Phys. At. Nucl.* **62**, 1993 (1999)].
7. B. Hyams *et al.*, *Nucl. Phys. B* **64**, 134 (1973).
8. G. Grayer *et al.*, *Nucl. Phys. B* **75**, 189 (1974).
9. P. Estabrooks and A. D. Martin, *Nucl. Phys. B* **79**, 301 (1974); **95**, 322 (1975).
10. B. Hyams *et al.*, *Nucl. Phys. B* **100**, 205 (1975).
11. H. Becker *et al.*, *Nucl. Phys. B* **151**, 46 (1979).
12. R. Kamiński, L. Leśniak, and K. Rybicki, *Z. Phys. C* **74**, 79 (1997).
13. Particle Data Group (K. Hagiwara *et al.*), *Phys. Rev. D* **66**, 010001 (2002).
14. N. N. Achasov, *Usp. Fiz. Nauk* **168**, 1257 (1998); *Nucl. Phys. A* **675**, 279c (2000); *Yad. Fiz.* **65**, 573 (2002) [*Phys. At. Nucl.* **65**, 546 (2002)].
15. N. N. Achasov, in *Proceedings of the 9th International Conference on Hadron Spectroscopy, Protvino, Russia, 2001*, Ed. by D. Amelin and A. M. Zaitsev; AIP Conf. Proc. **619**, 112 (2002); W. Ochs, in *Proceedings of the 9th International Conference on Hadron Spectroscopy, Protvino, Russia, 2001*, Ed. by D. Amelin and A. M. Zaitsev; AIP Conf. Proc. **619**, 167 (2002); T. Barnes, in *Proceedings of the 9th International Conference on Hadron Spectroscopy, Protvino, Russia, 2001*, Ed. by D. Amelin and A. M. Zaitsev; AIP Conf. Proc. **619**, 447 (2002); E. Klempt, in *Proceedings of the 9th International Conference on Hadron Spectroscopy, Protvino, Russia, 2001*, Ed. by D. Amelin and A. M. Zaitsev; AIP Conf. Proc. **619**, 463 (2002).
16. N. N. Achasov, S. A. Devyanin, and G. N. Shestakov, *Phys. Lett. B* **102B**, 196 (1981); *Yad. Fiz.* **32**, 1098 (1980) [*Sov. J. Nucl. Phys.* **32**, 566 (1980)].
17. W. Hoogland *et al.*, *Nucl. Phys. B* **126**, 109 (1977).
18. N. B. Durusoy *et al.*, *Phys. Lett. B* **45B**, 517 (1973).
19. N. N. Achasov and G. N. Shestakov, *Phys. Rev. D* **49**, 5779 (1994); M. Harada, F. Sannino, and J. Schechter, *Phys. Rev. D* **54**, 1991 (1996); S. Ishida *et al.*, *Prog. Theor. Phys.* **98**, 1005 (1997).
20. P. Estabrooks, A. D. Martin, *et al.*, in *Proceedings of the International Conference on $\pi\pi$ Scattering, Tallahassee, 1973*, Ed. by D. K. Williams and V. Hagopian; AIP Conf. Proc. **13**, 37 (1973).
21. N. N. Biswas *et al.*, *Phys. Rev. Lett.* **47**, 1378 (1981); N. M. Cason *et al.*, *Phys. Rev. Lett.* **48**, 1316 (1982); *Phys. Rev. D* **28**, 1586 (1983).
22. S. D. Protopopescu *et al.*, *Phys. Rev. D* **7**, 1279 (1973).
23. A. D. Martin, E. N. Ozmutlu, and E. J. Squires, *Nucl. Phys. B* **121**, 514 (1977); N. N. Achasov, S. A. Devyanin, and G. N. Shestakov, *Usp. Fiz. Nauk* **142**, 361 (1984) [*Sov. Phys. Usp.* **27**, 161 (1984)]; *Z. Phys. C* **22**, 53 (1984).
24. A. A. Kondashov and Yu. D. Prokoshkin, *Nuovo Cimento A* **107**, 1903 (1994); Yu. D. Prokoshin, *Yad. Fiz.* **62**, 396 (1999).
25. N. N. Achasov and G. N. Shestakov, *Mod. Phys. Lett. A* **8**, 2343 (1993).
26. C. Bromberg *et al.*, *Nucl. Phys. B* **232**, 189 (1984).
27. N. N. Achasov and G. N. Shestakov, *Phys. Rev. D* **58**, 054011 (1998); *Yad. Fiz.* **62**, 548 (1999) [*Phys. At. Nucl.* **62**, 505 (1999)].
28. M. Svec, *Phys. Rev. D* **47**, 2132 (1993); **53**, 2343 (1996).
29. R. Kamiński, L. Leśniak, and K. Rybicki, *Eur. Phys. J. C* **4**, 4 (2002).
30. A. D. Martin and C. Michael, *Nucl. Phys. B* **84**, 83 (1975).
31. S. Hagopian *et al.*, *Phys. Rev. Lett.* **25**, 1050 (1970); G. S. Adams *et al.*, *Phys. Rev. D* **4**, 653 (1971); N. N. Achasov and G. N. Shestakov, *Fiz. Élem. Chastits At. Yadra* **9**, 48 (1978) [*Sov. J. Part. Nucl.* **9**, 19 (1978)].

Translated by A. Isaakyan

The Pole Heavy-Quark Masses in the Hamiltonian Approach*

A. M. Badalian**, B. L. G. Bakker¹⁾, and A. I. Veselov

*Institute of Theoretical and Experimental Physics,
Bol'shaya Cheremushkinskaya ul. 25, Moscow, 117259 Russia*

Received November 4, 2003

Abstract—From the fact that nonperturbative self-energy contribution C_{SE} to the heavy-meson mass is small, $C_{SE}(b\bar{b}) = 0$ and $C_{SE}(c\bar{c}) \cong -40$ MeV, strong restrictions on the pole masses m_b and m_c are obtained. The analysis of the $b\bar{b}$ and the $c\bar{c}$ spectra with the use of the relativistic (string) Hamiltonian gives $m_b(2\text{-loop}) = 4.78 \pm 0.05$ GeV and $m_c(2\text{-loop}) = 1.39 \pm 0.06$ GeV, which correspond to the \overline{MS} running masses $\overline{m}_b(\overline{m}_b) = 4.19 \pm 0.04$ GeV and $\overline{m}_c(\overline{m}_c) = 1.14 \pm 0.05$ GeV. © 2004 MAIK “Nauka/Interperiodica”.

1. INTRODUCTION

The spectrum of heavy quarkonia (HQ) is very rich and provides a unique opportunity to study static interaction in the infrared (IR) region and hyperfine- and fine-structure effects. To use that opportunity, one needs to know, besides such fundamental parameters as the string tension and the strong coupling, the heavy-quark mass, which cannot directly be measured since a quark is not observed as a physical particle. Therefore, the heavy-quark mass m_Q has to be determined indirectly, e.g., from the study of hadronic properties like $e^+e^- \rightarrow b\bar{b}$, hadronic decays, and the $Q\bar{Q}$ spectra.

In the QCD Lagrangian, the mass parameter depends on the renormalization scheme, and by convention, this current mass is taken in the \overline{MS} scheme. In perturbation theory, it is convenient to introduce the pole quark mass, i.e., the pole of the quark propagator, and at present the \overline{MS} pole mass is known to 3-loops [1, 2]:

$$m_Q = \overline{m}_Q(\overline{m}_Q) \quad (1)$$

$$\times \left\{ 1 + \frac{4}{3} \frac{\alpha_s(\overline{m}_Q)}{\pi} + \xi_2 \left(\frac{\alpha_s}{\pi} \right)^2 + \xi_3 \left(\frac{\alpha_s}{\pi} \right)^3 \right\},$$

where ξ_2, ξ_3 are known numbers and the Lagrangian current masses,

$$\begin{aligned} \overline{m}_b(\overline{m}_b) &= 4.25 \pm 0.25 \text{ GeV}, \\ \overline{m}_c(\overline{m}_c) &= 1.20 \pm 0.20 \text{ GeV}, \end{aligned} \quad (2)$$

are known now with an accuracy of 6% (17%) for the b quark (c quark). Most calculations of the pole masses m_b and m_c have been done in the QCD sum rules [3, 4], lattice QCD [5], and different perturbative approaches [1, 2].

For three decades, many properties of HQ like the spectra, electromagnetic transitions, and hadronic and semileptonic decays were successfully studied in different potential models (PM) [6–13]; however, the heavy-quark masses used in PM are considered “to make sense in the limited context of a particular quark model” [1], i.e., as fitting parameters.

Meanwhile, in the last decade, the situation changed when in [11] the relativistic (string) Hamiltonian was derived directly from the QCD Lagrangian, starting with the gauge-invariant meson Green’s function in the Fock–Feynman–Schwinger (FFS) representation. In [11–13], it was established that, for orbital momentum $L \leq 5$ and not overly large string corrections, as in HQ, the string Hamiltonian reduces to the well-known Hamiltonian H_0 used in the relativized potential model (RPM) for many years [7, 8]:

$$H = H_0 + C_{SE}, \quad H_0 = 2\sqrt{\mathbf{p}^2 + m_q^2} + V_{\text{stat}}(r). \quad (3)$$

It follows from the derivation of H_0 in [11] that the mass m_q in (3) (it refers to any quark mass, including $m_q = 0$) coincides with the \overline{MS} running mass $\overline{m}_q(\overline{m}_q)$ if the perturbative interaction is neglected or with the pole mass of a heavy quark m_Q (1) if the perturbative self-energy corrections are taken into account. The nonperturbative (NP) self-energy contribution to the meson mass C_{SE} was calculated in [14] and a choice of the static potential $V_{\text{stat}}(r)$ will be

*This article was submitted by the authors in English.

¹⁾Free University, Amsterdam, The Netherlands.

**e-mail: badalian@heron.itep.ru

discussed later. Therefore, this Hamiltonian can be used to extract the pole mass m_Q from the analysis of the HQ spectrum.

Nevertheless, if one looks at the heavy-quark masses used in PM, a large variety of m_b and m_c values can be found in different analyses: m_c in the range 1.30–1.84 GeV and m_b in the range 4.20–5.17 GeV [7–10]. The main reason behind this wide spread in the m_b and m_c values (even for the same Hamiltonian H_0) is the presence of a negative arbitrary constant C_0 in the mass formula (or in the chosen static potential). We give three examples: in [7], $m_c = 1.327$ GeV and $C_0 = 0$ are used by the Wisconsin Group; in [8], $m_c = 1.628$ GeV and $C_0 = -253$ MeV (in both cases, the Hamiltonian H_0 (3) was used); in [6], $m_c = 1.84$ GeV and $C_0 \cong -800$ MeV are taken—i.e., the magnitude of C_0 is always larger for larger heavy-quark mass.

The meaning of the constant C_0 was understood recently when in [14] it was shown that the negative contribution to the meson mass comes from the NP color-magnetic quark (antiquark) interaction with the background (vacuum) field which gives rise to the self-energy NP term denoted as C_{SE} ; it was analytically calculated with 10% accuracy [14] [see Eq. (A.13) in Appendix]:

$$C_{SE}(nL) = -\frac{4\sigma}{\pi\omega_q(nL)}\eta(m_q) \quad (4)$$

for a quark and an antiquark with equal masses. This constant appears to be different for the states with different quantum numbers nL .

In expression (4), m_q is the pole mass which defines the factor $\eta(m_q)$ (A.11), while the average over the kinetic energy operator

$$\omega_q(nL) = \left\langle \sqrt{\mathbf{p}^2 + m_q^2} \right\rangle_{nL} \quad (5)$$

is the dynamical quark mass. For low-lying states in charmonium and bottomonium, the mass ω_Q turns out to be ~ 200 MeV larger than m_Q .

The essential fact (for light and heavy–light mesons) is that $C_{SE}(nL)$ depends on the quantum numbers, and just due to this the correct intercept of the Regge trajectory was obtained in [13]. In HQ, the situation appears to be much simpler. The factor $\eta(m_q)$ in (4) depends on the flavor through the pole mass m_q , and from the analytical expression (A.11), one obtains a small value: $\eta_c \cong 0.35$ – 0.27 for m_c in the range 1.37–1.70 GeV and $\eta_b \cong 0.07$ for $m_b \cong 4.7$ – 5.0 GeV. As a result, $C_{SE}(b\bar{b}) \cong -3$ MeV (i.e., it can be taken equal to zero), and $C_{SE}(c\bar{c})$ is also small:

$$C_{SE}(b\bar{b}) = 0; \quad C_{SE}(c\bar{c}) \cong -40 \text{ MeV}. \quad (6)$$

Thus, the self-energy contributions to the HQ states are well defined and therefore there is no longer an opportunity to vary the pole mass by introducing a fitting constant. We shall show in our paper that the condition (6) puts strong restrictions on the $m_b(m_c)$ needed to describe the $b\bar{b}(c\bar{c})$ spectrum. The extracted pole masses m_b and m_c in our analysis will be determined with an accuracy better than 60 MeV, and the main uncertainty in their values comes not from the method used (for fixed string tension and the strong coupling, or the QCD constant Λ_{QCD} , the uncertainty is ± 10 MeV), but from uncertainty in our knowledge of the strong coupling in the IR region. We shall show that HQ spectra, in particular, high excitations and the recently discovered $1D$ state in bottomonium [15], can give very important information about the strong coupling in the IR region.

Our analysis of HQ spectra shows that, in bottomonium, $m_b(2\text{-loop}) < 4.70$ GeV and the values $m_b > 4.85$ GeV turn out to be incompatible with the condition $C_{SE} = 0$. In charmonium, the extracted m_c values, $m_c = 1.39 \pm 0.06$ GeV, appear to be rather small and agree with that obtained by Narison with the use of the QCD sum rules for the (pseudo)scalar current [3]. Our calculations of the HQ spectra are done with the use of only three parameters: the string tension, the QCD constant $\Lambda(n_f)$ (in this paper, we mostly take the number of flavors $n_f = 4$), and the pole mass m_Q . The main emphasis in our fit lies on the excited (not ground) states.

The paper is organized as follows. In Section 2, the mass formula, following from the relativistic Hamiltonian, as well as the approximations to that, is presented and the notion of the dynamical mass is introduced. In Section 3, the static potential and the strong coupling in the IR region, defined as in background perturbation theory (BPT), are discussed. In Section 4, from the analysis of the $b\bar{b}$ spectrum (with special accent on high excitations), the restrictions on the pole mass $m_b(2\text{-loop})$ are obtained. In Section 5, the pole mass m_c is extracted from the $c\bar{c}$ spectrum. In Section 6, our conclusions are presented, and in the Appendix the method and NP self-energy term are discussed.

2. THE MASS FORMULA

The string corrections are small in HQ and therefore the simplified form of the relativistic Hamiltonian H_R [11] may be used (see Appendix):

$$H_R = \frac{\mathbf{p}^2}{\omega} + \omega + \frac{m_q^2}{\omega} + V_{\text{stat}}(r). \quad (7)$$

To derive this Hamiltonian in the FFS representation, one needs to go over from the proper time τ in the

meson Green's function [formula (A.2) in Appendix] to the actual time t , and at this point, the new variable $\omega(t)$ must be introduced [11]:

$$\omega(t) = \frac{1}{2} \frac{dt}{d\tau}. \tag{8}$$

This variable is the einbein (canonical) coordinate and, since H_R does not depend on its derivative $\dot{\omega}$, the requirement that the canonical momentum $\pi_\omega = 0$ is preserved in time corresponds to the extremum condition

$$\dot{\pi}_\omega = \frac{\partial H}{\partial \omega} = 0. \tag{9}$$

From this extremum condition, the operator ω ,

$$\omega = \sqrt{\mathbf{p}^2 + m_q^2}, \tag{10}$$

is defined as the kinetic energy operator. Substituting the definition (10) into the H_R (7), one comes to the Hamiltonian H_0 (3),

$$H_0 = 2\sqrt{\mathbf{p}^2 + m_q^2} + V_{\text{stat}}(r), \tag{11}$$

which does not explicitly depend on the variable ω . However, to calculate different corrections to the meson mass (like spin, string, and the self-energy corrections), which can be considered as a perturbation and depend on ω , we shall use an approximation where for a given nL state the operator ω will be replaced by its average:

$$\omega_q(nL) = \langle \omega \rangle_{nL} = \left\langle \sqrt{\mathbf{p}^2 + m_q^2} \right\rangle_{nL}. \tag{12}$$

This mass $\omega_q(nL)$ can be called the dynamical mass, since its difference in comparison to the current (pole) mass m_q is fully defined by the dynamics. Note that, for vanishing pole mass ($m_q = 0$), the value of $\omega_q(nL)$ is finite and defines the constituent quark mass [12, 13].

It is also important that perturbative corrections to the current mass, which are essential at small quark–antiquark separations, $r \lesssim 0.1$ fm [16, 17], are included in the pole mass m_q present in H_0 . On the other hand, the static potential $V_{\text{stat}}(r)$ is well defined at the $Q\bar{Q}$ separations $r \gtrsim T_g \cong 0.2$ fm, where T_g is the gluonic correlation length [14]. The eigenvalues (e.v.) of H_0 , denoted as $M_0(nL)$,

$$\left\{ 2\sqrt{\mathbf{p}^2 + m_q^2} + V_{\text{stat}}(r) \right\} \psi_{nL}(r) = M_0(nL)\psi_{nL}(r), \tag{13}$$

together with the self-energy term (6) define the heavy-meson masses. As shown in the Appendix, in bottomonium $C_{\text{SE}} = 0$ and therefore the spin-averaged mass $M(nL)$ for a given $b\bar{b}$ state coincides with the e.v. $M_0(nL)$,

$$M(nL, b\bar{b}) = M_0(nL), \tag{14}$$

while in charmonium from Eq. (A.13) $C_{\text{SE}} \cong -40$ MeV and

$$M(nL, c\bar{c}) = M_0(nL) + C_{\text{SE}}. \tag{15}$$

There exist two approximations to the solution of spinless Salpeter equation (SSE) (13) or to the meson mass $M(nL)$. The first one is the nonrelativistic (NR) approximation, where the mass $M_{\text{NR}}(nL)$ is the following:

$$M_{\text{NR}}(nL) = 2m_Q + E_{nL}^{\text{NR}}(m_Q) + C_{\text{SE}}, \tag{16}$$

where $E_{nL}^{\text{NR}}(m_Q)$ is the eigenvalue of the Schrödinger equation with the reduced mass equal to $m_Q/2$.

There is also another, so-called “einbein,” approximation (EA) to the solutions of SSE (13) [12], where the meson mass is given by the expression

$$M_{\text{EA}}(nL) = \omega_Q(nL) + \frac{m_Q^2}{\omega_Q(nL)} + E_{nL}(\omega_Q) + C_{\text{SE}}, \tag{17}$$

and it appears to be closer to the exact solution $M(nL)$ than the NR approximation [12]. In EA, the binding energy $E_{nL}(\omega_Q)$ is defined as the solution of Schrödinger equation with the reduced mass equal to $\omega_Q(nL)/2$ (not with the mass $m_Q/2$), while $\omega_Q(nL) \equiv \omega_{nL}$ is to be defined from the extremum condition for the meson mass (17)

$$\frac{\partial M_{\text{EA}}}{\partial \omega_{nL}} = 0, \text{ or } \omega_{nL} = \frac{m_Q^2}{\omega_{nL}} - \omega_{nL} \frac{\partial E_{nL}(\omega)}{\partial \omega_{nL}}. \tag{18}$$

In EA, the relativistic corrections are taken into account through ω_{nL} in the mass formula (17). Moreover, due to the special form of the mass formula (17), the value of the dynamical mass $\omega_b(nL) \cong 5.0$ GeV turns out to be compatible with the condition $C_{\text{SE}} = 0$, while in NR approximation (16) the admissible values of the pole mass m_b are about 200 MeV smaller.

It is worthwhile to note that, in bottomonium, when both $\omega_b(nL)$ and m_b are large, around 5 GeV, the difference between the NR, EA, and relativistic cases is small, $|\delta_R| = M(nL) - M^{\text{NR}}(nL)$ being about 10–20 MeV. In charmonium, this difference depends on the quantum numbers and for high excitations can reach ~ 100 MeV (see the discussion in Section 5).

3. STATIC POTENTIAL

The static potential contains perturbative and NP contributions, where the NP linear potential can directly be derived from the meson Green's function if the $q\bar{q}$ separation is larger than the gluonic correlation length. From analysis of the Regge trajectories of light and heavy–light mesons, the value of the string

tension, $\sigma = 0.185 \pm 0.005 \text{ GeV}^2$ [6, 13], is fixed, while the perturbative interaction in coordinate space can be represented in the form

$$V_P(r) = -\frac{4}{3} \frac{\alpha_{\text{stat}}(r)}{r}, \quad (19)$$

where $\alpha_{\text{stat}}(r)$ is well known only in the perturbative region, i.e., at very small distances, $r \lesssim 0.1 \text{ fm}$ [16, 17].

In bottomonium, however, the rms radii span a very wide range,

$$\begin{aligned} R(\Upsilon(1S)) &= 0.2 \text{ fm}, & R(\chi_b(1P)) &= 0.4 \text{ fm}, \\ R(\chi_b(2P)) &= 0.65 \text{ fm}, & R(\Upsilon(4S)) &= 0.9 \text{ fm}, \\ R(\Upsilon(6S)) &\cong 1.3 \text{ fm}, \end{aligned} \quad (20)$$

and in charmonium,

$$\begin{aligned} R(J/\psi) &\cong 0.4 \text{ fm}, & R(\chi_c(1P)) &= 0.6 \text{ fm}, \\ R(\psi(1D)) &= 0.8 \text{ fm}, & R(\psi(3S)) &= 1.1 \text{ fm}, \\ R(\psi(4S)) &\cong 1.40 \text{ fm}. \end{aligned} \quad (21)$$

Apparently, with the exception of $\Upsilon(1S)$, the sizes of HQ states lie outside the perturbative region.

Therefore, the problem arises how to define the strong coupling $\alpha_{\text{stat}}(r)$ at all distances, i.e., in the IR region. In PM, it has always been assumed, and later this fact has been supported by direct measurement of the static potential in lattice QCD [16], that the strong coupling freezes and reaches a critical (saturated) value at large r . Unfortunately, at present there is no consensus about the true value of α_{crit} . At present, different critical values are used in phenomenological analysis ($\alpha_{\text{crit}} = 0.60$ in [8], $\alpha_{\text{crit}} \cong 1.4$ in analytical perturbation theory [18], and in BPT $\alpha_{\text{crit}} \cong 0.56$ being fully defined by Λ_{QCD} [17, 19]).

For the definition of $\alpha_{\text{stat}}(r)$, it is better to start with the vector coupling in the momentum space $\alpha_B(q)$, entering the static (vector) potential $V_B(q)$:

$$V_B(q) = -4\pi C_F \frac{\alpha_B(q)}{q^2}. \quad (22)$$

The coupling $\alpha_B(q)$ in BPT is defined in Euclidean momentum space at all q^2 , including $q^2 = 0$ (i.e., it has no Landau singularity), and in the two-loop approximation is given by the standard expression

$$\alpha_B(q, 2\text{-loop}) = \frac{4\pi}{\beta_0 t_B} \left\{ 1 - \frac{\beta_1 \ln t_B}{\beta_0^2 t_B} \right\}. \quad (23)$$

Here, $\beta_1 = 11 - \frac{2}{3}n_f$, $\beta_0 = 102 - \frac{38}{3}n_f$, and the logarithm

$$t_B = \ln \frac{q^2 + M_B^2}{\Lambda_B^2} \quad (24)$$

contains the background mass M_B , which appears due to the interaction of a gluon with the background field at small q^2 . This mass $M_B \cong 1 \text{ GeV}$ has the meaning of the lowest hybrid excitation: $M_B = M(Q\bar{Q}gg) - M(Q\bar{Q}g)$ [19]. From the comparison of $V_B(q)$ (22) with the lattice static potential, the background mass M_B was found to be equal to $1 \pm 0.05 \text{ GeV}$ [17]. The logarithm t_B (24) coincides in form with the parametrization of $\alpha_s(q)$ suggested in [20], where, instead of the background mass M_B , two gluonic masses ($2m_g$) enter. However, because of gauge invariance, the physical gluon cannot have mass, while the mass of hybrid excitation is a well-defined physical quantity and can be calculated in different theoretical approaches [21] and in the lattice QCD.

By definition, $\alpha_B(q)$ has correct asymptotic freedom (AF) behavior at large q^2 , and in this region, the connection between the vector coupling $\alpha_B(q)$ and $\alpha_s(q)$ in the \overline{MS} renormalization scheme is very simple, so that the QCD constant Λ_B (in vector scheme) can be expressed through $\Lambda_{\overline{MS}}$ [22]:

$$\Lambda_B^{(n_f)} = \Lambda_{\overline{MS}}^{(n_f)} \exp\left(\frac{a_1}{2\beta_0}\right). \quad (25)$$

Here, $a_1 = \frac{31}{3} - \frac{10}{9}n_f$. At present, the value $\Lambda_{\overline{MS}}^{(5)}(2\text{-loop}) = 215 \pm 25 \text{ MeV}$ is established from high-energy processes [1], while in quenched QCD the value $\Lambda_{\overline{MS}}^{(0)} = 240 \pm 20 \text{ MeV}$ was calculated on the lattice [23]. Then, from relation (25), it follows that, in the quenched approximation, the QCD constant in the vector scheme (25)

$$\Lambda_B^{(0)} = 385 \pm 30 \text{ MeV} \quad (26)$$

and for $n_f = 4, 5$

$$\Lambda_B^{(4)} = 370 \pm 35 \text{ MeV}; \quad \Lambda_B^{(5)} = 293 \pm 34 \text{ MeV}. \quad (27)$$

Our choice of Λ_B in this paper will be in accordance with the numbers (26) and (27).

In coordinate space, the background coupling $\alpha_B(r)$ is defined as the Fourier transform of $\alpha_B(q)$,

$$\alpha_B(r) = \frac{2}{\pi} \int_0^\infty dq \frac{\sin qr}{q} \alpha_B(q), \quad (28)$$

so that the perturbative part of the static potential is

$$V_B(r) = -\frac{4}{3} \frac{\alpha_B(r)}{r} \quad (29)$$

Table 1. The effective coupling $\alpha_{\text{eff}}(nL)$ (33) for different $b\bar{b}$ and $c\bar{c}$ states for the static potential (30) with $m_b = 4.78$ GeV, $m_c = 1.45$ GeV, $\alpha_{\text{crit}} = 0.547$; $\sigma = 0.185$ GeV², $\Lambda^{(4)} = 360$ GeV ($n_f = 4$)

State	$b\bar{b}$	$c\bar{c}$
1S	0.386	0.441
2S	0.419	0.447
3S	0.427	0.446
4S	0.430	0.446
5S	0.431	—
6S	0.432	—
1P	0.474	0.510
2P	0.480	0.505
3P	0.482	0.505
1D	0.508	0.531
2D	0.508	0.526

and the static potential is the sum of $V_B(r)$ and NP linear potential:

$$V_{\text{stat}}(r) = \sigma r - \frac{4}{3} \frac{\alpha_B(r)}{r}. \quad (30)$$

In phenomenological potentials, the coupling $\alpha_B(r)$, equal to a constant, is often used. This approximation is valid because at distances $r \gtrsim 0.4$ fm $\alpha_B(r)$ approaches the freezing (critical) value. Note that, at large distances, $r \gtrsim 1.2$ fm, the confining linear potential, due to the creation of $q\bar{q}$ pairs, becomes flatter [24, 25], and this effect can be important not only for light mesons but also for high excitations in charmonium.

The critical values of $\alpha_B(q)$ and $\alpha_B(r)$ coincide,

$$\alpha_B(q = 0) = \alpha_B(r \rightarrow \infty) = \alpha_{\text{crit}}, \quad (31)$$

and their characteristic values in the two-loop approximation are given below:

$$\alpha_{\text{crit}}^{(0)}(\Lambda_B^{(0)} = 385 \text{ MeV}) = 0.428, \quad (32)$$

$$\alpha_{\text{crit}}^{(3)}(\Lambda_B^{(3)} = 370 \text{ MeV}) = 0.510,$$

$$\alpha_{\text{crit}}^{(4)}(\Lambda_B^{(4)} = 340 \text{ MeV}) = 0.515.$$

Our calculations show that the bottomonium spectrum appears to be rather sensitive to AF behavior, while in charmonium the approximation $\alpha_B = \text{const}$ can be used with good accuracy. It is also instructive to look at the effective coupling α_{eff} for different $c\bar{c}$ and $b\bar{b}$ states, which can be defined as

$$\left\langle \frac{\alpha_B(r)}{r} \right\rangle_{nL} = \alpha_{\text{eff}}(nL) \langle r^{-1} \rangle_{nL}, \quad (33)$$

Table 2. The spin-averaged masses $M(nL)$ (in GeV) in bottomonium for the potential (30) with the parameters (35) (NR case)

State	Set I	Set II	Set III	Experiment
1S	9.460	9.406*	9.379*	9.4603 ± 0.0003
2S	10.013	10.001	9.988	10.0233 ± 0.0003
3S	10.367	10.359	10.359	10.3552 ± 0.0005
1P	9.900	9.900	9.900	9.9001 ± 0.0006
2P	10.267	10.267	10.270	10.2601 ± 0.0006
1D	10.150	10.156	10.161	10.1622 ± 0.0016
Above $B\bar{B}$ threshold, $M_{\text{th}} = 10.558$ GeV				
4S	10.659	10.647	10.649	10.580 ± 0.0035
5S	10.917	10.900	10.902	10.865 ± 0.008
6S	11.146	11.131	11.132	10.019 ± 0.008

* The mass $M(1S)$ increases by $\sim 50\text{--}80$ MeV if the AF correction is taken into account.

and, being dependent on the quantum numbers (see Table 1), it is $\sim 10\text{--}20\%$ smaller than α_{crit} .

From Table 1, one can see that, in bottomonium, because of the different behavior of the wave functions, the effective coupling is smaller for the nS states and larger for orbital excitations like nD states.

4. BOTTOMONIUM

To extract the pole mass m_b from the spin-averaged masses ($M_{\text{cog}}(nL) \equiv M(nL)$), the $b\bar{b}$ spectrum will be studied here as a whole. Moreover, we mostly concentrate not on the ground state—the $\Upsilon(1S)$ mass—for which perturbative corrections are important [2], but on the following experimental splittings [1, 15]:

$$M(1D) - M(1P) \cong M(1^3D_2) - M(1P) \quad (34)$$

$$= 261.1 \pm 2.2 \text{ MeV}(\text{exp.}),$$

$$M(2P) - M(1P) = 360.0 \pm 1.2 \text{ MeV}(\text{exp.}).$$

The important feature of the $1P, 2P, 1D$ states is that they lie below the $B\bar{B}$ threshold and have no hadronic shifts. Also, for the mass splittings (34), small relativistic corrections are partly (or totally for the Δ_1) canceled and therefore the calculations can be done either with the use of SSE or in the NR approximation.

First, we consider the case with $\alpha_{\text{stat}} = \text{const}$ and give the $b\bar{b}$ spectrum in Table 2 for three sets of parameters with different m_b :

$$\text{set I: } m_b = 4.727 \text{ GeV}, \quad \sigma = 0.20 \text{ GeV}^2, \quad (35)$$

Table 3. The dynamical mass $\omega_b(nL)$ for SSE with Cornell potential ($m_b = 4.78$ GeV, $\sigma = 0.185$ GeV², $\alpha_{\text{stat}} = 0.4125$)

State	1S	2S	3S	4S	5S	6S	1P	2P	1D
$\omega_b(nL)$ [GeV]	5.04	5.01	5.03	5.06	5.09	5.13	4.96	4.99	4.96
$\omega_b(nL) - m_b$ [MeV]	263	228	248	277	308	347	179	209	182

Table 4. The $b\bar{b}$ spectrum ($M(nL)$ in MeV) defined by the mass formula (16) for spinless Salpeter equation

State	Set A	Set B	Set C	Experiment*
	$m_b = 4.828$ GeV, $\sigma = 0.178$ GeV ² , $\Lambda_B^{(5)} = 330$ MeV	$m_b = 4.83$ GeV, $\sigma = 0.19$ GeV ² , $\Lambda_B^{(4)} = 390$ MeV	$m_b = 4.817$ GeV, $\sigma = 0.185$ GeV ² , $\Lambda_B^{(0)}(1\text{-loop}) = 365$ MeV	
1S	9469	9478	9470	9460
2S	10 022	10 032	10 023	10 023
3S	10 369	10 386	10 375	10 355
1P	9900	9901	9900	9900
2P	10 267	10 278	10 266	10 260
1D	10 158	10 162	10 152	10 162

* The experimental errors in the masses are given in Table 2.

$$\alpha_{\text{stat}} = 0.3345;$$

$$\text{set II: } m_b = 4.765 \text{ GeV, } \sigma = 0.19 \text{ GeV}^2,$$

$$\alpha_{\text{stat}} = 0.390;$$

$$\text{set III: } m_b = 4.778 \text{ GeV, } \sigma = 0.188 \text{ GeV}^2,$$

$$\alpha_{\text{stat}} = 0.415.$$

In all cases, $C_{\text{SE}} = 0$ is taken as in the mass formula (14).

From the masses presented in Table 2, one can see the following:

(i) For small $m_b = 4.727$ GeV (set I), the mass $M(1D)$ appears to be ~ 10 MeV lower than the experimental number even for very large $\sigma = 0.20$ GeV².

(ii) For sets II and III, almost identical fits are obtained, with exception of the $1D$ state, when good agreement with experiment can be reached only for a larger value of the coupling, as for set III.

(iii) The $1D-1P$ splitting,

$$\Delta = M_{\text{cog}}(1D) - M_{\text{cog}}(1P), \quad (36)$$

has remarkable properties: it is practically independent both of relativistic correction δ_R and of the small variations of the string tension, and therefore Δ can be considered as the best and very stable criterion to determine the critical value of strong coupling as well as the pole mass m_b .

(iv) In NR approximation (16) and for SSE for b -quark masses $m_b \leq 4.70$ GeV or $m_b \geq 4.85$ GeV, the condition $C_{\text{SE}} = 0$ cannot be combined with a reasonably good fit to the $b\bar{b}$ spectrum.

However, if one uses EA (17) instead of NR mass formula (16), then the values of the dynamical mass $\omega_b(nL)$ are larger and the difference $\omega_b(nL) - m_b$ varies in the range (180–300 MeV) (see Table 3), from which one can see that the dynamical mass $\omega_b(nL)$ is slightly different for different nL states, $\omega_b(nL) - m_b \cong 200 \pm 50$ MeV. The $b\bar{b}$ spectrum calculated with $\omega_b(nL) = 5.0$ GeV and $m_b = 4.78$ GeV with the use of the mass formula (17) gives numbers within ± 5 MeV, coinciding with those from Table 2.

Thus, from our fits with the coupling α_{stat} taken as constant, the extracted value of the pole mass is

$$m_b = 4.76 \pm 0.02 \text{ GeV} \quad (\alpha_{\text{stat}} = \text{const}). \quad (37)$$

The picture does not change much if the AF behavior of $\alpha_B(r)$ (in two-loop approximation) is taken into account. However, in this case, the admissible values of m_b appear to be larger by ~ 50 MeV. The $b\bar{b}$ spectrum for $m_b \cong 4.82$ GeV and $m_b = 4.83$ GeV for the number of the flavors $n_f = 4, 5$ and also in the quenched approximation is presented in Table 4.

As seen from Table 4, for sets A, B, good agreement is obtained for the $1P, 1D$ states, but for the

1*S* level the mass is ~ 10 MeV higher than the spin-averaged $M(1S)$. This fact can be considered as an indication of possible contribution of the three-loop perturbative corrections, which are neglected here.

Our conclusion is that, for the background coupling (24) with $\Lambda_B^{(4)} = 390$ MeV ($n_f = 4$), or $\Lambda_B^{(5)} = 330$ MeV ($n_f = 5$), and $\sigma = 0.183 \pm 0.006$ GeV², the extracted pole mass lies in the narrow range

$$m_b(2\text{-loop}) = 4.81 \pm 0.02 \text{ GeV}. \quad (38)$$

Thus, if the AF behavior of $\alpha_B(r)$ is taken into account, the extracted pole mass is ~ 50 MeV larger than m_b (37) for $\alpha_{\text{stat}} = \text{const}$. Then, combining (35) and (38) for above considered choices of α_B , one finds that the extracted pole mass of the *b* quark lies in the range

$$m_b(2\text{-loop}) = 4.78 \pm 0.05 \text{ GeV}. \quad (39)$$

From here, by definition of the two-loop pole mass (1) ($n_f = 5$), where the parameter ξ_2 is

$$\begin{aligned} \xi_2(n_f = 5) & \quad (40) \\ &= -1.0414 \sum_k^{N_L} \left(1 - \frac{4}{3} \frac{\overline{m}_{Q_k}}{\overline{m}_Q} \right) + 13.4434, \end{aligned}$$

and the sum over *k* extends over the N_L flavors Q_k , which are lighter than *Q*, one finds $\xi_2(n_f = 5) \cong 9.6\text{--}9.7$. Then, for the conventional $\alpha_s(\overline{m}_b) = 0.217$, from (37) it follows that

$$\overline{m}_b(\overline{m}_b) = 4.19 \pm 0.04 \text{ GeV}. \quad (41)$$

This number for \overline{MS} current mass (41) appears to be in good agreement with the conventional value (2) but has smaller theoretical error, ~ 40 MeV, as compared to the PDG number (2).

5. CHARMONIUM

The $c\bar{c}$ spectrum has several differences in comparison to bottomonium.

First, the self-energy contribution to the mass $M(nL)$ is nonzero, being equal to ~ -40 MeV (6), and the value of C_{SE} is practically the same for different nL states; therefore, C_{SE} can be taken equal to a constant for all states (with an accuracy of 1–3 MeV).

Secondly, relativistic (*R*) corrections are negative and not small in charmonium, so that $M(nL)$ in *R* case is always smaller, and

$$\delta_R(nL) = M(nL) - M^{\text{NR}}(nL) \quad (42)$$

is negative. Note that the self-energy contribution must be the same in the *R* and NR cases (see third and fourth columns in Table 5). However, if for comparison one uses the fit to the spin-averaged mass

of the 1*S* state, $M(1S) = 3067$ MeV, then C_{SE} are different in the *R* and NR cases and $\delta_R(nL)$ has irregular behavior (see Table 5, sixth column). Such a fit is often used in HQ. From Table 5, where $C_{SE} = -35$ MeV in the *R* case and $C_{SE}^{\text{NR}} = -57$ MeV in the NR case are taken, one can see that $\delta_R(nL)$ is even positive ($\sim 10\text{--}20$ MeV) for the 1*P*, 1*D* states; equal to zero for the 1*F* state; and negative for the excited nS states, 2*P*, 2*D*, and other higher states. It is important that, for the 4*S* (3*S*) state, $|\delta_R|$ is large, ~ 100 MeV (60 MeV), and therefore the $c\bar{c}$ spectrum has to be calculated with a relativistic Hamiltonian.

An interesting observation is that, while the ground-state mass is fitted, the relativistic corrections for 1*P*, 1*D* states turn out to be positive (since for such fit a negative C_{SE}^{NR} has larger magnitude than in the *R* case).

The third difference refers to the choice of $\alpha_B(r)$. Since the $c\bar{c}$ states have larger sizes, than the $b\bar{b}$ ones, the AF behavior of $\alpha_B(r)$ appears to be less important in charmonium and the approximation $\alpha_B(r) = \text{const}$ is valid with good accuracy. For example, for two sets of parameters

$$\text{set A: } m_c = 1.42 \text{ GeV}, \quad \sigma = 0.18 \text{ GeV}^2, \quad (43)$$

$$\alpha_B = 0.42; \quad C_{SE} = -35 \text{ MeV},$$

$$\text{set B: } m_c = 1.42 \text{ GeV}, \quad \sigma = 0.185 \text{ GeV}^2,$$

$$\Lambda_B^{(4)} = 360 \text{ MeV}, \quad C_{SE} = -30 \text{ MeV},$$

close values of $M(nL)$ in the *R* case are obtained (see Table 6).

As seen from Table 6, the high excitations, like 3*S*, 4*S*, and 2*D* states, lie higher by ~ 40 MeV than the experimental values. All these states have large rms radii: $R(3S) = 1.1$ fm, $R(4S) \cong 1.4$ fm, $R(2D) \cong 1.4$ fm. At such distances, as was observed on the lattice [24], the confining potential flattens due to the quark–antiquark pair creation, and this phenomenon results in the correlated shift of all radial excitations down for light mesons [25]. The flattening of the static potential can be illustrated by taking, instead of the linear $\sigma_0 r$ potential, the modified confining potential $\sigma(r)r$, which was suggested in [25]:

$$\sigma(r) = \sigma_0(1 - \gamma_0 f(r)), \quad (44)$$

$$f(r) = \frac{\exp(\sqrt{\sigma_0}(r - a))}{B + \exp(\sqrt{\sigma_0}(r - a))},$$

with the parameters

$$\sigma_0 = 0.185 \text{ GeV}^2, \quad \gamma_0 = 0.40, \quad (45)$$

$$a = 6.0 \text{ GeV}^{-1}, \quad B = 20.$$

For this set of parameters, the $c\bar{c}$ spectrum (*R* case) is given in Table 7 together with that for the standard

Table 5. The $c\bar{c}$ spin-averaged masses $M(nL)$ (in MeV) in R and NR cases with the same static potential ($\alpha_{\text{static}} = 0.42$, $\sigma = 0.18 \text{ GeV}^2$, $m_c = 1.42 \text{ GeV}$) and different C_{SE}

State	Experiment	R	NR	NR ($C_{SE}^{\text{NR}} = -57 \text{ MeV}$)	$\delta_R = M(nL) - M^{\text{NR}}(nL)$
		$C_{SE} = -35 \text{ MeV}$			
$1S$	3067 ± 0.7	3067	3089	3067 (fit)	0
$2S$	3673 ± 6	3661	3710	3688	-27
$1P$	3525 ± 0.6	3528	3532	3510	+18
Above $D\bar{D}$ threshold					
$1D$	3770 ± 2.5 3872 ± 1.2	3823	3834	3812	+11
$2P$	—	3964	4006	3984	-20
$1F$	—	4067		4067	0
$3S$	4040 ± 10	4081	4163	4141	-60
$2D$	4159 ± 20	4200	4249	4227	-27
$4S$	4415 ± 6	4431	4549	4527	-96

Note: δ_R is the difference between the masses given in third and fifth columns.

Table 6. The spin-averaged masses (in MeV) in charmonium in R case for static potential with the parameters (43)

State	Set A	Set B	Experiment
$1S$	3067	3067	3067 ± 0.7
$2S$	3660	3668	3673 ± 8
$1P$	3528	3500	3525 ± 0.6
Above $D\bar{D}$ threshold			
$1D$	3823	3805	3871.8 ± 1.2 3770.0 ± 2.5
$2D$	4199	4193	4159 ± 20
$3S$	4080	4099	4040 ± 10
$4S$	4424	4459	4415 ± 6
$2P$	3964	3954	—
$1F$	4067	4064	—

linear $\sigma_0 r$ potential ($\sigma_0 = 0.185 \text{ GeV}^2$); the value $\alpha_{\text{stat}} = 0.42$ is taken in both cases.

From Table 7, one can see that the modified potential $\sigma(r)r$ does not affect orbital excitations, but the masses $M(4S)$ and $M(3S)$ of radial excitations for the modified potential are shifted down by ~ 50 and $\sim 20 \text{ MeV}$, respectively, and turn out to be close to experimental numbers.

For spin structure of a meson, one needs to know

Table 7. The comparison of the spin-averaged masses (in MeV) in charmonium (R case) for confining $\sigma_0 r$ potential and modified potential (44) ($m_c = 1.42 \text{ GeV}$, $C_{SE} = -42 \text{ MeV}$, $\alpha_{\text{stat}} = 0.42$ in both cases)

State	$\sigma_0 = \text{const} = 0.185 \text{ GeV}^2$	$\sigma = \sigma(r)$ with parameters (45)	Experiment
$1S$	3068	3067	3067
$2S$	3670	3664	3672
$3S$	4097	4077	4040 ± 10
$4S$	4454	4403	4415 ± 6
$1P$	3525	3530	3525 ± 0.6
$2P$	3979	3965	Absent
$1D$	3835	3828	3770 ± 2.5
$2D$	4217	4194	4159 ± 20
$1F$	4076	4070	Absent

the dynamical masses $\omega_c(nL)$, which are larger than the pole mass, and for low-lying states

$$\omega_c(nL) - m_c \cong 220\text{--}250 \text{ MeV}, \quad (46)$$

while for high excitations this difference can reach 300–340 MeV (see Table 8).

The observed difference between the dynamical and the pole mass can be essential for such physical characteristics as hyperfine- and fine-structure

Table 8. The dynamical masses $\omega_c(nL)$ for the potential with the parameters (43) (set A)

State	1S	2S	3S	4S	1P	2P	1D	2D
$\omega_c(nL)$ [GeV]	1.65	1.69	1.74	1.76	1.63	1.69	1.66	1.77

splittings, which are determined by the dynamical mass [26] and give rise to a decrease in spin splitting in charmonium [27].

From our analysis, the best fit to the $c\bar{c}$ spectrum [together with the correct choice of the self-energy constant (6)] is obtained for the pole mass m_c , which lies in the range

$$m_c(2\text{-loop}) = 1.39 \pm 0.03 (\text{theory}) \pm 0.03(\alpha_B) \text{ GeV.} \tag{47}$$

Then, from (1), the following \overline{MS} running mass ($n_f = 4$, the coefficient $\xi_2 \cong 10.5$, $\alpha_s(m_c) = 0.30$) can be obtained:

$$\overline{m}_c(\overline{m}_c) = 1.14 \pm 0.05 \text{ GeV.} \tag{48}$$

The extracted value turns out to be in good agreement with the conventional number for $\overline{m}_c(\overline{m}_c)$ (2), but has a smaller theoretical error.

6. CONCLUSION

Our study of the $b\bar{b}$ and $c\bar{c}$ spectra is performed with the use of the relativistic Hamiltonian H_0 and correct NP self-energy contribution to the meson mass.

By derivation, the kinetic part of H_0 contains the pole heavy-quark mass m_Q and it can directly be extracted from the analysis of the $Q\bar{Q}$ spectrum. In our study, all the meson masses are expressed through two parameters, the string tension and the QCD constant $\Lambda_B^{(n_f)}$ (in the vector scheme), which at present are known with $\sim 5\%$ accuracy. The variations of σ in the range $0.185 \pm 0.005 \text{ GeV}^2$ and $\Lambda_B^{(4)}$ in the range $385 \pm 15 \text{ MeV}$ give the uncertainty in the pole mass $m_b(m_c)$ around 50 MeV. In charmonium, the strong coupling $\alpha_B(r)$ can be approximated as a constant with good accuracy.

The spin-averaged splittings like $1D-1P$, $2P-1P$ in bottomonium and $2S-1P$, $1P-1S$ in charmonium appear to be very sensitive to the chosen freezing (critical) value of the strong coupling. A good description of the HQ spectra is reached only if α_{crit} is rather large, $\alpha_{\text{crit}} \cong 0.56 \pm 0.02$, while the effective $\alpha_{\text{eff}} = \text{const}$, present in the Cornell potential, is $\sim 20\%$ smaller.

From our analysis, one can conclude the following:

(i) The dynamical quark mass $\omega_b(\omega_c)$ is about 200 MeV larger than the pole mass $m_b(m_c)$ for low-lying states. This difference should be taken into account when the spin structure in heavy quarkonia is studied, and it is especially important in charmonium.

(ii) The pole masses $m_b(2\text{-loop}) = 4.78 \pm 0.05 \text{ GeV}$ and $m_c(2\text{-loop}) = 1.39 \pm 0.06 \text{ GeV}$ were extracted from our fit to the $Q\bar{Q}$ spectra, which correspond to the \overline{MS} running masses $\overline{m}_b(\overline{m}_b) = 4.19 \pm 0.04 \text{ GeV}$ and $\overline{m}_c(\overline{m}_c) = 1.14 \pm 0.05 \text{ GeV}$. The obtained numbers are in good agreement with the conventional values but have smaller theoretical error. Our theoretical error is small because in our analysis only one parameter, $\Lambda_{\overline{MS}}$ (or α_{crit}), is actually varied while the second parameter, the string tension, is taken to be the same as for light mesons.

APPENDIX

Below, we present the main steps to derive the Hamiltonian $H_R(7)$ [11] and NP self-energy term (4) from [14]. The starting point is the gauge-invariant meson Green's function written in the FFS representation [14, 24] with the use of the QCD action:

$$G_M(x, y) = \langle \text{tr} \Gamma_1 G_q(x, y) \Gamma_2 G_{\bar{q}}(x, y) \rangle_B. \tag{A.1}$$

Here, $\Gamma_1(\Gamma_2)$ is the matrix defining the quantum numbers of the initial (final) state of a meson. For a spinless quark (antiquark), $\Gamma_1 = \Gamma_2 = 1$. In (A.1), the averaging goes over the background field B_μ and $G_q(x, y)$ ($G_{\bar{q}}(x, y)$) is the Euclidean quark (antiquark) Green's function:

$$\begin{aligned} G_q(x, y) &= (\overline{m}_q + \hat{D})_{x,y}^{-1} \\ &= (\overline{m}_q - \hat{D})_x (\overline{m}_q^2 - \hat{D}^2)_{x,y}^{-1} \\ &= (\overline{m}_q - \hat{D})_x \int_0^\infty ds (Dz)_{xy} e^{-K} \mathcal{R}_a \mathcal{R}_B \mathcal{R}_F, \end{aligned} \tag{A.2}$$

where the factors \mathcal{R}_a , \mathcal{R}_B , \mathcal{R}_F are the following:

$$\mathcal{R}_a = P_a \exp \left(ig \int_y^x a_\mu dz_\mu \right), \tag{A.3}$$

$$\mathcal{R}_B = P_B \exp \left(ig \int_y^x B_\mu dz_\mu \right), \tag{A.4}$$

$$\mathcal{R}_F = P_F \exp \left(\int_0^s g \sigma_{\mu\nu} F_{\mu\nu} d\tau \right). \tag{A.5}$$

Here, P_a , P_B , and P_F are the ordering operators of the matrices a_μ (the field of valence gluon), B_μ (the

background NP field), and the NP field strength $F_{\mu\nu}$, respectively, and

$$\sigma_{\mu\nu}F_{\mu\nu} = \begin{pmatrix} \boldsymbol{\sigma} \cdot \mathbf{H} & \boldsymbol{\sigma} \cdot \mathbf{E} \\ \boldsymbol{\sigma} \cdot \mathbf{E} & \boldsymbol{\sigma} \cdot \mathbf{H} \end{pmatrix} \quad (\text{A.6})$$

with $\sigma_{\mu\nu} = \frac{1}{4i}(\gamma_\mu\gamma_\nu - \gamma_\nu\gamma_\mu)$, represents the interaction of the quark (antiquark) color magnetic moment with NP field strength $F_{\mu\nu}$.

In Eq. (A.2), the kinetic energy term K contains the integral over the proper time τ :

$$K = \bar{m}_q^2 s + \frac{1}{4} \int_0^s (\dot{z}_\mu)^2 d\tau. \quad (\text{A.7})$$

The quark, moving along the trajectory $z_\mu(\tau)$, interacts with the field of valence gluon a_μ and by its color charge also interacts with the NP background field B_μ .

In Eq. (A.7), the quantity \bar{m}_q , which refers to a quark with any mass, is the Lagrangian current mass taken in the \overline{MS} renormalization scheme. The factor \mathcal{R}_a is to be responsible for standard perturbative corrections to the quark mass \bar{m}_q [as for the heavy-quark mass m_Q in Eq. (2)], i.e., for the appearance of the pole mass in the QCD action (Hamiltonian) [2]. Also, the factors \mathcal{R}_a and $\bar{\mathcal{R}}_a$ (from the quark and the antiquark) provide the perturbative static interaction [26].

The other two factors \mathcal{R}_B and $\bar{\mathcal{R}}_B$ (from the quark and the antiquark) in $G_M(x, y)$ (A.1), (A.2) are responsible for the full NP (string) dynamics and were considered in detail in [11], where after several steps the meson Green's function was presented in the following form:

$$G_M = \int d\omega d\nu d\mathbf{r} \exp(-A_R), \quad (\text{A.8})$$

where the action A_R in coordinate space is expressed through two auxiliary fields ω and ν . Since this action (see [11]) does not depend on the derivatives $\dot{\omega}$ and $\dot{\nu}$, the integration over ω, ν in (A.8) is equivalent to the canonical quantization of the Hamiltonian H_R which corresponds to the action A_R . It results in the following Hamiltonian:

$$\begin{aligned} H_R = & \frac{p_r^2 + m_q^2}{\omega} + \omega(t) \\ & + \frac{\mathbf{L}^2}{r^2} \left[\omega + 2 \int_0^1 d\beta \cdot \beta \nu(\beta) \right]^{-1} \\ & + \frac{1}{2} \sigma^2 r^2 \int_0^1 \frac{d\beta}{\omega(\beta)} + \frac{1}{2} \int_0^1 d\beta \nu(\beta), \end{aligned} \quad (\text{A.9})$$

where \mathbf{L} is the orbital momentum and by definition the field operator $\omega(t)$ is $\omega(t) = \frac{1}{2} \frac{dt}{d\tau}$ (t is the actual time).

With the use of the extremal conditions (it gives the solution $\nu_0 = \sigma r$) and considering the string corrections as the perturbation (the procedure is described in [13]), one arrives at the Hamiltonian H_0 (3).

The terms \mathcal{R}_F and $\bar{\mathcal{R}}_F$ (from quark and antiquark) provide the NP self-energy (gauge-invariant) contribution C_{SE} to the meson mass [14], where the total self-energy correction Δm_q^2 to the pole mass m_q appears to be expressed only through the string tension σ and the factor $\eta(m_q)$:

$$\Delta m_q^2(m_q) = -\frac{4\sigma}{\pi} \eta(m_q). \quad (\text{A.10})$$

The factor $\eta(m_q)$ is calculated in analytical form in [14] and, for $m_q > T_g$, where T_g is the gluonic correlation length ($\delta = T_g^{-1}$), is given by the expression

$$\begin{aligned} \eta(m_q) = & -\frac{3m_q^2 \delta^3}{(m_q^2 - \delta^2)^{5/2}} \\ & \times \arctan \frac{\sqrt{m_q^2 - \delta^2}}{\delta} + \frac{\delta^2(2m_q^2 + \delta^2)}{(m_q^2 - \delta^2)^2}. \end{aligned} \quad (\text{A.11})$$

The direct calculations give for bottomonium $\eta(m_b \cong 5.0 \text{ GeV}) \cong 0.07$ and for charmonium $\eta(m_c \cong 1.70 \text{ GeV}) = 0.24$ and $\eta(m_c \cong 1.40 \text{ GeV}) \cong 0.30$. Then the string Hamiltonian (7) acquires the correction (A.10),

$$\begin{aligned} H'_R = H_0 + \frac{\Delta m_q^2}{\omega_q} = & \frac{\mathbf{p}^2 + m_q^2 + \Delta m_q^2}{\omega_q} \\ & + \omega_q + V_{\text{stat}} = H_0 + C_{SE}, \end{aligned} \quad (\text{A.12})$$

with the self-energy correction

$$C_{SE} = \frac{\Delta m_q^2}{\omega_q} = -\frac{4\sigma}{\pi \omega_q} \eta(m_q). \quad (\text{A.13})$$

In the self-energy correction, considered as a perturbation, the operator $\hat{\omega}$ in (7) can be replaced by the average of this operator (5), which is called by the dynamical mass,

$$\hat{\omega} \rightarrow \omega_q = \left\langle \sqrt{\mathbf{p}^2 + m_q^2} \right\rangle_{nL}. \quad (\text{A.14})$$

The NP self-energy term C_{SE} appears to be dependent on the quantum numbers nL just through the dynamical mass ω_q . However, in bottomonium for $m_b \cong 5.0 \text{ GeV}$,

$$C_{SE}(b\bar{b}) \cong -3 \text{ MeV} \quad (\text{A.15})$$

is very small and can be neglected. In charmonium for $m_c \cong 1.40$ GeV, the factor $\eta(m_c) = 0.29$ and the value of $C_{SE} \cong -40 \pm 10$ MeV is obtained, which is practically the same for different nL states because of weak dependence of $\omega_c(nL)$ on the quantum numbers nL (see Table 8).

REFERENCES

1. Particle Data Group, Phys. Rev. D **66**, 010001 (2002), and references therein.
2. F. J. Yndurain, *The Theory of Quark–Gluon Interaction* (Springer, Berlin, 1999), p. 230; N. Gray *et al.*, Z. Phys. **48**, 673 (1990); K. Melnikov and T. van Ritbergen, Phys. Lett. B **482**, 99 (2000).
3. S. Narison, Phys. Lett. B **520**, 115 (2001); hep-ph/0307248.
4. J. Kuhn and M. Steinhauser, Nucl. Phys. B **619**, 588 (2001); **640**, 415(E) (2002); A. Khodjamirian, hep-ph/0306253, and references therein; M. Eidemuller, Phys. Rev. D **67**, 113002 (2003).
5. L. Lellouch, Nucl. Phys. B (Proc. Suppl.) **117**, 127 (2003); A. Dougall, C. M. Maynard, and C. McNeill, hep-lat/0309081, and references therein.
6. E. J. Eichten *et al.*, Phys. Rev. D **21**, 203 (1980); E. J. Eichten, K. Lane, and C. Quigg, Phys. Rev. Lett. **89**, 162002 (2002).
7. D. P. Stanley and D. Robson, Phys. Rev. D **21**, 3180 (1980); Phys. Rev. Lett. **45**, 235 (1980); J. L. Basdevant and S. Boukraa, Z. Phys. C **28**, 413 (1985); S. Jacobs, M. G. Olsson, and C. Suchyta, Phys. Rev. D **33**, 3338 (1986); F. Halsen *et al.*, Phys. Rev. D **47**, 3013 (1993); L. P. Fulcher, Phys. Rev. D **44**, 2079 (1991).
8. S. Godfrey and N. Isgur, Phys. Rev. D **32**, 189 (1985), and references therein.
9. D. Ebert, R. N. Faustov, and V. O. Galkin, Phys. Rev. D **62**, 034014 (2000); **67**, 014027 (2003); W. Buchmuller and S. Tye, Phys. Rev. D **24**, 132 (1981).
10. A. M. Badalian and V. L. Morgunov, Phys. Rev. D **60**, 116008 (1999); A. M. Badalian and B. L. G. Bakker, Phys. Rev. D **62**, 094031 (2000).
11. A. Yu. Dubin, A. B. Kaidalov, and Yu. A. Simonov, Phys. Lett. B **323**, 41 (1994); Yad. Fiz. **56** (12), 213 (1993) [Phys. At. Nucl. **56**, 1745 (1993)].
12. Yu. S. Kalashnikova, A. V. Nefediev, and Yu. A. Simonov, Phys. Rev. D **64**, 014037 (2001).
13. A. M. Badalian and B. L. G. Bakker, Phys. Rev. D **66**, 034025 (2002).
14. Yu. A. Simonov, Phys. Lett. B **515**, 137 (2001).
15. S. E. Csorna *et al.* (CLEO Collab.), hep-ex/0207060; hep-ex/0404021; H. Mahlke-Krüger, hep-ph/0309015.
16. G. S. Bali, Phys. Lett. B **460**, 170 (1999).
17. A. M. Badalian, Yad. Fiz. **63**, 2269 (2000) [Phys. At. Nucl. **63**, 2173 (2000)]; A. M. Badalian and D. S. Kuzmenko, Phys. Rev. D **65**, 016004 (2002).
18. D. V. Shirkov and I. L. Solovtsov, Phys. Lett. B **442**, 344 (1998); Phys. Rev. Lett. **79**, 1209 (1997).
19. Yu. A. Simonov, Yad. Fiz. **66**, 796 (2003) [Phys. At. Nucl. **66**, 764 (2003)]; Pis'ma Zh. Éksp. Teor. Fiz. **57**, 513 (1993) [JETP Lett. **57**, 525 (1993)]; Yad. Fiz. **58**, 113 (1995) [Phys. At. Nucl. **58**, 107 (1995)]; A. M. Badalian and Yu. A. Simonov, Yad. Fiz. **60**, 714 (1997) [Phys. At. Nucl. **60**, 630 (1997)].
20. G. Parisi and R. Petronzio, Phys. Lett. B **94B**, 51 (1980); J. M. Cornwall, Phys. Rev. D **26**, 1453 (1982); A. C. Mattingly and P. M. Stevenson, Phys. Rev. D **49**, 437 (1994).
21. Yu. A. Simonov, Yad. Fiz. **65**, 140 (2002) [Phys. At. Nucl. **65**, 135 (2002)].
22. A. Billiøre, Phys. Lett. B **92B**, 343 (1980); M. Peter, Phys. Rev. Lett. **78**, 602 (1997); Y. Schröder, Phys. Lett. **447**, 321 (1999).
23. S. Capitani, M. Lüscher, R. Sommer, and H. Wittig, Nucl. Phys. B **544**, 669 (1999).
24. A. Duncan, E. Eichten, and H. Tacker, Phys. Rev. D **63**, 111501 (2001).
25. A. M. Badalian, B. L. G. Bakker, and Yu. A. Simonov, Phys. Rev. D **66**, 034025 (2002).
26. Yu. A. Simonov, in *Proceedings of the XVII International School on QCD: Perturbative or Nonperturbative, Lisbon, 1999*, Ed. by L. S. Ferreira *et al.* (World Sci., Singapore, 1999), p. 60; Phys. At. Nucl. **60**, 2069 (1997); Phys. Rev. D **65**, 116004 (2002); Yu. A. Simonov and J. A. Tjon, Ann. Phys. (N.Y.) **300**, 54 (2002).
27. A. M. Badalian and B. L. G. Bakker, Phys. Rev. D **67**, 071901 (2003).

ELEMENTARY PARTICLES AND FIELDS
Theory

Breit–Wigner Parameters of the $S_{11}(1535)$ Nucleon Resonance

E. V. Balandina, E. M. Leikin, and N. P. Yudin*

*Institute of Nuclear Physics, Moscow State University,
Vorob'evy gory, Moscow, 119899 Russia*

Received February 11, 2003; in final form, June 23, 2003

Abstract—The results of a partial-wave analysis of the angular distributions for the process $\gamma p \rightarrow \eta p$ over the energy range up to 2 GeV are presented. Reliable estimates of the Breit–Wigner parameters of the $S_{11}(1535)$ resonance, as well as the energy dependence of the real and imaginary parts of the electric dipole amplitude E_{0+} and its phase, are derived from the energy dependence of the regression coefficient $a_0(W)$.

© 2004 MAIK “Nauka/Interperiodica”.

1. INTRODUCTION

The present article completes our phenomenological analysis of experimental data on η -meson photoproduction on protons. The first part of our study [1] was devoted to a partial-wave analysis of the angular distributions and polarization observables, including the asymmetry Σ in a beam of linearly polarized γ radiation and the asymmetry T for a polarized proton target, which were measured over the photon-energy range from the threshold to about 1 GeV. In order to estimate the regression coefficients correctly, the contributions of various partial waves were determined on the basis of a linear nonparametric model: each observable was represented as a series in Legendre polynomials, all nonnegligible terms being retained.

At the second stage of the analysis, we solved a set of nonlinear equations involving bilinear combinations of the real and imaginary parts of the electric ($E_{l\pm}$) and magnetic ($M_{l\pm}$) multipole amplitudes for the production of an η meson in the $l \pm 1/2$ states. The nonlinearities generally give rise to some additional difficulties [2]; however, it is shown below that, in the case of η -meson photoproduction on protons, the situation becomes simpler.

2. RESULTS OF THE PARTIAL-WAVE ANALYSIS

The main results of the partial-wave analysis performed in [1] are as follows:

(i) We confirm the well-known fact that, over the energy range from the threshold to about 1 GeV, η mesons are produced predominantly in the s -wave state, the photoproduction process, described by the amplitude E_{0+} , being of a resonance character.

(ii) Higher partial waves manifest themselves only in sp and sd interferences, whose contributions are small in relation to the dominant s -wave contribution. Data obtained in different experiments [3–5] are contradictory.

Thus, only the $S_{11}(1535)$ resonance is seen over the indicated photon-energy range being considered, whereas the contribution of the $P_{11}(1440)$ and $D_{13}(1520)$ resonances, which lie in the same energy region, is on the same order of magnitude as non-resonance contributions, which, according to [3], do not exceed a few percent of the $S_{11}(1535)$ -resonance contribution.

In this connection, an analysis of the differential cross sections for the process $\gamma p \rightarrow \eta p$ is of particular interest. In the experiment reported in [6], angular distributions for this process over the energy range from 0.795 to 1.925 GeV were measured with a step of 50 MeV. In all, 24 distributions were obtained, each being measured at eight values of the η -meson emission angle. Our analysis was based on expanding the respective differential cross section in a series in Legendre polynomials and on retaining the first three terms of this expansion (linear model) [7]. In just the same way as in the region of lower energies, the linear model proved to be statistically justified. The coefficients a_0 , a_1 , and a_2 are given in Fig. 1 versus energy according to the analysis of the angular distributions measured in [6] (the expressions for the regression coefficients a_0 , a_1 , and a_2 in terms of the multipole photoproduction amplitudes to E_{3-} and M_{3-} terms inclusive are presented in [1]).

As can be seen from Fig. 1, the s -wave amplitude E_{0+} is dominant, the P - and D -wave contributions being an order of magnitude less. Also, the absence of noticeable resonance contributions over the energy range between 1 and 2 GeV, where there are

* e-mail: yudin@helene.sinp.msu.ru

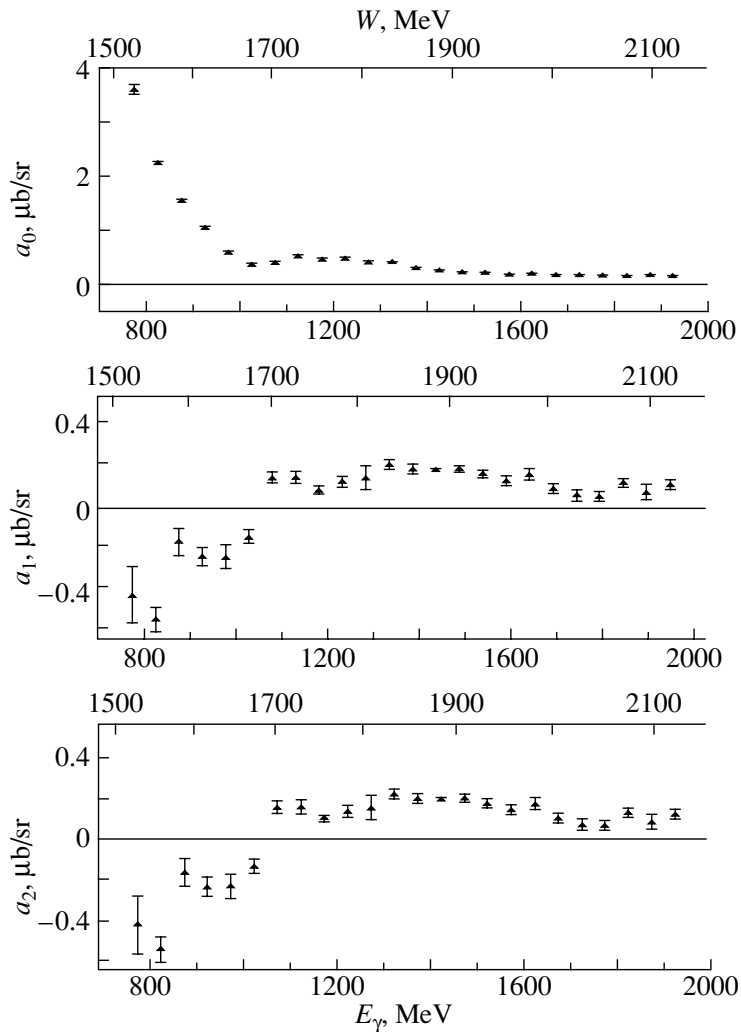


Fig. 1. Regression coefficients a_0 , a_1 , and a_2 versus the photon energy E_γ and the total energy W in the c.m. frame according to data from [6].

many well-established nucleon resonances, including $S_{11}(1650)$, $D_{15}(1675)$, $F_{15}(1680)$, $D_{13}(1700)$, $P_{11}(1710)$, and $P_{13}(1720)$ [8], is worthy of note. A rather smooth behavior of the coefficients a_0 , a_1 , and a_2 with increasing energy suggests that resonances do not play a significant role in the energy range under consideration. Thus, the $S_{11}(1535)$ resonance is an isolated broad resonance, whose parameters are estimated below.

3. DETERMINATION OF THE BREIT-WIGNER PARAMETERS FOR THE $S_{11}(1535)$ RESONANCE AND FOR THE AMPLITUDE E_{0+} OF η -MESON PHOTOPRODUCTION ON PROTONS

The results obtained by assessing the contributions of various partial waves to η -meson photoproduction on protons over the energy range from the

threshold to about 2 GeV made it possible to simplify the determination of the parameters of the $S_{11}(1535)$ resonance. This simplification is due to the fact that, over the entire energy range under consideration, the process $\gamma p \rightarrow \eta p$ can be adequately described by the first three terms of the expansion in Legendre polynomials. The validity of this description implies that, in formulas (2), (4), and (5) from [1], it is sufficient to retain only terms involving the amplitude E_{0+} . This being so, the leading s -wave contribution appears only in the first equation,

$$a_0(W) = |E_{0+}|^2. \quad (1)$$

Assuming that the electric dipole amplitude can be approximated by a Breit-Wigner resonance curve, one can determine its parameters by using the respective parametric model either for the energy dependence of the regression coefficient $a_0(W)$ or for the total cross section $(k/q)\sigma(W)$ for the reaction

Table 1. Parameters of the $S_{11}(1535)$ resonance that were determined from an analysis of data obtained in [3]

$(k/q)(d\sigma/d\Omega)$	$b_\eta = 0.55, b_\pi = 0.35$	$b_\eta = 0.45, b_\pi = 0.45$	$b_\eta = 0.35, b_\pi = 0.55$
$\sigma(W_R)$ [μb]	33.51 ± 1.5	35.88 ± 1.48	38.18 ± 1.57
W_R [MeV]	1563.68 ± 9.53	1555.32 ± 8.32	1547.68 ± 7.86
Γ_R [MeV]	270.42 ± 41.18	264.02 ± 40.5	271.34 ± 46.61
ξ [10^{-4} MeV^{-1}]	2.08 ± 0.05	2.15 ± 0.04	2.22 ± 0.05
$A_{1/2}$ [$10^{-3} \text{ GeV}^{-1/2}$]	129.25 ± 6.78	142.32 ± 7.46	164.28 ± 9.53
χ^2/ν	1.2	1.21	1.24

$4\pi a_0(W)$	$b_\eta = 0.55, b_\pi = 0.35$	$b_\eta = 0.45, b_\pi = 0.45$	$b_\eta = 0.35, b_\pi = 0.55$
$\sigma(W_R)$ [μb]	34.63 ± 0.82	36.92 ± 0.8	39.25 ± 0.76
W_R [MeV]	1558.73 ± 4.79	1551.32 ± 4.16	1543.9 ± 3.57
Γ_R [MeV]	244.09 ± 20.32	238.41 ± 19.83	240.16 ± 20.44
ξ [10^{-4} MeV^{-1}]	2.11 ± 0.02	2.18 ± 0.02	2.25 ± 0.02
$A_{1/2}$ [$10^{-3} \text{ GeV}^{-1/2}$]	122.96 ± 3.51	135.31 ± 3.83	154.43 ± 4.42
χ^2/ν	0.52	0.52	0.49

Table 2. Parameters of the $S_{11}(1535)$ resonance that were determined from an analysis of data obtained in [4]

$4\pi a_0(W)$	$b_\eta = 0.55, b_\pi = 0.35$	$b_\eta = 0.45, b_\pi = 0.45$	$b_\eta = 0.35, b_\pi = 0.55$
$\sigma(W_R)$ [μb]	41.06 ± 1.24	42.89 ± 1.28	44.79 ± 1.35
W_R [MeV]	1537.33 ± 1.47	1533.53 ± 1.54	1529.4 ± 1.69
Γ_R [MeV]	139.7 ± 5.76	137.08 ± 5.49	134.99 ± 5.3
ξ [10^{-4} MeV^{-1}]	2.3 ± 0.03	2.35 ± 0.04	2.4 ± 0.04
$A_{1/2}$ [$10^{-3} \text{ GeV}^{-1/2}$]	93.43 ± 1.54	102.71 ± 1.67	115.62 ± 1.9
χ^2/ν	15.27	15.29	15.54

Table 3. Parameters of the $S_{11}(1535)$ resonance that were determined from an analysis of data obtained in [5]

$4\pi a_0(W)$	$b_\eta = 0.55, b_\pi = 0.35$	$b_\eta = 0.45, b_\pi = 0.45$	$b_\eta = 0.35, b_\pi = 0.55$
$\sigma(W_R)$ [μb]	29.83 ± 0.76	31.16 ± 0.71	32.51 ± 0.66
W_R [MeV]	1559.18 ± 2.83	1554.0 ± 2.46	1548.47 ± 2.13
Γ_R [MeV]	199.61 ± 13.86	196.17 ± 13.43	194.25 ± 13.25
ξ [10^{-4} MeV^{-1}]	1.96 ± 0.02	2.0 ± 0.02	2.05 ± 0.02
$A_{1/2}$ [$10^{-3} \text{ GeV}^{-1/2}$]	103.35 ± 2.45	113.83 ± 2.63	128.63 ± 2.92
χ^2/ν	2.3	2.3	2.31

under study. Although these quantities coincide apart from the factor 4π , they are determined with different errors. The energy dependence of the resonance width

is taken into account by means of the formula [3]

$$\frac{k}{q}\sigma(W) = 4\pi a_0(W) = \frac{\sigma(W_R)W_R^2\Gamma_R^2}{(W_R^2 - W^2)^2 + W_R^2\Gamma^2(W)}, \quad (2)$$

Table 4. Parameters of the $S_{11}(1535)$ resonance that were determined from an analysis of data obtained in [6]

$4\pi a_0(W)$	$b_\eta = 0.55, b_\pi = 0.35$	$b_\eta = 0.45, b_\pi = 0.45$	$b_\eta = 0.35, b_\pi = 0.55$
$\sigma(W_R)$ [μb]	43.18 ± 9.13	46.15 ± 11.43	49.25 ± 14.19
W_R [MeV]	1530.63 ± 12.13	1525.6 ± 13.74	1520.34 ± 15.46
Γ_R [MeV]	152.4 ± 18.7	147.94 ± 16.4	143.97 ± 14.53
ξ [10^{-4} MeV^{-1}]	2.36 ± 0.25	2.44 ± 0.3	2.52 ± 0.36
$A_{1/2}$ [$10^{-3} \text{ GeV}^{-1/2}$]	96.86 ± 8.32	106.03 ± 10.47	118.47 ± 13.74
χ^2/ν	11.22	11.22	11.25

where W is the total energy in the c.m. frame (that is, the resonance mass); Γ_R is the total resonance width;

$$\Gamma(W) = \Gamma_R \left(b_\eta \frac{q_\eta}{q_{\eta R}} + b_\pi \frac{q_\pi}{q_{\pi R}} + b_{\pi\pi} \right); \quad (3)$$

b_η , b_π , and $b_{\pi\pi}$ are the branching fractions for the decays of the S_{11} resonance through the corresponding channels; and q_η and q_π are the momenta of the η and π mesons, respectively, $q_{\eta R}$ and $q_{\pi R}$ being their values at the resonance peak. The parameters were estimated by fitting $a_0(W)$ to data from [3–6], the results being presented in Tables 1–4 {in the case of data from [3], $(k/q)\sigma(W)$ was also subjected to fit-

ting}. The estimates given in these tables correspond to three sets of values of the parameters b_η and b_π at $b_{\pi\pi} = 0.1$. Tables 1–4 also display values of the helicity amplitudes calculated by the formula

$$A_{1/2}^2 = \frac{W_R \Gamma_R}{2m_p b_\eta} \sigma(W_R), \quad (4)$$

where m_p is the proton mass, and values of the parameter ξ , which is independent of b_η ,

$$\xi = \frac{1}{2} \sqrt{\frac{k}{q} \sigma(W_R)}. \quad (5)$$

Table 1 demonstrates that, within the errors, the values of the parameters obtained from a fit to the cross section agree with those obtained from a fit to the regression coefficient, the errors being much smaller in the latter case. There is a substantial distinction between the value obtained for the total width of the $S_{11}(1535)$ resonance from data presented in [3, 5] and that extracted from data quoted in [4, 6]. The origin of this distinction is illustrated by the Breit–Wigner curves for $b_\eta = 0.55$ and $b_\pi = 0.35$ in Figs. 2–4. It

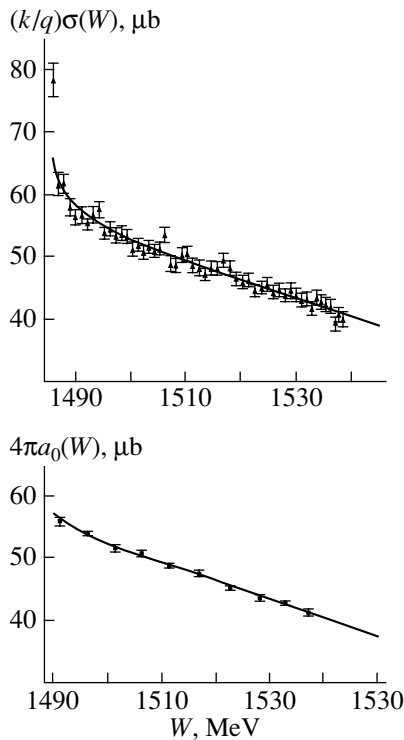


Fig. 2. Theoretical description (curves) of experimental data from [3] (points) on the basis of the parametric model at $b_\eta = 0.55$ and $b_\pi = 0.35$ [see formulas (2) and (3)].

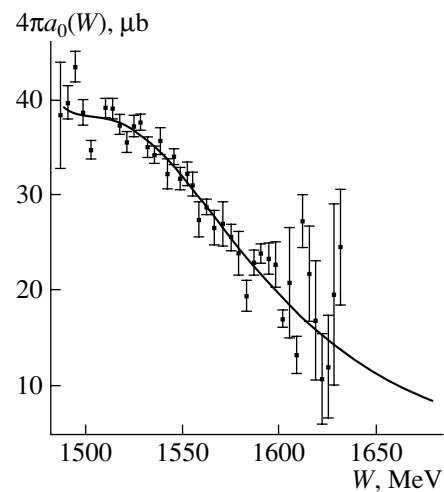


Fig. 3. As in Fig. 2, but for data from [5].

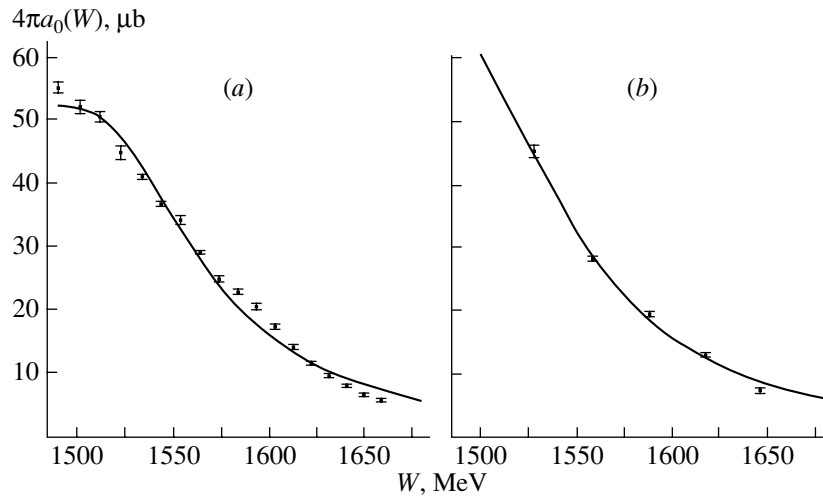


Fig. 4. Theoretical description (curves) of experimental data (points) from (a) [4] and (b) [6] on the basis of the parametric model at $b_\eta = 0.55$ and $b_\pi = 0.35$ [see formulas (2) and (3)].

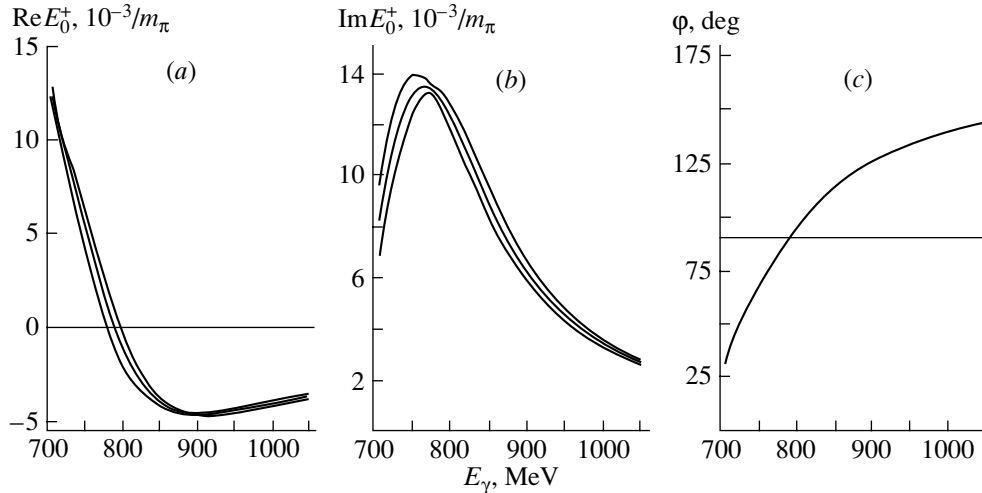


Fig. 5. (a) Real part, (b) imaginary part, and (c) phase φ of the multipole amplitude E_{0+} versus the photon energy E_γ .

should be noted that the results obtained by analyzing data presented in [4, 6] remove the disagreement between the values of Γ obtained from hadron processes and those obtained from η -meson photoproduction [8].

It is worth noting that the values of χ^2/ν (that is, χ^2 per degree of freedom) for an analysis of the data from [4, 6] are anomalously large, but that the estimates of the parameters agree within the errors. The reason is that the actual deviations of the experimental points considerably exceed the respective errors, as can be seen from Fig. 3. Therefore, the scatter of the experimental values of $4\pi a_0(W)$ with respect to the Breit–Wigner curve cannot be described by a Gaussian distribution with zero central value; that is, the experimental values cannot be considered

as random independent variables, in which case the standard χ^2 criterion does not work. It is known [9] that, if the expectation values of some terms of the χ^2 distribution are nonzero, then the goodness of a fit can be estimated on the basis of the noncentral criterion χ_{nc}^2 characterized by the noncentrality parameter δ^2 defined as the sum of the squares of the expectation values of individual terms [9]. For the $4\pi a_0(W)$ values obtained from the partial-wave analysis of data reported in [4], we present in Table 5 the deviations from the Breit–Wigner curve for $b_\eta = 0.55$ and $b_\pi = 0.35$. These deviations were used as estimates of the expectation values of individual terms in the noncentral criterion χ_{nc}^2 . The respective value of the noncentrality parameter is $\delta^2 = 46.8$. The expectation value of χ_{nc}^2 is $M_{nc} = \nu + \delta^2$, where, in the present case, ν is the

Table 5. Difference Δ of the experimental values of $4\pi a_0(W)$ and the results of the fit

W, MeV	Δ	W, MeV	Δ	W, MeV	Δ
1490.16	2.9 ± 0.91	1553.9	1.41 ± 0.71	1612.92	0.83 ± 0.4
1501.14	0.36 ± 1.05	1564.08	0.98 ± 0.28	1622.26	-0.06 ± 0.13
1511.98	0.09 ± 0.78	1574.06	0.82 ± 0.54	1631.55	-0.67 ± 0.37
1522.61	-2.6 ± 1.08	1583.98	2.3 ± 0.46	1640.78	-1.09 ± 0.23
1533.85	-1.59 ± 0.42	1593.49	2.78 ± 0.56	1649.79	-1.53 ± 0.25
1543.61	-1.06 ± 0.42	1603.12	2.03 ± 0.42	1658.81	-1.55 ± 0.27

number of independent terms. According to [9], the value of χ_{nc}^2 per effective degree of freedom ν_{nc} is evaluated as $M_{\text{nc}}/\nu_{\text{nc}} = 1.05$. It characterizes statistical reliability of the results presented in Table 2. A similar argument is valid for the results of the partial-wave analysis of data from [6]. Thus, the estimates given in Tables 2 and 4 for the parameters of the $S_{11}(1535)$ resonance are quite reliable.

Both the real and the imaginary part of the electric dipole amplitude E_{0+} describing the production of the $S_{11}(1535)$ resonance, as well as the phase of this amplitude, can readily be determined from the energy dependence predicted for $4\pi a_0(W)$ by the parametric model on the basis of the Breit–Wigner formula. The data obtained with the aid of the energy dependence of $4\pi a_0(W)$ from [4] (under the assumption that the arbitrary phase of E_{0+} is zero) are shown in Fig. 5 by way of illustration. The upper and lower curves in Figs. 5a and 5b were calculated with allowance for the covariance matrix for the errors in the parameters W_R , $\sigma(W_R)$, and Γ_R . At $b_\eta = 0.55$ and $b_\pi = 0.35$ (see Table 2), this matrix has the form

$$\begin{pmatrix} 1.54 & -1.23 & -4.71 \\ -1.23 & 2.16 & 1.84 \\ -4.71 & 1.84 & 33.20 \end{pmatrix}.$$

Upon determining the real and imaginary parts of E_{0+} , the equations that involve the interference with the amplitude E_{0+} reduce to a set of linear equations. Unfortunately, the errors in the regression coefficients b_0 , b_1 , c_0 , and c_1 are significant; moreover, these coefficients were determined only for six (b_0 , b_1) or eight (c_0 , c_1) values of energy. Therefore, a considerable enlargement of the relevant database and refinement of data on polarization observables, including the data on the angular distribution of the polarization of recoil protons, are required for performing a further analysis

and for reliably estimating p , d , and higher multipole amplitudes.

4. CONCLUSION

The partial-wave analyses of the observables of η -meson photoproduction on protons in [1] and in the present study confirmed that the s -wave contribution dominates the photon energy range from the threshold to about 2 GeV. This contribution exhibits resonance behavior, corresponding to the production of the $S_{11}(1535)$ nucleon resonance. Moreover, the experimental data on the differential cross sections over the energy range under study do not show any contribution from $l > 2$ partial waves. The p - and d -wave contributions manifest themselves only in the interference with the s wave. These contributions are small, and data on them from different studies are contradictory. In all cases, a statistically reliable description of the experimental data is achieved by retaining the three lowest terms in the expansion of the differential cross section in Legendre polynomials. Thus, we conclude that, throughout the range of photon energies up to 2 GeV, experimental data do not reveal many of the well-established nucleon resonances [8].

Isolating the s -wave contribution made it possible to determine the energy dependence of the multipole amplitude E_{0+} and the parameters of the $S_{11}(1535)$ resonance. Unfortunately, the data from [3, 5] are inconsistent with those from [4, 6], the latter leading to resonance parameters closer to those obtained from an analysis of other processes [8]. In view of insufficiently vast statistics and a low precision of available experimental data and in view of the aforementioned inconsistencies in determining the p - and d -wave contributions, other multipole amplitudes for the process $\gamma p \rightarrow \eta p$ can hardly be evaluated at present.

REFERENCES

1. E. V. Balandina *et al.*, *Yad. Fiz.* **65**, 1755 (2002) [*Phys. At. Nucl.* **65**, 1711 (2002)].
2. V. F. Grushin *et al.*, *Yad. Fiz.* **38**, 1448 (1983) [*Sov. J. Nucl. Phys.* **38**, 881 (1983)].
3. B. Krusche *et al.*, *Phys. Rev. Lett.* **74**, 3736 (1995); **75**, 3023 (1995).
4. F. Renard *et al.*, *Phys. Lett. B* **528**, 215 (2002).
5. L. Soezueer *et al.*, <http://gwdac.phys.gwu.edu>.
6. M. Dugger *et al.*, *Phys. Rev. Lett.* **89**, 222002 (2002).
7. E. V. Balandina *et al.*, Preprint No. 2002-12/696, NIIYaF MGU (Inst. Nucl. Phys., Moscow State Univ., 2002).
8. Review of Partical Physics, <http://pdg.lbl.org>.
9. H. Scheffé, *The Analysis of Variance* (Wiley, New York, 1959; Nauka, Moscow, 1980).

Translated by R. Rogalyov

Cherenkov Detectors in Particle Physics

Yu. K. Akimov

Joint Institute for Nuclear Research, Dubna, Moscow oblast, 141980 Russia

Received December 24, 2003

Abstract—The most impressive examples of the application of Cherenkov detectors in modern-physics experiments are considered. © 2004 MAIK “Nauka/Interperiodica”.

In 1934, Pavel A. Cherenkov, who was at that time S.I. Vavilov’s postgraduate student, discovered blue luminescence of transparent liquids under the effect of gamma rays. Analyzing the properties of this radiation, which were explored by Cherenkov, Vavilov assumed that it is caused by the motion of a charged particle in a medium. The mechanism of this new effect—the emergence of light in response to the motion of a charged particle at a speed v exceeding the phase velocity of light c/n in a medium whose refraction index is n —was revealed in the study of I.E. Tamm and I.M. Frank of 1937, who also proposed its quantitative theory. This outstanding discovery was recognized by the physics community worldwide, and its authors (Cherenkov, Tamm, and Frank) were awarded the Nobel prize of 1960 in physics.

Since the advent of photomultiplier tubes, which are capable of recording weak light splashes, the characteristic properties of Cherenkov radiation have become a basis for developing highly efficient methods for recording various types of nuclear radiation. The threshold character of Cherenkov radiation made it possible to separate charged particles reliably by their velocities. That the optical-photon emission angle is strictly correlated with the particle velocity is a remarkable property of Cherenkov radiation. As a result, a light ring whose radius carries information about the particle velocity can be observed at a certain distance from the radiator. Rather thick Cherenkov radiators were used as a basis for constructing many full-absorption spectrometers for electromagnetic showers.

A special international seminar dedicated to the 50th anniversary of the discovery of the Cherenkov effect was held in 1984 at the Lebedev Institute of Physics (USSR Academy of Sciences, Moscow). The reports presented at this seminar [1] reflected great advances made in constructing Cherenkov detectors of various types and in applying them in cosmic-ray and accelerator experiments. The results

obtained in further development of Cherenkov detectors and in their applications in subsequent years proved to be even more impressive.

Cherenkov detectors made it possible to implement numerous experiments in various realms of physics, whose range is extremely wide. Our consideration below covers only a modest part of the most important lines of investigation. Also, we briefly touch upon a number of studies at accelerators and in space where use has been made of the latest achievement in the field of radiators of Cherenkov light and photorecorders detecting it.

SEARCHES FOR NEUTRINO OSCILLATIONS

Cherenkov detectors play a special role in studying the properties of the neutrino. First of all, this concerns searches for neutrino oscillations, which were hypothesized by B. Pontecorvo in 1957. The presence of transitions between different neutrino flavors implies a violation of the postulated law of lepton-number conservation and a nonzero neutrino mass [2]. The number of such transitions depends on the ratio of the distance R between the point of production and the point of detection of a neutrino state pure in flavor to the neutrino energy E_ν . The amplitude of vacuum neutrino oscillations depends on the angle of mixing of massive neutrino states (within a model where only two neutrinos are mixed, this amplitude depends on one mixing angle θ), while the period of these oscillations depends on the difference of the squares of their masses, Δm^2 . The existence of such oscillations may in principle explain the problem of solar neutrinos (recall that the problem is that of why the result obtained by recording the electron-neutrino flux from the Sun in the known Cl–Ar [3] and Ga–Ge [4, 5] radiochemical experiments is much lower than that which is predicted by the standard solar model). A number of new underground facilities that employ various detection procedures were created for solving

the problem of solar neutrinos (see [1–12] in [6]). Important results were obtained in experiments with the Cherenkov detectors Kamiokande (2140 t of water, Japan) [7] and SuperKamiokande (50 000 t of water, 11 200 photomultiplier tubes of diameter 50 cm) [8] and especially with the SNO (Sudbury Neutrino Observatory) detector (1000 t of heavy water, Canada) [9]. The flux of boron neutrinos was measured in each case. In the Kamiokande facility, neutrinos were recorded via elastic $\nu_e e$ scattering, and a 49% deficit in relation to the calculated value of their flux was found there. The choice of D₂O in the SNO experiments was motivated by the fact that, in this transparent liquid, neutrinos can be recorded owing to the reactions

$$\nu_e + d \rightarrow p + p + e^- \quad (Q = -1.44 \text{ MeV}), \quad (1)$$

$$\nu_x + d \rightarrow \nu_x + p + n \quad (Q = -2.2 \text{ MeV}), \quad (2)$$

$$\nu_x + e \rightarrow \nu_x + e. \quad (3)$$

The first process involves only electron neutrinos, while the second and the third one are possible for any neutrino flavor. Thus, the SNO detector records individually the flux of electron neutrinos and the total flux of active neutrinos of all flavors. The experiment resulted in proving the existence of neutrino oscillations and the correctness of the prediction of the neutrino flux on the basis of the standard solar model.

The discovery of the anomaly in the ratio of the number of atmospheric muon and electron neutrinos was another important result of investigations at the Kamiokande Cherenkov detector: the number of recorded muon neutrinos was 40% less than the value expected on the basis of the calculation of their production mechanism in the atmosphere [10]. In addition, an experiment was performed in a ν_μ beam ($E_\nu \approx 1.3 \text{ GeV}$) formed at the K2K accelerator situated at a distance of 250 km from the SuperKamiokande detector [11]. Light images from Cherenkov radiation generated by electrons and muons were recorded in that experiment. The different shapes of these light images from electrons and muons permitted separating these particles to a rather high degree of reliability.

DETECTION OF COSMIC RAYS OF EXTREMELY HIGH ENERGIES

Entering the Earth's atmosphere, primary protons and nuclei of extremely high energy generate extensive air showers through the interaction with the atmosphere. The value of $E_l \approx 5 \times 10^{19} \text{ eV}$, which followed from generally accepted ideas of particle production and acceleration in the Universe, was taken for an upper limit on the cosmic-ray energy. However,

a few extensive air showers of energy $E > E_l$ had been recorded at the early 1990s, and this was an astrophysical puzzle. It is assumed that sources of cosmic rays having extremely high energies are beyond the Milky Way Galaxy. Since intergalactic magnetic fields are not sufficiently strong to deflect such cosmic rays considerably, there is the hope that the sources of their generation can be found by the direction of the axes of extensive air showers, each such shower containing billions of particles and covering an area of $S \sim 10 \text{ km}^2$. However, cosmic rays of extremely high energy come to the Earth's atmosphere very rarely—there occurs one event of this kind per kilometer squared over 100 years for $E > 10^{20} \text{ eV}$; therefore, observatories of giant area are necessary to reach a reasonably high efficiency in recording such cosmic rays.

In particular, it is planned to enlarge manyfold the observatory in Utah (USA), where extensive air showers are recorded by the fluorescence of atmospheric nitrogen excited by charged particles. In order to view the sky both in the Northern and in the Southern Hemisphere of the Earth, an observatory that is supposed to have an area of about 3000 km² is presently being constructed in Argentina [12]. There, Cherenkov detectors will be basic elements. Water in tanks of volume 11 m³ that are arranged at a distance of 1.5 km from one another are used as the radiators of Cherenkov light. In each tank, the light is recorded by three large photomultiplier tubes ($\varnothing 22 \text{ cm}$). The angle of the shower-axis slope can be determined by the time difference between the emergence of light splashes in different tanks.

Cherenkov light in tanks can be recorded 24 hours a day, while fluorescence in air is visible only in the case of a dark and cloudless sky. Herein lies an important advantage of the Cherenkov procedure over the fluorescence procedure.

In order to implement searches for cosmic rays of extremely high energy, the project of an experiment that employs the International Space Station, from which a surface area $S \sim 150\,000 \text{ km}^2$ of the Earth can be seen, is presently being discussed [13]. It is planned to record, in air, not only fluorescence but also Cherenkov radiation, a considerable fraction of which is reflected from the Earth's surface, sea surface, and clouds.

NEUTRINO ASTRONOMY

Since the neutrino is a neutral particle weakly interacting with matter, it provides rich possibilities for seeking, in the Universe, objects emitting neutrinos and for studying various phenomena in the Universe. Of particular interest are ultrahigh-energy muons, which form the only cosmic-ray component that can

traverse the entire thickness of the Earth, forming muons in it. For an observer, these muons propagate upward. The directions of the neutrino and muon momenta are nearly collinear, within an angle of $\alpha \approx 1.5/\sqrt{E_\nu}$ (in angular degrees), where the energy is taken in TeV.

Albeit being positive in the sense indicated above, the neutrino property of propagating through matter almost freely is simultaneously negative since it causes considerable difficulties in detecting neutrinos. However, nature itself is helpful in this respect, providing enormous water reservoirs, which are used as radiators of Cherenkov light and shields from atmospheric cosmic rays.

The first such detector (NT-200 neutrino telescope [14]) was constructed in Lake Baikal, where modules equipped with photomultiplier tubes ($\varnothing 37$ cm) and separated by a typical distance of about 6 m from one another were arranged at a depth of 1.1 km. The geometric volume of this telescope in 1998 was $V \approx 10^5$ m³, and its effective volume was $2V$ to 6×10^6 m³ for detecting neutrinos of energy 10 to 10^4 TeV. An observation of not less than 50 upward directed light signals with this telescope was reported in [15]. Still larger neutrino Cherenkov detectors (the planned volume of these detectors range up to 1 km³) are presently under construction in the Mediterranean Sea at the shores of France (ANTARES) [16] and Greece (NESTOR) [17].

The AMANDA Cherenkov detector embedded deep in the extremely transparent ice of Antarctica is very unusual [18]. In the region of the highest sensitivity of photomultiplier tubes (about 400 nm), the light-absorption length is 85 to 225 m. Modules equipped with photomultiplier tubes are arranged at a depth of 1.5 to 1.9 km with a step of 10 to 20 m. At the beginning of 1997, the effective area of the detector for recording upward-going muons was 10^4 m². An analysis of events recorded there within half a year revealed that 153 to 188 of them were generated by such muons. At the present time, the effective area of the detector is about 10^5 m², and it is planned to enlarge it to 1 km² (IceCube project).

The enormous amounts of transparent ice in Antarctica proved to be highly appealing for employing yet another wonderful property of Cherenkov radiation, the Askaryan effect, which consists in the coherent emission of radio waves of frequency about 1 GHz from neutrino-induced electromagnetic showers [19]. It is of importance that radio-wave emission is enhanced in proportion to the squared energy of particles inducing it [20]. The existence of the Askaryan effect was recently confirmed experimentally [21]. This experiment involved irradiating a target from 3.5 t of quartz sand with a beam of

photons of energy in excess of 1 GeV and seeking radio waves of frequency 0.3 to 6 GHz by means of antennae. As a result, distinct pulses of subnanosecond radio-frequency range that were generated by showers were recorded.

The ice of Antarctica is so pure that radio waves can be transmitted over a few hundred or even a thousand meters. At the present time, a prototype of the RICE (Radio Ice Cherenkov Experiment) radio detector of ultrahigh-energy neutrinos operates at the South Pole [22]. The antennae used, together with the modules of the AMANDA photodetector, are arranged in holes deep in the ice. Experimental data obtained with this detector, which already involve a few candidates for the sought effect, are presently being processed. ANITA, which is yet another Cherenkov radio detector and which will be arranged on board a balloon to be launched in 2006, is at the stage of preparation [23]. This telescope will make it possible to scan an enormously large layer of Antarctic ice from one horizon to the other.

The proposal to use geological deposits of ultrapure salt, which is twice as heavy as ice, so that more intense Cherenkov radio emission is expected to be generated there by showers, is also of great interest [24].

DETECTORS FOR INVESTIGATIONS AT ACCELERATORS AND IN SPACE

Cherenkov detectors have become an irreplaceable tool in numerous experiments with elementary particles and relativistic ions. Compelling results on *CP* violation in a *B*-meson system that were obtained in experiments at the *B*-meson factories at SLAC (USA) and KEK (Japan) (see, for example, [25]) are among the most important advancements made by using, among other things, Cherenkov detectors for identifying particles. This initiated the development of new *B*-meson physics, whose fundamental task is to explain the relationships existing in the family of quarks and between matter and antimatter. An extensive program of investigations into *B*-meson physics was proposed for LHC and Tevatron, where the rate of *B*-meson production is expected to be severalfold higher than at *B*-meson factories. In such and in other experiments [25], so-called Rich Imaging Cherenkov (RICH) detectors recording rings from Cherenkov radiation ensure the highest efficiency of particle identification.

Gases or an aerogel, which is a transparent solid-state material successfully replacing cumbersome gas radiators at threshold particle velocities not exceeding 0.993, is predominantly used as a radiating medium in RICH detectors.

The aerogel structure is formed by spherical quartz clusters of diameter about 4 nm that are arranged in a three-dimensional network whose hollows are filled with air (see, for example, [26] and references therein). The dimensions of the hollows are many times as great as the dimensions of the clusters and can be controlled during the preparation of an aerogel; as a result, it is possible to obtain a material whose refraction index ranges from 1.007 to 1.1.

Being a solid-state medium, an aerogel makes it possible to design compact Cherenkov detectors, and this is especially important for applying them in satellite-borne experiments. In particular, an aerogel RICH detector enters into the composition of the magnetic spectrometer of the AMS experiment, whose start is planned in 2004 at the International Space Station Alpha [27]. This experiment is intended for solving the fundamental problem of searches for antimatter and dark matter via a precision measurement of the composition of cosmic rays.

In media characterized by low values of n , the intensity of a light splash is usually very weak; therefore, it is necessary to ensure a highly efficient detection of even single photons, frequently under conditions of a high level of the background from accompanying processes. An important advantage of this mode of photorecorder operation is that a reliable energy calibration of the detector is automatically implemented in this case.

Photorecorders, especially those in RICH detectors, must ensure the required spatial accuracy in detecting light rings, this being achieved by using a relatively large number of photosensitive channels. For this purpose, industry proposes multichannel vacuum photomultiplier tubes featuring 16 to 256 diminutive channels ($\geq 2.5 \times 2.5$ mm) within one vessel about 5 cm in diameter. Up to 2048 channels are arranged in a hybrid photodiode, which is an image amplifier where photoelectrons are accelerated by an electric field of strength about 20 kV. Hitting a silicon detector, each accelerated photoelectron generates about 10^5 electron-positron pairs in it. Owing to modern technologies, multichannel recording microelectronics can be arranged within the same vacuum vessel of diameter about 8 cm, these microelectronics being in immediate contact with a position-sensitive silicon detector.

A system of such hybrid photodiodes was chosen, for example, as a photorecorder in the RICH detector for experiments at LHC [28]. However, a second version was also provided there, that which employs multichannel vacuum photomultiplier tubes, whose operational stability with time was better tested.

Gas position-sensitive instruments, whose highest precision and fast operation are achieved if use

is made of CsI photocathodes, which are sensitive to light of wavelength below 220 nm, permit obtaining the largest photosensitive area. For example, the area of the photocathode manufactured from segmented CsI is 5.3 m^2 in the RICH detector for the COMPASS experiment (CERN) [29].

Physics problems solved with the aid of Cherenkov detectors are quite diverse. Cherenkov detectors provide the most efficient way to seek sources of particles having extremely high energies and to study the nature of their emergence, and this is the most important problem in contemporary astrophysics.

The use of transparent and deep water reservoirs and enormous masses of ice as radiators of Cherenkov light and shields from atmospheric cosmic rays makes it possible to create unique telescopes for neutrino astronomy.

Without Cherenkov detectors, it would be impossible to identify particles in numerous experiments at accelerators and in space vehicles. The resulting need for fast multichannel photorecorders of large area that are able to detect single photons is a decisive factor in the development of many types of photosensitive instruments.

The observation of the Cherenkov effect was one of the outstanding discoveries in the 20th century. Without its application, many physical experiments of fundamental importance would have been impossible. The name of its author, Pavel A. Cherenkov, a recipient of a Nobel Prize in physics, is known among the physics community worldwide. It will forever remain in the history of science.

REFERENCES

1. *Proceedings of the Seminar on Cherenkov Detectors*, Nucl. Instrum. Methods Phys. Res. A **248** (1986).
2. S. M. Bilen'kiĭ and B. M. Pontekorvo, Usp. Fiz. Nauk **123**, 181 (1977) [Sov. Phys. Usp. **20**, 776 (1977)].
3. B. T. Cleveland *et al.*, Nucl. Phys. B (Proc. Suppl.) **38**, 47 (1995).
4. J. N. Abdurashitov *et al.*, astro-ph/0204245.
5. W. Hampel *et al.*, Phys. Lett. B **447**, 127 (1999).
6. V. Barger *et al.*, Phys. Rev. D **65**, 053016 (2002).
7. Y. Fukuda *et al.*, Phys. Rev. Lett. **77**, 1683 (1996).
8. Y. Fukuda *et al.*, Phys. Lett. B **539**, 179 (2002).
9. Q. R. Ahmad *et al.* (SNO Collab.), Phys. Rev. Lett. **89**, 011301 (2002).
10. Y. Fukuda *et al.*, Phys. Lett. B **433**, 9 (1998); Phys. Rev. Lett. **85**, 3999 (2000).
11. S. H. Ahn *et al.* (K2K Collab.), Phys. Lett. B **511**, 178 (2001).
12. <http://www.auger.org/>.
13. M. Pallavicini, Nucl. Instrum. Methods Phys. Res. A **502**, 155 (2003).

14. I. A. Belolaprikov *et al.*, *Astropart. Phys.* **7**, 263 (1997).
15. B. K. Lubsandorzhev, *Nucl. Instrum. Methods Phys. Res. A* **502**, 145 (2003).
16. G. D. Hallewell, *Nucl. Instrum. Methods Phys. Res. A* **502**, 138 (2003).
17. S. E. Tzamaras, *Nucl. Instrum. Methods Phys. Res. A* **502**, 150 (2003).
18. E. Andres *et al.*, *Nature* **401**, 441 (2001).
19. M. Markov and I. Zheleznykh, *Nucl. Instrum. Methods Phys. Res. A* **248**, 242 (1986).
20. G. M. Frichter *et al.*, *Phys. Rev. D* **53**, 1684 (1996).
21. D. Saltzberg *et al.*, *AIP Conf. Proc.* **579**, 225 (2001).
22. I. Kravchenko *et al.*, *Astropart. Phys.* **19**, 15 (2003).
23. <http://www.ps.uci.edu/~anita>.
24. M. Shiba, *CERN Courier* **41** (3), 20 (2001).
25. R. Forty, *Nucl. Instrum. Methods Phys. Res. A* **502**, 275 (2003).
26. Yu. K. Akimov, *Prib. Tekh. Éksp.*, No. 3, 5 (2003).
27. J. Alcaraz *et al.* (AMS Collab.), *Phys. Lett. B* **461**, 387 (1999).
28. A. Braem *et al.*, *Nucl. Instrum. Methods Phys. Res. A* **442**, 128 (2000).
29. E. Albrecht *et al.*, *Nucl. Instrum. Methods Phys. Res. A* **502**, 112 (2003).

Translated by A. Isaakyan

Cherenkov Quartz Calorimeter

V. B. Gavrilov* and M. V. Danilov

*Institute of Theoretical and Experimental Physics,
Bol'shaya Cheremushkinskaya ul. 25, Moscow, 117259 Russia*

Received November 28, 2003

Abstract—A Cherenkov quartz detector possesses a high radiation resistance because of the radiation resistance of quartz fibers in which a light signal is formed and which are used to transfer signals to photodetectors. Owing to properties of Cherenkov radiation, such as the existence of a threshold with respect to the velocity of radiating charged particles and an instantaneous character of the radiation, this type of calorimeter is not sensitive to neutrons and the majority of radiative-decay products and generates a short signal within a narrow spatial region. In view of these special features of a Cherenkov quartz calorimeter, it is advantageous (with respect to other calorimetric methods) in detecting narrow jets of high-energy particles against the background of high-density energy fluxes, this being necessary, for example, in experiments at the Large Hadron Collider, which is presently under construction at CERN. The results obtained by measuring the radiation resistance of quartz fibers and the main features of a Cherenkov quartz calorimeter that were measured for prototypes are discussed in the present article.
© 2004 MAIK “Nauka/Interperiodica”.

1. INTRODUCTION

Calorimeters—that is, detectors intended for measuring energy fluxes associated with particles of various types—have been extensively used in contemporary experimental physics. Calorimeters enter into the composition of all operating facilities, as well as those that are under construction, for various colliders of high-energy particles. Calorimeters will play an important role in experiments at the Large Hadron Collider, which is presently being constructed at CERN and which is intended for implementing collisions between 7-TeV proton beams. In searches for new types of fundamental particles, it would be necessary to measure the fluxes of energy of all secondary particles, with the exception of those that are emitted within narrow regions (of angular dimension smaller than 1°) around colliding beams. High energies and high luminosities of the Large Hadron Collider will create extremely unfavorable conditions for the operation of the detecting equipment used. This concerns above all regions adjacent to colliding beams, where the bulk of the energy of secondary particles is concentrated. Calorimeters installed in these parts of the facilities will have to operate under conditions of extremely high radiation doses (up to 100 Mrad/yr) and neutron fluxes [up to 10^{16} neutron/(cm² yr)]. Therefore, the requirement of a high radiation resistances of the calorimeter components and the requirement of a reliable operation for many years in the

situation where the maintenance of the calorimeter is complicated by high levels of induced radioactivity impose stringent constraints on the choice of possible calorimetric technologies.

A Cherenkov quartz calorimeter is able to solve the above tasks. Optical quartz fibers, which possess the necessary radiation resistance and which will not require replacement in the course of operation, are active elements of such a calorimeter that are situated in the region of high radiation fields. Moreover, the nature of Cherenkov light, on which the operation of the calorimeter is based, makes it possible to obtain a number of advantages over other calorimetric technologies relying on ionization or scintillation. These advantages include a very fast and short signal and a low sensitivity to neutrons and products of radiative decays. In view of this, a group of physicists from the Institute of Theoretical and Experimental Physics (ITEP, Moscow) proposed that an international collaboration involved in the CMS experiment employ a Cherenkov quartz calorimeter for the region of small angles with respect to the colliding-beam axes. The radiation resistance of various quartz fibers was measured, a full-scale calorimeter prototype was manufactured, and the main parameters of the forward calorimeters for the CMS experiment were optimized. At the present time, these calorimeters are being assembled at CERN.

* e-mail: Vladimir.Gavrilov@cern.ch

2. RADIATION RESISTANCE OF QUARTZ FIBERS

The main advantage of Cherenkov quartz calorimeters over the majority of calorimeters of other types is a high radiation resistance of its components—first of all, quartz fibers. In [1], the results obtained by measuring signals from various quartz fibers irradiated with a 2-MeV electron beam are presented versus the absorbed irradiation dose of up to 2.2 Grad. The light signal was formed owing to Cherenkov radiation from electrons in fibers. It was shown that fibers whose reflecting layer was obtained by saturating quartz in the reflecting fiber layer with fluorine possess the highest radiation resistance.

The spectra of absorption in quartz fibers irradiated up to a dose of 1 Grad with the aid of a ⁶⁰Co radioactive source were investigated in [2]. Figure 1 shows the light-wavelength dependence of the absorption defined in terms of the transmission loss

$$A(\lambda) = \frac{10}{L} \log \frac{I_2(\lambda)}{I_1(\lambda)}$$

in a fiber irradiated to various doses. Here, λ is the wavelength of light; L is the length of the irradiated fiber; and I_1 and I_2 are the intensities of light transmitted by the fiber, respectively, prior to and after the irradiation. From Fig. 1, it is obvious that the wavelength range between 400 and 550 nm is the operating wavelength range for a Cherenkov quartz calorimeter, since, in the region of shorter waves, quartz fibers become nontransparent upon irradiation. Similar dependences were observed for various types of quartz fibers.

The results of further investigations into the problem of the radiation resistance of quartz fibers were given in [3, 4]. Measurement of the absorption spectra for fibers directly during their irradiation was the main feature that distinguished the procedure used in [3, 4] from that in [2]. It was found that the transparency of quartz fibers is restored to some extent immediately after irradiation, but the general character of the absorption spectra measured during irradiation remained by and large similar to that in Fig. 1. The absorbed-dose dependence of the loss of transparency of quartz fibers can be approximated by a power-law function:

$$A(D, \lambda) = \alpha(\lambda)D^{\beta(\lambda)}.$$

The results of the measurements reported in [3, 4] revealed that quartz fibers featuring a new type of polymer reflecting coating possess the required radiation resistance and are cheaper than fibers where the reflecting coating is obtained by doping quartz with fluorine.

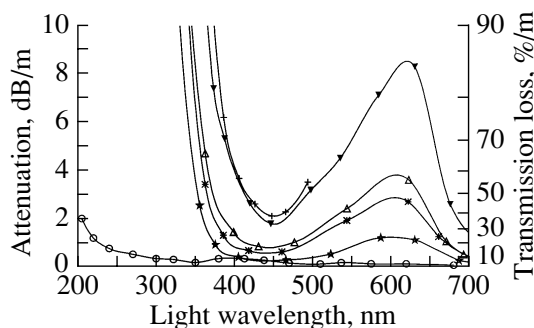


Fig. 1. Spectra of absorption in a quartz fiber irradiated to various doses [2]: (o) without irradiation, (*) after the dose of 10 Mrad, (*) after the dose of 57 Mrad, (Δ) after the dose of 100 Mrad, (▼) after the dose of 680 Mrad, and (+) after the dose of 1000 Mrad. The curves are drawn to guide the eye.

3. PRINCIPLE OF CALORIMETER OPERATION

A Cherenkov quartz calorimeter consists of optical quartz fibers embedded in an absorbing host material. In calorimeters, use is made of optical fibers whose core of radius about a few hundred micrometers is formed by a molten quartz and whose reflecting coating has a lower refraction index, whereby the propagation of light along a fiber is ensured owing to total internal reflection at the boundary between the quartz core and this coating. High-energy particles (hadrons, electrons, photons) finding their way to the calorimeter give rise to showers that develop in a calorimeter material. Relativistic charged particles belonging to such a shower that travel through quartz fibers radiate Cherenkov light, part of which propagates along fibers to photodetectors transforming it into an electric signal. The number of Cherenkov photons emitted by charged particles can be estimated by the formula

$$\frac{d^2 N_{ph}}{dLd\lambda} = 2\pi\alpha z^2 \frac{\sin^2 \vartheta_C}{\lambda^2},$$

where α is the fine-structure constant, ϑ_C is the angle at which Cherenkov light is emitted, λ is the light wavelength, and L is the distance that a particle of charge z travels in matter. The angle at which Cherenkov light is radiated with respect to the momentum of the radiating particle is given by

$$\cos \vartheta_C = \frac{1}{n\beta},$$

where $\beta = v/c$ and n is the medium's refraction index. For quartz, $\vartheta_C \approx 45^\circ$ for visible light and $\beta = 1$.

It was Gorodetzky [1] who first proposed widely employing quartz calorimeters in high-energy physics in view of a high radiation strength of quartz

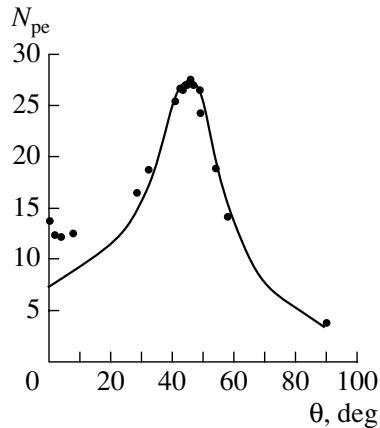


Fig. 2. The amplitude of the signal (mean number N_{pe} of photoelectrons in a signal) in a quartz-calorimeter prototype for electrons of energy 4 GeV as a function of the angle θ between the beam axis and the quartz-fiber direction [6]: (point) results of measurements and (curve) results of a Monte Carlo calculation.

fibers. The results obtained by measuring signals that arise in quartz fibers as single ultrarelativistic charged particles propagate through them at various angles are quoted in [5]. The signal from a single particle is maximal if the particle travels at the angle ϑ_C with respect to the fiber axis, since, in this case, the largest part of the emitted Cherenkov light satisfies the condition of total internal reflection and propagates along the fiber to the photodetector used. In order to attain a maximum signal from a quartz calorimeter (at a given relationship between the masses of the quartz and absorber), the fibers must therefore be arranged at the angle ϑ_C with respect to the direction of detected-particle incidence [1].

The forward calorimeters of the CMS facility will serve for reconstructing hadronic jets emitted at small angles with respect to colliding proton beams and (together with central and end-face calorimeters) for measuring the missing transverse energy carried away by particles that have not undergone any interaction in the detector (neutrinos and, possibly, new hypothetical particles). For this purpose, it is not sufficient to measure the total energy of all particles entering the calorimeter; it is necessary to measure energy fluxes in calorimeter cells corresponding to different polar and azimuthal angles of secondary-particle emission. The most natural way to ensure the transverse segmentation of a quartz calorimeter is to arrange fibers in the absorber along a direction close to that of the detected-particle trajectories and to group fibers in front of the photodetector in accordance with the required segmentation. Although the collection of Cherenkov light is lower for such an arrangement of fibers than for the configuration in which fibers lie at the angle ϑ_C with

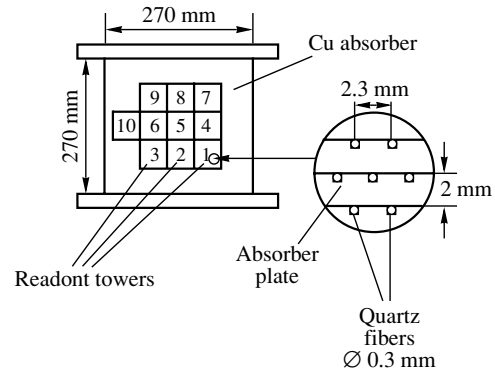


Fig. 3. Schematic of the cross section of a quartz-calorimeter prototype [7].

respect to the momentum of detected particles, the energy resolution of the calorimeter will remain at an acceptable level. According to the results of the measurements performed at ITEP for a calorimeter prototype [6], the amplitude of the quartz-calorimeter signal for electrons of energy 4 GeV is displayed in Fig. 2 versus the angle between the quartz-fiber direction and the electron-beam axis. The results of these measurements reveal that, for the orientation of fibers along the beam, the signal is only one-half as great as that for the orientation of fibers at the angle $\vartheta_C \approx 45^\circ$. This behavior is explained by a broad angular distribution of electrons and positrons in an electromagnetic shower.

4. CALORIMETER PROTOTYPE AND ITS PROPERTIES

In order to determine experimentally the main properties of signals from a quartz calorimeter that are caused by electromagnetic and hadronic showers, a full-scale prototype of such a calorimeter was manufactured [7]. The prototype absorber had a cross-sectional area of $27 \times 27 \text{ cm}^2$ and was made from copper plates having channels for fibers. These channels formed a hexagonal structure characterized by a distance of 2.3 mm between the nearest neighbors (see Fig. 3). In the prototype, use was made of quartz fibers having a quartz core of diameter $300 \mu\text{m}$ and a reflecting coating $15 \mu\text{m}$ thick from quartz doped with fluorine. The fraction of the sensitive fiber volume in the calorimeter was 1.5%. The total length of the calorimeter absorber was 135 cm, which corresponded to 8.5 nuclear-absorption-length units. About 6000 quartz fibers were employed in the prototype, which were grouped into ten bundles, each corresponding to a region of area $5.3 \times 5.4 \text{ cm}^2$ in cross section. Each such bundle was viewed by a photomultiplier tube (see Fig. 3).

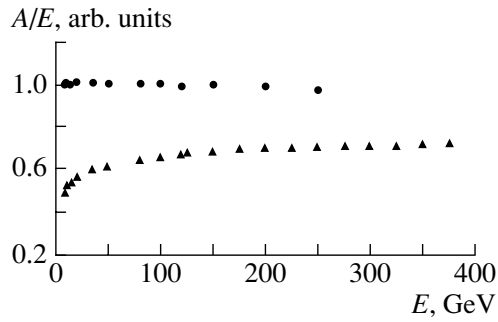


Fig. 4. Ratios of the mean amplitudes of signals to the energies of detected particles [7] for (●) electrons and (▲) pions. The amplitude of the signal for 150-GeV electrons was taken for a normalization.

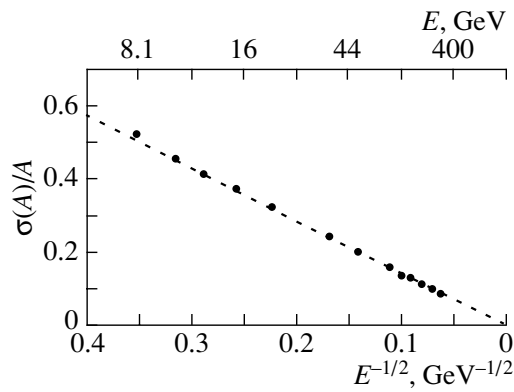


Fig. 5. Energy dependence of the energy resolution for electrons [7].

The calorimeter prototype was exposed to electron and pion beams of various energies. The amplitude distributions of signals from electrons are fully determined by fluctuations of the numbers of photoelectrons produced at the photocathodes of the multiplier phototubes used and are described by Poisson distributions. In the case of pion detection, fluctuations in the development of the hadronic shower in the absorber material play a more important role, dominating over fluctuations of the number of photoelectrons. The ratios of the mean amplitudes of signals to the energies of detected particles are shown in Fig. 4 versus energy. For electrons, the ratio in question is independent of energy, this being indicative of a good linearity of the calorimeter signal for electromagnetic showers. In the case of pions, the particle-energy dependence of the amplitude of the signal is seen to be nonlinear, the mean signal for pions being much less than that for electrons of identical energy. The reason behind these properties of a quartz calorimeter is that the number of relativistic charged particles traversing quartz fibers at angles close to ϑ_C is

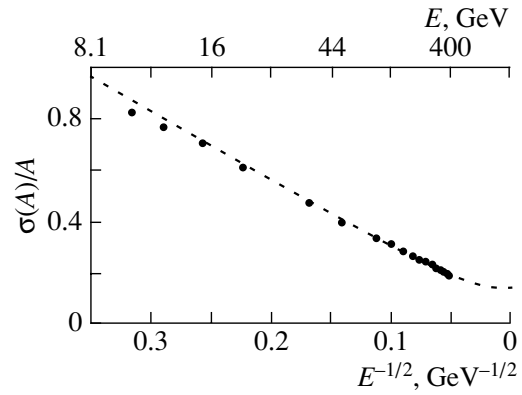


Fig. 6. Energy dependence of the energy resolution for charged pions [7].

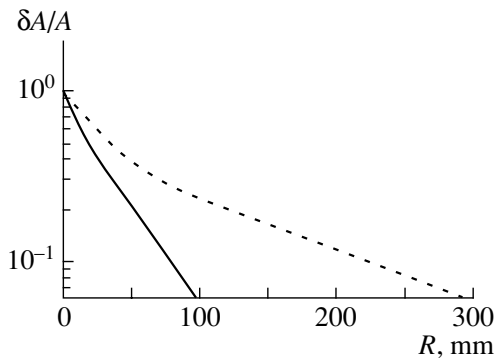


Fig. 7. Fraction of the calorimeter signal formed beyond a cylindrical region whose axis is aligned with the incident-particle momentum versus the radius of this region [8]: (solid curve) results for a quartz calorimeter and (dashed curve) results for the SPACAL scintillation calorimeter.

much less in hadronic than in electromagnetic showers.

Figure 5 shows the energy resolution of the calorimeter prototype as a function of the electron energy. The energy resolution can be approximated as follows:

$$\frac{\sigma(E)}{E} = \frac{A}{\sqrt{E}}.$$

The parameter value of $A = 1.37$ complies well with the number of photoelectrons (0.6 ph.el./GeV) that was determined from the position of the single-photoelectron peak. Figure 6 shows the calorimeter resolution as a function of the pion energy. In this case, the resolution can be approximated by the dependence

$$\frac{\sigma(E)}{E} = \sqrt{\left(\frac{A^2}{E} + B^2\right)}.$$

In the case of pions, the contribution of photostatistical fluctuations to the energy resolution is less

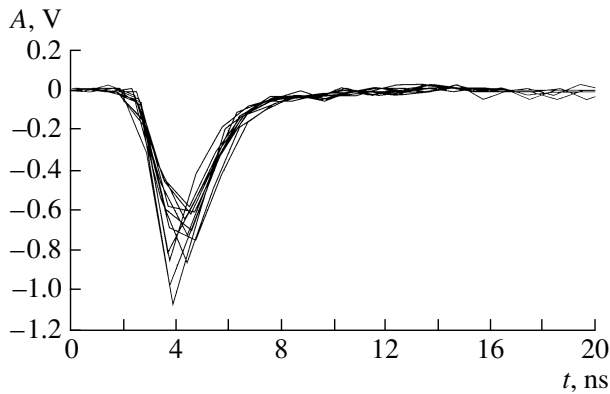


Fig. 8. Oscillograms of prototype signals for pions of energy 375 GeV [8].

than the contribution of fluctuations in the development of the hadronic shower, which are caused primarily by fluctuations of the total energy of neutral pions formed in the shower. It should be borne in mind that the energy resolution of a Cherenkov quartz calorimeter is much poorer than the energy resolution of the majority of calorimeters of other types, and this constrains the applicability range of quartz calorimeters; however, a quartz calorimeter is adequate to problems to be solved in the CMS experiment.

The fraction of the calorimeter signal formed beyond a cylindrical region whose axis is aligned with the incident-particle momentum is shown in Fig. 7 as a function of the radius of this region [7, 8]. For the sake of comparison, the analogous dependence is also given there for a calorimeter of the SPACAL type, where scintillation fibers were used for active elements. It can be seen that the sensitive region is much narrower in a Cherenkov calorimeter than in a scintillation calorimeter of the above type (by way of example, we indicate that, in a Cherenkov calorimeter, 90% of the signal is collected from a region of radius 9 cm, this radius being 22 cm in a scintillation calorimeter). This feature of a Cherenkov calorimeter is of paramount importance in reconstructing narrow hadronic jets formed in the region of small angles, since, in this case, the dimensions of the calorimeter region within which the jet deposits the bulk of its energy are smaller than the transverse size of a hadronic shower. Figure 8 displays the oscillograms of prototype signals for pions of energy 375 GeV [8]. These data confirm that signals from a Cherenkov calorimeter are very short and, as a matter of fact, are determined by the time characteristics of the photodetectors used.

5. DETECTION OF ENERGY FLUXES AND HADRONIC JETS

The quartz Cherenkov calorimeter of the CMS facility is intended for recording and measuring the energies of hadronic jets and energy fluxes associated with particles that are emitted at small angles (0.5° – 5.7°) with respect to the axis of colliding-proton beams. The bulk of the energy recorded in this calorimeter comes from hadrons and high-energy photons from decays of neutral pions and other short-lived particles. The fraction of energy carried by hadrons and photons is expected to fluctuate strongly from one event to another; therefore, the distinction between the amplitudes of the calorimeter signals for hadronic and electromagnetic showers will be a source of errors in measuring the energy of hadronic jets, and this error will be added to the intrinsic energy resolution of the calorimeter. This additional error can be reduced by introducing a longitudinal segmentation of the calorimeter and a corresponding calibration of signals from different segments.

The results obtained by simulating the detection of hadronic jets in a longitudinally segmented Cherenkov quartz calorimeter are presented in [9]. This simulation was based on data from an experiment where two calorimeter prototypes arranged one after the other in close proximity were exposed to electron and pions of various energies. The two prototypes had the same transverse structure (see Fig. 3) and differed only in length. The upstream prototype had a length of 34 cm, while the other (downstream) prototype (it has already been discussed above) was 135 cm long. The length of the first prototype corresponded to 24 radiation-length units; therefore, it absorbed electromagnetic showers from electrons almost completely. This prototype played the role of an electromagnetic (EM) segment of the calorimeter. In order to determine the energy of hadronic showers, it was necessary to sum signals from both segments; therefore, the second segment was referred to, by convention, as a hadronic (HAD) segment.

This, longitudinally segmented, prototype was exposed to electron and pion beams of energy 10 to 200 GeV and 12 to 350 GeV, respectively. An initial calibration of signals from all cells of both segments was performed in a 80-GeV electron beam (the EM segment was removed from the beam in calibrating the HAD beam). The shower energy was determined by the formula

$$E = W_{t_{EM}} E_{EM} + W_{t_{HAD}} E_{HAD},$$

where $W_{t_{EM}}$ and $W_{t_{HAD}}$ are calibration coefficients that were introduced in order to reduce the distinction between the signals from electrons and pions of the same energy. The optimum values of these

coefficients were determined by optimizing the energy resolution for hadronic jets.

At $W_{t_{EM}} = W_{t_{HAD}}$, the energy dependences of the mean amplitudes of signals and the energy resolutions both for electrons and for pions were in agreement, within the experimental uncertainties, with the results for the nonsegmented prototype. In this case, the amplitude of signals from pions (as is shown in Fig. 4) proves to be much less than that for electrons. This difference can be reduced by using, for the calibration coefficients, values satisfying the condition $W_{t_{EM}} < W_{t_{HAD}}$. However, the energy resolution for pions then becomes poorer since the uniformity of the calorimeter is lost, so that the amplitude of the signal becomes dependent on the character of the longitudinal development of a hadronic shower.

Data obtained for the calorimeter segmented in the way indicated above were used to simulate signals from hadronic jets that will be produced at small angles in collisions of 7-TeV protons at the Large Hadron Collider. Such jets of energy in the range between 400 GeV and 2 TeV were simulated with the aid of the PYTHIA package. Each jet consisted of hadrons (predominantly charged pions) and photons emitted into a narrow cone around the momentum of a primary quark that initiated its production. The response of the calorimeter was simulated as the sum of signals from hadronic and electromagnetic showers of corresponding energy that were chosen at random from the library of showers that were recorded with the aid of the prototypes of two segments of a Cherenkov quartz calorimeter. The resolution of the longitudinally segmented calorimeter for hadronic jets is shown in Fig. 9 as a function of energy for three values of the ratio of $W_{t_{HAD}}$ to $W_{t_{EM}}$. The value of $W_{t_{HAD}}/W_{t_{EM}} = 1$ corresponds to a uniform (nonsegmented) calorimeter, while the value of $W_{t_{HAD}}/W_{t_{EM}} = 1.97$ makes it possible to reach an approximate equality of signals for hadronic and electromagnetic showers; as to the value of $W_{t_{HAD}}/W_{t_{EM}} = 1.45$, it corresponds to the optimum energy resolution for high-energy hadronic jets. It can be seen that the optimum value of the ratio of $W_{t_{HAD}}$ to $W_{t_{EM}}$ remains unchanged over a broad range of jet energies.

6. CHERENKOV CALORIMETERS FOR THE CMS EXPERIMENT

The calorimetric system of the CMS facility is predominantly intended for performing an efficient measurement of hadronic jets and energy fluxes over a wide pseudorapidity interval, $|\eta| < 5$,

$$\eta = -\ln \tan \frac{\vartheta}{2}.$$

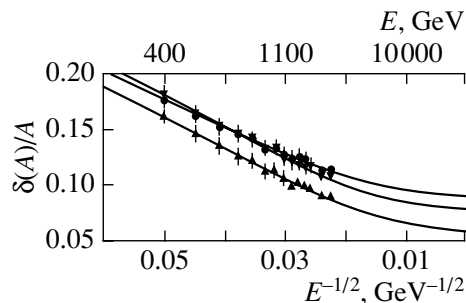


Fig. 9. Energy dependence of the resolution of a longitudinally segmented calorimeter for hadronic jets at $W_{t_{HAD}}/W_{t_{EM}} = (\bullet) 1.00, (\blacktriangle) 1.45, \text{ and } (\blacktriangledown) 1.97$ [9].

Here, ϑ is the emission angle of a secondary particle with respect to the axis of one of the colliding beams. Electromagnetic calorimeters involving lead tungstate crystal and hadronic calorimeters employing scintillator plates as sensitive elements will be installed in the central part of the facility and in its end-face parts. In the region of angles adjacent to the beam axis, such calorimeters cannot operate, primarily because of an insufficiently high radiation resistance. In the region of forward angles, the radiation doses expected in the high-luminosity ($L = 10^{34} \text{ cm}^{-2} \text{ s}^{-1}$) mode of Large Hadron Collider operation are as high as 100 Mrad/yr. Therefore, Cherenkov quartz calorimeters, which possess the required radiation resistance, will be used in the CMS facility in the region of small angles with respect to the axes of colliding beams. The energy resolution of a Cherenkov calorimeter is poorer than that of a scintillation calorimeter at the same energy of detected hadrons. If, however, these resolutions are compared at identical transverse (with respect to beam axes) energies, it turns out that, in the CMS facility, the resolution of the forward calorimeters with respect to transverse energy is not inferior to the resolution of the central calorimeters. Moreover, special features of a Cherenkov calorimeter, such as a short signal, a low sensitivity to neutrons and products of radiative decays, and a narrow region of signal formation, will make it possible to attain significant advantages over different calorimetric methods in suppressing backgrounds in reconstructing hadronic jets.

In the CMS facility, the forward calorimeters are positioned beyond the central part of the detector and its end-face parts [10]. This arrangement of the forward calorimeters will considerably facilitate access to other elements of the facility during exploitation, since, within the period of servicing the facility, the forward calorimeters, which are powerful radioactive sources, can be removed to specially provided shielded zones. Moreover, the disposition of the forward calorimeters beyond other units of the facil-



Fig. 10. Quartz-fiber-equipped sectors of the forward calorimeters of the CMS facility.

ity will make it possible to reduce significantly the backgrounds in the central part of the CMS from secondary particles (first of all, neutrons), which will be copiously produced in the forward calorimeters.

The absorber of the forward calorimeters of CMS are manufactured from steel in the form of 20-degree sectors 165 cm long and 123 cm in height. This form of the absorber makes it possible to assemble the calorimeter sectors as independent units (including the absorber, quartz fibers, and blocks involving photodetectors) and to ensure an optimum transverse segmentation of the calorimeter for reconstructing hadronic jets ($\Delta\eta \times \Delta\varphi = 0.175 \times 0.175$, where η is a pseudorapidity and φ is an azimuthal angle). In the absorber, there are holes about 1 mm in diameter that are separated by a distance of 5 mm in the transverse direction. Quartz fibers featuring a core of diameter 0.6 mm and a radiation-resistant polymer coating are inserted into these holes. One-half of the fibers pass over the entire length of the absorber, while the other half stop short of reaching the forward end face of the absorber (at a distance of 22 cm from it). The long and short fibers, which alternate in a staggered order, are grouped into separate bundles for the readout of signals by photodetectors. This ensures a longitudinal segmentation of the calorimeters, whereby one reduces the difference of the signals from electromagnetic and hadronic showers and improves the energy resolution for hadronic jets. An external view of the calorimeter sectors equipped with quartz fibers is illustrated in Fig. 10. Two forward calorimeters will have a total weight of about 200 t and will contain about 1000 km of quartz fibers. At the present time, the CMS quartz calorimeters are the largest

Cherenkov quartz calorimeters. Other examples illustrating the use of Cherenkov calorimeters can be found in [11].

7. CONCLUSION

A Cherenkov quartz calorimeter is radically different from calorimeters that are based on ionization or scintillation signals. In a shower initiated by a high-energy particle in a calorimeter, the fraction of energy going into the formation of a Cherenkov signal is much less than the fraction of energy going into ionization or scintillation. In what is concerned with the energy resolution, a Cherenkov quartz calorimeter is therefore inferior to calorimeters of traditional types. Owing to the nature of Cherenkov radiation, however, such a calorimeter has a very short signal and a considerably narrower sensitive region than other calorimeters and is not sensitive to neutrons and products of radiative decays. These advantages are of greatest importance for calorimeter operation under conditions of high particle fluxes. A high radiation resistance of quartz fibers is a property that enables one to make use of the advantages of Cherenkov calorimeters. At the present time, the assembly of the two largest Cherenkov quartz calorimeters, which will operate in the region of small angles of the CMS facility at the Large Hadron Collider, is being completed.

REFERENCES

1. P. Gorodetzky *et al.*, Nucl. Instrum. Methods Phys. Res. A **361** 161 (1995).
2. V. B. Gavrilov *et al.*, Prib. Tekh. Éksp., No. 4, 23 (1997).

3. I. Dumanoglu *et al.*, Nucl. Instrum. Methods Phys. Res. A **490**, 444 (2002).
4. A. V. Andriyash *et al.*, Prib. Tekh. Éksp., No. 5, 20 (2003).
5. G. Anzivino *et al.*, Nucl. Instrum. Methods Phys. Res. A **357**, 369 (1995).
6. G. Anzivino *et al.*, Nucl. Instrum. Methods Phys. Res. A **360**, 237 (1995).
7. N. Akchurin *et al.*, Nucl. Instrum. Methods Phys. Res. A **399**, 202 (1997).
8. N. Akchurin *et al.*, Nucl. Instrum. Methods Phys. Res. A **379**, 526 (1996).
9. N. Akchurin *et al.*, Nucl. Instrum. Methods Phys. Res. A **409**, 593 (1998).
10. The CMS Collab., HCAL Technical Design Report, CERN/LHCC 97–31 (1997).
11. N. Akchurin and R. Wigmans, Rev. Sci. Instrum. **74**, 2955 (2003).

Translated by A. Isaakyan

Alternative Technique for Standard Model Estimation of the Rare Kaon Decay Branchings $\text{BR}(K \rightarrow \pi\nu\bar{\nu})|_{\text{SM}}^*$

S. H. Kettell¹⁾, L. G. Landsberg²⁾, and H. Nguyen³⁾

Received November 30, 2003; in final form, February 2, 2004

Abstract—We estimate $\text{BR}(K \rightarrow \pi\nu\bar{\nu})$ in the context of the Standard Model by fitting for $\lambda_t \equiv V_{td}V_{ts}^*$ of the “kaon unitarity triangle” relation. To find the vertex of this triangle, we fit data from $|\varepsilon_K|$, the CP -violating parameter describing K mixing, and $a_{\psi K}$, the CP -violating asymmetry in $B_d^0 \rightarrow J/\psi K^0$ decays, and obtain the values $\text{BR}(K^+ \rightarrow \pi^+\nu\bar{\nu})|_{\text{SM}} = (7.07 \pm 1.03) \times 10^{-11}$ and $\text{BR}(K_L^0 \rightarrow \pi^0\nu\bar{\nu})|_{\text{SM}} = (2.60 \pm 0.52) \times 10^{-11}$. Our estimate is independent of the CKM matrix element V_{cb} and of the ratio of B -mixing frequencies $\Delta m_{B_s}/\Delta m_{B_d}$. We also use the constraint estimation of λ_t with additional data from Δm_{B_d} and $|V_{ub}|$. This combined analysis slightly increases the precision of the rate estimation of $K^+ \rightarrow \pi^+\nu\bar{\nu}$ and $K_L^0 \rightarrow \pi^0\nu\bar{\nu}$ (by $\simeq 10$ and $\simeq 20\%$, respectively). The measured value of $\text{BR}(K^+ \rightarrow \pi^+\nu\bar{\nu})$ can be compared both to this estimate and to predictions made from $\Delta m_{B_s}/\Delta m_{B_d}$. © 2004 MAIK “Nauka/Interperiodica”.

The ultrarare FCNC (Flavor Changing Neutral Currents) kaon decays $K^+ \rightarrow \pi^+\nu\bar{\nu}$ and $K_L^0 \rightarrow \pi^0\nu\bar{\nu}$ are of particular interest as these “gold-plated decays” can be predicted in the Standard Model (SM) framework with very high theoretical accuracy.

The $K \rightarrow \pi\nu\bar{\nu}$ decays are treated in detail in a number of papers [1–34]. We list some of the key aspects of these decays.

(a) The main contribution to these FCNC processes arises at small distances $r \sim 1/m_t, 1/m_Z$; therefore, a very accurate description for the strong interactions at the quark level is possible in the framework of perturbative QCD. This analysis has been carried out in the leading logarithmic order (LLO) with corrections to next-to-leading order (NLO) [1–4].

(b) The calculation of the matrix element $\langle \pi | H_w | K \rangle_{\pi\nu\bar{\nu}}$ from quark-level processes involves long-distance physics. However, these long-distance effects can be avoided by the renormalization procedure developed by Inami and Lim [5], relating the matrix element to that of the well-known decay $K^+ \rightarrow \pi^0 e^+ \nu_e$ through isotopic-spin symmetry. Other possible long-distance contributions to $\text{BR}(K^+ \rightarrow \pi^+\nu\bar{\nu})$ have been shown to be negligible [6].

(c) Since the effective vertex $Zd\bar{s}$ in the diagrams of Fig. 1 is short-distance, these processes are also sensitive to the contributions from new heavy objects (e.g., supersymmetric particles).

A very important step in the study of $K^+ \rightarrow \pi^+\nu\bar{\nu}$ was achieved by the E787 experiment [7] at BNL in which two clean events were found in favorable background conditions, indicating a branching ratio of $\text{BR}(K^+ \rightarrow \pi^+\nu\bar{\nu}) = (15.7_{-8.2}^{+17.5}) \times 10^{-11}$. This observation has opened the door for future more precise study of the $K^+ \rightarrow \pi^+\nu\bar{\nu}$ decay [8, 9].

In the SM, the $K^+ \rightarrow \pi^+\nu\bar{\nu}$ decay is described by penguin and box diagrams presented in Fig. 1. The partial widths have the form

$$\begin{aligned} \Gamma(K^+ \rightarrow \pi^+\nu\bar{\nu}) &= \kappa^+ |\lambda_c F(x_c) + \lambda_t X(x_t)|^2 \quad (1) \\ &= \kappa^+ [(F(x_c)\text{Re}\lambda_c + X(x_t)\text{Re}\lambda_t)^2 \\ &\quad + (F(x_c)\text{Im}\lambda_c + X(x_t)\text{Im}\lambda_t)^2] \\ &\simeq \kappa^+ [(F(x_c)\text{Re}\lambda_c + X(x_t)\text{Re}\lambda_t)^2 + (X(x_t)\text{Im}\lambda_t)^2], \end{aligned}$$

where

$$\begin{aligned} \kappa^+ &= \left(\frac{G_F}{\sqrt{2}}\right)^2 |\langle \pi^+\nu\bar{\nu} | H_w | K^+ \rangle|^2 \\ &\quad \times 3 \left(\frac{\alpha}{2\pi \sin^2 \vartheta_W}\right)^2. \end{aligned}$$

The factor of 3 in the expression for κ^+ results from the three flavors of neutrinos (ν_e, ν_μ, ν_τ) participating in the $K^+ \rightarrow \pi^+\nu\bar{\nu}$ decays. The factors $F(x_c)$ and $X(x_t)$ are functions corresponding to the quark loops.

*This article was submitted by the authors in English.

¹⁾Brookhaven National Laboratory, Upton, New York, USA.

²⁾Institute of High Energy Physics, Protvino, Moscow oblast, 142280 Russia.

³⁾Fermi National Accelerator Laboratory, Batavia, USA.

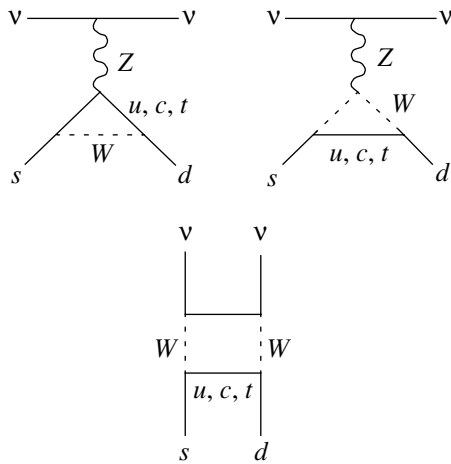


Fig. 1. The dominant contributions to $K \rightarrow \pi\nu\bar{\nu}$.

These functions include the Inami–Lim functions [5] and the QCD corrections that have been calculated to NLO [1–4, 10]. They depend on the variables $x_i = (m_i/m_W)^2$ with the masses of the $+$ $\frac{2}{3}$ quarks, $m_i, i = c, t$. The $\lambda_i \equiv V_{id}V_{is}^*$ are vectors in the complex plane that satisfy the unitarity relation

$$\lambda_t + \lambda_c + \lambda_u = 0 \quad (\lambda_i = V_{id}V_{is}^*; i = u, c, t). \quad (2)$$

This equation describes the “kaon unitarity triangle,” which can be completely determined from measurement of the three kaon decays: $K^+ \rightarrow \pi^0 e^+ \nu_e$, $K^+ \rightarrow \pi^+ \nu\bar{\nu}$, and $K_L^0 \rightarrow \pi^0 \nu\bar{\nu}$. This triangle is highly elongated with a base-to-height ratio of ~ 1000 .

Using the values of m_c and m_t in the table (see below), the calculations from [1] yield $F(x_c) = (9.82 \pm 1.78) \times 10^{-4}$ and $X(x_t) = 1.52 \pm 0.05$. The accuracy improves with increasing quark mass, and there are systematic dependences on QCD scale parameter $\Lambda_{\overline{MS}}^{(4)}$ (see [1]). The c -quark contribution in (1) is smaller than the t -quark contribution, but is non-negligible. Although $F(x_c)/X(x_t) \sim 10^{-3}$, $\text{Re}\lambda_c$ is much larger than $\text{Re}\lambda_t$ and $\text{Im}\lambda_t$ ($\text{Re}\lambda_c \sim \lambda$, while $\text{Re}\lambda_t, \text{Im}\lambda_t$, and $\text{Im}\lambda_c$ are less than λ^5).

For the CP -violating [11, 12] $K_L^0 \rightarrow \pi^0 \nu\bar{\nu}$ decay,

$$\begin{aligned} &\Gamma(K_L^0 \rightarrow \pi^0 \nu\bar{\nu}) \quad (3) \\ &\simeq \frac{1}{2} |A(K^0 \rightarrow \pi^0 \nu\bar{\nu}) - A(\bar{K}^0 \rightarrow \pi^0 \nu\bar{\nu})|^2 \\ &= \kappa^0 \frac{1}{2} |\lambda_c F(x_c) + \lambda_t X(x_t) - \text{h.c.}|^2 \\ &= \kappa^0 \cdot 2 [F(x_c) \text{Im}\lambda_c + X(x_t) \text{Im}\lambda_t]^2 \\ &\simeq \kappa^0 \cdot 2 [X(x_t) \text{Im}\lambda_t]^2, \end{aligned}$$

where

$$\kappa^0 = \left(\frac{G_F}{\sqrt{2}}\right)^2 |\langle \pi^0 \nu\bar{\nu} | H_w | K^0 \rangle|^2 \cdot 3 \left(\frac{\alpha}{2\pi \sin^2 \vartheta_W}\right)^2.$$

The c -quark contribution is negligible since $F(x_c) \text{Im}\lambda_c \ll X(x_t) \text{Im}\lambda_t$.

The partial width for the well-known decay mode $K^+ \rightarrow \pi^0 e^+ \nu_e$ is given by

$$\begin{aligned} &\Gamma(K^+ \rightarrow \pi^0 e^+ \nu_e) \\ &= \left(\frac{G_F}{\sqrt{2}}\right)^2 |V_{us}|^2 |\langle \pi^0 e^+ \nu_e | H_w | K^+ \rangle|^2. \end{aligned}$$

As mentioned above, one can relate this to $\langle \pi^+ \nu\bar{\nu} | H_w | K^+ \rangle$ and $\langle \pi^0 \nu\bar{\nu} | H_w | K^0 \rangle$ with the help of isotopic-spin symmetry:

$$\left| \frac{\langle \pi^+ \nu\bar{\nu} | H_w | K^+ \rangle}{\langle \pi^0 e^+ \nu_e | H_w | K^+ \rangle} \right|^2 = \left| \frac{\langle \pi^+ | H_w | K^+ \rangle}{\langle \pi^0 | H_w | K^+ \rangle} \right|^2 = 2r_+, \quad (4)$$

$$\left| \frac{\langle \pi^0 \nu\bar{\nu} | H_w | K^0 \rangle}{\langle \pi^0 e^+ \nu_e | H_w | K^+ \rangle} \right|^2 = \left| \frac{\langle \pi^0 | H_w | K^0 \rangle}{\langle \pi^0 | H_w | K^+ \rangle} \right|^2 = r_0. \quad (5)$$

The factor 2 in (4) accounts for the pion quark structure $|\pi^0\rangle = \frac{1}{\sqrt{2}}|u\bar{u} - d\bar{d}\rangle$ and $|\pi^+\rangle = |u\bar{d}\rangle$. The factors $r_+ = 0.901$ and $r_0 = 0.944$ arise from the phase-space corrections and the breaking of isotopic symmetry [13].

Hence, from (1), (4), and (5), the branching ratio for the $K^+ \rightarrow \pi^+ \nu\bar{\nu}$ decay is

$$\begin{aligned} &\text{BR}(K^+ \rightarrow \pi^+ \nu\bar{\nu})|_{\text{SM}} = R_+ \frac{X(x_t)^2}{\lambda^2} \quad (6) \\ &\times \left\{ \left[(\text{Re}\lambda_c) f \frac{F(x_c)}{X(x_t)} + \text{Re}\lambda_t \right]^2 + [\text{Im}\lambda_t]^2 \right\}, \end{aligned}$$

where

$$\begin{aligned} &R_+ = \text{BR}(K^+ \rightarrow \pi^0 e^+ \nu_e) \frac{3\alpha^2}{2\pi^2 \sin^4 \vartheta_W} r_+ \quad (7) \\ &= 7.50 \times 10^{-6}, \end{aligned}$$

$$f \frac{F(x_c)}{X(x_t)} = (6.66 \pm 1.23) \times 10^{-4},$$

$$f = 1.03 \pm 0.02.$$

Here, f is an additional correction factor to the c -quark term to take into account nonperturbative effects of dimension-8 operators [14]. The branching ratio for the $K_L^0 \rightarrow \pi^0 \nu\bar{\nu}$ decay is

$$\text{BR}(K_L^0 \rightarrow \pi^0 \nu\bar{\nu})|_{\text{SM}} = R_0 \frac{X(x_t)^2}{\lambda^2} [\text{Im}\lambda_t]^2 \quad (8)$$

with

$$R_0 = R_+ \frac{r_0}{r_+} \frac{\tau(K_L^0)}{\tau(K^+)} = 3.28 \times 10^{-5},$$

$$r_0/r_+ = 1.048, \quad \tau(K_L^0)/\tau(K^+) = 4.17.$$

The intrinsic theoretical uncertainty of the SM prediction for $\text{BR}(K^+ \rightarrow \pi^+ \nu \bar{\nu})|_{\text{SM}}$ is $\sim 7\%$ and is limited by the c -quark contribution, whereas for $\text{BR}(K_L^0 \rightarrow \pi^0 \nu \bar{\nu})|_{\text{SM}}$ the uncertainty is 1–2%. However, in practice, the uncertainties of the numerical evaluations of the $K \rightarrow \pi \nu \bar{\nu}$ branching ratios are dominated by the current uncertainties in the CKM quark mixing matrix parameters.

The parameters $\text{Im}\lambda_t$, $\text{Re}\lambda_t$, $\text{Re}\lambda_c$ can be estimated within the standard unitarity triangle (UT) framework using the improved Wolfenstein parametrization [15] $\bar{\eta}$, $\bar{\rho}$, A , and λ (with $A\lambda^2 = |V_{cb}|$, $\bar{\rho} \equiv \rho(1 - \lambda^2/2)$, and $\bar{\eta} \equiv \eta(1 - \lambda^2/2)$). To $O(\lambda^4)$, the CKM matrix is

$$V_{\text{CKM}} = \begin{pmatrix} V_{ud} & V_{us} & V_{ub} \\ V_{cd} & V_{cs} & V_{cb} \\ V_{td} & V_{ts} & V_{tb} \end{pmatrix} \quad (9)$$

$$= \begin{pmatrix} 1 - \lambda^2/2 & \lambda & A\lambda^3(\rho - i\eta) \\ -\lambda & 1 - \lambda^2/2 & A\lambda^2 \\ A\lambda^3(1 - \rho - i\eta) & -A\lambda^2 & 1 \end{pmatrix} + O(\lambda^4),$$

and to higher order we have

$$\text{Re}\lambda_c = -\lambda(1 - \lambda^2/2) + O(\lambda^5), \quad (10)$$

$$\text{Re}\lambda_t = -A^2\lambda^5(1 - \lambda^2/2)(1 - \bar{\rho}) + O(\lambda^7),$$

$$\text{Im}\lambda_t = \eta A^2\lambda^5 + O(\lambda^9).$$

The current values of these and other parameters used in this paper can be found below in the table. Using (10) and PDG [35] (see table), Eqs. (6) and (8) can be naively solved to give the branching ratios for $K^+ \rightarrow \pi^+ \nu \bar{\nu}$ and $K_L^0 \rightarrow \pi^0 \nu \bar{\nu}$:

$$\text{BR}(K^+ \rightarrow \pi^+ \nu \bar{\nu})|_{\text{SM}} \quad (11)$$

$$= R_+ A^4 \lambda^8 X(x_t)^2 \left\{ \frac{1}{\sigma} [(\rho_0 - \bar{\rho})^2 + (\sigma \bar{\eta})^2] \right\}$$

$$= R_+ |V_{cb}|^4 X(x_t)^2 \left\{ \frac{1}{\sigma} [(\rho_0 - \bar{\rho})^2 + (\sigma \bar{\eta})^2] \right\}$$

$$= 7.50 \times 10^{-6} [2.88 \times 10^{-6} \pm (19.4\%)]$$

$$\times [2.30 \pm (6.9\%)] \{1.44 \pm (20\%)\}$$

$$= [7.15 \pm (28.9\%)] \times 10^{-11} = [7.2 \pm 2.1] \times 10^{-11};$$

$$\text{BR}(K_L^0 \rightarrow \pi^0 \nu \bar{\nu})|_{\text{SM}} \quad (12)$$

$$= R_0 A^4 \lambda^8 X(x_t)^2 \{ \sigma \bar{\eta}^2 \}$$

$$= R_0 |V_{cb}|^4 X(x_t)^2 \{ \sigma \bar{\eta}^2 \}$$

$$= 3.28 \times 10^{-5} [2.88 \times 10^{-6} \pm (19.4\%)]$$

$$\times [2.30 \pm (6.9\%)] \{0.129 \pm (28.6\%)\}$$

$$= [2.8 \pm (35\%)] \times 10^{-11} = [2.8 \pm 1.0] \times 10^{-11}$$

with $\rho_0 = 1 + \Delta = 1 + fF(x_c)/(|V_{cb}|^2 X(x_t)) = 1.40 \pm 0.08$ and $\sigma = 1/(1 - \lambda^2/2)^2 = 1.051$.

The uncertainties of $\text{BR}(K \rightarrow \pi \nu \bar{\nu})$ in (11) and (12) are dominated by the current uncertainties in the CKM parameters and are significantly larger than the intrinsic theoretical uncertainties. The uncertainty of $|V_{cb}|$ is quite significant in the evaluation of $\text{BR}(K \rightarrow \pi \nu \bar{\nu})$ due to the $|V_{cb}|^4$ dependence. CLEO has recently measured [36] a somewhat higher $|V_{cb}|$ value of $(46.9 \pm 3.0) \times 10^{-3}$, which would cause a significant increase in $\text{BR}(K \rightarrow \pi \nu \bar{\nu})$ in Eqs. (11) and (12).

The numerical solutions of Eqs. (11) and (12) do not include correlations between $\bar{\rho}$, $\bar{\eta}$, X , and V_{cb} . Rather, these calculations are used to demonstrate the influence of different factors in the calculation of $\text{BR}(K \rightarrow \pi \nu \bar{\nu})$. An evaluation [16] employing a scanning method and conservative errors for V_{CKM} obtained the following values: $\text{BR}(K^+ \rightarrow \pi^+ \nu \bar{\nu})|_{\text{SM}} = (7.5 \pm 2.9) \times 10^{-11}$ and $\text{BR}(K_L^0 \rightarrow \pi^0 \nu \bar{\nu})|_{\text{SM}} = (2.6 \pm 1.2) \times 10^{-11}$. A more recent evaluation with similar CKM inputs but employing a Gaussian fit obtained $\text{BR}(K^+ \rightarrow \pi^+ \nu \bar{\nu})|_{\text{SM}} = (7.2 \pm 2.1) \times 10^{-11}$ [17]. These values are not very different from the results in Eqs. (11) and (12). In some recent analyses [18–21] with correlations included, higher precision on the $\text{BR}(K \rightarrow \pi \nu \bar{\nu})$ predictions has been obtained.

For the values of the parameters $|V_{cb}|$, $\bar{\rho}$, and $\bar{\eta}$ in Eqs. (11) and (12), we adopt the more conservative approach of PDG [35]. A more aggressive approach [22] for the evaluation of these errors can significantly increase the precision for $\text{BR}(K \rightarrow \pi \nu \bar{\nu})$. Solving Eqs. (11) and (12) with the values of [22] gives $\text{BR}(K^+ \rightarrow \pi^+ \nu \bar{\nu})|_{\text{SM}} = (7.4 \pm 1.2) \times 10^{-11}$ and $\text{BR}(K_L^0 \rightarrow \pi^0 \nu \bar{\nu})|_{\text{SM}} = (2.8 \pm 0.5) \times 10^{-11}$. The precision of the outputs of the standard UT fits is dependent on the value of ξ , the $SU(3)$ -breaking correction to $\Delta m_{B_s}/\Delta m_{B_d}$. The generally accepted value of ξ is $\xi = 1.15 \pm 0.06$; however, recent works would suggest a higher value of $\xi = 1.18 \pm 0.04_{-0.0}^{+0.12}$ [37] (or even as high as $\xi = 1.32 \pm 0.10$ [38]).

Given the strong dependence of Eqs. (11) and (12) on $|V_{cb}|$, we consider an estimate of $\text{BR}(K^+ \rightarrow \pi^+ \nu \bar{\nu})$ that is essentially independent of $|V_{cb}|$. This estimate is also independent of $\Delta m_{B_s}/\Delta m_{B_d}$. It is based solely

on $|\varepsilon_K|$ and $a_{\psi K}$, is remarkably competitive to other estimates, and has the advantage of simplicity.

In this work, we directly evaluate λ_t to calculate $\text{BR}(K \rightarrow \pi\nu\bar{\nu})$ from (6) and (8). This avoids the use of $\bar{\rho}$ and $\bar{\eta}$, as has been used in previous calculations of $\text{BR}(K \rightarrow \pi\nu\bar{\nu})$. This approach has been discussed in the literature [23, 24], but as far as we know, no calculations of $\text{BR}(K \rightarrow \pi\nu\bar{\nu})$ exist by this method. In order to minimize uncertainty from $|V_{cb}|$, it is natural to consider $|\varepsilon_K|$ and $a_{\psi K}$ in terms of the kaon UT.⁴⁾ We recall that $\lambda_u = V_{ud}V_{us}^* \simeq \lambda(1 - \lambda^2/2)$ is real, and $\lambda_c = V_{cd}V_{cs}^*$ has a very small complex phase $\varphi(\lambda_c) \simeq \text{Im}\lambda_t/\lambda \simeq 6 \times 10^{-4}$. The phase of V_{ts} is $\varphi(V_{ts}) \simeq -\pi + (\text{Im}\lambda_t)\lambda/|V_{cb}|^2 = -\pi + 0.0172 = -\pi + 1.0^\circ$. The phase of V_{td} is $\varphi(V_{td}) = -\beta$ and the angle (β_K) between λ_t and λ_u is

$$\begin{aligned} \beta_K &= \pi - \varphi(V_{td}V_{ts}^*) = \pi - \varphi(V_{td}) + \varphi(V_{ts}) \quad (13) \\ &= \beta + 1.0^\circ = 24.6^\circ \pm 2.3^\circ. \end{aligned}$$

This angle is very close to β , which in the SM is extracted cleanly from the precise measurement of $a_{\psi K}$, the CP asymmetry in $B_d^0 \rightarrow J/\psi K^0$ decays: $\sin(2\beta) = 0.734 \pm 0.054$ [39]. We use an iterative procedure, starting with $\beta_K = \beta$, from our fit to derive $\text{Im}\lambda_t$ [as will be explained later in (15)] and then recalculate β_K as $\beta_K = \beta + (\text{Im}\lambda_t)\lambda/|V_{cb}|^2$. This procedure converges after one iteration since the correction to β is small. There is also a small dependence on $|V_{cb}|$; however, a 10% change in $|V_{cb}|$ results in only a 0.6% shift in $\text{BR}(K^+ \rightarrow \pi^+\nu\bar{\nu})$, which is significantly less than the uncertainty in our result. For all practical purposes, our result is independent of $|V_{cb}|$. The preferred solution for β , based on other SM input, such as V_{ub}/V_{cb} , is $\beta = 23.6^\circ \pm 2.3^\circ$, so we shall only consider this particular solution. The extraction of $\sin(2\beta)$ from $a_{\psi K}$ is also clean in models with minimal flavor violation (MFV) [22, 25, 26]. In these models, there are no new phases and all of the influences of new physics are in modifications to the Inami–Lim functions.

In the SM, the apex of the kaon UT ($\lambda_t^{(a)}$) is constrained by various measurements as shown in Fig. 2 (without errors). The constraint from $|\varepsilon_K|$ is

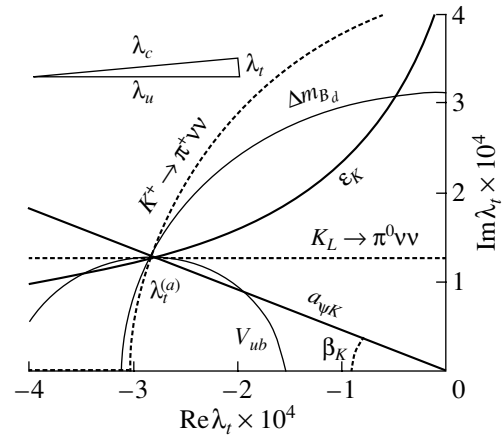


Fig. 2. The apex of the kaon unitarity triangle is $\lambda_t^{(a)}$ (no errors are shown). The circle labeled V_{ub} is described by (26) with a radius $R_2 \simeq |V_{ub}V_{cb}|$. The thick black lines ($|\varepsilon_K|$ and $a_{\psi K}$) illustrate the main constraints used in this paper. The dashed lines illustrate the constraints from $K \rightarrow \pi\nu\bar{\nu}$. The constraint from Δm_{B_d} is shown as the circle centered at the origin. The inset shows the triangle (not drawn to scale).

expressed as [10, 40–43]⁵⁾

$$\begin{aligned} |\varepsilon_K| &= L\hat{B}_K \text{Im}\lambda_t \{ \text{Re}\lambda_c [\eta_{cc}S_0(x_c) \\ &\quad - \eta_{ct}S_0(x_c; x_t)] - \text{Re}\lambda_t \eta_{tt}S_0(x_t) \} \quad (14) \end{aligned}$$

with parameters as shown below in the table. We can find the apex of the kaon UT as the intercept of the $|\varepsilon_K|$ curve with the line representing the constraint from $a_{\psi K}$:

$$\text{Im}\lambda_t = -\tan\beta_K \cdot \text{Re}\lambda_t = (-0.458 \pm 0.049)\text{Re}\lambda_t. \quad (15)$$

To calculate a probability density function (PDF) for $\lambda_t^{(a)}$, we follow the Bayesian approach of [44, 45] and [22]. Let $f(\mathbf{x})$ be the PDF for \mathbf{x} , where \mathbf{x} is a point in the space of $(\beta_K, |\varepsilon_K|, \hat{B}_K, m_t, m_c, \lambda, \alpha_s, \eta_{cc}, \eta_{ct}, \eta_{tt})$. Equations (14) and (15) define the mapping from \mathbf{x} to $\lambda_t^{(a)}$. Through these equations and $f(\mathbf{x})$, we derive $f(\lambda_t^{(a)})$, the PDF for $\lambda_t^{(a)}$. Probability density $f(\mathbf{x})$ depends on the PDFs for the components of \mathbf{x} . We assume that the component PDFs are independent from one another except for the small dependence of η_{cc} on m_c and α_s (discussed below). The component PDFs are taken from the table (see below).

Figure 3 shows the PDF for $\lambda_t^{(a)}$. We find the following central values:

$$\text{Re}\lambda_t^{(a)} = (-2.84 \pm 0.31) \times 10^{-4}, \quad (16)$$

⁴⁾We expect that a precise determination of the apex of the kaon UT ($\lambda_t^{(a)}$) will be available, entirely from kaon decay data, in the near future. In the meantime, it is necessary to use some data from the B system, so we chose to augment $|\varepsilon_K|$ with the theoretically clean measurement of the CP asymmetry $a_{\psi K}$ from the B system.

⁵⁾We stress that the loop functions $S_0(x_t)$, $S_0(x_t, x_c)$, and $S_0(x_c)$ and their QCD corrections η_{tt} , η_{ct} , and η_{cc} for the expression for $|\varepsilon_K|$ [see (14)] were first introduced in the pioneering work of Vysotsky [40].

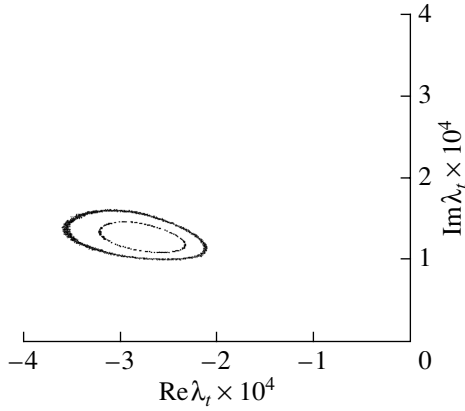


Fig. 3. 1σ (internal ellipsis) and 2σ (external ellipsis) C.L. intervals on $\lambda_t^{(a)}$ obtained from the measurements of $|\varepsilon_K|$ and $a_{\psi K}$.

$$\text{Im}\lambda_t^{(a)} = (1.30 \pm 0.13) \times 10^{-4}.$$

For $\text{BR}(K^+ \rightarrow \pi^+ \nu \bar{\nu})|_{\text{SM}}$, we obtain from Eqs. (6) and (16)

$$\begin{aligned} \text{BR}(K^+ \rightarrow \pi^+ \nu \bar{\nu})|_{\text{SM}} & \quad (17) \\ & = \left\{ [(\text{Re}\lambda_c) f F(x_c) \right. \\ & \quad \left. + X(x_t) \text{Re}\lambda_t^{(a)}]^2 + [X(x_t) \text{Im}\lambda_t^{(a)}]^2 \right\} \frac{R_+}{\lambda^2} \\ & = \frac{R_t}{\lambda^2} [X(x_t)]^2 \left\{ \left[\frac{(\text{Re}\lambda_c) f F(x_c)}{X(x_t)} + \text{Re}\lambda_t^{(a)} \right]^2 \right. \\ & \quad \left. + [\text{Im}\lambda_t^{(a)}]^2 \right\} = (7.07 \pm 1.03) \times 10^{-11}. \end{aligned}$$

The three largest contributions to the uncertainty are due to \hat{B}_K (0.69×10^{-11}), m_c (0.44×10^{-11}), and $a_{\psi K}$ (0.49×10^{-11}). The probability distribution for $\text{BR}(K^+ \rightarrow \pi^+ \nu \bar{\nu})|_{\text{SM}}$ is presented in Fig. 4.

In obtaining the results of Eq. (17), we have accounted for the correlations between the terms $\lambda_t^{(a)}$ and $(\text{Re}\lambda_c) f F(x_c)/X(x_t)$ through the variables x_c , x_t , and $\Lambda_{\overline{MS}}^{(4)}$. The functions $X(x_t)$ and $F(x_c, \Lambda_{\overline{MS}}^{(4)})$ are given in [1], from which we have parametrized Table 1 (in [1]) to get (here and below m_c and $\Lambda_{\overline{MS}}^{(4)}$ are in GeV)

$$\begin{aligned} F(x_c, \Lambda_{\overline{MS}}^{(4)}) \times 10^4 & = 9.82 + 16.58(m_c - 1.3) \quad (18) \\ & + 7.8(0.325 - \Lambda_{\overline{MS}}^{(4)}), \end{aligned}$$

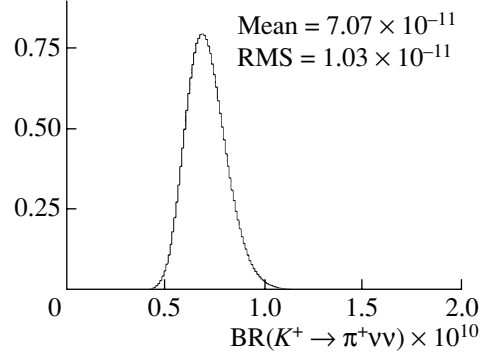


Fig. 4. The relative values of PDF for $\text{BR}(K^+ \rightarrow \pi^+ \nu \bar{\nu})|_{\text{SM}}$ obtained from the measurements of $|\varepsilon_K|$ and $a_{\psi K}$. The 95% C.L. upper limit is 8.9×10^{-11} and 95% C.L. lower limit is 5.6×10^{-11} . Here, MEAN is the weighted average of BR; RMS is the root-mean-squared standard deviation for BR.

where

$$\Lambda_{\overline{MS}}^{(4)}[\text{GeV}] = 0.341 + 16.7(-0.119 + \alpha_s(m_Z)). \quad (19)$$

Equation (19) is accurate to 0.7% for α_s in the range 0.116 to 0.122 [46]. The expression for $|\varepsilon_K|$ (and the determination of the apex, $\lambda_t^{(a)}$) has a dependence on x_c and x_t through the Inami–Lim functions $S_0(x_c)$, $S_0(x_t)$, and $S_0(x_c, x_t)$. In addition, the NLO correction η_{cc} has the following dependence [46]:

$$\begin{aligned} \eta_{cc} & = (1.46 \pm \sigma_1) \left(1 - 1.2 \left(\frac{m_c}{1.25} - 1 \right) \right) \quad (20) \\ & \quad \times (1 + 52(\alpha_s(m_Z) - 0.118)) \end{aligned}$$

with

$$\begin{aligned} \sigma_1 & = 0.31 \left(1 - 1.8 \left(\frac{m_c}{1.25} - 1 \right) \right) \quad (21) \\ & \quad \times (1 + 80(\alpha_s(m_Z) - 0.118)). \end{aligned}$$

It is seen that the inclusion of the correlations between $\lambda_t^{(a)}$ and $(\text{Re}\lambda_c) f F(x_c)/X(x_t)$ through x_c , x_t , and $\Lambda_{\overline{MS}}^{(4)}$ (the most important is the correlation through $x_c = (m_c/m_W)^2$) partly compensates the uncertainties in these terms and reduces the uncertainty in $\text{BR}(K^+ \rightarrow \pi^+ \nu \bar{\nu})|_{\text{SM}}$ by $\sim 20\%$ compared to the case of ignoring these correlations.

For $K_L^0 \rightarrow \pi^0 \nu \bar{\nu}$, we obtain from (8) and (16)

$$\begin{aligned} \text{BR}(K_L^0 \rightarrow \pi^0 \nu \bar{\nu})|_{\text{SM}} & = R_0 \frac{X(x_t)^2}{\lambda^2} [\text{Im}\lambda_t^{(a)}]^2 \\ & = (2.60 \pm 0.52) \times 10^{-11}. \quad (22) \end{aligned}$$

The four largest contributions to the uncertainty are due to \hat{B}_K (0.37×10^{-11}), $a_{\psi K}$ (0.23×10^{-11}), m_c

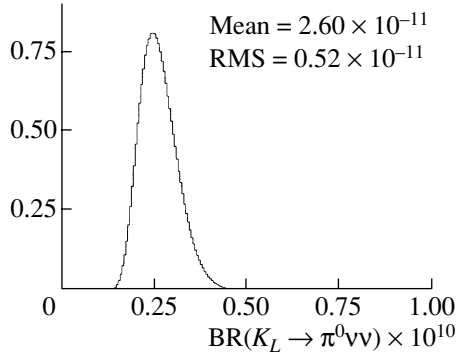


Fig. 5. The relative values of PDF for $\text{BR}(K_L^0 \rightarrow \pi^0 \nu \bar{\nu})|_{\text{SM}}$ obtained from the measurement of $|\varepsilon_K|$ and $a_{\psi K}$ (notation is the same as in Fig. 4).

(0.16×10^{-11}), and m_t (0.08×10^{-11}). The probability distribution for $\text{BR}(K_L^0 \rightarrow \pi^0 \nu \bar{\nu})$ is presented in Fig. 5.

The results of these new calculations (17) and (22) of $K \rightarrow \pi \nu \bar{\nu}$ branching ratios from fits to λ_t are in good agreement with the calculations based on the standard UT variables (11) and (12) but are free of uncertainties in $|V_{cb}|$ and are independent of $\Delta m_{B_s}/\Delta m_{B_d}$. The main source of uncertainty in (17) and (22) is the lattice calculation of $\hat{B}_K = 0.86 \pm 0.15$. (We note that some lattice calculations using domain-wall fermions [18, 47, 48] find values of \hat{B}_K that are 10–15% lower than the recent world average [37, 49] that we use in the table—see below.) If future lattice QCD calculations [50] can significantly reduce the uncertainty in \hat{B}_K , an improvement in $\text{BR}(K \rightarrow \pi \nu \bar{\nu})|_{\text{SM}}$ will be possible.

Given the difficulty of assigning PDFs to theoretical uncertainties, we explore the influence of a more conservative scanning technique on the uncertainty in $\text{BR}(K^+ \rightarrow \pi^+ \nu \bar{\nu})|_{\text{SM}}$. We determine $\lambda_t^{(a)}$ again from only $|\varepsilon_K|$ and $a_{\psi K}$, using Gaussian errors for all quantities except \hat{B}_K and m_c , which are scanned throughout their ranges: $0.72 < \hat{B}_K < 1.0$ and $1.2 < m_c < 1.4$ GeV. For $\hat{B}_K = 0.72$ and $m_c = 1.4$ GeV, which maximizes $\text{BR}(K^+ \rightarrow \pi^+ \nu \bar{\nu})$, the 95% C.L. upper limit is $\text{BR}(K^+ \rightarrow \pi^+ \nu \bar{\nu})|_{\text{SM}} < 9.9 \times 10^{-11}$. For $\hat{B}_K = 1.00$ and $m_c = 1.2$ GeV, which minimizes $\text{BR}(K^+ \rightarrow \pi^+ \nu \bar{\nu})$, the 95% C.L. lower limit is $\text{BR}(K^+ \rightarrow \pi^+ \nu \bar{\nu})|_{\text{SM}} > 5.0 \times 10^{-11}$. These limits are not much worse than those derived from Fig. 4.

We have emphasized that our estimate uses only $a_{\psi K}$ and $|\varepsilon_K|$. Nevertheless, it is interesting to consider how the measurements of Δm_{B_d} and $|V_{ub}|$ would constrain $\lambda_t^{(a)}$. Here, we will use the more aggressive treatment of $|V_{cb}|$ errors (see table below)

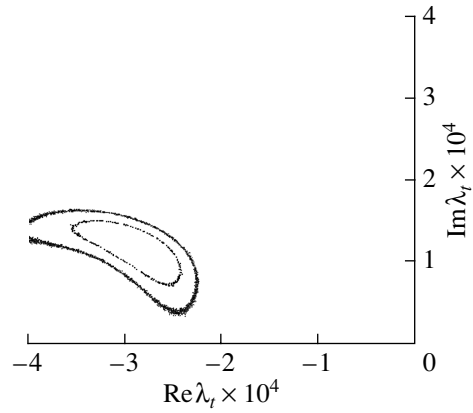


Fig. 6. 1σ and 2σ C.L. intervals on $\lambda_t^{(a)}$ obtained from the constraints of Δm_{B_d} and $|V_{ub}|$ (notation is the same as in Fig. 3).

in order to obtain the smallest errors on $\text{BR}(K^+ \rightarrow \pi^+ \nu \bar{\nu})$. From the following relations (here and in other places, we use standard notation—see, for example, reviews [30–33])

$$\Delta m_{B_d} = \frac{G_F}{6\pi^2} m_W^2 m_{B_d} f_{B_d}^2 \hat{B}_{B_d} \eta_{B_d} S_0(x_t) |V_{td} V_{tb}^*|^2,$$

$$0 = V_{ud} V_{ub}^* + V_{cd} V_{cb}^* + V_{td} V_{tb}^*,$$

and using the approximations of (9), $V_{tb}^* \approx 1$, $V_{us} = \lambda$, $V_{ud} \approx 1 - \lambda^2/2$, and $V_{cb} \approx -V_{ts}$, we convert the equations above into

$$\Delta m_{B_d} = \frac{G_F}{6\pi^2} m_W^2 m_{B_d} f_{B_d}^2 \hat{B}_{B_d} \eta_{B_d} S_0(x_t) |V_{td} V_{tb}^*|^2$$

$$= N^2 |V_{td} V_{tb}^*|^2 \simeq N^2 \frac{|\lambda_t|^2}{|V_{cb}|^2}, \tag{23}$$

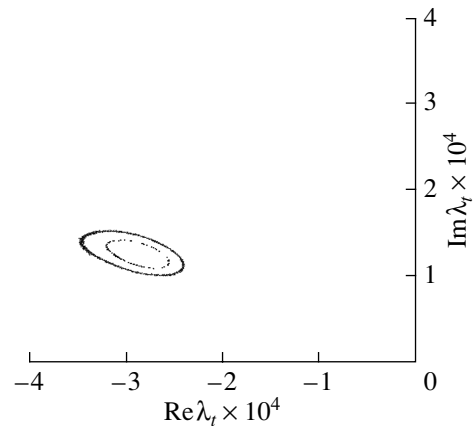


Fig. 7. 1σ and 2σ C.L. intervals on $\lambda_t^{(a)}$ obtained from combined analysis (with constraints of $|\varepsilon_K|$, $a_{\psi K}$, Δm_{B_d} , and $|V_{ub}|$) (notation is the same as in Fig. 3).

Some SM parameters used for evaluation of the standard unitarity triangle, the kaon unitarity triangle, and $\text{BR}(K \rightarrow \pi\nu\bar{\nu})|_{\text{SM}}$ [the subscript G(U) denotes the Gaussian (uniform) probability density distribution for the errors; errors shown without subscripts are assumed to be Gaussian]

$$\begin{aligned}
 &\lambda = V_{us} = 0.222 \pm 0.002 \\
 &\left. \begin{aligned}
 \bar{\rho} &= 0.22 \pm 0.10 \\
 \bar{\eta} &= 0.35 \pm 0.05 \\
 |V_{cb}| &= (41.2 \pm 2.0) \times 10^{-3} \\
 |V_{ub}| &= (3.6 \pm 0.7) \times 10^{-3}
 \end{aligned} \right\} \text{PDG-2002 [35]} \\
 &\left. \begin{aligned}
 \bar{\rho} &= 0.173 \pm 0.046 \\
 \bar{\eta} &= 0.357 \pm 0.027 \\
 |V_{cb}| &= (40.6 \pm 0.8) \times 10^{-3} \\
 \beta_K &= \beta + 1^\circ = 24.6^\circ \pm 2.3^\circ
 \end{aligned} \right\} [22] \\
 &|\varepsilon_K| = (2.282 \pm 0.017) \times 10^{-3} [35] \\
 &\hat{B}_K = 0.86 \pm 0.06_{\text{G}} \pm 0.14_{\text{U}} \simeq 0.86 \pm 0.15 [37, 49, 52] \\
 &m_c = \bar{m}_c = 1.3 \pm 0.1 \text{ GeV}/c^2 \\
 &m_t = \bar{m}_t = 166 \pm 5 \text{ GeV}/c^2 \\
 &\left. \begin{aligned}
 X(x_t) &= 1.52 \pm 0.05 \\
 F(x_c) &= \frac{2}{3} X_{\text{NL}}^e(x_c) + \frac{1}{3} X_{\text{NL}}^r(x_c) = (9.82 \pm 1.78) \times 10^{-4} \\
 \Lambda_{\overline{MS}}^{(4)} &= 0.325 \pm 0.08 \text{ GeV}
 \end{aligned} \right\} [1] \\
 &f = 1.03 \pm 0.02 [14] \\
 &fF(x_c)/X(x_t) = (6.66 \pm 1.23) \times 10^{-4} \\
 &\left. \begin{aligned}
 S_0(x_c) &= (2.42 \pm 0.39) \times 10^{-4} \\
 S_0(x_c, x_t) &= (2.15 \pm 0.31) \times 10^{-3} \\
 S_0(x_t) &= 2.38 \pm 0.11 \\
 \eta_{cc} &= 1.45 \pm 0.38 [41] \\
 \eta_{ct} &= 0.47 \pm 0.04 [42] \\
 \eta_{tt} &= 0.57 \pm 0.01 [43] \\
 L &= 3.837 \times 10^4 [30]
 \end{aligned} \right\} \text{Inami-Lim functions and QCD} \\
 &\hspace{10em} \text{corrections for } K^0 \rightleftharpoons \bar{K}^0 \text{ and } |\varepsilon_K| \\
 &\hspace{10em} \text{evaluation} \\
 &\left. \begin{aligned}
 |V_{cb}|(\text{incl.}) &= (40.4 \pm 0.7_{\text{G}} \pm 0.8_{\text{U}}) \times 10^{-3} [53] \\
 |V_{cb}|(\text{excl.}) &= (42.1 \pm 1.1_{\text{G}} \pm 1.9_{\text{U}}) \times 10^{-3} [53] \\
 |V_{ub}|(\text{incl.}) &= (40.9 \pm 4.6_{\text{G}} \pm 3.6_{\text{U}}) \times 10^{-4} [22] \\
 |V_{ub}|(\text{excl.}) &= (32.5 \pm 2.9_{\text{G}} \pm 5.5_{\text{U}}) \times 10^{-4} [22] \\
 \Delta m_{B_d} &= 0.489 \pm 0.008 \text{ ps}^{-1} [35] \\
 \Delta m_{B_s} &> 14.4 \text{ ps}^{-1} \text{ (95\% C.L.) [51]} \\
 f_{B_d} \sqrt{\hat{B}_{B_d}} &= 230 \pm 30_{\text{G}} \pm 15_{\text{U}} \text{ MeV}
 \end{aligned} \right\} |V_{ub}| \text{ and } \Delta m_{B_d} \text{ parameters used in} \\
 &\hspace{10em} \text{evaluating the constraint on } \lambda_t^{(a)} \text{ in} \\
 &\hspace{10em} \text{Fig. 6} \\
 &\xi = \frac{f_s}{f_d} \sqrt{\frac{\hat{B}_s}{\hat{B}_d}} = 1.15 \pm 0.06 \text{ } \} \text{Old value} \\
 &\left. \begin{aligned}
 \xi &= 1.32 \pm 0.10 [38] \\
 \xi &= 1.18 \pm 0.04_{-0.0}^{+0.12} [37] \\
 \xi &= 1.22 \pm 0.07 [54]
 \end{aligned} \right\} \text{New data with chiral log extrapolation}
 \end{aligned}$$

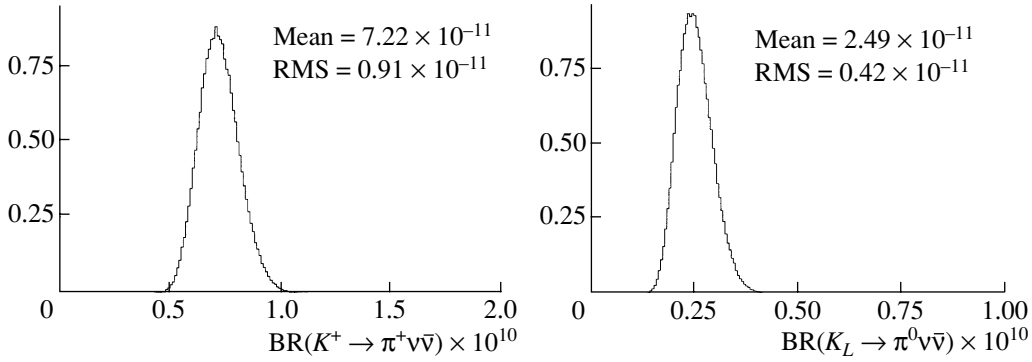


Fig. 8. The relative values of PDF for $\text{BR}(K^+ \rightarrow \pi^+ \nu \bar{\nu})|_{\text{SM,comb.}}$ (left) and $\text{BR}(K_L^0 \rightarrow \pi^0 \nu \bar{\nu})|_{\text{SM,comb.}}$ (right) obtained from the combined analysis with constraints from $|\varepsilon_K|$, $a_{\psi K}$, Δm_{B_d} , and $|V_{ub}|$ (notation is the same as in Fig. 4).

where $N^2 = \frac{G_F^2}{6\pi^2} m_W^2 m_{B_d} f_{B_d}^2 \hat{B}_{B_d} \eta_{B_d} S_0(x_t)$ and

$$\begin{aligned} \lambda_t &= V_{ub}^* V_{cb}^* (1 - \lambda^2/2) - \lambda (V_{cb}^*)^2 \quad (24) \\ &\simeq V_{ub}^* V_{cb}^* (1 - \lambda^2/2) - \lambda |V_{cb}|^2. \end{aligned}$$

These two equations describe two circles in the $(\text{Re}\lambda_t, \text{Im}\lambda_t)$ plane (see Fig. 2):

$$(\text{Re}\lambda_t)^2 + (\text{Im}\lambda_t)^2 = R_1^2 = \frac{\Delta m_{B_d} |V_{cb}|^2}{N^2} \quad (25)$$

(with the center at $\text{Re}\lambda_t = 0, \text{Im}\lambda_t = 0$ and the radius $R_1 = \sqrt{\Delta m_{B_d} |V_{cb}|/N}$) and

$$(\text{Re}\lambda_t + |V_{cb}|^2 \lambda)^2 + (\text{Im}\lambda_t)^2 = R_2^2 \quad (26)$$

(with the center at $\text{Re}\lambda_t = -\lambda |V_{cb}|^2, \text{Im}\lambda_t = 0$ and the radius $R_2 = (1 - \lambda^2/2) |V_{ub} V_{cb}| \simeq |V_{ub} V_{cb}|$).

The intersections of these circles contain the apex of the kaon UT $\lambda_t^{(a)}$. Equations (25) and (26) are correlated somewhat through V_{cb} . Similar to the case of $|\varepsilon_K|$, with large uncertainties from \hat{B}_K , there are large uncertainties in the extraction of $\lambda_t^{(a)}$ from the Δm_{B_d} and $|V_{ub}|$ constraints, with large uncertainties from $f_{B_d}^2 \hat{B}_{B_d}$, $|V_{ub}|$, and V_{cb} . The uncertainty on the constraint from B mixing may be significantly improved by the addition of Δm_{B_s} , once the situation with ξ is resolved (this will be further improved once Δm_{B_s} is actually observed). Using the Bayesian procedure described earlier and the parameters in the table (see also [51–54]), the PDF for $\lambda_t^{(a)}$ derived solely from the constraints of Δm_{B_d} and $|V_{ub}|$ is shown in Fig. 6. We see that this PDF does not constrain the kaon UT apex as well as $a_{\psi K}$ and $|\varepsilon_K|$. Combining all four constraints, we get the PDF for $\lambda_t^{(a)}$ (Fig. 7) and the PDF for $\text{BR}(K \rightarrow \pi \nu \bar{\nu})$ (Fig. 8). Thus, the results of this combined analysis are only slightly more precise than Fig. 3–5 and (16), (17), and (22):

$$\text{Re}\lambda_{t,\text{comb}}^{(a)} = (-2.91 \pm 0.22) \times 10^{-4}, \quad (27)$$

$$\text{Im}\lambda_{t,\text{comb}}^{(a)} = (1.27 \pm 0.11) \times 10^{-4}$$

and

$$\text{BR}(K^+ \rightarrow \pi^+ \nu \bar{\nu})|_{\text{SM,comb}} = (7.22 \pm 0.91) \times 10^{-11}, \quad (28)$$

$$\text{BR}(K_L^0 \rightarrow \pi^0 \nu \bar{\nu})|_{\text{SM,comb}} = (2.49 \pm 0.42) \times 10^{-11}.$$

The CKM matrix appears to be the dominant source of CP violation. However, some models [55] allow for a significant contribution of new physics to $\text{BR}(K \rightarrow \pi \nu \bar{\nu})$, while preserving the equality between $\sin(2\beta)$ as measured from $a_{\psi K}$ and global CKM fits. A crucial test of the CKM description will be to compare β derived from $\text{BR}(K \rightarrow \pi \nu \bar{\nu})$ to that from $a_{\psi K}$ [12, 27–29]. The most important new information on the CKM matrix will be measurements of $\text{BR}(K^+ \rightarrow \pi^+ \nu \bar{\nu})$ [9] and $\text{BR}(K_L^0 \rightarrow \pi^0 \nu \bar{\nu})$ [56] to 10% precision. The combination of these, in context of the SM, will determine $\sin(2\beta)$ to 0.05 [30], competitive with the current uncertainty on $\sin(2\beta)$. The comparison of this angle obtained from $\text{BR}(K \rightarrow \pi \nu \bar{\nu})$ with that from $a_{\psi K}$ will provide a very strong test of the SM description of CP violation.

Another critical test of the SM will be the direct comparison of $\text{BR}(K^+ \rightarrow \pi^+ \nu \bar{\nu})$ to either $\Delta m_{B_s}/\Delta m_{B_d}$, which in the SM both directly measure $|V_{td}|$, or to evaluations of $\text{BR}(K^+ \rightarrow \pi^+ \nu \bar{\nu})|_{\text{SM}}$ such as this work. Currently, the E787 measurement of $\text{BR}(K^+ \rightarrow \pi^+ \nu \bar{\nu}) = (15.7_{-8.2}^{+17.5}) \times 10^{-11}$ is consistent with the SM expectation, but the central experimental value exceeds it by a factor of two. To date, there is only a limit on $\Delta m_{B_s} > 14.4 \text{ ps}^{-1}$ (95% C.L.) [51], but it is likely to be observed soon. Until Δm_{B_s} is observed, this limit can be used to set an upper limit on $\text{BR}(K^+ \rightarrow \pi^+ \nu \bar{\nu})$ [1]. A recent calculation of this limit [17] gives $\text{BR}(K^+ \rightarrow \pi^+ \nu \bar{\nu})|_{\text{SM}} < 13.2 \times 10^{-11}$, which is below the central experimental value [7]. This work used a value of

$\xi = 1.15 \pm 0.06$, whereas a higher value of ξ would raise this upper limit. Our work is an estimation of $\text{BR}(K^+ \rightarrow \pi^+ \nu \bar{\nu})|_{\text{SM}}$ based solely on $|\varepsilon_K|$ and $a_{\psi K}$ and is not dependent on $|V_{cb}|$ or $\Delta m_{B_s}/\Delta m_{B_d}$. Our 95% C.L. upper limit is 8.9×10^{-11} with the largest systematic error of this approach coming from \hat{B}_K . The uncertainty from our prediction is comparable to the expected experimental uncertainties that might be achieved in the future measurements of $K^+ \rightarrow \pi^+ \nu \bar{\nu}$ [8, 9]. An experimental measurement significantly larger than that determined from $\Delta m_{B_s}/\Delta m_{B_d}$ or our 99% C.L. limit of $\text{BR}(K^+ \rightarrow \pi^+ \nu \bar{\nu})|_{\text{SM}} < 10 \times 10^{-11}$ will be a strong indication of new physics.

ACKNOWLEDGMENTS

We would like to thank P. Cooper, G. Isidori, D.E. Jaffe, P. Mackenzie, U. Nierste, L. Okun, and A. Soni for useful discussions and comments and W. Marciano for the original stimulation to perform this type of calculation.

This work was supported in part by the US Department of Energy through contract no. DE-AC02-98CH10886, in part by the Fermilab Particle Physics Division, and in part by IHEP. L.G.L. is grateful to the Fermilab Administration and Particle Physics Division for their hospitality and support for his stay at Fermilab during the preparation of this work.

Note. During the final preparation of this work for publication (as hep-ex/0212321), we found that [57] considered fitting for the apex of the UT from the CP -violating data only ($|\varepsilon_K|$ and $a_{\psi K}$), as we do. However, [57] used $(\bar{\rho}, \bar{\eta})$, which is dependent on $|V_{cb}|$ and is not as suitable for analysis of $K \rightarrow \pi \nu \bar{\nu}$.

Notes added in proof:

1) The new experimental value of $\text{BR}(K^+ \rightarrow \pi \nu \bar{\nu})|_{\text{exp}} = (1.47_{-0.89}^{+1.30}) \times 10^{-10}$ was obtained as a combined result of E787 and E949 experiments (V.V. Anisimovsky *et al.* (E949 Collab.), hep-ex/0403036).

2) New estimates of $\text{BR}(K \rightarrow \pi \nu \bar{\nu})|_{\text{SM}}$ were obtained in a global fit of standard CKM unitarity triangle:

a) $\text{BR}(K^+ \rightarrow \pi^+ \nu \bar{\nu})|_{\text{SM}} = (0.77 \pm 0.11) \times 10^{-10}$;
 $\text{BR}(K_L^0 \rightarrow \pi^0 \nu \bar{\nu})|_{\text{SM}} = (0.26 \pm 0.05) \times 10^{-10}$ (G. Isidori, hep-ph/0307014).

b) $\text{BR}(K^+ \rightarrow \pi^+ \nu \bar{\nu})|_{\text{SM}} = (0.80 \pm 0.11) \times 10^{-10}$;
 $\text{BR}(K_L^0 \rightarrow \pi^0 \nu \bar{\nu})|_{\text{SM}} = (0.32 \pm 0.06) \times 10^{-10}$ (A. Buras *et al.*, hep-ph/0402112).

REFERENCES

1. G. Buchalla and A. J. Buras, Nucl. Phys. B **548**, 309 (1999); hep-ph/9901288.
2. M. Misiak and J. Urban, Phys. Lett. B **451**, 161 (1999); hep-ph/9901278.
3. G. Buchalla and A. J. Buras, Nucl. Phys. B **412**, 106 (1994); hep-ph/9308272.
4. G. Buchalla and A. J. Buras, Nucl. Phys. B **398**, 285 (1993); **400**, 225 (1993).
5. T. Inami and C. S. Lim, Prog. Theor. Phys. **65**, 297 (1981).
6. J. S. Hagelin and L. S. Littenberg, Prog. Part. Nucl. Phys. **23**, 1 (1989); D. Rein and L. M. Sehgal, Phys. Rev. D **39**, 3325 (1989); M. Lu and M. B. Wise, Phys. Lett. B **324**, 461 (1994); C. Q. Geng *et al.*, Phys. Lett. B **355**, 569 (1995); S. Fajfer, Nuovo Cimento A **110**, 397 (1997).
7. S. Adler *et al.*, Phys. Rev. Lett. **79**, 2204 (1997); hep-ex/9708031; **84**, 3768 (2000); hep-ex/0002015; **88**, 041803 (2002); hep-ex/0111091; S. Adler *et al.*, Phys. Lett. B **537**, 211 (2002); hep-ex/0201037.
8. B. Bassalleck *et al.*, BNL 949 Experiment, BNL-67247 (1999); <http://www.phy.bnl.gov/e949>.
9. J. Frank *et al.*, *Fermilab Proposal for Precision Measurement of the Decay $K^+ \rightarrow \pi^+ \nu \bar{\nu}$ and Other Rare K^+ Processes at Fermilab Using the Main Injector*, Fermilab, 2001; <http://www.fnal.gov/projects/ckm/Welcome.html>
10. G. Buchalla *et al.*, Rev. Mod. Phys. **68**, 1125 (1996); hep-ph/9512380.
11. L. Littenberg, Phys. Rev. D **39**, 3322 (1989).
12. Y. Grossman and Y. Nir, Phys. Lett. B **398**, 163 (1997); hep-ph/9701313.
13. W. Marciano and Z. Parsa, Phys. Rev. D **53**, R1 (1996).
14. A. Falk *et al.*, Phys. Lett. B **505**, 107 (2001); hep-ph/0012099.
15. L. Wolfenstein, Phys. Rev. Lett. **51**, 1945 (1983); A. J. Buras *et al.*, Phys. Rev. D **50**, 3433 (1994); hep-ph/9403384.
16. A. J. Buras, hep-ph/0109197.
17. G. D'Ambrosio and G. Isidori, Phys. Lett. B **530**, 108 (2002); hep-ph/0112135.
18. D. Atwood and A. Soni, hep-ph/0212071.
19. D. Atwood and A. Soni, Phys. Lett. B **508**, 17 (2001); hep-ph/0103197.
20. S. Laplace, hep-ph/0209188.
21. A. Hocker *et al.*, AIP Conf. Proc. **618**, 27 (2002); hep-ph/0112295.
22. A. J. Buras *et al.*, J. High Energy Phys. **0301**, 29 (2003); hep-ph/0207101.
23. W. Marciano, in *Kaon Physics*, Ed. by J. L. Rosner and B. D. Winstein (The University of Chicago Press, Chicago, 2001), p. 603.
24. A. R. Barker and S. H. Kettell, Ann. Rev. Nucl. Part. Sci. **50**, 249 (2000); hep-ex/0009024.
25. A. J. Buras *et al.*, Phys. Lett. B **500**, 161 (2001); hep-ph/0007085.

26. G. D'Ambrosio *et al.*, Nucl. Phys. B **645**, 155 (2003); hep-ph/0207036; A. J. Buras and R. Fleischer, Phys. Rev. D **64**, 115010 (2001); hep-ph/0104238; S. Bergmann and G. Perez, Phys. Rev. D **64**, 115009 (2001); hep-ph/0103299; A. J. Buras and R. Buras, Phys. Lett. B **501**, 223 (2001); hep-ph/0008273.
27. S. Bergmann and G. Perez, J. High Energy Phys. **0008**, 34 (2000); hep-ph/0007170.
28. Y. Nir and M. P. Worah, Phys. Lett. B **423**, 319 (1998); hep-ph/9711215.
29. G. Buchalla and A. J. Buras, Phys. Lett. B **333**, 221 (1994).
30. A. J. Buras, hep-ph/9806471; hep-ph/9905437; hep-ph/0101336.
31. A. J. Buras and R. Fleischer, Adv. Ser. Direct. High Energy Phys. **15**, 65 (1998); hep-ph/9704376.
32. A. J. Buras, hep-ph/0210291.
33. L. G. Landsberg, Yad. Fiz. **64**, 1811 (2001)[Phys. At. Nucl. **64**, 1729 (2001)]; Usp. Fiz. Nauk **173**, 1025 (2003).
34. G. C. Branco *et al.*, *CP Violation* (Clarendon Press, Oxford, 1999).
35. K. Hagiwara *et al.* (Particle Data Group), Phys. Rev. D **66**, 010001 (2002).
36. R. A. Briere *et al.* (CLEO Collab.), Phys. Rev. Lett. **89**, 081803 (2002).
37. L. Lellouch, hep-ph/0211359.
38. A. S. Kronfeld and S. M. Ryan, Phys. Lett. B **543**, 59 (2002); hep-ph/0206058.
39. T. Affolder *et al.* (CDF Collab.), Phys. Rev. D **61**, 072005 (2000); hep-ex/9909003; B. Aubert *et al.* (BaBar Collab.), Phys. Rev. Lett. **89**, 201802 (2002); hep-ex/0207042; A. Abe *et al.* (Belle Collab.), Phys. Rev. D **66**, 071102 (2002); hep-ex/0207098; see also J. L. Rosner, hep-ph/0208243.
40. M. I. Vysotsky, Yad. Fiz. **31**, 1535 (1980) [Sov. J. Nucl. Phys. **31**, 797 (1980)].
41. S. Herrlich and U. Nierste, Nucl. Phys. B **419**, 292 (1994); hep-ph/9310311.
42. S. Herrlich and U. Nierste, Phys. Rev. D **52**, 6505 (1995); hep-ph/9507262; Nucl. Phys. B **476**, 27 (1996); hep-ph/9604330.
43. A. J. Buras *et al.*, Nucl. Phys. B **347**, 491 (1990).
44. M. Ciuchini *et al.*, J. High Energy Phys. **0107**, 13 (2001); hep-ph/0012308.
45. D. E. Jaffe and S. Youssef, Comput. Phys. Commun. **101**, 206 (1997); hep-ph/9607469.
46. U. Nierste, private communication.
47. A. Ali Kahn *et al.* (CP-PACS Collab.), Phys. Rev. D **64**, 114506 (2001); hep-lat/0105020.
48. T. Blum *et al.* (RBC Collab.), hep-lat/0110075.
49. N. Garron *et al.*, hep-lat/0212015.
50. P. Mackenzie, *Talk on Fermilab Joint Experimental Theoretical Seminar, 2002*.
51. http://lepbos.web.cern.ch/LEPBOSC/combined_results/amsterdam_2002
52. M. Battaglia *et al.*, *Results Presented at the CKM Unitary Triangle Workshop, CERN, 2002*; <http://ckm-workshop.web.cern.ch/ckm-workshop>; hep-ph/0304132.
53. M. Artuso and E. Barberio, hep-ph/0205163.
54. D. Becirevic *et al.*, hep-ph/0211271.
55. J. A. Aguilaz-Saavedra, Phys. Rev. D **67**, 035003 (2003); hep-ph/0210112.
56. D. A. Bryman and L. Littenberg, Nucl. Phys. B (Proc. Suppl.) **99**, 61 (2001); <http://pubweb.bnl.gov/users/e926/www>
57. A. Stocchi, hep-ph/0211245.

100th ANNIVERSARY OF P.A. CHERENKOV

Investigation of the Reaction $\pi^- p \rightarrow \eta' \pi^0 n$ at the VES Spectrometer

D. V. Amelin, Yu. G. Gavrilo, Yu. P. Gouz*, V. A. Dorofeev, R. I. Dzhelyadin,
A. M. Zaitsev, A. V. Zenin, A. V. Ivashin, I. A. Kachaev, V. V. Kabachenko, A. N. Karyukhin,
A. N. Konoplyannikov, V. F. Konstantinov, V. V. Kostyukhin, V. D. Matveev,
V. I. Nikolaenko, A. P. Ostankov, B. F. Polyakov, D. I. Ryabchikov, A. A. Solodkov,
A. V. Solodkov, O. V. Solovianov, E. A. Starchenko, A. B. Fenyuk, and Yu. A. Khokhlov

Institute for High Energy Physics, Protvino, Moscow oblast, 142284 Russia

Received February 2, 2004

Abstract—Results obtained by investigating the reaction $\pi^- p \rightarrow \eta' \pi^0 n$ at the VES spectrometer (Institute for High Energy Physics, Protvino) are presented. The effective-mass spectrum and angular distributions of $\eta' \pi^0$ events are compared with their counterparts for $\eta \pi^0$ and $\eta' \pi^-$ events selected from the same data sample. The ratio R of the branching fractions for the decays of $a_2^0(1320)$ mesons into $\eta' \pi$ and $\eta \pi$ is measured. The result is $R = 0.047 \pm 0.018$, which agrees with the value measured previously for a_2^- . An investigation of P -wave production in the $\eta' \pi^0$ and $\eta \pi^0$ systems over the effective-mass interval 1.45–1.9 GeV/ c^2 leads to the conclusion that the coupling of the exotic object $\pi_1(1600)$ to the $\rho \pi$ channel is suppressed in relation to its coupling to the $\eta' \pi$ or the $b_1(1235)\pi$ channel. © 2004 MAIK “Nauka/Interperiodica”.

INTRODUCTION

The main reason why it is of interest to study the production of $\eta(\eta')\pi$ systems is that, in the case of the orbital angular momentum equal to unity, they have exotic quantum numbers: $J^{PC} = 1^{-+}$. The $\eta \pi^-$ [1–4], $\eta' \pi^-$ [1, 4, 5], and $\eta \pi^0$ [6, 7] systems were explored in the VES, KEK E-179, GAMS/NA12, and E852 experiments on the basis of vast statistics. The exotic partial wave 1^{-+} behaved differently in all three final states.

In the $\eta \pi^-$ and $\eta \pi^0$ systems, the exotic-wave spectrum features a broad peak at a mass value of $M \approx 1.4$ GeV/ c^2 . For the $\eta \pi^-$ system, the behavior of the phase shift suggests the possible existence of an exotic resonance [it is referred to as $\pi_1(1400)$] in this mass region [3], while, for the $\eta \pi^0$ system, there is no resonance behavior of the phase shift [6, 7]. This difference may be due to different production mechanisms: the $\eta \pi^0$ system can be produced only via the exchange of isospin-1 particles [predominantly, ρ and b_1 (ρ_2) trajectories for positive- and negative-naturality exchanges, respectively], while the system $\eta \pi^-$ can also emerge from exchanges of isoscalar particles (Pomeron, f_2).

The 1^{-+} wave with positive-naturality exchange is dominant in the $\eta' \pi^-$ system and forms a broad peak at a mass value of $M \approx 1.6$ GeV/ c^2 , its width being $\Gamma \approx 0.3$ GeV/ c^2 . This object, known as $\pi_1(1600)$, can be interpreted as a manifestation of an exotic meson [4, 5, 8]. The peak near 1.6 GeV/ c^2 in the 1^{-+} wave is also observed in the $b_1(1235)\pi$ and $f_1(1285)\pi$ final states [4, 9, 10].

The P -wave states in the $\eta' \pi$ and $\eta \pi$ systems have substantially different $SU(3)_f$ properties: in the $\eta' \pi$ system, it is mainly an octet state, while, in the $\eta \pi$ system, the P -wave state belongs to the representation $10 \oplus \overline{10}$ [11]. In terms of the quark model, the P -wave state of the $\eta \pi$ system is predominantly a multiquark state ($q\bar{q}q\bar{q}$), while that in the $\eta' \pi$ system can be either a multiquark or a hybrid ($q\bar{q}g$) state. This can explain the observed distinctions between the P -wave spectra of the $\eta' \pi$ and $\eta \pi$ systems. This also means that the hypothetical resonance $\pi_1(1400)$ cannot be a hybrid state.

It is worth emphasizing that, at the present time, $\pi_1(1400)$ and $\pi_1(1600)$ are not firmly established resonances. The peaks in the P -wave spectra of the $\eta' \pi^-$ and $\eta \pi^-$ systems can be explained by a dynamical enhancement that is generated by an anomalous chiral Lagrangian of the Wess–Zumino type for $VPPP$ interaction [12] or a Lagrangian of a different form [13].

* e-mail: gouz@mx.ihep.su

Also, attempts were made to explain these peaks by nonresonance amplitudes associated with the Deck effect [14].

In this study, we have first examined the fourth final state of this type, $\eta'\pi^0$. The P -wave state in the $\eta'\pi^0$ system is also predominantly an $SU(3)_f$ octet, this making it possible to obtain new information about the properties of the hypothetical $\pi_1(1600)$ meson and to check it for compatibility with available information. We will compare the distributions for the $\eta'\pi^0$ system with the corresponding distributions obtained for the $\eta'\pi^-$ and $\eta\pi^0$ systems from the same data sample.

EVENT SELECTION AND DATA ANALYSIS

We selected events of the reaction $\pi^-p \rightarrow \eta'\pi^0n$ from the entire body of data obtained in the VES experiment for the decay mode

$$\eta' \rightarrow \pi^+\pi^-\eta, \quad \eta \rightarrow \gamma\gamma, \quad \pi^0 \rightarrow \gamma\gamma. \quad (1)$$

The VES facility was described earlier in [15]. We applied the following selection criteria:

(i) An event should contain two tracks of opposite charges and generate, in the electromagnetic calorimeter, four clusters that can be interpreted as photons. One additional photon cluster of energy not exceeding 1 GeV is allowed.

(ii) The effective masses of two photon pairs should be close to the masses of π^0 and η : $0.105 < M(\gamma_1\gamma_2) < 0.165$ GeV/ c^2 and $0.478 < M(\gamma_3\gamma_4) < 0.618$ GeV/ c^2 . In the ensuing calculations, we use the most probable photon energies calculated under the assumption that the corresponding photon pairs products of the decay of π^0 and η to two photons.

(iii) The photon sample should not obey the $\pi^0\pi^0$ hypothesis for any possible photon combination; this criterion suppresses the background from the production of the $\pi^+\pi^-\pi^0\pi^0$ system.

(iv) Charged particles should not admit identification with electrons (positrons). This criterion was specified on the basis of the energy deposition in the electromagnetic calorimeter: $E_{\text{Cal}}/|p| < 0.8$.

(v) The effective mass of the $\pi^+\pi^-\eta$ system should be close to the η' -meson mass: $0.938 < M(\pi^+\pi^-\eta) < 0.978$ GeV/ c^2 . Events from the control intervals around the η' -meson mass, $0.916 < M(\pi^+\pi^-\eta) < 0.936$ GeV/ c^2 and $0.980 < M(\pi^+\pi^-\eta) < 1.0$ GeV/ c^2 , were used to estimate and subtract the background.

(vi) We rejected events generating a signal in the veto system of the target in order to suppress processes where an isobar decaying into a neutron and a π^0 meson is produced instead of a neutron.

(vii) The $\pi^+\pi^-\pi^0$ system should not admit identification with an η meson: $|M(\pi^+\pi^-\pi^0) - m_\eta| > 0.02$ GeV/ c^2 . This requirement suppresses the $\eta\eta$ -production background, which is significant near the $\eta'\pi^0$ threshold.

Figures 1a–1c display the $M(\gamma\gamma)$ distributions near the masses of π^0 and η and the $M(\pi^+\pi^-\eta)$ distribution. Against a linear background, these distributions feature peaks associated with π^0 , η , and η' mesons. We selected 1955 “signal” and 809 “background” events. Figures 1d and 1e show the distributions with respect to effective masses and the square of the momentum transfer. In the effective-mass distribution, we can see a peak associated with the $a_2(1320)$ meson.

By using similar selection criteria, we separated events of the reaction $\pi^-p \rightarrow \eta\pi^0n$ from the same sample of the experimental data for the decay mode

$$\eta \rightarrow \pi^+\pi^-\pi^0, \quad \pi^0 \rightarrow \gamma\gamma. \quad (2)$$

We selected signal events from an interval of $\pi^+\pi^-\pi^0$ effective masses around the η -meson mass, $0.528 < M(\pi^+\pi^-\pi^0) < 0.568$ GeV/ c^2 . Events from the control intervals $0.506 < M(\pi^+\pi^-\pi^0) < 0.526$ GeV/ c^2 and $0.570 < M(\pi^+\pi^-\pi^0) < 0.590$ GeV/ c^2 were used in estimating background and subtracting it. Figures 2a–2c show the effective-mass distributions for “free” π^0 and for π^0 from η -meson decay and the distribution with respect to the effective mass $M(\pi^+\pi^-\pi^0)$. For a further analysis, we selected 18 547 “signal” and 8436 “background” events. Figures 2d and 2e display the distributions of events with respect to the effective mass and the square of the momentum transfer. The effective-mass distribution exhibits distinct peaks associated with $a_0(980)$ and $a_2(1320)$ mesons, this being in agreement with the results presented in [6, 7].

On the basis of the effective-mass distribution, the ratio of the branching fractions for the decays of $a_2^0(1320)$ meson to $\eta'\pi^0$ and $\eta\pi^0$ was found to be $\bar{R} \approx 0.047 \pm 0.018$, which agrees with the tabular value [16] previously obtained for the $\eta'\pi^-$ and $\eta\pi^-$ final states [1, 5]. Figures 3a and 3b display the results obtained by correcting the effective-mass distributions of the $\eta'\pi^0$ and $\eta\pi^0$ systems for the detection probability. The curves represent fits to the distributions in terms of the Breit–Wigner formula for resonances against a smooth polynomial background.

A conventional partial-wave analysis of the $\eta\pi^0$ system [6, 7] was performed over 50-MeV/ c^2 effective-mass intervals by using a standard set of waves that includes the S_0 , P_0 , P^- , D_0 , and D^- waves for negative-naturality exchange and the $P+$ and $D+$ waves for positive-naturality exchange. In order to

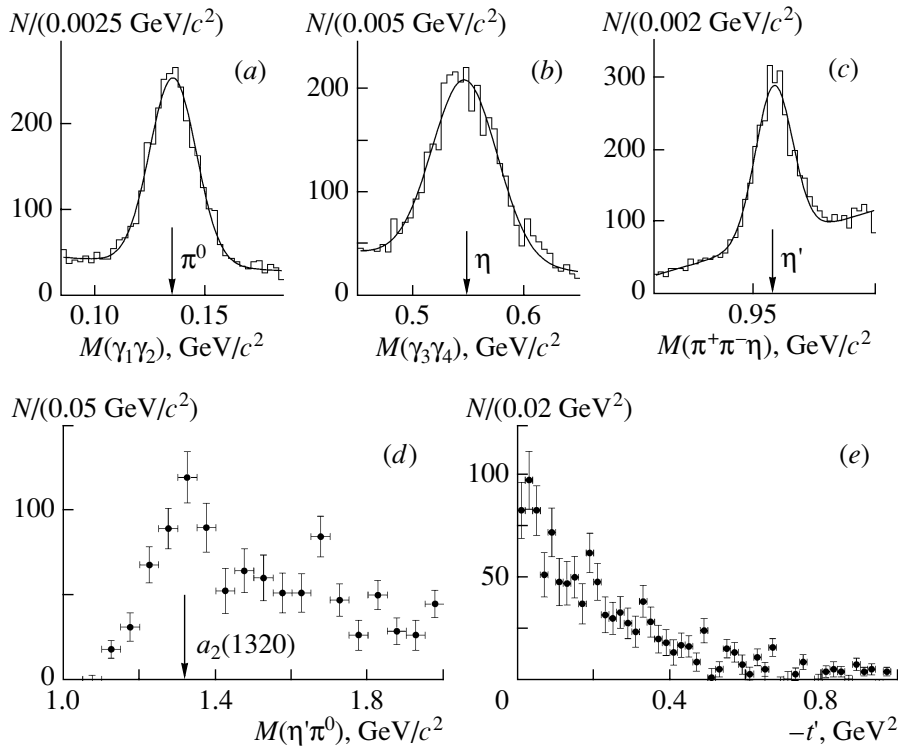


Fig. 1. Selection of $\eta'\pi^0$ events: $M(\gamma\gamma)$ distributions for (a) π^0 and (b) η ; (c) $M(\pi^+\pi^-\eta)$ and (d) $M(\eta'\pi^0)$ effective mass distributions; and (e) $|t'|$ distribution for $\eta'\pi^0$ events.

subtract the background, we added “background” events with an opposite sign to the minimized functional having the form of the logarithm of likelihood [1]. The results are shown in Fig. 4. They agree with the results of the GAMS/NA12 and E852 experiments performed earlier on the basis of vaster statistics [6, 7]: the mass spectra of the S_0 and $D+$ waves show peaks caused by $a_0(980)$ and $a_2(1320)$ mesons, respectively; the spectrum of the $P+$ wave features a broad peak; also, we observe a fast change in the phase difference between the $P+$ and $D+$ waves near $1.3 \text{ GeV}/c^2$ due to the $a_2(1320)$ meson.

DISCUSSION OF THE RESULTS

Figure 5 displays the effective-mass distributions for the $\eta'\pi^0$ and $\eta'\pi^-$ systems selected from the same data sample. The scales along the ordinate are chosen in such a way that the visible heights of the peaks due to the $a_2(1320)$ meson are approximately identical. We can see that the shapes of the distributions are significantly different. The production of the $J^{PC} = 1^{-+}$ exotic state $\pi_1(1600)$ [1, 8] dominates the spectrum of the $\eta'\pi^-$ system. In contrast, the production of the $a_2(1320)$ meson is dominant for the $\eta'\pi^0$ system, the production of the $\eta'\pi^0$ system being substantially less intensive for $M > 1.4 \text{ GeV}/c^2$. The

reason behind the difference of the spectra is that the $\eta'\pi^0$ system can be produced only in isovector-exchange processes, while the $\eta'\pi^-$ system can also be generated by isoscalar-exchange processes. Since $a_2^0(1320)$ mesons emerge primarily from ρ -exchange processes [6, 7, 17], the branching fraction for their decay into $\eta'\pi$ is about 0.5% because of suppression by the barrier factor. In view of this and in view of the fact that the probability of $\pi_1(1600)$ decay into $\eta'\pi$ is not small, the coupling of the $\pi_1(1600)$ meson to the $\rho\pi$ channel is substantially lower than the coupling of the $a_2(1320)$ meson to this channel.

In order to study the coupling of the $\pi_1(1600)$ state to the $\rho\pi$ channel more comprehensively, it is necessary to estimate the fraction of the $P+$ wave in the $\eta'\pi^0$ system in the mass region around $1.6 \text{ GeV}/c^2$. Figures 6a and 6b display the angular distributions of the $\eta'\pi^0$ system in the effective-mass interval $1.45\text{--}1.9 \text{ GeV}/c^2$. For the sake of comparison, the analogous distributions for the $\eta\pi^0$ system in the same mass interval are shown in Figs. 6c and 6d. The distribution of the cosine of the polar angle in the Gottfried–Jackson frame features a clear asymmetry for both systems. The dominance of positive-naturality exchanges for the $\eta\pi^0$ system manifests itself in the distribution with respect to the

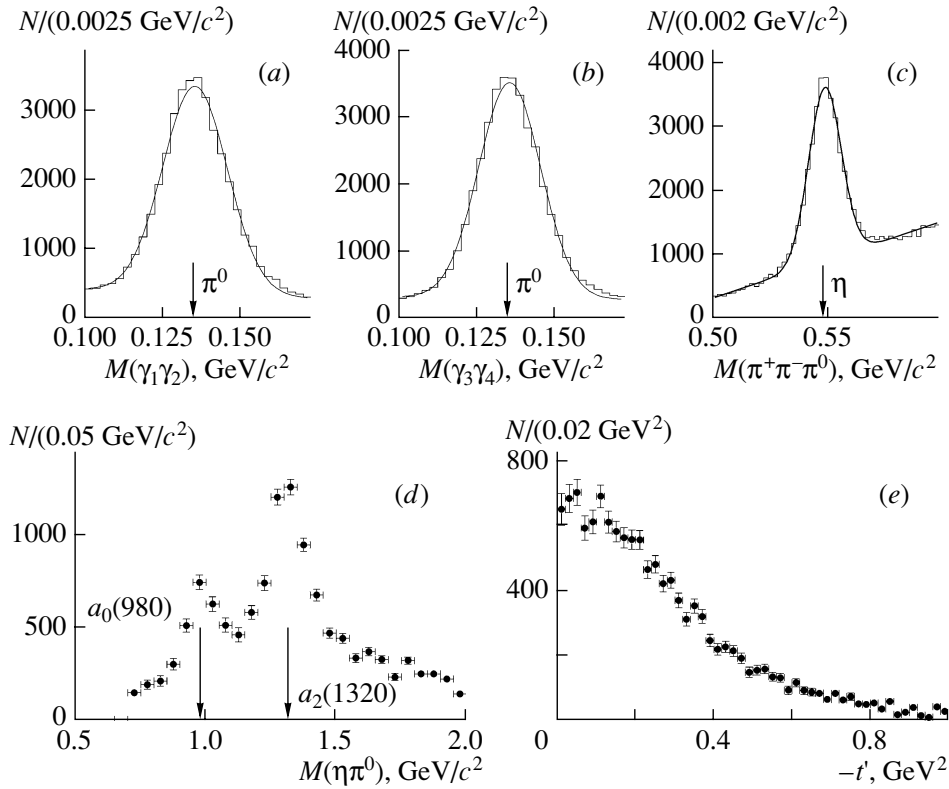


Fig. 2. Selection of $\eta\pi^0$ events: $M(\gamma\gamma)$ distributions for (a) “free” π^0 and (b) π^0 from η decay, (c) $M(\pi^+\pi^-\pi^0)$, and (d) effective-mass and (e) $|t'|$ distributions for $\eta\pi^0$ events.

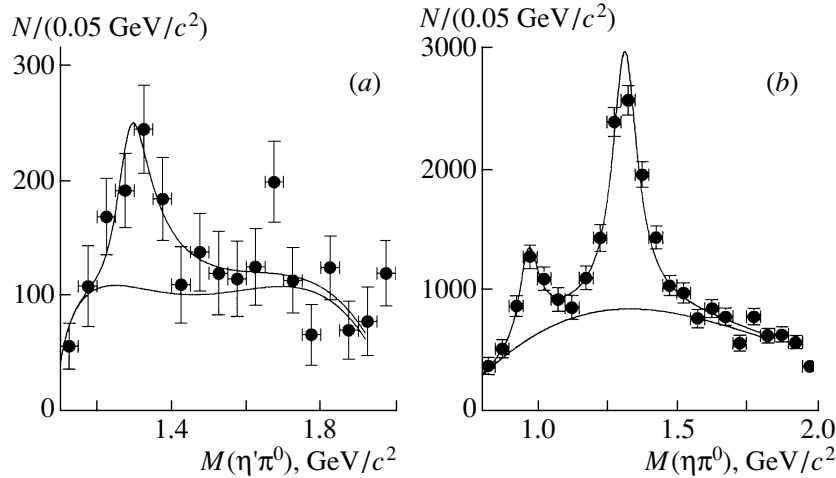


Fig. 3. $a_2^0(1320)$ meson in the effective-mass distributions of the (a) $\eta'\pi^0$ and (b) $\eta\pi^0$ systems. The distributions are corrected for the detection probability. The points represent experimental data.

polar angle (Treiman–Yang angle ϕ_{TY}) in the form of a large component proportional to $\sin^2 \phi_{\text{TY}}$. The fraction of the component $\sin^2 \phi_{\text{TY}}$ in the distribution with respect to ϕ_{TY} for the $\eta'\pi^0$ system is substantially lower.

The number of $\eta'\pi^0$ events is insufficient for performing a mass-independent partial-wave analysis and for studying the shape of the wave $P+$ and the behavior of its phase. Nevertheless, we can perform a partial-wave analysis for events from the effective-mass interval 1.45–1.9 GeV/c^2 , assuming that the

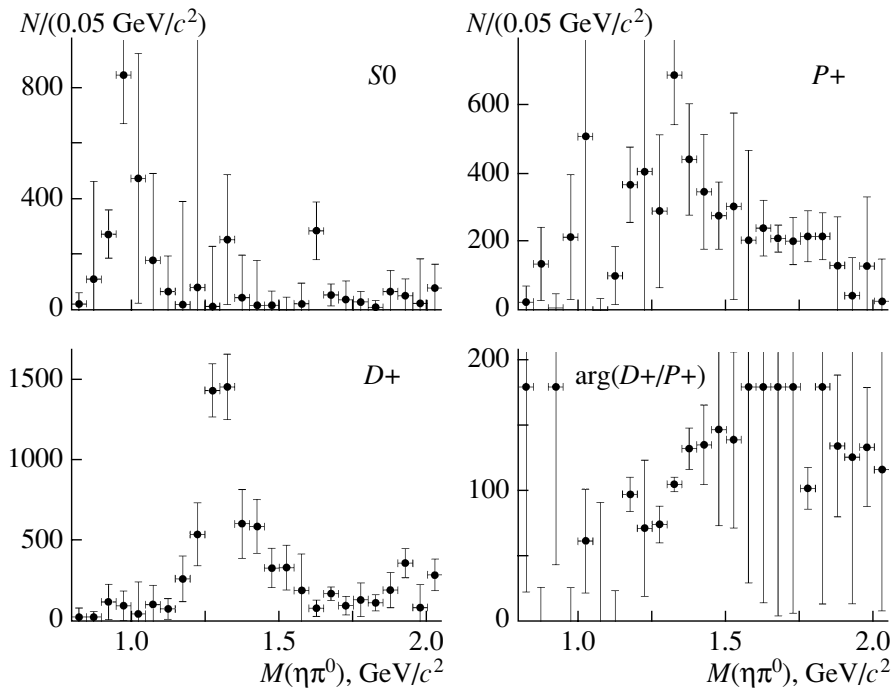


Fig. 4. Results of a partial-wave analysis of the $\eta\pi^0$ system: the mass spectra of the S_0 , P_+ , and D_+ waves and the behavior of the phase difference between the D_+ and P_+ waves.

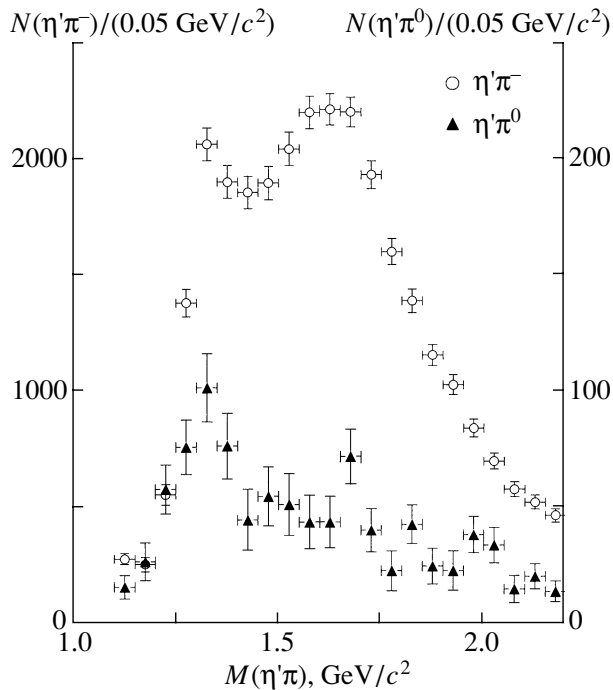


Fig. 5. Comparison of the effective-mass distributions of the $\eta'\pi^-$ and $\eta'\pi^0$ systems.

relative phase of any pair of partial waves does not undergo significant variations over the entire mass interval (this being true for the $\eta\pi^-$, $\eta'\pi^-$, and $\eta\pi^0$

systems) and considering that there is no abrupt variations in the detection efficiency of the facility. Figures 7a and 7b show the results of such an analysis for the $\eta'\pi^0$ and $\eta\pi^0$ systems. Each cell of the histogram represents the intensity of one wave. All possible solutions [18] are represented by the dashed lines within the cells. The thick lines correspond to one solution that we consider to be physical. The physical solution for $\eta\pi^0$ is chosen in such a way that it is compatible with the results presented in [6]. Since, for the same naturality of exchange, waves characterized by the orbital-angular-momentum projection equal to unity are usually suppressed in relation to waves characterized by the orbital-angular-momentum projection of zero, the requirement that the intensity of the P_0 wave exceed that of the P_- wave is taken to be a criterion for choosing a solution for the $\eta'\pi^0$ system. However, the main conclusions of the present study remain valid for any choice of physical solution.

In the $\eta'\pi^0$ system, the D_0 wave has the maximum intensity in all solutions; the P_0 wave is also significant. For any choice of solution, the contribution of the P_+ wave does not exceed 20% of the total intensity of $\eta'\pi^0$ production. Assuming that the whole intensity of the P_+ wave in the $\eta'\pi^0$ system is due to the production of the $\pi_1(1600)$ state through ρ exchange, we can compare it with the peak of the $a_2^0(1320)$ meson, which is also produced through ρ exchange, in the spectrum of the D_+ wave in the $\eta\pi^0$

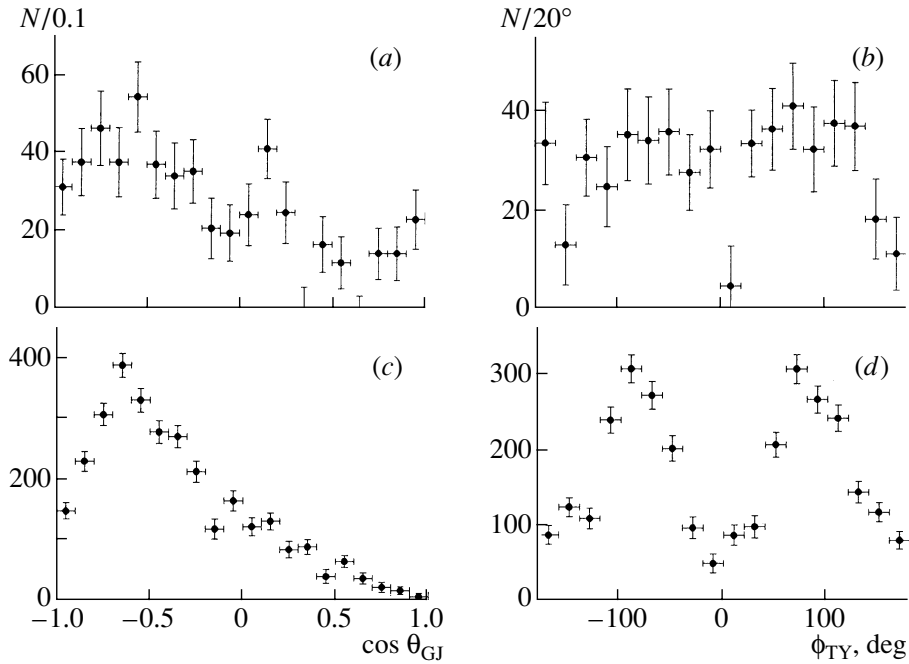


Fig. 6. Distributions with respect to the azimuthal and polar angles of π^0 emission in the Gottfried–Jackson frame for the (a, b) $\eta'\pi^0$ and (c, d) $\eta\pi^0$ systems for events in the effective-mass interval $1.45\text{--}1.90\text{ GeV}/c^2$.

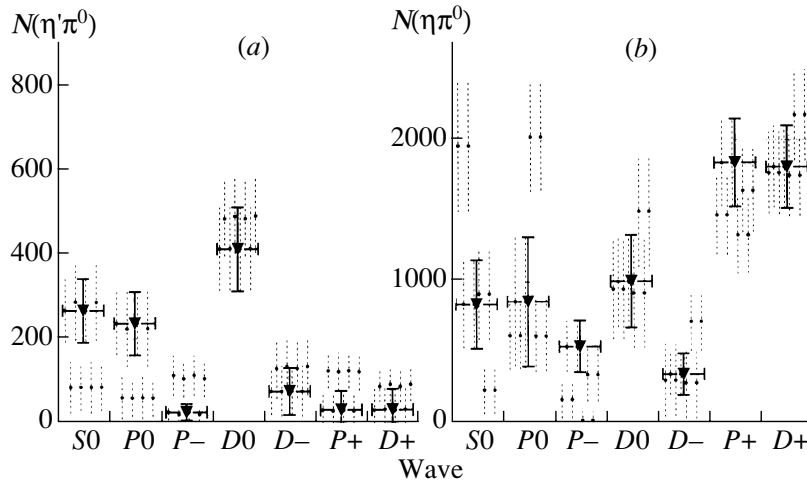


Fig. 7. Results of a partial-wave analysis of events from the effective-mass interval $1.45\text{--}1.90\text{ GeV}/c^2$ for the (a) $\eta'\pi^0$ and (b) $\eta\pi^0$ systems.

system (see Fig. 4). Assuming the same dependence of the coupling of a_2 and π_1 to $\rho\pi$ on the ρ -meson virtuality, we then obtain

$$\frac{\text{Br}(\pi_1 \rightarrow \rho\pi)\text{Br}(\pi_1 \rightarrow \eta'\pi)}{\text{Br}(a_2 \rightarrow \rho\pi)\text{Br}(a_2 \rightarrow \eta\pi)} \lesssim 3 \times 10^{-2}$$

or

$$\text{Br}(\pi_1 \rightarrow \rho\pi)\text{Br}(\pi_1 \rightarrow \eta'\pi) \lesssim 3 \times 10^{-3}. \quad (3)$$

The object $\pi_1(1600)$ is observed in the $f_1\pi$, $\eta'\pi$, and $b_1\pi$ decay channels with probabilities in the ratio $(1.1 \pm 0.3) : 1 : (1 \pm 0.3)$ [10, 19]. Searches for a signal of $\pi_1(1600)$ in other channels, $f_2\pi^-$, K^*K , and $\eta(1295)\pi^-$, in the VES experiment show that the signal in any of these channels is substantially lower than that in the $\eta'\pi^-$ channel. With allowance for the

errors, this leads to the constraint $\text{Br}(\pi_1 \rightarrow \eta'\pi) > 0.1$. It follows from (3) that $\text{Br}(\pi_1 \rightarrow \rho\pi) < 0.03$.

In order to compare the production of the $P+$ wave in the $\eta'\pi^0$ and $\eta\pi^0$ systems, we determined the ratio of the squares of the corresponding matrix elements. Taking into account the probabilities of η and η' decays into the final states (1) and (2) and the phase space, we obtain $|T_{P+}^{\eta'\pi^0}|^2/|T_{P+}^{\eta\pi^0}|^2 \approx 0.1 \pm 0.1$. The error includes the statistical error and the ambiguity in choosing the solution of the partial-wave analysis. A small value of this ratio indicates that, in ρ exchange, the 1^{-+} wave is predominantly produced in the $SU(3)_f$ -decuplet state. This value is on the same order of magnitude as η - η' mixing; therefore, a significant part of the $P+$ wave in the $\eta'\pi^0$ state can indeed be due to the decuplet state rather than to the $\pi_1(1600)$ state.

In the physical solution that we chose for the $\eta'\pi^0$ system, the ratio of the intensities of the $P+$ and $P0$ waves is 0.15 ± 0.2 . The ratio of the intensities of production in the positive- (ρ exchange) and negative-naturality [$b_1(\rho_2)$ exchange] exchanges was measured in the VES experiments for $a_2(1320)$ and $\omega_3(1670)$ [17] and was found to be 1.3 ± 0.2 and 1.1 ± 0.3 , respectively. Since the probabilities of $\pi_1(1600)$ decays into $b_1\pi$ and $\eta'\pi$ are on the same order of magnitude [9], a small value of the $P+/P0$ ratio agrees with our conclusion that the coupling of $\pi_1(1600)$ to the $\rho\pi$ channel is weak.

The results of direct searches for the decay of $\pi_1(1600)$ to $\rho^0\pi$ are ambiguous. The peak of $\pi_1(1600)$ in the $J^{PC} = 1^{-+}$ wave of the $\rho\pi$ system in the case of positive-naturality exchange was observed in the $\pi^+\pi^-\pi^-$ final state in the analysis of E852 data [20] and in early results of the VES experiment [10, 19]; according to these data, the probabilities of $\pi_1(1600)$ decays to $\rho\pi$, $\eta'\pi$, and $b_1\pi$ are approximately in the ratio 1.5 : 1 : 1. Later, it turned out [21, 22] that the shape of the 1^{-+} wave of the $\rho\pi$ system in the $\pi^+\pi^-\pi^-$ final state is highly model-dependent and that, at a reasonable choice of model parameters, the peak of $\pi_1(1600)$ disappears.

The majority of the theoretical models predict the suppression of the decays of the $J^{PC} = 1^{-+}$ hybrid meson to $\rho\pi$ [23, 24]. This conclusion is based on the fact that the ρ -meson wave function is approximately identical to the π -meson wave function. In [25], it was shown that, within the pointlike-pion model, the probability of hybrid-meson decay to $\rho\pi$ can reach 10–25%. Our investigation of the $\eta'\pi^0$ final state has provided an indirect piece of evidence that the coupling of $\pi_1(1600)$ to the $\rho\pi$ channel is indeed suppressed, thereby disproving the ratio $\rho\pi : \eta'\pi(b_1\pi) \sim 1$.

CONCLUSION

The reaction $\pi^-p \rightarrow \eta'\pi^0n$ has been studied in the VES experiment. The effective-mass spectrum and the angular distributions of $\eta'\pi^0$ events have been compared with the analogous distributions in $\eta\pi^0$ and $\eta'\pi^-$ events selected from the same data sample. The ratio of the branching fractions for the decay of the $a_2^0(1320)$ meson to $\eta'\pi$ and $\eta\pi$ has been found to be $R = 0.047 \pm 0.018$, which is in agreement with the tabular value of this quantity measured earlier for a_2^- . That the production of the exotic object $\pi_1(1600)$ has not been observed in positive-naturality exchange leads to the conclusion that its coupling to the $\rho\pi$ channel is suppressed in relation to coupling to the $\eta'\pi$ or the $b_1(1235)\pi$ channel. This feature was predicted for the decays of hybrid mesons in various phenomenological models.

ACKNOWLEDGMENTS

This work was supported in part by the Russian Foundation for Basic Research (RFBR), project nos. 02-02-17479 and 00-15-96689, and by the RFBR program for support of leading scientific schools, project no. NSh1695.2003.2.

REFERENCES

1. G. M. Beladidze *et al.*, Phys. Lett. B **313**, 276 (1993).
2. H. Aoyagi *et al.*, Phys. Lett. B **314**, 246 (1993).
3. S. U. Chung *et al.*, Phys. Rev. D **60**, 092001 (1999).
4. V. Dorofeev *et al.*, in *Proceedings of the IX International Conference on Hadron Spectroscopy "HADRON 2001," Protvino, 2001*, Ed. by D. Amelin and A. Zaitsev (Melville, New York, 2002); AIP Conf. Proc. **619**, 143 (2002).
5. E. I. Ivanov *et al.*, Phys. Rev. Lett. **86**, 3977 (2001).
6. D. Alde *et al.*, Yad. Fiz. **62**, 462 (1999) [Phys. At. Nucl. **62**, 421 (1999)].
7. A. R. Dzierba *et al.*, Phys. Rev. D **67**, 094015 (2003).
8. Yu. Khokhlov *et al.*, Nucl. Phys. A **663**, 596 (2000).
9. D. V. Amelin *et al.*, Yad. Fiz. **62**, 487 (1999) [Phys. At. Nucl. **62**, 445 (1999)].
10. Yu. Gouz *et al.*, in *Proceedings of the XXVI International Conference on High Energy Physics "ICHEP 1992,"* Ed. by J. R. Sanford; AIP Conf. Proc. **272**, 572 (1992).
11. S. U. Chung, E. Klempt, and J. G. Korner, Eur. Phys. J. A **15**, 539 (2002).
12. N. N. Achasov and G. N. Shestakov, Yad. Fiz. **65**, 579 (2002) [Phys. At. Nucl. **65**, 552 (2002)].
13. A. P. Szczepaniak *et al.*, hep-ph/0304095.
14. A. Donnachie and P. R. Page, Phys. Rev. D **58**, 114012 (1998).
15. S. Bitjukov *et al.*, Phys. Lett. B **268**, 137 (1991).
16. K. Hagiwara *et al.*, Phys. Rev. D **66**, 010001 (2002).
17. D. V. Amelin *et al.*, Z. Phys. C **70**, 71 (1996).

18. S. A. Sadovsky, Preprint No. IFVE-91-75 (Inst. High Energy Phys., Protvino, 1991).
19. A. Zaitsev *et al.*, Nucl. Phys. A **675**, 155 (2000).
20. G. S. Adams *et al.*, Phys. Rev. Lett. **81**, 5760 (1998).
21. A. Zaitsev *et al.*, in *Proceedings of the VII International Conference on Hadron Spectroscopy "HADRON 1997"*, Ed. by S. Chung and H. Willutzki; AIP Conf. Proc. **432**, 461 (1998).
22. I. Kachaev *et al.*, in *Proceedings of the IX International Conference on Hadron Spectroscopy "HADRON 2001"*, Protvino, 2001, Ed. by D. Amelin and A. Zaitsev; AIP Conf. Proc. **619**, 577 (2002).
23. F. E. Close and P. R. Page, Nucl. Phys. B **433**, 233 (1995).
24. P. R. Page, Phys. Lett. B **402**, 183 (1997).
25. F. E. Close and J. J. Dudek, hep-ph/0308099.

Translated by M. Kobrinsky